

INFLUENCE OF LIGAND MODIFICATION AND ELECTRONIC STRUCTURE
IN HOMOGENEOUS CATALYSIS WITH REDUCED IRON COMPLEXES

A Dissertation

Presented to the Faculty of the Graduate School

of Cornell University

In Partial Fulfillment of the Requirements for the Degree of

Doctor of Philosophy

by

Jonathan Michael Darmon

August 2012

© 2012 Jonathan Michael Darmon

INFLUENCE OF LIGAND MODIFICATION AND ELECTRONIC STRUCTURE
IN HOMOGENEOUS CATALYSIS WITH REDUCED IRON COMPLEXES

Jonathan Michael Darmon, Ph. D.

Cornell University 2012

The synthesis of a family of *para*-substituted pyridine di(imine) ligands, and their corresponding iron dihalide, dicarbonyl and dinitrogen complexes are described. The influence of the substituents on the electronic structure of each derivative was investigated using a combination of X-ray diffraction, cyclic voltammetry, infrared, Mößbauer, and NMR spectroscopies as well as density functional theory. No dramatic changes to the electronic structure description were observed as a result of the *para*-substituent. However, significant differences in catalytic activity were observed for the hydrogenation of olefins and the $[2\pi + 2\pi]$ cycloaddition of α,ω -heptadienes, and were also found to be substrate dependent.

The electronic structure and catalytic activity of a structurally related pyridine di(carbene) complex, $(iPrCNC)Fe(N_2)_2$ was investigated. The spectroscopic data establish that $(iPrCNC)Fe(N_2)_2$ and several of its derivatives are redox non-innocent. They are best described as hybrid structures with $[(iPrCNC^0)Fe^0]$ and $[(iPrCNC^{2-})Fe^{II}]$ resonance forms with the $iPrCNC$ ligand acting as a π -acceptor. The activity of $(iPrCNC)Fe(N_2)_2$ for the catalytic hydrogenation of olefins and $[2\pi + 2\pi]$ cyclization of α,ω -diolefins was also investigated. $(iPrCNC)Fe(N_2)_2$ exhibited hydrogenation activities that were consistent with the trends observed in pyridine di(imine) iron olefin hydrogenation, but exhibited no activity for the $[2\pi + 2\pi]$ cycloaddition of α,ω -heptadienes. Isotopic experiments indicated that a competitive, unproductive 2,1-insertion

pathway or a vinylic C–H activation mechanism was responsible for the deviation in hydrogenation activity trends observed with 1,1-diphenylethylene and the electron-rich iron catalysts.

A series of dialkyl dinitrogen complexes were prepared from treatment of (*i*PrCNC)FeBr₂ with two equivalents of the corresponding alkyl lithium reagent. The iron dialkyl dinitrogen complexes were characterized by infrared, NMR and Mößbauer spectroscopies as low-spin, ferrous compounds. One member of the series, (*i*PrCNC)Fe(CH₃)₂(N₂) underwent extrusion of ethane at 23 °C. The mechanism of this transformation was investigated by isotopic cross-over experiments.

The dimeric iron bis(dinitrogen) complex, [(^{Me}BPDI)Fe(N₂)]₂(μ₂-N₂) was prepared by sodium naphthalenide reduction of the corresponding iron dichloride. This complex was established to be more susceptible to contamination by THF complexes, and underwent the irreversible formation of η⁶-arene species in solution. [(^{Me}BPDI)Fe(N₂)]₂(μ₂-N₂) and (*i*PrBPDI)Fe(N₂)₂ exhibited remarkably lower activity for the hydrogenation of ethyl 3,3-dimethylacrylate relative to (*i*PrPDI)Fe(N₂)₂. NMR studies and stoichiometric experiments established that this was due to the more electrophilic iron center as engendered by the BPDI chelate, resulting in a greater affinity for carbonyl coordination.

A family of bis(oxazoline) iron dialkyl complexes were prepared by treatment of their ferrous dihalide precursors with the appropriate alkyl lithium reagent and examined for the asymmetric hydrosilylation of ketones using PhSiH₃ as the stoichiometric reductant. While these complexes expressed high levels of activity, low enantiomeric inductions were observed regardless of the identity of the auxiliary ligand or the alkyl substituent. Activation of these

complexes *in situ* using $\text{B}(\text{C}_6\text{F}_5)_3$ resulted in higher levels of enantiomeric induction; however, synthetically useful e.e.'s were not observed.

BIOGRAPHICAL SKETCH

Jonathan Michael Darmon was born to Michael and Virginia Darmon on October 2, 1984 in Philadelphia, Pennsylvania. Jonathan attended Chichester Middle and High School, where he followed in his older sister, Sarah's footsteps and left a legacy for his younger brother, David. In high school, Jonathan was privileged to be in Mr. Lavender's Honors and AP Chemistry courses, where he developed a passion for chemistry that would forever change his future plans.

After graduating Valedictorian in 2003, Jonathan continued his chemical education at Ursinus College, where he was extremely fortunate to have Dr. Ronald Hess as his faculty advisor, organic chemistry professor, research advisor and friend. Jonathan conducted basic research in the area of substituent effects on ketene trimers beginning in his sophomore year. It was in the laboratory where Jonathan forged some of his most important friendships and his plans to attend graduate school to pursue research solidified. During his Junior year, Jonathan attended a lecture given by a Cornell professor, Dr. Paul Chirik, that captured his interest.

Jonathan was thus lured to Cornell University after graduating from Ursinus in 2007, to continue doing research in the laboratory of Dr. Chirik in the area of substituent effects on the electronic structure and catalysis of reduced iron and cobalt complexes. During his graduate career, Jonathan worked in four different laboratory spaces and helped transition the group through three difficult moves. By the beginning of 2012, the time had come for Jon to take the next step in his career, and he made plans to move West to join the laboratory of Morris Bullock at Pacific Northwest National Laboratory in Richland, Washington.

My parents, Michael and Virginia

My siblings, Sarah and David

Past, Present and Future members of the “Freak Show”

ACKNOWLEDGMENTS

Without any adieu, I must thank my advisor, Professor Paul J. Chirik for allowing me to join his group in the summer of 2007, and for his support and guidance throughout my time in graduate school. Never in my wildest imagination did I think that my decision to come to Cornell would lead me down this rabbit hole, which has encompassed four different laboratories and two prestigious universities.

I'd like to thank my other committee members, Professor Peter Wolczanski and Professor Bruce Ganem for their assistance in molding me into the scientist I am today. Pete, in particular, has always been straight with me, and in conjunction with Paul, the two taught me to critically analyze both scientific data and myself. For this, I will always be grateful. Several members of the Cornell support staff deserve thanks as well: Dave Neish and Dave Wise, in particular, for all of the assistance they have rendered to both myself and to the group. Emil Lobkovsky also deserves a thank you for solving all of the tricky crystal structures I obtained while at Cornell.

I would also like to thank the Ursinus crew: Professor Thomas Ruttledge, Kevin Sylvester and Elliott Hulley. I have never regretted my decision to follow these three to Cornell. Tom is a long-time friend and mentor, and I will always be thankful for all of the opportunities and advice that he has given me. Kevin and Elliott have always been my role models, both during my time at Ursinus and while at Cornell. Their friendship and advice have meant more to me than I can put into words, and I have always treasured their presence in my life. I would need to split in two to follow both of them now (which I promised Kevin I wouldn't do – especially after following him to Princeton).

I owe a debt of gratitude to the Wolczanski group (Elliott, Brenda, Emily, Erika, Wes, Valerie and Brian). Although I was not a member of their group, they have always treated me like I was one of them, and I have worn my Wolczanski sweatshirt with pride. I don't think I would have survived graduate school without their friendship and willingness to drag me out of lab when the occasion called for it. Erika, in particular, deserves a special thanks for being a shoulder I could lean on and someone I could talk to honestly the past few years.

I also owe a huge debt of gratitude to many of the past members of the “freak show.” I would have been lost in the lab without Doris. I often tell her now that I think that she was a saint, and I do not think she truly understands how thankful I really am. Amanda will always hold a special place in my heart because of her willingness to help me prevent a box regen at 3 AM. Seeing her come down the hallway with a call of "Hey guys, it's just me, Jooooon Darmon" always put a smile on my face. I would also like to thank Aaron, my box mate, and Sarah for their friendship and assistance in the laboratory these last four years. Aaron has always been generous with his resources and with his incredible ideas, and I was truly lucky to be partnered with him. Sarah was equally amazing, and one of my biggest regrets will always be that I never got up the courage to know her better.

I must also thank the people who helped me most when we were called upon to organize a move: Helen, David and Bastian. Without these people, the group never would have been able to pull off a move as painlessly as we did—all *three* times. David and Bastian deserve particular thanks, though. Besides assisting me – the “move Czar” – and being amazing friends, they introduced me to my current vices: “celebrations” and German beer!

The current members of the Chirik group (Crisita, Scott, Chantal, Jordan, Carsten, Seb, Zoë, Pony, Grant, Max and Brian) also deserve thanks for helping me keep my sanity these last few months. Carsten has been a good friend and house mate, and I am thankful that he was willing to assist me with the calculations that you will find herein, as well as attempt to teach me the fine art of BS (broken symmetry, that is). I will always remember the very late nights at Princeton that we spent discussing electronic structure and magnetochemistry. He is a very intelligent individual, and I have no doubt this will take him far in his future endeavors. Crisita has been a good friend and confidante, and I have the utmost faith that her abilities will take her far. I wish her and her husband, Jason all the happiness in the world. Scott, aside from being the reason for all of the “tension” in the lab, was kind enough to solve many of the structures I obtained at Princeton and has become a good friend of mine. His “secrets” are something I will never forget. Zoë is thanked for solving many of my crystal structures, for bringing her crystal growing luck to our box and for being an endless source of optimism. Chantal is responsible for all of the XAS data in this dissertation, and is thanked for this as well as all of the snacks and treats she brought in for us to enjoy. Lastly, I’d like to thank both Jordan and Seb, my fellow catalysis subgroup members: Jordan, for sharing a box with me and carrying on the legacy, and Seb for all of your help with substrates, mechanisms, etc. It has been an honor serving with you. To the first years, all I can do is wish you luck on your own journey through graduate school!

Most importantly, I’d like to thank my family, for without their faith, trust and understanding, I would not have become the person I am today. My mother has always been the person I could turn to – she is my rock and my best friend – and I’d like to think she is the source of all of my best qualities. My father has both served as an inspiration and warned me early on

that graduate school would be “no picnic.” Even still, I often tell him he did not properly prepare me for the reality that awaited. I have deeply treasured all of our graduate school/war story conversations. My sister, Sarah, has paved the way as the oldest child, and my brother, David, has carried on the Darmon legacy proudly – even though he’s a vegetarian and went into applied math.

TABLE OF CONTENTS

Biographical Sketch	iii
Dedication	iv
Acknowledgements	v
Table of Contents	ix
List of Figures	xiv
List of Tables	xxv

Chapter 1: Synthesis, Electronic Structure, and Reactivity of *para*-Substituted Pyridine

Di(imine) Iron Compounds

1.1	Abstract	1
1.2	Introduction	2
1.3	Synthesis of <i>para</i> -Substituted Pyridine Di(imine) Ligands, and their Iron Dicarbonyl and Dinitrogen Complexes	5
1.4	Electronic Structure Comparison of 4-Substituted Pyridine Di(imine) Ligands and their Iron Complexes	14
1.5	Computational Studies: (4-R- <i>i</i> PrPDI)Fe(N ₂) and (4-R- <i>i</i> PrPDI)Fe(DMAP)	29
1.6	Hydrogenation: Catalytic Comparison of (4-R- <i>i</i> PrPDI)Fe(N ₂) ₂ Complexes	36
1.7	[2 π + 2 π] Cycloaddition: Catalytic Comparison of (4-R- <i>i</i> PrPDI)Fe(N ₂) ₂	

Complexes	43
1.8 Conclusions	48
1.9 Experimental	49
References	65

Chapter 2: Electronic Structure Elucidation and Reactivity of the Pyridine Di(carbene)

Iron Bis(dinitrogen) Complex, (*i*PrCNC)Fe(N₂)₂

2.1 Abstract	69
2.2 Introduction	70
2.3 Synthesis, Characterization and Electronic Structure Elucidation of Pyridine Di(carbene) Iron Complexes	73
2.4 Hydrogenation: Catalytic Evaluation of (<i>i</i> PrCNC)Fe(N ₂) ₂	84
2.5 Hydrogenation: Mechanistic Insight into the Activity of (<i>i</i> PrCNC)Fe(N ₂) ₂	87
2.6 Evaluation of (<i>i</i> PrCNC)Fe(N ₂) ₂ for the Cyclization of 1,6-Diolefins	104
2.7 Conclusions	112
2.8 Experimental	113
References	120

Chapter 3: Synthesis, Electronic Structure and Reactivity of Pyridine Di(carbene) Iron

Dialkyl Dinitrogen Complexes

3.1	Abstract	124
3.2	Introduction	125
3.3	Synthesis and Characterization of Pyridine Di(carbene) Iron Dialkyl Dinitrogen Complexes	129
3.4	Reactivity of Di(carbene)pyridine Iron Dialkyl Complexes	137
3.5	Conclusions	150
3.6	Experimental	151
	References	156

Chapter 4: Synthesis and Reactivity of an Aryl-Substituted Bis(phenylimino)pyridine Iron Dinitrogen Compound

4.1	Abstract	160
4.2	Introduction	161
4.3	Characterization of the Reduction Products of $(^{\text{Me}}\text{BPDI})\text{FeCl}_2$	164
4.4	Catalytic Olefin Hydrogenation Activity of $[(^{\text{Me}}\text{BPDI})\text{Fe}(\text{N}_2)]_2(\mu_2\text{-N}_2)$	175
4.5	Conclusions	179
4.6	Experimental	180
	References	187

Chapter 5: Application of Enantiopure Bis(oxazoline) Iron Dialkyl Complexes towards Catalytic, Asymmetric Ketone Hydrosilylation

5.1	Abstract	191
5.2	Introduction	191
5.3	Synthesis and Characterization of Bis(Oxazoline) Iron Dichloride and Iron Dialkyl Complexes	194
5.4	Catalytic, Asymmetric Hydrosilylation of Ketones	195
5.5	<i>In situ</i> Activation of Bis(oxazoline) Iron Dialkyl Complexes	198
5.6	Conclusions	200
5.7	Experimental	201
	References	207

Appendix A: Preliminary Investigations

A.1	Reduced <i>para</i> -Substituted Pyridine Di(imine) Cobalt Complexes	210
A.2	Reduced Pyridine Di(carbene) Cobalt Complexes	223
A.3	Synthesis of a Reduced Pyridine Di(carbene) Manganese Dicarbonyl Complex	237
	References	241

Appendix B: Computational Investigations

B.1	Pyridine Di(carbene) Iron Complexes with Neutral Ligands	243
-----	--	-----

B.2	Electronic Structure of Bis(oxazoline), Terpyridine, Bipyridine and Pyridine Di(carbene) Iron Dialkyl Complexes as Suggested by Density Functional Theory	253
B.3.	Summary of Results for other Complexes	265
B.4.	Converged Geometries for Theoretical Molecules at the B3LYP Level of DFT	266
B.5.	Experimental	275
	References	277
	Appendix C: Crystal Structure Data	279
	Appendix D: Permissions	337

LIST OF FIGURES

1.1. Electronic structure of redox non-innocent pyridine di(imine) iron complexes.	3
1.2. Electronic structure of redox-active pyridine di(imine) iron complexes.	4
1.3. Prepared <i>para</i> -substituted pyridine di(imine) ligands.	5
1.4. Synthesis of 4-Me ₂ N- <i>i</i> PrPDI and 4-CF ₃ - <i>i</i> PrPDI.	7
1.5. Synthesis of (4-R- <i>i</i> PrPDI)FeX ₂ .	8
1.6. Solid state structures of (4-CF ₃ - <i>i</i> PrPDI)FeCl ₂ and (4-Me ₂ N- <i>i</i> PrPDI)FeCl ₂ shown at 30% probability ellipsoids.	9
1.7. Synthesis of (4-R- <i>i</i> PrPDI)Fe(CO) ₂ .	10
1.8. Solid state structure of (4-Me ₂ N- <i>i</i> PrPDI)Fe(CO) ₂ shown at 30% probability ellipsoids.	11
1.9. Synthesis of (4-R- <i>i</i> PrPDI)Fe(N ₂) ₂ .	12
1.10. Solid state structures of (4- ^t Bu- <i>i</i> PrPDI)Fe(N ₂) ₂ and (4-Me ₂ N- <i>i</i> PrPDI)Fe(N ₂) ₂ at 30% probability ellipsoids.	14
1.11. Cathodic CV scans of <i>para</i> -substituted bis(imino)pyridine ligands.	16
1.12. CV scans of <i>para</i> -substituted bis(imino)pyridine iron dicarbonyl complexes.	18
1.13. Plot of the [(4-R- <i>i</i> PrPDI)Fe(CO) ₂] ^{+1/0} redox couple vs. σ_{para} value.	20
1.14. Zero-field ⁵⁷ Fe Mößbauer spectra of (4-R- <i>i</i> PrPDI)Fe(CO) ₂ .	21
1.15. Zero-field ⁵⁷ Fe Mößbauer spectra of mixtures of (4-R- <i>i</i> PrPDI)Fe(N ₂) _n	

(n = 1, 2) obtained at 80 K.	23
1.16. Benzene- <i>d</i> ₆ ¹ H NMR spectra of (4-R- <i>i</i> PrPDI)Fe(N ₂) _n (n = 1, 2) at 23 °C.	24
1.17. Synthesis of (4-Me ₂ N- <i>i</i> PrPDI)Fe(DMAP).	26
1.18. Solid state structure of (4-Me ₂ N- <i>i</i> PrPDI)Fe(DMAP) shown at 30% probability ellipsoids.	27
1.19. Qualitative MO diagrams of (4-R- <i>i</i> PrPDI)Fe(N ₂) obtained from a BS(2,2) DFT calculation at the B3LYP level.	31
1.20. Qualitative MO diagrams of (4-R- <i>i</i> PrPDI)Fe(N ₂) obtained from an unrestricted triplet and BS(4,2) DFT calculation at the B3LYP level.	32
1.21. Qualitative MO diagrams of (4-R- <i>i</i> PrPDI)Fe(DMAP) obtained from BS(2,2) (top) and unrestricted triplet (bottom) DFT calculations at the B3LYP level.	35
1.22. Electronic structure descriptions for the singlet and triplet solutions investigated for (<i>i</i> PrPDI)Fe(N ₂) and (<i>i</i> PrPDI)Fe(DMAP).	36
1.23. Reaction of ethyl 3,3-dimethylacrylate with (<i>i</i> PrPDI)Fe(N ₂).	37
1.24. Hydrogenation of ethyl 3,3-dimethylacrylate using (4-R- <i>i</i> PrPDI)Fe(N ₂).	38
1.25. Proposed mechanism for selective deuterium incorporation into the isopropyl methyl groups.	42
1.26. Proposed mechanism of [2π + 2π] cyclization of α,ω-heptadienes.	44
1.27. Proposed mechanisms accounting for formation A - and B -type products.	45
1.28. [2π + 2π] cycloaddition of <i>N,N</i> -diallylaniline using reduced metal iron and cobalt dinitrogen complexes.	46

2.1. Product obtained from the attempted reduction of (<i>i</i> PrPNP)FeCl ₂ with two equivalents of sodium triethylborohydride.	70
2.2. Comparison of CO infrared stretching frequencies for (<i>i</i> PrPDI)Fe(CO) ₂ , (<i>i</i> PrCNC)Fe(CO) ₂ and (<i>i</i> PrPNP)Fe(CO) ₂ .	71
2.3. Electronic structure of the four- and five-coordinate pyridine di(imine) iron dinitrogen compounds, (<i>i</i> PrPDI)Fe(N ₂) and (<i>i</i> PrPDI)Fe(N ₂) ₂ .	72
2.4. Synthesis of (<i>i</i> PrCNC)Fe(N ₂) ₂ according to the method of Danopoulos.	74
2.5. Benzene- <i>d</i> ₆ ¹⁵ N NMR spectrum of (<i>i</i> PrCNC)Fe(¹⁵ N ₂) ₂ at 22 °C.	75
2.6. Benzene- <i>d</i> ₆ ¹ H NMR spectra of <i>i</i> PrCNC and (<i>i</i> PrCNC)Fe(N ₂) ₂ at 22 °C.	76
2.7. Synthesis of (<i>i</i> PrCNC)Fe(DMAP)(N ₂).	77
2.8. Solid state structure of (<i>i</i> PrCNC)Fe(DMAP)(N ₂) at 30% probability ellipsoids.	78
2.9. Zero-field ⁵⁷ Fe Mößbauer spectra for pyridine di(carbene) iron complexes.	80
2.10. Normalized Fe K-edge X-ray absorption spectra of pyridine di(carbene) iron complexes.	82
2.11. Normalized Fe K-edge X-ray absorption spectra of pyridine di(carbene) iron complexes and their pyridine di(imine) analogs.	83
2.12. Electronic structure of (<i>i</i> PrCNC)Fe(L)(L').	84
2.13. Synthesis of (<i>i</i> PrCNC)Fe(η^2 -C ₂ H ₄)(N ₂).	85
2.14. Benzene- <i>d</i> ₆ ¹ H NMR spectrum of (<i>i</i> PrCNC)Fe(N ₂) ₂ at 22 °C.	86
2.15. Assay for the hydrogenation activity of (<i>i</i> PrCNC)Fe(N ₂) ₂ using 4 atm of H ₂ .	86

2.16. Benzene- <i>d</i> ₆ ¹ H NMR spectrum of the three species from exposure of a solution of (<i>i</i> PrCNC)Fe(N ₂) ₂ to H ₂ for 2 hours.	88
2.17. Proposed structures for compounds A , B , and C .	89
2.18. Recovered (<i>i</i> PrCNC)Fe(N ₂) ₂ after exposure to H ₂ in benzene- <i>d</i> ₆ and re-exposure to N ₂ .	90
2.19. Examples of <i>i</i> PrCNC deprotonation/activation and aryl C–H activation by (<i>i</i> PrCNC)Fe(N ₂) ₂ .	91
2.20. Intermolecular detetrium incorporation into (<i>i</i> PrCNC)Fe(CO) ₂ .	92
2.21. Deuteration of norbornene using (<i>i</i> PrCNC)Fe(N ₂) ₂ , (4-Me ₂ N- <i>i</i> PrPDI)Fe(N ₂) ₂ , and (<i>i</i> PrPDI)Fe(N ₂) ₂ with 1 atm of D ₂ .	92
2.22. Deuteration of 1,1-diphenylethylene under 4 atmospheres of D ₂ for 60 hours using 5 mol % (<i>i</i> PrCNC)Fe(N ₂) ₂ .	93
2.23. Mechanisms accounting for vinylic deuteration of 1,1-diphenylethylene.	95
2.24. Geometry optimization of the theoretical molecules, (<i>i</i> PrCNC)Fe(CH ₂ CH(Ph) ₂)(H) and (<i>i</i> PrCNC)Fe(C(Ph) ₂ CH ₃)(H), at the B3LYP level of DFT.	96
2.25. Deuteration of α -methylstyrene using (4-R- <i>i</i> PrPDI)Fe(N ₂) (R = H, NMe ₂).	97
2.26. Proposed mechanisms accounting for hydrogen incorporation at the isopropyl methine position.	100
2.27. Catalytic deuteration of 1-butene using 5 mol % (<i>i</i> PrCNC)Fe(N ₂) ₂ and 1 atm of D ₂ .	101
2.28. Catalytic deuteration of ethyl 3,3-dimethylacrylate using 5 mol %	

$(i^{\text{Pr}}\text{CNC})\text{Fe}(\text{N}_2)_2$ and 4 atm D_2 .	101
2.29. (a) Primary and secondary iron alkyl equilibrium studied by Holland and co-workers. (b) Isolated and crystallographically characterized example of a tertiary iron alkyl.	103
2.30. ^1H NMR spectra of a 0.22 M benzene- d_6 solution of N,N -diallyl- <i>tert</i> -butylamine containing 10 mol % $(i^{\text{Pr}}\text{CNC})\text{Fe}(\text{N}_2)_2$ over time.	105
2.31. Addition of 1 atmosphere H_2 to a 0.22 M benzene- d_6 solution of N,N -diallyl- <i>tert</i> -butylamine containing 10 mol % $(i^{\text{Pr}}\text{CNC})\text{Fe}(\text{N}_2)_2$.	106
2.32. Synthesis of $(i^{\text{Pr}}\text{CNC})\text{Fe}(\eta^2, \eta^2\text{-(CH}_2\text{CHCH}_2)_2\text{N}^i\text{Bu})$.	106
2.33. Benzene- d_6 ^1H NMR spectrum of $(i^{\text{Pr}}\text{CNC})\text{Fe}(\eta^2, \eta^2\text{-(CH}_2\text{CHCH}_2)_2\text{N}^i\text{Bu})$.	107
2.34. Solid-state structure of $(i^{\text{Pr}}\text{CNC})\text{Fe}(\eta^2, \eta^2\text{-(CH}_2\text{CHCH}_2)_2\text{N}^i\text{Bu})$ at 30% probability ellipsoids.	108
2.35. Zero-field ^{57}Fe Mößbauer spectrum of $(i^{\text{Pr}}\text{CNC})\text{Fe}(\eta^2, \eta^2\text{-(CH}_2\text{CHCH}_2)_2\text{N}^i\text{Bu})$ obtained at 80 K.	109
2.36. Reaction of $(i^{\text{Pr}}\text{CNC})\text{Fe}(\eta^2, \eta^2\text{-(CH}_2\text{CHCH}_2)_2\text{N}^i\text{Bu})$ with H_2 and D_2 .	110
2.37. Proposed mechanisms for the synthesis of <i>cis-D</i> .	111
3.1. Reaction of pyridine di(imine) iron dichloride with two equivalents of alkyl lithium.	126
3.2. Iron bis(neosilyl) complexes competent for hydrosilylation.	127
3.3. Synthesis of $(i^{\text{Pr}}\text{CNC})\text{Fe}(\text{R})_2(\text{N}_2)$ ($\text{R} = \text{CH}_2\text{Si}(\text{CH}_3)_3, 4\text{-CH}_3\text{-C}_6\text{H}_4, \text{CH}_3$).	130
3.4. Selected iron dialkyl complexes exhibiting an $S = 0$ ground state.	131

3.5. Solid state structure of (<i>i</i> PrCNC)Fe(R) ₂ (N ₂) (R = CH ₂ Si(CH ₃) ₃ , 4-CH ₃ -C ₆ H ₄) at 30% probability ellipsoids, and a ball and stick representation of (<i>i</i> PrCNC)Fe(CH ₃) ₂ (N ₂).	132
3.6. Benzene- <i>d</i> ₆ ¹ H NMR spectra of (<i>i</i> PrCNC)Fe(CH ₂ Si(CH ₃) ₃) ₂ (N ₂) and (<i>i</i> PrCNC)Fe(CH ₃) ₂ (N ₂) collected at 22 °C.	135
3.7. Representative zero-field ⁵⁷ Fe Mößbauer spectra for (<i>i</i> PrCNC)Fe(R) ₂ (N ₂).	136
3.8. Reductive C–C coupling of <i>cis,trans,cis</i> -Fe(CO) ₂ (PMe ₃) ₂ RR'.	137
3.9. Potential pathways for ethane elimination from (<i>i</i> PrCNC)Fe(CH ₃) ₂ (N ₂).	139
3.10. Synthesis of (<i>i</i> PrCNC)Fe(CH ₂ Si(CH ₃) ₃) ₂ (CO).	140
3.11. Solid state structure of (<i>i</i> PrCNC)Fe(CH ₂ Si(CH ₃) ₃) ₂ (CO) at 30% probability ellipsoids.	141
3.12. ¹ H NMR spectrum of (<i>i</i> PrCNC)Fe(CH ₂ Si(CH ₃) ₃) ₂ (CO) in benzene- <i>d</i> ₆ at 22 °C.	142
3.13. Zero-field ⁵⁷ Fe Mößbauer spectrum of (<i>i</i> PrCNC)Fe(CH ₂ Si(CH ₃) ₃) ₂ (CO) obtained at 80 K.	143
3.14. Reaction of (<i>i</i> PrCNC)Fe(CH ₃) ₂ (N ₂) with CO.	144
3.15. Proposed crossover experiments and expected results from a concerted reductive elimination mechanism.	145
3.16. Final ¹ H and ² H NMR spectra resulting from the mixture of (<i>i</i> PrCNC)Fe(CH ₃) ₂ (N ₂) and (<i>i</i> PrCNC)Fe(CD ₃) ₂ (N ₂).	147
3.17. Final ¹ H and ² H NMR spectra resulting from the addition of a 1:1 mixture of CH ₃ Li and CD ₃ Li·LiI to (<i>i</i> PrCNC)FeBr ₂ .	148

3.18. Favored mechanism of reductive elimination for (<i>i</i> PrCNC)Fe(CH ₃) ₂ (N ₂).	148
4.1. Modularity of the pyridine di(imine) ligand architecture.	162
4.2. Sodium amalgam reduction of pyridine di(imine) iron dihalides with less steric protection.	163
4.3. Synthetic methods for the preparation of ^{Me} BPDI.	164
4.4. Synthesis of [(^{Me} BPDI)Fe(N ₂)] ₂ (μ ₂ -N ₂) from reduction of (^{Me} BPDI)FeCl ₂ using catalytic sodium naphthalenide.	165
4.5. Solid-state structure of [(^{Me} BPDI)Fe(N ₂)] ₂ (μ ₂ -N ₂) at 30% probability ellipsoids.	166
4.6. <i>In situ</i> , toluene solution infrared spectra of isolated [(^{Me} BPDI)Fe(N ₂)] ₂ (μ ₂ -N ₂).	168
4.7. Zero-field ⁵⁷ Fe Mößbauer spectrum of [(^{Me} BPDI)Fe(N ₂)] ₂ (μ ₂ -N ₂) obtained at 80 K.	169
4.8. Zero-field ⁵⁷ Fe Mößbauer spectrum of the isolated THF adduct obtained at 80 K.	171
4.9. Qualitative molecular orbital diagram of (^{Me} BPDI)Fe(THF) obtained from a BS(2,2) calculation at the B3LYP level.	173
4.10. Solution equilibrium between (^{Me} PDI)Fe(THF) and [(^{Me} BPDI)Fe(N ₂)] ₂ (μ ₂ -N ₂).	174
4.11. Formation of the η ⁶ -arene complexes, (κ ² - ^{Me} BPDI)Fe(η ⁶ -phenyl) and (κ ² - ^{Me} BPDI)Fe(η ⁶ -aryl).	175

4.12. Synthesis of (^R BPDI)Fe(OC(OEt)(CHC(CH ₃) ₂)).	178
4.13. Addition of H ₂ to (^R BPDI)Fe(OC(OEt)(CHC(CH ₃) ₂)).	178
5.1. Morris' asymmetric transfer hydrogenation catalyst for the reduction of ketones.	192
5.2. Synthesis of (S,S)-(^R Box)FeCl ₂ (R = ⁱ Pr, Ph).	194
5.3. Synthesis of (S,S)-(^R Box)Fe(R') ₂ .	195
5.4. Conditions used for the catalytic, asymmetric hydrosilylation of ketones.	196
5.5. Alkyl abstraction of (S,S)-(^t BuBox)Fe(CH ₂ Si(CH ₃) ₃) ₂ with B(C ₆ F ₅) ₃ .	200
A.1.1. Synthesis of (4-Me ₂ N- ⁱ PrPDI)CoCl ₂ .	210
A.1.2. Synthesis of (4-Me ₂ N- ⁱ PrPDI)Co(CH ₃).	212
A.1.3. In situ synthesis of (4-Me ₂ N- ⁱ PrPDI)Co(H).	213
A.1.4. Benzene- <i>d</i> ₆ ¹ H NMR spectra of (4-Me ₂ N- ⁱ PrPDI)Co(CH ₃) and (4-Me ₂ N- ⁱ PrPDI)Co(H) at 22 °C.	214
A.1.5. Solid-state structure of (4-Me ₂ N- ⁱ PrPDI)Co(H) at 30% probability ellipsoids.	215
A.1.6. Reactivity of (4-Me ₂ N- ⁱ PrPDI)Co(H) with 1,1-diphenylethylene under 1 atmosphere of N ₂ .	216
A.1.7. Mechanisms accounting for the formation of (4-Me ₂ N- ⁱ PrPIEA)Co(N ₂) from (4-Me ₂ N- ⁱ PrPDI)Co(H) and 1,1-diphenylethylene.	217
A.1.8. Synthesis of (4-Me ₂ N- ⁱ PrPDI)Co(N ₂).	217

A.1.9. Solid-state structure of (4-Me ₂ N- <i>i</i> PrPDI)Co(N ₂) at 30% probability ellipsoids.	218
A.1.10. Toluene solution EPR spectrum of (4-Me ₂ N- <i>i</i> PrPDI)Co(N ₂) recorded at 23 °C	220
A.2.1. Synthetic routes to (<i>i</i> PrCNC)Co(CH ₃).	224
A.2.2. Benzene- <i>d</i> ₆ ¹ H NMR spectra of (<i>i</i> PrPDI)Co(CH ₃) and (<i>i</i> PrCNC)Co(CH ₃) at 22 °C.	225
A.2.3. Qualitative MO diagrams of (<i>i</i> PrCNC)Co(CH ₃). Spin density plot for (<i>i</i> PrCNC)Co(CH ₃) obtained from Mulliken population analysis.	227
A.2.4. Electronic structure of (<i>i</i> PrCNC)Co(CH ₃).	227
A.2.5. In situ synthesis of (<i>i</i> PrCNC)Co(H).	228
A.2.6. Benzene- <i>d</i> ₆ ¹ H NMR spectra of (<i>i</i> PrCNC)Co(CH ₃) and (<i>i</i> PrCNC)Co(H) at 22 °C.	229
A.2.7. Deuterium scrambling resulting from in situ synthesis of (<i>i</i> PrCNC)Co(D).	229
A.2.8. Proposed product arising from the exposure of (<i>i</i> PrCNC)Co(H) with 1 atm of N ₂ or from reduction of (<i>i</i> PrCNC)CoBr ₂ .	230
A.2.9. Hydrogenation of ethyl 3,3-dimethylacrylate with 5 mol % (<i>i</i> PrCNC)Co(CH ₃) and 4 atmospheres of H ₂ .	231
A.2.10. Reactivity of (<i>i</i> PrCNC)Co(H) with 1,1-diphenylethylene under 1 atmosphere of N ₂ .	232
A.2.11. Benzene- <i>d</i> ₆ ¹ H NMR spectra of (4-C(Ph) ₂ CH ₃ -4-H- <i>i</i> PrCNC)Co(N ₂)	

at 22 °C.	232
A.2.12. Solid state structure of (4-C(Ph) ₂ CH ₃ -4-H- <i>i</i> PrCNC)Co(N ₂) at 30% probability ellipsoids.	233
A.2.13. Mechanisms accounting for the formation of (4-C(Ph) ₂ CH ₃ -4-H- <i>i</i> PrCNC)Co(N ₂) from (<i>i</i> PrCNC)Co(H) and 1,1-diphenylethylene.	235
A.2.14. Geometry optimization of the theoretical molecules, (<i>i</i> PrCNC)Co(<i>t</i> Bu) and (<i>i</i> PrCNC)Co(C(Ph) ₂ CH ₃), at the B3LYP level of DFT.	236
A.3.1. Synthesis of (<i>i</i> PrCNC)Mn(CO) ₂ .	238
A.3.2. Solid-state structure of (<i>i</i> PrCNC)Mn(CO) ₂ at 30% probability ellipsoids.	239
B.1.1. Qualitative MO diagrams of (<i>i</i> PrCNC)Fe(N ₂) ₂ obtained from a RKS and BS(2,2) DFT calculation at the B3LYP level. Spin density plot for (<i>i</i> PrCNC)Fe(N ₂) ₂ obtained from Mulliken population analysis.	246
B.1.2. Electronic structure of (<i>i</i> PrCNC)Fe(N ₂) ₂ and (<i>i</i> PrPDI)Fe(N ₂) ₂ .	247
B.1.3. Qualitative MO diagrams of hypothetical (<i>i</i> PrCNC)Fe(N ₂) obtained from a RKS and BS(2,2) singlet DFT calculation as well as an unrestricted triplet DFT calculation at the B3LYP level.	249
B.1.4. Qualitative MO diagrams of (<i>i</i> PrCNC)Fe(DMAP)(N ₂) obtained from a spin-restricted and BS(2,2) DFT calculation and of hypothetical (<i>i</i> PrCNC)Fe(DMAP) obtained from a BS(2,2) DFT calculation at the B3LYP level.	251

B.2.1. Qualitative MO diagram for (<i>S,S</i>)-(<i>t</i> BuBox)Fe(CH ₂ Si(CH ₃) ₃) ₂ obtained from a spin-unrestricted quintet DFT calculation at the B3LYP level.	254
B.2.2. Synthetic routes to (terpy)Fe(CH ₂ Si(CH ₃) ₃) ₂ and (bipy) ₂ Fe(Et) ₂ .	255
B.2.3. Spin density plots obtained from a Mulliken population analysis of the spin-unrestricted quintet and BS(5,1) solutions. Qualitative MO diagram of (terpy)Fe(CH ₂ Si(CH ₃) ₃) ₂ obtained from a BS(5,1) DFT calculation at the B3LYP level.	257
B.2.4. Spin density plot obtained from a Mulliken population analysis of the BS(1,1) solutions. Qualitative MO diagram for (bipy) ₂ Fe(Et) ₂ obtained from a BS(1,1) DFT calculation at the B3LYP level.	259
B.2.5. Qualitative MO diagrams of (<i>i</i> PrCNC)Fe(R) ₂ (N ₂) obtained from a spin-restricted singlet DFT calculation at the B3LYP level.	262
B.2.6. Computed LUMO of the proposed intermediate, (<i>i</i> PrCNC)Fe(CH ₃) ₂ , involved in the reductive elimination of ethane obtained from a spin-restricted singlet DFT calculation at the B3LYP level.	264

LIST OF TABLES

1.1. Bond distances and angles for (4-CF ₃ - ⁱ PrPDI)FeCl ₂ , (4-Me ₂ N- ⁱ PrPDI)FeCl ₂ , and (ⁱ PrPDI)FeCl ₂ .	9
1.2. Bond distances and angles for (4-Me ₂ N- ⁱ PrPDI)Fe(CO) ₂ and (ⁱ PrPDI)Fe(CO) ₂ .	11
1.3. Bond distances and angles for (4-Me ₂ N- ⁱ PrPDI)Fe(N ₂) ₂ , (4- ^t Bu- ⁱ PrPDI)Fe(N ₂) ₂ and (ⁱ PrPDI)Fe(N ₂) ₂ .	15
1.4. Reduction potentials of various pyridine di(imine) compounds versus Fc/Fc ⁺ and SCE.	16
1.5. Cyclic voltammetry data for (4-R- ⁱ PrPDI)Fe(CO) ₂ complexes.	18
1.6. Carbonyl stretching frequencies of (4-R- ⁱ PrPDI)Fe(CO) ₂ measured by infrared spectroscopy in pentane.	20
1.7. Zero-field ⁵⁷ Fe Mössbauer parameters for (4-R- ⁱ PrPDI)Fe(CO) ₂ at 80 K.	21
1.8. Dinitrogen stretching frequencies for (4-R- ⁱ PrPDI)Fe(N ₂) _n (n = 1, 2) compounds recorded in pentane solution.	22
1.9. Zero-field ⁵⁷ Fe Mössbauer parameters for (4-R- ⁱ PrPDI)Fe(N ₂) _n compounds recorded at 80 K.	23
1.10. ¹ H NMR shifts of the in-plane pyridine di(imine) hydrogens of (4-R- ⁱ PrPDI)Fe(N ₂) collected in benzene- <i>d</i> ₆ at 23 °C.	24
1.11. Bond distances and angles for (4-Me ₂ N- ⁱ PrPDI)Fe(DMAP) and (ⁱ PrPDI)Fe(DMAP) ₂ .	28

1.12. Zero-Field ^{57}Fe Mössbauer parameters for (4-R- i^{Pr} PDI)Fe(DMAP).	28
1.13. ^1H NMR shifts of in-plane pyridine di(imine) resonances of (4-R- i^{Pr} PDI)Fe(DMAP) collected in benzene- d_6 at 23 °C.	29
1.14. Electronic descriptions and relative energies for singlet and triplet solutions of (4-R- i^{Pr} PDI)Fe(N_2) (R = CF_3 , NMe_2).	31
1.15. Comparison of selected experimental and computed bond distances and angles for (4- Me_2N - i^{Pr} PDI)Fe(DMAP) and (i^{Pr} PDI)Fe(DMAP).	33
1.16. Electronic descriptions and relative energies for the computed singlet and triplet solutions of (4-R- i^{Pr} PDI)Fe(DMAP) (R = NMe_2 , H, CF_3).	34
1.17. Hydrogenation of unactivated olefins using (4-R- i^{Pr} PDI)Fe(N_2).	40
2.1. Dinitrogen stretching frequencies for selected five-coordinate iron bis(dinitrogen) complexes recorded in pentane.	74
2.2. Bond distances and angles for ($i^{\text{Pr}}\text{CNC}$)Fe(DMAP)(N_2).	78
2.3. Zero-field ^{57}Fe Mössbauer parameters for pyridine di(carbene) and pyridine di(imine) iron complexes recorded at 80 K.	80
2.4. Bond distances and angles for ($i^{\text{Pr}}\text{CNC}$)Fe(η^2, η^2 -(CH_2CHCH_2) $_2\text{N}^t\text{Bu}$).	108
2.5. Experimental and computed Mössbauer parameters for ($i^{\text{Pr}}\text{CNC}$)Fe(η^2, η^2 -(CH_2CHCH_2) $_2\text{N}^t\text{Bu}$).	109
3.1. Coupling of alkyl halides with aryl Grignards using ($i^{\text{Pr}}\text{CNC}$)FeBr $_2$.	128
3.2. Infrared stretching frequencies of ($i^{\text{Pr}}\text{CNC}$)Fe(R) $_2$ (N_2)	

(CH ₂ Si(CH ₃) ₃ , 4-CH ₃ -C ₆ H ₄ , CH ₃).	131
3.3. Representative bond distances and angles for (ⁱ PrCNC)Fe(R) ₂ (N ₂) (R = CH ₂ Si(CH ₃) ₃ , 4-CH ₃ -C ₆ H ₄).	133
3.4. Zero-field ⁵⁷ Fe Mößbauer parameters for the pyridine di(carbene) iron dialkyl dinitrogen complexes at 80 K.	136
3.5. Selected bond distances and angles for (ⁱ PrCNC)Fe(CH ₂ Si(CH ₃) ₃) ₂ (CO).	141
4.1. Bond distances and angles for [(^{Me} BPDI)Fe(N ₂)] ₂ (μ ₂ -N ₂).	167
4.2. Zero-field ⁵⁷ Fe Mößbauer parameters for representative four- and five-coordinate pyridine di(imine) iron dinitrogen complexes.	170
4.3. Comparison of experimental and computed bond lengths and angles for (ⁱ PrPDI)Fe(NHC ₆ H ₁₀) and (^{Me} BPDI)Fe(THF), respectively.	173
4.4. Catalytic hydrogenation of ethyl 3,3-dimethylacrylate using aryl substituted bis(imino)pyridine iron bis(dinitrogen) complexes.	176
5.1. Catalytic Ketone Hydrosilylation with (<i>S,S</i>)-(^R Box)Fe(CH ₂ E(CH ₃) ₃) ₂ Complexes.	197
5.2. Catalytic Ketone Hydrosilylation with (<i>S,S</i>)-(ⁱ PrBox)Fe(CH ₂ Si(CH ₃) ₃) ₂ Activated with B(C ₆ F ₅) ₃ .	199
A.1.1. ¹ H NMR chemical shifts of the in-plane pyridine di(imine) hydrogens of (4-R- ⁱ PrPDI)Co(CH ₃) collected in benzene- <i>d</i> ₆ at 23 °C.	212

A.1.2. Selected bond distances and angles for (4-Me ₂ N- <i>i</i> PrPDI)Co(H).	215
A.1.3. Dinitrogen stretching frequencies of (4-R- <i>i</i> PrPDI)Co(N ₂) measured by infrared spectroscopy in toluene.	218
A.1.4. Bond distances and angles for (4-Me ₂ N- <i>i</i> PrPDI)Co(N ₂) and (<i>i</i> PrPDI)Co(N ₂).	219
A.2.1. Comparison of experimental and computational bond distances and angles for (<i>i</i> PrCNC)Co(CH ₃).	226
A.2.2. Bond distances (Å) and angles (°) for (4-C(Ph) ₂ CH ₃ -4-H- <i>i</i> PrCNC)Co(N ₂).	234
A.3.1. Bond distances and angles for (<i>i</i> PrCNC)Mn(CO) ₂ .	239
B.1.1. Comparison of experimental and computational bond distances and angles for (<i>i</i> PrCNC)Fe(N ₂) ₂ .	244
B.1.2. Comparison of computed bond distances and angles for hypothetical (<i>i</i> PrCNC)Fe(N ₂).	248
B.1.3. Comparison of selected computed bond distances and angles for the (<i>i</i> PrCNC)Fe(DMAP)(N ₂) and the theoretical (<i>i</i> PrCNC)Fe(DMAP) computed solutions.	251
B.2.1. Experimental and computed bond distances for (<i>S,S</i>)-(<i>t</i> BuBox)Fe(CH ₂ Si(CH ₃) ₃) ₂ .	254
B.2.2. Experimental and computed bond distances for (terpy)Fe(CH ₂ Si(CH ₃) ₃) ₂ .	256

B.2.3. Experimental and computed bond distances for (bipy) ₂ Fe(Et) ₂ .	259
B.2.4. Computed bond distances and angles for (ⁱ PrCNC)Fe(R) ₂ (N ₂).	261
B.2.5. Experimental and computed Mößbauer parameters for (ⁱ PrCNC)Fe(R) ₂ (N ₂).	262
B.2.6. Computed bond distances and angles for (ⁱ PrCNC)Fe(CH ₃) ₂ (N ₂) and (ⁱ PrCNC)Fe(CH ₃) ₂ .	264

CHAPTER 1

SYNTHESIS, ELECTRONIC STRUCTURE, AND REACTIVITY OF *para*-SUBSTITUTED PYRIDINE DI(IMINE) IRON COMPLEXES*

1.1 Abstract

A series of *para*-substituted pyridine di(imine) ligands, 4-R-ⁱPrPDI (4-R-ⁱPrPDI = 2,6-(2,6-ⁱPr₂-C₆H₃N=CCH₃)₂-4-R-C₅H₂N; R = CF₃, Bn, ^tBu, NMe₂) and the corresponding iron dihalide, dicarbonyl, and dinitrogen complexes were prepared. One example of a *para*-substituted pyridine di(imine) iron complex bearing a principally σ -donating ligand, (4-Me₂N-ⁱPrPDI)Fe(DMAP), was also prepared. Each variant was studied by a combination of electrochemical and spectroscopic (infrared, NMR, and Mößbauer) techniques to systematically investigate the influence of each *para*-substituent on the electronic structure of the complex. While no gross change in the ground state electronic structure was observed, ¹H NMR spectroscopy provided a relative measure of the thermal population and mixing of paramagnetic states for the four-coordinate complexes, (4-R-ⁱPrPDI)Fe(N₂) and (4-R-ⁱPrPDI)Fe(DMAP). This phenomenon was further investigated by density functional theory. The influence of the *para*-substituent on the catalytic activity of (4-R-ⁱPrPDI)Fe(N₂) was also studied. For catalytic hydrogenation, introduction of electron-donating substituents resulted in higher turnover frequencies for ethyl 3,3-dimethylacrylate and *trans*-methylstilbene. However, a lower turnover frequency for 1,1-diphenylethylene was observed, indicating that catalyst activity is substrate dependent. For the [2 π + 2 π] cycloaddition of *N,N*-diallylaniline, (4-Me₂N-ⁱPrPDI)Fe(N₂)₂

* Reproduced in part with permission from Darmon, J. M.; Turner, Z. R.; Lobkovsky, E.; Chirik, P. J. *Organometallics*. **2012**, *31*, 2275–2285. Copyright 2012 American Chemical Society.

exhibited a lower turnover frequency than (*i*PrPDI)Fe(N₂)₂, but was more active and selective than [(^{Me}PDI)Fe(N₂)₂](μ₂-N₂) and (*i*PrPDI)Co(N₂).

1.2 Introduction

Metal-ligand cooperativity, defined as the ability of a metal and ligand to undergo mutual redox events in order to facilitate a chemical transformation, has been one strategy identified to confer 2nd and 3rd row transition metal-like “nobility” to base metals.¹ This methodology has been exploited by Nature to carry out numerous catalytic processes.^{2,3} One fundamental requirement is the capability of the ligand to undergo at least one reversible redox event. The pyridine di(imine) ligand framework, popularized by Brookhart⁴ and Gibson^{5,6} for the base metal (*i.e.* iron and cobalt) catalyzed polymerization of ethylene upon activation with methylaluminoxane (MAO), possesses this ability, and is well known for its ability to accept between one and three electrons.⁷

In 2004, Bart *et al.* reported the synthesis of (*i*PrPDI)Fe(N₂)₂ (*i*PrPDI = 2,6-(2,6-*i*Pr₂-C₆H₃N=CCH₃)₂-C₅H₂N) from the reduction of (*i*PrPDI)FeCl₂ using an excess of 0.5% sodium amalgam under an atmosphere of dinitrogen.⁸ This complex has exhibited remarkable activity for the hydrogenation of olefins,⁹ intra-,^{10,11} and intermolecular¹² cyclization of unsaturates as well as the regioselective, anti-Markovnikov hydrosilylation of α-olefins with tertiary silanes.¹³ Mechanistic understanding of these processes has proven non-trivial, as the ability of the ligand to effect the overall electronic structure of the metal complex, and therefore the redox events required for fundamental transformations such as oxidative addition and reductive elimination, prevents straightforward interpretation. The synthesis and isolation of likely intermediates,^{8,10,12}

model complexes,¹⁴ and the use of modified ligand architectures^{15,16,17,18} has provided mechanistic insight; however, elucidation of the electronic structure of these complexes often requires exhaustive spectroscopic, structural and computational analyses.

Until recently, elucidation of the ground state of the pre-catalyst, $(i\text{PrPDI})\text{Fe}(\text{N}_2)_2$ had proven to be a challenge, as rapid loss of one molecule of dinitrogen in solution gave an equilibrium mixture of the five- and four-coordinate iron dinitrogen compounds.¹⁹ The five-coordinate compound, $(i\text{PrPDI})\text{Fe}(\text{N}_2)_2$ is a highly covalent compound, and is best described as a hybrid structure between $[(i\text{PrPDI}^0)\text{Fe}^0]$ and $[(i\text{PrPDI}^{2-})\text{Fe}^{\text{II}}]$. It is important to denote that in the $[(i\text{PrPDI}^{2-})\text{Fe}^{\text{II}}]$ formalism, the dianionic ligand is in a closed-shell configuration. This description is analogous to that of $(i\text{PrPDI})\text{Fe}(\text{CO})_2$,²⁰ and under this regime, these complexes are described as “redox non-innocent” (**Figure 1.1**). This term was first used by Jørgenson in the context of nitrosyl ligands to indicate ambiguity in the metal oxidation state assignment.²¹

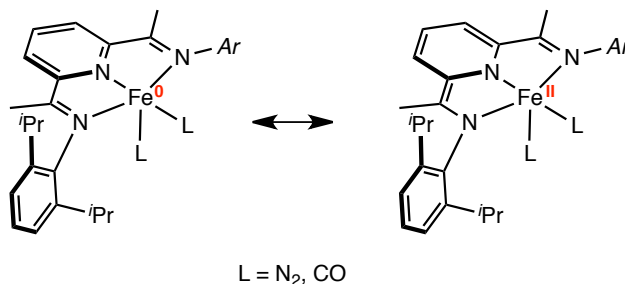


Figure 1.1. Electronic structure of redox non-innocent pyridine di(imine) iron complexes.

The electronic structure of the four-coordinate compound, $(i\text{PrPDI})\text{Fe}(\text{N}_2)_2$, as elucidated by NMR, Mößbauer, X-ray absorption and X-ray emission spectroscopies, in combination with density functional theory calculations, was characterized as a low-spin, Fe^{II} metal center antiferromagnetically coupled to a pyridine di(imine) triplet diradical.¹⁹ While this description is

similar to other four-coordinate pyridine di(imine) iron complexes previously described with σ -donating ligands (*i.e.* (*i*PrPDI)Fe(DMAP)),^{22,23} the degree of coupling between the metal and ligand magnetic orbitals was found to vary. This resulted in observation of two different NMR spectroscopic behaviors. For (*i*PrPDI)Fe(N₂), the coupling is weak, giving rise to a thermally accessible triplet state at 20 °C and temperature dependent chemical shifts. In contrast, (*i*PrPDI)Fe(DMAP), exhibits strong coupling which results in temperature independent paramagnetism (TIP). This phenomenon arises from mixing of a triplet excited state into the singlet ground state through spin-orbit coupling. These two complexes represent a second regime, in which the complex is referred to as “redox-active” (**Figure 1.2**). This nomenclature denotes the presence of ligand radicals that interact with the metal orbitals through antiferromagnetic coupling with an iron atom in a well-characterized spectroscopic oxidation state.

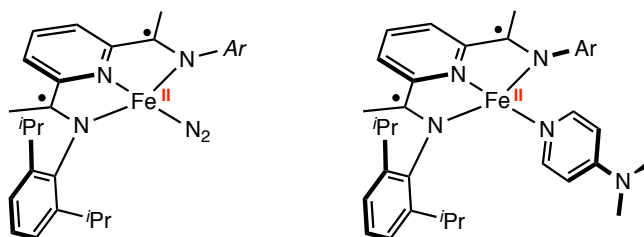


Figure 1.2. Electronic structure of redox-active pyridine di(imine) iron complexes.

One fundamental question arising from the study of the reduced pyridine di(imine) iron complexes is the importance of metal-ligand cooperativity in promoting the many types of catalytic reactions observed for (*i*PrPDI)Fe(N₂)_n (*n* = 1,2). One strategy for elucidating the importance of this phenomenon is the introduction of electron-donating and -withdrawing substituents with the intention of perturbing the interaction between the metal and chelate

magnetic orbitals. Using computations, Zhu and Budzelaar have investigated the effect of ligand modifications to the pyridine di(imine) ligand scaffold, and have demonstrated that the introduction of *para*-substituents to the pyridine ring affect the σ -donating and π -accepting ability of the ligand scaffold by a few kcal/mol.²⁴ Presented here is the synthesis, characterization and systematic evaluation of the electronic effects of *para*-substituents on the electronic structure and catalytic activity of the iron complexes.

1.3 Synthesis of *para*-Substituted Pyridine Di(Imine) Ligands, and their Iron Dicarbonyl and Dinitrogen Complexes

The family of *para*-substituted pyridine di(imine) complexes prepared for this study is presented in **Figure 1.3**. Substituents were selected that would influence the electronics of the ligand either in an electron-donating (4-Me₂N-*i*PrPDI) or -withdrawing (4-CF₃-*i*PrPDI) fashion, and for compatibility with the reducing conditions utilized to prepare the iron bis(dinitrogen) and dicarbonyl derivatives. The 2,6-diisopropyl aryl variant of the ligand was chosen in each case such that the steric environment of all derived metal complexes would be, to a first approximation, indistinguishable. Two examples, 4-Bn-*i*PrPDI and 4-*t*Bu-*i*PrPDI were prepared according to the previously reported methods of Cámpora²⁵ and Burger,²⁶ respectively.

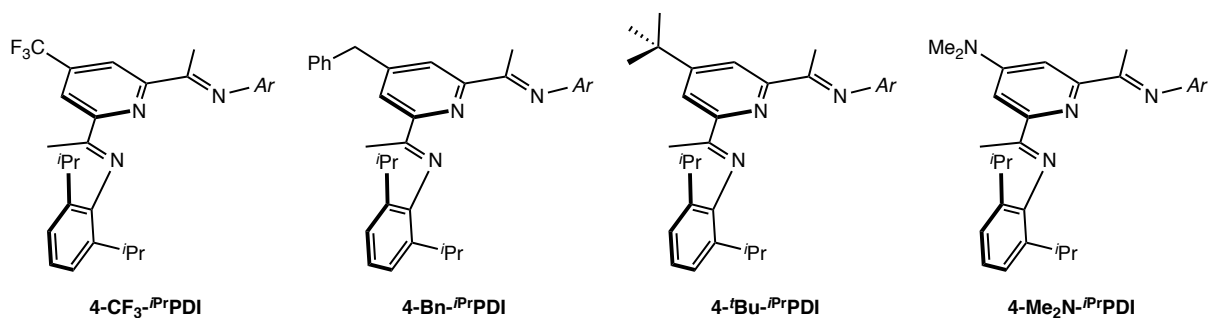


Figure 1.3. Prepared *para*-substituted pyridine di(imine) ligands.

The synthesis of 4-Me₂N-*i*PrPDI and 4-CF₃-*i*PrPDI are presented in **Figure 1.4**. Both syntheses were initiated by treatment of commercially available chelidamic acid with thionyl chloride, followed by addition of water or methanol to yield 4-chloropyridine-2,6-dicarboxylic acid or dimethyl 4-chloropyridine-2,6-dicarboxylate, respectively. 4-Chloropyridine-2,6-dicarboxylic acid served as the precursor to 4-Me₂N-*i*PrPDI, and was treated with dimethyl amine (aqueous, 35%) at 160 °C for 24 hours to afford 4-dimethylaminopyridine-2,6-dicarboxylic acid. This diacid was then converted to the dimethyl ester using methanolic thionyl chloride. With dimethyl 4-dimethylaminopyridine-2,6-dicarboxylate in hand, conversion to 4-dimethylamino-2,6-diacetylpyridine, and ultimately 4-Me₂N-*i*PrPDI, was accomplished using standard methods.²⁷

Dimethyl 4-chloropyridine-2,6-dicarboxylate served as the precursor to 4-CF₃-*i*PrPDI, and was sonicated in the presence of NaI and acetyl chloride in acetonitrile to give the corresponding iodide, dimethyl 4-iodopyridine-2,6-dicarboxylate.²⁸ Following a procedure of Johnson, the trifluoromethyl group was introduced using FSO₂CF₂CO₂CH₃ with five equivalents of CuI and 5% (dppf)PdCl₂·CH₂Cl₂ in DMF at 100 °C.²⁹ Conversion of this material to 4-CF₃-*i*PrPDI was also accomplished using standard methods.²⁷

Preparation of each *para*-substituted pyridine di(imine) iron dihalide was accomplished by stirring with either FeCl₂ or FeBr₂ in THF for 12–24 hours. Precipitation with pentane and collection by filtration yielded each pyridine di(imine) iron dihalide as a blue or green-blue solid in excellent yield (88–98%, **Figure 1.5**). All of the iron dihalides exhibited an *S* = 2 ground state and were routinely characterized by ¹H NMR spectroscopy in dichloromethane-*d*₂ or benzene-*d*₆ at 22 °C. Each ¹H NMR spectrum displayed the number of paramagnetically shifted and

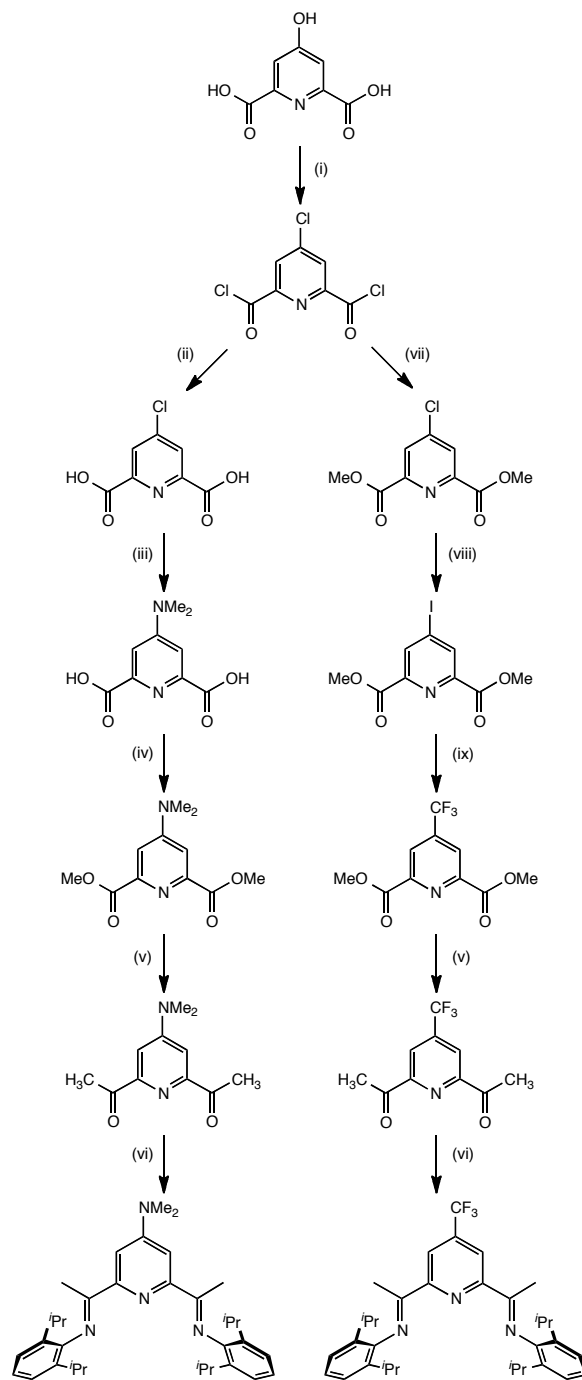


Figure 1.4. Synthesis of 4-Me₂N-*i*PrPDI and 4-CF₃-*i*PrPDI. Reagents and Conditions: (i) SOCl₂; (ii) H₂O, 0 to 45 °C; (iii) Me₂NH (aq., 35%), 160 °C; (iv) SOCl₂, MeOH; (v) NaOEt, EtOAc; HCl; (vi) 2,6-diisopropylaniline, MeOH, H⁺ (cat); (vii) MeOH, 0 to 45 °C; (viii) NaI, CH₃C(O)Cl, CH₃CN; (ix) FSO₂CF₂CO₂CH₃, 5 eq CuI, 5% (dppf)PdCl₂·CH₂Cl₂, DMF, 100 °C.

broadened resonances associated with a C_{2v} symmetric molecule over a chemical shift range of approximately 125 ppm.

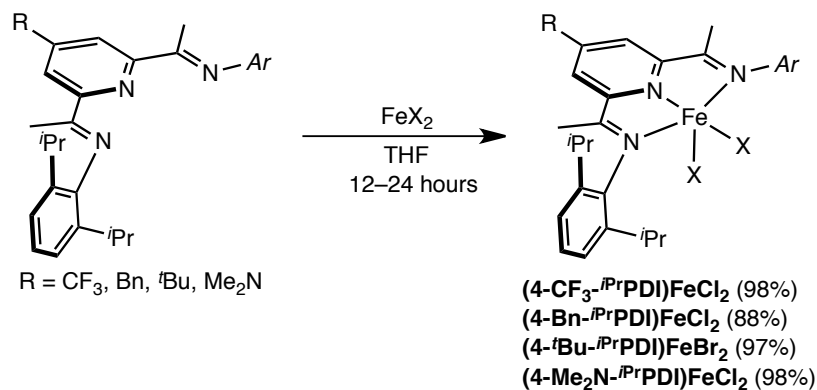


Figure 1.5. Synthesis of (4-R- $i\text{PrPDI}$) FeX_2 .

Single crystals of (4- Me_2N - $i\text{PrPDI}$) FeCl_2 and (4- CF_3 - $i\text{PrPDI}$) FeCl_2 suitable for X-ray diffraction were obtained as blue blocks by slow evaporation of concentrated THF and diethyl ether solutions, respectively, at 23 °C. The asymmetric unit of each crystal contained two molecules of the corresponding dihalide with statistically indistinguishable metrical parameters. Representations of the solid-state structures are presented in **Figure 1.6**, and selected metrical parameters are reported in **Table 1.1**. The metrical parameters for ($i\text{PrPDI}$) FeCl_2 are included for reference.^{4b} The intraligand bond distances were insensitive to the influence of a *para*-substituent. For example, the $C_{\text{ipso}}\text{--}C_{\text{imine}}$ and $C_{\text{imine}}\text{--}N_{\text{imine}}$ bond distances are statistically indistinguishable among the three pyridine di(imine) variants. In contrast, the metal-ligand bond distances exhibited statistical differences. The complex bearing the *para*-dimethylamino substituent, (4- Me_2N - $i\text{PrPDI}$) FeCl_2 , displayed the longest iron-nitrogen bond distances of the series, while the trifluoromethyl substituted compound, (4- CF_3 - $i\text{PrPDI}$) FeCl_2 , exhibited the shortest. These differences likely result from the varying *trans*-influence of each pyridine di(imine) ligand.

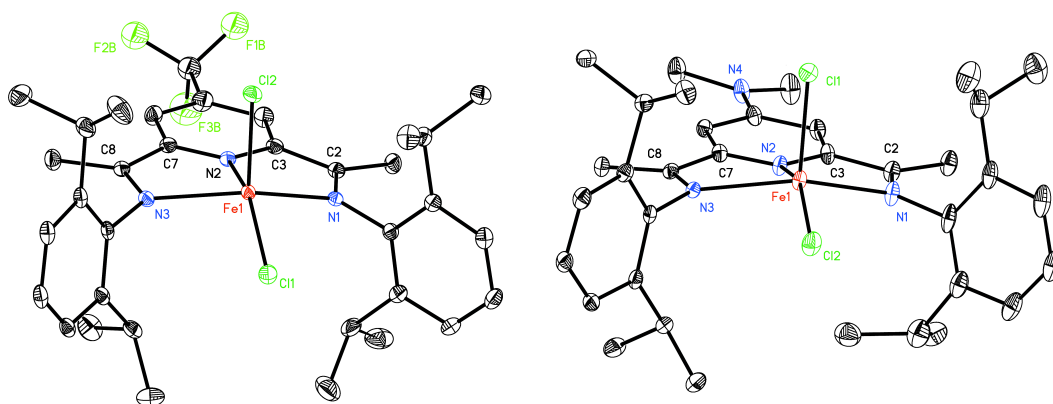


Figure 1.6. Solid-state structures of (4-CF₃-*i*PrPDI)FeCl₂ (left) and (4-Me₂N-*i*PrPDI)FeCl₂ (right) at 30% probability ellipsoids. In both cases, only one molecule from the asymmetric unit is shown. Hydrogen atoms are omitted for clarity.

Table 1.1. Bond distances (Å) and angles (°) for (4-CF₃-*i*PrPDI)FeCl₂, (4-Me₂N-*i*PrPDI)FeCl₂, and (*i*PrPDI)FeCl₂.

	(4-CF ₃ - <i>i</i> PrPDI)FeCl ₂	(4-Me ₂ N- <i>i</i> PrPDI)FeCl ₂	(<i>i</i> PrPDI)FeCl ₂
Fe(1)–N(1)	2.177(3)	2.284(3)	2.222(4)
Fe(1)–N(2)	2.058(3)	2.100(2)	2.091(4)
Fe(1)–N(3)	2.184(3)	2.253(3)	2.225(5)
Fe(1)–Cl(1)	2.2535(9)	2.3339(10)	2.2627(17)
Fe(1)–Cl(2)	2.2940(10)	2.2828(9)	2.3173(19)
N(1)–C(2)	1.291(4)	1.286(4)	1.301(7)
N(3)–C(8)	1.285(4)	1.284(4)	1.295(7)
C(2)–C(3)	1.479(4)	1.497(4)	1.466(8)
C(7)–C(8)	1.480(5)	1.497(4)	1.482(8)
N(1)–Fe(1)–N(2)	73.92(10)	71.90(10)	73.67(16)
N(1)–Fe(1)–Cl(1)	96.31(7)	100.22(8)	98.14(12)
N(1)–Fe(1)–Cl(2)	103.81(7)	104.19(8)	100.57(12)
N(2)–Fe(1)–Cl(1)	149.11(8)	96.77(8)	147.90(13)
N(2)–Fe(1)–Cl(2)	93.92(8)	152.67(8)	94.52(13)
N(2)–Fe(1)–N(3)	73.01(10)	72.92(9)	72.59(16)
N(3)–Fe(1)–Cl(1)	101.68(7)	101.28(7)	99.28(12)
N(3)–Fe(1)–Cl(2)	98.22(7)	98.78(7)	102.47(12)
Cl(1)–Fe(1)–Cl(2)	116.95(4)	110.47(4)	117.58(7)

To better evaluate the electronic effects of the *para*-substituents, a series of iron dicarbonyl compounds was prepared. Reduction of the iron dihalide complexes was accomplished using excess 0.5% sodium amalgam in toluene under one atmosphere of carbon monoxide, and yielded the corresponding iron dicarbonyl, (4-R-*i*PrPDI)Fe(CO)₂ as green or yellow-brown crystalline solids in moderate (63–69%) yields (**Figure 1.7**). The pyridine di(imine) iron dicarbonyl complexes were routinely characterized by ¹H and ¹³C NMR, solution infrared, and zero-field ⁵⁷Fe Mößbauer spectroscopies as well as combustion analysis.

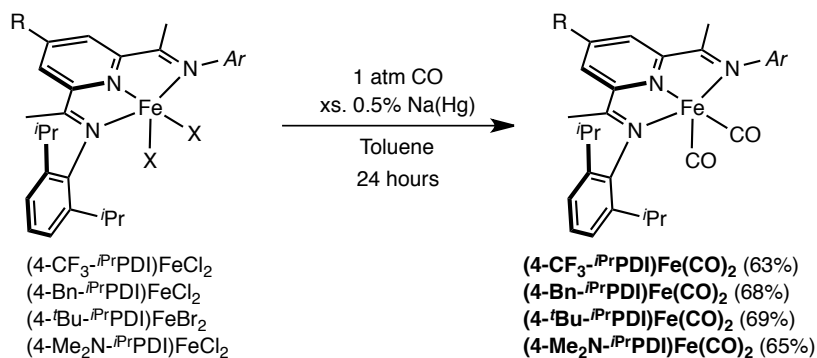


Figure 1.7. Synthesis of (4-R-*i*PrPDI)Fe(CO)₂.

One example, (4-Me₂N-*i*PrPDI)Fe(CO)₂ was characterized by X-ray diffraction. A representation of the solid-state structure is presented in **Figure 1.8** and selected metrical parameters are reported in **Table 1.2**. Single crystals were obtained from a concentrated diethyl ether solution at -35 °C as orange plates. Analogous to (*i*PrPDI)Fe(CO)₂,⁸ an idealized square pyramidal geometry was observed in the solid state with apical and basal carbonyl ligands. Observation of a C_{2v} symmetric molecule in benzene-*d*₆ solution by ¹H and ¹³C NMR spectroscopy at 22 °C for each of the *para*-substituted pyridine di(imine) iron dicarbonyl complexes indicates rapid exchange of these positions by rocking of the dicarbonyl ligands

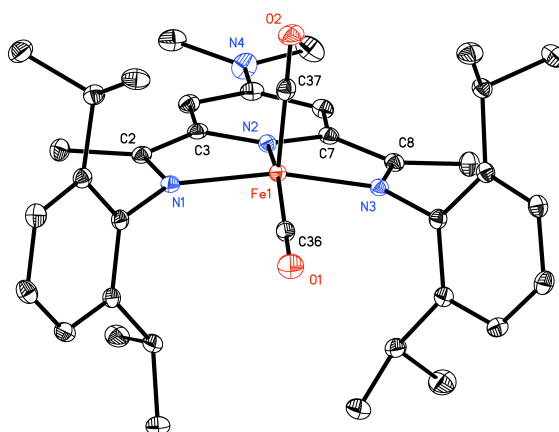


Figure 1.8. Solid-state structure of (4-Me₂N-*i*PrPDI)Fe(CO)₂ at 30% probability ellipsoids. Hydrogen atoms omitted for clarity.

Table 1.2. Bond distances (Å) and angles (°) for (4-Me₂N-*i*PrPDI)Fe(CO)₂ and (*i*PrPDI)Fe(CO)₂^a.

	(4-Me ₂ N- <i>i</i> PrPDI)Fe(CO) ₂	(<i>i</i> PrPDI)Fe(CO) ₂ ^a
Fe(1)–N(1)	1.9540(14)	1.9622(15)
Fe(1)–N(2)	1.8648(14)	1.8488(14)
Fe(1)–N(3)	1.9582(14)	1.9500(14)
Fe(1)–C(36)	1.7806(18)	1.7809(19)
Fe(1)–C(37)	1.7839(18)	1.7823(19)
N(1)–C(2)	1.330(2)	1.330(2)
N(3)–C(8)	1.327(2)	1.335(2)
C(2)–C(3)	1.427(2)	1.425(2)
C(7)–C(8)	1.438(2)	1.423(2)
N(1)–Fe(1)–N(2)	78.49(6)	79.10(6)
N(1)–Fe(1)–N(3)	148.83(6)	152.56(6)
N(1)–Fe(1)–C(36)	103.98(7)	101.54(7)
N(1)–Fe(1)–C(37)	97.41(7)	96.36(7)
N(2)–Fe(1)–N(3)	78.55(6)	79.32(6)
N(3)–Fe(1)–C(36)	102.33(7)	100.30(7)
N(3)–Fe(1)–C(37)	97.35(7)	97.27(7)
C(36)–Fe(1)–C(37)	93.56(8)	97.01(9)

^a Data taken from reference 8.

through the iron-chelate plane on the timescale of the experiment. The *para*-dimethylamino group is approximately coplanar with the pyridine ring, with a dihedral angle of 10.3(3)° between the two idealized planes. The $C_{ipso}-C_{imine}$ and $C_{imine}-N_{imine}$ bond distances are statistically indistinguishable from those of $(iPr)PDI)Fe(CO)_2$, consistent with backbonding between the iron center and the pyridine di(imine) ligand.

Synthesis of the *para*-substituted pyridine di(imine) iron bis(dinitrogen) complexes was targeted, as access to these complexes may allow evaluation of the effect of the *para*-substituent on catalytically relevant systems (*i.e.* hydrogenation). Employing the conditions used to prepare $(iPr)PDI)Fe(N_2)_2$,⁸ each of the iron dihalide complexes was stirred with an excess of 0.5% sodium amalgam in toluene under an atmosphere of dinitrogen. In one instance, $(4-Me_2N-iPr)PDI)Fe(N_2)_2$, an equivolume amount of THF was added to improve solubility and facilitate the reduction. Filtration and recrystallization from pentane or pentane-diethyl ether mixtures at -35 °C furnished the iron bis(dinitrogen) complexes, $(4-R-iPr)PDI)Fe(N_2)_2$ as green or brown-green solids in modest yields (39–65%, **Figure 1.9**).

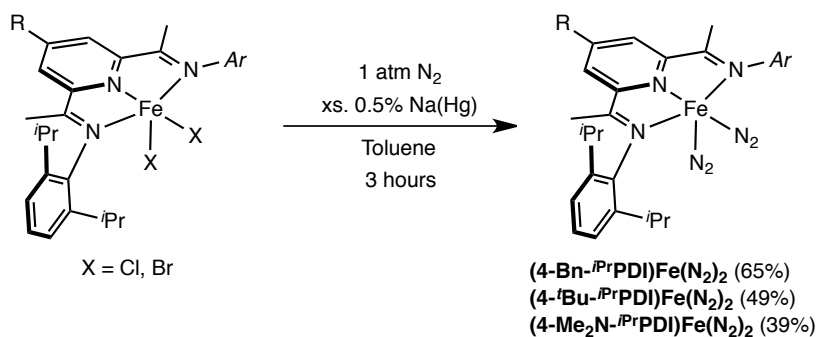


Figure 1.9. Synthesis of $(4-R-iPr)PDI)Fe(N_2)_2$.

Only one of the pyridine di(imine) iron dihalides, $(4-CF_3-iPr)PDI)FeCl_2$, failed to form the iron bis(dinitrogen) complex. Reduction of $(4-CF_3-iPr)PDI)FeCl_2$ under one atmosphere of

dinitrogen afforded an intractable mixture of products, principally comprised of free 4-CF₃-*i*PrPDI. Monitoring the reaction by ¹H NMR and solution infrared spectroscopy demonstrated clean one-electron reduction to yield a paramagnetic intermediate, tentatively assigned as (4-CF₃-*i*PrPDI)FeCl.³⁰ However, further reduction consumed the intermediate. No new compounds were identified by ¹H NMR spectroscopy and no strong bands assignable to N₂ stretching frequencies were identified in the solution infrared spectrum, suggesting that no iron dinitrogen complex was formed.

As with the pyridine di(imine) iron dicarbonyl complexes, each of the iron dinitrogen compounds was characterized by ¹H and ¹³C NMR, infrared and zero-field ⁵⁷Fe Mößbauer spectroscopies. Consistent with other monomeric pyridine di(imine) iron dinitrogen complexes^{8,15} recrystallization at -35 °C yielded predominantly the five-coordinate, bis(dinitrogen) adduct, (4-R-*i*PrPDI)Fe(N₂)₂; however, in solution at 23 °C, the four-coordinate complex, (4-R-*i*PrPDI)Fe(N₂), dominates. The benzene-*d*₆ ¹H and ¹³C NMR spectra exhibited the number of resonances consistent for a single C_{2v} symmetric compound, indicating rapid conversion between the four- and five-coordinate complexes on the NMR timescale. Bulk samples of the iron dinitrogen complexes underwent rapid loss of dinitrogen in the solid state, giving rise to a mixture of the four- and five-coordinate complexes, which made isolation and handling challenging. Observation of both species was accomplished using techniques with shorter observation timescales (*i.e.* infrared and Mößbauer spectroscopies, *vide infra*).

Two of the new *para*-substituted pyridine di(imine) iron dinitrogen complexes, (4-*t*Bu-*i*PrPDI)Fe(N₂)₂ and (4-Me₂N-*i*PrPDI)Fe(N₂)₂, were characterized by X-ray diffraction. Single crystals of (4-*t*Bu-*i*PrPDI)Fe(N₂)₂ and (4-Me₂N-*i*PrPDI)Fe(N₂)₂ were obtained from concentrated

pentane-diethyl ether solutions as green shards and dark blocks, respectively. The asymmetric unit of the crystals of $(4\text{-}^t\text{Bu-}^i\text{PrPDI})\text{Fe}(\text{N}_2)_2$ contained two independent molecules with statistically indistinguishable metrical parameters. Representations of both complexes in the solid state are presented in **Figure 1.10** and their metrical parameters are reported in **Table 1.3**. As with other five-coordinate pyridine di(imine) iron complexes possessing neutral ligands, an idealized square pyramidal geometry was observed in each case with one apical and one basal dinitrogen ligand. For $(4\text{-Me}_2\text{N-}^i\text{PrPDI})\text{Fe}(\text{N}_2)_2$, the two idealized planes created by the pyridine ring and the dimethylamino group deviate from planarity by approximately three degrees. The intraligand bond distances, suggestive of an iron(II) oxidation state assignment, were insensitive to the presence of a *para*-substituent, and the steric environment of each complex is virtually indistinguishable.

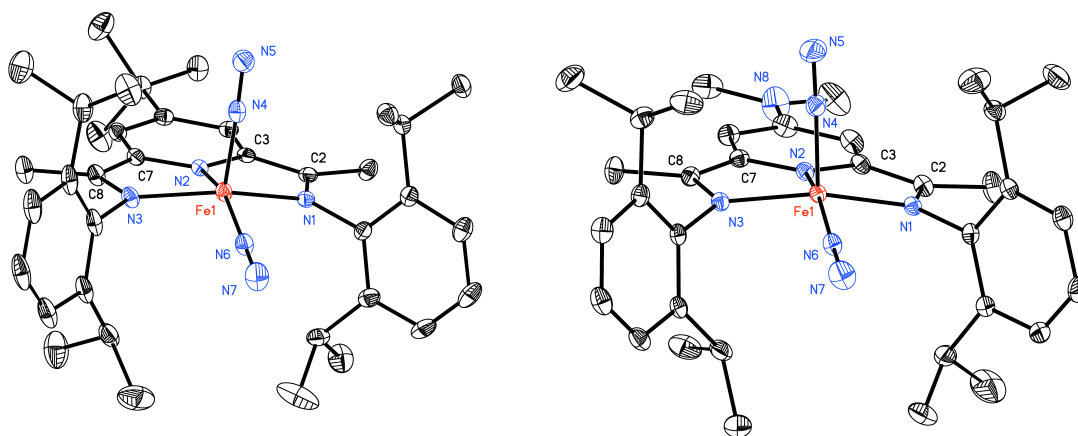


Figure 1.10. Solid-state structure of $(4\text{-}^t\text{Bu-}^i\text{PrPDI})\text{Fe}(\text{N}_2)_2$ and $(4\text{-Me}_2\text{N-}^i\text{PrPDI})\text{Fe}(\text{N}_2)_2$ at 30% probability ellipsoids. Hydrogen atoms omitted for clarity.

1.4 Electronic Structure Comparison of 4-Substituted Pyridine Di(imine) Ligands and their Iron Complexes

Electrochemical and spectroscopic measurements were collected on each class of

Table 1.3. Bond distances (Å) and angles (°) for (4-Me₂N-ⁱPrPDI)Fe(N₂)₂, (4-^tBu-ⁱPrPDI)Fe(N₂)₂ and (ⁱPrPDI)Fe(N₂)₂.

	(4-Me ₂ N- ⁱ PrPDI)Fe(N ₂) ₂	(4- ^t Bu- ⁱ PrPDI)Fe(N ₂) ₂	(ⁱ PrPDI)Fe(N ₂) ₂ ^a
Fe(1)–N(1)	1.9738(14)	1.9444(16)	1.9473(16)
Fe(1)–N(2)	1.8500(14)	1.8415(16)	1.8362(14)
Fe(1)–N(3)	1.9134(14)	1.9444(16)	1.9452(16)
Fe(1)–N(4)	1.8386(16)	1.9013(19)	1.8800(19)
Fe(1)–N(6)	1.8670(15)	1.8347(18)	1.8341(16)
N(1)–C(2)	1.332(2)	1.342(2)	1.333(2)
N(3)–C(8)	1.362(2)	1.334(3)	1.332(2)
C(2)–C(3)	1.464(3)	1.423(3)	1.427(2)
C(7)–C(8)	1.419(3)	1.425(3)	1.428(3)
N(1)–Fe(1)–N(2)	80.42(6)	79.42(7)	79.90(6)
N(1)–Fe(1)–N(4)	104.73(6)	99.33(7)	98.92(7)
N(1)–Fe(1)–N(6)	94.17(6)	97.00(7)	97.41(7)
N(2)–Fe(1)–N(4)	97.49(7)	103.16(7)	102.89(7)
N(2)–Fe(1)–N(6)	161.58(7)	159.45(8)	159.09(8)
N(2)–Fe(1)–N(3)	79.31(6)	79.64(7)	79.49(6)
N(3)–Fe(1)–N(4)	94.78(6)	99.06(7)	99.74(7)
N(3)–Fe(1)–N(6)	99.71(6)	97.65(7)	96.65(7)
N(4)–Fe(1)–N(6)	100.91(7)	97.38(8)	98.02(8)

^a Data taken from reference 8.

compounds (free ligand, iron dicarbonyl and iron dinitrogen derivatives) to evaluate the electronic influence of each *para*-substituent. Cyclic voltammograms were obtained for each of the pyridine di(imine) ligands and are presented in **Figure 1.11**. Each voltammogram was recorded in THF solution (approximately 1 mM in compound and 0.1 M in [ⁿBu₄N]PF₆ supporting electrolyte). Silver wire was used as the reference electrode, platinum wire as the counter electrode and glassy carbon as the working electrode. Reduction potentials versus ferrocene/ferrocenium (Fc/Fc⁺) and SCE³¹ are reported in **Table 1.4**. Values for ⁱPrBPDI, a pyridine di(imine) known to be electron withdrawing relative to ⁱPrPDI, and ^{Cy}APDI, a pyridine

di(imine) where the aryl-substituent has been replaced by a cyclohexyl group, are included for comparison.³²

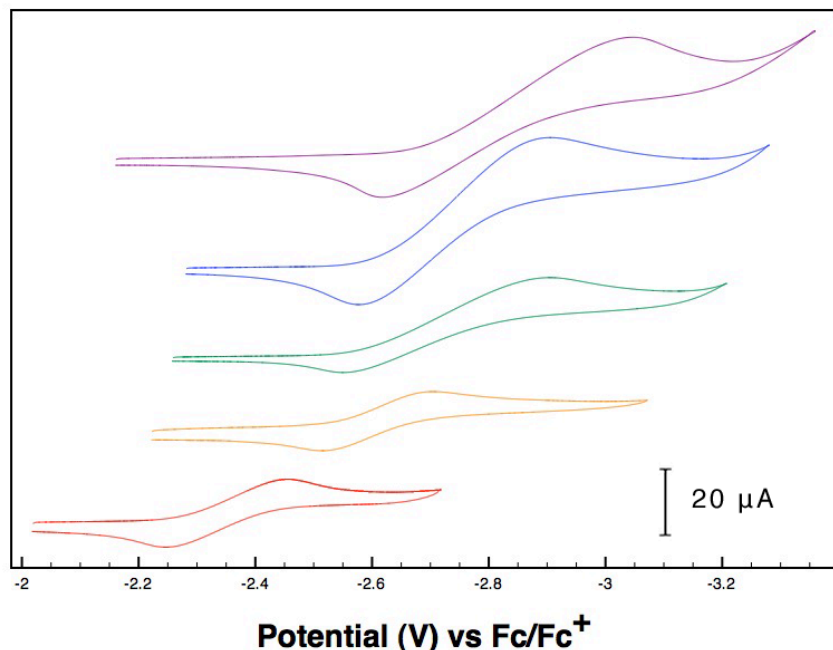


Figure 1.11. Cathodic CV scans of *para*-substituted pyridine di(imine) ligands: 4-CF₃-*iPr*PDI (red), *iPr*PDI (orange), 4-Bn-*iPr*PDI (green), 4-*t*Bu-*iPr*PDI (blue), and 4-Me₂N-*iPr*PDI (purple).

Table 1.4. Reduction potentials of various pyridine di(imine) compounds versus Fc/Fc⁺ and SCE.^a

Ligand	Reduction Potential (V vs. Fc/Fc ⁺)	Reduction Potential (V vs. SCE) ^a
4-CF ₃ - <i>iPr</i> PDI	-2.35	-1.79
<i>iPr</i> BPDI ^b	-2.55	-1.99
<i>iPr</i> PDI	-2.62	-2.06
4-Bn- <i>iPr</i> PDI	-2.72	-2.16
4- <i>t</i> Bu- <i>iPr</i> PDI	-2.76	-2.20
4-Me ₂ N- <i>iPr</i> PDI	-2.82	-2.26
CyAPDI ^b	-2.83	-2.27

^a Formal potential for the ferrocene^{+1/0} couple vs. SCE with [nBu₄N][PF₆] taken from reference 31.

^b Data taken from reference 32.

Each of the pyridine di(imine) ligands exhibited a single, reversible reduction wave in THF solution, and no other redox waves were observed in the solvent window. As expected,

electron-withdrawing substituents (*i.e.* 4-CF₃-^{*i*}PrPDI and ^{*i*}PrBPDI) stabilized formation of the radical anion, resulting in an anodic shift relative to the unsubstituted pyridine di(imine), ^{*i*}PrPDI, whereas electron-donating substituents (*i.e.* 4-Bn-^{*i*}PrPDI, 4-^{*t*}Bu-^{*i*}PrPDI, *etc.*) destabilized formation of the radical anion, resulting in a cathodic shift. 4-CF₃-^{*i*}PrPDI was the most readily reduced of the series of pyridine di(imine) ligands, with a reduction potential 200 and 270 mV more positive than ^{*i*}PrBPDI and ^{*i*}PrPDI, respectively. The two *para*-alkyl substituted pyridine di(imine) ligands, 4-Bn-^{*i*}PrPDI and 4-^{*t*}Bu-^{*i*}PrPDI were virtually indistinguishable, and were only 100 and 140 mV more negative than ^{*i*}PrPDI, respectively. The *para*-dimethylamino derivative, 4-Me₂N-^{*i*}PrPDI was the most difficult aryl-substituted pyridine di(imine) to reduce, 200 mV more negative than ^{*i*}PrPDI, and was virtually indistinguishable from the alkyl-substituted pyridine di(imine), ^{Cy}APDI. It should be noted that selection of the *para*-substituent resulted in the ability to tune the reduction potential of the pyridine di(imine) ligand by 470 mV.

Because the electrochemical behavior of (^{*i*}PrPDI)Fe(CO)₂ has previously been investigated,²⁰ electrochemical data for each of the *para*-substituted pyridine di(imine) iron dicarbonyl complexes were collected using identical conditions to those used for the free ligand. Representative cyclic voltammograms are presented in **Figure 1.12**, and the oxidation and reduction potentials are reported in **Table 1.5**. As with (^{*i*}PrPDI)Fe(CO)₂, each of the *para*-substituted pyridine di(imine) iron dicarbonyl complexes undergoes a clean, reversible one-electron oxidation and reduction. The electronic structure of these species has been elucidated by isolation following chemical oxidation and reduction of (^{*i*}PrPDI)Fe(CO)₂. The oxidation event is principally ligand-based, and gives rise to an *S* = 1/2 iron(I) compound with a neutral pyridine di(imine) chelate, [(^{*i*}PrPDI⁰)Fe^I(CO)₂]⁺. The reduction event, in contrast, is principally metal-

based and also gives rise to an $S = 1/2$ iron(I) species with a dianionic chelate, $[(i\text{PrPDI}^{2-})\text{Fe}^{\text{I}}(\text{CO})_2]^-$. Computational studies have suggested that these formalisms are oversimplifications, as oxidation state assignments are complicated by covalency between metal- and ligand-based orbitals.

The redox behavior exhibited by the *para*-substituted pyridine di(imine) iron dicarbonyl

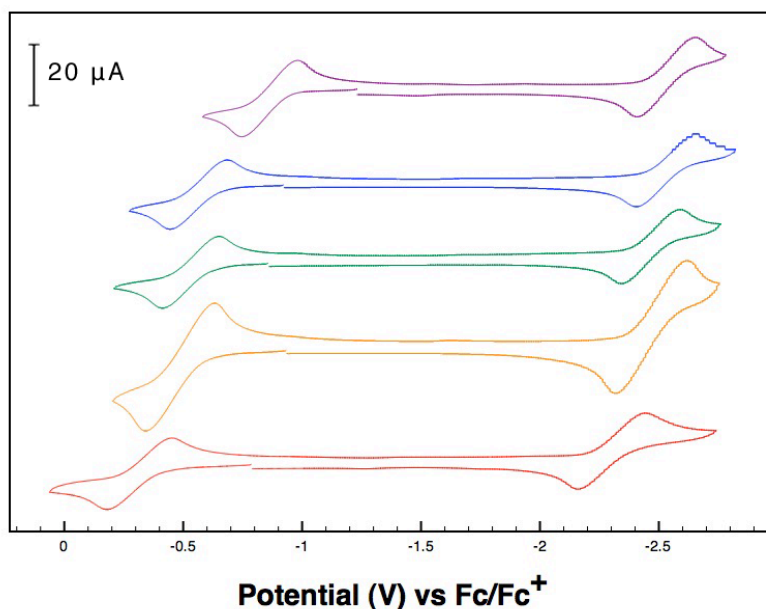


Figure 1.12. CV scans of *para*-substituted pyridine di(imine) iron dicarbonyl complexes: (4-CF₃-*i*PrPDI)Fe(CO)₂ (red), (*i*PrPDI)Fe(CO)₂ (orange), (4-Bn-*i*PrPDI)Fe(CO)₂ (green), (4-*t*Bu-*i*PrPDI)Fe(CO)₂ (blue), and (4-Me₂N-*i*PrPDI)Fe(CO)₂ (purple). The scans were initiated anodically.

Table 1.5. Cyclic voltammetry data for (4-R-*i*PrPDI)Fe(CO)₂ complexes.

Compound	Oxidation (V vs Fc/Fc ⁺)	Reduction (V vs Fc/Fc ⁺)	Oxidation (V vs SCE) ^a	Reduction (V vs SCE) ^a
(4-CF ₃ - <i>i</i> PrPDI)Fe(CO) ₂	-0.27	-2.27	0.29	-1.71
(<i>i</i> PrPDI)Fe(CO) ₂ ^b	-0.49	-2.46	0.07	-1.90
(4-Bn- <i>i</i> PrPDI)Fe(CO) ₂	-0.53	-2.47	0.03	-1.91
(4- <i>t</i> Bu- <i>i</i> PrPDI)Fe(CO) ₂	-0.56	-2.53	0.00	-1.97
(4-Me ₂ N- <i>i</i> PrPDI)Fe(CO) ₂	-0.86	-2.53	-0.30	-1.97

^a Formal potential for the ferrocene^{+1/0} couple vs. SCE with [Bu₄N][PF₆] taken from reference 31.

^b Data taken from reference 20.

complexes mimics the trend observed with free pyridine di(imine) compounds. Those complexes bearing electron-withdrawing substituents were more easily reduced than their electron-donating derivatives, while the opposite trend was observed for oxidation of the neutral iron dicarbonyl compounds. The *para*-trifluoromethyl derivative, (4-CF₃-*i*PrPDI)Fe(CO)₂, was the most easily reduced by +190 mV relative to (*i*PrPDI)Fe(CO)₂. This is a less dramatic difference than the +270 mV difference observed between the free pyridine di(imine) compounds. The oxidation event occurred at a potential 220 mV more positive. The oxidation and reduction of the two *para*-alkyl substituted pyridine di(imine) iron dicarbonyl complexes, (4-Bn-*i*PrPDI)Fe(CO)₂ and (4-*t*-Bu-*i*PrPDI)Fe(CO)₂ did not significantly deviate from (*i*PrPDI)Fe(CO)₂, and were less than 100 mV different. While the oxidation of (4-Me₂N-*i*PrPDI)Fe(CO)₂ occurred at a potential 360 mV more negative than (*i*PrPDI)Fe(CO)₂, the reduction event was indistinguishable from that of (4-*t*-Bu-*i*PrPDI)Fe(CO)₂. As expected, the oxidation event, which is principally ligand-based, was more sensitive to the identity of the *para*-substituent, and a linear relationship between the [(4-R-*i*PrPDI)Fe(CO)₂]^{+1/0} redox event and σ_{para} value³³ was observed ($R^2 = 0.9992$, **Figure 1.13**).

The infrared stretching frequency of the carbonyl ligands provided another diagnostic probe for studying the electronic effects of the *para*-substituents. The infrared spectrum of each of the *para*-substituted pyridine di(imine) iron dicarbonyl complexes was recorded in pentane solution and the symmetric and asymmetric stretching frequencies of the dicarbonyl ligands are reported in **Table 1.6**. (*i*PrPDI)Fe(CO)₂ and (*i*PrBPDI)Fe(CO)₂ are included for reference. As expected from the electrochemical measurements, (4-CF₃-*i*PrPDI)Fe(CO)₂ exhibited the least reduced carbonyl stretching frequencies by approximately 10 wavenumbers from (*i*PrPDI)Fe(CO)₂. The stretching frequencies of the two *para*-alkyl substituted complexes, (4-Bn-

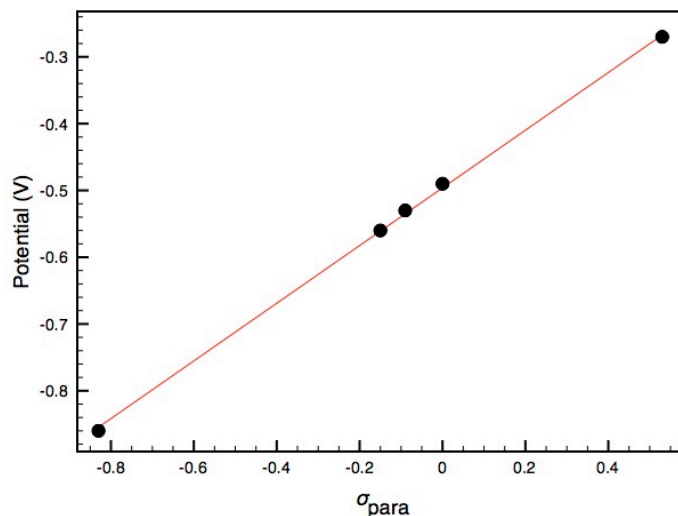


Figure 1.13. Plot of the $[(4\text{-R-}^i\text{PrPDI})\text{Fe}(\text{CO})_2]^{+1/0}$ redox couple vs. σ_{para} value. ($y = 0.4319x - 0.4962$; $R^2 = 0.9992$)

$^i\text{PrPDI})\text{Fe}(\text{CO})_2$ and $(4\text{-}^t\text{Bu-}^i\text{PrPDI})\text{Fe}(\text{CO})_2$ were almost indistinguishable from $(^i\text{PrPDI})\text{Fe}(\text{CO})_2$, differing by one to three wavenumbers. The *para*-dimethylamino variant, $(4\text{-Me}_2\text{N-}^i\text{PrPDI})\text{Fe}(\text{CO})_2$, exhibited the most reduced carbonyl stretching frequencies, indicating increased π -backbonding into the carbonyl ligands as a result of a more electron-rich metal center imparted by the $4\text{-Me}_2\text{N-}^i\text{PrPDI}$ ligand.

Table 1.6. Carbonyl stretching frequencies of $(4\text{-R-}^i\text{PrPDI})\text{Fe}(\text{CO})_2$ measured by infrared spectroscopy in pentane.

Complex	$\nu(\text{C}\equiv\text{O})$ (cm^{-1})
$(4\text{-CF}_3\text{-}^i\text{PrPDI})\text{Fe}(\text{CO})_2$	1925, 1983
$(^i\text{PrBPDI})\text{Fe}(\text{CO})_2^a$	1921, 1979
$(^i\text{PrPDI})\text{Fe}(\text{CO})_2^b$	1914, 1974
$(4\text{-Bn-}^i\text{PrPDI})\text{Fe}(\text{CO})_2$	1913, 1972
$(4\text{-}^t\text{Bu-}^i\text{PrPDI})\text{Fe}(\text{CO})_2$	1911, 1971
$(4\text{-Me}_2\text{N-}^i\text{PrPDI})\text{Fe}(\text{CO})_2$	1906, 1965

^a Data from reference 8.

^b Data from reference 15.

To probe the overall electronic structure of the pyridine di(imine) iron dicarbonyl complexes, solid-state, zero-field ^{57}Fe Mössbauer spectra were collected at 80 K. Representative

spectra are presented in **Figure 1.14**, and the isomer shift (δ) and quadrupole splitting (ΔE_Q) parameters are reported in **Table 1.7**. The parameters of each variant were indistinguishable from those of the parent complex, (*i*PrPDI)Fe(CO)₂, indicating that no gross electronic structure change had occurred, and that Mößbauer spectroscopy was not sufficiently sensitive to distinguish electronic perturbations caused by the *para*-substituents.

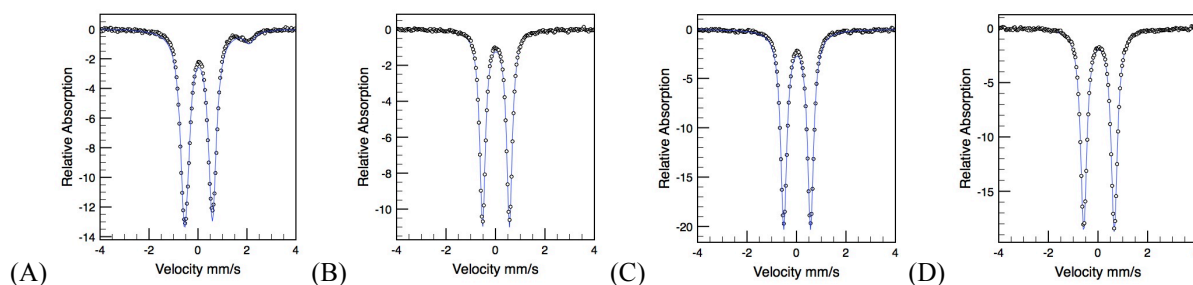


Figure 1.14. Zero-field ⁵⁷Fe Mößbauer spectra for (4-R-*i*PrPDI)Fe(CO)₂: (A) (4-CF₃-*i*PrPDI)Fe(CO)₂, (B) (4-Bn-*i*PrPDI)Fe(CO)₂, (C) (4-^tBu-*i*PrPDI)Fe(CO)₂, and (D) (4-Me₂N-*i*PrPDI)Fe(CO)₂.

Table 1.7. Zero-field ⁵⁷Fe Mößbauer parameters for (4-R-*i*PrPDI)Fe(CO)₂ at 80 K.

Compound	δ (mm·s ⁻¹)	$ \Delta E_Q $ (mm·s ⁻¹)
(4-CF ₃ - <i>i</i> PrPDI)Fe(CO) ₂	0.02	1.14
(<i>i</i> PrPDI)Fe(CO) ₂ ^a	0.03	1.17
(4-Bn- <i>i</i> PrPDI)Fe(CO) ₂	0.02	1.09
(4- ^t Bu- <i>i</i> PrPDI)Fe(CO) ₂	0.03	1.08
(4-Me ₂ N- <i>i</i> PrPDI)Fe(CO) ₂	0.04	1.23

^a Data from reference 8.

The *para*-substituted pyridine di(imine) iron dinitrogen complexes, (4-R-*i*PrPDI)Fe(N₂)_n (*n* = 1, 2) were characterized in a similar manner. The infrared stretching frequencies of the dinitrogen ligands for both the four- and five-coordinate complexes were recorded in pentane solution at 23 °C, and the dinitrogen stretching frequencies are presented in **Table 1.8**. One exception was (4-Me₂N-*i*PrPDI)Fe(N₂)₂, which was collected in toluene solution at -30 °C. Among the four-coordinate complexes, the alkyl substituted pyridine di(imine) complexes, (4-

Bn-ⁱPrPDI)Fe(N₂) and (4-^tBu-ⁱPrPDI)Fe(N₂) were modestly more reduced than (ⁱPrPDI)Fe(N₂) by 2 and 5 wavenumbers, respectively. The *para*-dimethylamino variant (4-Me₂N-ⁱPrPDI)Fe(N₂) showed the most dramatic change, and was 12 wavenumbers more reduced than (ⁱPrPDI)Fe(N₂). The same trend was observed with the five-coordinate bis(dinitrogen) complexes. (4-Me₂N-ⁱPrPDI)Fe(N₂)₂ exhibited the lowest energy N₂ stretching frequencies, consistent with having the most electron-rich metal center.

Table 1.8. Dinitrogen stretching frequencies for (4-R-ⁱPrPDI)Fe(N₂)_n (n = 1, 2) compounds recorded in pentane solution.

Complex	n = 1	n = 2
	$\nu(\text{N}\equiv\text{N})$ (cm ⁻¹)	$\nu(\text{N}\equiv\text{N})$ (cm ⁻¹)
(ⁱ PrPDI)Fe(N ₂) _n ^a	2046	2132, 2073
(4-Bn- ⁱ PrPDI)Fe(N ₂) _n	2044	2129, 2071
(4- ^t Bu- ⁱ PrPDI)Fe(N ₂) _n	2041	2128, 2067
(4-Me ₂ N- ⁱ PrPDI)Fe(N ₂) _n	2034	2117, 2055 ^b

^a Data from reference 8. ^b Values were recorded in toluene at -30 °C.

The solid-state, zero-field ⁵⁷Fe Mößbauer spectra of mixtures of the four- and five-coordinate *para*-substituted pyridine di(imine) iron dinitrogen complexes were collected at 80 K. Representative spectra are presented in **Figure 1.15**, and the Mößbauer parameters are reported in **Table 1.9**. As with the pyridine di(imine) iron dicarbonyl complexes, the Mößbauer parameters do not deviate significantly within the family of four- and five-coordinate complexes, indicating no gross change in the electronic structure. The isomer shifts are consistent with an iron(II) designation in all cases. As was previously observed,²² the quadrupole splitting of the five-coordinate complexes is larger than that observed for the four-coordinate complexes and is likely due to a change in the electric field gradient arising from different ordering and population of the cloverleaf *d*-orbitals and d_{z²} between the two geometries.

In order to more closely examine the influence of the *para*-substituent on the electronic

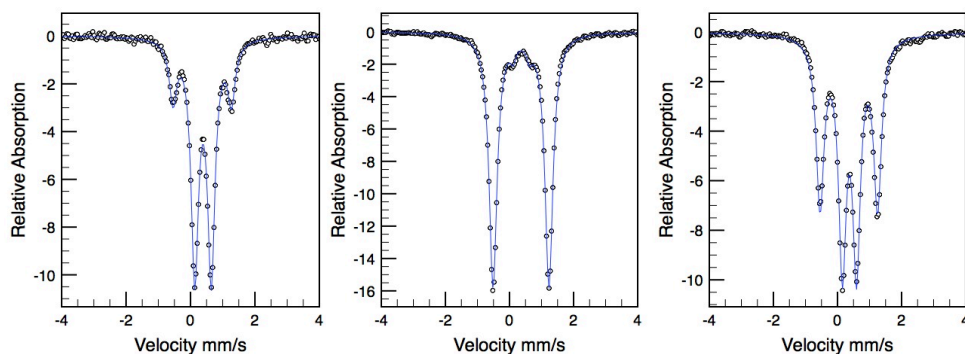


Figure 1.15. Zero-field ^{57}Fe Mössbauer spectra of mixtures of $(4\text{-R-}^i\text{PrPDI})\text{Fe}(\text{N}_2)_n$ ($n = 1, 2$) obtained at 80 K: $(4\text{-Bn-}^i\text{PrPDI})\text{Fe}(\text{N}_2)_n$ (left), $(4\text{-}^t\text{Bu-}^i\text{PrPDI})\text{Fe}(\text{N}_2)_n$ (middle), and $(4\text{-Me}_2\text{N-}^i\text{PrPDI})\text{Fe}(\text{N}_2)_n$ (right).

Table 1.9. Zero-field ^{57}Fe Mössbauer parameters for $(4\text{-R-}^i\text{PrPDI})\text{Fe}(\text{N}_2)_n$ ($n = 1, 2$) compounds recorded at 80 K.

Compound	δ ($\text{mm}\cdot\text{s}^{-1}$)	$ \Delta E_Q $ ($\text{mm}\cdot\text{s}^{-1}$)
$(^i\text{PrPDI})\text{Fe}(\text{N}_2)_2^a$	0.39	0.53
$(^i\text{PrPDI})\text{Fe}(\text{N}_2)^a$	0.38	1.72
$(4\text{-Bn-}^i\text{PrPDI})\text{Fe}(\text{N}_2)_2$	0.39	0.51
$(4\text{-Bn-}^i\text{PrPDI})\text{Fe}(\text{N}_2)$	0.36	1.81
$(4\text{-}^t\text{Bu-}^i\text{PrPDI})\text{Fe}(\text{N}_2)_2$	0.37	0.51
$(4\text{-}^t\text{Bu-}^i\text{PrPDI})\text{Fe}(\text{N}_2)$	0.36	1.74
$(4\text{-Me}_2\text{N-}^i\text{PrPDI})\text{Fe}(\text{N}_2)_2$	0.37	0.44
$(4\text{-Me}_2\text{N-}^i\text{PrPDI})\text{Fe}(\text{N}_2)$	0.35	1.79

^aData from reference 8.

structure of the *para*-substituted pyridine di(imine) iron dinitrogen compounds, benzene- d_6 ^1H NMR spectra for each $(4\text{-R-}^i\text{PrPDI})\text{Fe}(\text{N}_2)$ complex ($\text{R} = \text{Bn}, ^t\text{Bu}, \text{NMe}_2$) were collected at 23 °C (**Figure 1.16**). As with $(^i\text{PrPDI})\text{Fe}(\text{N}_2)$, the resonances of the in-plane hydrogens of each complex exhibit unusual shifts relative to the values for the free ligands. The chemical shifts of the *m*-pyr and imine methyl hydrogens are reported in **Table 1.10**. Values for the free ligand and $(^i\text{PrPDI})\text{Fe}(\text{N}_2)$ are included for reference.

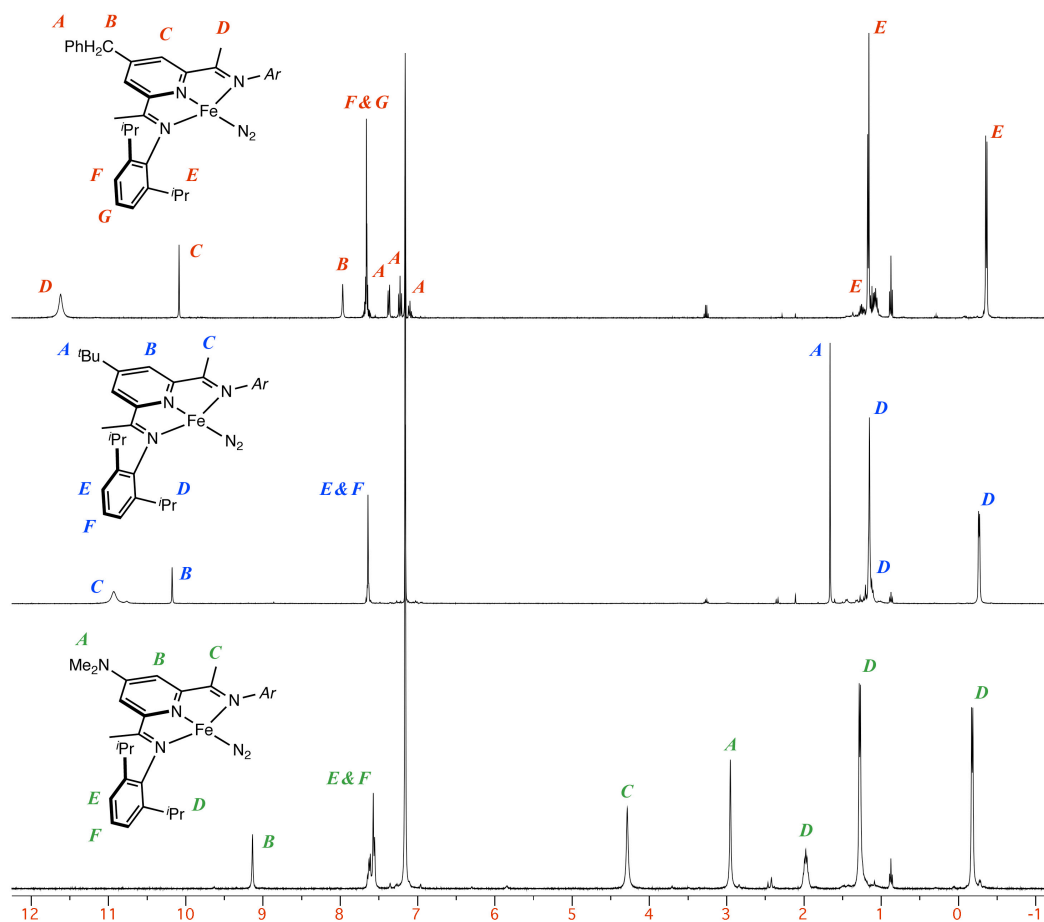


Figure 1.16. Benzene- d_6 ^1H NMR spectra of $(4\text{-R-}i\text{PrPDI})\text{Fe}(\text{N}_2)_n$ ($n = 1, 2$) at $23\text{ }^\circ\text{C}$.

Table 1.10. ^1H NMR chemical shifts (ppm) of the in-plane pyridine di(imine) hydrogens of $(4\text{-R-}i\text{PrPDI})\text{Fe}(\text{N}_2)$ collected in benzene- d_6 at $23\text{ }^\circ\text{C}$. Free ligand reference values are provided in parentheses.

Complex	<i>m</i> -pyr	imine CH_3
$(i\text{PrPDI})\text{Fe}(\text{N}_2)^a$	10.11 (8.51)	13.61 (2.28)
$(4\text{-Bn-}i\text{PrPDI})\text{Fe}(\text{N}_2)$	10.09 (8.55)	11.62 (2.31)
$(4\text{-}^t\text{Bu-}i\text{PrPDI})\text{Fe}(\text{N}_2)$	10.18 (8.86)	10.93 (2.36)
$(4\text{-Me}_2\text{N-}i\text{PrPDI})\text{Fe}(\text{N}_2)$	9.13 (8.04)	4.23 (2.4)

^a Data from reference 8.

The ^1H NMR shifts of the in-plane hydrogens of the four-coordinate pyridine di(imine) iron nitrogen compounds, $(i\text{PrRPDI})\text{Fe}(\text{N}_2)$ ($i\text{PrRPDI} = 2,6\text{-}(2,6\text{-}^i\text{Pr}_2\text{-C}_6\text{H}_3\text{-N=CR})_2\text{C}_5\text{H}_3\text{N}$; R = Me, Et, ^iPr) are temperature dependent.¹⁹ This behavior arises due to thermal population of an

energetically-accessible triplet state. First observed in pyridine di(imine) chemistry by Budzelaar and coworkers for the (^RPDI)Co(R) class of complexes.^{34,35} Our laboratory later verified this phenomenon by studying the spin-crossover behavior of *N*-alkyl substituted pyridine di(imine) cobalt halide complexes.³⁶ The magnitude of the shift of the proton resonances from the value of the free ligand directly relates to the accessibility of the excited state, and gives a very sensitive metric of the *d*-orbital energetics.

The chemical shifts of the *m*-pyridine hydrogens for the *para*-substituted pyridine di(imine) iron nitrogen complexes were relatively insensitive to the presence of a *para*-substituent at 23 °C; however, downfield shifts relative to the chemical shifts of the free ligand did occur. The *para*-alkyl substituted pyridine di(imine) iron nitrogen complexes, (4-Bn-ⁱPrPDI)Fe(N₂) and (4-^tBu-ⁱPrPDI)Fe(N₂) shift slightly less downfield, by 1.54 and 1.32 ppm, respectively than the parent complex, (ⁱPrPDI)Fe(N₂) (which shifts by 1.60 ppm). The *para*-dimethylamino derivative, (4-Me₂N-ⁱPrPDI)Fe(N₂) experiences the least downfield shift of the series (by 1.09 ppm).

While the same overall trend is observed for the imine methyl resonances of the pyridine di(imine) iron nitrogen complexes, sensitivity to the *para*-substituent was significantly more pronounced. The parent complex, (ⁱPrPDI)Fe(N₂) experiences the most dramatic downfield shift ($\Delta\delta = 11.33$ ppm) at 23 °C, whereas the *para*-alkyl substituted derivatives, (4-Bn-ⁱPrPDI)Fe(N₂) and (4-^tBu-ⁱPrPDI)Fe(N₂) shift slightly less downfield by 9.31 and 8.57 ppm, respectively. Distinct from the other *para*-substituted complexes, the imine methyl resonance of (4-Me₂N-ⁱPrPDI)Fe(N₂) only shifts downfield by 1.83 ppm to 4.23 ppm. The minor chemical shift deviations experienced by the in-plane hydrogens of (4-Me₂N-ⁱPrPDI)Fe(N₂) suggest that

introduction of electron-donating groups result in a less thermally accessible triplet state.

While the ground state description of the four-coordinate dinitrogen complex, (*i*PrPDI)Fe(N₂) is similar to other four-coordinate pyridine di(imine) iron complexes with principally σ-donating ligands, the strength of the coupling between the metal-chelate magnetic orbitals, as dictated by the *d*-orbital energetics, gave rise to different NMR spectroscopic behaviors.^{19,22} To investigate the effect of *para*-substitution on pyridine di(imine) iron complexes with principally σ-donating ligands, the synthesis of (4-Me₂N-*i*PrPDI)Fe(DMAP) was targeted.

Inspired by the conditions used to prepare (*i*PrPDI)Fe(DMAP), one equivalent of 4-*N,N*-dimethylaminopyridine was added to (4-Me₂N-*i*PrPDI)Fe(N₂) in diethyl ether solution, and resulted in an immediate color change from brown-green to purple-orange. Following filtration and recrystallization, (4-Me₂N-*i*PrPDI)Fe(DMAP) was isolated as a dark red-purple solid in 88% yield (**Figure 1.17**).

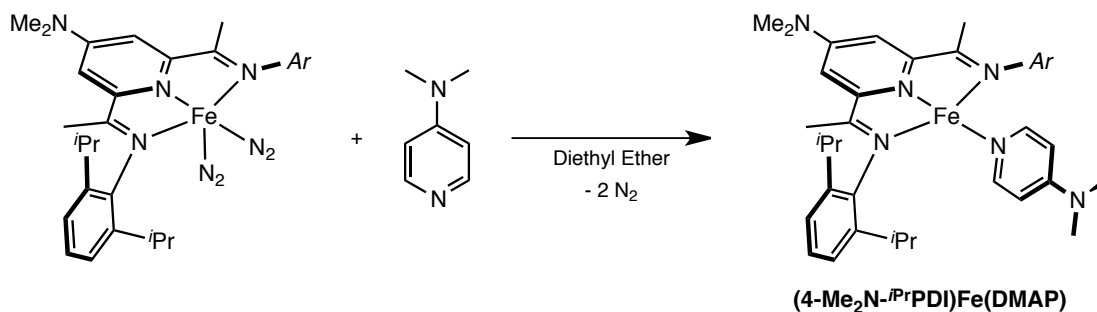


Figure 1.17. Synthesis of (4-Me₂N-*i*PrPDI)Fe(DMAP).

Single crystals of (4-Me₂N-*i*PrPDI)Fe(DMAP) suitable for X-ray diffraction were obtained from a concentrated diethyl ether solution at -35 °C as dark red-purple plates. A representation of the solid-state structure of (4-Me₂N-*i*PrPDI)Fe(DMAP) is presented in **Figure 1.18**, and selected metrical parameters are reported in **Table 1.11**. Values for (*i*PrPDI)Fe(DMAP)

are included for comparison.²² Analogously to (*i*PrPDI)Fe(DMAP), an idealized square planar geometry is observed in the solid state. The idealized plane, as defined by the *para*-dimethylamino substituent of the pyridine di(imine), and the plane of the pyridine ring exhibit a torsion angle of approximately six degrees. As with the five-coordinate dinitrogen analogue, (4-Me₂N-*i*PrPDI)Fe(N₂)₂, intraligand bond distances do not deviate significantly from the parent complex, (*i*PrPDI)Fe(DMAP), and are consistent with a two-electron reduced chelate, 4-Me₂N-*i*PrPDI²⁻.

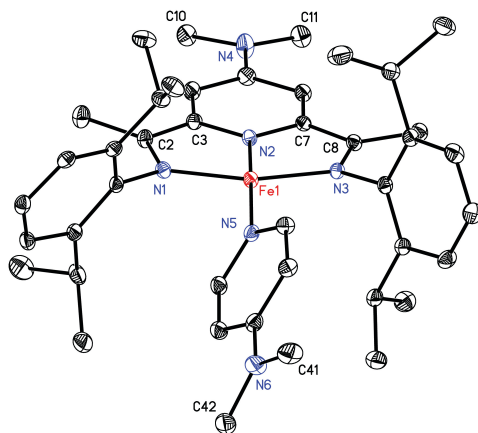


Figure 1.18. Solid-state structure of (4-Me₂N-*i*PrPDI)Fe(DMAP) at 30% probability ellipsoids. Hydrogen atoms omitted for clarity.

The solid-state, zero-field ⁵⁷Fe Mößbauer spectrum of (4-Me₂N-*i*PrPDI)Fe(DMAP) collected at 80 K yielded parameters that were nearly identical to the unsubstituted analog, (*i*PrPDI)Fe(DMAP). The parameters for (4-R-*i*PrPDI)Fe(DMAP) (R = H, Me₂N) are reported in **Table 1.12**. These parameters are consistent with a ferrous oxidation state assignment and indicate no gross change in electronic structure.

Like (*i*PrPDI)Fe(N₂), the in-plane hydrogen atoms of (*i*PrPDI)Fe(DMAP) exhibit ¹H NMR chemical shifts that significantly deviate from the values of the free ligand; however, the direction of the shift (upfield or downfield) is opposite of what is observed for (*i*PrPDI)Fe(N₂).

Table 1.11. Bond distances (Å) and angles (°) for (4-Me₂N-ⁱPrPDI)Fe(DMAP) and (ⁱPrPDI)Fe(DMAP)₂.

	(4-Me ₂ N- ⁱ PrPDI)Fe(DMAP)	(ⁱ PrPDI)Fe(DMAP)
Fe(1)–N(1)	1.9279(18)	1.942(3)
Fe(1)–N(2)	1.8357(18)	1.822(3)
Fe(1)–N(3)	1.9119(18)	1.908(3)
Fe(1)–N(5)	1.9901(19)	1.978(3)
N(1)–C(2)	1.370(3)	1.358(5)
N(3)–C(8)	1.369(3)	1.350(5)
C(2)–C(3)	1.415(3)	1.405(5)
C(7)–C(8)	1.415(3)	1.406(5)
N(1)–Fe(1)–N(2)	81.08(8)	81.05(14)
N(1)–Fe(1)–N(5)	98.72(8)	97.77(14)
N(2)–Fe(1)–N(5)	173.91(8)	175.58(14)
N(2)–Fe(1)–N(3)	80.60(8)	80.74(14)
N(3)–Fe(1)–N(5)	99.84(8)	100.68(14)

^a Data taken from reference 22.**Table 1.12.** Zero-Field ⁵⁷Fe Mössbauer parameters for (4-R-ⁱPrPDI)Fe(DMAP).

Compound	δ (mm·s ⁻¹)	ΔE _Q (mm·s ⁻¹)
(ⁱ PrPDI)Fe(DMAP) ^a	0.31	1.94
(4-Me ₂ N- ⁱ PrPDI)Fe(DMAP)	0.33	1.80

^a Data from reference 22.

For (ⁱPrPDI)Fe(DMAP), this results from temperature independent paramagnetism, whereby a mixing of excited states into the singlet ground state occurs by spin-orbit coupling. In order to determine the influence of the electron-donating *para*-dimethyl amino substituent, the benzene-*d*₆ ¹H NMR spectrum of (4-Me₂N-ⁱPrPDI)Fe(DMAP) was collected at 23 °C. Under this regime (electron-donating pyridine di(imine) chelate/σ-donating ligand), the resonances for the in-plane hydrogen atoms of (4-Me₂N-ⁱPrPDI)Fe(DMAP) experienced more dramatic deviations than (ⁱPrPDI)Fe(DMAP). The chemical shifts are reported in **Table 1.13**, and values for

(*i*PrPDI)Fe(DMAP) are included for reference. Consistent with the NMR behavior of (4-R-*i*PrPDI)Fe(N₂), the shift of the *m*-pyr was less sensitive to the presence of a *para*-substituent than the imine methyl group. However, the deviation of the *m*-pyr and the imine methyl resonances from their free ligand values for (4-Me₂N-*i*PrPDI)Fe(DMAP) were more dramatic ($\Delta\delta = 4.92$ and 11.38 ppm, respectively) than those for (*i*PrPDI)Fe(DMAP) ($\Delta\delta = 3.91$ and 8.13 ppm, respectively). This suggests that (4-Me₂N-*i*PrPDI)Fe(DMAP) experiences a greater degree of mixing into the singlet ground state; however, the reason for this phenomenon is not currently well understood.

Table 1.13. ¹H NMR shifts of in-plane pyridine di(imine) resonances of (4-R-*i*PrPDI)Fe(DMAP) collected in benzene-*d*₆ at 23 °C. Free ligand reference values are provided in parentheses.

Complex	<i>m</i> -pyr	imine CH ₃
(<i>i</i> PrPDI)Fe(DMAP) ^a	12.42 (8.51)	-5.85 (2.28)
(4-Me ₂ N- <i>i</i> PrPDI)Fe(DMAP)	12.96 (8.04)	-8.98 (2.4)

^a Data from reference 22.

1.5 Computational Studies: (4-R-*i*PrPDI)Fe(N₂) and (4-R-*i*PrPDI)Fe(DMAP)

To more thoroughly understand the *d*-orbital energetics and the influence of the *para*-substituent, full molecule density functional theory calculations on (4-R-*i*PrPDI)Fe(N₂) and (4-R-*i*PrPDI)Fe(DMAP) (R = CF₃, H, NMe₂) were performed at the B3LYP level. Ground states were investigated using spin-restricted (RKS) and broken-symmetry (BS) approaches, while triplet states were explored using spin-unrestricted and broken-symmetry models. This approach, similar to one taken by Budzelaar and coworkers,³⁴ resulted in a correlation between the magnitude of the chemical shifts and the energy differences between the singlet and triplet computed solutions.

For (*i*PrPDI)Fe(N₂), the ground state was best described as an intermediate-spin, iron(II) ion ($S = 1$) antiferromagnetically coupled to a PDI²⁻ triplet diradical ($S = 1$), which was 17.1 kcal/mol lower in energy than the spin-restricted approach.¹⁹ Two low-lying triplet excited states were identified that were in good agreement with the temperature dependent magnetic behavior. One state corresponded to a low-spin, Fe^I ion ($S = 1/2$) and a PDI¹⁻ radical with parallel spin alignment. The other state corresponded to a high-spin, Fe^I ion ($S = 3/2$) antiferromagnetically coupled to a PDI¹⁻ radical ($S = 1/2$), and was obtained through a BS(4,2) approach. These two states were 1.1 and 6.2 kcal/mol higher in energy, respectively, than the diamagnetic ground state.

Using these results as a model for (4-Me₂N-*i*PrPDI)Fe(N₂) and the theoretical dinitrogen compound, (4-CF₃-*i*PrPDI)Fe(N₂), the spin-restricted singlet (RKS), BS(2,2), and unrestricted triplet states were calculated. The results are reported in **Table 1.14**. The unrestricted BS(2,2) states were consistently lower in energy than the restricted singlet states by 17.8 and 16.2 kcal/mol for (4-Me₂N-*i*PrPDI)Fe(N₂) and (4-CF₃-*i*PrPDI)Fe(N₂), respectively. Qualitative molecular orbital diagrams are presented in **Figure 1.19**. The degree of overlap between the d_{yz} and a_2 magnetic orbitals increased as a function of electron donation into the pyridine di(imine) π -system, whereas no systematic trend was observed between the d_{z^2} and b_2 magnetic orbitals. This is likely because the d_{z^2} and b_2 magnetic orbitals do not have the proper symmetry to interact, and therefore ligand electronic effects are negligible.

The unrestricted triplet solution of (4-Me₂N-*i*PrPDI)Fe(N₂) was higher in energy than that of (*i*PrPDI)Fe(N₂) and (4-CF₃-*i*PrPDI)Fe(N₂), which is consistent with the reduced contribution of the thermally accessible excited state observed from the chemical shifts of (4-Me₂N-

Table 1.14. Electronic descriptions and relative energies (kcal/mol) for singlet and triplet solutions of (4-R-*i*PrPDI)Fe(N₂) (R = CF₃, NMe₂).

	Converged Description	Relative Energy
(4-Me₂N-<i>i</i>PrPDI)Fe(N₂)		
RKS	<i>RKS</i>	17.8
BS(2,2)	<i>BS(2,2)</i>	0.0
Triplet	<i>Triplet</i>	2.4
(4-CF₃-<i>i</i>PrPDI)Fe(N₂)		
RKS	<i>RKS</i>	16.2
BS(2,2)	<i>BS(2,2)</i>	0.0
Triplet	<i>Triplet</i>	0.6

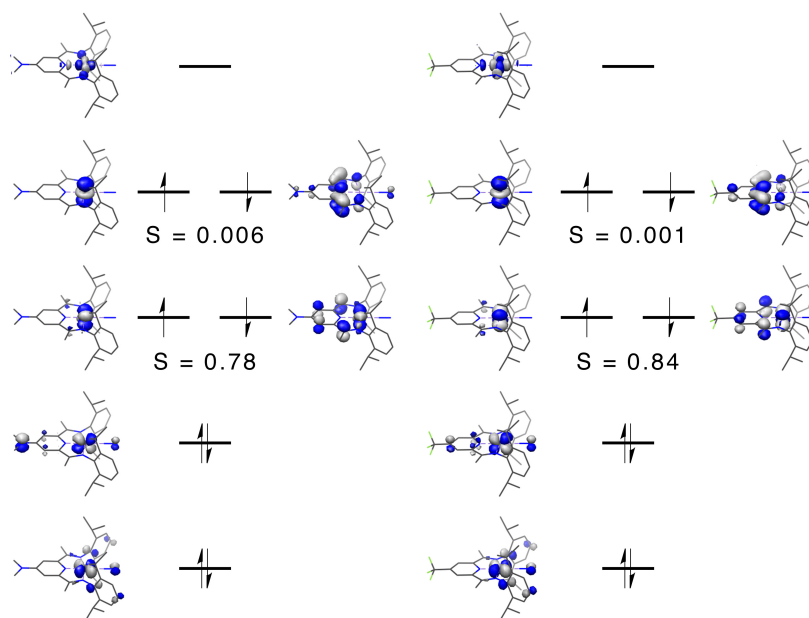


Figure 1.19. Qualitative MO diagrams of (4-R-*i*PrPDI)Fe(N₂) (R = NMe₂, CF₃) obtained from a BS(2,2) DFT calculation at the B3LYP level.

*i*PrPDI)Fe(N₂) at 23 °C by ¹H NMR spectroscopy. The unrestricted triplet solution for (4-Me₂N-*i*PrPDI)Fe(N₂) and (4-CF₃-*i*PrPDI)Fe(N₂) was 2.4 and 0.6 kcal/mol higher in energy, respectively, than the BS(2,2) ground state. Relatively minor changes in energy were expected for the *para*-substituted analogues given that the difference in energy between the BS(2,2) and unrestricted triplet solutions for (*i*PrPDI)Fe(N₂) was calculated to be 1.1 kcal/mol. This can be rationalized on

the basis of the metal oxidation state for the singlet and triplet solutions. The more reducing 4-Me₂N-*i*PrPDI ligand has the potential to better stabilize higher oxidation states, leading to a net stabilization of the diamagnetic Fe(II) state ground state. This rationale, however, is an oversimplification as the metal oxidation state assignments are complicated by covalency. Qualitative molecular orbital diagrams for the unrestricted triplet solutions are presented in

Figure 1.20.

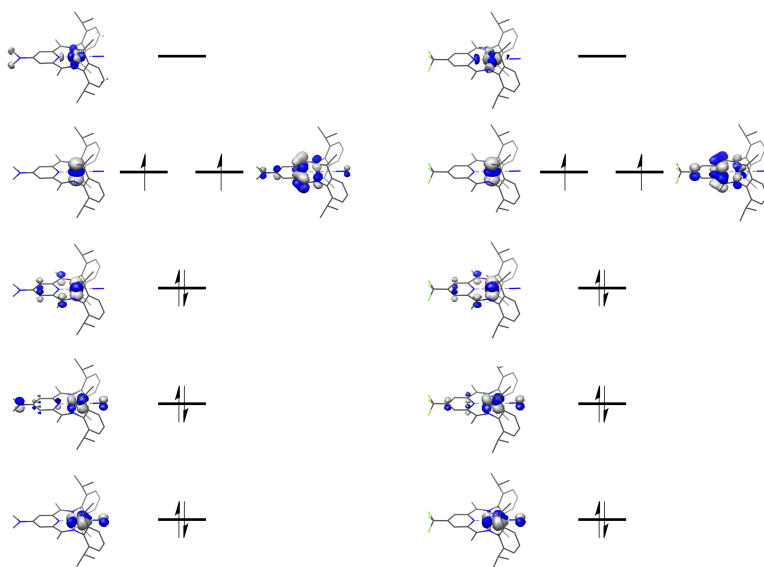


Figure 1.20. Qualitative MO diagrams of (4-R-*i*PrPDI)Fe(N₂) (R = NMe₂, CF₃) obtained from an unrestricted triplet calculation at the B3LYP level.

For (*i*PrPDI)Fe(DMAP), the ground state was best described as an intermediate-spin, iron(II) ion ($S = 1$) antiferromagnetically coupled to a triplet PDI²⁻ diradical ($S = 1$).²² A triplet solution that likely mixes with the ground state was identified on the basis of computed isomer shifts, and can be described as an intermediate-spin, Fe^{II} ion ($S = 1$) with a singlet PDI²⁻ diradical ($S = 0$). This solution was 2.5 kcal/mol higher in energy. Because the initial computations regarding (*i*PrPDI)Fe(DMAP) were performed on a truncated model, the energetics of the full

molecule were reinvestigated. It should be reiterated here that the ground state of (*i*PrPDI)Fe(DMAP) cannot accurately be described at this level of theory, because (*i*PrPDI)Fe(DMAP) does not exhibit a pure ground state. Mixing of excited states likely by spin-orbit coupling prevents straightforward interpretation of DFT results. However, this methodology has been used in a qualitative sense to better understand the electronic structure of pyridine di(imine) iron species exhibiting TIP.²² The broken-symmetry singlet and unrestricted triplet states of (4-Me₂N-*i*PrPDI)Fe(DMAP), (*i*PrPDI)Fe(DMAP) and the theoretical molecule, (4-CF₃-*i*PrPDI)Fe(DMAP) were calculated at the B3LYP level using these models. The restricted singlet solution was also computed for comparison. The geometric parameters of the RKS and broken-symmetry solutions for (4-Me₂N-*i*PrPDI)Fe(DMAP) and (*i*PrPDI)Fe(DMAP) were in excellent agreement with the crystallographic data (**Table 1.15**).

Table 1.15. Comparison of selected experimental and computed bond distances (Å) and angles (°) for (4-Me₂N-*i*PrPDI)Fe(DMAP) and (*i*PrPDI)Fe(DMAP).

	(4-Me ₂ N- <i>i</i> PrPDI)Fe(DMAP)			(<i>i</i> PrPDI)Fe(DMAP)		
	Exp.	RKS	BS(2,2)	Exp.	RKS	BS(2,2)
Fe(1)–N(1)	1.928	1.967	1.986	1.942	1.983	1.985
Fe(1)–N(2)	1.836	1.815	1.871	1.822	1.801	1.873
Fe(1)–N(3)	1.912	1.964	1.985	1.908	1.982	1.986
Fe(1)–N(5)	1.990	2.046	2.054	1.978	2.055	2.053
N(1)–C(2)	1.370	1.345	1.372	1.358	1.340	1.368
N(2)–C(3)	1.372	1.378	1.365	1.390	1.391	1.369
N(2)–C(7)	1.369	1.378	1.365	1.387	1.391	1.369
N(3)–C(8)	1.369	1.345	1.372	1.350	1.340	1.368
C(2)–C(3)	1.415	1.427	1.423	1.405	1.425	1.421
C(7)–C(8)	1.415	1.427	1.423	1.406	1.426	1.422

The full-molecule singlet state calculations on (*i*PrPDI)Fe(DMAP) were consistent with the truncated model calculated previously.²² The energetics of each computed singlet and triplet

state for each (4-R-*i*PrPDI)Fe(DMAP) complex are presented in **Table 1.16**, and qualitative molecular orbital diagrams are presented in **Figure 1.21**. Several similarities were observed between the calculations for (4-R-*i*PrPDI)Fe(DMAP) and the calculations for (4-R-*i*PrPDI)Fe(N₂). For one, the BS(2,2) solutions of (4-Me₂N-*i*PrPDI)Fe exhibits the most stabilization relative to the spin-restricted singlet state as well as unrestricted triplet state. This would imply that (4-Me₂N-*i*PrPDI)Fe(DMAP) should exhibit the least paramagnetically shifted resonances in the series if this phenomenon were due to thermal population of an excited state. However, because this behavior is believed to be due to the mixing of excited states into a singlet ground state, the energetics of these solutions are likely less important in causing the observed NMR spectroscopic behavior. The exact mechanism by which this behavior occurs has not yet been elucidated.

Table 1.16. Electronic descriptions and relative energies (kcal/mol) for the computed singlet and triplet solutions of (4-R-*i*PrPDI)Fe(DMAP) (R = NMe₂, H, CF₃).

Converged Description		Relative Energy
(4-Me₂N-<i>i</i>PrPDI)Fe(DMAP)		
RKS	<i>RKS</i>	26.2
BS(2,2)	<i>BS(2,2)</i>	0.0
BS(3,1)	<i>Triplet</i>	4.7
(<i>i</i>PrPDI)Fe(DMAP)		
RKS	<i>RKS</i>	23.3
BS(2,2)	<i>BS(2,2)</i>	0
BS(3,1)	<i>Triplet</i>	3.5
(4-CF₃-<i>i</i>PrPDI)Fe(DMAP)		
RKS	<i>RKS</i>	22.3
BS(2,2)	<i>BS(2,2)</i>	0.0
BS(3,1)	<i>BS(3,1)</i>	2.72

In summary, the DFT calculations for both the (4-R-*i*PrPDI)Fe(N₂) and (4-R-*i*PrPDI)Fe(DMAP) complexes do demonstrate significant commonalities and differences between

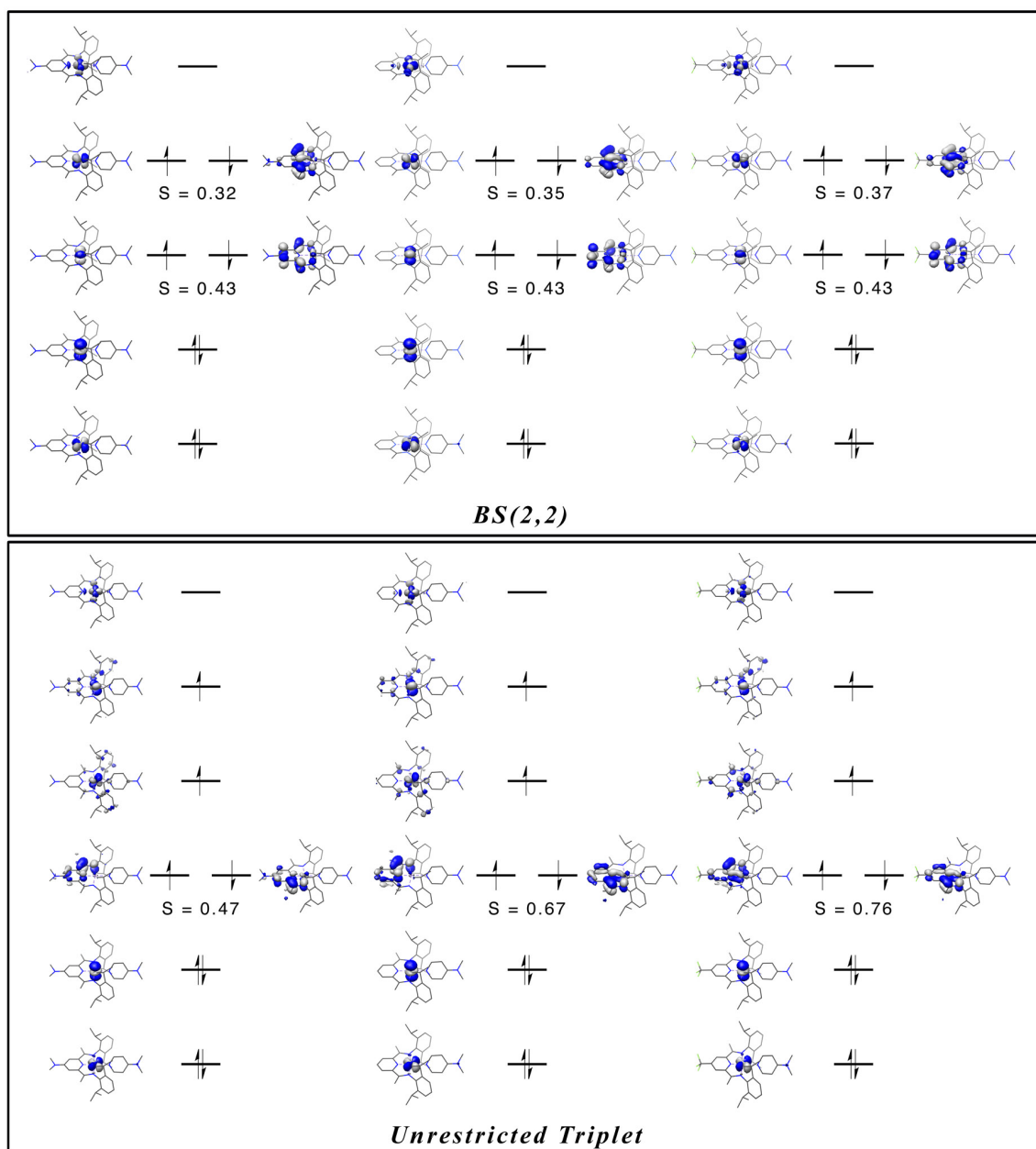


Figure 1.21. Qualitative MO diagrams of (4-R-ⁱPrPDI)Fe(DMAP) (R = NMe₂, left; H, middle; CF₃, right) obtained from BS(2,2) (top) and unrestricted triplet (bottom) DFT calculations at the B3LYP level.

the BS(2,2) and unrestricted triplet solutions (**Figure 1.22**). The BS(2,2) solutions are nearly identical; however, different ordering of the cloverleaf *d*-orbitals and *d*² results in a dissimilar degree of overlap between the metal and ligand magnetic orbitals. The triplet solutions for both

$(i\text{PrPDI})\text{Fe}(\text{N}_2)$ and $(i\text{PrPDI})\text{Fe}(\text{DMAP})$ correspond to different electronic structure descriptions. For $(i\text{PrPDI})\text{Fe}(\text{N}_2)$, the metal is formally reduced and the ligand and metal SOMOs align in parallel spin; whereas for $(i\text{PrPDI})\text{Fe}(\text{DMAP})$, the pyridine di(imine) changes from a triplet diradical in the singlet state to a singlet diradical in the triplet state nearest in energy. For the *para*-substituted series, electron-donating substituents resulted in broken-symmetry solutions that were lower in energy for both the RKS and higher in energy for the unrestricted triplet solutions. While this is consistent with the observed NMR behavior of $(4\text{-R-}i\text{PrPDI})\text{Fe}(\text{N}_2)$, the exact mechanism by which $(4\text{-R-}i\text{PrPDI})\text{Fe}(\text{DMAP})$ experiences TIP is not yet understood, and is likely less sensitive to the energetics of excited states.

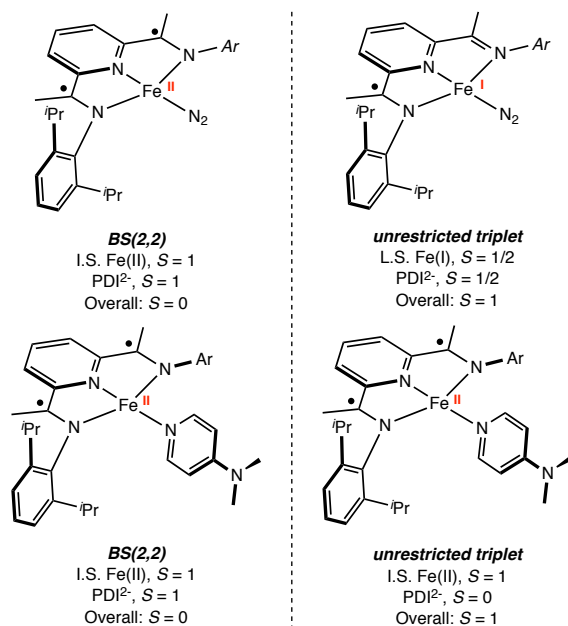


Figure 1.22. Electronic structure descriptions for the singlet and triplet solutions investigated for $(i\text{PrPDI})\text{Fe}(\text{N}_2)$ and $(i\text{PrPDI})\text{Fe}(\text{DMAP})$.

1.6 Hydrogenation: Catalytic Comparison of $(4\text{-R-}i\text{PrPDI})\text{Fe}(\text{N}_2)_2$ Complexes

Having established the electronic influence of the *para*-substituents on the ground state

structure of several pyridine di(imine) iron complexes, the impact on catalytic activity was investigated. Prior work established that hydrogenation of ethyl 3,3-dimethylacrylate served as a useful benchmark for substituted pyridine di(imine) iron complexes because of the lower turnover frequency exhibited by (*i*PrPDI)Fe(N₂) relative to other olefins.^{9,17} A maximum of 65% conversion was observed at 24 hours due to competitive catalyst deactivation by irreversible C–O bond cleavage (**Figure 1.23**).^{9,37} Standard conditions used to assay the activity of the *para*-substituted pyridine di(imine) iron complexes employed a 0.92 M solution of substrate in benzene-*d*₆, 5 mol % (4-*R*-*i*PrPDI)Fe(N₂) and four atmospheres of dihydrogen. When possible, each reaction was carried out to greater than 95% conversion as judged by ¹H NMR spectroscopy.

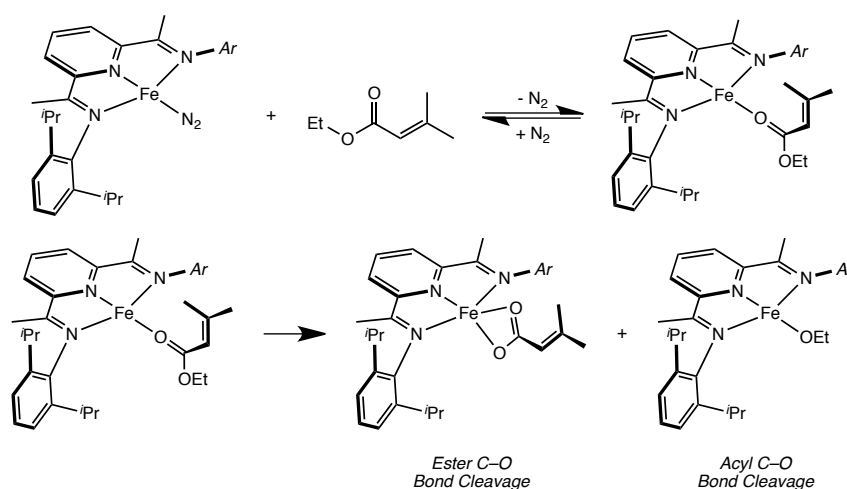


Figure 1.23. Reaction of ethyl 3,3-dimethylacrylate with (*i*PrPDI)Fe(N₂).

The introduction of electron-donating substituents resulted in higher activities for the catalytic hydrogenation of ethyl 3,3-dimethylacrylate (**Figure 1.24**). The benzyl substituted pyridine di(imine) iron dinitrogen compound, (4-Bn-*i*PrPDI)Fe(N₂) reached 80% conversion at 24 hours. Longer reaction times (36 hours) did not result in further conversion of the olefin, likely

due to competitive C–O bond cleavage. The *tert*-butyl derivative, (4-*t*Bu-*i*PrPDI)Fe(N₂), achieved > 95% conversion at 24 hours. Consistent with this trend, the most reduced pyridine di(imine) complex, (4-Me₂N-*i*PrPDI)Fe(N₂), reached > 95% conversion in approximately seven hours. Thus, modest changes to the ligand electronics, but not the overall electronic structure or steric environment, results in dramatic differences in hydrogenation activity.

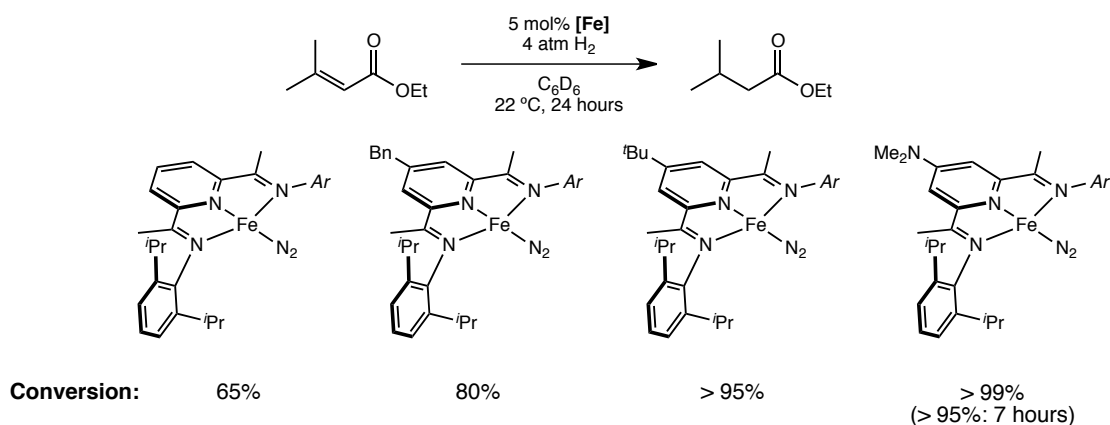


Figure 1.24. Hydrogenation of ethyl 3,3-dimethylacrylate using (4-R-*i*PrPDI)Fe(N₂).

In order to better understand the increased hydrogenation activity exhibited by the pyridine di(imine) iron dinitrogen compounds bearing electron-donating substituents, a series of stoichiometric experiments and NMR studies were conducted. Addition of one equivalent of ethyl 3,3-dimethylacrylate to (4-R-*i*PrPDI)Fe(N₂) (R = H, NMe₂) in benzene-*d*₆ resulted in no color change. Analysis by ¹H NMR spectroscopy indicated that an equilibrium mixture of (4-R-*i*PrPDI)Fe(N₂) and (4-R-*i*PrPDI)Fe(OC(OEt)(CHC(CH₃)₂)) was present (see **Figure 1.23**). The iron ester complex, (4-R-*i*PrPDI)Fe(OC(OEt)(CHC(CH₃)₂)) was identified in each case by the characteristic *m*-pyridine and imine methyl resonances which exhibit temperature independent paramagnetism and are significantly shifted from the value of the free ligand.⁹ The ratio of iron dinitrogen to iron ester complex was sensitive to the nature of the *para*-substituent. Under one

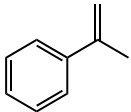
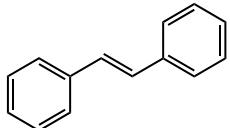
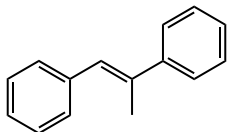
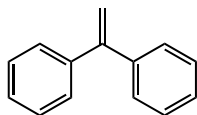
atmosphere of dinitrogen, a ratio of 1:1 (iron dinitrogen:iron ester) was observed for (*i*PrPDI)Fe upon addition of 1 equivalent of ethyl 3,3-dimethylacrylate, and a 3:1 ratio was observed for (4-Me₂N-*i*PrPDI)Fe. This result is in agreement with previous experiments demonstrating the increased affinity of iron for the carbonyl oxygen for less reducing pyridine di(imine) iron complexes (see Chapter 4).³⁸ This was postulated to be the reason for the significant decrease in activity of (*i*PrBPDI)Fe(N₂) with ethyl 3,3-dimethylacrylate. With 20 equivalents of ethyl 3,3-dimethylacrylate, however, the iron ester complex, (4-R-*i*PrPDI)Fe(OC(OEt)(CHC(CH₃)₂)) predominates for both the parent and *para*-dimethylamino derivative under 1 atmosphere of nitrogen.

One potential explanation for the apparent increase in activity for (4-Me₂N-*i*PrPDI)Fe(N₂) would be a less competitive rate of irreversible C–O bond cleavage (*i.e.* slower catalyst deactivation). Addition of 20 equivalents of ethyl 3,3-dimethylacrylate to a 25 mM solution of (4-R-*i*PrPDI)Fe(N₂) in benzene-*d*₆ allowed for a qualitative measure of catalyst deactivation by monitoring the disappearance of the iron ester resonances at 23 °C under an atmosphere of dinitrogen. Ferrocene was used as an internal standard. The rate of disappearance of the iron ester complex was observed to be virtually indistinguishable between (*i*PrPDI)Fe(OC(OEt)(CHC(CH₃)₂)) and (4-Me₂N-*i*PrPDI)Fe(OC(OEt)(CHC(CH₃)₂)), thereby demonstrating that (4-Me₂N-*i*PrPDI)Fe(N₂) does not undergo deactivation at a sufficiently slower rate to account for the observed increase in activity. Thus, the rate of hydrogenation is faster when electron-rich pyridine di(imine) iron complexes are utilized.

The complexity of the system involving ethyl 3,3-dimethylacrylate prompted an investigation of unactivated olefins. In contrast to the activated ester, an ideal substrate would

distinguish between the hydrogenation activity of (*i*PrPDI)Fe(N₂) and (4-Me₂N-*i*PrPDI)Fe(N₂). To this end, the following olefins were screened under identical hydrogenation conditions: α -methylstyrene, *trans*-stilbene, *trans*-methylstilbene and 1,1-diphenylethylene. One exception was *trans*-stilbene, which was assayed as a 0.24 M olefin solution in a 1:4 mixture of benzene-*d*₆ and toluene due to partial solubility of stilbene under the standard conditions. The time to reach > 95% conversion for each catalyst-substrate combination as determined by GC-FID is reported in **Table 1.17**.

Table 1.17. Hydrogenation of unactivated olefins using (4-R-*i*PrPDI)Fe(N₂) (R = H, NMe₂).

Substrate	Time ^a	
	(<i>i</i> PrPDI)Fe(N ₂)	(4-Me ₂ N- <i>i</i> PrPDI)Fe(N ₂)
	< 1 hour	< 1 hour
	< 1 hour	< 1 hour
	20% (at 24 hours)	76% ^b (at 24 hours)
	12 hours	30 hours

^a Time required to reach > 95% conversion as determined by GC-FID.

^b > 95% conversion observed at 60 hours.

Both α -methylstyrene and *trans*-stilbene were hydrogenated to their hydrocarbon products, isopropylbenzene and 1,2-diphenylethane, respectively, in less than an hour under standard reaction conditions. In contrast, *trans*-methylstilbene and 1,1-diphenylethylene exhibited dramatically lower turnover frequencies, allowing for a distinction in activity for

(*i*PrPDI)Fe(N₂) and (4-Me₂N-*i*PrPDI)Fe(N₂). However, opposing trends were observed. For *trans*-methylstilbene, an unactivated tri-substituted olefin, (*i*PrPDI)Fe(N₂) exhibited significantly reduced activity compared with (4-Me₂N-*i*PrPDI)Fe(N₂). For (4-Me₂N-*i*PrPDI)Fe(N₂), longer reaction periods (60 hours) resulted in > 95% conversion to propane-1,2-diyldibenzene. Significant amounts of black precipitate were observed during the reaction and the solution color bleached, indicating catalyst decomposition was also occurring. However, this trend is in agreement with the observations made for ethyl 3,3-dimethylacrylate.

In contrast, 1,1-diphenylethylene reached > 95% conversion, yielding 1,1-diphenylethane, in 12 and 30 hours for (*i*PrPDI)Fe(N₂) and (4-Me₂N-*i*PrPDI)Fe(N₂), respectively, suggesting that electron-donating substituents retard the activity of pyridine di(imine) iron precatalysts towards the hydrogenation of certain unsubstituted olefins. These results are inconsistent with those observed for ethyl 3,3-dimethylacrylate and *trans*-methylstilbene. The less sterically hindered iron dinitrogen precatalyst, [(^{Me}PDI)Fe(N₂)]₂(μ₂-N₂), reached greater than 95% conversion for 1,1-diphenylethylene in less than an hour under identical reaction conditions. Mechanistic investigations into the hydrogenation of 1,1-diphenylethylene with pyridine di(imine) iron precatalysts will be discussed in Chapter 2.

In order to obtain mechanistic insight into the hydrogenation of olefins, the reaction of (4-Me₂N-*i*PrPDI)Fe(N₂) with deuterium gas was examined. Previous work has demonstrated that reaction of (*i*PrPDI)Fe(N₂) with D₂ results in complete, selective incorporation of deuterium into the methyl groups of the 2,6-diisopropyl aryl substituents; (*i*Pr*PDI)Fe(N₂) (*i*Pr*PDI = 2,6-(2,6-((CD₃)₂CH)₂-C₆H₃N=CCH₃)-C₅H₂N) is obtained upon exposure to N₂.⁸ Deuteration likely results from formation of a cyclometallated hydride species, which may serve as a catalytic

intermediate. The currently proposed mechanism is presented in **Figure 1.25**. Many mechanistic questions remain unanswered as to the coordination number of such an intermediate, the potential for imine dissociation resulting in a κ^2 -pyridine imine chelate, and ground state electronic structures. Bart *et al.* demonstrated that deuteration of 1-hexene under catalytic conditions yielded 1,2-*d*₂-hexane with little evidence for deuterium incorporation into the pyridine di(imine) ligand. In contrast, the cyclometallated intermediate was implicated in the mechanism of ethane loss from (*i*PrPDI)Fe(CH₂CH₃).³⁹

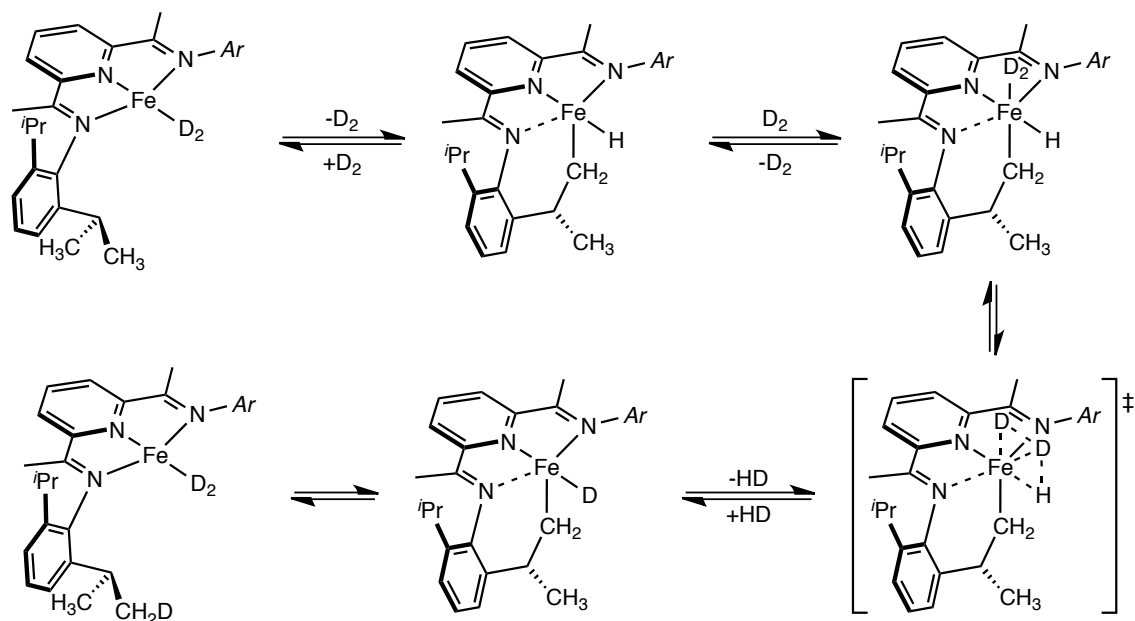


Figure 1.25. Proposed mechanism for selective deuterium incorporation into the isopropyl methyl groups.

Because the cyclometallated species represents a potential intermediate in the mechanism of olefin hydrogenation, the relative rate of deuterium incorporation into (*i*PrPDI)Fe(N₂) and (4-Me₂N-*i*PrPDI)Fe(N₂) was assayed. Exposure of 6.7 mM toluene solutions of (*i*PrPDI)Fe(N₂) and (4-Me₂N-*i*PrPDI)Fe(N₂) to 4 atm of D₂ for 12 hours at 23 °C, followed by addition of 1 atmosphere of carbon monoxide, yielded mixtures of the isotopologues of (4-R-*i*Pr*PDI)Fe(CO)₂

(R = H, NMe₂). Addition of CO following deuteration ensured that the absence of deuterium incorporation was not a result of decomposition. Analysis by ¹H NMR spectroscopy following isolation and recrystallization revealed > 90% and 40–43% deuterium incorporation for (ⁱPrPDI)Fe(N₂) and (4-Me₂N-ⁱPrPDI)Fe(N₂), respectively.

This data suggests that either the rate of C–H oxidative addition (and all preceding steps) is retarded by more reducing pyridine di(imine) iron complexes, or that the rate of reductive elimination is significantly faster than the rate of sigma-bond metathesis or β-hydrogen elimination. This hypothesis is also consistent with the observation that the iron alkyl complex, (4-^tBu-ⁱPrPDI)Fe(CH₂CH₃) was demonstrated to have a significantly longer half-life than (ⁱPrPDI)Fe(CH₂CH₃),⁴⁰ implying that more reduced pyridine di(imine) iron alkyl complexes are either less susceptible to β-hydrogen elimination or that the rate of β-hydrogen insertion becomes competitive with olefin dissociation. The observed trends for (4-Me₂N-ⁱPrPDI)Fe(N₂) are unusual: strongly electron-donating ligands typically promote oxidative addition and retard the rate of reductive elimination for second- and third-row metals.⁴¹ We would therefore expect faster deuteration of (4-Me₂N-ⁱPrPDI)Fe(N₂). This trend is rationalized on the basis of thermodynamic arguments; however, exceptions have been reported.⁴²

1.7 [2π + 2π] Cycloaddition: Catalytic Comparison of (4-R-ⁱPrPDI)Fe(N₂)₂ Complexes

Another catalytic process that is a hallmark of reduced pyridine di(imine) iron dinitrogen complexes is the formal [2π + 2π] cycloaddition of α,ω-heptadienes.¹⁰ This methodology has been expanded to the reductive cyclization of 1,6-enynes and diynes,⁴³ from which metallocyclic intermediates have been isolated.⁴⁴ Studies on the electronic structure of a model complex,

(*i*PrPDI)Fe(2,2'-biphenyl), prepared from the reaction of (*i*PrPDI)Fe(N₂) with biphenylene, indicate that the ground state of the complex at 295 K is an intermediate-spin Fe^{III} center (*S* = 3/2) antiferromagnetically coupled to a pyridine di(imine) radical anion (*S* = 1/2).¹⁴ Therefore, the net transformation of the proposed iron diolefin compound to the metallocyclic intermediate is believed to involve cooperative loss of one electron from the metal center and one electron from the pyridine di(imine) chelate. The current, proposed mechanism is presented in **Figure 1.26**. It should be noted that very little is known about the mechanism of oxidative coupling, and that several steps—including potential imine dissociation—may be required for this event to occur. Additionally, little is known about the electronic structure of the proposed diolefin adduct. Bouwkamp *et al.*¹⁰ originally proposed the electronic structure of this intermediate using the butadiene adduct, (*i*PrPDI)Fe(η²,η²-C₄H₆) as a model. The fate of the iron complex following catalysis was found to vary depending upon the substrate; however, in the simplest situation, where the substrate was *N,N*-diallyl-*tert*-butylamine, (*i*PrPDI)Fe(N₂) was regenerated.

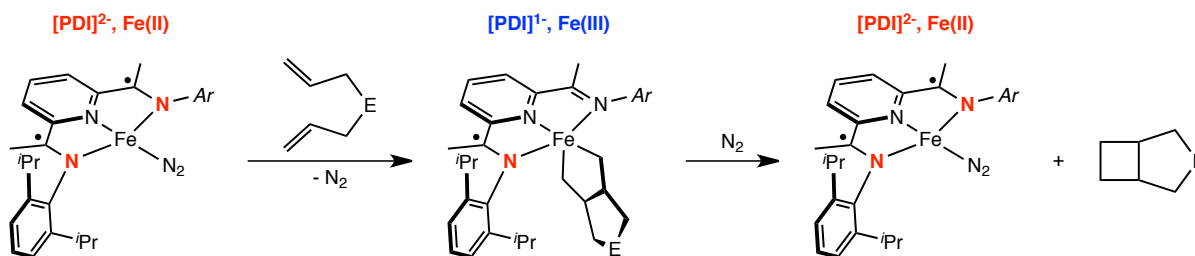


Figure 1.26. Proposed mechanism of [2π + 2π] cyclization of α,ω-heptadienes.

Preliminary investigation regarding the [2π + 2π] cycloaddition of *N,N*-diallyltosylamine with [(^{Me}PDI)Fe(N₂)]₂(μ₂-N₂) and (*i*PrPDI)Co(N₂) demonstrated loss of selectivity for the bicyclo[3.2.0]heptane product.¹¹ In addition to the expected [2π + 2π] product, 3-tosyl-3-azabicyclo[3.2.0]heptane (**A**), the pyrrolidine, 3-methyl-4-methylene-1-tosylpyrrolidine (**B**) was

observed in a 3:7 (**A**:**B**) ratio and a 1:1 ratio for $[(^{\text{Me}}\text{PDI})\text{Fe}(\text{N}_2)]_2(\mu_2\text{-N}_2)$ and $(^{\text{iPr}}\text{PDI})\text{Co}(\text{N}_2)$, respectively. Pyrrolidine formation is currently proposed to result from β -hydride elimination of the pyridine di(imine) metalocycle and is followed by rapid C–H reductive elimination (**Figure 1.27**). For the less sterically demanding catalyst, $[(^{\text{Me}}\text{PDI})\text{Fe}(\text{N}_2)]_2(\mu_2\text{-N}_2)$, the rate of β -hydride elimination becomes competitive and determines the product ratios of **A** and **B** type substrates.

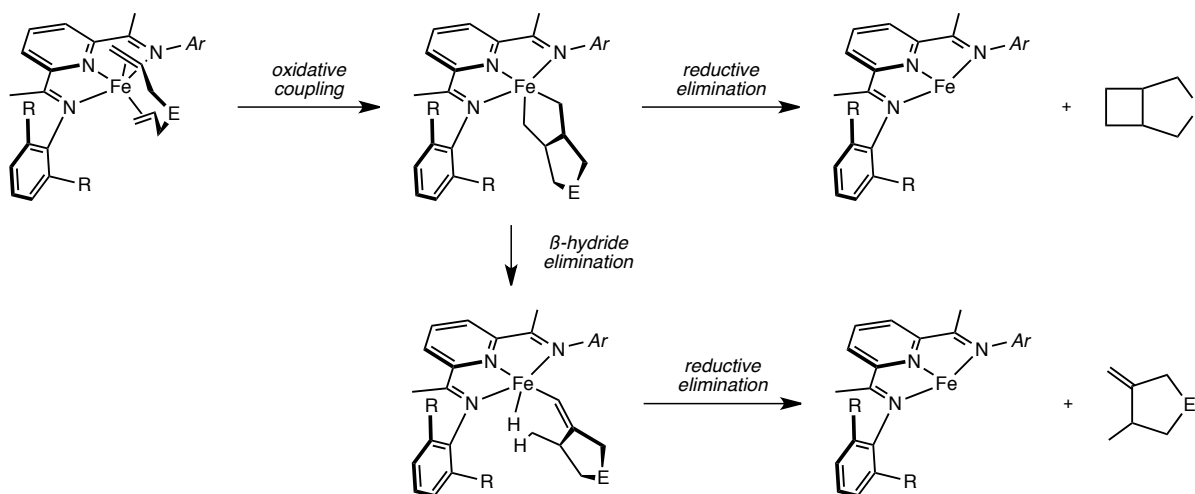


Figure 1.27. Proposed mechanisms accounting for formation **A**- and **B**-type products.

In order to probe the influence of *para*-substituents on the activity of the pyridine di(imine) iron nitrogen compounds towards the $[2\pi + 2\pi]$ cycloaddition of α,ω -heptadienes, the cyclization of *N,N*-diallylaniline using the most reduced *para*-substituted pyridine di(imine) iron nitrogen compound, $(4\text{-Me}_2\text{N-}^{\text{iPr}}\text{PDI})\text{Fe}(\text{N}_2)$ was investigated. $[(^{\text{Me}}\text{PDI})\text{Fe}(\text{N}_2)]_2(\mu_2\text{-N}_2)$ and $(^{\text{iPr}}\text{PDI})\text{Co}(\text{N}_2)$ were also included in this study for comparison. Typical reaction conditions used to assay the activity of the pyridine di(imine) metal dinitrogen complexes utilized 0.49 M benzene- d_6 solutions of *N,N*-diallylaniline and 5 mol % of the metal complex (2.5 mol % of the dimeric iron dinitrogen compound) at 23 °C under 1 atmosphere of dinitrogen. In all cases, the reaction was run to > 95% consumption of the 1,6-diolefin as determined by ^1H NMR spectroscopy. The results of these experiments are presented in **Figure 1.28**.

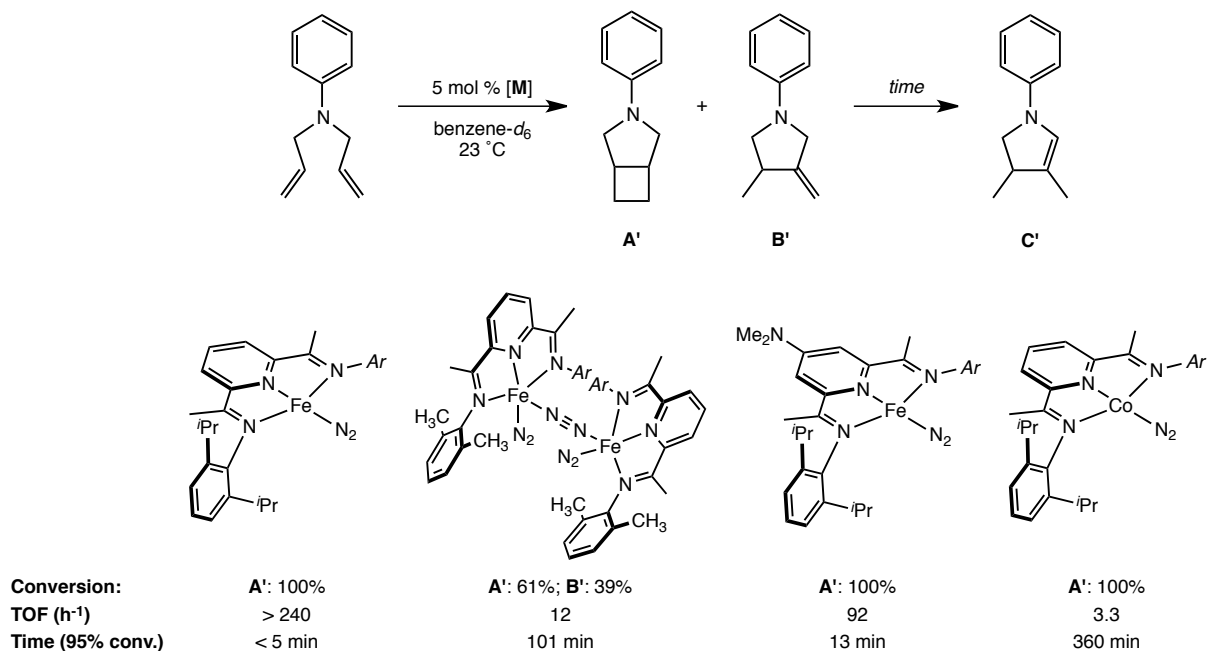


Figure 1.28. $[2\pi + 2\pi]$ cycloaddition of *N,N*-diallylaniline using reduced metal iron and cobalt dinitrogen complexes.

Consistent with previous results, the less sterically congested pyridine di(imine) iron dinitrogen compound, $[(^{\text{Me}}\text{PDI})\text{Fe}(\text{N}_2)]_2(\mu_2\text{-N}_2)$, was significantly less active than the parent complex, $(^{\text{iPr}}\text{PDI})\text{Fe}(\text{N}_2)$. However, a 3:2 mixture of **A'** (3-phenyl-3-azabicyclo[3.2.0]heptane) to **B'** (3-methyl-4-methylene-1-phenylpyrrolidine) was obtained following consumption of *N,N*-diallylaniline. Compared with the result obtained for *N,N*-diallyltosylamine (which favored formation of the **B**-type product), this experiment demonstrates that the ratio of **A**- and **B**-type products is substrate-dependent, and is most likely a result of the steric environment of the substrate. Allowing this mixture to stand at 23 °C under these conditions for hours resulted in further isomerization of **B'** to **C'** (3,4-dimethyl-1-phenyl-2,3-dihydro-1H-pyrrole). Addition of 1 atm of H_2 to this product mixture at 23 °C resulted in hydrogenation of **C'** to yield **D'**, 3,4-dimethyl-1-phenylpyrrolidine.

All diisopropyl-aryl substituted pyridine di(imine) precatalysts were selective for the

formation of **A'** (azabicyclo[3.2.0]heptane). The cobalt dinitrogen complex, (*i*PrPDI)Co(N₂) exhibited the lowest turnover frequency of the series (3.3 h⁻¹). The *para*-dimethylamino variant, (4-Me₂N-*i*PrPDI)Fe(N₂) was less active than (*i*PrPDI)Fe(N₂) and exhibited a turnover frequency of approximately 90 h⁻¹ (as compared to > 240 h⁻¹). The cause of the lower activity exhibited by (4-Me₂N-*i*PrPDI)Fe(N₂) is currently unknown. However, isotope studies conducted by Sylvester demonstrated that turnover of *N,N*-bis(2-deuteroallyl)-tosylamine by (*i*PrPDI)Fe(N₂) resulted in deuterium incorporation into the methyl group of the isopropyl aryl substituent, and scrambling of deuterium into the olefin methylene position.⁴⁵ The mechanism currently proposed for [2π + 2π] cycloaddition of α,ω-heptadienes does not rationalize this data, suggesting that a fundamental step is not yet completely understood. However, given that deuterium incorporation into (4-Me₂N-*i*PrPDI)Fe(N₂) was found to be significantly slower than (*i*PrPDI)Fe(N₂)₂, this step most likely rationalizes the observed decrease in activity for electron-donating substituents.

Synthesis of the (4-Me₂N-*i*PrPDI)Fe(2,2'-biphenyl) was targeted in an attempt to understand the mechanism of oxidative addition by reduced pyridine di(imine) iron complexes. Addition of one equivalent of biphenylene to (4-Me₂N-*i*PrPDI)Fe(N₂) in benzene-*d*₆ did not yield formation of any new diamagnetic or paramagnetic species at 23 °C over the course of hours as determined by ¹H NMR spectroscopy. After one week, approximately 35% conversion of biphenylene to biphenyl was observed. This occurs presumably through oxidative addition and subsequent transfer hydrogenation from the isopropyl aryl substituent, resulting in the intramolecular iron olefin complex. The intramolecular iron olefin complex of (*i*PrPDI)Fe(N₂) is NMR-silent,⁴⁶ and it is therefore unsurprising that no new species were identified by ¹H NMR spectroscopy. The inability to observe the biphenyl adduct, (4-Me₂N-*i*PrPDI)Fe(2,2'-biphenyl),

might also suggest that oxidation of biphenylene is rate-limiting, and that irreversible transfer dehydrogenation occurs at a rate that prevents observation of the metallocycle by ^1H NMR. This hypothesis has not yet been experimentally demonstrated. While rate limiting oxidative addition is consistent with the deuterium incorporation experiment described in Section 1.6, rapid transfer dehydrogenation is not. Little is currently known about the mechanism of transfer dehydrogenation from formally iron(II) pyridine di(imine) complexes.

1.8 Conclusions

A series of *para*-substituted pyridine di(imine) ligands and their iron dihalide, dicarbonyl, and dinitrogen complexes were prepared, as well as one example of a neutral pyridine di(imine) iron complex bearing a principally σ -donating ligand, (4-Me₂N-*i*PrPDI)Fe(DMAP). The ability to tune the redox behavior of the pyridine di(imine) scaffold by 470 mV through rational ligand design was demonstrated. Despite this, no significant change was observed in the ground state description of any of the *para*-substituted pyridine di(imine) iron complexes, (4-R-*i*PrPDI)Fe(L)_n (L = CO, n = 2; L = N₂, n = 1; L = DMAP, n = 1). Cyclic voltammetry, infrared and NMR spectroscopies were more sensitive to the energetic perturbations caused by substitution of the pyridine di(imine) chelate.

The ^1H NMR spectroscopic behavior of the four-coordinate complexes, (4-R-*i*PrPDI)Fe(N₂) and (4-R-*i*PrPDI)Fe(DMAP), provided insight into the coupling of the metal-chelate magnetic orbitals. For the four-coordinate iron dinitrogen complex, spectroscopic and computational data demonstrated that introduction of electron-donating substituents resulted in a more thermally inaccessible triplet state. Contrastingly, for the four-coordinate iron DMAP

complexes, spectroscopic data indicated that electron-donating substituents increased the degree of excited state mixing into the ground state. Although this phenomenon was investigated by DFT, a higher level of theory is necessary to accurately describe and understand the ground state of (4-R-*i*PrPDI)Fe(DMAP).

Relatively small perturbations to the coupling of the metal-chelate magnetic orbitals significantly affected the catalytic performance of the *para*-substituted pyridine di(imine) iron dinitrogen compounds. In general, introduction of electron-donating substituents resulted in dramatically increased turnover frequencies for many of the olefins examined in this study. One exception was 1,1-diphenylethylene, which will be further discussed in Chapter 2. This example definitively illustrates that the rate effect of *para*-substitution is substrate dependent. The *para*-dimethylamino substituted pyridine di(imine) complex, (4-Me₂N-*i*PrPDI)Fe(N₂) was also demonstrated to be less active towards the [2 π + 2 π] cyclization of *N,N*-diallylaniline than (*i*PrPDI)Fe(N₂); however, selectivity for the azabicycl[3.2.0]heptane product was maintained.

1.9 Experimental

All air- and moisture-sensitive manipulations were carried out using standard vacuum line, Schlenk, and cannula techniques or in an MBraun inert atmosphere dry box containing an atmosphere of purified nitrogen. Solvents for air- and moisture-sensitive manipulations were initially dried and deoxygenated using literature procedures.⁴⁷ Benzene-*d*₆ was purchased from Cambridge Isotope Laboratories and dried over 4 Å molecular sieves. The following compounds were prepared according to literature procedure: 4-Bn-*i*PrPDI,²⁵ 4-*t*Bu-*i*PrPDI,²⁶ dimethyl 4-(trifluoromethyl)pyridine-2,6-dicarboxylate,²⁹ dimethyl 4-(dimethylamino)pyridine-2,6-

dicarboxylate,⁴⁸ [(^{Me}PDI)Fe(N₂)]₂(μ₂-N₂),¹⁷ and (^{iPr}PDI)Co(N₂).⁴⁹ Ethyl 3,3-dimethylacrylate and α-methylstyrene, were purchased from commercial sources and stirred over calcium hydride for at least 24 hours prior to being vacuum transferred to a dry flask, brought into a nitrogen-filled glovebox, and filtered through activated, neutral alumina. *Trans*-stilbene and *trans*-methylstilbene were purchased from commercial sources and dried under vacuum for 16 hours prior to use. 1,1-diphenylethylene was purchased from a commercial source and stirred over calcium hydride for 24 hours, freeze-pump degassed on a high vacuum line, brought into a dinitrogen filled glovebox, and passed through activated, neutral alumina prior to use.

¹H NMR spectra were recorded on Varian Mercury 300, Inova 400, 500, and 600 spectrometers operating at 299.76, 399.78, 500.62, and 599.78 MHz, respectively. ¹³C NMR spectra were recorded on an Inova 500 spectrometer operating at 125.893 MHz. All ¹H and ¹³C NMR chemical shifts are reported relative to SiMe₄ using the ¹H (residual) and ¹³C chemical shifts of the solvent as a secondary standard. For diamagnetic complexes, many assignments were made based on COSY and HSQC NMR experiments. Solution magnetic moments were determined by Evans method⁵⁰ using a ferrocene standard and are the average value of at least two independent measurements. Magnetic susceptibility balance measurements were performed with a Johnson Matthey instrument that was calibrated with HgCo(SCN)₄. All solid-state values were recorded at 21 °C unless otherwise noted. Peak widths at half height are reported for paramagnetically broadened and shifted resonances. Infrared spectra were collected on a Thermo Nicolet spectrometer. High-resolution mass spectra were collected on an Agilent 6220 Accurate-Mass Time-of-Flight LC/MS. The mass spectrometer was calibrated externally before each use with purine and the Agilent ES-TOF tuning mix (part number = G1969-85000). These

compounds were assigned a (M+H)⁺ *m/z* ratio of 121.050873 and 922.009798 respectively. Elemental analyses were performed at Robertson Microlit Laboratories, Inc., in Ledgewood, NJ.

Cyclic voltammograms (CVs) were collected in THF solution (1 mM in compound) with [nBu₄N][PF₆] (0.1 M), using a 3 mm glassy carbon working electrode, platinum wire as the counter electrode, and silver wire as the reference in a drybox equipped with electrochemical outlets. CVs were recorded using a BASi EC Epsilon electrochemical workstation and analyzed using the BASi Epsilon-EC software. All CVs were run at a scan rate of 100 mV/s at 295 K. Potentials are reported versus ferrocene/ferrocenium, and were obtained using the *in situ* method.⁵¹

Single crystals suitable for X-ray diffraction were coated with polyisobutylene oil in a drybox, transferred to a nylon loop and then quickly transferred to the goniometer head. Data for (4-Me₂N-ⁱPrPDI)Fe(N₂)₂ was collected using a Bruker X8 APEX2 diffractometer equipped with a molybdenum X-ray tube ($\lambda = 0.71073 \text{ \AA}$). The space group was identified and the data were processed using the Bruker SAINT+ program and corrected for absorption using SADABS. The structures were solved using direct methods (SHELXS) completed by subsequent Fourier synthesis and refined by full-matrix least-squares procedures. A Bruker APEX2 Duo diffractometer equipped with molybdenum and copper X-ray tubes ($\lambda = 0.71073$ and 1.54178 \AA , respectively) was used to collect data for (4-CF₃-ⁱPrPDI)FeCl₂ (Cu source), (4-Me₂N-ⁱPrPDI)FeCl₂ (Cu source), (4-^tBu-ⁱPrPDI)Fe(N₂)₂ (Cu source), (4-Me₂N-ⁱPrPDI)Fe(CO)₂ (Cu source), and (4-Me₂N-ⁱPrPDI)Fe(DMAP) (Cu source). The space group was identified and the data were processed using the Bruker SAINT+ program and corrected for absorption using SADABS. The

structures were solved using direct methods (SIR92) completed by subsequent Fourier synthesis and refined by full-matrix least-squares procedures.

^{57}Fe Mössbauer spectra were recorded on a SEE Co. Mössbauer spectrometer (MS4) at 80 K in constant acceleration mode. $^{57}\text{Co/Rh}$ was used as the radiation source. WMOSS software was used for the quantitative evaluation of the spectral parameters (least squares fitting to Lorentzian peaks. The temperature of the samples was controlled by a Janis Research Co. CCS-850 He/N₂ cryostat within an accuracy of ± 1 K. Isomer shifts were determined relative to α -iron at 298K.

All DFT calculations were performed with the *ORCA* program package.⁵² The geometry optimizations of the complexes and single-point calculations on the optimized geometries were carried out at the B3LYP level⁵³ of DFT. This hybrid functional often gives better results for transition-metal compounds than pure gradient-corrected functionals, especially with regard to metal-ligand covalency.⁵⁴ The all-electron Gaussian basis sets were those developed by Ahlrichs' group.⁵⁵ Triple- ζ quality basis sets def2-TZVP with one set of polarization functions on the metals and on the atoms directly coordinated to the metal center were used. For the carbon and hydrogen atoms, slightly smaller polarized split-valence def2-SV(P) basis sets were used that were of double- ζ quality in the valence region and contained a polarizing set of d functions on the non-hydrogen atoms. Auxiliary basis sets were chosen to match the orbital basis.⁵⁶ The RIJCOSX⁵⁷ approximation was used to accelerate the calculations.

Throughout this dissertation, computational results are described using the BS approach by Ginsberg⁵⁸ and Noodleman et al.⁵⁹ Because several BS solutions to the spin-unrestricted Kohn-Sham equations may be obtained, the general notation BS(m,n)⁶⁰ has been adopted, where

m (n) denotes the number of spin-up (spin-down) electrons at the two interacting fragments. Canonical and corresponding⁶¹ orbitals, as well as spin density plots, were generated with the program *Molekel*.⁶²

Nonrelativistic single-point calculations employed the CP(PPP) basis set for iron.⁶³ The Mößbauer isomer shifts were calculated from the computed electron densities at the iron centers as previously described.⁶⁴

Preparation of 4-dimethylamino-2,6-diacetylpyridine. A 250-mL, round-bottom flask was charged with dimethyl 4-(dimethylamino)pyridine-2,6-dicarboxylate (5.00 g, 21.0 mmol) and sodium ethoxide (6.14 g, 90.2 mmol, 4.3 eq). To this mixture was added 50 mL ethyl acetate with rapid stirring. After 1 hour, the reaction was brought to reflux, and an additional 75 mL of ethyl acetate was added once the reaction mixture thickened. After 6 hours, the mixture was allowed to cool to room temperature and 20 mL of conc. HCl was added dropwise. Refluxing was resumed for an additional 12 hours, after which the reaction was allowed to cool to room temperature and water was added until the salt was dissolved. The resulting mixture was neutralized with sodium bicarbonate, and extracted three times with dichloromethane. The organic extracts were dried with magnesium sulfate, filtered, and concentrated *in vacuo* to yield 3.67 g (84% yield) of a light brown solid identified as 4-dimethylamino-2,6-diacetylpyridine. HR-MS (+ESI): Calc'd for C₁₁H₁₅N₂O₂, [M+H]⁺, m/z 207.11280. Found, m/z 207.11284. ¹H NMR (chloroform-*d*, 22 °C): δ = 2.78 (s, 6H, CCH₃), 3.17 (s, 6H, N(CH₃)₂), 7.46 (s, 2H, *m*-pyr). ¹³C {¹H} NMR (chloroform-*d*, 22 °C): δ = 25.9 (C(O)CH₃), 39.6 (N(CH₃)₂), 106.8 (*m*-pyr), 153.4 (*o*-pyr), 155.6 (*p*-pyr), 201.2 (C(O)CH₃).

Preparation of 4-Me₂N-ⁱPrPDI. A 100-mL, round-bottom flask was charged with 2.0 g (9.7 mmol) 4-dimethylamino-2,6-diacetylpyridine, 4.3 g (24 mmol) 2,6-diisopropylaniline, 2 drops of formic acid and 25 mL methanol. The reaction was brought to reflux and stirred for 72 hours. After this time, the reaction mixture was allowed to cool to room temperature, and then placed in an ice bath. Filtration of the resulting solid yielded 3.2 g (63% yield) of a pale yellow solid identified as 4-Me₂N-ⁱPrPDI. HR-MS (+ESI): Calc'd for C₃₅H₄₉N₄, [M+H]⁺, *m/z* 525.39517. Found, *m/z* 525.39521. ¹H NMR (benzene-*d*₆, 22 °C): δ = 1.19 (d, 7 Hz, 12H, CH(CH₃)₂), 1.25 (d, 7 Hz, 12H, CH(CH₃)₂), 2.38 (s, 6H, N(CH₃)₂ or CCH₃), 2.43 (s, 6H, N(CH₃)₂ or CCH₃), 3.05 (spt, 4H, CH(CH₃)₂), 7.16–7.23 (m, 6H, *m*-, *p*-aryl), 8.04 (s, 2H, *m*-pyr). ¹³C {¹H} NMR (benzene-*d*₆, 22 °C): δ = 17.7 (C(N)CH₃), 23.1 (CH(CH₃)₂), 23.5 (CH(CH₃)₂), 28.8 (CH(CH₃)₂), 38.6 (N(CH₃)₂), 105.3 (*m*-pyr), 123.6 (*aryl*), 124.1 (*aryl*), 136.1 (*aryl*), 147.4 (*aryl*), 155.6 (*o*-pyr), 156.1 (*p*-pyr), 168.1 (C(N)CH₃).

Preparation of 4-CF₃-ⁱPrPDI. 4-trifluoromethyl-2,6-diacetylpyridine was first prepared in a similar manner to 4-dimethylamino-2,6-diacetylpyridine with 1.76 g (6.65 mmol) dimethyl 4-(trifluoromethyl)pyridine-2,6-dicarboxylate, 1.96 g (36.3 mmol) sodium ethoxide, and 15 mL ethyl acetate. An additional 50 mL of ethyl acetate was added during the course of the reaction. The crude, golden oil (1.50 g) isolated from the reaction, identified as 4-trifluoromethyl-2,6-diacetylpyridine was used without purification for the synthesis of 4-CF₃-ⁱPrPDI. ¹H NMR (chloroform-*d*, 22 °C): δ = 2.82 (s, 6H, CCH₃), 8.43 (s, 2H, *m*-pyr). ¹⁹F NMR (benzene-*d*₆, 22 °C): δ = -63.5. 4-CF₃-ⁱPrPDI was prepared in a similar manner to 4-Me₂N-ⁱPrPDI with 1.00 g (4.32

mmol) 4-trifluoromethyl-2,6-diacetylpyridine, 2.30 g (12.9 mmol) 2,6-diisopropylaniline and two drops of formic acid in 15 mL methanol. Following filtration, 0.78 g (33% yield) of 4-CF₃-ⁱPrPDI was isolated as a light yellow solid. HR-MS (+ESI): Calc'd for C₁₀H₉F₃NO₂, [M+H]⁺, *m/z* 550.34036. Found, *m/z* 550.34072. ¹H NMR (benzene-*d*₆, 22 °C): δ = 1.11 (d, 4 Hz, 12H, CH(CH₃)₂), 1.13 (d, 4Hz, 12H, CH(CH₃)₂), 2.18 (s, 6H, CCH₃), 2.82 (m, 4H, CH(CH₃)₂), 7.12–7.18 (m, 6H, *m*-, *p*-*aryl*), 8.88 (s, 2H, *m*-*pyr*). ¹³C {¹H} NMR (benzene-*d*₆, 22 °C): δ = 17.2 (C(N)CH₃), 23.0 (CH(CH₃)₂), 23.4 (CH(CH₃)₂), 28.9 (CH(CH₃)₂), 118.0 (3 Hz, *m*-*pyr*), 123.1 (*aryl*), 123.5 (273 Hz, CF₃), 123.6 (*aryl*), 135.8 (*aryl*), 140.1 (q, 34 Hz, *p*-*pyr*), 146.4 (*aryl*), 157.1 (*o*-*pyr*), 166.1 (C(N)CH₃). ¹⁹F NMR {¹H} (benzene-*d*₆, 22 °C): δ = -63.3.

Preparation of (4-Me₂N-ⁱPrPDI)FeCl₂. A 20-mL scintillation vial was charged with 0.083 g (0.65 mmol) of FeCl₂ and 2 mL THF. A solution of 0.36 g (0.68 mmol) 4-Me₂N-ⁱPrPDI in 5 mL THF was then added to the slurry with rapid stirring, causing an immediate color change to dark blue-green. After 12 hours, 10 mL of pentane was added, causing the product to precipitate from solution. Filtration from THF/pentane and washing with diethyl ether yielded 0.42 g (98% yield) of analytically pure blue-green solid identified as (4-Me₂N-ⁱPrPDI)FeCl₂. Analysis for C₃₅H₄₈N₄FeCl₂: Calc. C, 64.52; H, 7.43; N, 8.60. Found: C, 64.58; H, 7.69; N, 8.34. Solid state magnetic susceptibility: μ_{eff} = 4.5 μ_B. ¹H NMR (dichloromethane-*d*₂, 22 °C): δ = -22.4 (200 Hz, 4H, CH(CH₃)₂), -7.6 (22 Hz, 2H, *p*-*aryl*), -4.7 (42 Hz, 6H, CCH₃), -4.6 (66 Hz, 12H, CH(CH₃)₂), -3.7 (21 Hz, 12H, CH(CH₃)₂), 15.2 (21 Hz, 4H, *m*-*aryl*), 27.8 (22 Hz, 6H, N(CH₃)₂), 91.9 (45 Hz, 2H, *m*-*pyr*).

Preparation of (4-*t*-Bu-^{*i*}PrPDI)FeBr₂. The compound was prepared in a similar manner to (4-Me₂N-^{*i*}PrPDI)FeCl₂ with 1.50 g (2.79 mmol) of 4-*t*-Bu-^{*i*}PrPDI and 0.57 g (2.6 mmol) FeBr₂. Filtration from THF/pentane and washing with diethyl ether yielded 1.93 g (97% yield) of analytically pure, dark blue solid identified as (4-*t*-Bu-^{*i*}PrPDI)FeBr₂. Analysis for C₃₇H₅₁N₃FeBr₂: Calc. C, 58.98; H, 6.82; N, 5.58. Found: C, 59.11; H, 6.71; N, 5.29. Magnetic susceptibility (magnetic susceptibility balance): $\mu_{\text{eff}} = 4.5 \mu_{\text{B}}$. ¹H NMR (dichloromethane-*d*₂, 22 °C): $\delta = -23.7$ (30 Hz, 6H, CCH₃), -14.2 (290 Hz, 4H, CH(CH₃)₂), -10.6 (18 Hz, 2H, *p*-aryl), -5.2 (15 Hz, 12H, CH(CH₃)₂), -1.9 (66 Hz, 12H, CH(CH₃)₂), 4.8 (7 Hz, 9H, C(CH₃)₃), 14.8 (16 Hz, 4H, *m*-aryl), 78.0 (44 Hz, 2H, *m*-pyr).

Preparation of (4-Bn-^{*i*}PrPDI)FeCl₂. The compound was prepared in a similar manner to (4-Me₂N-^{*i*}PrPDI)FeCl₂ with 0.40 g (0.70 mmol) of 4-Bn-^{*i*}PrPDI and 0.084 g (0.66 mmol) FeCl₂. Filtration from THF/pentane and washing with diethyl ether yielded 0.41 g (88% yield) of analytically pure, blue solid identified as (4-Bn-^{*i*}PrPDI)FeCl₂. Analysis for C₄₀H₄₉N₃FeCl₂: Calc. C, 68.77; H, 7.07; N, 6.02. Found: C, 68.75; H, 6.71; N, 5.82. Magnetic susceptibility (magnetic susceptibility balance): $\mu_{\text{eff}} = 4.6 \mu_{\text{B}}$. ¹H NMR (dichloromethane-*d*₂, 22 °C): $\delta = -35.1$ (19 Hz, 2H, *p*-Bn), -32.8 (39 Hz, 6H, CCH₃), -25.2 (279 Hz, 4H, CH(CH₃)₂), -10.6 (21 Hz, 2H, *p*-aryl), -6.8 (19 Hz, 12H, CH(CH₃)₂), -5.6 (70 Hz, 12H, CH(CH₃)₂), 9.3 (20 Hz, 1H, *p*-Bn), 9.7 (23 Hz, 2H, *p*-Bn), 13.2 (20 Hz, 2H, *p*-Bn), 14.4 (23 Hz, 4H, *m*-aryl), 83.5 (49 Hz, 2H, *m*-pyr).

Preparation of (4-CF₃-^{*i*}PrPDI)FeCl₂. The compound was prepared in a similar manner to (4-Me₂N-^{*i*}PrPDI)FeX₂ with 0.40 g (0.73 mmol) of 4-CF₃-^{*i*}PrPDI and 0.090 g (0.71 mmol) FeCl₂.

Filtration from THF/pentane and washing with diethyl ether yielded 0.47 g (98% yield) of analytically pure blue-green solid identified as (4-CF₃-*i*PrPDI)FeCl₂. Analysis for C₃₄H₄₂F₃N₃FeCl₂: Calc. C, 60.37; H, 6.26; N, 6.21. Found C, 60.32; H, 6.54; N, 5.92. Solid state magnetic susceptibility: $\mu_{\text{eff}} = 4.5 \mu_{\text{B}}$. ¹H NMR (benzene-*d*₆, 22 °C): $\delta = -75.1$ (120 Hz, 6H, CCH₃), -13.5 (26 Hz, 2H, *p*-aryl), -3.6 (191 Hz, 12H, CH(CH₃)₂), -3.3 (75 Hz, 16H, CH(CH₃)₂ and *m*-aryl), 16.2 (44 Hz, 4H, CH(CH₃)₂), 67.9 (98 Hz, 2H, *m*-pyr).

Preparation of (4-Me₂N-*i*PrPDI)Fe(CO)₂. A thick-walled vessel was charged with 8.8 g mercury, approximately 10 mL of toluene, and a stir bar. Sodium (0.044 g, 1.9 mmol) was cut into small pieces and added slowly to the rapidly stirred slurry. The resulting amalgam was allowed to stir for an additional 30 min to ensure complete dissolution. A slurry of (4-Me₂N-*i*PrPDI)FeCl₂ (0.25 g, 0.38 mmol) in 10 mL toluene was added to the reaction vessel, which was then sealed. The resulting mixture was brought to -196 °C and the vessel was evacuated. One atmosphere of CO was introduced, and the reaction mixture was allowed to stir for 24 hours. The resulting green-yellow mixture was then decanted away from the amalgam and filtered through a pad of Celite. The solvent was removed *in vacuo* and the residue recrystallized from pentane/ether at -35 °C to give 0.16 g (65% yield) of an olive green solid identified as (4-Me₂N-*i*PrPDI)Fe(CO)₂. Dissolving the compound in benzene gave a dark yellow-brown solution. Analysis for C₃₇H₄₈N₄O₂Fe: Calc. C, 69.80; H, 7.60; N, 8.80. Found: C, 69.46; H, 7.57; N, 8.66. ¹H NMR (benzene-*d*₆, 22 °C): $\delta = 1.04$ (d, 7 Hz, 12H, CH(CH₃)₂), 1.47 (d, 7 Hz, 12H, CH(CH₃)₂), 2.10 (s, 6H, CCH₃ or N(CH₃)₂), 2.65 (s, 6H, CCH₃ or N(CH₃)₂), 2.98 (spt, 7 Hz, 4H, CH(CH₃)₂), 7.16–7.17 (m, 6H, *m*-, *p*-aryl), 7.33 (s, 2H, *m*-pyr). ¹³C NMR {¹H} (benzene-*d*₆, 22

°C): δ = 16.5 (C(N)CH₃), 24.8 (CH(CH₃)₂), 25.4 (CH(CH₃)₂), 27.9 (CH(CH₃)₂), 40.6 (N(CH₃)₂), 106.6, 123.9, 126.6, 140.47, 146.9, 150.5, 153.3, 184.3 (*aryl, pyr, imine*), 215.2 (CO). IR (pentane): ν_{CO} = 1905, 1965 cm⁻¹.

Preparation of (4-*t*-Bu-*i*PrPDI)Fe(CO)₂. The compound was prepared in a similar manner to (4-Me₂N-*i*PrPDI)Fe(CO)₂ with 0.25 g (0.32 mmol) of (4-*t*-Bu-*i*PrPDI)FeBr₂, 10.9 g mercury and 0.053 g (2.3 mmol) sodium. Recrystallization from pentane/ether at -35 °C yielded 0.15 g (69% yield) of a yellow-brown solid identified as (4-*t*-Bu-*i*PrPDI)Fe(CO)₂. Analysis for C₃₉H₅₃FeN₃O₂: Calc. C, 71.88; H, 8.20; N, 6.45. Found: C, 72.03; H, 7.96; N, 6.55. ¹H NMR (benzene-*d*₆, 22 °C): δ = 0.97 (d, 7 Hz, 12H, CH(CH₃)₂), 1.37 (s, 9H, C(Me)₃), 1.41 (d, 7 Hz, 12H, CH(CH₃)₂), 2.19 (s, 6H, CMe), 2.84 (spt, 7 Hz, 4 Hz, CH(CH₃)₂), 7.10–7.18 (m, *p, m*-aryl), 8.04 (s, *m*-pyr, 2H). ¹³C {¹H} NMR (benzene-*d*₆, 22 °C): δ = 16.4 (C(N)CH₃), 24.8 (CH(CH₃)₂), 25.2 (CH(CH₃)₂), 27.9 (CH(CH₃)₂), 31.5 (C(CH₃)₃), 35.1 (C(CH₃)₃), 118.5, 123.9, 126.8, 140.5, 142.0, 145.9, 150.1, 155.4 (*aryl, pyr, imine*), 214.8 (CO). IR (pentane): ν_{CO} = 1911, 1971 cm⁻¹.

Preparation of (4-Bn-*i*PrPDI)Fe(CO)₂. The compound was prepared in a similar manner to (4-Me₂N-*i*PrPDI)Fe(CO)₂ with 0.15 g (0.21 mmol) of (4-Bn-*i*PrPDI)FeCl₂, 7.0 g mercury and 0.035 g (1.5 mmol) sodium. Recrystallization from pentane/ether at -35 °C yielded 0.10 g (68% yield) of a yellow-brown solid identified as (4-Bn-*i*PrPDI)Fe(CO)₂. Analysis for C₄₂H₄₉N₃O₂Fe: Calc. C, 73.78; H, 7.22; N, 6.15. Found: C, 73.68; H, 7.48; N, 6.05. ¹H NMR (benzene-*d*₆, 22 °C): δ = 0.99 (d, 7 Hz, 12H, CH(CH₃)₂), 1.45 (d, 7 Hz, 12H, CH(CH₃)₂), 2.08 (s, 6H, CCH₃), 2.85 (spt, 4H, CH(CH₃)₂), 4.06 (s, 2H, CH₂Ph), 7.10–7.28 (m, 11H, CH₂Ph, *m-, p*-aryl), 7.76 (s, 2H, *m-*

pyr). ^{13}C $\{^1\text{H}\}$ NMR (benzene- d_6 , 22 °C): δ = 16.4 (C(N)CH $_3$), 24.8 (CH(CH $_3$) $_2$), 25.2 (CH(CH $_3$) $_2$), 27.9 (CH(CH $_3$) $_2$), 42.4 (CH $_2$ (C $_6$ H $_5$)), 122.0, 123.9, 126.8, 128.1, 129.1, 129.5, 131.7, 140.4, 140.6, 150.0, 155.5, 198.0 (*aryl*, *phenyl*, *pyr*, *imine*), 228.1 (CO). IR (pentane): ν_{CO} = 1913, 1972 cm^{-1} .

Preparation of (4-CF $_3$ - i PrPDI)Fe(CO) $_2$. The compound was prepared in a similar manner to (4-Me $_2$ N- i PrPDI)Fe(CO) $_2$ with 0.11 g (0.20 mmol) of (4-CF $_3$ - i PrPDI)FeCl $_2$, 3.67 g mercury and 0.018 g (0.78 mmol) sodium. Recrystallization from pentane/ether at -35 °C yielded 0.083 g (63% yield) of a yellow-brown solid identified as (4-CF $_3$ - i PrPDI)Fe(CO) $_2$. Analysis for C $_{36}$ H $_{42}$ F $_3$ N $_3$ O $_2$ Fe: Calc. C, 65.36; H, 6.40; N, 6.35. Found: C, 65.95; H, 6.42; N, 5.95. ^1H NMR (benzene- d_6 , 22 °C): δ = 0.91 (d, 7 Hz, 12H, CH(CH $_3$) $_2$), 1.36 (d, 7 Hz, 12H, CH(CH $_3$) $_2$), 1.87 (s, 6H, CCH $_3$), 2.61 (spt, 4H, CH(CH $_3$) $_2$), 7.06–7.20 (m, 6H, *m*-, *p*-*aryl*), 8.02 (s, 2H, *m*-*pyr*). ^{13}C $\{^1\text{H}\}$ NMR (benzene- d_6 , 22 °C): δ = 16.2 (C(N)CH $_3$), 24.8 (CH(CH $_3$) $_2$), 25.0 (CH(CH $_3$) $_2$), 27.9 (CH(CH $_3$) $_2$), 117.4 (q, 4 Hz, *m*-*pyr*), 117.8 (q, 33 Hz, *p*-*pyr*), 124.1 (*aryl*), 127.2 (*pyr* or *aryl*), 140.2 (*aryl*), 144.4 (*pyr* or C(N)CH $_3$), 149.4 (*aryl*), 158.4 (*pyr* or C(N)CH $_3$), 213.9 (CO), CF $_3$ peak not located. ^{19}F $\{^1\text{H}\}$ NMR (benzene- d_6 , 22 °C): δ = -59.9. IR (pentane): ν_{CO} = 1925, 1983 cm^{-1} .

Preparation of (4-Me $_2$ N- i PrPDI)Fe(N $_2$) $_2$. A round bottom flask was charged with 17.6 g mercury, approximately 10 mL of toluene and a stir bar. Sodium (0.088 g, 3.8 mmol) was cut into small pieces and added slowly to the rapidly stirred slurry. The resulting amalgam was stirred for an additional 30 min to ensure complete dissolution. A solution containing 0.50 g

(0.77 mmol) of (4-Me₂N-ⁱPrPDI)FeCl₂ in 10 mL of toluene and 10 mL of THF was added to the vessel. The reaction mixture was stirred vigorously forming a brown solution. After three hours, the reaction mixture was decanted from the amalgam and concentrated *in vacuo* to remove the THF. The residue was extracted with pentane and yielded a brown-green mixture that was filtered through a pad of Celite and concentrated to ~15 mL. The concentrated solution was stored at -35 °C and deposited 0.19 g (39%) of a green-brown solid identified as (4-Me₂N-ⁱPrPDI)Fe(N₂)₂. ¹H NMR (benzene-*d*₆, 22 °C): δ = -0.17 (d, 7 Hz, 12H, CH(CH₃)₂), 1.28 (d, 7 Hz, 12 H, CH(CH₃)₂), 1.98 (spt, 7 Hz, 4H, CH(CH₃)₂), 2.95 (s, Δ_{v1/2} = 11 Hz, 6H, N(CH₃)₂), 4.23 (bs, 6H, CCH₃), 7.56 (d, 7 Hz, 4H, *m*-aryl), 7.63 (m, 2H, *p*-aryl), 9.13 (s, 2H, *m*-pyr). ¹³C {¹H} NMR (benzene-*d*₆, 22 °C): δ = 13.7 (C(N)CH₃), 24.0 (CH(CH₃)₂), 27.5 (CH(CH₃)₂), 34.6 (CH(CH₃)₂), 40.8 (N(CH₃)₂), 80.5 (*m*-pyr), 125.3 (*aryl*), 125.6 (*aryl*), 145.6 (*aryl*), 151.2 (*aryl*), 162.4 (*pyr* or C(N)CH₃), 173.0 (*pyr* or C(N)CH₃), 190.5 (*pyr* or C(N)CH₃). In solution, under a dinitrogen atmosphere, the compound is in equilibrium with (4-Me₂N-ⁱPrPDI)Fe(N₂). IR (pentane, 23 °C): ν_{NN} = 2034 cm⁻¹.

Preparation of (4-^tBu-ⁱPrPDI)Fe(N₂)₂. The compound was prepared in a similar manner to (4-Me₂N-ⁱPrPDI)Fe(N₂)₂ with 0.25 g (0.33 mmol) of (4-^tBu-ⁱPrPDI)FeBr₂, 10.7 g mercury, 0.055 g (2.4 mmol) sodium and approximately 30 mL toluene. Filtration of the green reaction mixture through Celite, concentration *in vacuo*, and recrystallization from pentane/ether at -35 °C yielded 0.10 g (49%) of a green solid identified as (4-^tBu-ⁱPrPDI)Fe(N₂)₂. ¹H NMR (benzene-*d*₆, 22 °C): δ = -0.26 (d, 5 Hz, 12H, CH(CH₃)₂), 1.08–1.20 (m, 16H, CH(CH₃)₂ and CH(CH₃)₂), 1.66 (s, 9H, C(CH₃)₃), 7.59–7.68 (m, 6H, *m*- and *p*-aryl), 10.18 (s, 2H, *m*-pyr), 10.93 (bs, Δ_{v1/2} = 28 Hz, 6H,

CCH₃). ¹³C {¹H} NMR (benzene-*d*₆, 22 °C): δ = -0.9 (C(N)CH₃), 24.4 (CH(CH₃)₂), 27.7 (C(CH₃)₃), 30.7 (CH(CH₃)₂), 38.6 (CH(CH₃)₂), 39.5 (C(CH₃)₃), 125.5 (*aryl*), 79.8 (*m-pyr*), 126.3 (*aryl*), 143.1 (*aryl*), 148.4 (*o-pyr*), 153.2 (*aryl*), 187 (*p-pyr*, located by HMBC), one resonance not located. IR (pentane, 23 °C): ν_{NN} = 2128, 2067 cm⁻¹. In solution, under a dinitrogen atmosphere, the compound is in equilibrium with (4-^tBu-ⁱPrPDI)Fe(N₂). IR (pentane, 23 °C): ν_{NN} = 2041 cm⁻¹.

Preparation of (4-Bn-ⁱPrPDI)Fe(N₂)₂. The compound was prepared in a similar manner to (4-Me₂N-ⁱPrPDI)Fe(N₂)₂ with 0.25 g (0.36 mmol) of (4-Bn-ⁱPrPDI)FeCl₂, 8.4 g mercury, 0.042 g (1.8 mmol) sodium, and 20 mL toluene. Filtration of the green reaction mixture through Celite, concentration *in vacuo*, and recrystallization from pentane/ether at -35 °C yielded 0.16 g (65% yield) of a green solid identified as (4-Bn-ⁱPrPDI)Fe(N₂)₂. ¹H NMR (benzene-*d*₆, 22 °C): δ = -0.36 (d, 7 Hz, 12H, CH(CH₃)₂), 1.06 (spt, 7 Hz, 4H, CH(CH₃)₂), 1.17 (d, 7 Hz, 12H, CH(CH₃)₂), 7.10 (t, 7 Hz, 1H, *p-phenyl*), 7.23 (t, 7 Hz, 2H, *m-phenyl*), 7.37 (d, 7 Hz, 2H, *o-phenyl*), 7.70–7.61 (m, 6H, *m-* and *p-aryl*), 7.97 (s, 2H, CH₂Phenyl), 10.09 (s, 2H, *m-pyr*), 11.62 (bs, Δν_{1/2} = 20 Hz, 6H, CCH₃). ¹³C {¹H} NMR (benzene-*d*₆, 22 °C): δ = -1.6 (C(N)CH₃), 24.4 (CH(CH₃)₂ or CH(CH₃)₂), 31.2 (CH(CH₃)₂), 33.8 (CH₂Ph), 39.5 (CH(CH₃)₂ or CH(CH₃)₂), 81.9 (*m-pyr*), 125.5 (*aryl*), 126.3 (*aryl*), 126.8 (*phenyl*), 129.1 (*phenyl*), 142.3 (*aryl*), 147.1 (*phenyl*), 147.7 (*o-pyr*), 153.9 (*aryl*), 154.4 (*phenyl*), 181 (*p-pyr*, located by HMBC), one resonance not located. IR (pentane): ν_{NN} = 2129, 2071 cm⁻¹. In solution, under a dinitrogen atmosphere, the compound is in equilibrium with (4-Bn-ⁱPrPDI)Fe(N₂). IR (pentane, 23 °C): ν_{NN} = 2044 cm⁻¹.

Preparation of (4-Me₂N-ⁱPrPDI)Fe(DMAP). To a 20-mL scintillation vial containing 0.015 g (0.12 mmol) 4-*N,N*-dimethylaminopyridine was added a solution of 0.075 g (0.12 mmol) (4-Me₂N-ⁱPrPDI)Fe(N₂)₂ in approximately 10 mL diethyl ether. Addition caused an immediate color change from brown-green to maroon. The reaction mixture was stirred for 15 minutes, after which point the solution was filtered through Celite and concentrated to approximately 2 mL. A dark purple-red crystals (0.073 g, 88%) identified as (4-Me₂N-ⁱPrPDI)Fe(DMAP) were deposited upon layering the solution with approximately 5 mL of pentane and cooling to -35 °C. Analysis for C₄₂H₅₈N₆Fe: Calc. C, 71.78; H, 8.32; N, 11.96. Found: C, 71.61; H, 7.99; N, 11.45. ¹H NMR (benzene-*d*₆, 22 °C): δ = -8.98 (s, 6H, CCH₃), -0.02 (d, 6 Hz, 12H, CH(CH₃)₂), 1.37 (d, 6 Hz, 12H, CH(CH₃)₂), 1.88 (s, 6H, N(CH₃)₂), 2.27 (s, 6H, N(CH₃)₂), 2.49 (spt, 6 Hz, 4H, CH(CH₃)₂), 5.83 (bs, 4H, *o*- and *m*-DMAP), 7.16 (d, 7 Hz, 4H, *m*-pyr), 7.71 (t, 7 Hz, 2H, *p*-aryl), 12.96 (s, 2H, *m*-pyr). ¹³C {¹H} NMR (benzene-*d*₆, 22 °C): δ = 22.5 (CH(CH₃)₂), 24.1 (CH(CH₃)₂), 27.7 (CH(CH₃)₂), 37.8 (N(CH₃)₂), 40.7 (N(CH₃)₂), 89.0 (*m*-pyr), 106.8 (DMAP), 123.2 (*m*-aryl), 123.5 (*p*-aryl), 132.9 (aryl), 150.4 (DMAP), 150.8, 160.1, 169.6, 173.8, 199.3, one resonance not located.

General Procedure for the Catalytic Olefin Hydrogenation. In a typical experiment, a thick-walled glass vessel was charged with a solution containing 0.032 mmol of the desired iron compound in 0.65 g (7.72 mmol) of benzene-*d*₆ and a magnetic stir bar. The vessel was placed in a liquid nitrogen cooled cold well for 20 min. Once the solution was frozen, 0.63 mmol of the olefin was layered onto the solution of iron nitrogen compound. The vessel was taken out of the drybox and transferred to a high vacuum line while continuously submerged in liquid nitrogen.

Following evacuation of the dinitrogen atmosphere, 1 atm of dihydrogen was admitted at 80 K. The solution was then thawed and stirred in an ambient temperature water bath. After the desired reaction time, the vessel was vented of dihydrogen and exposed to air. Decomposed iron compound was removed by filtration through Celite, and the filtrate collected for analysis by ^1H NMR. Conversions were determined by ^1H NMR spectroscopy for ethyl 3,3-dimethylacrylate and α -methylstyrene, and by GC-FID for all other olefins.

Characterization of Hydrogenated Products by Gas Chromatography. GC analyses were performed using a Shimadzu GC-2010 gas chromatograph equipped with a Shimadzu AOC-20s autosampler and a Shimadzu SHRXI-5MS capillary column (15m x 250 μm). The instrument was set to an injection volume of 1 μL , an inlet split ratio of 100:1, and inlet and detector temperatures of 120 $^\circ\text{C}$ and 250 $^\circ\text{C}$, respectively. UHP-grade helium was used as carrier gas with a flow rate of 1.12 mL/min. The temperature program used for the various alkanes are as follows:

1,2-Diphenylethane. 60 $^\circ\text{C}$ for 1 min; 15 $^\circ\text{C}/\text{min}$ to 250 $^\circ\text{C}$ and hold for 2 min. Retention Time: 7.96 min.

Propane-1,2-diylidibenzene. 60 $^\circ\text{C}$ for 1 min; 15 $^\circ\text{C}/\text{min}$ to 250 $^\circ\text{C}$ and hold for 2 min. Retention Time: 8.22 min.

Ethane-1,1-diylidibenzene. 60 $^\circ\text{C}$ for 1 min; 15 $^\circ\text{C}/\text{min}$ to 180 $^\circ\text{C}$ and hold for 2 min. Retention Time: 7.73 min.

General Procedure for the Catalytic $[2\pi + 2\pi]$ Cycloaddition of *N,N*-Diallylaniline. In a typical experiment, a 20 mL scintillation vial was charged with 0.017 mmol of the desired monomeric iron dinitrogen compound or 8.4 μmol of the desired dimeric iron dinitrogen compound, and 0.650 g (7.72 mmol) of benzene- d_6 . *N,N*-diallylaniline (0.34 mmol) was added, in most cases eliciting an immediate color change, and the resulting reaction mixture was filtered through a glass frit into a J. Young tube. Conversion was monitored by ^1H NMR spectroscopy.

REFERENCES

- ¹ (a) Chirik, P. J.; Wieghardt, K. *Science* **2010**, *327*, 794–795. (b) de Bruin, B. *Eur. J. Inorg. Chem.* **2012**, 340–342.
- ² a) Stubbe, J.; van Der Donk, W. A. *Chem. Rev.* **1998**, *98*, 705–762. b) Jazdewski, B. A.; Tolman, W. B. *Coord. Chem. Rev.* **2000**, *200-202*, 633–685. c) Lewis, E. A.; Tolman, W. B. *Chem. Rev.* **2004**, *104*, 1047–1076. d) Kaim, W.; Schwederski, B. *Coord. Chem. Rev.* **2010**, *254*, 1580–1588.
- ³ Rittle, J.; Green, M. T. *Science* **2010**, *330*, 933–937.
- ⁴ (a) Small, B. M.; Brookhart, M. *J. Am. Chem. Soc.* **1998**, *120*, 7143–7144. (b) Small, B. L.; Brookhart, M.; Bennett, A. M. A. *J. Am. Chem. Soc.* **1998**, *120*, 4049–4050.
- ⁵ Britovsek, G. J. P.; Gibson, V. C.; Kimberley, B. S.; Maddox, S. J.; Solan, G. A.; White, A. J. P.; Williams, D. J. *Chem. Commun.* **1998**, 849–850.
- ⁶ Britovsek, G. J. P.; Bruce, M.; Gibson, V. C.; Kimberley, B. S.; Maddox, P. J.; Mastroianni, S.; McTavish, S. J.; Redshaw, C.; Solan, G. A.; Strömberg, S.; White, A. J. P.; Williams, D. J. *J. Am. Chem. Soc.* **1999**, *121*, 8728–8748.
- ⁷ (a) Knijnenburg, Q.; Gambarotta, S.; Budzelaar, P. H. M. *Dalton Trans.* **2006**, 5442–5448. (b) Gibson, V. C.; Redshaw, C.; Solan, G. A. *Chem. Rev.* **2007**, *107*, 1745–1776. and references therein.
- ⁸ Bart, S. C.; Lobkovsky, E.; Chirik, P. J. *J. Am. Chem. Soc.* **2004**, *126*, 13794–13807.
- ⁹ Trovitch, R. J.; Lobkovsky, E.; Bill, E.; Chirik, P. J. *Organometallics* **2008**, *27*, 1470–1478.
- ¹⁰ Bouwkamp, M. W.; Bowman, A. C.; Lobkovsky, E.; Chirik, P. J. *J Am Chem Soc* **2006**, *128*, 13340–13341.
- ¹¹ Sylvester, K. T.; Chirik, P. J. *J. Am. Chem. Soc.* **2009**, *131*, 8772–8774.
- ¹² Russell, S. K.; Lobkovsky, E.; Chirik, P. J. *J. Am. Chem. Soc.* **2011**, *133*, 8858–8861.
- ¹³ Tondreau, A. M.; Atienza, C. C. H.; Weller, K. J.; Nye, S. A.; Lewis, K. M.; Delis, J. G. P.; Chirik, P. J. *Science* **2012**, *335*, 567–570.
- ¹⁴ Sylvester, K. T.; Darmon, J. M.; Stieber, S. C. E.; Fernández, I.; Semproni, S. P.; Lobkovsky, E.; Bill, E.; Wieghardt, K.; DeBeer, S.; Chirik, P. J. *manuscript in preparation*.
- ¹⁵ Archer, A.; Bouwkamp, M.; Cortez, M.; Lobkovsky, E.; Chirik, P. J. *Organometallics* **2006**, *25*, 4269–4278.
- ¹⁶ Wile, B. M.; Trovitch, R. J.; Bart, S. C.; Tondreau, A. M.; Lobkovsky, E.; Milsman, C.; Bill, E.; Wieghardt, K.; Chirik, P. J. *Inorg. Chem.* **2009**, *48*, 4190–4200.

- ¹⁷ Russell, S. K.; Darmon, J. M.; Lobkovsky, E.; Chirik, P. J. *Inorg. Chem.* **2010**, *49*, 2782–2792.
- ¹⁸ Russell, S. K.; Milsman, C.; Lobkovsky, E.; Weyhermüller, T.; Chirik, P. J. *Inorg. Chem.* **2011**, *50*, 3159–3169.
- ¹⁹ Stieber, S. C. E.; Milsman, C.; Hoyt, J. M.; Turner, Z. R.; Finkelstein, K. D.; Wieghardt, K.; DeBeer, S.; Chirik, P. J. *Inorg. Chem.* **2012**, *51*, 3770–3785.
- ²⁰ Tondreau, A. M.; Milsman, C.; Lobkovsky, E.; Chirik, P. J. *Inorg. Chem.* **2011**, *50*, 9888–9895.
- ²¹ Jørgensen, C. K. *Coord. Chem. Rev.* **1966**, *1*, 164–178.
- ²² Bart, S. C.; Chłopek, K.; Bill, E.; Bouwkamp, M. W.; Lobkovsky, E.; Neese, F.; Wieghardt, K.; Chirik, P. J. *J. Am. Chem. Soc.* **2006**, *128*, 13901–13912.
- ²³ Bart, S. C.; Lobkovsky, E.; Bill, E.; Wieghardt, K. *Inorg. Chem.* **2007**, *46*, 7055–7063.
- ²⁴ Zhu, D.; Budzelaar, P. H. A. *Organometallics* **2008**, *27*, 2699–2705.
- ²⁵ (a) Cámpora, J.; Pérez, C. M.; Rodríguez-Delgado, A.; Naz, A. M.; Palma, P.; Alvarez, E. *Organometallics* **2007**, *26*, 1104–1107. (b) Cámpora, J.; Naz, A. M.; Palma, P.; Rodríguez-Delgado, A.; Álvarez, E.; Tritto, I.; Boggioni, L. *Eur. J. Inorg. Chem.* **2008**, 1871–1879.
- ²⁶ Nüchel, S.; Burger, P. *Organometallics* **2001**, *20*, 4345–4359.
- ²⁷ Su, B.; Zhao, J.; Cui, Y.; Liang, Y.; Sun, W. *Synth. Commun.* **2005**, *35*, 2317–2324.
- ²⁸ Chessa, G.; Canovese, L.; Visentin, F.; Santo, C.; Seraglia, R. *Tetrahedron* **2005**, *61*, 1755–1763.
- ²⁹ Parsons, A. T.; Johnson, J. S. *J. Am. Chem. Soc.* **2009**, *131*, 3122–3123.
- ³⁰ Bouwkamp, M. W.; Hawrelak, E. J.; Trovitch, R. J.; Lobkovsky, E.; Chirik, P. J. *Chem. Commun.* **2005**, 3406–3408.
- ³¹ Connelly, N. G.; Geiger, W. E. *Chem. Rev.* **1996**, *96*, 877–910.
- ³² Tondreau, A. M.; Darmon, J. M.; Wile, B. M.; Floyd, S. K.; Lobkovsky, E.; Chirik, P. J. *Organometallics* **2009**, *28*, 3928–3940.
- ³³ Hansch, C.; Leo, A.; Taft, R. W. *Chem. Rev.* **1991**, *91*, 165–195.
- ³⁴ Knijnenburg, Q.; Hettterscheid, D.; Kooistra, T. M.; Budzelaar, P. H. M. *Eur. J. Inorg. Chem.* **2004**, *2004*, 1204–1211.
- ³⁵ Zhu, D.; Thapa, I.; Korobkov, I.; Gambarotta, S.; Budzelaar, P. H. M. *Inorg. Chem.* **2011**, *50*, 9879–9887.

- ³⁶ Bowman, A. C.; Milsmann, C.; Bill, E.; Lobkovsky, E.; Weyhermüller, T.; Wieghardt, K.; Chirik, P. J. *Inorg Chem* **2010**, *49*, 6110–6123.
- ³⁷ Trovitch, R. J.; Lobkovsky, E.; Bouwkamp, M. W.; Chirik, P. J. *Organometallics* **2008**, *27*, 6264–6278.
- ³⁸ This topic is more thoroughly discussed in Chapter 5.
- ³⁹ Trovitch, R. J.; Lobkovsky, E.; Chirik, P. J. *J. Am. Chem. Soc.* **2008**, *130*, 11631–11640.
- ⁴⁰ Patrick, A. D.; Hoyt, H. M.; Chirik, P. J. *unpublished results*.
- ⁴¹ (a) Hartwig, J. F. *Inorg Chem* **2007**, *46*, 1936–1947. (b) Jones, W. D.; Kuykendall, V. L. *Inorg. Chem.* **1991**, *30*, 2615–2622. (c) Abis, L.; Santi, R.; Halpern, J. J. *J. Organomet. Chem.* **1981**, *215*, 263–267.
- ⁴² Abu-Hasanayn, F.; Krogh-Jespersen, K.; Goldman, A. S. *Inorg. Chem.* **1993**, *32*, 495–496.
- ⁴³ Sylvester, K. T.; Chirik, P. J. *J. Am. Chem. Soc.* **2009**, *131*, 8772–8774.
- ⁴⁴ Hoyt, J. M.; Semproni, S. P.; Chirik, P. J. *unpublished results*.
- ⁴⁵ Sylvester, K. T. Ph.D. Thesis, Cornell University, Ithaca, NY, 2011.
- ⁴⁶ Bart, S. C.; Bowman, A. C.; Lobkovsky, E.; Chirik, P. J. *J. Am. Chem. Soc.* **2007**, *129*, 7212–7213.
- ⁴⁷ Pangborn, A. B.; Giardello, M. A.; Grubbs, R. H.; Rosen, R. K.; Timmers, F. J. *Organometallics* **1996**, *15*, 1518–1520.
- ⁴⁸ Bhattacharya, S.; Snehalatha, K.; George, S. *J. Org. Chem.* **1998**, *63*, 27–35.
- ⁴⁹ Bowman, A. C.; Milsmann, C.; Atienza, C. C. H.; Lobkovsky, E.; Wieghardt, K.; Chirik, P. J. *J. Am. Chem. Soc.* **2010**, *132*, 1676–1684.
- ⁵⁰ Sur, S. K. *J. Mag. Res.* **1989**, *82*, 169–173.
- ⁵¹ Geiger, W. E. *Organometallics* **2007**, *26*, 5738–5765.
- ⁵² Neese, F. *ORCA: an ab initio, DFT and Semiempirical Electronic Structure Package*, version 2.8, revision 2287; Institut für Physikalische und Theoretische Chemie, Universität Bonn: Bonn, Germany, Nov 2010.
- ⁵³ (a) Becke, A. D. *J. Chem. Phys.* **1986**, *84*, 4524–4529. (b) Becke, A. D. *J. Chem. Phys.* **1993**, *98*, 5648–5652. (c) Lee, C. T.; Yang, W. T.; Parr, R. G. *Phys. Rev. B.* **1998**, *37*, 785–789.
- ⁵⁴ Neese, F.; Solomon, E. I. In *Magnetism: From Molecules to Materials*; Miller, J. S., Drillon, M., Eds.; Wiley: New York, 2002; Vol. 4, p 345.

- ⁵⁵ (a) Schäfer, A.; Horn, H.; Ahlrichs, R. *J. Chem. Phys.* **1992**, *97*, 2571–2577. (b) Schäfer, A.; Huber, C.; Ahlrichs, R. *J. Chem. Phys.* **1994**, *100*, 5829–5835. (c) Weigend, F.; Ahlrichs, R. *Phys. Chem. Chem. Phys.* **2005**, *7*, 3297–3305.
- ⁵⁶ (a) Eichkorn, K.; Weigend, F.; Treutler, O.; Ahlrichs, R. *Theor. Chem. Acc.* **1997**, *97*, 119–124. (b) Eichkorn, K.; Treutler, O.; Öhm, H.; Häser, M.; Ahlrichs, R. *Chem. Phys. Lett.* **1995**, *240*, 283–290. (c) Eichkorn, K.; Treutler, O.; Öhm, H.; Häser, M.; Ahlrichs, R. *Chem. Phys. Lett.* **1995**, *242*, 652–660.
- ⁵⁷ (a) Neese, F.; Wennmohs, F.; Hansen, A.; Becker, U. *Chem. Phys.* **2009**, *356*, 98–109. (b) Kossmann, S.; Neese, F. *Chem. Phys. Lett.* **2009**, *481*, 240–243. (c) Neese, F. *J. Comput. Chem.* **2003**, *24*, 1740–1747.
- ⁵⁸ Ginsberg, A. P. *J. Am. Chem. Soc.* **1980**, *102*, 111–117.
- ⁵⁹ Noodleman, L.; Peng, C. Y.; Case, D. A.; Mouesca, J. M. *Coord. Chem. Rev.* **1995**, *144*, 199–244.
- ⁶⁰ Kirchner, B.; Wennmohs, F.; Ye, S.; Neese, F. *Curr. Opin. Chem. Biol.* **2007**, *11*, 134–141.
- ⁶¹ Neese, F. *J. Phys. Chem. Solids* **2004**, *65*, 781–785.
- ⁶² *Molekel*, Advanced Interactive 3D-Graphics for Molecular Sciences, available under <http://www.cscs.ch/molkel/>.
- ⁶³ Neese, F. *Inorg. Chim. Acta.* **2002**, *337*, 181–192.
- ⁶⁴ (a) Sinnecker, S.; Slep, L. D.; Bill, E.; Neese, F. *Inorg. Chem.* **2005**, *44*, 2245–2254. (b) Römelt, M.; Ye, S.; Neese, F. *Inorg. Chem.* **2009**, *48*, 784–785.

CHAPTER 2

ELECTRONIC STRUCTURE ELUCIDATION AND REACTIVITY OF THE PYRIDINE DI(CARBENE) IRON BIS(DINITROGEN) COMPLEX, (*i*PrCNC)Fe(N₂)₂

2.1 Abstract

The electronic structure of a series of reduced pyridine di(carbene) iron complexes, (*i*PrCNC)Fe(L)(L') (*i*PrCNC = 2,6-((2,6-*i*Pr₂-C₆H₃)-imidazolin-2-ylidene)₂-C₅H₃N; L = L' = N₂; L = L' = CO; L = DMAP and L' = N₂) was investigated by a combination of NMR, infrared, Mößbauer and X-ray absorption spectroscopies. The spectroscopic data establish that these complexes are redox non-innocent. They are best described as hybrid structures with [*i*PrCNC⁰)Fe⁰] and [*i*PrCNC²⁻)Fe^{II}] resonance forms with the *i*PrCNC ligand acting as a π -acceptor. No decomposition to or detectable formation of a potentially redox-active four-coordinate pyridine di(carbene) iron dinitrogen complex, (*i*PrCNC)Fe(N₂)₂ was observed by ¹H NMR or solution infrared spectroscopies under 1 atmosphere of dinitrogen over the course of a week, although dinitrogen exchange with atmospheric dinitrogen was established by ¹⁵N NMR spectroscopy. The activity of (*i*PrCNC)Fe(N₂)₂ for the catalytic hydrogenation of olefins and [2 π + 2 π] cyclization of α,ω -diolefins was also investigated. Activity relationships consistent with those observed in olefin hydrogenation using electron-donating pyridine di(imine) iron precatalysts were observed. Isotopic experiments indicated that a competitive, unproductive 2,1-insertion pathway or a vinylic C–H activation mechanism was responsible for the deviation in hydrogenation activity trends observed with 1,1-diphenylethylene and the electron-rich iron catalysts. Instead of [2 π + 2 π] cyclization, olefin isomerization was observed for *N,N*-diallyl-*tert*-

butylamine in the presence of catalytic $(i\text{PrCNC})\text{Fe}(\text{N}_2)_2$. Stoichiometric experiments resulted in the isolation of $(i\text{PrCNC})\text{Fe}(\eta^2, \eta^2\text{-(CH}_2\text{CHCH}_2)_2\text{N}^t\text{Bu})$.

2.2 Introduction

Reduced, aryl-substituted pyridine di(imine) iron complexes are competent catalysts for a variety of organic transformations (see Section 1.2), and are well known for their ability to undergo metal-ligand electron transfer.¹ Metal-ligand cooperativity arising from this interplay may diminish kinetic barriers and facilitate unprecedented reactivity,² and is a well recognized strategy for coaxing “noble” behavior from base metal complexes.³ However, novel reactivity may not alone result from the presence of a redox-active ligand.

One strategy taken by our laboratory to demonstrate the importance of metal-ligand cooperativity for catalytically competent iron centers was replacement of the imine donors. To this end, the reduction of $(i\text{PrPNP})\text{FeCl}_2$ ($i\text{PrPNP} = 2,6\text{-(}i\text{Pr}_2\text{PCH}_2)_2\text{-C}_5\text{H}_3\text{N}$) was explored.⁴ The decreased conjugation of the chelate was expected to raise the barrier for metal-ligand redox events to occur. Addition of two equivalents of sodium triethylborohydride to $(i\text{PrPNP})\text{FeCl}_2$ furnished the low-spin, ferrous dihydride dinitrogen complex, $(i\text{PrPNP})\text{Fe}(\text{H})_2(\text{N}_2)$ (**Figure 2.1**). $(i\text{PrPNP})\text{Fe}(\text{H})_2(\text{N}_2)$ was unstable at 23 °C, and exhibited low activity for the hydrogenation of 1-

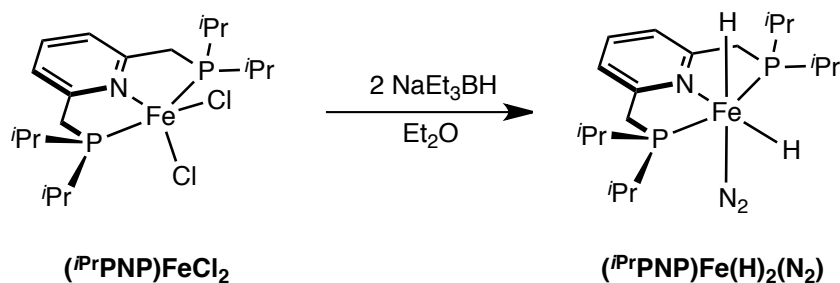


Figure 2.1. Product obtained from the attempted reduction of $(i\text{PrPNP})\text{FeCl}_2$ with two equivalents of sodium triethylborohydride.

hexene at 0.3 mol % under 4 atmospheres of H₂. Unfortunately, many influences typically impact catalyst (in)activity aside from metal-ligand transfer events, and demonstrating the role of redox activity in catalysis remains a challenge.

In 2005, Danopoulos and co-workers published the synthesis of a formally Fe⁰ pyridine di(carbene) bis(dinitrogen) complex, (*i*PrCNC)Fe(N₂)₂ (*i*PrCNC = 2,6-((2,6-*i*Pr₂-C₆H₃)-imidazolin-2-ylidene)₂-C₅H₃N).⁵ *N*-heterocyclic carbenes (NHCs) are ubiquitous and have found widespread application in the field of homogeneous catalysis.⁶ NHCs are significantly stronger σ -donors than the most basic phosphine ligands.^{6h} Recent work has also indicated that NHCs are strong π -accepting ligands.⁷ A comparison of the carbonyl stretching frequencies of (*i*PrPDI)Fe(CO)₂ (*i*PrPDI = 2,6-(2,6-*i*Pr₂-C₆H₃N=CCH₃)₂-C₅H₃N), (*i*PrCNC)Fe(CO)₂ and (*i*PrPNP)Fe(CO)₂ revealed that the pyridine di(carbene) complex exhibited intermediate values relative to the phosphine and imine analogs (**Figure 2.2**). Computational studies by Danopoulos and co-workers has suggested that the iron exhibits less π -backbonding into the carbonyl ligands than expected due to competitive π -backbonding into the pyridine ring.⁸ This is also consistent

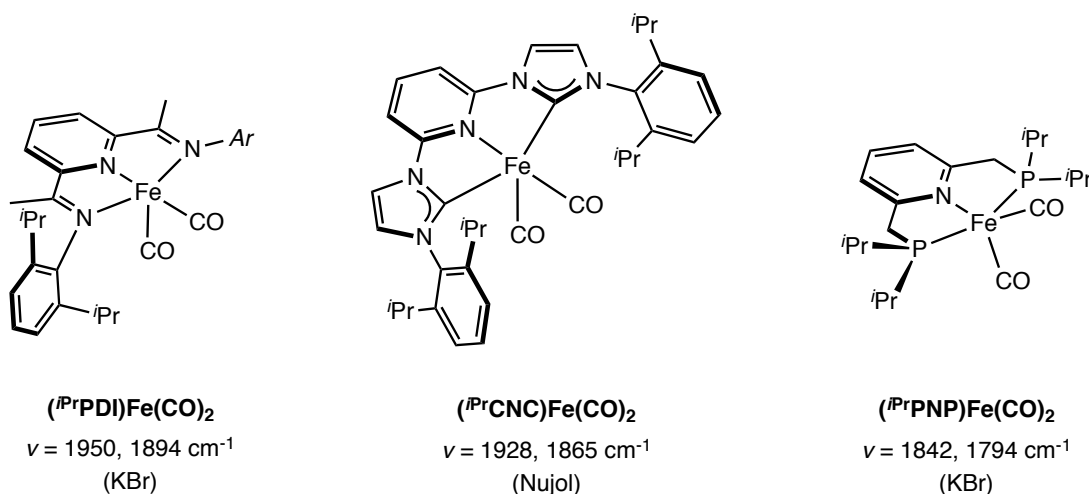


Figure 2.2. Comparison of CO infrared stretching frequencies for (*i*PrPDI)Fe(CO)₂, (*i*PrCNC)Fe(CO)₂ and (*i*PrPNP)Fe(CO)₂.

with the computational work of Zhu *et al.*, which indicates that the pyridine di(carbene) ligand is a significantly stronger π -accepting ligand than a variety of pyridine di(imine) analogues.⁹

The structural similarities between $(i^{\text{Pr}}\text{CNC})\text{Fe}(\text{N}_2)_2$ and the pyridine di(imine) iron bis(dinitrogen) analog, $(i^{\text{Pr}}\text{PDI})\text{Fe}(\text{N}_2)_2$ raised questions regarding the ability of the pyridine di(carbene) ligand scaffold to support ligand-centered radicals as well as the electronic structure and catalytic competency of the iron bis(dinitrogen) complex. Prior work by our laboratory has shown that the four- and five-coordinate pyridine di(imine) iron dinitrogen complexes have distinct electronic structures (**Figure 2.3**).¹⁰ The four-coordinate compound, $(i^{\text{Pr}}\text{PDI})\text{Fe}(\text{N}_2)$ is redox-active and is best described by an intermediate-spin ferrous ion antiferromagnetically coupled to a pyridine di(imine) triplet dianion. In contrast, the five-coordinate complex, $(i^{\text{Pr}}\text{PDI})\text{Fe}(\text{N}_2)_2$ is a highly covalent molecule best described as a hybrid structure with $(i^{\text{Pr}}\text{PDI})\text{Fe}(\text{N}_2)$ and $(i^{\text{Pr}}\text{PDI})\text{Fe}(\text{N}_2)_2$ resonance forms, and is considered redox non-innocent. This term was first used by Jørgenson in the context of nitrosyl ligands to indicate ambiguity in the metal oxidation state assignment.¹¹ Here, we elucidate the electronic structure of the five-coordinate pyridine di(carbene) iron bis(dinitrogen) complex, $(i^{\text{Pr}}\text{CNC})\text{Fe}(\text{N}_2)_2$ and evaluate its catalytic activity for the hydrogenation of olefins and the $[2\pi + 2\pi]$ cyclization of α,ω -dienes.

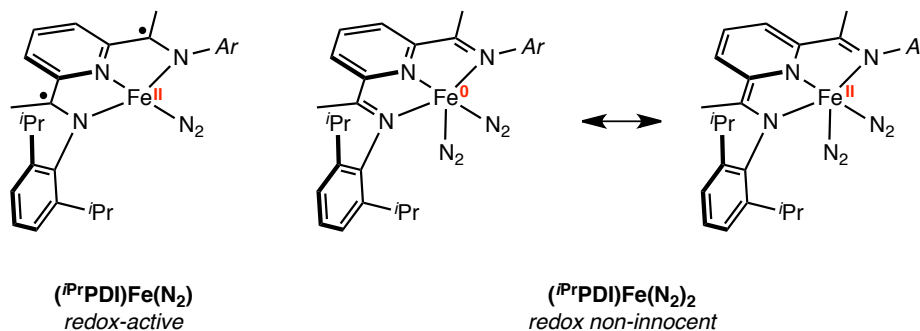


Figure 2.3. Electronic structure of the four- and five-coordinate pyridine di(imine) iron dinitrogen compounds, $(i^{\text{Pr}}\text{PDI})\text{Fe}(\text{N}_2)$ and $(i^{\text{Pr}}\text{PDI})\text{Fe}(\text{N}_2)_2$.

2.3 *Synthesis, Characterization and Electronic Structure Elucidation of Pyridine Di(carbene) Iron Complexes*

Two studies have definitively illustrated the ability of the pyridine di(imine) ligand to accept electrons. Gaboratta, Budzelaar and coworkers isolated paramagnetic and diamagnetic pyridine di(imine) trianions by treatment of *i*PrPDI with lithium or lithium naphthalenide.¹² Our group has also experimentally measured the reduction potential of various pyridine di(imine) ligands using cyclic voltammetry.^{13,14} These methods were also employed for the free pyridine di(carbene), *i*PrCNC. Attempts to reduce *i*PrCNC by stirring with sodium metal in either diethyl ether or THF did not yield a color change suggestive of free radical formation. Attempts to obtain the reduction potential for *i*PrCNC by cyclic voltammetry in THF solution (approximately 1 mM in compound and 0.1 M in [ⁿBu₄N]PF₆ supporting electrolyte) were unsuccessful, and no reversible redox waves were observed.¹⁵ This data suggests that either the pyridine di(carbene) framework is unable to accept electrons, or that the reduction potential is more negative than -3.04 V (vs. ferrocene), the formal potential of sodium in THF,¹⁶ and was not observable within the solvent window employed for cyclic voltammetry.

Elucidation of the ground state electronic structure of (*i*PrCNC)Fe(N₂)₂ was pursued for comparison with the pyridine di(imine) analog. Utilizing the methodology of Danopoulos,⁵ (*i*PrCNC)FeBr₂ was stirred with excess 0.5% sodium amalgam in THF under an atmosphere of dinitrogen. The iron bis(dinitrogen) complex, (*i*PrCNC)Fe(N₂)₂ was isolated as a green solid following the literature procedure in comparable yields (**Figure 2.4**).⁵ Pentane solution infrared spectroscopy exhibited two strong absorptions at 2112 and 2046 cm⁻¹ at 23 °C, and were assigned as the symmetric and asymmetric N₂ stretching frequencies of the five-coordinate complex,

respectively. The solution dinitrogen stretching frequencies of $(i\text{PrCNC})\text{Fe}(\text{N}_2)_2$ are significantly more reduced than the parent pyridine di(imine) iron complex, $(i\text{PrPDI})\text{Fe}(\text{N}_2)_2$ by approximately 20–30 cm^{-1} (**Table 2.1**); however, they are only 5–10 cm^{-1} different than the *para*-substituted complex, $(4\text{-Me}_2\text{N-}i\text{PrPDI})\text{Fe}(\text{N}_2)_2$. It is important to note that comparisons between $(i\text{PrCNC})\text{Fe}(\text{N}_2)_2$ and $(4\text{-Me}_2\text{N-}i\text{PrPDI})\text{Fe}(\text{N}_2)_2$ are less reliable due to the different solvents and conditions in which the values were recorded. These data illustrate the more reducing environment imparted by the pyridine di(carbene) chelate.

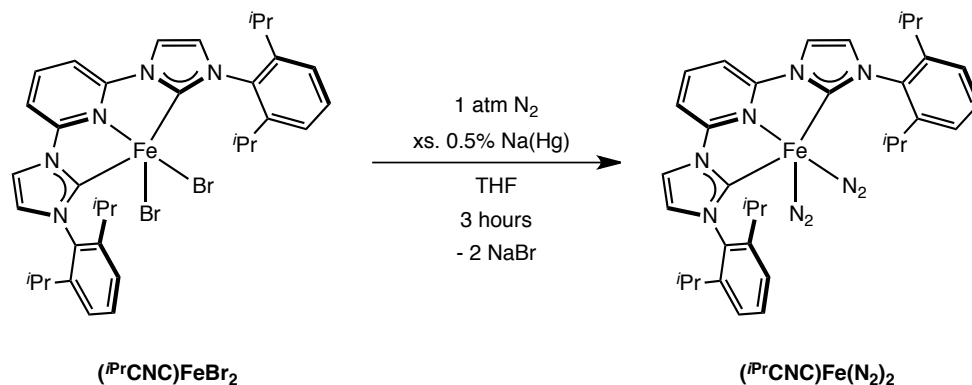


Figure 2.4. Synthesis of $(i\text{PrCNC})\text{Fe}(\text{N}_2)_2$ according to the method of Danopoulos.¹⁰

Table 2.1. Dinitrogen stretching frequencies for selected five-coordinate iron bis(dinitrogen) complexes recorded in pentane.

Complex	$\nu(\text{N}\equiv\text{N})$ (cm^{-1})
$(i\text{PrBPDI})\text{Fe}(\text{N}_2)_2$	2138, 2086
$(i\text{PrPDI})\text{Fe}(\text{N}_2)_2$	2132, 2073
$[(\text{Me}^e\text{PDI})\text{Fe}(\text{N}_2)]_2(\mu_2\text{-N}_2)$	2102, 2085 ^a
$(4\text{-Me}_2\text{N-}i\text{PrPDI})\text{Fe}(\text{N}_2)_2$	2117, 2055 ^b
$(i\text{PrCNC})\text{Fe}(\text{N}_2)_2$	2112, 2046

^a Values were recorded in toluene at 22 °C. ^b Values were recorded in toluene at -30 °C.

No evidence for a four-coordinate species was observed by solution IR spectroscopy. This behavior contrasts $(i\text{PrPDI})\text{Fe}(\text{N}_2)_2$,¹⁷ which loses an equivalent of dinitrogen in solution at 23 °C under 1 atmosphere of dinitrogen and exists as the minor species in equilibrium with the

four-coordinate iron dinitrogen compound, (*i*PrPDI)Fe(N₂). This phenomenon is particularly noteworthy because the two pyridine di(imine) iron dinitrogen complexes possess distinct electronic structures (see **Section 2.2**).¹⁰ Exposure of a benzene-*d*₆ solution of (*i*PrCNC)Fe(N₂)₂ to one atmosphere of ¹⁵N₂ resulted in rapid incorporation of ¹⁵N₂ as measured by ¹⁵N NMR spectroscopy (**Figure 2.5**). Two broad resonances, consistent with solution C_{2v} symmetry (*vide infra*), were located in the ¹⁵N NMR spectrum at 323.4 and 348.4 ppm ($\Delta\nu_{1/2} = 36$ and 33 Hz, respectively). The broadness of the signals is attributed to rapid exchange between the terminal N₂ ligands and atmospheric N₂.

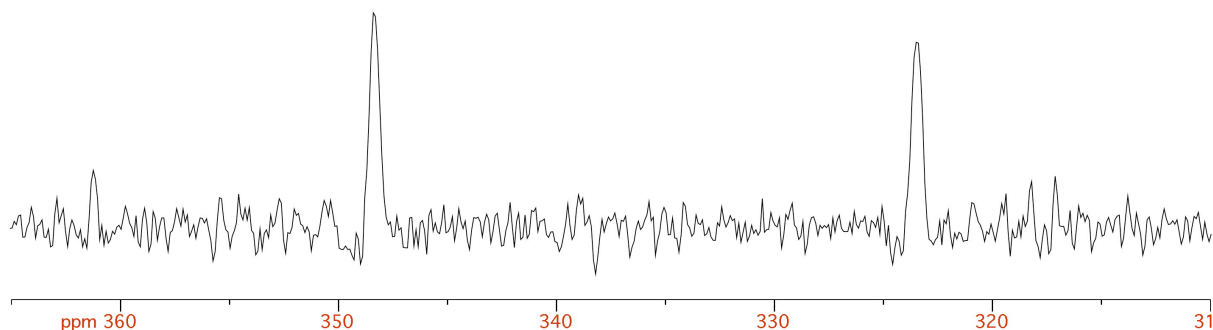


Figure 2.5. Benzene-*d*₆ ¹⁵N NMR spectrum of (*i*PrCNC)Fe(¹⁵N₂)₂ at 22 °C.

In his original report,⁵ Danopoulos described (*i*PrCNC)Fe(N₂)₂ as having limited stability in benzene-*d*₆. This was interpreted by Zhang as decomposition through dissociation of dinitrogen to yield a four-coordinate iron dinitrogen complex, (*i*PrCNC)Fe(N₂).¹⁸ In our hands, (*i*PrCNC)Fe(N₂)₂ exhibited no signs of decomposition under an atmosphere of dinitrogen in benzene-*d*₆ over the course of one week at 23 °C (as judged by ¹H NMR spectroscopy). Analysis of this solution by infrared spectroscopy provided no evidence for significant formation of a four-coordinate dinitrogen complex.

The benzene-*d*₆ ¹H NMR spectrum of (*i*PrCNC)Fe(N₂)₂, as described by Danopoulos,⁵ is

consistent with solution C_{2v} symmetry, and indicates either trigonal bipyramidal geometry or fluxionality on the timescale of the experiment. The ^{15}N NMR spectrum of $(i\text{PrCNC})\text{Fe}(^{15}\text{N}_2)_2$ suggests this is caused by rapid exchange of dinitrogen on the NMR timescale. The benzene- d_6 ^1H NMR spectroscopic features of $(i\text{PrCNC})\text{Fe}(\text{N}_2)_2$ are noteworthy, particularly in the context of the pyridine di(imine) analog. The chemical shift of protons in the iron-chelate plane do not significantly deviate from the values of free pyridine di(carbene) (**Figure 2.6**). This contrasts the behavior of $(i\text{PrPDI})\text{Fe}(\text{N}_2)_2$, which is reported to exhibit several temperature-dependent resonances that significantly deviate from the chemical shift values of free $i\text{PrPDI}$.¹⁷ This phenomenon has recently been attributed to the presence of the four-coordinate species, $(i\text{PrPDI})\text{Fe}(\text{N}_2)$ in solution, which has a thermally accessible triplet state at 23 °C.¹⁰ It is therefore

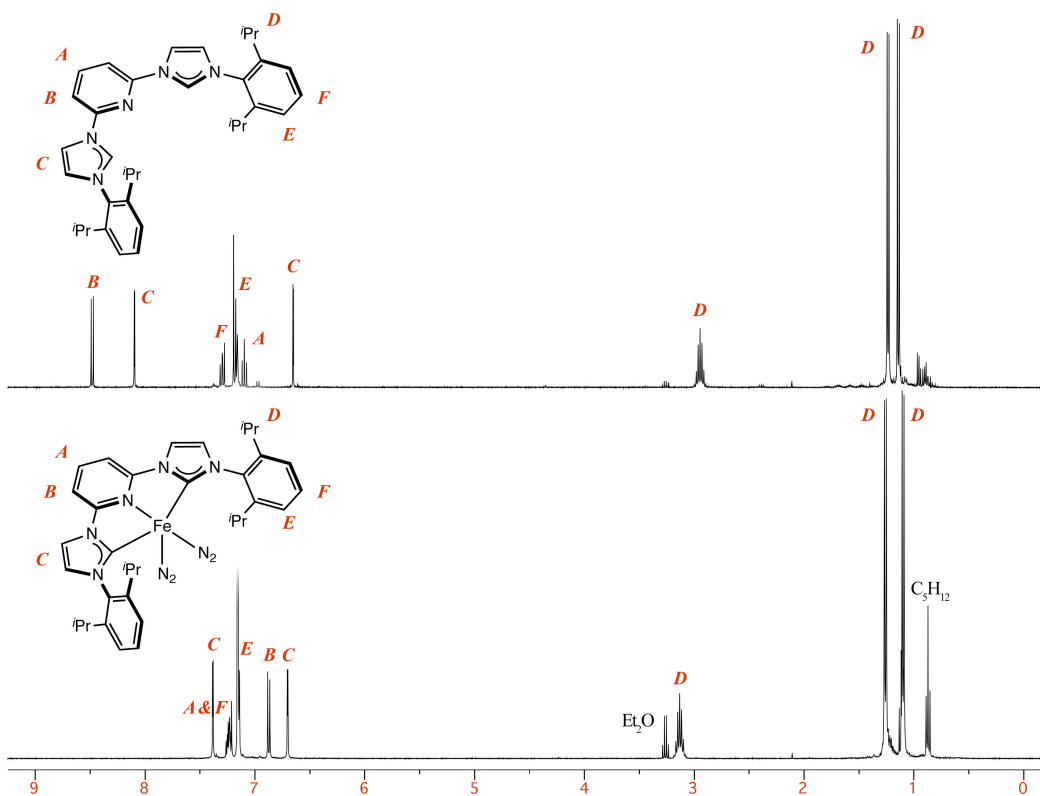


Figure 2.6. Benzene- d_6 ^1H NMR spectra of $i\text{PrCNC}$ (top) and $(i\text{PrCNC})\text{Fe}(\text{N}_2)_2$ (bottom) at 22 °C.

unsurprising that the ^1H NMR spectrum of $(i^{\text{Pr}}\text{CNC})\text{Fe}(\text{N}_2)_2$ is straightforward and reminiscent of $i^{\text{Pr}}\text{CNC}$.

Given that $(i^{\text{Pr}}\text{CNC})\text{Fe}(\text{N}_2)_2$ was not detected, another analog to a pyridine di(imine) iron compound exhibiting redox-activity was sought. Spectroscopic and computational studies of the four-coordinate pyridine di(imine) iron 4-*N,N*-dimethylaminopyridine (DMAP) complex, $(i^{\text{Pr}}\text{PDI})\text{Fe}(\text{DMAP})$, established two-electron reduction of the pyridine di(imine) chelate.¹⁹ Synthesis of the analogous pyridine di(carbene) iron complex was targeted. Inspired by the conditions used to prepare $(i^{\text{Pr}}\text{PDI})\text{Fe}(\text{DMAP})$,¹⁹ a diethyl ether solution of $(i^{\text{Pr}}\text{CNC})\text{Fe}(\text{N}_2)_2$ was treated with one equivalent of DMAP, resulting in an immediate color change from green to orange-red. A dark, crystalline solid, identified as the five-coordinate pyridine di(carbene) iron DMAP dinitrogen complex, $(i^{\text{Pr}}\text{CNC})\text{Fe}(\text{DMAP})(\text{N}_2)$, was isolated from this reaction in good yield (80%, **Figure 2.7**). The pentane solution infrared spectrum exhibited a strong N_2 absorption at 1998 cm^{-1} , which is significantly more reduced ($>10\text{ cm}^{-1}$) than those observed for $(i^{\text{Pr}}\text{CNC})\text{Fe}(\text{L})(\text{N}_2)$ ($\text{L} = \text{ethylene, PMe}_3$) in Nujol.⁵

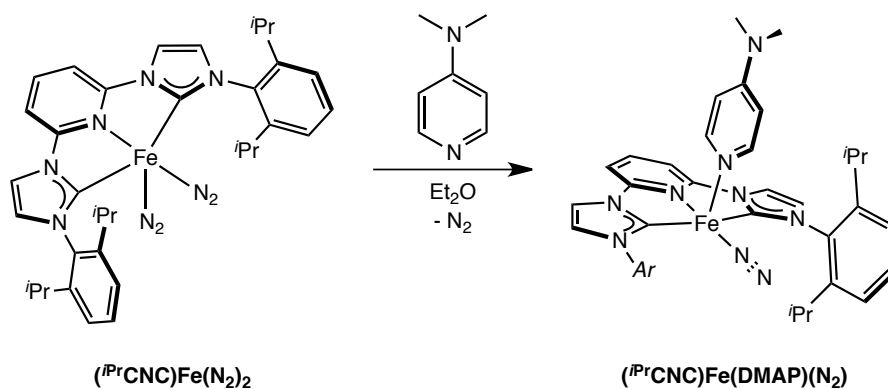


Figure 2.7. Synthesis of $(i^{\text{Pr}}\text{CNC})\text{Fe}(\text{DMAP})(\text{N}_2)$.

Single crystals of $(i^{\text{Pr}}\text{CNC})\text{Fe}(\text{DMAP})(\text{N}_2)$ suitable for X-ray diffraction were obtained from a concentrated diethyl ether solution at $-35\text{ }^\circ\text{C}$ as deep-red cubes. A representation of the

solid-state structure is presented in **Figure 2.8** and selected metrical parameters are reported in **Table 2.2**. The geometry of $(i^{\text{Pr}}\text{CNC})\text{Fe}(\text{DMAP})(\text{N}_2)$ is best described as distorted square-pyramidal with the DMAP ligand occupying the apical site. No significant geometric distortions were observed throughout the DMAP ligand,²⁰ confirming the absence of significant metal-ligand back-bonding. The five-coordinate bonding motif observed for this complex is consistent with $(i^{\text{Pr}}\text{CNC})\text{Fe}(\eta^2\text{-C}_2\text{H}_4)(\text{N}_2)$ and $(i^{\text{Pr}}\text{CNC})\text{Fe}(\text{PR}_3)(\text{N}_2)$ ($\text{R} = \text{CH}_3, \text{Cy}$),⁵ but is relatively rare for

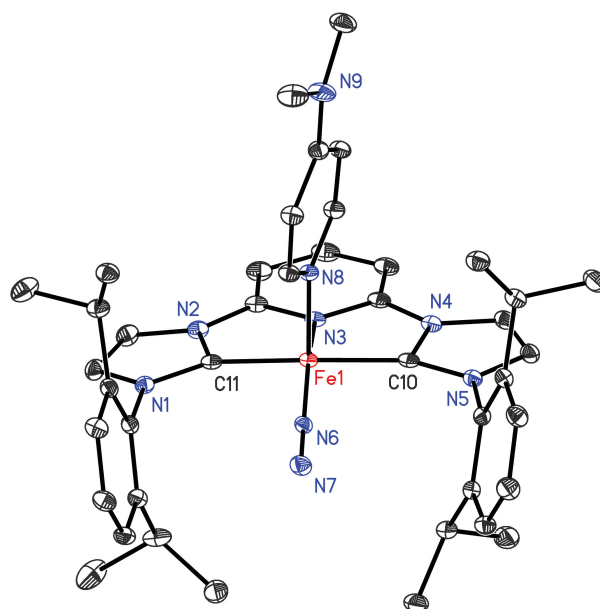


Figure 2.8. Solid-state structure of $(i^{\text{Pr}}\text{CNC})\text{Fe}(\text{DMAP})(\text{N}_2)$ at 30% probability ellipsoids. Hydrogen atoms omitted for clarity.

Table 2.2. Bond distances (Å) and angles (°) for $(i^{\text{Pr}}\text{CNC})\text{Fe}(\text{DMAP})(\text{N}_2)$.

Fe(1)–N(3)	1.8903(14)	N(1)–C(11)	1.387(2)
Fe(1)–C(10)	1.9156(17)	C(11)–N(2)	1.406(2)
Fe(1)–C(11)	1.9179(17)	N(4)–C(10)	1.405(2)
Fe(1)–N(6)	1.7797(14)	C(10)–N(5)	1.387(2)
Fe(1)–N(8)	2.0467(16)	N(6)–N(7)	1.1323(19)
N(3)–Fe(1)–N(6)	160.62(6)	N(1)–C(11)–N(2)	101.73(13)
N(3)–Fe(1)–N(8)	102.36(6)	N(4)–C(10)–N(5)	101.55(13)

pyridine di(imine) iron complexes.

Only two examples of a pyridine di(imine) iron complexes bearing both a neutral ligand donor and a molecule of dinitrogen in the basal position have been reported.²¹ The ¹H NMR spectra of the five-coordinate pyridine di(imine) iron complexes, (ⁱPrPDI)Fe(PET₃)(N₂) and (ⁱPrPDI)Fe(THT)(N₂) (THT = tetrahydrothiophene) exhibit different spectroscopic behaviors as reported by Bart *et al.*²¹ In the case of (ⁱPrPDI)Fe(PET₃)(N₂), broad resonances indicative of a dynamic process were observed at 23 °C in benzene-*d*₆. Upon cooling a toluene-*d*₈ solution of the compound to -80 °C, sharp resonances consistent with an iron compound of *C*_s symmetry were observed. No evidence of temperature independent paramagnetism was obtained under these conditions, and the in-plane protons were not shifted significantly from their diamagnetic reference values. In contrast, the benzene-*d*₆ ¹H NMR spectrum of (ⁱPrPDI)Fe(THT)(N₂) established temperature independent paramagnetism. This is unusual for five-coordinate pyridine di(imine) iron complexes, which are typically redox non-innocent.¹⁰ Temperature independent paramagnetism has been associated with redox-active complexes, and suggests N₂ dissociation from (ⁱPrPDI)Fe(THT)(N₂) in solution.

The benzene-*d*₆ ¹H NMR spectrum of (ⁱPrCNC)Fe(DMAP)(N₂) at 22 °C exhibits the number of resonances consistent with an iron complex of *C*_s symmetry, suggesting that the solid-state geometry is preserved in solution. Additionally, the chemical shift for the protons in the idealized iron-chelate plane do not significantly shift from the values of ⁱPrCNC. The most notable feature of the spectrum is the upfield shift of the *ortho*- and *meta*-hydrogens on the coordinated DMAP to 6.95 and 5.19 ppm, respectively. Broad resonances corresponding to free DMAP were also observed, suggesting competitive binding between DMAP and dinitrogen.

Removal of the dinitrogen headspace from this sample resulted in the disappearance of these signals.

In order to investigate the electronic structure of the reduced pyridine di(carbene) iron complexes, ^{57}Fe Mössbauer spectra were collected at 80 K in the solid state. The parameters of $(i\text{PrCNC})\text{FeBr}_2$ and $(i\text{PrCNC})\text{Fe}(\text{CO})_2$ were also obtained. Representative Mössbauer spectra are presented in **Figure 2.9** and the parameters are reported in **Table 2.3**. Values for the corresponding pyridine di(imine) iron complexes are included for comparison. The isomer shift and quadrupole splitting observed for $(i\text{PrCNC})\text{FeBr}_2$ are consistent with a high-spin, Fe^{II} ion.

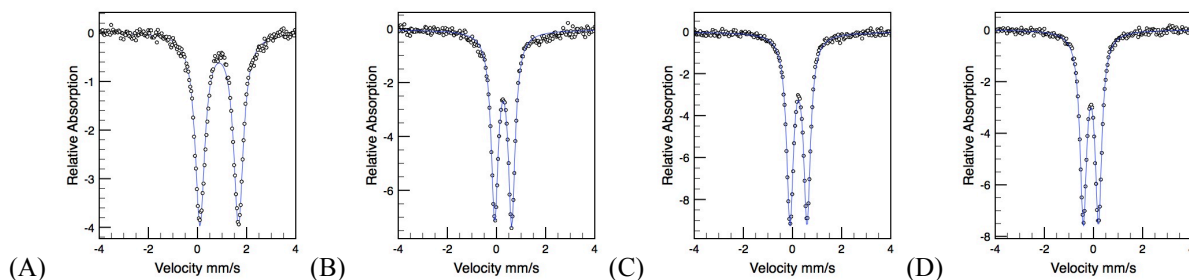


Figure 2.9. Zero-field ^{57}Fe Mössbauer spectra for pyridine di(carbene) iron complexes: (A) $(i\text{PrCNC})\text{FeBr}_2$, (B) $(i\text{PrCNC})\text{Fe}(\text{N}_2)_2$, (C) $(i\text{PrCNC})\text{Fe}(\text{DMAP})(\text{N}_2)$, and (D) $(i\text{PrCNC})\text{Fe}(\text{CO})_2$.

Table 2.3. Zero-field ^{57}Fe Mössbauer parameters for pyridine di(carbene) and pyridine di(imine) iron complexes recorded at 80 K.^a

Compound	δ ($\text{mm}\cdot\text{s}^{-1}$)	$ \Delta E_Q $ ($\text{mm}\cdot\text{s}^{-1}$)
$(i\text{PrCNC})\text{FeBr}_2$	0.88	1.57
$(i\text{PrPDI})\text{FeCl}_2^a$	0.89	2.40
$(i\text{PrCNC})\text{Fe}(\text{N}_2)_2$	0.27	0.69
$(i\text{PrPDI})\text{Fe}(\text{N}_2)_2$	0.39	0.53
$(i\text{PrCNC})\text{Fe}(\text{DMAP})(\text{N}_2)$	0.24	0.70
$(i\text{PrPDI})\text{Fe}(\text{DMAP})^a$	0.31	1.94
$(i\text{PrCNC})\text{Fe}(\text{CO})_2$	-0.10	0.62
$(i\text{PrPDI})\text{Fe}(\text{CO})_2^a$	0.03	1.17

^a Data from reference 19.

The isomer shifts of the formally Fe⁰ complexes are consistent with low- or intermediate-spin configurations, corresponding to either redox non-innocent or redox-active descriptions, respectively, and suggest no gross differences in electronic structure as a result of the nature or identity of the non-chelate ligands. The isomer shifts of the pyridine di(carbene) iron complexes are consistently lower than those of the pyridine di(imine) analogues, a result of increased covalency and shorter iron-ligand bonds. The quadrupole splitting parameters for all of the reduced species are indistinguishable, which is unsurprising given the geometry similarities in the solid state, and suggest a similar electronic structure.

These complexes were further investigated by X-ray absorption spectroscopy (XAS). This technique is sensitive to the oxidation state of the metal absorber, local site symmetry, and coordination environment,²² and has been used to gain insight into the electronic structure of pyridine di(imine) iron complexes – particularly for distinguishing between redox non-innocent and redox-active species.^{10,23} The normalized XAS data for (*i*PrCNC)FeBr₂, (*i*PrCNC)Fe(N₂)₂, (*i*PrCNC)Fe(DMAP)(N₂) and (*i*PrCNC)Fe(CO)₂ are presented in **Figure 2.10**. The spectrum of (*i*PrCNC)FeBr₂, an established high-spin Fe^{II} complex,²⁴ was collected as a calibration for comparison. The spectrum is comparable to the pyridine di(imine) analog with respect to the spectral shape and energy.¹⁰ The shape of the edge for each of the reduced pyridine di(carbene) iron complexes are nearly indistinguishable from one another, supporting similar electronic structure and coordination. Additionally, the rising edges of each of the reduced species shift ~5 eV to higher energy when compared to (*i*PrCNC)FeBr₂, with (*i*PrCNC)Fe(CO)₂ exhibiting the highest energy. This is likely attributed to the relative ability of the iron to back-bond into the dinitrogen and carbonyl ligands in the coordination sphere, and results in the appearance of a

more highly oxidized center.²⁵

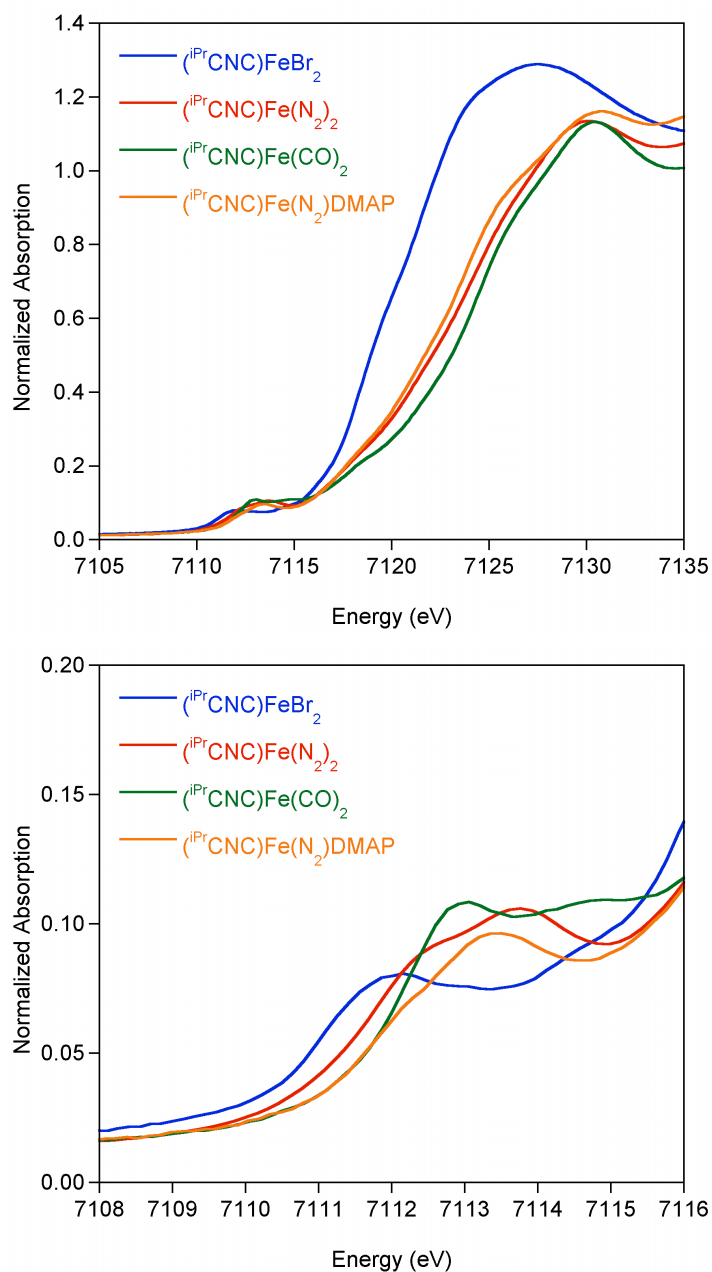


Figure 2.10. Normalized Fe K-edge X-ray absorption spectra of pyridine di(carbene) iron complexes. Data collected at 10 K.

The pre-edge of each formally Fe^0 species is shifted to higher energy as compared to the Fe^{II} species, $(iPrCNC)FeBr_2$, and are more consistent with typical Fe^{III} compounds. This effect is likely a combination of the iron oxidation state and the strongly backbonding ligands, making a

conclusive assignment challenging. As in the pyridine di(imine) iron analogues (**Figure 2.11**), the pre-edges of the formally Fe⁰ compounds display two features. Based on the assignments for (ⁱPrPDI), the lower energy feature corresponds to a metal 1s to 3d transition and the second feature has tentatively been assigned as a 1s to ligand π* transition, and is similar, although relatively less intense as compared with the first feature, to absorptions exhibited by the pyridine di(imine) iron analogues. Computational investigations are needed to understand the differences in intensities. These data, in conjunction with density functional theory (see **Appendix B.1**) indicate that the reduced pyridine di(carbene) iron complexes are redox non-innocent and are

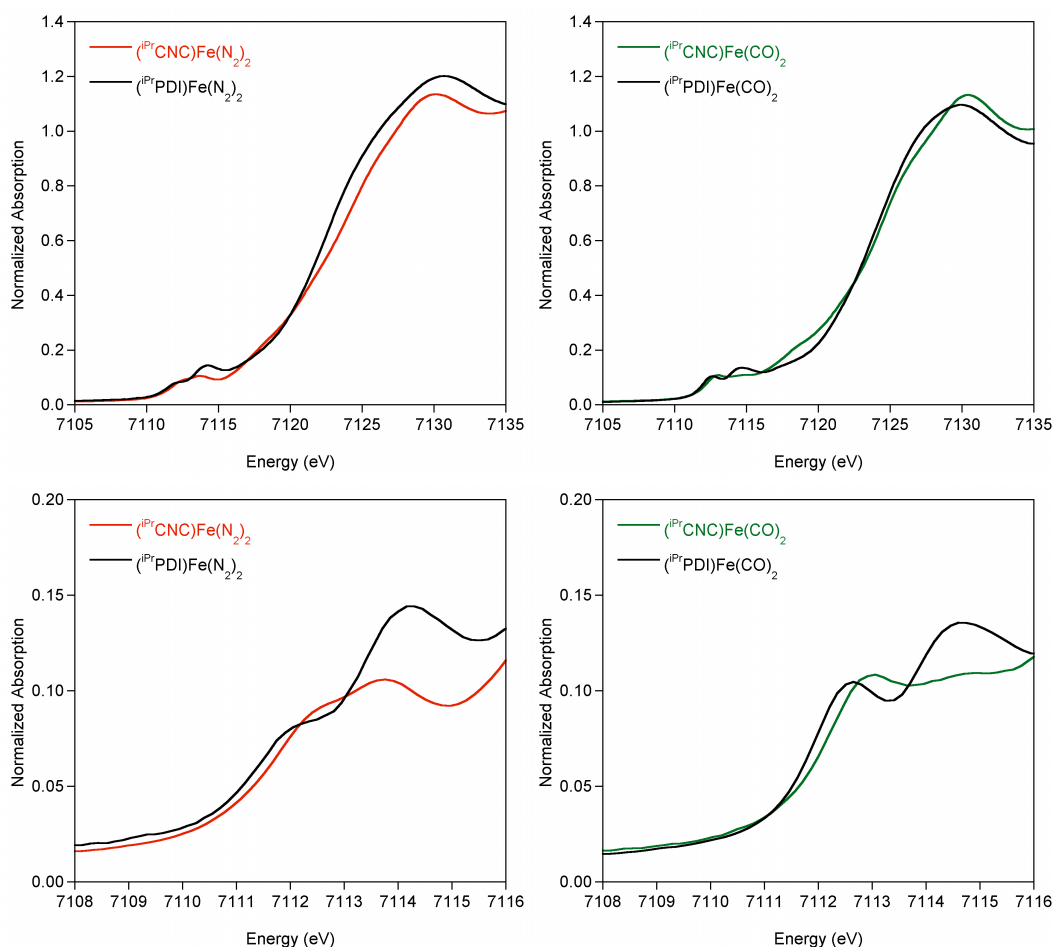


Figure 2.11. Normalized Fe K-edge X-ray absorption spectra of pyridine di(carbene) iron complexes and their pyridine di(imine) analogs. Data collected at 10 K.

best described as a hybrid structure between $(i\text{PrCNC}^0)\text{Fe}^0$ and $(i\text{PrCNC}^{2-})\text{Fe}^{\text{II}}$ resonance forms with $i\text{PrCNC}$ functioning as a π -acceptor (**Figure 2.12**).

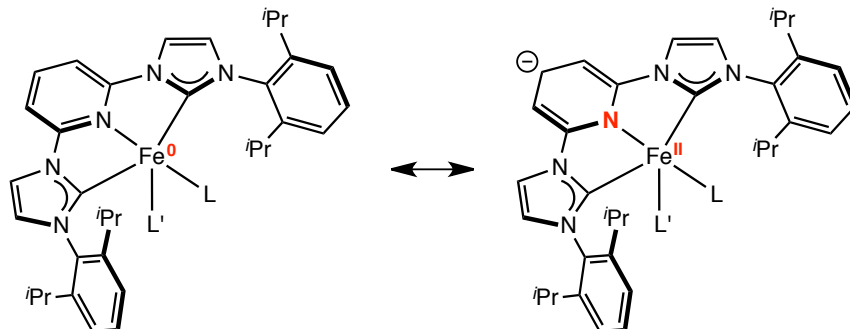


Figure 2.12. Electronic structure of $(i\text{PrCNC})\text{Fe}(\text{L})(\text{L}')$
($\text{L} = \text{L}' = \text{N}_2$; $\text{L} = \text{L}' = \text{CO}$; $\text{L} = \text{N}_2$, $\text{L}' = \text{DMAP}$).

2.4 Hydrogenation: Catalytic Evaluation of $(i\text{PrCNC})\text{Fe}(\text{N}_2)_2$

Our laboratory, inspired by the thermal²⁶ and photochemical²⁷ activity of $\text{Fe}(\text{CO})_5$ for olefin hydrogenation and hydrosilylation, sought to use $[(i\text{PrPDI})\text{Fe}]$ as a mimic for the proposed $[\text{Fe}(\text{CO})_3]$ active species.²⁸ Because $(i\text{PrPDI})\text{Fe}(\text{N}_2)_2$ and $(i\text{PrCNC})\text{Fe}(\text{N}_2)_2$ have similar electronic structures,¹⁰ the competency and activity of the latter complex for olefin hydrogenation was of interest. To evaluate catalytic activity, the hydrogenation of ethylene was investigated. Danopoulos and coworkers reported that addition of excess ethylene to $(i\text{PrCNC})\text{Fe}(\text{N}_2)_2$ resulted in substitution of only one molecule of dinitrogen (**Figure 2.13**).⁵ The resulting compound, $(i\text{PrCNC})\text{Fe}(\eta^2\text{-C}_2\text{H}_4)(\text{N}_2)$ was characterized by infrared and ^1H NMR spectroscopies as well as X-ray diffraction.

Addition of 20 equivalents of ethylene to a 23 mM solution of $(i\text{PrCNC})\text{Fe}(\text{N}_2)_2$ in benzene- d_6 resulted in an immediate color change from green to red-brown accompanied by formation of the bis(ethylene) complex, $(i\text{PrCNC})\text{Fe}(\eta^2\text{-C}_2\text{H}_4)_2$. The benzene- d_6 ^1H NMR

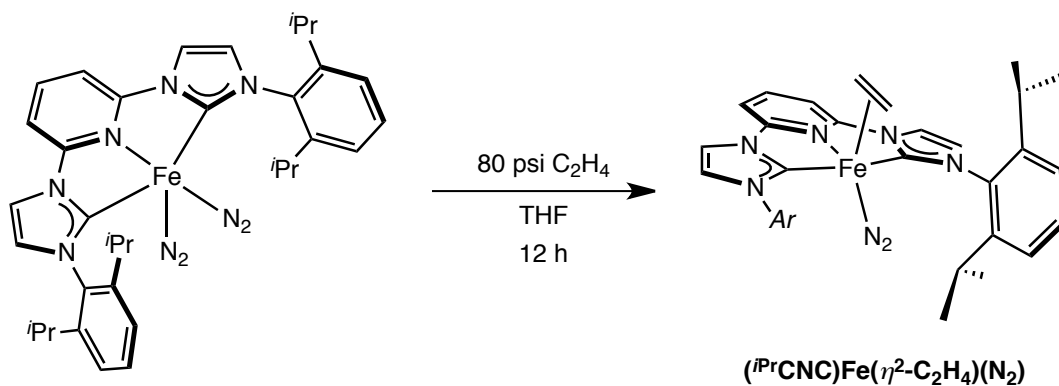


Figure 2.13. Synthesis of $(iPrCNC)Fe(\eta^2-C_2H_4)(N_2)$.

spectrum of $(iPrCNC)Fe(\eta^2-C_2H_4)_2$ exhibits C_{2v} symmetry (**Figure 2.14**), distinguishing it from the mono(ethylene) complex reported by Danopoulos and coworkers. A singlet for coordinated ethylene was located at 2.46 ppm. The resonance corresponding to the uncoordinated ethylene was broad, suggesting rapid exchange with coordinated ethylene on the timescale of the experiment. Addition of 1 atmosphere of H_2 to this solution and monitoring by 1H NMR spectroscopy resulted in the rapid appearance of ethane, demonstrating that $(iPrCNC)Fe(N_2)_2$ was active for olefin hydrogenation. During the course of the reaction, only the bis(ethylene) complex was observed.

Building upon the preliminary investigations presented in Section 1.6, the hydrogenation activity of $(iPrCNC)Fe(N_2)_2$ was assessed using ethyl 3,3-dimethylacrylate, *trans*-methylstilbene and 1,1-diphenylethylene. For consistency, the conditions used to assay the activity of the *para*-substituted pyridine di(imine) iron complexes were employed.²⁹ The results of this study are presented in **Figure 2.15**.

The trends exhibited by $(iPrCNC)Fe(N_2)_2$ for the hydrogenation of these selected substrates were consistent with those demonstrated for $(4-R-iPrPDI)Fe(N_2)$. As the most reduced iron dinitrogen complex, $(iPrCNC)Fe(N_2)_2$ exhibited significantly higher activity for the

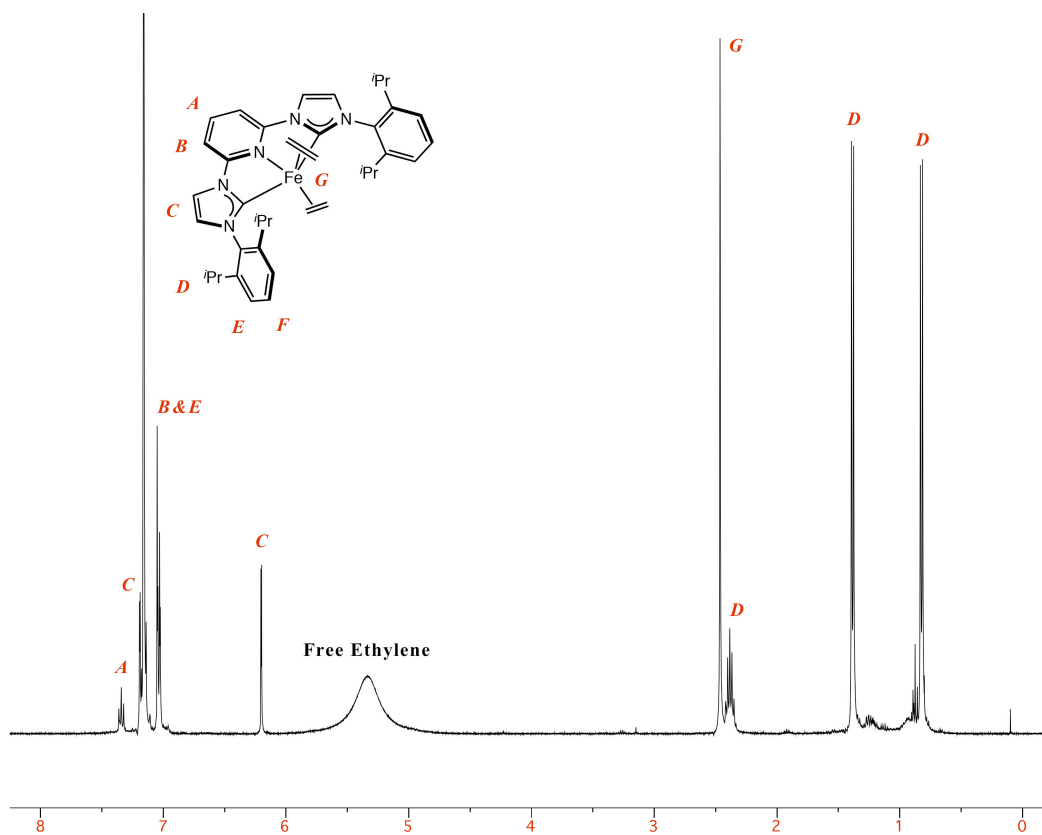


Figure 2.14. Benzene- d_6 ^1H NMR spectrum of $(i\text{PrCNC})\text{Fe}(\text{N}_2)_2$ (bottom) at 22 °C.

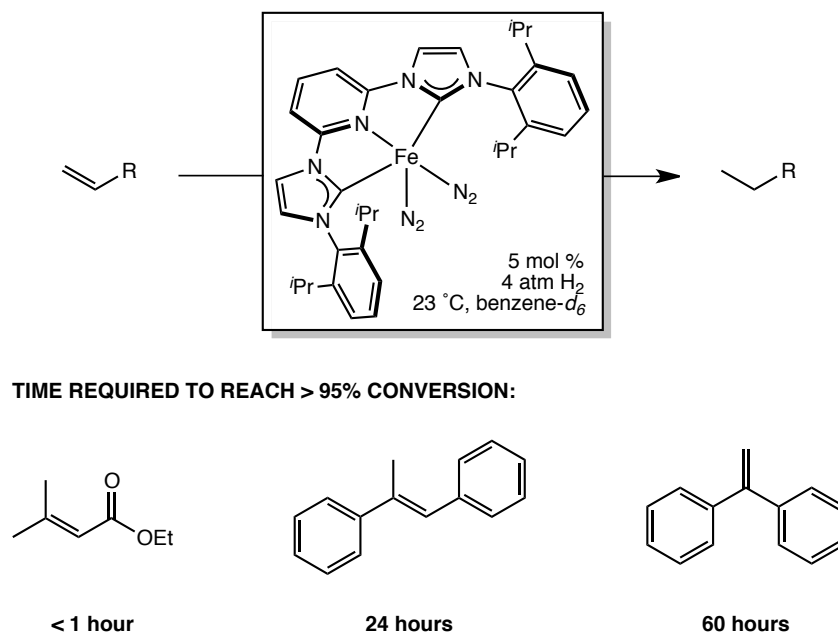


Figure 2.15. Assay for the hydrogenation activity of $(i\text{PrCNC})\text{Fe}(\text{N}_2)_2$ using 4 atm of H_2 .

hydrogenation of ethyl 3,3-dimethylacrylate and *trans*-methylstilbene. Conversion to >95% for these two olefins was accomplished in <1 h and within 24 h, respectively, as determined by ¹H NMR or GC-FID analysis. The relative activity of (*i*PrCNC)Fe(N₂)₂ for the hydrogenation of ethyl 3,3-dimethylacrylate under these conditions cannot be distinguished from [(^{Me}PDI)Fe(N₂)]₂(μ₂-N₂), the most active pyridine di(imine) iron dinitrogen complex reported to date.³⁰ However, prior work has shown that (*i*PrPDI)Fe(N₂)₂ and [(^{Me}PDI)Fe(N₂)]₂(μ₂-N₂) are not very active for the hydrogenation of unactivated tri-substituted olefins.^{31,32} Therefore, (*i*PrCNC)Fe(N₂)₂ may be the most synthetically useful iron catalyst for this class of substrate.

The activity of (*i*PrCNC)Fe(N₂)₂ towards the hydrogenation of 1,1-diphenylethylene, although consistent with the trend observed for (4-R-*i*PrPDI)Fe(N₂), was inconsistent with the general trend observed for the other substrates. Conversion of 1,1-diphenylethylene to 1,1-diphenylethane in >95% was observed within 60 hours under standard conditions. The substrate dependence on the activity of pyridine di(imine) and the pyridine di(carbene) iron dinitrogen complexes prompted further investigation.

2.5 Hydrogenation: Mechanistic Insight into the Activity of (*i*PrCNC)Fe(N₂)₂

In order to investigate the mechanism of olefin hydrogenation, the reactivity of (*i*PrCNC)Fe(N₂)₂ with dihydrogen was explored. Addition of 1 atm of H₂ to a (23 mM) benzene-*d*₆ solution of (*i*PrCNC)Fe(N₂)₂ resulted in an immediate color change from green to green-brown. The ¹H NMR spectrum of the resulting solution revealed the presence of three species (**A**, **B**, and **C**; **Figure 2.16**) – each with C_{2v} molecular symmetry. The resonances of species **A** were consistent with the chemical shift values of the bis(dinitrogen) complex, and with the exception

of the most upfield isopropyl methyl doublet, were broad and featureless. Over the course of two hours at 23 °C, the downfield isopropyl methyl and imidazolylidine resonances of each species decreased in intensity, while the corresponding upfield isopropyl methyl and imidazolylidine resonances were unchanged. The solution was then re-exposed to an atmosphere of dinitrogen. Analysis by ^1H NMR spectroscopy revealed that complex **C** had immediately and cleanly reverted to $(i\text{PrCNC})\text{Fe}(\text{N}_2)_2$ while species **B** persisted for several hours before reverting to $(i\text{PrCNC})\text{Fe}(\text{N}_2)_2$. Similar observations were made upon addition of D_2 to a 23 mM solution of $(i\text{PrCNC})\text{Fe}(\text{N}_2)_2$ in benzene- d_6 .

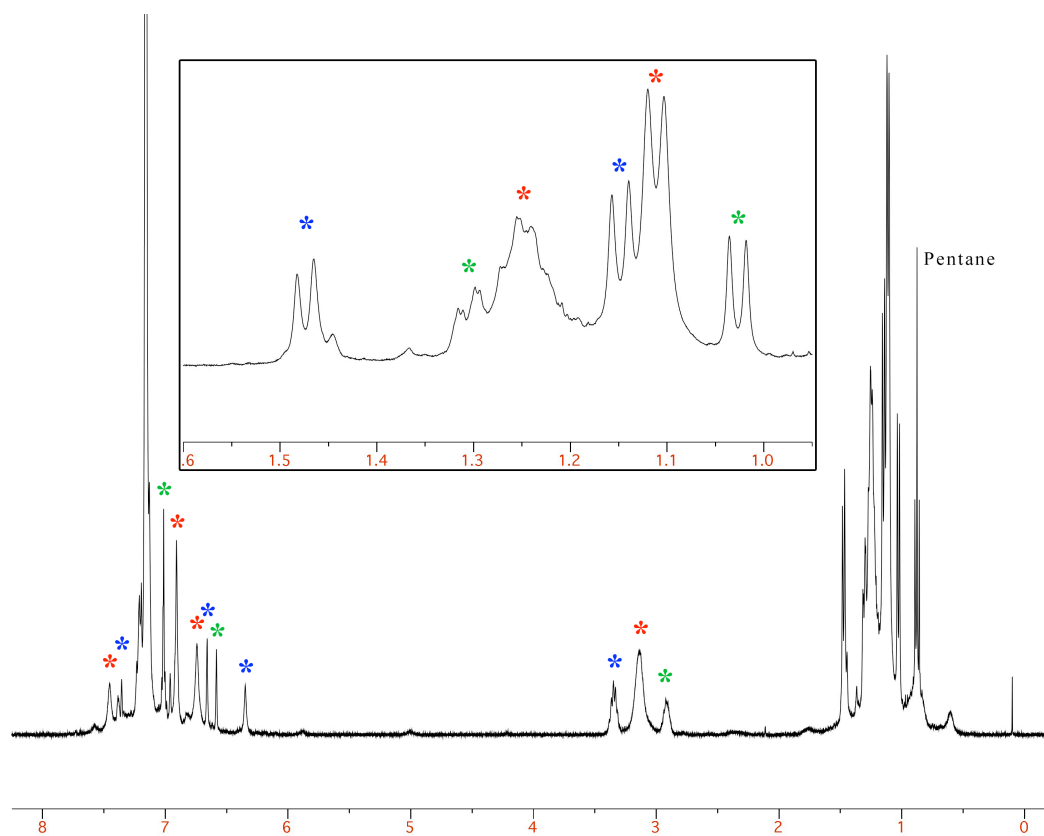


Figure 2.16. Benzene- d_6 ^1H NMR spectrum of the three species – **A** (red), **B** (blue), and **C** (green) – arising from exposure of a 23 mM solution of $(i\text{PrCNC})\text{Fe}(\text{N}_2)_2$ to H_2 for 2 hours. Inset shows the region from 0.95 to 1.60 ppm.

The identity of compounds **A**, **B** and **C** are currently unknown; however, proposed

structures are presented in **Figure 2.17**. The similarity between the chemical shift values of **A** and $(i\text{PrCNC})\text{Fe}(\text{N}_2)_2$ suggest that these species are closely related, and the broadness of those signals indicate a dynamic process. We propose that compound **A** is the dihydrogen, dinitrogen compound, $(i\text{PrCNC})\text{Fe}(\text{H}_2)(\text{N}_2)$. Rapid dissociation of dihydrogen accounts for the observed solution C_{2v} symmetry and the broadness of the resonances. The chemical shift values of compound **B** are similar to those of the iron dialkyl species presented in **Chapter 3**, and on this basis, we propose that compound **B** is the iron dihydride dinitrogen complex, $(i\text{PrCNC})\text{Fe}(\text{H})_2(\text{N}_2)$. The slow disappearance of this species upon re-exposure to N_2 suggests relatively slow reductive elimination of H_2 . The chemical shift values of **C**, particularly the upfield shift of the isopropyl methine, are relatively uncommon for $[(i\text{PrCNC})\text{Fe}]$ species, with the exception of the bis(ethylene) complex. Therefore, compound **C** is proposed to be the bis(dihydrogen) complex, $(i\text{PrCNC})\text{Fe}(\text{H}_2)_2$. Rapid displacement of H_2 by N_2 accounts for the immediate disappearance of this compound upon re-exposure to N_2 .

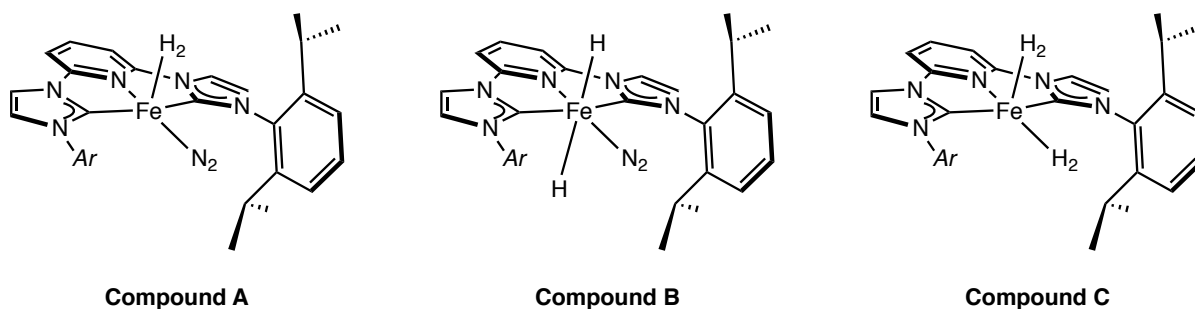


Figure 2.17. Proposed structures for compounds **A**, **B**, and **C**.

The benzene- d_6 ^1H NMR spectrum of recovered $(i\text{PrCNC})\text{Fe}(\text{N}_2)_2$ revealed several interesting features. The *p*-pyridine resonance was not present and the downfield imidazolylidene and isopropyl methyl resonances were reduced in intensity. These results established deuterium

incorporation into these positions, which was also confirmed by ^2H NMR spectroscopy in benzene. Deuterium incorporation occurred exclusively at the positions indicated in **Figure 2.18**, and was confirmed by NOESY correlation. The only source of deuterium during the course of this reaction was benzene- d_6 , conclusively demonstrating that $(i\text{PrCNC})\text{Fe}(\text{N}_2)_2$ activates benzene upon addition of H_2 .

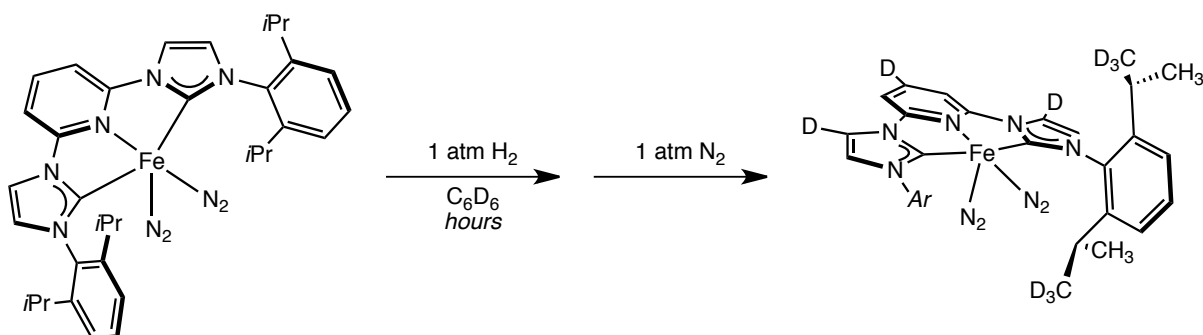
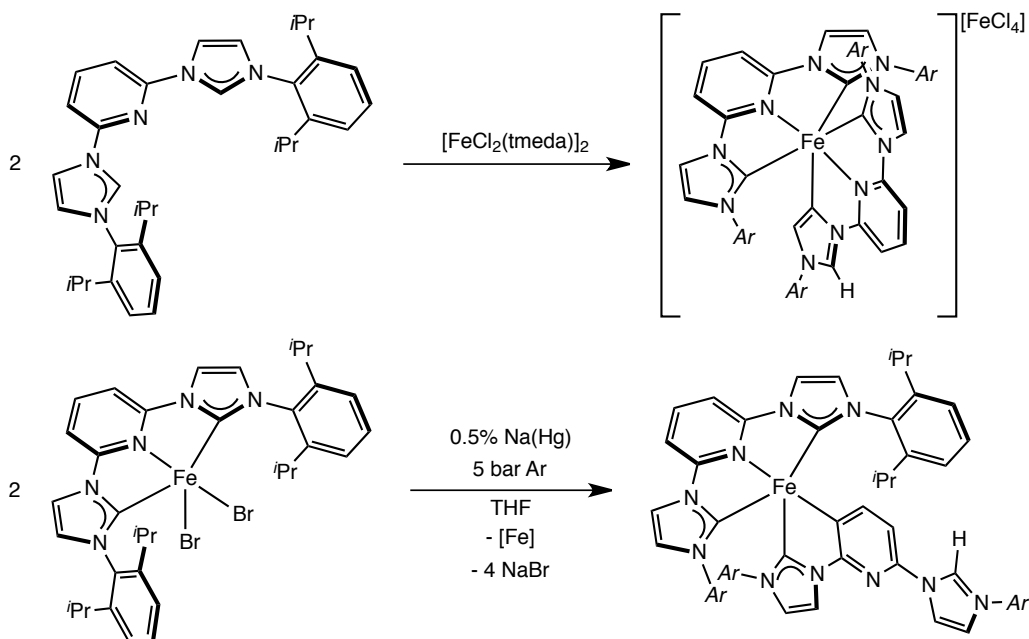


Figure 2.18. Recovered $(i\text{PrCNC})\text{Fe}(\text{N}_2)_2$ after exposure to H_2 in benzene- d_6 and re-exposure to N_2 .

Danopoulos and coworkers have previously reported two iron complexes arising from deprotonation or activation of $i\text{PrCNC}$, and one example of photolytically induced aryl C–H activation by $(i\text{PrCNC})\text{Fe}(\text{N}_2)_2$ (**Figure 2.19**).^{8,24} The first example was a bis(ligand)-type complex prepared from the addition of $[\text{FeCl}_2(\text{tmeda})]_2$ to free $i\text{PrCNC}$.²⁴ Notably, one of the ligands is an abnormal carbene, and is proposed to arise from deprotonation of the imidazolylidene protons by tmeda. The second example, involving C–H activation of a *meta*-pyridine, was prepared in low yield from sodium amalgam reduction of $(i\text{PrCNC})\text{FeBr}_2$ under argon and is proposed to be a common decomposition product for reduced $[(i\text{PrCNC})\text{Fe}]$ complexes.⁸ Lastly, aryl C–H activation by $(i\text{PrCNC})\text{Fe}(\text{N}_2)_2$ of a benzaldehyde anilide was observed upon photolysis ($\lambda = 254\text{ nm}$) resulting in formation of the formally iron(II) *cis*-phenyl hydride.⁸

***i*PrCNC DEPROTONATION/ACTIVATION:**



ARYL C–H ACTIVATION:

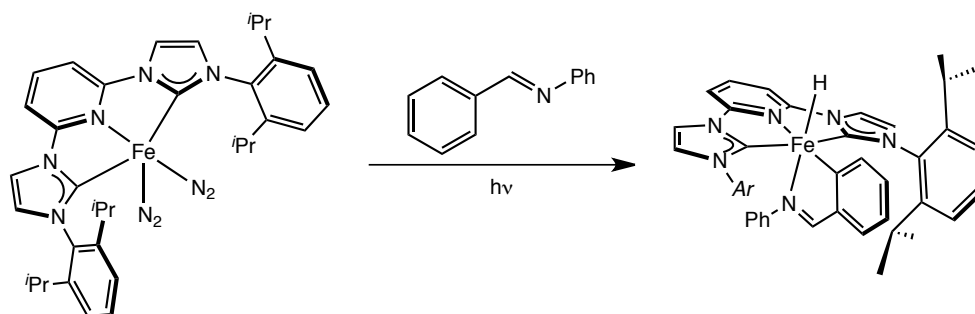


Figure 2.18. Examples of *i*PrCNC deprotonation/activation and aryl C–H activation by $(i\text{PrCNC})\text{Fe}(\text{N}_2)_2$.

To determine if *i*PrCNC ligand deuteration occurred by an inter- or intramolecular process, D_2 gas was added to a 1:1 mixture of $(i\text{PrCNC})\text{Fe}(\text{N}_2)_2$ and $(i\text{PrCNC})\text{Fe}(\text{CO})_2$ in benzene- d_6 . Monitoring the reaction over the course of one day at 23°C by ^1H NMR spectroscopy established deuterium incorporation into the *p*-pyridine and imidazolylidene positions of $(i\text{PrCNC})\text{Fe}(\text{CO})_2$, as evidenced by the appearance of a singlet for the *m*-pyridine resonance, and disappearance of the downfield imidazolylidene resonance. Deuterium incorporation was not observed at the isopropyl methyl position. The results of this experiment are presented in **Figure**

2.20. These data demonstrate that deuterium incorporation at the *p*-pyridine and imidazolylidene positions occurs from an intermolecular process, while deuterium incorporation at the isopropyl methyl resonance is exclusively intramolecular. Deuterium incorporation at these positions was not observed in the absence of $(i\text{PrCNC})\text{Fe}(\text{N}_2)_2$ under identical conditions.

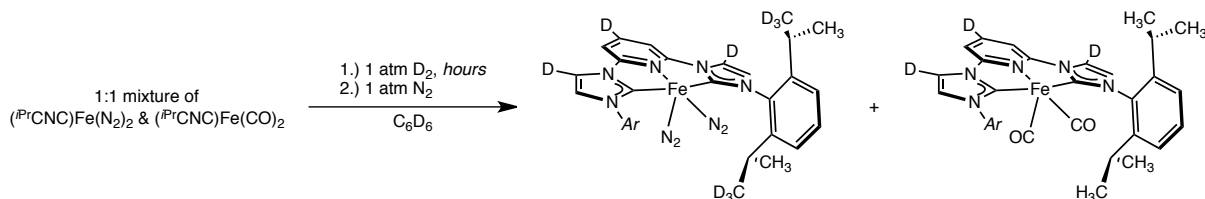


Figure 2.20. Intermolecular deuterium incorporation into $(i\text{PrCNC})\text{Fe}(\text{CO})_2$.

A series of isotopic labeling experiments was performed in order to probe the regioselectivity of olefin hydrogenation with $(i\text{PrCNC})\text{Fe}(\text{N}_2)_2$. Norbornene was used to evaluate *cis/trans* and *exo/endo* selectivity and as a potential probe for 1-electron chemistry. $(4\text{-Me}_2\text{N-}i\text{PrPDI})\text{Fe}(\text{N}_2)_2$ was also examined for completeness. Prior work demonstrated that the stereochemistry of initial hydrogen addition with $(i\text{PrPDI})\text{Fe}(\text{N}_2)_2$ takes place in a *syn* fashion across the C=C bond.¹⁷ Addition of 1 atmosphere of D_2 to a 0.5 M solution of norbornene in benzene- d_6 containing 5 mol % [Fe] resulted in selective formation of *exo,exo*-2,3- d_2 -norbornane with each of the iron dinitrogen complexes (**Figure 2.21**).³³ Therefore, each of the complexes likely exhibits similar regioselectivity for the insertion of olefins.

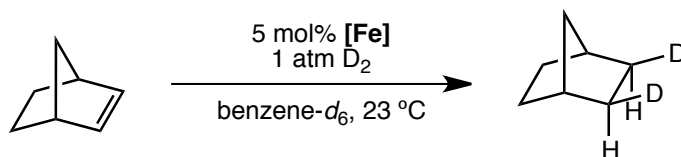


Figure 2.21. Deuteration of norbornene using $(i\text{PrCNC})\text{Fe}(\text{N}_2)_2$, $(4\text{-Me}_2\text{N-}i\text{PrPDI})\text{Fe}(\text{N}_2)_2$, and $(i\text{PrPDI})\text{Fe}(\text{N}_2)_2$ under 1 atm of D_2 .

To examine the divergence in hydrogenation activity observed with 1,1-diphenylethylene,

deuteration was performed with 5 mol % (*i*PrCNC)Fe(N₂)₂ in benzene-*d*₆ employing 4 atmospheres of D₂.²⁹ After 60 hours, the reaction mixture was quenched. Analysis by ¹H NMR spectroscopy revealed the absence of resonances in the aliphatic and olefinic region (0–6 ppm). However, both 1,1-diphenylethylene and 1,1-diphenylethane were present in approximately a 1:1 ratio as determined by GC-FID analysis. This indicated both were present in their deuterated forms, 1,1-diphenylethylene-*d*₂ and 1,1-diphenylethane-*d*₄, respectively, and was confirmed by ²H NMR spectroscopy in benzene. No evidence for incorporation of the isotopic label in the phenyl substituents of the substrate or product was observed. These results are summarized in

Figure 2.22.

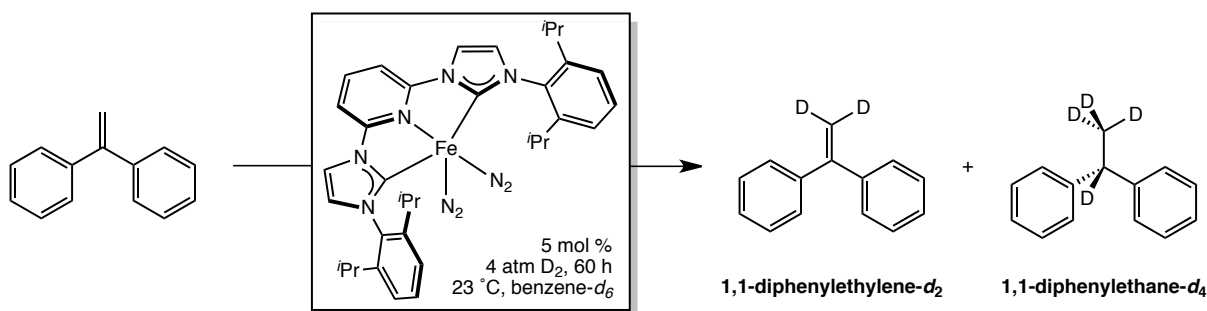


Figure 2.22. Deuteration of 1,1-diphenylethylene under 4 atmospheres of D₂ for 60 hours using 5 mol % (*i*PrCNC)Fe(N₂)₂.

Because benzene-*d*₆ is another likely source of deuterium, the catalytic and stoichiometric hydrogenation of 1,1-diphenylethylene was carefully monitored under one and four atmospheres of H₂, respectively. Benzene-*d*₆ served as the only source of deuterium under these conditions. The catalytic hydrogenation of 1,1-diphenylethylene was performed for 12 hours,²⁹ and the resulting mixture was filtered and analyzed by ¹H NMR spectroscopy. The starting material, 1,1-diphenylethylene and product, 1,1-diphenylethane, were observed in a 1:2 ratio (as judged by integration of the vinylic and methine resonances, respectively). Importantly, a second, smaller

vinyllic singlet resonance was located 0.015 ppm upfield of the starting material, and was assigned as 1,1-diphenylethylene- d_1 . Addition of 1 atmosphere of H_2 to a J. Young tube containing an equimolar (23 mM) solution of (^{iPr}CNC)Fe(N_2) $_2$ and 1,1-diphenylethylene, resulted in rapid growth of the signal corresponding to 1,1-diphenylethylene- d_1 with concomitant disappearance of the vinyllic resonance corresponding to the protio analog. Over time, both resonances disappeared without significant growth of those signals corresponding to 1,1-diphenylethane, indicating that at lower pressures of hydrogen, deuterium incorporation – and therefore benzene- d_6 activation – is competitive with hydrogenation. Deuterium incorporation was not observed in an equimolar (23 mM) benzene- d_6 solution of (^{iPr}CNC)Fe(N_2) $_2$ and 1,1-diphenylethylene over the course of one week, confirming that reaction with H_2 or D_2 is necessary. These results conclusively show that benzene- d_6 is a source of deuterium involved in vinyllic H/D exchange.

In summary, these reactions demonstrate that the relative rate of deuterium incorporation into the vinyllic position is significantly faster for 1,1-diphenylethylene than the rate of deuteration (or hydrogenation) under low pressures of H_2 in benzene- d_6 , or under 4 atmospheres of D_2 . Two mechanistic possibilities account for this behavior: **(A)** 2,1-insertion of an iron-deuteride into the olefin followed by rapid β -hydride elimination or **(B)** vinyllic C–H bond activation followed by hydride/deuteride exchange from D_2 or benzene- d_6 . These two mechanisms are presented in **Figure 2.23**. Benzene- d_6 C–D bond activation is not shown for clarity.

The accessibility of the tertiary iron alkyl hydride complex, (^{iPr}CNC)Fe(C(Ph) $_2$ CH $_3$)(H) was evaluated by DFT using a simple spin-restricted singlet approach. Geometry optimization

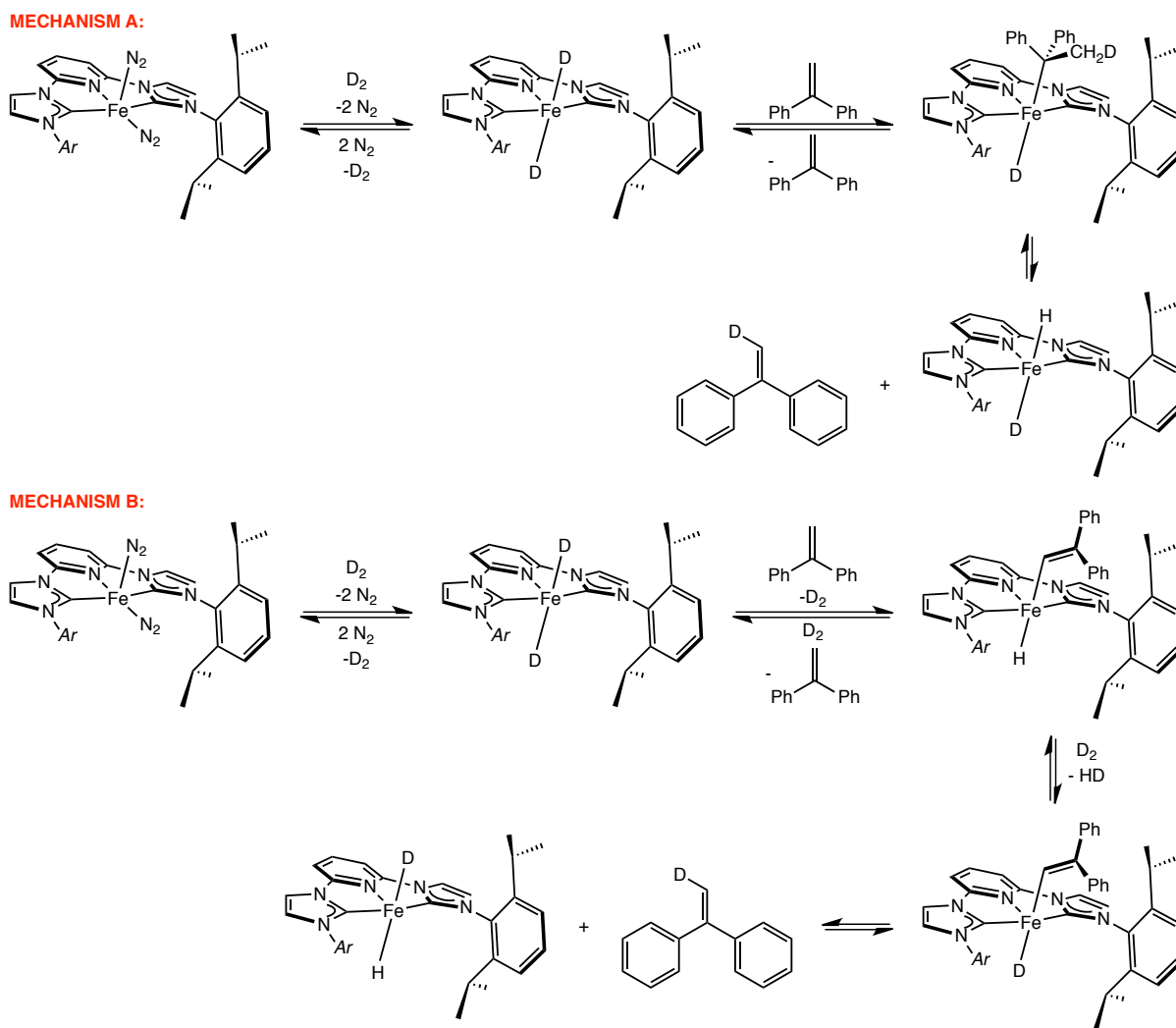


Figure 2.23. Mechanisms accounting for vinylic deuteration of 1,1-diphenylethylene.

was performed at the B3LYP level. The primary iron alkyl hydride, $(i\text{PrCNC})\text{Fe}(\text{CH}_2\text{CH}(\text{Ph})_2)(\text{H})$ was also computed. A comparison of the total energies showed that the primary iron alkyl was 10.0 kcal/mol less stable than the tertiary iron alkyl, which is most likely due to the steric congestion caused by the aryl rings of the alkyl ligand. This suggests that formation of the tertiary iron alkyl would be thermodynamically favored for this substrate. The optimized geometries are presented in **Figure 2.24**.

The deuteration of 1,1-diphenylethylene in benzene- d_6 using $(i\text{PrPDI})\text{Fe}(\text{N}_2)$ and (4-

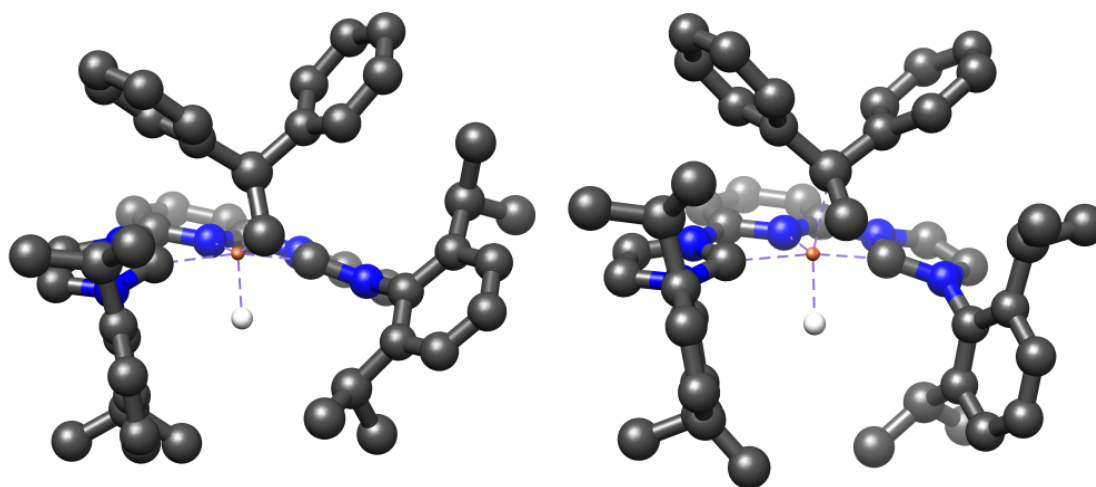


Figure 2.24. Geometry optimization of the theoretical molecules, $(iPrCNC)Fe(CH_2CH(Ph)_2)(H)$ (left) and $(iPrCNC)Fe(C(Ph)_2CH_3)(H)$ (right), at the B3LYP level of DFT.

$Me_2N-iPrPDI)Fe(N_2)$ was examined under standard conditions for comparison.²⁹ With $(iPrPDI)Fe(N_2)$, quenching the reaction after 24 hours revealed a 1:1 ratio of the isotopic label in the internal and terminal positions as determined by 2H NMR spectroscopy in benzene. These results are consistent with our previous findings favoring 1,2-insertion during catalytic hydrogenation. Using $(4-Me_2N-iPrPDI)Fe(N_2)$, significant catalyst decomposition was noted during the course of deuteration (as signaled by the precipitation of free iron). Analysis of the quenched reaction mixture after 48 hours by 1H NMR spectroscopy revealed both resonances associated with 1,1-diphenylene- d_1 and 1,1-diphenylene. The signals were of equal intensity, suggesting a 2:1 ratio of 1,1-diphenylene- d_1 to 1,1-diphenylene. Analysis of the same sample by 2H NMR spectroscopy in benzene confirmed deuterium incorporation at the vinylic position, but also revealed a 1:1 ratio of the isotopic label in the internal and terminal positions of the product. One likely explanation for this observations is that the mechanism resulting in vinylic H/D exchange is unproductive for deuteration, and is more consistent with mechanism **B**. These data indicated that in making the pyridine di(imine) chelate more electron-donating, and thereby

making the resulting iron dinitrogen complex more electron-rich, one of the two mechanisms proposed in **Figure.23** becomes competitive – and in the case of [$(i\text{PrCNC})\text{Fe}$] is preferred.

Intrigued by these results, deuteration of α -methylstyrene was investigated using $(i\text{PrPDI})\text{Fe}(\text{N}_2)$, $(4\text{-Me}_2\text{N-}i\text{PrPDI})\text{Fe}(\text{N}_2)$, and $(i\text{PrCNC})\text{Fe}(\text{N}_2)_2$ in benzene and benzene- d_6 . For reference, under 4 atm of H_2 in benzene- d_6 , $>95\%$ conversion was observed for all catalysts within one hour as judged by ^1H NMR spectroscopy. Each catalytic reaction was conducted using standard conditions and was stirred for 12 hours to ensure complete conversion of α -methylstyrene to isopropylbenzene. Transferring the volatiles following deuteration allowed for analysis of the product free of residual catalyst.²⁹ The solvent used for each catalytic reaction determined the method of NMR spectroscopic analysis (benzene- d_6 for ^1H NMR and benzene for ^2H NMR spectroscopy).

The results obtained for $(i\text{PrPDI})\text{Fe}(\text{N}_2)$ and $(4\text{-Me}_2\text{N-}i\text{PrPDI})\text{Fe}(\text{N}_2)$ were indistinguishable. ^1H NMR and ^2H NMR spectroscopic analysis of the reaction mixtures confirmed selective 1:1 incorporation of the isotopic label into the methyl and methine positions of the product following deuteration. These data suggest that with $(4\text{-R-}i\text{PrPDI})\text{Fe}(\text{N}_2)$ ($\text{R} = \text{H}, \text{Me}_2\text{N}$), the rate of deuteration is significantly greater than any competing process. These results are summarized in **Figure 2.25**.

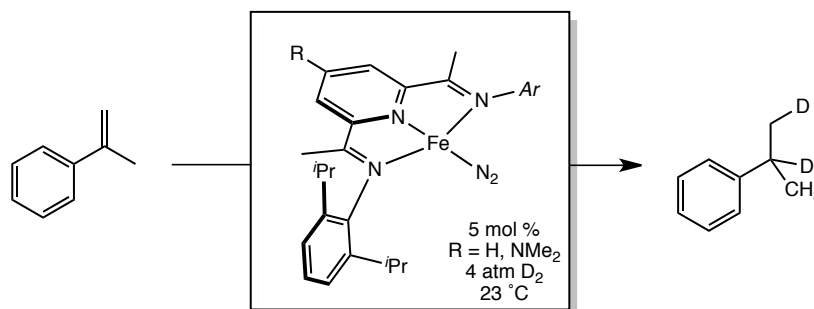


Figure 2.25. Deuteration of α -methylstyrene using $(4\text{-R-}i\text{PrPDI})\text{Fe}(\text{N}_2)$ ($\text{R} = \text{H}, \text{NMe}_2$).

The results obtained using ($i^{\text{Pr}}\text{CNC})\text{Fe}(\text{N}_2)_2$ were not as straightforward. The isotopic label was observed in a 1:6 ratio (methine:methyl) by ^2H NMR spectroscopy in benzene following deuteration. This result suggested complete deuterium incorporation into both vinylic and allylic positions prior to deuteration of the *gem*-olefin. However, ^1H NMR spectroscopic analysis of the catalytic reaction performed in benzene- d_6 also exhibited two signals in a 1:6 ratio corresponding to the methine and methyl resonances. Under these conditions, α -methylstyrene and $i^{\text{Pr}}\text{CNC}$ were the only sources of hydrogen.

The deuteration of two *para*-substituted α -methylstyrene derivatives (*p*- Me_2N and *p*- CF_3) was also investigated with ($i^{\text{Pr}}\text{PDI})\text{Fe}(\text{N}_2)$, (4- Me_2N - $i^{\text{Pr}}\text{PDI})\text{Fe}(\text{N}_2)$, and ($i^{\text{Pr}}\text{CNC})\text{Fe}(\text{N}_2)_2$. A similar approach was utilized, but with lower substrate concentrations (0.23 M) and 1 atmosphere of D_2 . The results obtained for ($i^{\text{Pr}}\text{PDI})\text{Fe}(\text{N}_2)$ and (4- Me_2N - $i^{\text{Pr}}\text{PDI})\text{Fe}(\text{N}_2)$ with either the *p*- Me_2 or *p*- CF_3 α -methylstyrene were not significantly different than from the parent α -methylstyrene. ^1H and ^2H NMR analysis of the solutions following deuteration revealed a 1:1 incorporation of the isotopic label into the methine and methyl positions. Similarly, the results obtained with ($i^{\text{Pr}}\text{CNC})\text{Fe}(\text{N}_2)_2$ were not significantly different from the parent α -methylstyrene. Qualitatively, a rate decrease was observed when using the *p*- Me_2N α -methylstyrene. Monitoring these reactions by ^2H NMR spectroscopy revealed incorporation of the isotopic label into the vinylic and allylic positions of the α -methylstyrenes in a 2:3 ratio, suggesting complete deuterium incorporation prior to deuteration, and accounting for the 1:6 ratio of the isotopic label observed for the product. No evidence for incorporation of the isotopic label at any of the aryl-positions was observed by ^2H NMR spectroscopy. When the deuteration reactions were performed in benzene- d_6 , the ^1H NMR spectrum exhibited an isopropyl methine resonance that integrated

nearly 1:2 with respect to the *ortho*- and *meta*-aryl resonances of the product. The isopropyl methyl resonances were also not significantly diminished, and integrated approximately 1:4 (isopropyl methyl:isopropyl methine).

Two mechanisms account for these observations (**Figure 2.26**). Mechanism **A** involves 2,1-insertion of an iron-deuteride bond, and β -hydrogen elimination to form an iron-hydride bond. Reversible 2,1-insertion accounts for deuterium incorporation into the vinylic and allylic positions of α -methylstyrene. In contrast, mechanism **B** involves allylic C–H activation to form $(i\text{PrCNC})\text{Fe}(\text{H})(\eta^1\text{-allyl})$. Exchange of the hydride for a deuteride, either by σ -bond metathesis or and oxidative addition-reductive elimination sequence, and reductive elimination accounts for deuterium incorporation into the allylic position. Transient formation of an η^3 -allyl (or a 1,3-sigmatropic rearrangement) results in deuterium incorporation into both the vinylic and allylic positions of α -methylstyrene. For both mechanisms, a productive 1,2-insertion of the iron-hydride, followed by C–H or C–D reductive elimination accounts for the presence of hydrogen at the isopropyl methine position. While the source of the hydrogen incorporated into the methine position likely originates from the substrate and is accounted for by close association of the olefin and the metal, the pyridine di(carbene) chelate may also serve as source of hydrogen by a mechanism not presented. This possibility cannot be ruled out on the basis of these experiments.

The deuteration of an α -olefin, 1-butene was also examined. Addition of 1 atmosphere of D_2 to a 0.24 M solution of 1-butene in benzene containing 5 mol % $(i\text{PrCNC})\text{Fe}(\text{N}_2)_2$ rapidly afforded butane- d_2 (**Figure 2.27**). Analysis of the product by ^2H NMR spectroscopy revealed a 1:1 ratio of the isotopic label in the terminal and internal positions. This result indicated that 2,1-insertion or allylic C–H activation were not competitive processes with deuteration of 1-butene.

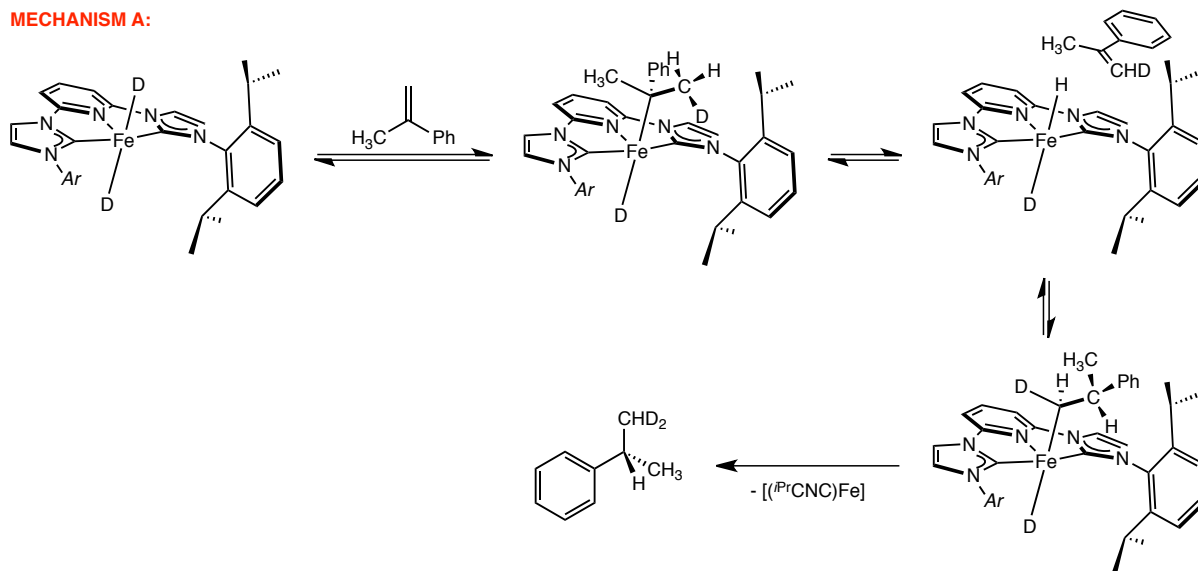
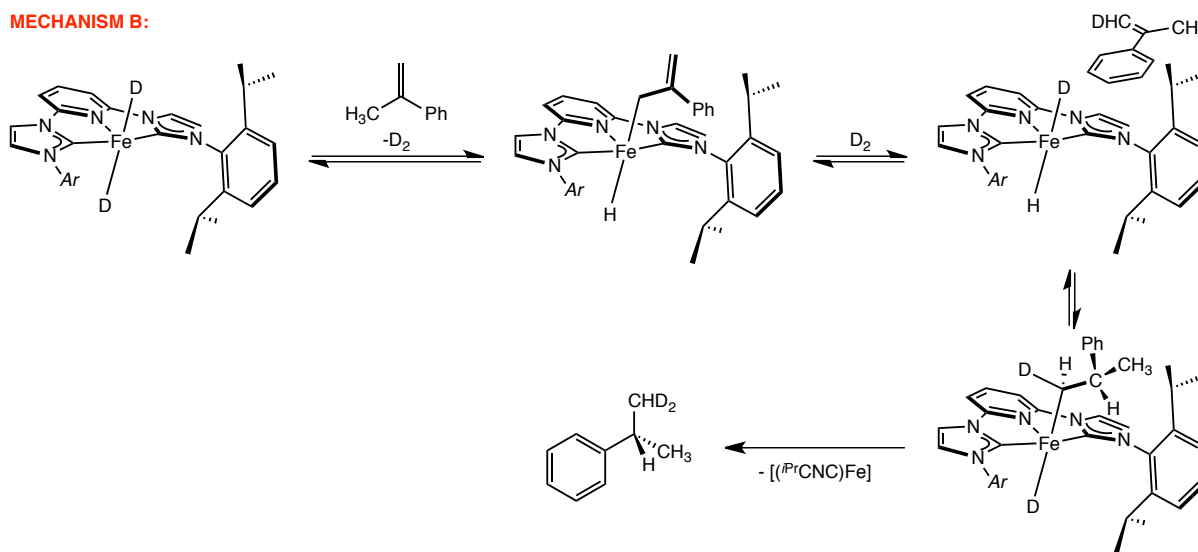
MECHANISM A:**MECHANISM B:**

Figure 2.26. Proposed mechanisms accounting for hydrogen incorporation at the isopropyl methine position. No stereochemistry is implied by the above mechanism.

Repeating the experiment in benzene- d_6 and analysis by ^1H NMR spectroscopy also revealed the presence of *cis*- and *trans*-2-butene – arising from competitive isomerization at lower pressures of D_2 .

For completion, the deuteration of ethyl 3,3-dimethylacrylate was examined using $(i\text{PrCNC})\text{Fe}(\text{N}_2)_2$ as the iron precatalyst under standard conditions with 4 atm of D_2 . The reaction was quenched after 2 hours, and analysis of the resulting solution by ^1H NMR spectroscopy

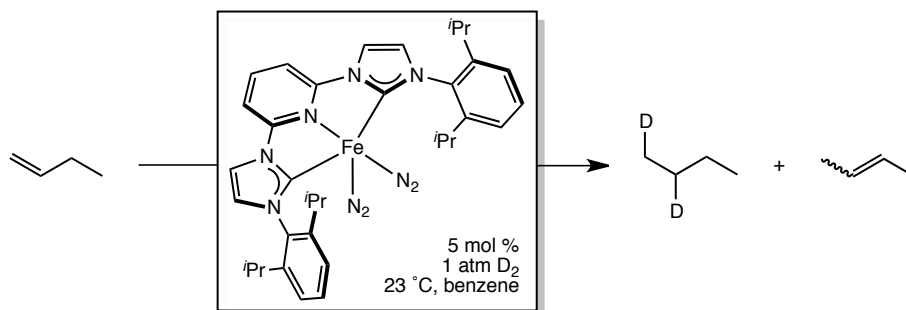


Figure 2.27. Catalytic deuteration of 1-butene using 5 mol % (*i*PrCNC)Fe(N₂)₂ and 1 atm of D₂.

demonstrated that deuterium had selectively been inserted into the olefin in a 1:1 ratio (**Figure 2.28**). One possibility to explain these results is that the ester functionality acts as a directing group; however, further experiments are necessary to examine this possibility.

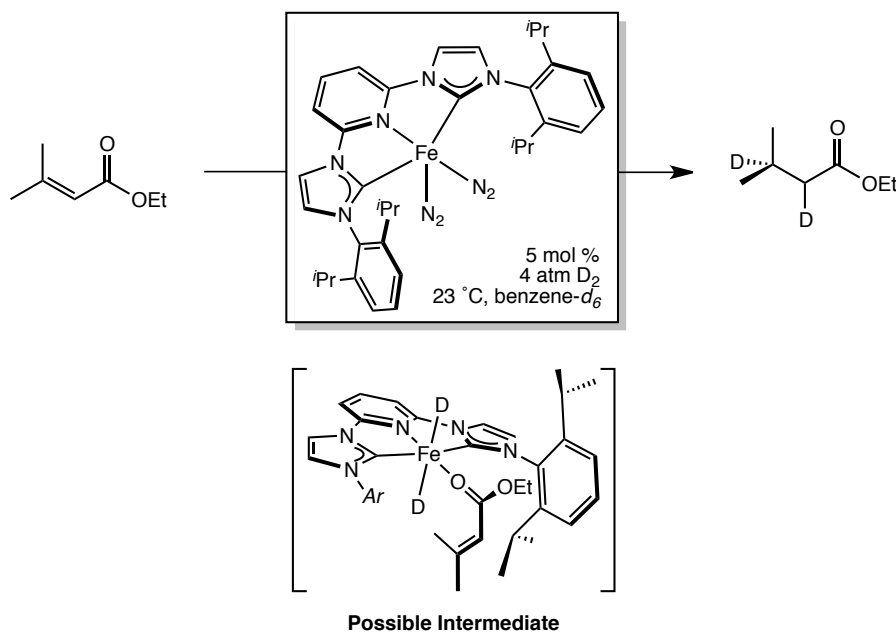


Figure 2.28. Catalytic deuteration of ethyl 3,3-dimethylacrylate using 5 mol % (*i*PrCNC)Fe(N₂)₂ and 4 atm D₂.

Alkyl isomerization – as defined by β -hydride elimination, olefin rotation and reinsertion – has been the subject of several investigations and is a likely mechanism accounting for the deuterium scrambling observed with (*i*PrCNC)Fe(N₂)₂. Lazzaroni and coworkers have studied

this phenomenon with regards to rhodium catalyzed deuterioformylation reactions; particularly with 1,1-diphenylethylene and α -methylstyrene.³⁴ Fortunately, the asymmetric addition across the C=C bond allows distinction of productive and non-productive insertions. Precedent for iron-alkyl isomerization was originally provided by Reger and coworkers studying $(\eta^5\text{-Cp})\text{Fe}(\text{CO})(\text{PR}_3)(\text{alkyl})$ complexes (Cp = C₅H₅).³⁵ Scrambling of the isotopic label in $(\eta^5\text{-Cp})\text{Fe}(\text{CO})(\text{PPh}_3)$ (isobutyl-1,1-*d*₂) at 65 °C in xylene supported formation of a tertiary alkyl intermediate following β -hydride elimination.

More recently, Holland and co-workers have measured Fe–C bond strengths by studying reversible β -hydrogen elimination reactions in a three-coordinate Fe^{II} alkyl system featuring a diketiminate ligand.^{36a} With styrene, a clear preference for 2,1-insertion was observed and allowed for crystallographic characterization of the secondary alkyl (**Figure 2.29**). Additionally, Holland and co-workers have isolated and crystallographically characterized an example of a tertiary iron alkyl.^{36b}

The stability of the alkyl isomers dominates the equilibrium, thereby dictating the preference for 1,2- or 2,1-insertion, and is often attributed to steric effects. However, Reger and coworkers have demonstrated that electronic effects are much more important.³⁷ Stated more explicitly, the ionic character of the resulting metal-alkyl bond decides the preference for primary vs. secondary and tertiary alkyls. Strongly polarized metal-carbon bonds favor the former whereas covalent metal-alkyl bonds favor the latter. In many of the systems described, a thermodynamic preference for the primary alkyls is expressed; however, for 1,1-diphenylethylene and α -methylstyrene, a thermodynamic preference for the tertiary alkyl is observed.^{34,36} Computational analysis of Reger's $(\eta^5\text{-Cp})\text{Fe}(\text{CO})(\text{L})(\text{alkyl})$ (L = PR₃ or CO)

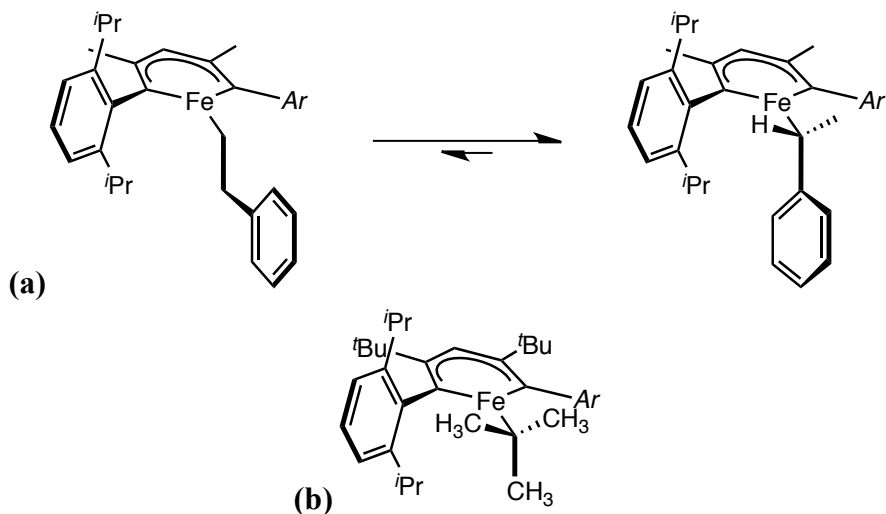


Figure 2.29. (a) Primary and secondary iron alkyl equilibrium studied by Holland and co-workers. No stereochemistry is implied by the above figure. (b) Isolated and crystallographically characterized example of a tertiary iron alkyl.

system by Harvey has clearly demonstrated that the supporting ligands play an integral role in determining the polarity of the metal-carbon bond.³⁸

Although alkyl isomerization is typically described by a series of two-electron processes, Arnold and co-workers have recently described a hydrotris(pyrazolyl)borate Co^{II} system in which the isomerization of secondary and tertiary alkyls is believed to occur from a radical pathway.³⁹ Radical trapping experiments provided evidence for this mechanism. This possibility cannot be discounted on the basis of our observed results.

The vinylic and allylic C–H oxidative addition pathways presented in **Figures 2.23** and **2.26** are equally relevant given the observation of benzene- d_6 activation by $(i^{\text{Pr}}\text{CNC})\text{Fe}(\text{N}_2)_2$. The vinylic C–H bond strength of ethylene and the allylic C–H bond strength of 1-propene are approximately 2 and 26 kcal/mol weaker than the C–H bond in benzene, respectively.⁴⁰ For α -olefins, the rate of hydrogenation (or deuteration) dominates and the effect of this alternative pathway is negligible, which accounts for the 1:1 observation of the isotopic label in these

substrates by ^2H NMR spectroscopy. Unfortunately, the experiments presented in this section do not allow for exclusion of either pathway presented.

2.6 Evaluation of $(i\text{PrCNC})\text{Fe}(\text{N}_2)_2$ for the Cyclization of 1,6-Diolefins

Given that $(i\text{PrCNC})\text{Fe}(\text{N}_2)_2$ and $(i\text{PrPDI})\text{Fe}(\text{N}_2)_2$ have similar ground states, and both are active for the hydrogenation of olefins, the reactivity of $(i\text{PrCNC})\text{Fe}(\text{N}_2)_2$ towards α,ω -dienes was investigated. *N,N*-diallyl-*tert*-butylamine was chosen as a representative substrate due to the exceptional activity with which it undergoes $[2\pi + 2\pi]$ cyclization with $(i\text{PrPDI})\text{Fe}(\text{N}_2)_2$.⁴¹ Addition of 10 equivalents of *N,N*-diallyl-*tert*-butylamine to a 22 mmol solution of $(i\text{PrCNC})\text{Fe}(\text{N}_2)_2$ in benzene-*d*₆ resulted in an immediate color change from green to brown. Monitoring the reaction by ^1H NMR spectroscopy at 23 °C over the course of hours revealed no evidence for formation of the $[2\pi + 2\pi]$ cyclized product, 3-(*tert*-butyl)-3-azabicyclo[3.2.0]heptane. Instead, olefin isomerization was observed (**Figure 2.28**).

Monitoring this reaction by ^1H NMR spectroscopy revealed consumption of *N,N*-diallyl-*tert*-butylamine within 20 hours of addition. Two new major organic species, **A** and **B**, were identified in a 3:2 ratio by their characteristic *tert*-butyl resonances at 1.02 and 0.99 ppm, respectively. **A** has been tentatively assigned as (*E*)-*N*-allyl-*N*-(*tert*-butyl)prop-1-en-1-amine due to the characteristic prop-1-en resonances (highlighted in **Figure 2.19**). After an additional 22 hours, **A** was consumed, and a new product, **C**, assigned as (*E*)-*N*-(*tert*-butyl)-*N*-((*E*)-prop-1-en-1-yl)prop-1-en-1-amine, was observed. Stereochemistry about the double bond was assigned on the basis of the large coupling ($J = 14$ Hz) observed between the olefinic proton resonances. After ten days, **C** appeared to be the dominant component in solution; however, analysis of the

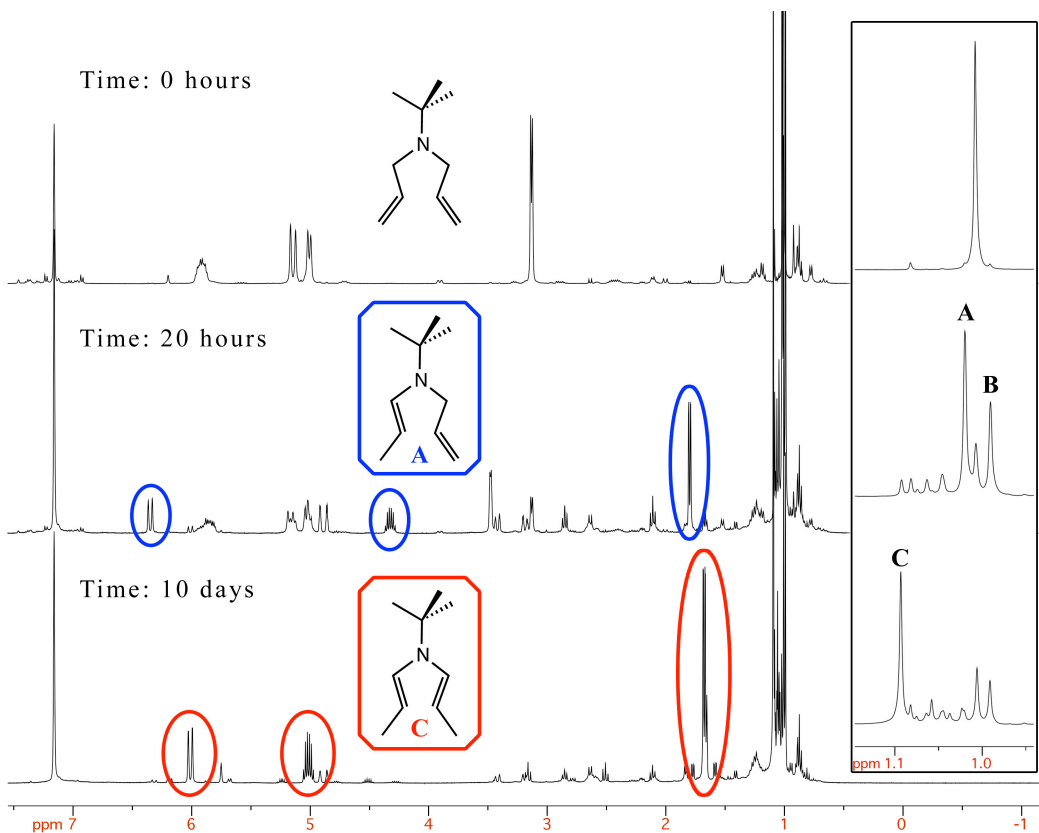


Figure 2.30. ^1H NMR spectra of a 0.22 M benzene- d_6 solution of *N,N*-diallyl-*tert*-butylamine containing 10 mol % (*i*PrCNC)Fe(N_2) $_2$ over time. Inset shows the region from 0.5–1.5 ppm.

reaction mixture by GC-FID indicated a number of organic species were present.

Addition of one atmosphere of H_2 to a 0.22 M benzene- d_6 solution of *N,N*-diallyl-*tert*-butylamine containing 10 mol % (*i*PrCNC)Fe(N_2) $_2$ resulted in rapid conversion of the starting material to two new products, **D** and **E**, in a 3:2 ratio on the basis of the number of *tert*-butyl resonances (1.05 and 1.02 ppm, respectively). Analysis of this mixture by GC-FID revealed the presence of three species in a 3:3:4 ratio. **D** was identified as a 1:1 mixture of diastereomers, 1-(*tert*-butyl)-*cis*- (*cis*-**D**) and *trans*-3,4-dimethylpyrrolidine (*trans*-**D**).⁴² The remaining organic component, **E** was tentatively assigned as the hydrogenated product, *N*-(*tert*-butyl)-*N*-propylpropan-1-amine. These results are summarized in **Figure 2.31**; however, it should be noted that the ratio of **D** to **E** is likely H_2 pressure dependent.

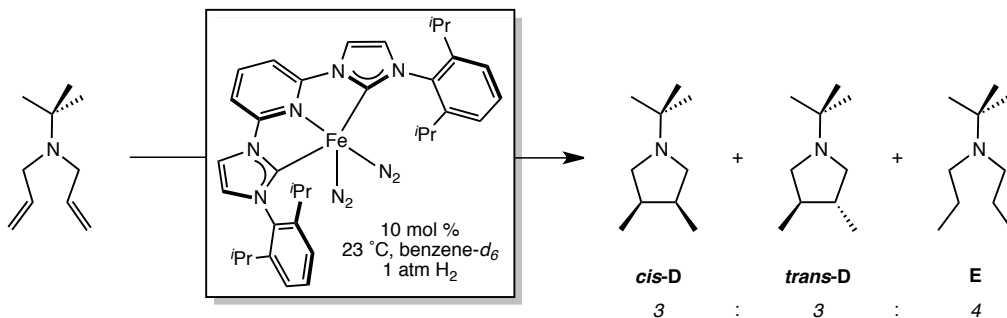


Figure 2.31. Addition of 1 atmosphere H_2 to a 0.22 M benzene- d_6 solution of *N,N*-diallyl-*tert*-butylamine containing 10 mol % $(iPrCNC)Fe(N_2)_2$. Only one enantiomer of ***trans*-D** is shown for simplicity.

In an attempt to gain a better understanding of the catalytic results, stoichiometric experiments with $(iPrCNC)Fe(N_2)_2$ and *N,N*-diallyl-*tert*-butylamine were conducted. Addition of one equivalent of *N,N*-diallyl-*tert*-butylamine to $(iPrCNC)Fe(N_2)_2$ resulted in formation of a brown solution. Recrystallization at -35 °C following removal of solvent yielded brown shards identified as the iron diene complex, $(iPrCNC)Fe(\eta^2, \eta^2-(CH_2CHCH_2)_2N^tBu)$ (**Figure 2.32**). This is the second example of a pyridine di(carbene) iron olefin complex,⁵ and the first isolated example of a diene compound.

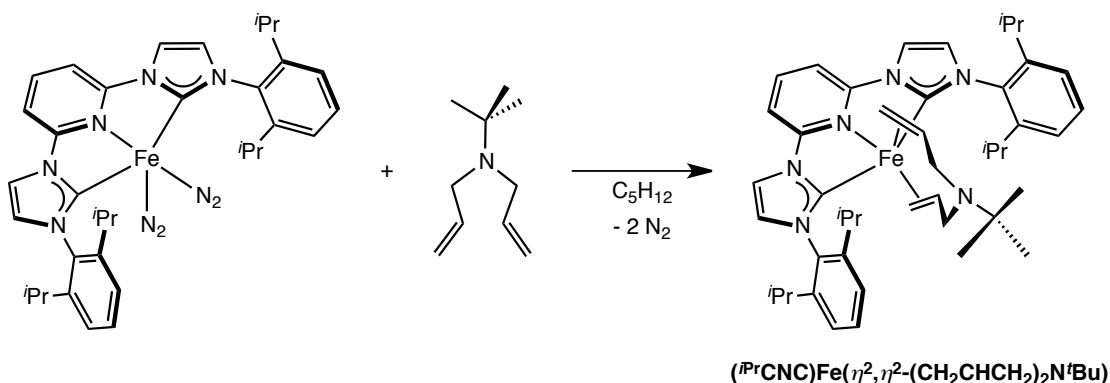


Figure 2.32. Synthesis of $(iPrCNC)Fe(\eta^2, \eta^2-(CH_2CHCH_2)_2N^tBu)$.

The benzene- d_6 1H NMR spectrum of $(iPrCNC)Fe(\eta^2, \eta^2-(CH_2CHCH_2)_2N^tBu)$ exhibited the number of resonances consistent with molecular C_s symmetry at 22 °C (**Figure 2.33**).

Coordination to iron causes the olefinic resonances to shift upfield from their free-ligand values, with the most extreme chemical shift appearing at 0.69 ppm. This phenomenon was also observed for the ethylene adduct, $(^{i\text{Pr}}\text{CNC})\text{Fe}(\eta^2\text{-C}_2\text{H}_4)(\text{N}_2)$.⁵

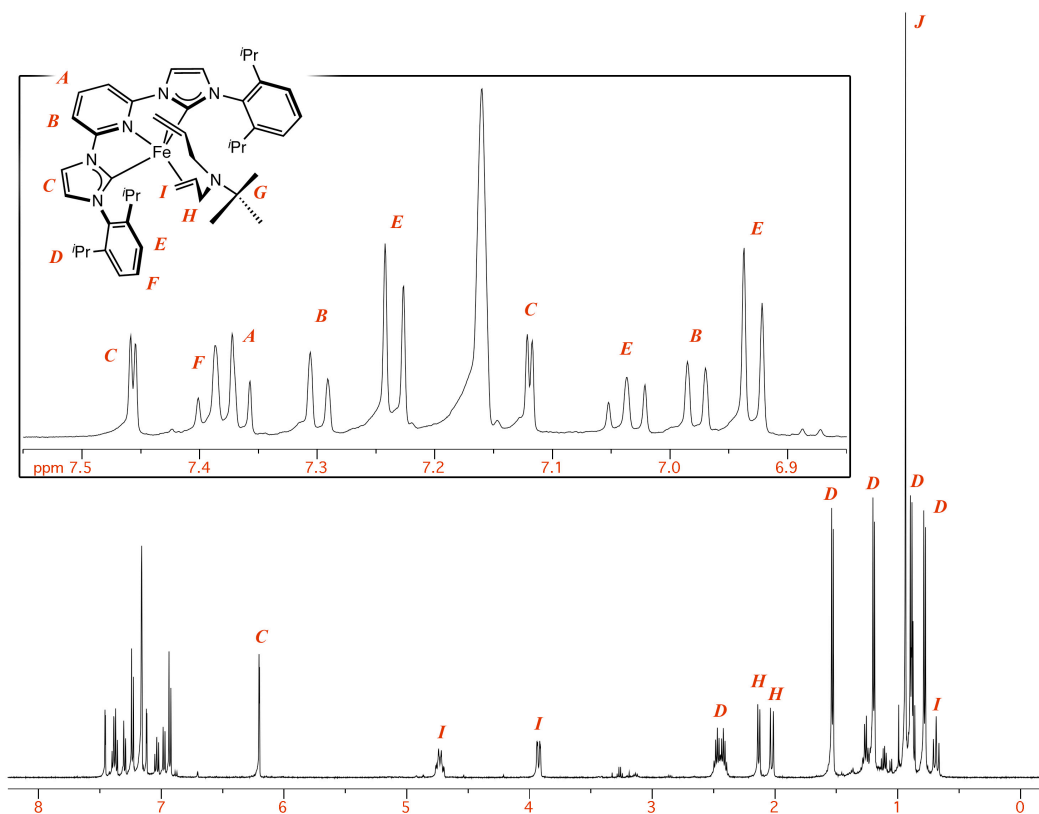


Figure 2.33. Benzene- d_6 ^1H NMR spectrum of $(^{i\text{Pr}}\text{CNC})\text{Fe}(\eta^2, \eta^2\text{-(CH}_2\text{CHCH}_2)_2\text{N}'\text{Bu})$ at 22 °C. Inset shows the region from 6.85–7.55 ppm.

The solid-state structure of $(^{i\text{Pr}}\text{CNC})\text{Fe}(\eta^2, \eta^2\text{-(CH}_2\text{CHCH}_2)_2\text{N}'\text{Bu})$ was determined by single-crystal X-ray diffraction (**Figure 2.34**). Selected metrical parameters are reported in **Table 2.4**. The diallyl and *tert*-butyl groups of the substrate were disordered over two positions, most likely resulting in the statistical differences observed between the allylic C=C bond lengths. The geometry of $(^{i\text{Pr}}\text{CNC})\text{Fe}(\eta^2, \eta^2\text{-(CH}_2\text{CHCH}_2)_2\text{N}'\text{Bu})$ is unique for reduced pyridine di(carbene) complexes. Typically, idealized square pyramidal geometries are adopted, and diatomic molecules capable of π -backbonding (N_2 and CO) occupy the basal site.^{5,8} Applying the Dewar–

Chat–Duncanson model for olefin coordination,⁴³ (*i*PrCNC)Fe(η^2,η^2 -(CH₂CHCH₂)₂N^tBu) can be described formally as a seven-coordinate Fe^{IV}, six-coordinate Fe^{II}, or five-coordinate Fe⁰ complex.

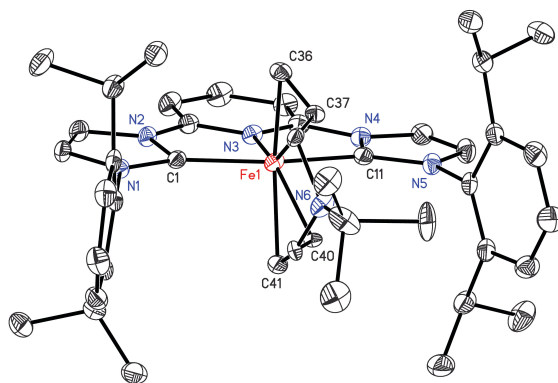


Figure 2.34. Solid-state structure of (*i*PrCNC)Fe(η^2,η^2 -(CH₂CHCH₂)₂N^tBu) at 30% probability ellipsoids. Hydrogen atoms omitted for clarity.

Table 2.4. Bond distances (Å) and angles (°) for (*i*PrCNC)Fe(η^2,η^2 -(CH₂CHCH₂)₂N^tBu).

Fe(1)–N(3)	1.9008(16)	N(1)–C(1)	1.398(3)
Fe(1)–C(1)	1.972(2)	C(1)–N(2)	1.406(2)
Fe(1)–C(11)	1.990(2)	N(4)–C(11)	1.404(3)
Fe(1)–C(36)	2.079(2)	C(11)–N(5)	1.400(3)
Fe(1)–C(37)	2.135(4)		
Fe(1)–C(40)	2.087(4)	C(36)–C(37)	1.315(5)
Fe(1)–C(41)	2.076(2)	C(40)–C(41)	1.413(5)
N(1)–C(1)–N(2)	100.43(16)	N(4)–C(11)–N(5)	99.81(18)

In order to investigate the electronic structure of (*i*PrCNC)Fe(η^2,η^2 -(CH₂CHCH₂)₂N^tBu), a solid-state ⁵⁷Fe Mößbauer spectrum was collected at 80 K (**Figure 2.35**). A quadrupole doublet was observed with an isomer shift of 0.31 mm·s⁻¹ and a quadrupole splitting of |0.60| mm·s⁻¹. These parameters are virtually indistinguishable from those of the other reduced pyridine di(carbene) iron complexes (see Section 2.1), suggesting a similar electronic structure. The Mößbauer parameters were reasonably reproduced by density functional theory from spin-

restricted and BS(1,1) solutions (Table 2.5). On the basis of these data, $(i\text{PrCNC})\text{Fe}(\eta^2, \eta^2\text{-(CH}_2\text{CHCH}_2)_2\text{N}^t\text{Bu})$ is best described as a five-coordinate complex with $(i\text{PrCNC}^0)\text{Fe}^0(\eta^2, \eta^2\text{-(CH}_2\text{CHCH}_2)_2\text{N}^t\text{Bu})$ and $(i\text{PrCNC}^{2-})\text{Fe}^{\text{II}}(\eta^2, \eta^2\text{-(CH}_2\text{CHCH}_2)_2\text{N}^t\text{Bu})$ resonance forms.

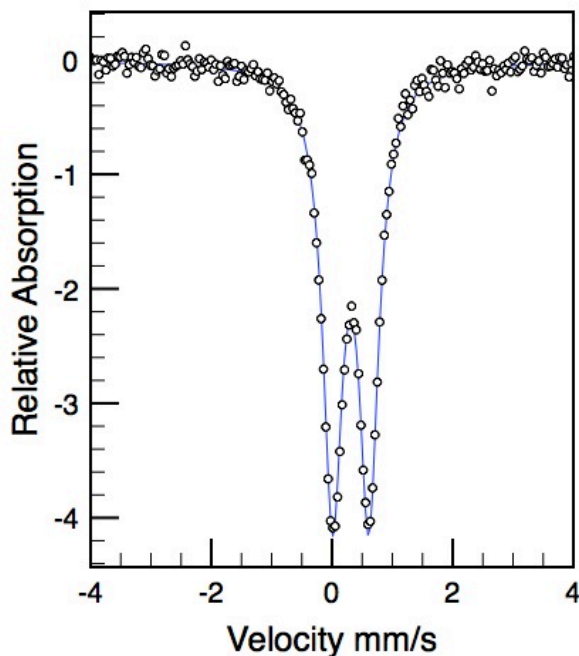


Figure 2.35. Zero-field ^{57}Fe Mössbauer spectrum of $(i\text{PrCNC})\text{Fe}(\eta^2, \eta^2\text{-(CH}_2\text{CHCH}_2)_2\text{N}^t\text{Bu})$ obtained at 80 K; $\delta = 0.31 \text{ mm}\cdot\text{s}^{-1}$, $|\Delta E_{\text{Q}}| = 0.60 \text{ mm}\cdot\text{s}^{-1}$.

Table 2.5. Experimental and computed Mössbauer parameters for $(i\text{PrCNC})\text{Fe}(\eta^2, \eta^2\text{-(CH}_2\text{CHCH}_2)_2\text{N}^t\text{Bu})$.

Method	δ ($\text{mm}\cdot\text{s}^{-1}$)	$ \Delta E_{\text{Q}} $ ($\text{mm}\cdot\text{s}^{-1}$)
Experimental	0.31	0.50
RKS	0.35	0.18
BS(1,1)	0.38	0.16

The reactivity of $(i\text{PrCNC})\text{Fe}(\eta^2, \eta^2\text{-(CH}_2\text{CHCH}_2)_2\text{N}^t\text{Bu})$ with H_2 was probed in an attempt to understand the catalytic activity observed with *N,N*-diallyl-*tert*-butylamine and excess hydrogen. Addition of 1 atmosphere of H_2 to a benzene- d_6 solution of $(i\text{PrCNC})\text{Fe}(\eta^2, \eta^2\text{-(CH}_2\text{CHCH}_2)_2\text{N}^t\text{Bu})$, resulted in rapid and selective formation of the organic product *cis*-**D**. In order to gain insight into the mechanism of this transformation, the experiment was repeated

using D₂. Isolation of the organic products by vacuum transfer, and subsequent analysis by ¹H and ²H NMR spectroscopy revealed selective formation of *cis-d₂-D* (**Figure 2.36**). The pyridine di(carbene) iron bis(dinitrogen) compound, (ⁱPrCNC)Fe(N₂)₂ was recovered following re-exposure to dinitrogen.

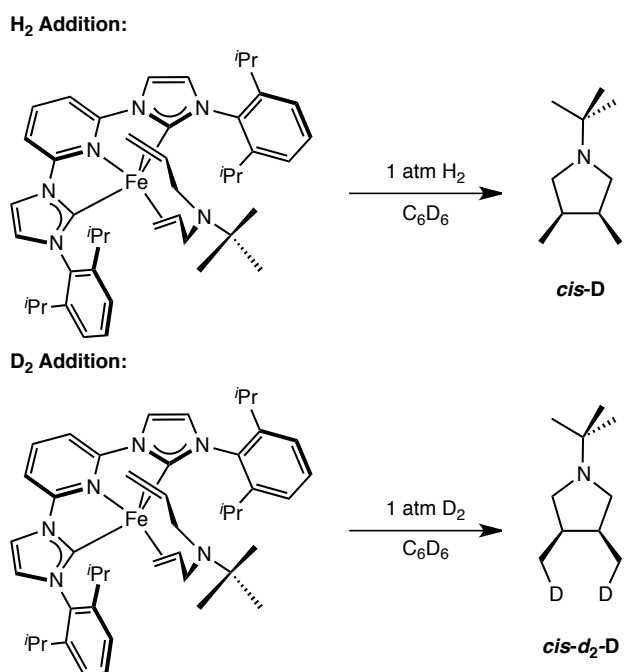


Figure 2.36. Reaction of (ⁱPrCNC)Fe(η^2,η^2 -(CH₂CHCH₂)₂N^tBu) with H₂ and D₂.

Three mechanisms are proposed to account for the formation of *cis-D* following hydrogenation of (ⁱPrCNC)Fe(η^2,η^2 -(CH₂CHCH₂)₂N^tBu) (**Figure 2.37**). Mechanism A involves oxidative coupling of the diolefin to form a metallocyclopentane. The formation of *cis-D* from this intermediate is accomplished either by oxidative addition of H₂ or by σ -bond metathesis with H₂ followed by rapid C–H reduction elimination. Dissociation of a carbene ligand to give an open coordination site is a possibility in both pathways. Under catalytic conditions, a competitive rate of olefin hydrogenation accounts for the presence of **E**. This mechanism is disfavored because of the H₂-induced oxidative coupling step. Alternative pathways of ligand-induced

oxidative coupling were explored.^{44,45} Addition of one atmosphere of CO to $(i\text{PrCNC})\text{Fe}(\eta^2,\eta^2\text{-(CH}_2\text{CHCH}_2)_2\text{N}^t\text{Bu})$ resulted in an intractable mixture of products, whereas addition of five equivalents of 1,3-butadiene produced no reaction.

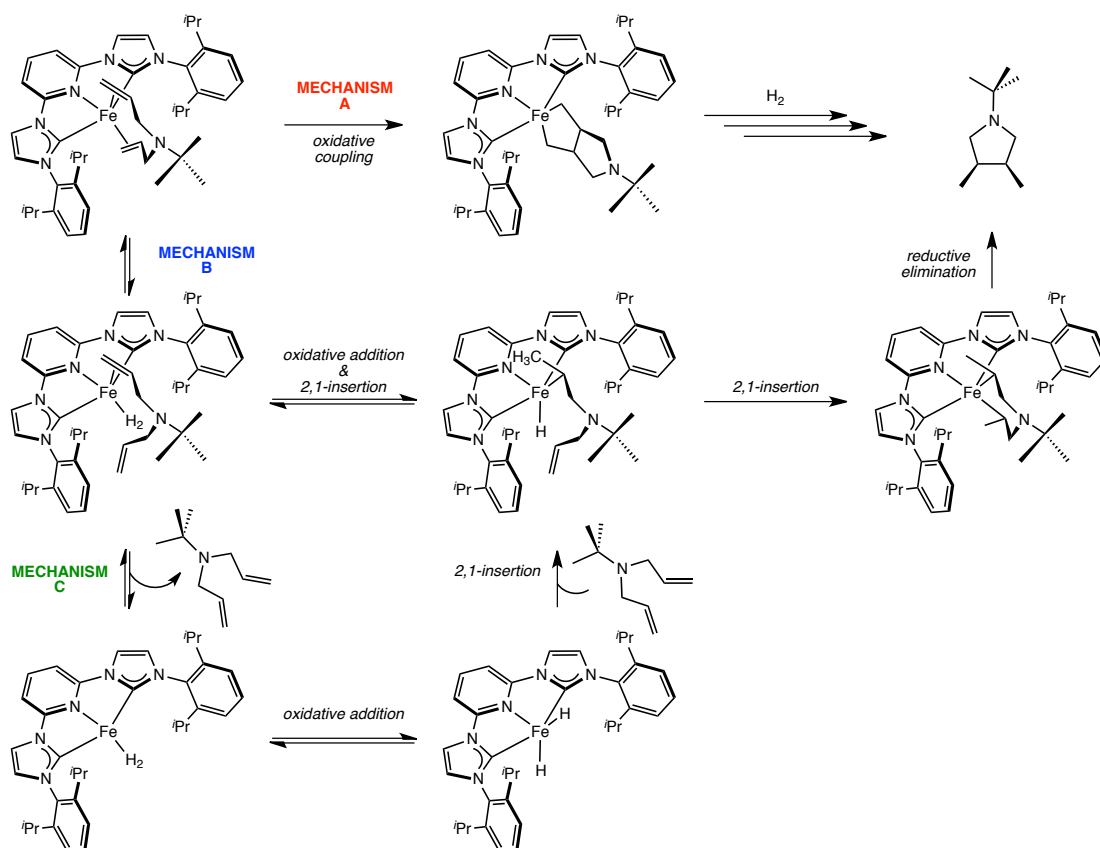


Figure 2.37. Proposed mechanisms for the synthesis of *cis-D*.

Alternatively, mechanism B initiates from dissociation of an olefin followed by coordination of H_2 . Oxidative addition of H_2 followed by two successive 2,1-insertion steps, and C–C bond reductive elimination also accounts for formation of *cis-D*. Mechanism C involves a subtle variation, requiring complete dissociation of *N,N*-diallyl-*tert*-butylamine prior to coordination and oxidative addition of H_2 to give an iron dihydride. As with mechanism B, two 2,1-insertion events and a C–C bond reductive elimination yield *cis-D*. Unfortunately, all of these mechanisms cannot be discounted on the basis of isotopic labeling experiments. In mechanism B

and C, competitive C–H reductive elimination results in the hydrogenated product, **E**.

As stated in Section 2.2, many factors typically affect catalyst (in)activity. Although it is tempting to attribute the inability of (*i*PrCNC)Fe(N₂)₂ to catalyze the [2π + 2π] cyclization of α,ω-dienes to the absence of observed redox-activity with pyridine di(carbene) iron complexes, other possibilities are equally probable. Most reduced pyridine di(carbene) iron complexes, as well as their dialkyl analogs (see **Chapter 3**) have been characterized with singlet ground states, whereas many intermediate- and high-spin pyridine di(imine) species have been observed. Thus, it also seems likely that the field strength of the pyridine di(carbene) ligand may prevent the formation of species that are competent for catalytic turnover. Another possibility is the difference in the lability of chelate substituents. Until more is known about the mechanism of [2π + 2π] cyclization, arguments are merely speculative.

2.7 Conclusions

A family of reduced pyridine di(carbene) iron complexes have been investigated by a combination of spectroscopic methods, including infrared, NMR, Mößbauer, and X-ray absorption spectroscopies and their electronic structures have been elucidated. These complexes are best described as hybrid structures with [(*i*PrCNC)Fe] and [(*i*PrCNC)Fe] resonance forms where the *i*PrCNC chelate acts as a π-acceptor. The iron bis(dinitrogen) compound, (*i*PrCNC)Fe(N₂)₂ was screened as a precatalyst for olefin hydrogenation and the [2π + 2π] cyclization of α,ω-diolefins. During these experiments, (*i*PrCNC)Fe(N₂)₂ demonstrated the ability to activate benzene-*d*₆. (*i*PrCNC)Fe(N₂)₂ was found to be one of the most active olefin hydrogenation iron precatalysts for substrates like ethyl 3,3-dimethylacrylate and *trans*-

methylstilbene, but exhibited diminished activity for the hydrogenation of 1,1-diphenylethylene. Isotopic experiments revealed that an unproductive process – either 2,1-insertion or vinylic C–H activation – was competitive with the rate of hydrogenation for this substrate, and in the case of $(i\text{PrCNC})\text{Fe}(\text{N}_2)_2$ was preferred. $(i\text{PrCNC})\text{Fe}(\text{N}_2)_2$ was not a competent catalyst for the $[2\pi + 2\pi]$ cyclization of *N,N*-diallyl-*tert*-butylamine. Stoichiometric experiments resulted in the isolation of $(i\text{PrCNC})\text{Fe}(\eta^2, \eta^2\text{-(CH}_2\text{CHCH}_2)_2\text{N}^t\text{Bu})$.

2.8 Experimental

All air- and moisture-sensitive manipulations were carried out using standard vacuum line, Schlenk, and cannula techniques or in an MBraun inert atmosphere dry box containing an atmosphere of purified nitrogen. Solvents for air- and moisture-sensitive manipulations were initially dried and deoxygenated using literature procedures.⁴⁶ Benzene-*d*₆ was purchased from Cambridge Isotope Laboratories and dried over 4 Å molecular sieves. The following compounds were prepared according to literature procedure: $(i\text{PrCNC})\text{FeBr}_2$,²⁴ $(i\text{PrCNC})\text{Fe}(\text{N}_2)_2$,⁵ $(i\text{PrCNC})\text{Fe}(\text{CO})_2$.⁵ Ethyl 3,3-dimethylacrylate and α -methylstyrene, were purchased from commercial sources and stirred over calcium hydride for at least 24 hours prior to being vacuum transferred to a dry flask, brought into a nitrogen-filled glovebox, and filtered through activated, neutral alumina. *Trans*-stilbene and *trans*-methylstilbene were purchased from commercial sources and dried under vacuum for 16 hours prior to use. 1,1-diphenylethylene was purchased from a commercial source and stirred over calcium hydride for 24 hours, freeze-pump degassed on a high vacuum line, brought into a dinitrogen filled glovebox, and passed through activated, neutral alumina prior to use. Preparation of *p*-trifluoromethyl- α -methylstyrene and *p*-

dimethylamino- α -methylstyrene were accomplished by reaction of $\text{Ph}_3\text{P}=\text{CH}_2$ with the appropriate acetophenone as described previously,⁴⁷ and the resulting product was distilled at reduced pressure from CaH_2 (for *p*-trifluoromethyl- α -methylstyrene) or dried under vacuum for 16 hours prior to use (for *p*-dimethylamino- α -methylstyrene).

^1H NMR spectra were recorded on Varian Mercury 300, Inova 400, 500, and 600 spectrometers operating at 299.76, 399.78, 500.62, and 599.78 MHz, respectively. ^{13}C NMR spectra were recorded on an Inova 500 spectrometer operating at 125.893 MHz. All ^1H and ^{13}C NMR chemical shifts are reported relative to SiMe_4 using the ^1H (residual) and ^{13}C chemical shifts of the solvent as a secondary standard. For diamagnetic complexes, many assignments were made based on COSY and HSQC NMR experiments. Solution magnetic moments were determined by Evans method⁴⁸ using a ferrocene standard and are the average value of at least two independent measurements. Magnetic susceptibility balance measurements were performed with a Johnson Matthey instrument that was calibrated with $\text{HgCo}(\text{SCN})_4$. All solid-state values were recorded at 21 °C unless otherwise noted. Peak widths at half height are reported for paramagnetically broadened and shifted resonances. Infrared spectra were collected on a Thermo Nicolet spectrometer. Elemental analyses were performed at Robertson Microlit Laboratories, Inc., in Ledgewood, NJ.

Single crystals suitable for X-ray diffraction were coated with polyisobutylene oil in a drybox, transferred to a nylon loop and then quickly transferred to the goniometer head. A Bruker APEX2 Duo diffractometer equipped with molybdenum and copper X-ray tubes ($\lambda = 0.71073$ and 1.54178 Å, respectively) was used to collect data for $(i\text{PrCNC})\text{Fe}(\text{DMAP})(\text{N}_2)$ (Cu source) and $(i\text{PrCNC})\text{Fe}(\eta^2, \eta^2\text{-(CH}_2\text{CHCH}_2)_2\text{N}^t\text{Bu})$ (Mo source). The space group was identified

and the data were processed using the Bruker SAINT+ program and corrected for absorption using SADABS. The structures were solved using direct methods (SIR92) completed by subsequent Fourier synthesis and refined by full-matrix least-squares procedures.

^{57}Fe Mössbauer spectra were recorded on a SEE Co. Mössbauer spectrometer (MS4) at 80 K in constant acceleration mode. $^{57}\text{Co/Rh}$ was used as the radiation source. WMOSS software was used for the quantitative evaluation of the spectral parameters (least squares fitting to Lorentzian peaks). The temperature of the samples was controlled by a Janis Research Co. CCS-850 He/N₂ cryostat within an accuracy of ± 1 K. Isomer shifts were determined relative to α -iron at 298K.

For X-ray absorption spectroscopy, samples were prepared in an inert atmosphere nitrogen glove box as finely ground dilutions in boron nitride pressed into 1 mm Al spacers and shipped to the experimental site in triple glass jars with fluoropolymer seals on the lids and sealed with teflon and electrical tape. X-ray absorption spectra were recorded at the Stanford Synchrotron Radiation Lightsource (SSRL) on BL7-3 under standard ring conditions. The beamline optics were optimized and the monochromator fully tuned at 7500 eV. The incident energy was calibrated by setting the first inflection of an iron foil to 7111.2 eV. Data were measured in transmission mode. Data was processed using EXAFSPAK,⁴⁹ and pictured using Kaleidagraph.⁵⁰

Preparation of (*i*PrCNC)Fe(DMAP)(N₂). A 20-mL scintillation vial was charged with a solution of 0.100 g (0.155 mmol) of (*i*PrCNC)Fe(N₂)₂ in approximately 10 mL of diethyl ether. With stirring, 0.019 g (0.16 mmol) of DMAP was added, resulting in an immediate color change to

red-orange. After stirring for 30 minutes, the solution was concentrated and layered with approximately 5 mL of pentane. Storing the solution at -35 °C resulted in crystallization of an analytically pure, dark solid (0.092 g, 80%) identified as (*i*PrCNC)Fe(DMAP)(N₂). Analysis for C₄₂H₅₁N₉Fe: Calc. C, 68.38; H, 6.97; N, 17.09. Found: C, 67.98; H, 6.76; N, 16.81. ¹H NMR (benzene-*d*₆, 22 °C): δ = 1.00 (d, 6 Hz, 6H, CH(CH₃)₂), 1.05 (d, 6 Hz, 6H, CH(CH₃)₂), 1.11 (d, 6 Hz, 6H, CH(CH₃)₂), 1.19 (d, 6 Hz, 6H, CH(CH₃)₂), 1.93 (s, 6H, N(CH₃)₂), 3.00 (spt, 6 Hz, 2H, CH(CH₃)₂), 3.12 (spt, 6 Hz, 2H, CH(CH₃)₂), 5.19 (d, 6 Hz, 2H, *m*-DMAP), 6.83 (s, 2H, *imidazolylidene backbone*), 6.95 (d, 6 Hz, 2H, *o*-DMAP), 7.20–7.33 (m, 6H, *m*-aryl and *m*-pyr), 7.38 (t, 7 Hz, 2H, *p*-aryl), 7.59–7.70 (m, 3H, *imidazolylidene backbone* and *p*-pyr). ¹³C NMR {¹H} (benzene-*d*₆, 22 °C): δ = 23.1 (CH(CH₃)₂), 23.3 (CH(CH₃)₂), 25.6 (CH(CH₃)₂), 26.7 (CH(CH₃)₂), 28.4 (CH(CH₃)₂), 28.5 (CH(CH₃)₂), 38.2 (N(CH₃)₂), 98.6 (*pyr*), 106.9 (DMAP), 109.8 (*imidazolylidene backbone*), 122.9 (*aryl*), 123.9 (*pyr*), 124.4 (*aryl*), 126.2 (*imidazolylidene backbone*), 129.1 (*aryl*), 139.0 (*aryl*), 140.9 (*pyr*), 146.7 (*aryl*), 148.8 (*aryl*), 151.8 (DMAP), 152.0 (DMAP), 203.6 (*carbene*). IR (pentane, 23 °C): ν_{NN} = 1998 cm⁻¹. IR (KBr): ν_{NN} = 1987 cm⁻¹.

Characterization of (*i*PrCNC)Fe(η²-C₂H₄)₂. A J. Young tube was charged with a solution of (*i*PrCNC)Fe(N₂)₂ (0.010 g, 15 μmol) in benzene-*d*₆ (0.650 g). On the vacuum line, the J. Young tube was degassed and 0.31 mmol of ethylene was admitted via a calibrated gas bulb. Upon thawing, an immediate color change from green to red-brown was observed. ¹H NMR (benzene-*d*₆, 22 °C): δ = 0.82 (d, 7 Hz, 12H, CH(CH₃)₂), 1.38 (d, 7 Hz, 12H, CH(CH₃)₂), 2.38 (spt, 7 Hz, 4H, CH(CH₃)₂), 2.46 (s, 8H, CH₂=CH₂), 6.20 (d, 2 Hz, 2H, *imidazolylidene backbone*), 7.01–

7.07 (m, 6H, *m*-aryl and *m*-pyr), 7.16 (t, 2H, *p*-aryl, located by COSY), 7.19 (d, 2 Hz, 2H, *imidazolylidene backbone*), 7.34 (t, 8 Hz, 1H, *p*-pyr). ^{13}C NMR $\{\text{}^1\text{H}\}$ (benzene- d_6 , 22 °C): δ = 21.9 ($\text{CH}(\text{CH}_3)_2$), 27.1 ($\text{CH}(\text{CH}_3)_2$), 28.1 ($\text{CH}(\text{CH}_3)_2$), 39.6 ($\text{CH}_2=\text{CH}_2$), 99.4 (*m*-pyr), 111.9 (*imidazolylidene backbone*), 118.9 (*p*-pyr), 123.0 (*m*-aryl), 126.0 (*imidazolylidene backbone*), 129.5 (*pyr*), 136.9 (*aryl*), 147.3 (*aryl*), 151.7 (*aryl*), 207.8 (*carbene*).

Preparation of $(i\text{PrCNC})\text{Fe}(\eta^2, \eta^2\text{-(CH}_2\text{CHCH}_2)_2\text{N}^t\text{Bu}$). A 20-mL scintillation vial was charged with a solution of 0.075 g (0.12 mmol) $(i\text{PrCNC})\text{Fe}(\text{N}_2)_2$ in approximately 5 mL of diethyl ether. With stirring, approximately 0.020 g (0.13 mmol) of *N,N*-diallyl-*tert*-butylamine was added, causing an immediate color change to brown. After stirring for 30 minutes, the solution was concentrated and layered with approximately 5 mL of pentane. Storing the solution at -35 °C resulted in crystallization of an analytically pure, brown solid (0.030 g, 35%) identified as $(i\text{PrCNC})\text{Fe}(\eta^2, \eta^2\text{-(CH}_2\text{CHCH}_2)_2\text{N}^t\text{Bu}$). ^1H NMR (benzene- d_6 , 22 °C): δ = 0.69 (t, 11 Hz, 2H, $\text{N}(\text{CH}_2\text{CHCH}_2)_2$), 0.78 (d, 7 Hz, 6H, $\text{CH}(\text{CH}_3)_2$), 0.89 (d, 7 Hz, 6H, $\text{CH}(\text{CH}_3)_2$), 0.94 (s, 9H, $\text{NC}(\text{CH}_3)_3$), 1.20 (d, 7 Hz, 6H, $\text{CH}(\text{CH}_3)_2$), 1.53 (d, 7 Hz, 6H, $\text{CH}(\text{CH}_3)_2$), 2.03 (d, 12 Hz, 2H, $\text{N}(\text{CH}_2\text{CHCH}_2)_2$), 2.13 (d, 8 Hz, 2H, $\text{N}(\text{CH}_2\text{CHCH}_2)_2$), 2.42 (spt, 7 Hz, 2H, $\text{CH}(\text{CH}_3)_2$), 2.47 (spt, 7 Hz, 2H, $\text{CH}(\text{CH}_3)_2$), 3.93 (dd, 12 Hz, 3 Hz, 2H, $\text{N}(\text{CH}_2\text{CHCH}_2)_2$), 4.70–4.76 (m, 2H, $\text{N}(\text{CH}_2\text{CHCH}_2)_2$), 6.20 (d, 2 Hz, 2H, *imidazolylidene backbone*), 6.93 (d, 8 Hz, 2H, *m*-aryl), 6.98 (d, 8 Hz, 1H, *m*-pyr), 7.04 (t, 8 Hz, 1H, *p*-aryl), 7.12 (d, 2 Hz, 1H, *imidazolylidene backbone*), 7.23 (d, 8 Hz, *m*-aryl), 7.30 (d, 8 Hz, 1H, *m*-pyr), 7.37 (t, 8 Hz, 1H, *p*-pyr), 7.40 (t, 8 Hz, 1H, *p*-aryl), 7.46 (d, 2 Hz, 1H, *imidazolylidene backbone*). ^{13}C NMR $\{\text{}^1\text{H}\}$ (benzene- d_6 , 22 °C): δ = 21.6 ($\text{CH}(\text{CH}_3)_2$), 22.2 ($\text{CH}(\text{CH}_3)_2$), 26.8 ($\text{CH}(\text{CH}_3)_2$), 27.0 ($\text{CH}(\text{CH}_3)_2$), 28.4 ($\text{CH}(\text{CH}_3)_2$ or

C(CH₃)₃), 28.5 (CH(CH₃)₂ or C(CH₃)₃), 28.6 (N(CH₂CHCH₂)₂), 28.8 (CH(CH₃)₂ or C(CH₃)₃), 52.4 (C(CH₃)₃), 54.0 (N(CH₂CHCH₂)₂), 61.4 (N(CH₂CHCH₂)₂), 99.4 (*m-pyr*), 100.4 (*m-pyr*), 110.2 (*imidazolylidene backbone*), 113.0 (*imidazolylidene backbone*), 114.8 (*p-pyr*), 123.2 (*m-aryl*), 124.1 (*m-aryl*), 127.0 (*imidazolylidene backbone*), 127.0 (*imidazolylidene backbone*), 129.5 (*p-aryl*), 130.3 (*p-aryl*), 138.4 (*aryl*), 139.1 (*aryl*), 146.2 (*pyr*), 146.5 (*aryl*), 147.6 (*aryl*), 152.4 (*pyr*), 195.8 (*carbene*), 208.8 (*carbene*).

General Procedure for the Catalytic Olefin Hydrogenation. Unless noted otherwise, a thick-walled glass vessel was charged with a solution containing 0.032 mmol of the desired iron compound in 0.65 g (7.72 mmol) of benzene-*d*₆ and a magnetic stir bar. The vessel was placed in a liquid nitrogen cooled cold well for 20 min. Once the solution was frozen, 0.63 mmol of the olefin was layered onto the solution of iron nitrogen compound. The vessel was taken out of the drybox and transferred to a high vacuum line while continuously submerged in liquid nitrogen. Following evacuation of the dinitrogen atmosphere, 1 atm of dihydrogen was admitted at 80 K. The solution was then thawed and stirred in an ambient temperature water bath. After the desired reaction time, the vessel was vented of dihydrogen and exposed to air. Decomposed iron compound was removed by filtration through Celite, and the filtrate collected for analysis by ¹H NMR. Conversions were determined by ¹H NMR spectroscopy for ethyl 3,3-dimethylacrylate and α -methylstyrene, and by GC-FID for all other olefins.

Characterization of Hydrogenated Products by Gas Chromatography. GC analyses were performed using a Shimadzu GC-2010 gas chromatograph equipped with a

Shimadzu AOC-20s autosampler and a Shimadzu SHRXI-5MS capillary column (15m x 250 μ m). The instrument was set to an injection volume of 1 μ L, an inlet split ratio of 100:1, and inlet and detector temperatures of 120 °C and 250 °C, respectively. UHP-grade helium was used as carrier gas with a flow rate of 1.12 mL/min. The temperature program used for the various alkanes are as follows:

Propane-1,2-diylidibenzene. 60 °C for 1 min; 15 °C/min to 250 °C and hold for 2 min.

Retention Time: 8.22 min.

Ethane-1,1-diylidibenzene. 60 °C for 1 min; 15 °C/min to 180 °C and hold for 2 min.

Retention Time: 7.73 min.

REFERENCES

- ¹ (a) Knijnenburg, Q.; Gambarotta, S.; Budzelaar, P. H. M. *Dalton Trans.* **2006**, 5442–5448. (b) Gibson, V. C.; Redshaw, C.; Solan, G. A. *Chem. Rev.* **2007**, *107*, 1745–1776. and references therein.
- ² For recent examples, see: (a) King, E. R.; Hennessy, E. T.; Betley, T. A. *J. Am. Chem. Soc.* **2011**, *133*, 4917–4923. (b) Heyduk, A. F.; Zarkesh, R. A.; Nguyen, A. I. *Inorg. Chem.* **2011**, *50*, 9849–9863.
- ³ (a) Chirik, P. J.; Wieghardt, K. *Science* **2010**, *327*, 794–795. (b) de Bruin, B. *Eur. J. Inorg. Chem.* **2012**, 340–342.
- ⁴ Trovitch, R.; Lobkovsky, E.; Chirik, P. J. *Inorg. Chem.* **2006**, *45*, 7252–7260.
- ⁵ Danopoulos, A. A.; Wright, J. A.; Motherwell, W. B. *Chem. Commun.* **2005**, 784–786.
- ⁶ For current reviews, see: (a) Mercks, L.; Albrecht, M. *Chem. Soc. Rev.* **2010**, *39*, 1903–1912. (b) Cazin, C. S. J. *Comp. Rend. Chim.* **2009**, *12*, 1173–1180. (c) Poyatos, M.; Mata, J. A.; Peris, E. *Chem. Rev.* **2009**, *109*, 3677–3707. (d) Schuster, O.; Yang, L.; Raubenheimer, H. G.; Albrecht, M. *Chem. Rev.* **2009**, *109*, 3445–3478. (e) Díez-González, S.; Marion, N.; Nolan, S. P. *Chem. Rev.* **2009**, *109*, 3612–3676. (f) Kühnl, O. *Coord. Chem. Rev.* **2009**, *253*, 2481–2492. (g) Sommer, W. J.; Weck, M. *Coord. Chem. Rev.* **2007**, *251*, 860–873. (h) Crabtree, R. H. *J. Organomet. Chem.* **2005**, *690*, 5451–5457. (i) Peris, E.; Crabtree, R. H. *Coord. Chem. Rev.* **2004**, *248*, 2239–2246. (j) Herrmann, W. A. *Angew. Chem., Int. Ed. Engl.* **2002**, *41*, 1290–1309.
- ⁷ (a) Nemcsok, D.; Wichmann, K.; Frenking, G. *Organometallics* **2004**, *23*, 3640–3646. (b) Hu, X.; Castro-Rodriguez, I.; Olsen, K.; Meyer, K. *Organometallics* **2004**, *23*, 755–764. (c) Danopoulos, A.; Tulloch, A.; Winston, S.; Eastham, G.; Hursthouse, M. *Dalton Trans.* **2003**, 1009–1015. (d) Fantasia, S.; Petersen, J. L.; Jacobsen, H.; Cavallo, L.; Nolan, S. P. *Organometallics* **2007**, *26*, 5880–5889. (e) Khramov, D. M.; Lynch, V. M.; Bielawski, C. W. *Organometallics* **2007**, *26*, 6042–6049. (f) Dorta, R.; Stevens, E. D.; Scott, N. M.; Costabile, C.; Cavallo, L.; Hoff, C. D.; Nolan, S. P. *J Am Chem Soc* **2005**, *127*, 2485–2495.
- ⁸ Danopoulos, A. A.; Pugh, D.; Smith, H.; Saßmannshausen, J. *Chem. Eur. J.* **2009**, *15*, 5491–5502.
- ⁹ Zhu, D.; Budzelaar, P. H. A. *Organometallics* **2008**, *27*, 2699–2705.
- ¹⁰ Stieber, S. C. E.; Milsman, C.; Hoyt, J. M.; Turner, Z. R.; Finkelstein, K. D.; Wieghardt, K.; DeBeer, S.; Chirik, P. J. *Inorg. Chem.* **2012**, *51*, 3770–3785.
- ¹¹ Jørgensen, C. K. *Coord. Chem. Rev.* **1966**, *1*, 164–178.
- ¹² Enright, D.; Gambarotta, S.; Yap, G. P. A.; Budzelaar, P. H. M. *Angew. Chem. Int. Ed.* **2002**, *41*, 3873–3876.

- ¹³ Tondreau, A. M.; Darmon, J. M.; Wile, B. M.; Floyd, S. K.; Lobkovsky, E.; Chirik, P. J. *Organometallics* **2009**, *28*, 3928–3940.
- ¹⁴ Darmon, J. M.; Turner, Z. R.; Lobkovsky, E.; Chirik, P. J. *Organometallics* **2012**, *31*, 2275–2285.
- ¹⁵ Silver wire was used as the reference electrode, platinum wire as the counter electrode and glassy carbon as the working electrode.
- ¹⁶ Connelly, N.; Geiger, W. *Chem. Rev.* **1996**, *96*, 877–910.
- ¹⁷ Bart, S. C.; Lobkovsky, E.; Chirik, P. J. *J. Am. Chem. Soc.* **2004**, *126*, 13794–13807.
- ¹⁸ Zhang, X. *International Journal of Quantum Chemistry* **2010**, *110*, 1880–1889.
- ¹⁹ Bart, S. C.; Chłopek, K.; Bill, E.; Bouwkamp, M. W.; Lobkovsky, E.; Neese, F.; Wieghardt, K.; Chirik, P. J. *J. Am. Chem. Soc.* **2006**, *128*, 13901–13912.
- ²⁰ Koleva, B. B.; Kolev, T.; Seidel, R. W.; Tsanev, T.; Mayer-Figge, H.; Spitteller, M.; Sheldrick, W. S. *Spectrochimica Acta Part A* **2008**, *71*, 695–702.
- ²¹ Bart, S. C.; Lobkovsky, E.; Bill, E.; Wieghardt, K. *Inorg. Chem.* **2007**, *46*, 7005–7063.
- ²² (a) Shulman, G. R.; Yafet, Y.; Eisenberger, P.; Blumberg, W. E. *Proc. Natl. Acad. Sci. U.S.A.* **1976**, *73*, 1384–1388. (b) Levina, A.; Armstrong, R. S.; Lay, P. A. *Coord. Chem. Rev.* **2005**, *249*, 141–160. (c) Westre, T. E.; Kennepohl, P.; DeWitt, J. G.; Hedman, B.; Hodgson, K. O.; Solomon, E. I. *J. Am. Chem. Soc.* **1997**, *119*, 6297–6314.
- ²³ Bowman, A. C.; Milsmann, C.; Bill, E.; Turner, Z. R.; Lobkovsky, E.; DeBeer, S.; Wieghardt, K.; Chirik, P. J. *J. Am. Chem. Soc.* **2011**, *133*, 17353–17369.
- ²⁴ Danopoulos, A. A.; Tsoureas, N.; Wright, J. A.; Light, M. E. *Organometallics* **2004**, *23*, 166–168.
- ²⁵ a) Ramallo-López, J. M.; Ledo, E. J.; Requejo, F. G.; Rodriguez, J. A.; Kim, J.-Y.; Rosas-Salas, R.; Domínguez, J. M. *J. Phys. Chem. B*, **2004**, *108*, 20005–20010. b) Honji, A.; Gron, L. U.; Chang, J. -R.; Gates, B. C. *Langmuir*, **1992**, *8*, 2715–2719.
- ²⁶ (a) Orchin, M. *Advances in Catalysis* **1953**, *5*, 385–415. (b) Frankel, E. N.; Emken, E. A.; Peters, H. M.; Davison, V. K.; Butterfield, R. O. *J. Org. Chem.* **1964**, *29*, 3292–3297. (c) Frankel, E. N.; Emken, E. A.; Davison, V. K. *J. Org. Chem.* **1965**, *30*, 2739–2745. (d) Harmon, R. E.; Gupta, S. K.; Brown, D. J.; *Chem. Rev.* **1973**, *73*, 21–52.
- ²⁷ Schroeder, M. A.; Wrighton, M. S. *J. Am. Chem. Soc.* **1976**, *98*, 551–558.

²⁸ (a) Mitchener, J. C.; Wrighton, M. S. *J. Am. Chem. Soc.* **1981**, *103*, 975–977. (b) Whetten, R. L.; Fu, K.-J.; Grant, E. R. *J. Am. Chem. Soc.* **1982**, *104*, 4270–4272. (c) Weiller, B. H.; Miller, M. E.; Grant, E. R. *J. Am. Chem. Soc.* **1987**, *109*, 352–356. (d) Weiller, B. H.; Grant, E. R. *J. Am. Chem. Soc.* **1987**, *109*, 1051–1055. (e) Miller, M. E.; Grant, E. R. *J. Am. Chem. Soc.* **1987**, *109*, 7951–7960. (f) Fleckner, H.; Grevels, F. –W.; Hess, D. *J. Am. Chem. Soc.* **1984**, *106*, 2027–2032. (g) Wu, Y. –M.; Bentsen, J. G.; Brinkley, C. G.; Wrighton, M. S. *Inorg. Chem.* **1987**, *26*, 530–540. (h) Hayes, D.; Weitz, E. *J. Phys. Chem.* **1991**, *95*, 2723–2727. (i) Cedeño, D. L.; Weitz, E. *Organometallics* **2003**, *22*, 2652–2659. (j) Kismartoni, L. C.; Weitz, E.; Cedeño, D. L. *Organometallics* **2005**, *24*, 4714–4720.

²⁹ Standard conditions used to assay the activity of the *para*-substituted pyridine di(imine) iron complexes employed a 0.92 M solution of substrate in benzene-*d*₆, 5 mol % (ⁱPrCNC)Fe(N₂)₂ and four atmospheres of dihydrogen.

³⁰ Russell, S. K.; Darmon, J. M.; Lobkovsky, E.; Chirik, P. J. *Inorg. Chem.* **2010**, *49*, 2782–2792.

³¹ Bart, S. C.; Lobkovsky, E.; Chirik, P. J. *J. Am. Chem. Soc.* **2004**, *126*, 13794–13807.

³² Russell, S. K. Ph.D. Thesis, Cornell University, Ithaca, NY, 2011.

³³ Marchand, A. P.; Marchand, N. W. *Tetrahedron Lett.* **1971**, *18*, 1365–1368.

³⁴ (a) Lazzaroni, R.; Uccello-Barretta, G.; Scamuzzi, S.; Settambolo, R.; Caiazzo, A. *Organometallics* **1996**, *15*, 4657–4659. (b) Lazzaroni, R.; Settambolo, R.; Uccello-Barretta, G.; Caiazzo, A.; Scamuzzi, S. *J. Mol. Cat. A: Chem.* **1999**, *143*, 123–130. (c) Lazzaroni, R.; Settambolo, R.; Rocchiccioli, S.; Paganelli, S.; Marchetti, M. *J. Organomet. Chem.* **2005**, *690*, 1699–1704. (d) Lazzaroni, R.; Settambolo, R.; Marchetti, M.; Paganelli, S.; Alagona, G.; Ghio, C. *Inorg. Chim. Acta.* **2009**, *362*, 1641–1644.

³⁵ (a) Reger, D. L.; Culbertson, E. C. *J. Am. Chem. Soc.* **1976**, *98*, 2789–2794. (b) Reger, D. L.; Culbertson, E. C. *Inorg. Chem.* **1977**, *16*, 3104–3107.

³⁶ (a) Vela, J.; Vaddadi, S.; Cundari, T. R.; Smith, J. M.; Gregory, E. A.; Lachicotte, R. J.; Flaschenriem, C. J.; Holland, P. L. *Organometallics* **2004**, *23*, 5226–5239. (b) Vela, J.; Smith, J. M.; Lachicotte, R. J.; Holland, P. L. *Chem. Comm.* **2002**, 2886–2887.

³⁷ (a) Reger, D. L.; Garza, D. G.; Lebioda, L. *Organometallics* **1991**, *10*, 902–906. (b) Reger, D. L.; Garza, D. G.; Lebioda, L. *Organometallics* **1992**, *11*, 4285–4292. (c) Reger, D. L.; Ding, Y.; Garza, D. G.; Lebioda, L. *J. Organomet. Chem.* **1993**, *452*, 263–270.

³⁸ Harvey, J. N. *Organometallics* **2001**, *20*, 4887–4895.

³⁹ Kunishita, A.; Gianetti, T. L.; Arnold, J. *Organometallics* **2012**, *31*, 372–380.

⁴⁰ Clot, E.; Mégrét, C.; Eisenstein, O.; Perutz, R. N. *J. Am. Chem. Soc.* **2006**, *128*, 8350–8357.

⁴¹ Bouwkamp, M. W.; Bowman, A. C.; Lobkovsky, E.; Chirik, P. J. *J. Am. Chem. Soc.* **2006**, *128*, 13340–13341.

⁴² See the following reference for characterization of **D'**: Sylvester, K. T.; Chirik, P. J. *J. Am. Chem. Soc.* **2009**, *131*, 8772–8774.

Note that the spectrum was not referenced correctly and 0.10 ppm needs to be added to all reported values to obtain the correct chemical shifts.

⁴³ Miessler, G. L.; Tarr, D. A. *Inorganic Chemistry*, 3rd ed.; Prentice Hall: Upper Saddle River, NJ, 2004; p 482.

⁴⁴ Collman, J.; Hegedus, L.; Norton, J.; Finke, R. *Principles and Applications of Organotransition Metal Chemistry*; University Science Books: Mill Valley, CA, 1987; p 392.

⁴⁵ Russell, S. K.; Lobkovsky, E.; Chirik, P. J. *J. Am. Chem. Soc.* **2011**, *133*, 8858–8861.

⁴⁶ Pangborn, A. B.; Giardello, M. A.; Grubbs, R. H.; Rosen, R. K.; Timmers, F. J. *Organometallics* **1996**, *15*, 1518–1520.

⁴⁷ Vogel, A. I. *Vogel's Textbook of Practical Organic Chemistry*, 5th ed.; John Wiley and Sons: New York, 1989; pp 495–498.

⁴⁸ Sur, S. K. *J. Mag. Res.* **1989**, *82*, 169-173.

⁴⁹ George, G.N. *EXAFSPAK, SSRL, SLAC*; Stanford University: Stanford, CA, 2000.

⁵⁰ Kaleidagraph: Tools for Discovery. Synergy Software, Version 4.03, Copyright 1986–2006.

CHAPTER 3

SYNTHESIS, ELECTRONIC STRUCTURE AND REACTIVITY OF PYRIDINE

DI(CARBENE) IRON DIALKYL DINITROGEN COMPLEXES

3.1 Abstract

A series of pyridine di(carbene) iron dialkyl dinitrogen complexes was prepared by addition of alkyl lithium solutions to the corresponding iron dibromide. The pyridine di(carbene) iron dialkyl dinitrogen complexes, $(^{i\text{Pr}}\text{CNC})\text{Fe}(\text{R})_2(\text{N}_2)$ ($^{i\text{Pr}}\text{CNC} = 2,6\text{-}((2,6\text{-}^i\text{Pr}_2\text{-C}_6\text{H}_3)\text{-imidazolin-2-ylidene})_2\text{-C}_5\text{H}_3\text{N}$; $\text{R} = \text{CH}_2\text{Si}(\text{CH}_3)_3, 4\text{-CH}_3\text{-C}_6\text{H}_4, \text{CH}_3$) exhibit $S = 0$ ground states, and were studied by a combination of NMR, infrared and Mößbauer spectroscopies, and X-ray crystallography. The bis(neosilyl) and di(tolyl) variants were thermally stable under an atmosphere of dinitrogen at 23 °C, whereas the dimethyl analog underwent loss of ethane to yield the reduced iron bis(dinitrogen) complex, $(^{i\text{Pr}}\text{CNC})\text{Fe}(\text{N}_2)_2$. Crossover experiments suggested that ethane formation results from intramolecular reductive elimination. Substitution of the dinitrogen moiety in the bis(neosilyl) complex was accomplished by addition of carbon monoxide and yielded $(^{i\text{Pr}}\text{CNC})\text{Fe}(\text{CH}_2\text{Si}(\text{CH}_3)_3)_2(\text{CO})$. Alternatively, addition of excess CO to $(^{i\text{Pr}}\text{CNC})\text{Fe}(\text{CH}_3)_2(\text{N}_2)$ yielded the dicarbonyl complex, $(^{i\text{Pr}}\text{CNC})\text{Fe}(\text{CO})_2$. Differences in reactivity are a result of the steric environment of the alkyl substituents as well as a mixture of ground and transition state effects.

3.2 *Introduction*

Metal-carbon bonds define organometallic chemistry.¹ Of particular interest is their role in catalytic transformations such as hydrogenation, hydroformylation and polymerization,² as well as in cross-coupling reactions.³ While precious metals have traditionally held the spotlight for their use in homogeneous catalysis, considerable effort has been made in recent decades towards finding iron alternatives.⁴ The cost, high natural abundance and low toxicity of iron make it a very attractive precious metal surrogate. The synthesis and study of iron alkyls has therefore become a significant area of research.⁵

One important highlight in this area is the independent reports of Brookhart⁶ and Gibson^{7,8} regarding the polymerization of ethylene by MAO-activated (MAO = methylaluminumoxane) aryl-substituted pyridine di(imine) iron and cobalt dihalide complexes. While these low-cost, first row metal alternatives rivaled the efficiency of metallocenes, the mechanism of olefin polymerization and the nature of the active species remain unknown. Significant work has been performed toward better understanding of this system, but the results of these efforts have often been controversial.⁹ The approach taken by Chirik and co-workers has been the synthesis of well-defined, single-component olefin polymerization catalysts.^{10,11,12} This effort began in 2005 with the synthesis of pyridine di(imine) iron mono- and dialkyl complexes from addition of two equivalents of alkyl lithium.¹³ The outcome, mono- or dialkylation, was dependent on the alkyl lithium reagent and the steric environment of the ligand, with reductive alkylation predominating (**Figure 3.1**).^{13,14}

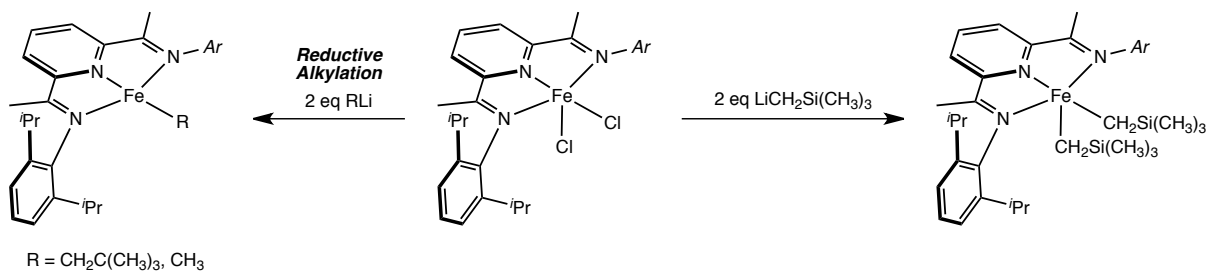


Figure 3.1. Reaction of pyridine di(imine) iron dichloride with two equivalents of alkyl lithium.

In 2008, Tondreau *et al.*¹⁵ demonstrated that aryl and alkyl-substituted pyridine di(imine) iron dialkyl complexes were extremely efficient pre-catalysts for the hydrosilylation of aldehydes and ketones using PhSiH₃ and Ph₂SiH₂ at low catalyst loadings (0.3 mol %). This methodology was expanded to asymmetric variants using enantiopure pyridine bis(oxazoline) (“Pybox”) and bis(oxazoline) (“Box”) iron dialkyl complexes.¹⁶ However, the enantiopure variants were less active than the pyridine di(imine) iron dialkyl complexes, and only low to moderate enantioselectivities were observed. One limitation to the aforementioned systems is that only primary and secondary silanes were effective. One significant breakthrough was the terpyridine derivative, (terpy)Fe(CH₂Si(CH₃)₃)₂, which was competent for the hydrosilylation of terminal olefins using tertiary silanes (Et₃SiH, *etc.*).¹⁷

It is notable that the dialkyl complexes mentioned above possess $S = 2$ ground states (**Figure 3.2**). The aryl- and alkyl-substituted pyridine di(imine), pyridine bis(oxazoline)¹⁷ and terpyridine¹⁸ iron dialkyl complexes are best described as high-spin, ferric ($S = 5/2$) compounds antiferromagnetically coupled to a ligand-centered radical ($S = 1/2$). This assignment is supported by the low isomer shifts which are inconsistent with a high-spin ferrous configuration, and is supported by density functional theory. In contrast, the bis(oxazoline) iron dialkyl compounds are best described as high-spin, ferrous complexes.¹⁹

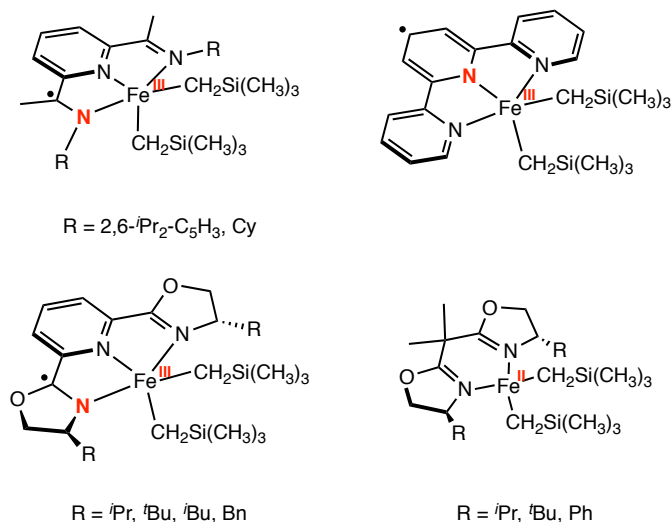


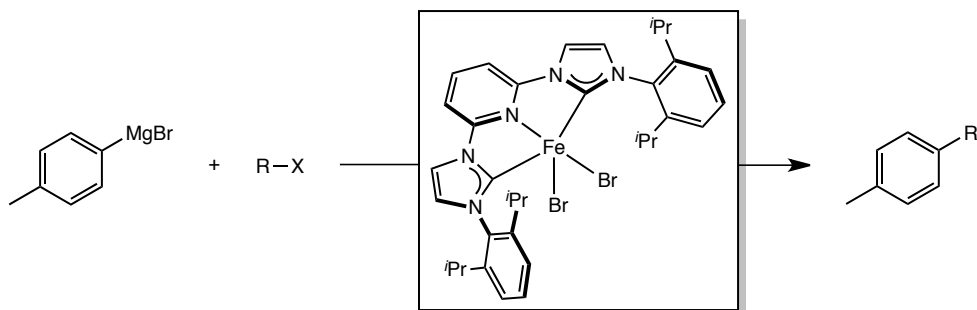
Figure 3.2. Iron bis(neosilyl) complexes competent for hydrosilylation.

The pyridine di(carbene) ligand is structurally similar to a pyridine di(imine), raising questions about the importance of redox-activity.^{20,21,22} Although early-metal pyridine di(carbene) complexes (*e.g.* Ti, V, Cr) were highly active for the polymerization of ethylene,^{20,23} Gibson and coworkers have shown that treatment of the pyridine di(carbene) iron dibromide, (ⁱPrCNC)FeBr₂ (ⁱPrCNC = 2,6-((2,6-ⁱPr₂-C₆H₃)-imidazolin-2-ylidene)₂-C₅H₃N) with MAO in the presence of ethylene did not yield polyethylene. Other precursors featuring slight modifications to the ligand architecture or FeCl₃ as the iron source were also inactive. Positive ion FAB (fast atom bombardment) mass spectrometry analysis of the solutions after treatment with MAO indicated that metal-ligand carbene elimination had occurred, a known decomposition pathway for late-metal carbene complexes.²⁴

Another area in which the two ligand frameworks have been distinguished is cross-coupling. To our knowledge, no reports of iron-catalyzed cross-coupling using the pyridine di(imine) framework have been published. On the other hand, Bedford and coworkers have reported that (ⁱPrCNC)FeBr₂ exhibited excellent activity for the cross-coupling of primary and

secondary alkyl bromides with 4-tolylmagnesium bromide (4-CH₃-C₆H₄MgBr).²⁵ Bedford's results are summarized in **Table 3.1**.

Table 3.1. Coupling of alkyl halides with aryl Grignards using (*i*PrCNC)FeBr₂.^a



R-X	Product	Conversion (%)
		94
		—
		89 ^b
		71

^a Conditions: Alkyl halide (2.0 mmol), ArMgBr (4.0 mmol), 5 mol % (*i*PrCNC)FeBr₂, Et₂O, 30 minute reflux. ^b Trans:cis = 69:31.

Presented here is an investigation into the reactivity of the pyridine di(carbene) iron dibromide with alkyl lithium reagents in an attempt to better differentiate this ligand architecture from that of the redox-active bis(imino)pyridines and to understand why these complexes are not competent for olefin polymerization.

3.3 *Synthesis and Characterization of Pyridine Di(Carbene) Iron Dialkyl Complexes*

A family of pyridine di(carbene) iron dialkyl dinitrogen complexes, $(i\text{PrCNC})\text{Fe}(\text{R})_2(\text{N}_2)$ ($\text{R} = \text{CH}_2\text{Si}(\text{CH}_3)_3$, $4\text{-CH}_3\text{-C}_6\text{H}_4$, CH_3) was prepared by slow addition of chilled ($-115\text{ }^\circ\text{C}$ or $-35\text{ }^\circ\text{C}$) diethyl ether solutions of alkyl lithium reagent to a slurry of $(i\text{PrCNC})\text{FeBr}_2$ in diethyl ether (**Figure 3.3**). Alkylation with $\text{LiCH}_2\text{Si}(\text{CH}_3)_3$ was virtually instantaneous, and $(i\text{PrCNC})\text{Fe}(\text{CH}_2\text{Si}(\text{CH}_3)_3)_2$ was isolated in modest yield (61%) without contamination from the salt byproducts following pentane filtration and recrystallization. Reaction of $(i\text{PrCNC})\text{FeBr}_2$ with 4-tolylithium resulted in an immediate color change from purple-red to yellow-brown. After stirring for three hours, the reaction mixture turned purple. Filtration and recrystallization from diethyl ether, furnished the dialkyl dinitrogen complex, $(i\text{PrCNC})\text{Fe}(4\text{-CH}_3\text{-C}_6\text{H}_4)_2(\text{N}_2)$. Bulk samples were difficult to purify due to the insolubility of the compound in pentane and hexane, making removal of the salt byproduct challenging. Samples were also contaminated with 4,4'-dimethyl-1,1'-biphenyl, which was removed by washing with pentane. Reaction of $(i\text{PrCNC})\text{FeBr}_2$ with methyllithium resulted in a rapid color change to deep purple, signifying formation of $(i\text{PrCNC})\text{Fe}(\text{CH}_3)_2(\text{N}_2)$. Stirring the reaction mixture for approximately 1 hour resulted in a color change to brown. Isolation and purification of the resulting material by filtration and recrystallization furnished the pyridine di(carbene) iron bis(dinitrogen) complex, $(i\text{PrCNC})\text{Fe}(\text{N}_2)_2$. Attempts to isolate $(i\text{PrCNC})\text{Fe}(\text{CH}_3)_2(\text{N}_2)$ shortly after addition of methyllithium by concentrating the solution to dryness *in vacuo* caused the color change to occur more rapidly. The isolated material was principally $(i\text{PrCNC})\text{Fe}(\text{N}_2)_2$ as judged by Mößbauer spectroscopy.

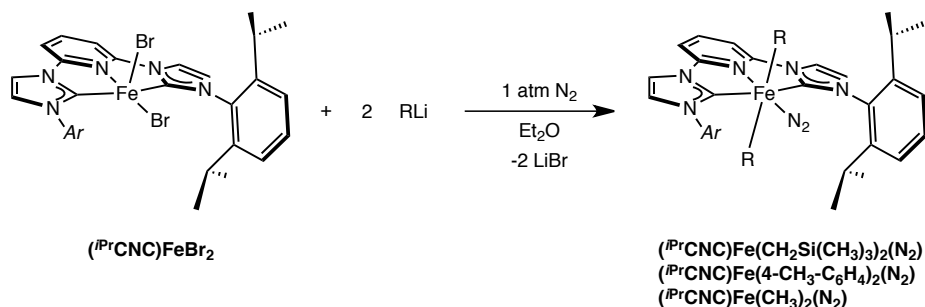


Figure 3.3. Synthesis of $(iPrCNC)Fe(R)_2(N_2)$ ($R = CH_2Si(CH_3)_3, 4-CH_3-C_6H_4, CH_3$).

Each of the pyridine di(carbene) iron dialkyl dinitrogen complexes is diamagnetic, demonstrating that the pyridine di(carbene) ligand imparts a significantly stronger ligand-field than other pincer-type tridentate ligands (i.e. pyridine di(imine),^{13,14,15} pyridine bis(oxazoline)¹⁶ and terpyridine¹⁷). Additionally, due to the low-spin d^6 configuration, the pyridine di(carbene) iron dialkyl complexes coordinate one molecule of dinitrogen, resulting in a coordinatively saturated iron center. These complexes therefore more closely resemble the bis(diphosphinoethane)^{26,27} and bis(phosphine) dicarbonyl²⁸ iron dialkyl complexes, which exhibit $S = 0$ ground states and octahedral coordination environments (**Figure 3.4**). To our knowledge, the pyridine di(phosphine) complexes,²⁹ $(iPrPNP)Fe(H)(SiH_2Ph)(L)$ ($L = N_2, CO$) are the only comparable, coordinatively saturated, neutral FeX_2 complexes bearing pincer-type tridentate ligands.

Coordination of dinitrogen by each of the pyridine di(carbene) iron dialkyl complexes was confirmed by solid-state and solution infrared spectroscopy. The values for the terminal $N\equiv N$ bands recorded in toluene are reported in **Table 3.2**, and $(iPrCNC)Fe(SiH_2(2,4,6-Me_3-C_6H_2))_2(N_2)$, prepared by Danopoulos and coworkers from the reaction of $(iPrCNC)Fe(N_2)_2$ and excess mesityl silane,²² is included for comparison. One exception is $(iPrCNC)Fe(CH_3)_2(N_2)$, where the reported value was recorded from a solid-state (KBr) spectrum due to sample isolation

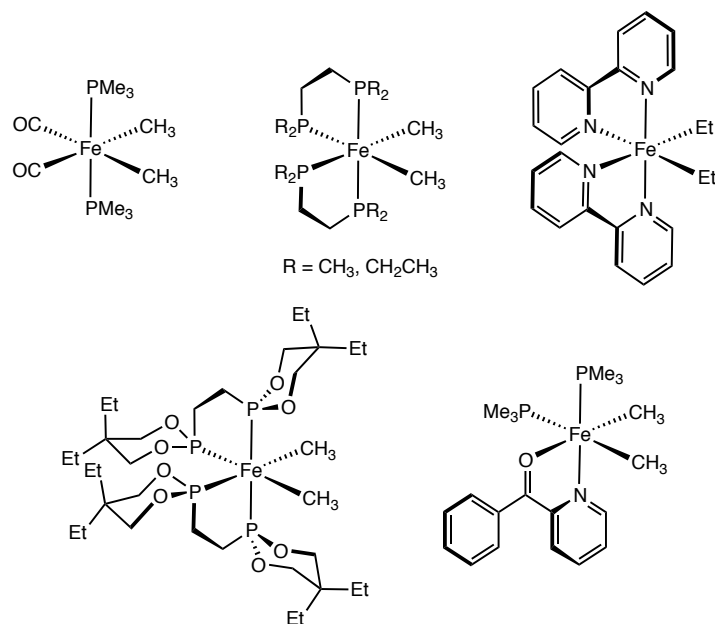


Figure 3.4. Selected iron dialkyl complexes exhibiting an $S = 0$ ground state.

difficulty. Significant differences of approximately 15–20 cm^{-1} distinguished each iron dialkyl. $(i\text{PrCNC})\text{Fe}(\text{CH}_3)_2(\text{N}_2)$ was the most reduced with a stretching frequency of 2094 cm^{-1} . $(i\text{PrCNC})\text{Fe}(\text{SiH}_2(2,4,6\text{-Me}_3\text{-C}_6\text{H}_2))_2(\text{N}_2)$, as reported by Danopoulos, exhibits the least activated dinitrogen ligand, which is expected due to the electropositive nature of silicon as compared to carbon.

Table 3.2. Infrared stretching frequencies (cm^{-1}) of $(i\text{PrCNC})\text{Fe}(\text{R})_2(\text{N}_2)$ (R = $\text{CH}_2\text{Si}(\text{CH}_3)_3$, 4- $\text{CH}_3\text{-C}_6\text{H}_4$, CH_3).

Complex	$\nu_{\text{N}\equiv\text{N}}$	Method
$(i\text{PrCNC})\text{Fe}(\text{SiH}_2\text{Mes})_2(\text{N}_2)^a$	2149	nujol
$(i\text{PrCNC})\text{Fe}(\text{CH}_2\text{Si}(\text{CH}_3)_2)_2(\text{N}_2)$	2133	toluene
$(i\text{PrCNC})\text{Fe}(4\text{-CH}_3\text{-C}_6\text{H}_4)_2(\text{N}_2)$	2118	toluene
$(i\text{PrCNC})\text{Fe}(\text{CH}_3)_2(\text{N}_2)$	2094	KBr

^a Data taken from reference 22.

Two of the pyridine di(carbene) iron dialkyl dinitrogen complexes were characterized by X-ray diffraction. Single crystals of $(i\text{PrCNC})\text{Fe}(\text{CH}_2\text{Si}(\text{CH}_3)_3)_2(\text{N}_2)$ were obtained at -35°C from

a concentrated pentane solution as dark purple needles, and single crystals of (*i*PrCNC)Fe(4-CH₃-C₆H₄)₂(N₂) were obtained at -35 °C from a concentrated diethyl ether solution as purple blocks. Representations of their solid-state structures are presented in **Figure 3.5**. Attempts to crystallize (*i*PrCNC)Fe(CH₃)₂(N₂) by filtration of a reaction mixture through Celite and cooling to -35 °C yielded purple crystals that were suitable for X-ray diffraction. Unfortunately, the crystals were weakly diffracting due to their size (15 micron thickness) and a publishable data set was not obtained; however, connectivity of the dialkyl dinitrogen complex was established. In the X-ray diffraction study of (*i*PrCNC)Fe(CH₂Si(CH₃)₃)₂(N₂), the asymmetric unit contained three

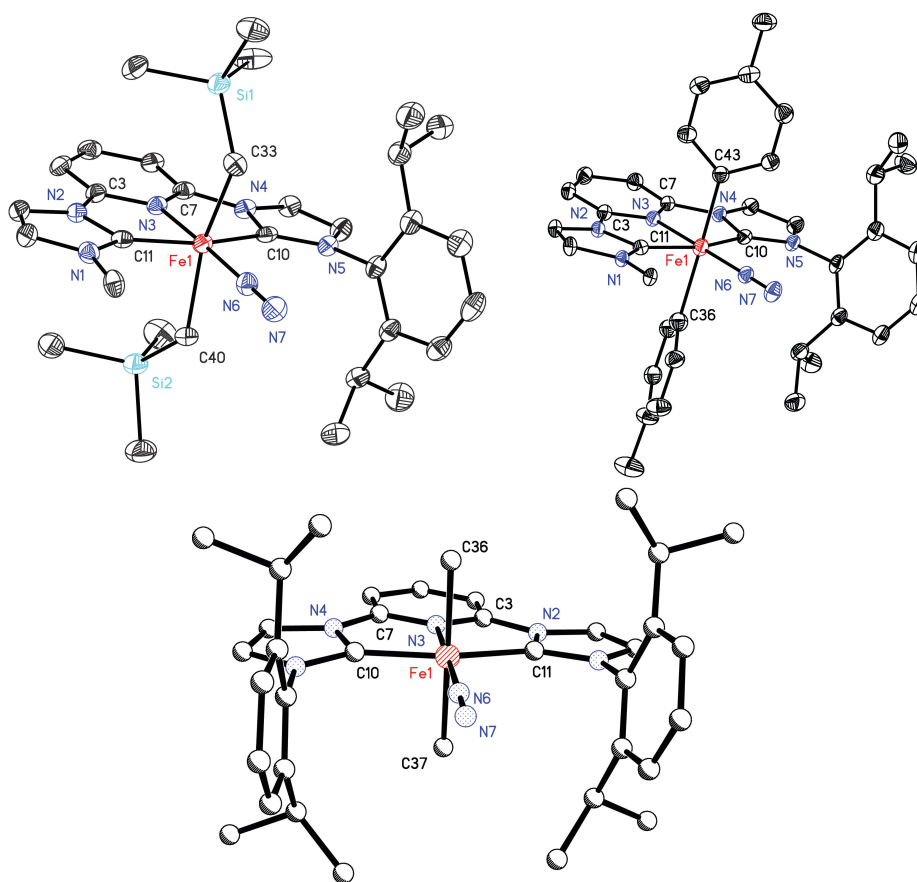


Figure 3.5. Solid state structure of (*i*PrCNC)Fe(R)₂(N₂) (R = CH₂Si(CH₃)₃, 4-CH₃-C₆H₄) at 30% probability ellipsoids, and a ball and stick representation of (*i*PrCNC)Fe(CH₃)₂(N₂). An aryl group, the hydrogen atoms, and molecules of [(Et₂O)₂LiBr]₂, where present, are omitted for clarity.

independent molecules with metrical parameters that are statistically indistinguishable, whereas for $(i\text{PrCNC})\text{Fe}(4\text{-CH}_3\text{-C}_6\text{H}_4)_2(\text{N}_2)$ and $(i\text{PrCNC})\text{Fe}(\text{CH}_3)_2(\text{N}_2)$, the asymmetric units contained one molecule of the iron dialkyl dinitrogen complex and one molecule of $[(\text{Et}_2\text{O})_4(\text{LiBr})_2]$.

Representative bond distances (Å) and angles (°) are presented in **Table 3.3**.

Table 3.3 Representative bond distances (Å) and angles (°) for $(i\text{PrCNC})\text{Fe}(\text{R})_2(\text{N}_2)$ (R = $\text{CH}_2\text{Si}(\text{CH}_3)_3$, 4- $\text{CH}_3\text{-C}_6\text{H}_4$).

$(i\text{PrCNC})\text{Fe}(\text{CH}_2\text{Si}(\text{CH}_3)_3)_2(\text{N}_2)$		$(i\text{PrCNC})\text{Fe}(4\text{-CH}_3\text{-C}_6\text{H}_4)_2(\text{N}_2)$	
Fe(1)–N(3)	1.829(4)	Fe(1)–N(3)	1.890(4)
Fe(1)–C(10)	1.937(4)	Fe(1)–C(10)	1.937(5)
Fe(1)–C(11)	1.932(4)	Fe(1)–C(11)	1.943(5)
Fe(1)–C(33)	2.138(4)	Fe(1)–C(36)	2.172(5)
Fe(1)–C(40)	2.137(4)	Fe(1)–C(43)	2.066(5)
Fe(1)–N(6)	1.829(4)	Fe(1)–N(6)	1.819(4)
N(6)–N(7)	1.118(5)	N(6)–N(7)	1.103(6)
N(3)–Fe(1)–C(33)	100.77(14)	N(3)–Fe(1)–C(36)	88.59(19)
C(33)–Fe(1)–N(6)	81.71(16)	C(36)–Fe(1)–N(6)	91.5(2)
N(3)–Fe(1)–C(10)	79.89(14)	N(3)–Fe(1)–C(10)	80.56(17)
C(33)–Fe(1)–C(40)	163.22(16)	C(36)–Fe(1)–C(43)	176.9(2)
N(4)–C(10)–N(5)	101.5(3)	N(4)–C(10)–N(5)	102.1(4)
N(3)–Fe(1)–C(40)	95.98(15)	N(3)–Fe(1)–C(43)	88.71(18)
C(40)–Fe(1)–N(6)	81.53(16)	C(43)–Fe(1)–N(6)	91.22(19)
N(3)–Fe(1)–C(11)	79.75(15)	N(3)–Fe(1)–C(11)	80.42(17)
N(1)–C(11)–N(2)	101.7(3)	N(1)–C(11)–N(2)	102.5(4)

The pyridine di(carbene) iron dialkyl dinitrogen complexes are six-coordinate, pseudo-octahedral compounds exhibiting idealized C_{2v} symmetry. The alkyl substituents are arranged in a *trans* configuration. For $(i\text{PrCNC})\text{Fe}(\text{CH}_2\text{Si}(\text{CH}_3)_3)_2(\text{N}_2)$, the two alkyl groups are arranged at an angle of $163.22(16)^\circ$ with the bulky $-\text{Si}(\text{CH}_3)_3$ groups positioned away from the isopropyl methyls to minimize steric interactions. For $(i\text{PrCNC})\text{Fe}(4\text{-CH}_3\text{-C}_6\text{H}_4)_2(\text{N}_2)$, the $C_{\text{aryl}}\text{-Fe-}C_{\text{aryl}}$ bond angle does not significantly deviate from linearity because of the decreased steric demand imparted by the tolyl groups. The iron-alkyl bond lengths of $(i\text{PrCNC})\text{Fe}(\text{CH}_2\text{Si}(\text{CH}_3)_3)_2(\text{N}_2)$ are

significantly longer than those of the pyridine di(imine),^{13,15} pyridine bis(oxazoline)¹⁶ and terpyridine iron dialkyls,¹⁷ which range from 2.045 to 2.085 Å. This is attributed to a strong *trans*-influence. For (ⁱPrCNC)Fe(4-CH₃-C₆H₄)₂(N₂), two statistically distinct Fe-C_{aryl} distances are observed; however, one of the carbons, C36, was disordered. As such, this carbon was left isotropic during refinement, and is therefore the less reliable value. The other Fe-C_{aryl} bond length, 2.066(5) Å, is significantly shorter than that of the bis(neosilyl) analog. This was expected due to the difference in hybridization: *sp*² vs *sp*³.

Unlike (ⁱPrCNC)Fe(SiH₂(2,4,6-Me₃-C₆H₂))₂(N₂), which is reported to exhibit signal broadening,²² (ⁱPrCNC)Fe(CH₂Si(CH₃)₃)₂(N₂) and (ⁱPrCNC)Fe(4-CH₃-C₆H₄)₂(N₂) were readily characterized by ¹H and ¹³C NMR spectroscopy. The benzene-*d*₆ ¹H NMR spectra display the number of resonances associated with a C_{2v} symmetric compound at 22 °C, consistent with the solid state structures. For (ⁱPrCNC)Fe(CH₂Si(CH₃)₃)₂(N₂) (**Figure 3.6**, top), the methylene and methyl resonances of the two alkyl ligands are located upfield at -1.13 and -0.45 ppm, respectively. The resonances for the pyridine di(carbene) ligand do not shift significantly from the diamagnetic reference values of the free carbene.²⁰ One exception, the *m*-pyridine resonance is shifted upfield from 8.47 (free ligand) to 6.60 ppm. The benzene-*d*₆ ¹H NMR spectrum of (ⁱPrCNC)Fe(4-CH₃-C₆H₄)₂(N₂) was similar. Both (ⁱPrCNC)Fe(CH₂Si(CH₃)₃)₂(N₂) and (ⁱPrCNC)Fe(4-CH₃-C₆H₄)₂(N₂) showed no signs of decomposition over the course of days at 23 °C under an atmosphere of dinitrogen by ¹H NMR spectroscopy.

Concentrating a sample of (ⁱPrCNC)Fe(CH₃)₂(N₂) to near dryness ten minutes after slow addition of methyllithium allowed observation of (ⁱPrCNC)Fe(CH₃)₂(N₂) by ¹H NMR spectroscopy in benzene-*d*₆ (**Figure 3.6**, bottom). Although significant amounts of diethyl ether were present

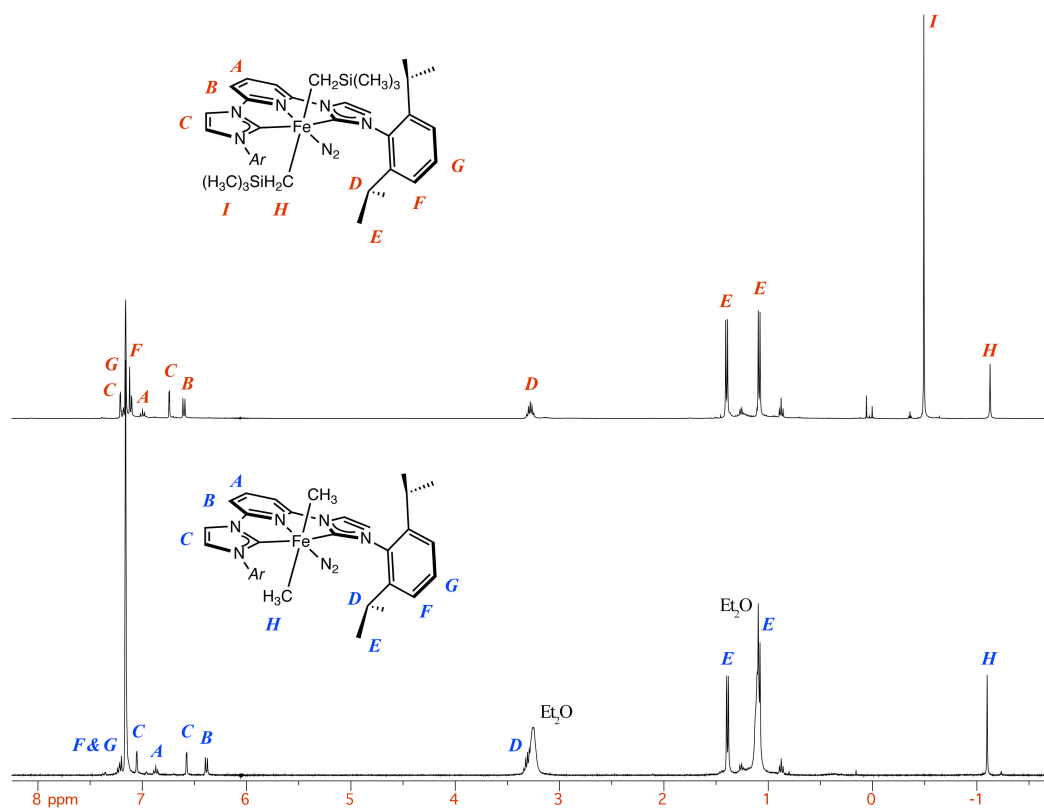


Figure 3.6. Benzene- d_6 ^1H NMR spectra of $(i\text{PrCNC})\text{Fe}(\text{CH}_2\text{Si}(\text{CH}_3)_3)_2(\text{N}_2)$ (top) and $(i\text{PrCNC})\text{Fe}(\text{CH}_3)_2(\text{N}_2)$ (bottom) collected at 22 °C.

in the spectrum, all proton resonances were located by COSY. The benzene- d_6 ^1H NMR spectrum of $(i\text{PrCNC})\text{Fe}(\text{CH}_3)_2(\text{N}_2)$ is similar to that of $(i\text{PrCNC})\text{Fe}(\text{CH}_2\text{Si}(\text{CH}_3)_3)_2(\text{N}_2)$ and $(i\text{PrCNC})\text{Fe}(4\text{-CH}_3\text{-C}_6\text{H}_4)_2(\text{N}_2)$. The chemical shift of the methyl groups is located at -1.10 ppm. Under an atmosphere of dinitrogen, $(i\text{PrCNC})\text{Fe}(\text{CH}_3)_2(\text{N}_2)$ cleanly converts to $(i\text{PrCNC})\text{Fe}(\text{N}_2)_2$ (as determined by ^1H NMR spectroscopy) with concomitant growth of the resonance at 0.80 ppm corresponding to ethane. The effect of additional diethyl ether or the influence of lithium bromide on this process has not yet been demonstrated.

The pyridine di(carbene) iron dialkyl dinitrogen complexes were further characterized by zero-field, ^{57}Fe Mößbauer spectroscopy at 80 K. Representative spectra are presented in **Figure 3.7** and the experimentally determined parameters are reported in **Table 3.4**.

$(i\text{PrPDI})\text{Fe}(\text{CH}_2\text{Si}(\text{CH}_3)_3)_2$ is included for reference. Because $(i\text{PrCNC})\text{Fe}(\text{CH}_3)_2(\text{N}_2)$ was not isolated cleanly as a solid, an aliquot of a 50 mM diethyl ether solution of the $(i\text{PrCNC})\text{Fe}(\text{CH}_3)_2(\text{N}_2)$ prepared *in situ* was frozen shortly after addition of methyllithium, yielding a sample suitable for Mößbauer spectroscopy. The isomer shifts of the pyridine di(carbene) iron dialkyl dinitrogen complexes are significantly lower than those of five-coordinate pyridine di(imine), pyridine bis(oxazoline), and terpyridine iron bis(neosilyl) complexes, 0.27–0.29 $\text{mm}\cdot\text{s}^{-1}$.¹⁷ This indicates a greater degree of covalency, and can be attributed to the difference in spin states. Low-spin configurations typically result in lower isomer shifts because of shorter metal-ligand bonds.³⁰ The pyridine di(carbene) iron dialkyls also

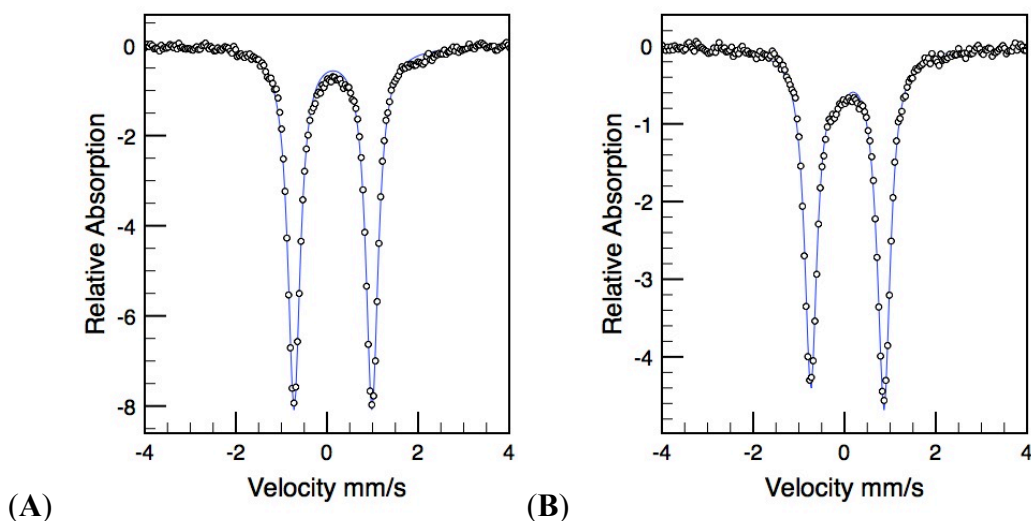


Figure 3.7. Representative zero-field ^{57}Fe Mößbauer spectra of $(i\text{PrCNC})\text{Fe}(\text{R})_2(\text{N}_2)$ collected at 80 K: **(A)** $(i\text{PrCNC})\text{Fe}(\text{CH}_2\text{Si}(\text{CH}_3)_3)_2(\text{N}_2)$, solid-state **(B)** $(i\text{PrCNC})\text{Fe}(\text{CH}_3)_2(\text{N}_2)$, diethyl ether solution.

Table 3.4. Zero-field ^{57}Fe Mößbauer parameters ($\text{mm}\cdot\text{s}^{-1}$) for the pyridine di(carbene) iron dialkyl dinitrogen complexes at 80 K.

Complex	δ	$ \Delta E_Q $
$(i\text{PrPDI})\text{Fe}(\text{CH}_2\text{Si}(\text{CH}_3)_3)_2$	0.27	2.60
$(i\text{PrCNC})\text{Fe}(\text{CH}_2\text{Si}(\text{CH}_3)_2)_2(\text{N}_2)$	0.13	1.71
$(i\text{PrCNC})\text{Fe}(4\text{-CH}_3\text{-C}_6\text{H}_4)_2(\text{N}_2)$	0.07	1.42
$(i\text{PrCNC})\text{Fe}(\text{CH}_3)_2(\text{N}_2)$	0.06	1.61

exhibit smaller quadrupole splitting values; however, a straightforward interpretation of the differences in the electric field gradients is challenging due to the differences in iron oxidation state and molecular geometry.

3.4 Reactivity of Pyridine Di(carbene) Iron Dialkyl Complexes

The formal carbon-carbon reductive elimination of iron dialkyls was previously reported by Venturi *et al.*²⁸ from decomposition of the iron bis(trimethylphosphine) dicarbonyl dialkyl complexes, *cis,trans,cis*-Fe(CO)₂(PMe₃)₂RR' (R = CH₃, R' = Ph; R = R' = CH=CH₂; R = R' = CH₃) (**Figure 3.8**). One feature that distinguishes these iron phosphine carbonyl complexes from the pyridine di(carbene) iron complexes is the *cis* arrangement of the alkyl fragments. Additionally, the iron dimethyl compound, *cis,trans,cis*-Fe(CO)₂(PMe₃)₂(CH₃)₂, is thermally stable at 23 °C and was stable up to 50 °C in solution in the absence of nucleophiles. The mechanism of reductive elimination for these complexes has not been thoroughly studied.

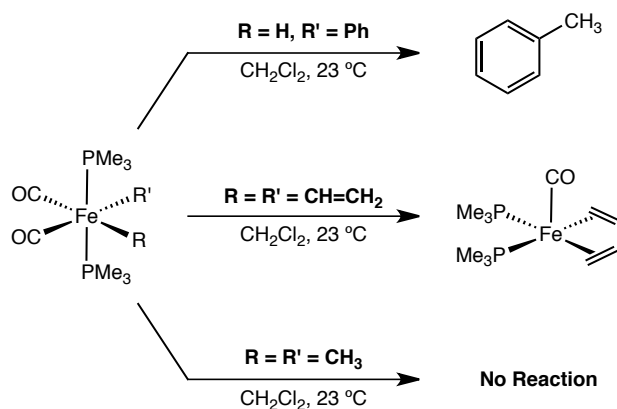


Figure 3.8. Reductive C–C coupling of *cis,trans,cis*-Fe(CO)₂(PMe₃)₂RR'.

Recently, Bernskoetter and coworkers investigated the mechanism of ethane elimination from the diamagnetic cobalt(III) dimethyl complex, *cis,mer*-(PMe₃)₃Co(CH₃)₂I.³¹ Loss of ethane yielded the paramagnetic cobalt(I) species, (PMe₃)₃CoI. Kinetic and deuterium labelling studies

avored a mechanism in which loss of phosphine preceded a “largely concerted” C–C bond coupling event, thus exhibiting significant commonalities with mechanisms investigated for second or third row transition metals.^{32,33} Understanding of this system was complicated by observation of intermolecular methyl exchange and the necessity for a spin-state change during the transformation.

The initially observed reactivity of the pyridine di(carbene) iron dialkyl dinitrogen complexes prompted further exploration as well as an investigation into the mechanism of ethane loss. At least three distinct mechanisms are possible that account for the formation of ethane from $(i\text{PrCNC})\text{Fe}(\text{CH}_3)_2(\text{N}_2)$ (**Figure 3.9**). Each mechanism begins with dissociation of dinitrogen from the coordinately saturated iron center. The reductive elimination of carbon-carbon bonds from six-coordinate, d^6 metal species undergoing ligand dissociation has been well established for base- and precious metals.^{31,33,34} Experimental evidence for this was observed, as attempts to isolate $(i\text{PrCNC})\text{Fe}(\text{CH}_3)_2(\text{N}_2)$ after addition of methyl lithium by removal of solvent resulted in material that was predominately $(i\text{PrCNC})\text{Fe}(\text{N}_2)_2$ (identified by Mößbauer spectroscopy), indicating an increase in the rate of ethane loss. Dissociation of dinitrogen would also allow for a *cis*-orientation of the methyl groups, which is a requirement for concerted reductive eliminations.³⁵ Mechanism A invokes iron-carbon bond homolysis. The resulting methyl radical could then combine with a second methyl radical, or abstract a methyl group from resulting formally iron(I) complex.^{12,36} This mechanism is often difficult to rule out, as the absence of significant amounts of methane could be due to a tightly caged radical or a rapid radical rebound version of Mechanism A.³⁷ In mechanism B, a concerted reductive elimination occurs likely via a three-centered transition state.^{32,38} The final pathway, mechanism C involves a

sequence beginning with α -hydride elimination to form a methyldiene, followed by methyl insertion and C–H reductive elimination.³⁹

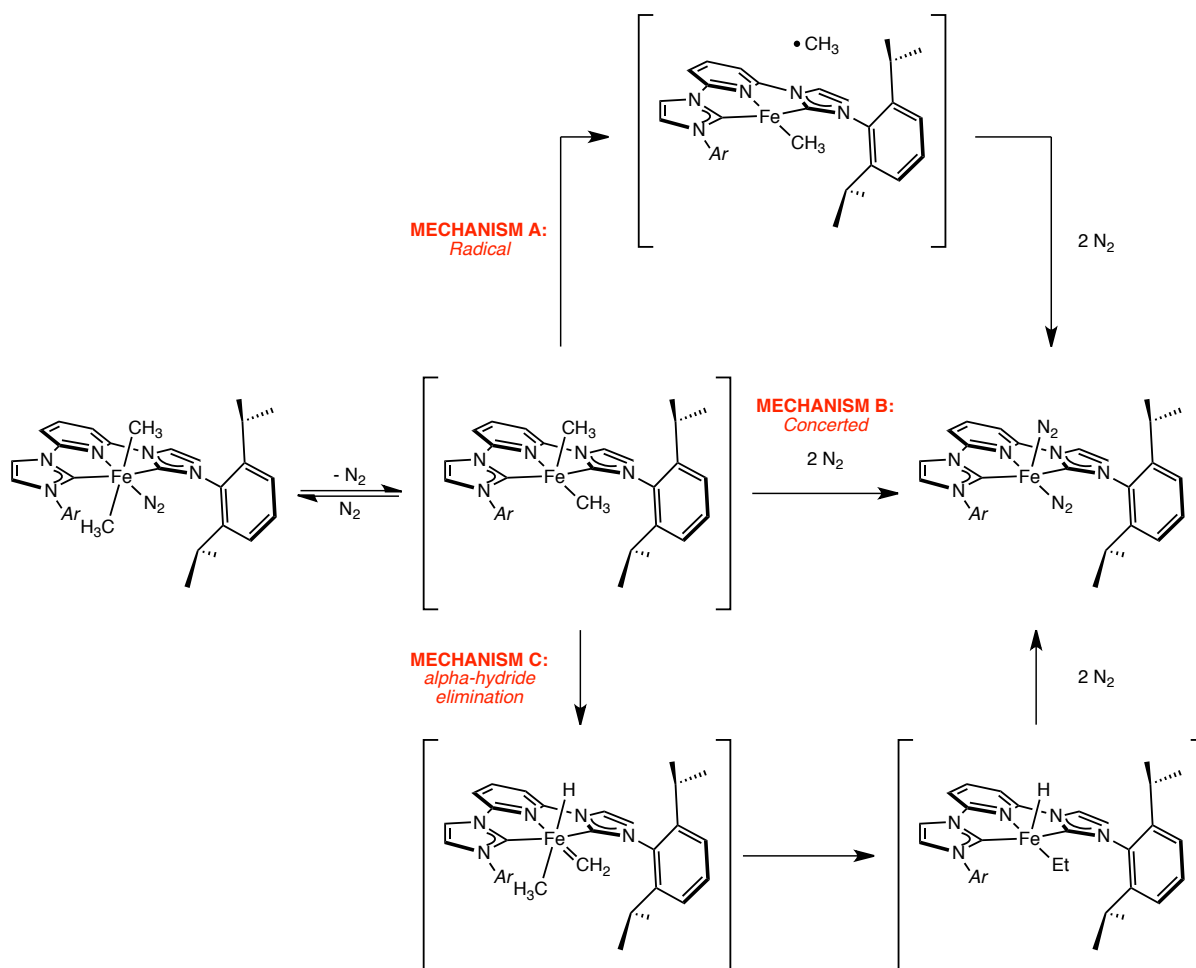


Figure 3.9. Potential pathways for ethane elimination from $(iPrCNC)Fe(CH_3)_2(N_2)$.

Danopoulos and coworkers postulated that lability of the dinitrogen moiety of the disilyl dinitrogen analog was a potential reason for broadening of the 1H NMR resonances.²² To investigate this hypothesis, $(iPrCNC)Fe(CH_2Si(CH_3)_3)_2(N_2)$ was studied by ^{15}N NMR spectroscopy. Addition of 1 atmosphere of $^{15}N_2$ to $(iPrCNC)Fe(CH_2Si(CH_3)_3)_2(N_2)$ in benzene- d_6 resulted in incorporation of ^{15}N into the terminal dinitrogen position. A very broad resonance

($\Delta\nu_{1/2} = 430$ Hz) centered at 386 ppm was observed in the ^{15}N NMR spectrum at 22 °C, supporting rapid exchange of dinitrogen on the ^{15}N NMR timescale.

In order to demonstrate that reductive elimination could not occur without loss of dinitrogen, the reactivity of the pyridine di(carbene) iron dialkyl dinitrogen complexes with carbon monoxide was probed. Presumably, carbon monoxide coordination would be irreversible and raises the barrier for reductive elimination. Addition of excess carbon monoxide to a benzene- d_6 solution of $(i\text{PrCNC})\text{Fe}(\text{CH}_2\text{Si}(\text{CH}_3)_2)_2(\text{N}_2)$ resulted in a color change from purple to deep pink, and furnished the CO adduct, $(i\text{PrCNC})\text{Fe}(\text{CH}_2\text{Si}(\text{CH}_3)_3)_2(\text{CO})$ (**Figure 3.10**). Similar reactivity has been observed with the pyridine di(phosphine) complex, $(i\text{PrPNP})\text{FeH}(\text{SiH}_2\text{Ph})\text{N}_2$ upon addition of CO,²⁹ and starkly contrasts the reactivity of high-spin, bis neosilyl complexes. Bart *et al.*⁴⁰ and Girolami *et al.*⁴¹ have demonstrated that addition of excess carbon monoxide to high-spin, ferrous dialkyl complexes with neutral ligands resulted in the formation of the iron dicarbonyl species and formal elimination of $((\text{CH}_3)_3\text{SiCH}_2)_2\text{CO}$.

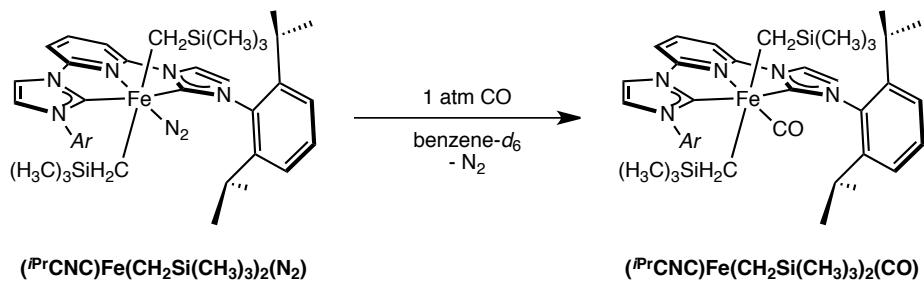


Figure 3.10. Synthesis of $(i\text{PrCNC})\text{Fe}(\text{CH}_2\text{Si}(\text{CH}_3)_3)_2(\text{CO})$.

The presence of bound carbon monoxide was confirmed by toluene solution infrared spectroscopy. The intense CO absorption was located at 1919 cm^{-1} , which is approximately 20 cm^{-1} less reduced than the average of the symmetric and asymmetric carbonyl absorptions of the

formally iron(0) dicarbonyl complex, $(i\text{PrCNC})\text{Fe}(\text{CO})_2$.²¹ This is consistent with metal-ligand backbonding from a less electron-rich metal center. It is also significantly less reduced (approximately 40 wavenumbers) than the di(phosphine) complex, $(i\text{PrPNP})\text{FeH}(\text{SiH}_2\text{Ph})(\text{CO})$.²⁹

Single crystals of $(i\text{PrCNC})\text{Fe}(\text{CH}_2\text{Si}(\text{CH}_3)_3)_2(\text{CO})$ suitable for X-ray diffraction were obtained from a concentrated pentane solution at $-35\text{ }^\circ\text{C}$ as dark purple plates (**Figure 3.11**). The asymmetric unit contained two independent molecules of $(i\text{PrCNC})\text{Fe}(\text{CH}_2\text{Si}(\text{CH}_3)_3)_2(\text{CO})$ with metrical parameters that are statistically indistinguishable. Representative bond distances (\AA) and

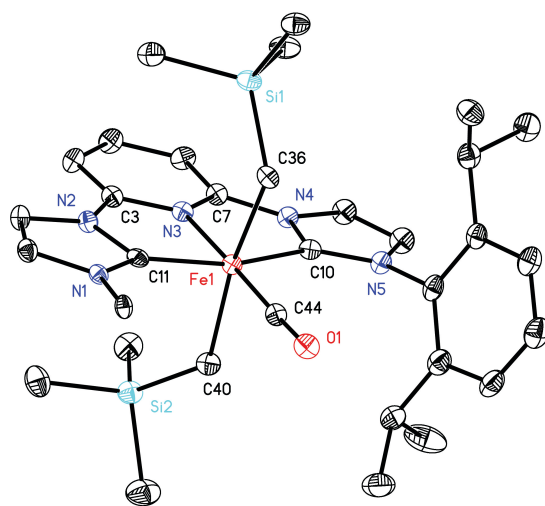


Figure 3.11. Solid state structure of $(i\text{PrCNC})\text{Fe}(\text{CH}_2\text{Si}(\text{CH}_3)_3)_2(\text{CO})$ at 30% probability ellipsoids. One representative molecule is shown from the asymmetric unit with hydrogen atoms and an aryl group omitted for clarity.

Table 3.5. Selected bond distances (\AA) and angles ($^\circ$) for $(i\text{PrCNC})\text{Fe}(\text{CH}_2\text{Si}(\text{CH}_3)_3)_2(\text{CO})$.

Fe(1)–N(3)	1.925(2)	Fe(1)–C(10)	1.931(3)
Fe(1)–C(11)	1.915(3)	Fe(1)–C(36)	2.137(2)
Fe(1)–C(40)	2.154(3)	Fe(1)–C(44)	1.730(3)
C(44)–O(1)	1.160(3)		
N(3)–Fe(1)–C(36)	100.20(10)	N(3)–Fe(1)–C(40)	89.40(10)
C(36)–Fe(1)–C(44)	81.55(11)	C(40)–Fe(1)–C(44)	88.85(12)
N(3)–Fe(1)–C(10)	79.64(10)	N(3)–Fe(1)–C(11)	79.81(10)
C(36)–Fe(1)–C(40)	170.16(11)	N(1)–C(11)–N(2)	102.7(2)
N(4)–C(10)–N(5)	103.1(2)		

angles ($^{\circ}$) are presented in **Table 3.5**. $(i\text{PrCNC})\text{Fe}(\text{CH}_2\text{Si}(\text{CH}_3)_3)_2(\text{CO})$, similar to the dinitrogen analog is a six-coordinate, pseudo-octahedral complex with idealized C_{2v} symmetry. The iron–carbene and iron–alkyl bond lengths are statistically indistinguishable from those $(i\text{PrCNC})\text{Fe}(\text{CH}_2\text{Si}(\text{CH}_3)_3)_2(\text{N}_2)$. However, the iron pyridine bond length is significantly longer at 1.925(2) Å, likely due to a stronger *trans* influence of the carbonyl ligand.

The ^1H NMR spectrum of $(i\text{PrCNC})\text{Fe}(\text{CH}_2\text{Si}(\text{CH}_3)_3)_2(\text{CO})$ in benzene- d_6 is consistent with molecular C_{2v} symmetry and an $S = 0$ ground state (**Figure 3.12**). Many of the resonances do not deviate significantly from those of the bis(neosilyl) dialkyl dinitrogen compound, suggesting that substitution of dinitrogen does not significantly alter the electronics of the complex.

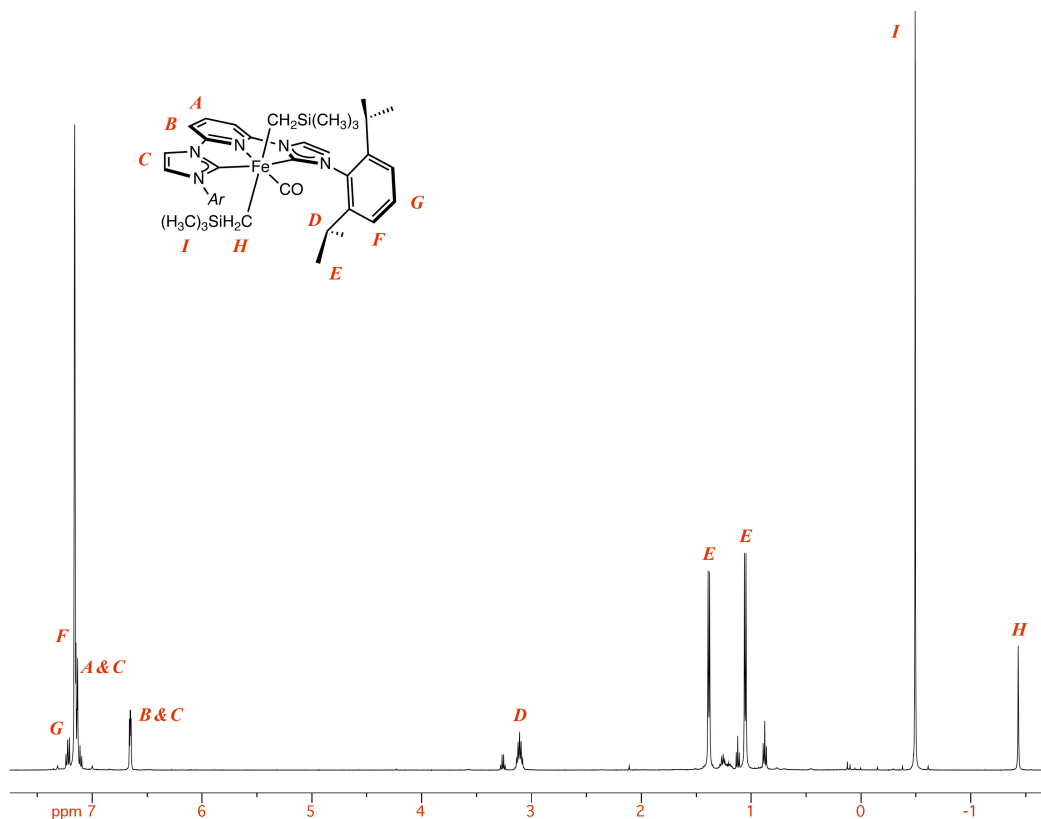


Figure 3.12. ^1H NMR spectrum of $(i\text{PrCNC})\text{Fe}(\text{CH}_2\text{Si}(\text{CH}_3)_3)_2(\text{CO})$ in benzene- d_6 at 22 °C.

In order to demonstrate that no gross change in electronic structure had occurred, $(i\text{PrCNC})\text{Fe}(\text{CH}_2\text{Si}(\text{CH}_3)_3)_2(\text{CO})$ was investigated by Mößbauer spectroscopy (**Figure 3.13**). A quadrupole doublet was observed with an isomer shift of $-0.03 \text{ mm}\cdot\text{s}^{-1}$ and a quadrupole splitting of $|0.65| \text{ mm}\cdot\text{s}^{-1}$. The lower isomer shift of the dialkyl carbonyl complex, as compared to the dinitrogen analog (see **Table 3.4**), is most likely due to the short Fe–CO bond and an increase in covalency due to metal-ligand back bonding. The difference in quadrupole splitting is attributed to a change in electric field gradient arising from different ordering and population of the cloverleaf d -orbitals and d_{z^2} orbitals in the two complexes. A minor impurity (6%) was also present with an isomer shift of $-0.10 \text{ mm}\cdot\text{s}^{-1}$ and a quadrupole splitting of $|1.98| \text{ mm}\cdot\text{s}^{-1}$.

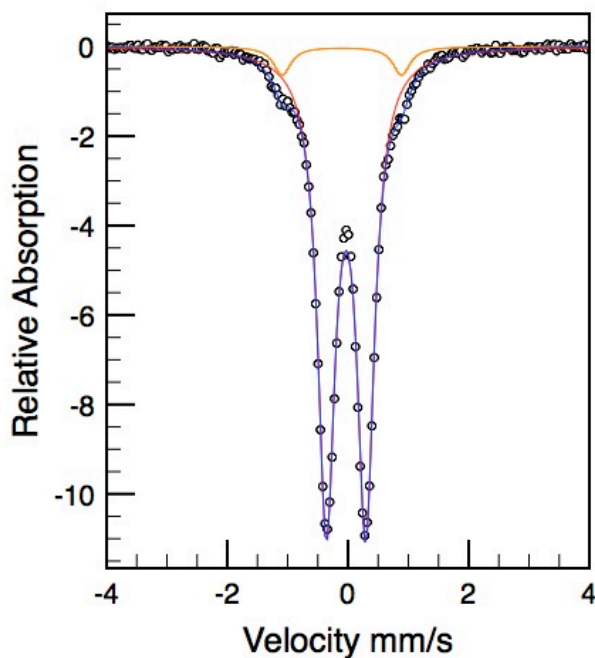


Figure 3.13. Zero-field ^{57}Fe Mößbauer spectrum of $(i\text{PrCNC})\text{Fe}(\text{CH}_2\text{Si}(\text{CH}_3)_3)_2(\text{CO})$ obtained at 80 K; $\delta = -0.03 \text{ mm}\cdot\text{s}^{-1}$, $|\Delta E_Q| = 0.65 \text{ mm}\cdot\text{s}^{-1}$.

$(i\text{PrCNC})\text{Fe}(\text{CH}_2\text{Si}(\text{CH}_3)_3)_2(\text{CO})$ did not revert to the bis(neosilyl) dialkyl dinitrogen compound under an atmosphere of dinitrogen at 23 °C, signifying that carbon monoxide binding

was irreversible. Additionally, the complex exhibited some modest air and moisture stability. Exposing a solution of $(i\text{PrCNC})\text{Fe}(\text{CH}_2\text{Si}(\text{CH}_3)_3)_2(\text{CO})$ in benzene- d_6 to air did not result in rapid decomposition; however, bleaching of the intensely pink solution did occur within a few hours.

Addition of an excess of CO to a diethyl ether solution of $(i\text{PrCNC})\text{Fe}(\text{CH}_3)_2(\text{N}_2)$ prepared *in situ* from the reaction of $(i\text{PrCNC})\text{FeBr}_2$ and methyllithium was performed in hopes of obtaining the iron dimethyl carbonyl species. Upon work-up, however, only the iron(0) dicarbonyl compound, $(i\text{PrCNC})\text{Fe}(\text{CO})_2$ was isolated (**Figure 3.14**). The fate of the alkyl groups has not yet been determined. Three likely possibilities exist: (1) CO addition induces reductive elimination to afford ethane, (2) the dimethyl monocarbonyl forms and the carbonyl inserts into the metal-alkyl bond to form the acyl, alkyl complex followed by rapid reductive elimination to form acetone or (3) carbon monoxide inserts into both metal-alkyl bonds to give a diacyl complex that undergoes reductive elimination to yield 2,3-butanedione. Bellachioma *et al.*⁴² reported that addition of an excess of carbon monoxide to *cis*, *trans*, *cis*- $\text{Fe}(\text{CO})_2(\text{PMe}_3)_2(\text{CH}_3)_2$ resulted in formation of $\text{Fe}(\text{CO})_3(\text{PMe}_3)_2$ and 2,3-butanedione. Monitoring the reaction by ^1H NMR spectroscopy in benzene- d_6 revealed the formation of $(i\text{PrCNC})\text{Fe}(\text{CO})_2$ and an unknown

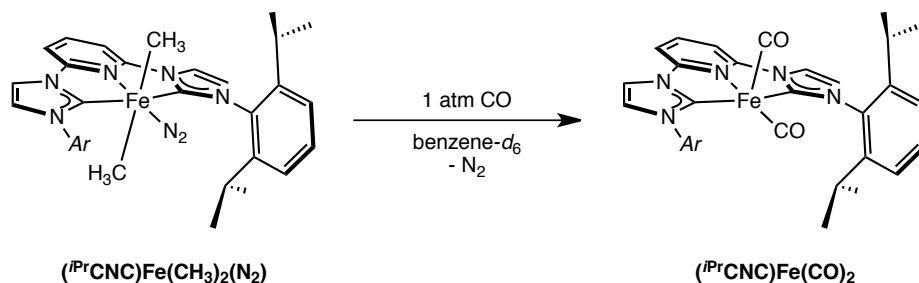


Figure 3.14. Reaction of $(i\text{PrCNC})\text{Fe}(\text{CH}_3)_2(\text{N}_2)$ with CO.

diamagnetic species, which has not yet been identified. Vacuum transfer of the volatiles did not reveal the presence of any significant amount of organics.

Having shown the lability of the dinitrogen moiety, crossover experiments were performed to probe the nature of the reductive elimination (**Figure 3.15**). One experiment (a) involved mixing of equimolar diethyl ether solutions of (*i*PrCNC)Fe(CH₃)₂(N₂) with deuterium labeled (*i*PrCNC)Fe(CD₃)₂(N₂). Assuming that reductive elimination takes place in a concerted fashion (mechanism B, **Figure 3.8**), ethane and ethane-*d*₆ would be observed exclusively. The presence of ethane-*d*₃ would indicate that the mechanism of reductive elimination occurs as an outer-sphere version of mechanism A. The other experiment (b) involved the addition of an equimolar solution of methyllithium and methyllithium-*d*₃. Under these conditions, a roughly equimolar amount of ethane, ethane-*d*₃, and ethane-*d*₆ should be observed, assuming mechanism B was operative. Unfortunately, these crossover experiments do not rule out the possibility of mechanism C, which would give similar results to those obtained for mechanism B (concerted elimination).

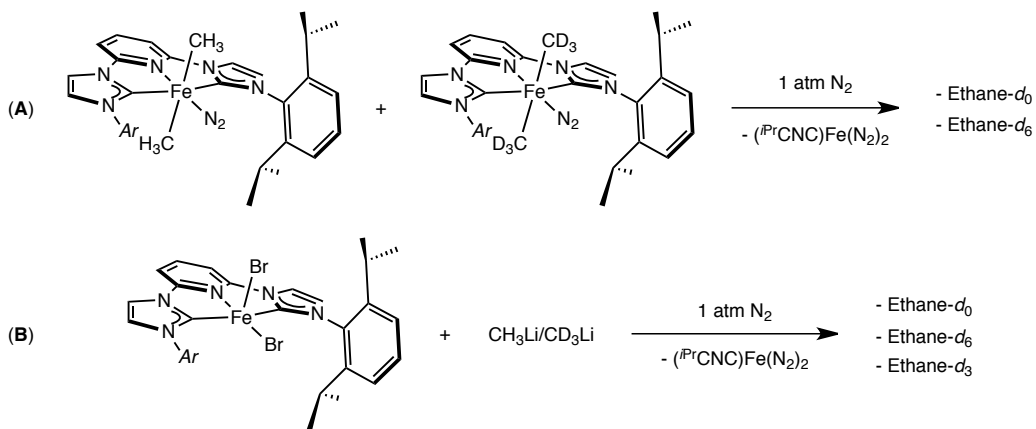


Figure 3.15. Proposed crossover experiments and expected results from a concerted reductive elimination mechanism.

The deuterated iron dimethyl dinitrogen compound, (i^{PrCNC})Fe(CD₃)₂(N₂) was prepared in a similar manner to the protio-analog. Addition of two equivalents of CD₃Li·LiI in melting diethyl ether to a thawing diethyl ether slurry of (i^{PrCNC})FeBr₂ resulted in a rapid color change to bright purple. This complex was analyzed by ²H NMR spectroscopy in C₆H₆. The methyl resonance was located at -1.20 ppm. Over time, this resonance diminished in intensity and a new resonance at 0.70 ppm (ethane-*d*₆) grew in, demonstrating consistent reactivity.

The first crossover experiment was performed by preparing both dimethyl dinitrogen isotopologues *in situ*, followed by a ten minute period of stirring before the two mixtures were combined. Aliquots from the resulting mixture were analyzed by ¹H and ²H NMR spectroscopy. The final spectra, after complete conversion of the dimethyl complexes to the iron bis(dinitrogen) compound, (i^{PrCNC})Fe(N₂)₂, are presented in **Figure 3.16**. Only the resonances for ethane (0.80 ppm in benzene-*d*₆) and ethane-*d*₆ (0.70 ppm in C₆H₆) were observed by ¹H and ²H NMR spectroscopy, respectively. This supports reductive elimination from a single iron center, and that the alkyl groups do not exchange on the timescale of the experiment.

The second crossover experiment was performed by pre-mixing solutions of methyllithium and methyllithium-*d*₃ complexed with lithium iodide prior to freezing the solutions and adding them to the melting ethereal slurry of (i^{PrCNC})FeBr₂. Aliquots from the final mixture were analyzed by ¹H and ²H NMR spectroscopy. The final spectra, after complete conversion of the dimethyl complexes to the iron bis(dinitrogen) compound, (i^{PrCNC})Fe(N₂)₂ are presented in **Figure 3.17**. A singlet resonance at 0.80 ppm corresponding to ethane-*d*₀ and a multiplet at 0.78 ppm corresponding to ethane-*d*₃ were observed in the ¹H NMR spectrum. Two

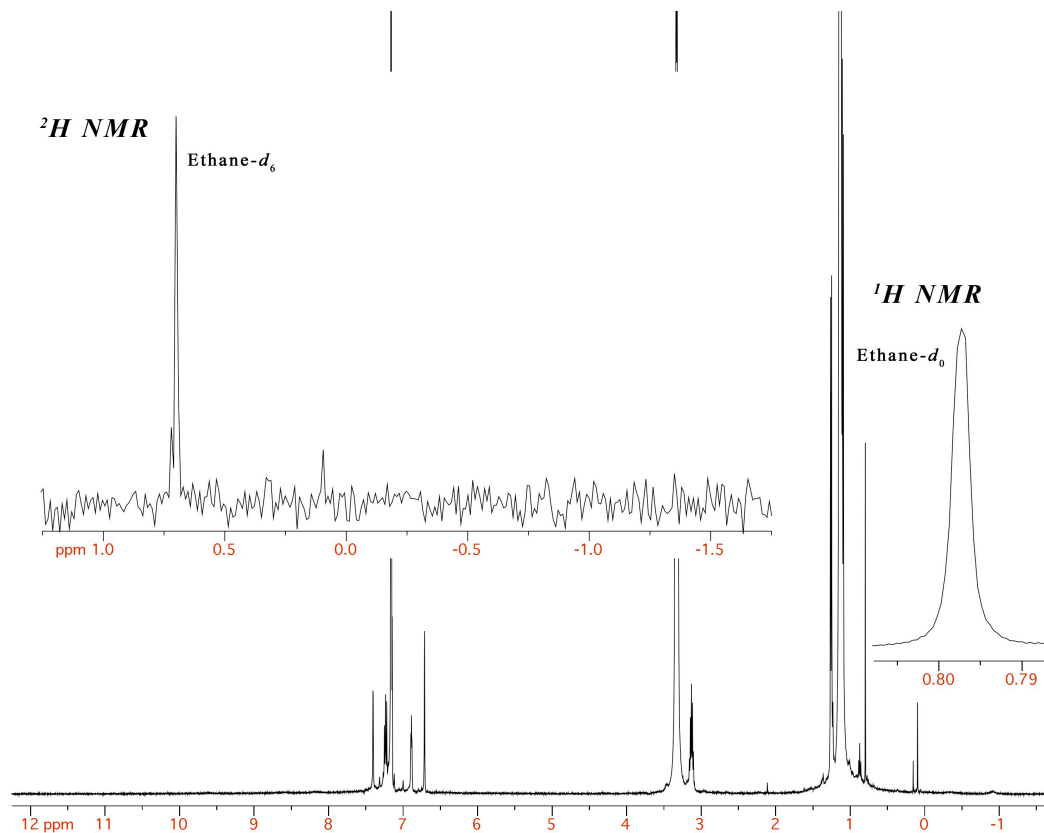


Figure 3.16. Final ^1H and ^2H NMR (inset) spectra resulting from the mixture of $(i^{\text{Pr}}\text{CNC})\text{Fe}(\text{CH}_3)_2(\text{N}_2)$ and $(i^{\text{Pr}}\text{CNC})\text{Fe}(\text{CD}_3)_2(\text{N}_2)$.

broad singlets corresponding to ethane- d_3 and ethane- d_6 were observed at 0.72 and 0.70 ppm, respectively, in the ^2H NMR spectrum.

The mechanism proposed in **Figure 3.18** is favored and accounts for all of the experimental observations: lability of the dinitrogen ligand and carbon-carbon coupling from a single iron center. Unfortunately, mechanism C could not be ruled out by the crossover experiments. Several questions arise from this proposed mechanism: Why is reductive elimination not observed with the bis(neosilyl) and ditolyl analogs? What is so special about the pyridine di(carbene) ligand framework as compared to other tridentate frameworks that two-electron chemistry is observed?

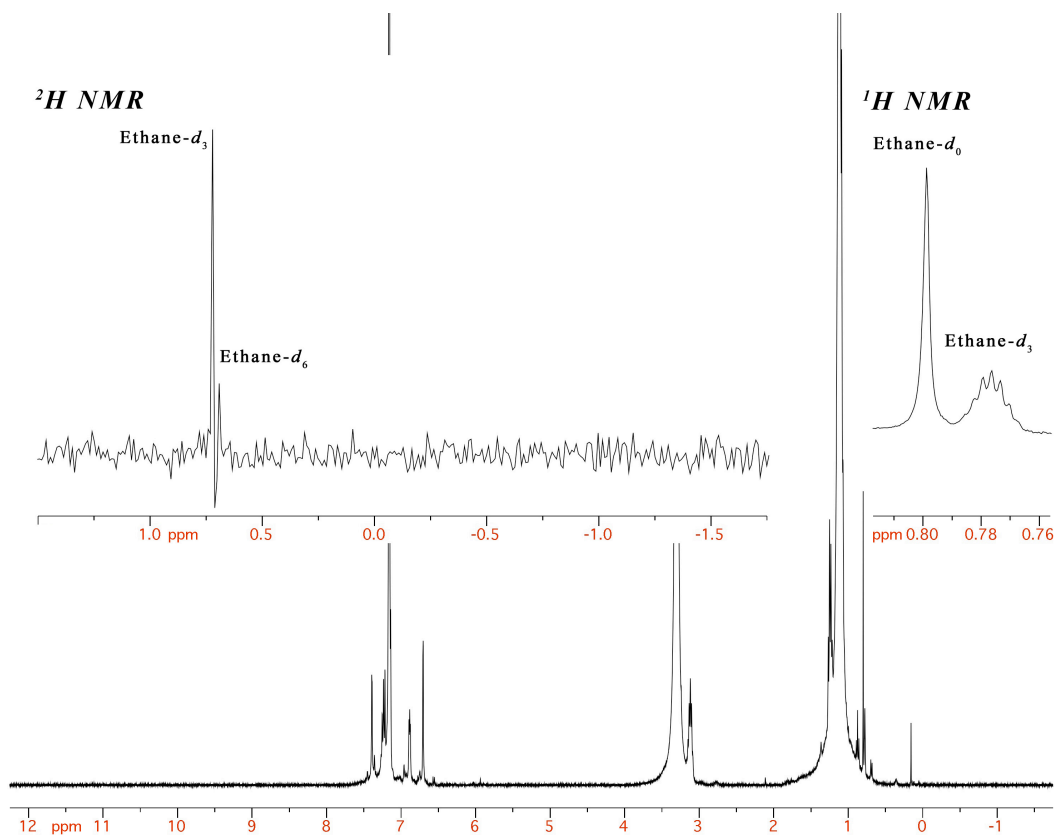


Figure 3.17. Final ^1H and ^2H NMR spectra resulting from the addition of a 1:1 mixture of CH_3Li and $\text{CD}_3\text{Li}\cdot\text{LiI}$ to $(i^{\text{Pr}}\text{CNC})\text{FeBr}_2$.

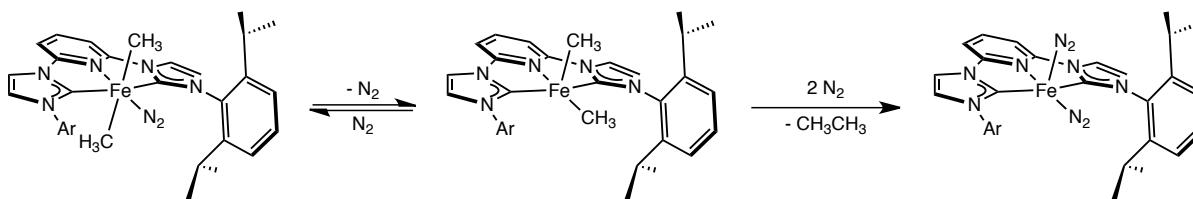


Figure 3.18. Favored mechanism of reductive elimination for $(i^{\text{Pr}}\text{CNC})\text{Fe}(\text{CH}_3)_2(\text{N}_2)$.

The origin of the stability of $(i^{\text{Pr}}\text{CNC})\text{Fe}(\text{CH}_2\text{Si}(\text{CH}_3)_3)_2(\text{N}_2)$ is unlikely due to thermodynamics, as metal–neosilyl bond strengths are slightly weaker than metal–methyl bonds.⁴³ The observed stability is instead attributed to sterics. Although the dinitrogen ligand has been demonstrated to be labile, the steric environment imparted by the 2,6-diisopropyl aryl substituents with respect to the bulky trimethylsilyl groups likely results in a high

thermodynamic barrier for the *cis-trans* isomerization of the alkyl substituents required for intramolecular reductive elimination. The use of less sterically demanding aryl substituents (i.e. 2,6-dimethyl) might allow for a facile and observable reductive elimination.

The stability of the (*i*PrCNC)Fe(C₆H₄CH₃)₂(N₂) complex on the other hand, is likely due to ground state effects. Metal-aryl bonds are notably stronger than their metal-alkyl counterparts due to a greater degree of *s*-orbital character in their hybridization as well as the potential for metal ligand backbonding through the unhybridized *p*-orbital.^{43,44} Investigations by Hartwig and coworkers regarding the reductive elimination of bis(aryl) platinum complexes have demonstrated that reductive elimination occurs more rapidly when the aryl ligands contain electron-donating substituents, or when the two aryl groups are electronically dissimilar.⁴⁵ Thus, the use of more electron-donating aryl Grignards might allow for a facile aryl-aryl reductive elimination.

In his initial report, Bernskoetter hypothesized that the observed mechanistic commonalities between *cis,mer*-(PMe₃)₃Co(CH₃)₂I reductive elimination and those of precious metals was due to the strong-field ligands supporting the metal.³¹ Our investigation into the reactivity of pyridine di(carbene) iron dialkyl dinitrogen complexes agrees with this assertion. Despite the *trans*-arrangement of the alkyl substituents, the pyridine di(carbene) iron dimethyl dinitrogen complex is significantly less thermally stable than the iron bis(phosphine) dicarbonyl dimethyl complex. This is likely attributed to the lability of the dinitrogen moiety as compared to PMe₃ or CO, which readily results in formation of a reactive 16-electron intermediate.

3.5 Conclusions

The synthesis and characterization of three pyridine di(carbene) iron dialkyl and diaryl dinitrogen complexes has been achieved by addition of two equivalents of the appropriate organolithium reagent to the ferrous iron dibromide precursor. Spectroscopic techniques, including NMR and Mößbauer spectroscopies, suggested that these complexes possessed similar, strongly covalent, $S = 0$ ground states. X-ray diffraction studies revealed that all complexes adopt similar molecular geometries in the solid state. However, divergent chemical reactivity for the iron alkyls was observed and is attributed to a mixture of steric and ground state effects. The iron bis(neosilyl) and di(tolyl) dinitrogen compounds were established to be thermally stable at 23 °C under an atmosphere of dinitrogen, whereas the iron dimethyl dinitrogen compound underwent extrusion of ethane to yield the formally iron(0) bis(dinitrogen) compound, $(iPrCNC)Fe(N_2)_2$. ^{15}N NMR spectroscopy and reactions with carbon monoxide, demonstrated the lability of the dinitrogen moiety, and also resulted in divergent behavior. For $(iPrCNC)Fe(CH_2Si(CH_3)_3)_2(N_2)$, ligand substitution took place, furnishing the CO adduct, $(iPrCNC)Fe(CH_2Si(CH_3)_3)_2(CO)$. Reaction with the dimethyl complex yielded the dicarbonyl complex, $(iPrCNC)Fe(CO)_2$. The fate of the methyl groups has not yet been identified.

Three potential mechanisms for formal C–C bond reductive elimination were identified and isotopic labeling experiments suggested that ethane loss occurred by a concerted intramolecular reductive elimination mechanism. The possibility of a tightly caged radical or a mechanism involving α -hydride elimination were not could not be discounted. Loss of dinitrogen, as implicated by ^{15}N NMR and the reactivity of the iron dialkyl dinitrogen complexes with carbon monoxide, yields a reactive, 16-electron intermediate species, $(iPrCNC)Fe(R)_2$. Steric

interactions between the bulky 2,6-diisopropyl aryl substituents and the iron alkyl groups are believed to dictate the reactivity of this intermediate. However, these findings suggest that methylation of the iron dibromide, (*i*PrCNC)FeBr₂ does not result in methyl-carbene elimination, as was postulated by Gibson and coworkers.²³

This work illustrates that two-electron transformations can be achieved using iron, a first-row transition metal, when strong field donors are used in conjunction with labile, small-molecules. Additionally, this work also demonstrates the ability of the pyridine di(carbene) ligand framework to stabilize iron in a low oxidation state. This has important mechanistic implications for the reactivity of other pyridine di(carbene) iron complexes as well as catalysis.

3.6 *Experimental*

All air- and moisture-sensitive manipulations were carried out using standard vacuum line, Schlenk, and cannula techniques or in an MBraun inert atmosphere dry box containing an atmosphere of purified nitrogen. Solvents for air- and moisture-sensitive manipulations were initially dried and deoxygenated using literature procedures.⁴⁶ Benzene-*d*₆ was purchased from Cambridge Isotope Laboratories and dried over 4 Å molecular sieves. (*i*PrCNC)FeBr₂⁴⁷ and 4-tolylithium⁴⁸ were prepared according to literature procedures.

¹H NMR spectra were recorded on Varian Mercury 300, Inova 400, 500, and 600 spectrometers operating at 299.76, 399.78, 500.62, and 599.78 MHz, respectively. ¹³C NMR spectra were recorded on an Inova 500 spectrometer operating at 125.893 MHz. All ¹H and ¹³C NMR chemical shifts are reported relative to SiMe₄ using the ¹H (residual) and ¹³C chemical shifts of the solvent as a secondary standard. For diamagnetic complexes, many assignments

were made based on COSY and HSQC NMR experiments. Infrared spectra were collected on a Thermo Nicolet spectrometer. Elemental analyses were performed at Robertson Microlit Laboratories, Inc., in Ledgewood, NJ.

Single crystals suitable for X-ray diffraction were coated with polyisobutylene oil in a drybox, transferred to a nylon loop and then quickly transferred to the goniometer head. Data for $(i\text{PrCNC})\text{Fe}(\text{CH}_3)_2(\text{N}_2) [(\text{Et}_2\text{O})_4(\text{LiBr})_2]$ was collected using a Bruker X8 APEX2 diffractometer equipped with a molybdenum X-ray tube ($\lambda = 0.71073 \text{ \AA}$). The space group was identified and the data were processed using the Bruker SAINT+ program and corrected for absorption using SADABS. The structures were solved using direct methods (SHELXS) completed by subsequent Fourier synthesis and refined by full-matrix least-squares procedures. A Bruker APEX2 Duo diffractometer equipped with molybdenum and copper X-ray tubes ($\lambda = 0.71073$ and 1.54178 \AA , respectively) was used to collect data for $(i\text{PrCNC})\text{Fe}(\text{CH}_2\text{Si}(\text{CH}_3)_3)_2(\text{N}_2)$ (Cu source), $(i\text{PrCNC})\text{Fe}(\text{C}_6\text{H}_4\text{CH}_3)_2(\text{N}_2)$ (Cu source), and $(i\text{PrCNC})\text{Fe}(\text{CH}_2\text{Si}(\text{CH}_3)_3)_2(\text{CO})$ (Cu source). The space group was identified and the data were processed using the Bruker SAINT+ program and corrected for absorption using SADABS. The structures were solved using direct methods (SIR92) completed by subsequent Fourier synthesis and refined by full-matrix least-squares procedures.

^{57}Fe Mößbauer spectra were recorded on a SEE Co. Mößbauer spectrometer (MS4) at 80 K in constant acceleration mode. $^{57}\text{Co}/\text{Rh}$ was used as the radiation source. WMOSS software was used for the quantitative evaluation of the spectral parameters (least squares fitting to Lorentzian peaks). The temperature of the samples was controlled by a Janis Research Co.

CCS-850 He/N₂ cryostat within an accuracy of ± 1 K. Isomer shifts were determined relative to α -iron at 298 K.

Preparation of (ⁱPrCNC)Fe(CH₂Si(CH₃)₃)₂(N₂). A 20 mL scintillation vial was charged with 0.500 g (0.669 mmol) of (ⁱPrCNC)FeBr₂ and approximately 5 mL of diethyl ether. The slurry was stored at -35 °C for 15 minutes before a chilled solution (-35 °C, 15 min) of LiCH₂Si(CH₃)₃ (0.125 g, 1.33 mmol) in approximately 10 mL diethyl ether was added dropwise with rapid stirring. The solution darkened to red-purple in minutes, and was stirred for 3 hours. The solution was then concentrated to dryness. The residue was extracted with pentane and filtered through a pad of Celite to give a purple solution. Removal of the solvent in vacuo gave a red-brown solid that became intensely purple upon re-exposure to dinitrogen. Recrystallization from pentane gave 0.325 g (61%) of a purple solid identified as (ⁱPrCNC)Fe(N₂)(CH₂Si(CH₃)₃)₂. ¹H NMR (benzene-*d*₆, 22 °C): δ = -1.13 (s, 4H, CH₂Si(CH₃)₃), -0.49 (s, 18H, CH₂Si(CH₃)₃), 1.09 (d, 7 Hz, 12H, CH(CH₃)₂), 1.40 (d, 7 Hz, 12H, CH(CH₃)₂), 3.28 (sep, 7 Hz, 4H, CH(CH₃)₂), 6.60 (d, 8 Hz, 2H, *m*-pyr), 6.74 (d, 2 Hz, 2H, *imidazolylidene backbone*), 6.99 (t, 8 Hz, 1H, *p*-pyr), 7.11 (d, 8 Hz, 4H, *m*-aryl), 7.17 (t, 8 Hz, 2H, *p*-aryl), 7.20 (d, 2 Hz, 2H, *imidazolylidene backbone*). ¹³C NMR {¹H} (benzene-*d*₆, 22 °C): δ = 2.8 (CH₂Si(CH₃)₃), 23.0 (CH(CH₃)₂), 27.1 (CH(CH₃)₂), 28.6 (CH(CH₃)₂), 99.9 (*m*-pyr), 112.7 (*imidazolylidene backbone*), 124.0 (*m*-aryl), 126.4 (*p*-pyr or *imidazolylidene backbone*), 126.5 (*p*-pyr or *imidazolylidene backbone*), 129.9 (*p*-aryl), 136.6 (*aryl*), 147.2 (*aryl*), 153.5 (*o*-pyr), 223.4 (*carbene*), CH₂Si(CH₃)₃ resonance not located. IR (toluene): $\nu_{\text{NN}} = 2133 \text{ cm}^{-1}$.

Characterization of (*i*PrCNC)Fe(4-CH₃-C₆H₄)₂(N₂). The compound was prepared in a similar manner to (*i*PrCNC)Fe(CH₂Si(CH₃)₃)₂(N₂) with 0.30 g (0.40 mmol) of (*i*PrCNC)FeBr₂ and 0.078 g (0.80 mmol) of tolyllithium. Both mixtures were frozen (-115 °C), and addition took place immediately upon thawing. The reaction was stirred for 8 hours, although a color change to purple took place after approximately three hours. Toluene was used to extract the residue following removal of solvent from the reaction mixture. The final product was washed several times with pentane to remove 4,4'-dimethyl-1,1'-biphenyl. This procedure yielded 0.062 g of a solid identified as (*i*PrCNC)Fe(4-CH₃-C₆H₄)₂(N₂). ¹H NMR (benzene-*d*₆, 22 °C): δ = 0.79 (d, 7 Hz, 12H, CH(CH₃)₂), 1.18 (d, 7 Hz, 12H, CH(CH₃)₂), 2.18 (s, 6H, C₄H₆CH₃), 2.80 (sep, 7 Hz, 4H, CH(CH₃)₂), 6.46 (d, 2 Hz, 2H, *imidazolylidene backbone*), 6.51 (d, 8 Hz, 2H, *m-pyr*), 6.67 (d, 7 Hz, 4H, C₆H₄CH₃), 6.77–6.82 (m, 6H, C₆H₄CH₃ and *imidazolylidene backbone*), 7.05 (t, 8 Hz, 1H, *p-pyr*), 7.16–7.22 (m, 6H, *m-* and *o-aryl*). ¹³C NMR (benzene-*d*₆, 22 °C): δ = 21.1 (C₄H₆CH₃), 23.3 (CH(CH₃)₂), 26.6 (CH(CH₃)₂), 28.2 (CH(CH₃)₂), 102.0 (*m-pyr*), 113.1 (*imidazolylidene backbone*), 123.9 (*aryl*), 127.3 (C₆H₄CH₃), 127.7 (C₆H₄CH₃), 129.9, 132.3, 136.8 (*aryl*), 138.2 (C₆H₄CH₃), 147.3 (*aryl*), 152.3, 164.6 (C₆H₄CH₃), 221.8 (*carbene*), one peak not located. IR (toluene): ν_{NN} = 2118 cm⁻¹.

Characterization of (*i*PrCNC)Fe(CH₃)₂(N₂). This compound was prepared *in situ* in a similar manner to (*i*PrCNC)Fe(4-CH₃-C₆H₄)₂(N₂) using 0.10 g (0.13 mmol) (*i*PrCNC)FeBr₂ and 0.128 g (0.26 mmol) of a 1.6 M solution of methyllithium in diethyl ether. The reaction mixture turned intensely purple shortly after addition of methyllithium. Once the color change had occurred, the reaction mixture was stirred for 10 minutes and an aliquot was taken and concentrated *in vacuo*,

yielding a sample that was suitably pure for ^1H NMR analysis. ^1H NMR (benzene- d_6 , 22 °C): δ = -1.10 (s, 6H, CH_3), 1.09 (d, 7 Hz, 12H, $\text{CH}(\text{CH}_3)_2$), 1.39 (d, 7 Hz, 12H, $\text{CH}(\text{CH}_3)_2$), 3.31 (s, 7 Hz, 4H, $\text{CH}(\text{CH}_3)_2$), 6.39 (d, 8 Hz, 2H, *m*-pyr), 6.58 (d, 2 Hz, 2H, *imidazolylidene backbone*), 6.87 (t, 8 Hz, 1H, *p*-pyr), 7.05 (d, 2 Hz, 2H, *imidazolylidene backbone*), 7.09–7.26 (m, 6H, *m*- and *p*-aryl). IR (KBr): $\nu_{\text{NN}} = 2094 \text{ cm}^{-1}$

Preparation of $(i\text{PrCNC})\text{Fe}(\text{CH}_2\text{Si}(\text{CH}_3)_3)_2(\text{CO})$. A thick-walled vessel was charged with a solution of $(i\text{PrCNC})\text{Fe}(\text{CH}_2\text{Si}(\text{CH}_3)_3)_2(\text{N}_2)$ (0.125 g, 0.158 mmol) in approximately 15 mL diethyl ether. The vessel was submerged in liquid nitrogen, the headspace was evacuated, and 1 atmosphere of CO was introduced. Upon thawing, a rapid color change from purple to intense pink occurred. The reaction was stirred at 23 °C for 30 minutes, and filtered through Celite. Removal of solvent and recrystallization of the burgundy residue from a pentane-diethyl ether mixture yielded 0.101 g (81%) of a solid identified as $(i\text{PrCNC})\text{Fe}(\text{CH}_2\text{Si}(\text{CH}_3)_2)(\text{CO})$. Anal. Calcd for $\text{C}_{44}\text{H}_{63}\text{FeN}_5\text{OSi}_2$: C, 66.89; H, 8.04; N, 8.86. Found; C, 66.74; H, 7.97; N, 8.69. ^1H NMR (benzene- d_6 , 22 °C): δ = -1.43 (s, 4H, $\text{CH}_2\text{Si}(\text{CH}_3)_3$), -0.49 (s, 18 H, $\text{CH}_2\text{Si}(\text{CH}_3)_3$), 1.05 (d, 7 Hz, 12H, $\text{CH}(\text{CH}_3)_2$), 1.39 (d, 7 Hz, 12H, $\text{CH}(\text{CH}_3)_2$), 3.11 (spt, 7 Hz, 4H, $\text{CH}(\text{CH}_3)_2$), 6.63–6.67 (m, 4H, *m*-pyr and *imidazolylidene backbone*), 7.09–7.15 (m, 7H, *m*-aryl, *imidazolylidene backbone* and *p*-pyr), 7.22 (t, 8 Hz, 2H, *p*-aryl). ^{13}C NMR $\{^1\text{H}\}$ (benzene- d_6 , 22 °C): δ = 2.9 ($\text{CH}_2\text{Si}(\text{CH}_3)_3$), 23.0 ($\text{CH}(\text{CH}_3)_2$), 27.0 ($\text{CH}(\text{CH}_3)_2$), 28.5 ($\text{CH}(\text{CH}_3)_2$), 100.4 (*m*-pyr), 112.7 (*imidazolylidene backbone*), 124.1 (*m*-aryl), 126.4 (*imidazolylidene backbone*), 130.0 (*p*-aryl), 136.7 (*aryl*), 147.0 (*aryl*), 151.6 (*o*-pyr), 227.6 (*carbene*), $\text{CH}_2\text{Si}(\text{CH}_3)_3$ resonance not located. IR (toluene): $\nu_{\text{CO}} = 1919 \text{ cm}^{-1}$.

REFERENCES

- ¹ Collman, J. P.; Hegedus, L. S.; Norton, J. R.; Finke, R. G. Survey of Organotransition-Metal Complexes According to Ligand. *Principles and Applications of Organotransition Metal Chemistry*; University Science Books: California, 1987; pp 57–234.
- ² Spessard, G. O.; Miessler, G. L. *Organometallic Chemistry*; Prentice Hall: Upper Saddle River, NJ, 1996; p 116.
- ³ Jana, R.; Pathak, T. P.; Sigman, M. S. *Chem. Rev.* **2011**, *111*, 1417–1492.
- ⁴ For recent reviews on iron catalysis see: (a) Bolm, C.; Legros, J.; Paith, J. L.; Zani, L. *Chem. Rev.* **2004**, *104*, 6217–6254. (b) Correa, A.; Mancheño, O. G.; Bolm, C. *Chem. Soc. Rev.* **2008**, *37*, 1108–1117. (c) Sherry, B. D.; Fürstner, A.; *Acc. Chem. Res.* **2008**, *41*, 1500–1511. (d) Bauer, E. B. *Curr. Org. Chem.* **2008**, *12*, 1341–1369. (e) Gaillard, S.; Renaud, J. L. *ChemSusChem.* **2008**, *1*, 505–509. (f) Sarhan, A. A. O.; Bolm, C. *Chem. Soc. Rev.* **2009**, *38*, 2730–2744. (g) Morris, R. H. *Chem. Soc. Rev.* **2009**, *38*, 2282–2291. (h) Czaplik, W. M.; Mayer, M.; Cvengros, J.; von Wangelin, J. *ChemSusChem.* **2009**, *2*, 396–417. (i) Liu, L. X. *Curr. Org. Chem.* **2010**, *14*, 1099. (j) Nakazawa, H.; Itazaki, M. *Top. Organomet. Chem.* **2011**, *33*, 27–81. (k) Junge, K.; Schröder, K.; Beller, M. *Chem. Commun.* **2011** *47*, 4849–4859.
- ⁵ Knorr, M. Mononuclear Iron Compounds with η^1 -Hydrocarbon Ligands. In *Comprehensive Organometallic Chemistry III*; Crabtree, R. H.; Mingos, D. M. P., Eds.; Elsevier: 2007; Vol. 8; pp 77–125.
- ⁶ (a) Small, B. M.; Brookhart, M. *J. Am. Chem. Soc.* **1998**, *120*, 7143–7144. (b) Small, B. L.; Brookhart, M.; Bennett, A. M. A. *J. Am. Chem. Soc.* **1998**, *120*, 4049–4050.
- ⁷ Britovsek, G. J. P.; Gibson, V. C.; Kimberley, B. S.; Maddox, S. J.; Solan, G. A.; White, A. J. P.; Williams, D. J. *Chem. Commun.* **1998**, 849–850.
- ⁸ Britovsek, G. J. P.; Bruce, M.; Gibson, V. C.; Kimberley, B. S.; Maddox, P. J.; Mastroianni, S.; McTavish, S. J.; Redshaw, C.; Solan, G. A.; Strömberg, S.; White, A. J. P.; Williams, D. J. *J. Am. Chem. Soc.* **1999**, *121*, 8728–8740.
- ⁹ For studies regarding the mechanism and nature of the active species, see the following and references therein: (a) Bryliakov, K. P.; Semikolvenova, N. V.; Zudin, V. N.; Zakharov, V. A.; Talsi, E. P. *Organometallics* **2004**, *23*, 5375–5378. (b) Barabanov, A. A.; Bukatov, G. D.; Zakharov, V. A.; Semikolvenova, N. V.; Mikenas, T. B.; Echevskaja, L. G.; Matsko, M. A. *Macromol. Chem. Phys.* **2006**, *207*, 1368–1375. (c) Kissin, Y. V.; Qian, C.; Xie, G.; Chen, Y. J. *Polym. Sci., Part A: Polym. Chem.* **2006**, *44*, 6159–6170. (d) Britovsek, G. J. P.; Clentsmith, G. K. B.; Gibson, V. C.; Goodgame, D. M. L.; McTavish, S. J.; Pankhurst, Q. A. *Catal. Commun.* **2002**, *3*, 207–2011. (e) Cruz, V. L.; Ramos, J.; Martinez-Salazar, J.; Gutierrez-Oliva, S.; Toro-Labbe, A. *Organometallics* **2009**, *28*, 5889–5895. (f) Bryliakov, K. P.; Talsi, E. P.; Semikolvenova, N. V.; Zakharov, V. A. *Organometallics* **2009**, *28*, 3225–3232.

- ¹⁰ Bouwkamp, M.; Lobkovsky, E.; Chirik, P. J. *J. Am. Chem. Soc.* **2005**, *127*, 9660–9661.
- ¹¹ Tondreau, A. M.; Milsmann, C.; Patrick, A. D.; Hoyt, H. M.; Lobkovsky, E.; Wieghardt, K.; Chirik, P. J. *J. Am. Chem. Soc.* **2010**, *132*, 15046–15059.
- ¹² Atienza, C. C. H.; Milsmann, C.; Lobkovsky, E.; Chirik, P. J. *Angew. Chem. Int. Ed.* **2011**, *50*, 8143–8147.
- ¹³ Bouwkamp, M. W.; Bart, S. C.; Hawrelak, E. J.; Trovitch, R. J.; Lobkovsky, E.; Chirik, P. J. *Chem. Comm.* **2005**, 3406–3408.
- ¹⁴ Fernández, I.; Trovitch, R. J.; Lobkovsky, E.; Chirik, P. J. *Organometallics* **2008**, *27*, 109–118.
- ¹⁵ Tondreau, A. M.; Lobkovsky, E.; Chirik, P. J. *Org. Lett.* **2008**, *10*, 2789–2792.
- ¹⁶ Tondreau, A. M.; Darmon, J. M.; Wile, B. M.; Floyd, S. K.; Lobkovsky, E.; Chirik, P. J. *Organometallics* **2009**, *28*, 3928–3940.
- ¹⁷ Tondreau, A. M. Ph.D. Thesis, Cornell University, Ithaca, NY, 2011.
- ¹⁸ Calculations for (terpy)Fe(CH₂Si(CH₃)₃)₂ and (S,S)-(RBox)Fe(CH₂Si(CH₃)₃)₂ are presented in Appendix B.2.
- ¹⁹ Calculations for (terpy)Fe(CH₂Si(CH₃)₃)₂ and (S,S)-(RBox)Fe(CH₂Si(CH₃)₃)₂ are presented in Appendix B.2.
- ²⁰ McGuinness, D. S.; Gibson, V. C.; Steed, J. W. *Organometallics* **2004**, *23*, 6288–6292.
- ²¹ Danopoulos, A. A.; Wright, J. A.; Motherwell, W. B. *Chem. Commun.* **2005**, 784–786.
- ²² Pugh, D.; Wells, N. J.; Evans, D. J.; Danopoulos, A. A. *Dalton Trans.* **2009**, 7189–7195.
- ²³ McGuinness, D. S.; Gibson, V. C.; Wass, D. F.; Steed, J. W. *J. Am. Chem. Soc.* **2003**, *125*, 12716–12717.
- ²⁴ McGuinness, D. S.; Saendig, N.; Yates, B. F.; Cavell, K. J. *J. Am. Chem. Soc.* **2001**, *123*, 4029–4040.
- ²⁵ Bedford, R. B.; Betham, M.; Bruce, D. W.; Danopoulos, A. A.; Frost, R. M.; Hird, M. *J. Org. Chem.* **2006**, *71*, 1104–1110.
- ²⁶ Girolami, G. S.; Wilkinson, G.; Galas, A. M. R.; Thornton-Pett, M.; Hursthouse, M. B. *Dalton Trans.* **1985**, 1339–1348.
- ²⁷ Allen, O. R.; Dalgarno, S. J.; Field, L. D.; Jensen, P.; Turnbull, A. J.; Willis, A. C. *Organometallics* **2008**, *27*, 2092–2098.
- ²⁸ Venturi, C.; Bellachioma, G.; Cardaci, G.; Macchioni, A.; Zuccaccia, C. *Inorg. Chimica Acta* **2005**, *358*, 3815–3823.

- ²⁹ Trovitch, R. J.; Lobkovsky, E.; Chirik, P. J. *Inorg. Chem.* **2006**, *45*, 7252–7260.
- ³⁰ Neese, F. *Inorg. Chim. Acta.* **2002**, *337*, 181–192.
- ³¹ Xu, H.; Bernskoetter, W. H. *J. Am. Chem. Soc.* **2011**, *133*, 14956–14959.
- ³² Hartwig, J. F. *Inorg Chem* **2007**, *46*, 1936–1947. and references therein.
- ³³ (a) Crumpton, D. M.; Goldberg, K. I. *J. Am. Chem. Soc.* **2000**, *122*, 962–963. (b) Procelewska, J.; Zahl, A.; Liehr, G.; van Eldik, R.; Smythe, N. A.; Williams, B. S.; Goldberg, K. I. *Inorg. Chem.* **2005**, *44*, 7732–7742.
- ³⁴ (a) DiCosimo, R.; Whitesides, G. M. *J. Am. Chem. Soc.* **1982**, *104*, 3601–3607. (b) Komiya, S.; Albright, T. A.; Hoffmann, R.; Kochi, J. K. *J. Am. Chem. Soc.* **1976**, *98*, 7255–7265. (c) Kuch, P. L.; Tobias, R. S. *J. Organomet. Chem.* **1976**, *122*, 429–446.
- ³⁵ Gillie, A.; Stille, J. K. *J. Am. Chem. Soc.* **1980**, *102*, 4933–4941.
- ³⁶ (a) Hager, E.; Sivaramakrishna, A.; Clayton, H. S.; Mogorosi, M. M.; Moss, J. R. *Coord. Chem. Rev.* **2008**, *252*, 1668–1688. (b) Khusnutdinova, J. R.; Rath, N. P.; Mirica, L. M. *J. Am. Chem. Soc.* **2010**, *132*, 7303–7305.
- ³⁷ (a) Braden, D. A.; Parrack, E. E.; Tyler, D. R. *Coord. Chem. Rev.* **2001**, *211*, 279–294. (b) Hlavica, P. *Eur. J. Biochem.* **2004**, *271*, 4335–4360.
- ³⁸ (a) Hill, G. S.; Puddephatt, R. J. *Organometallics* **1998**, *17*, 1478–1486. (b) Espinet, P.; Echavarren, A. M. *Angew. Chem., Int. Ed.* **2004**, *43*, 4704–4734. (c) Gatard, S.; Celeligil-Cetin, R.; Guo, C.; Foxman, B. M.; Ozerov, O. V. *J. Am. Chem. Soc.* **2006**, *128*, 2808–2809. (d) Ghosh, R.; Emge, T. J.; Krogh-Jespersen, K.; Goldman, A. S. *J. Am. Chem. Soc.* **2008**, *130*, 11317–11327. (e) Racowski, J. M.; Dick, A. R.; Sanford, M. S. *J. Am. Chem. Soc.* **2009**, *131*, 10974–10984.
- ³⁹ (a) Byers, P. K.; Canty, A. J.; Crespo, M.; Puddephatt, R. J.; Scott, J. D. *Organometallics* **1988**, *7*, 1363–1367. (b) de Graff, W.; Boersma, J.; Smeets, W. J. J.; Spek, A. L.; van Koten, G. *Organometallics* **1989**, *8*, 2907–2917.
- ⁴⁰ Bart, S. C.; Hawrelak, E. J.; Schmisser, A. K.; Lobkovsky, E.; Chirik, P. J. *Organometallics* **2004**, *23*, 237–246.
- ⁴¹ Schleis, T.; Spaniol, T. P.; Okuda, J.; Heinemann, J.; Mülhaupt, R. *Organomet. Chem.* **1998**, *569*, 159–167.
- ⁴² Bellachioma, G.; Cardaci, G.; Macchioni, A.; Zuccaccia, C. *J. Organometal. Chem.* **2001**, *628*, 255–261.
- ⁴³ (a) Bruno, J. W.; Marks, T. J.; Morss, L. R. *J. Am. Chem. Soc.* **1983**, *105*, 6824–6832. (b) Bennett, J. L.; Vaid, T. P.; Wolecanski, P. T. *Inorg. Chim. Acta* **1998**, *270*, 414–423. (c) Clot, E.; Mégret, C.; Eisenstein, O.; Perutz, R. N. *J. Am. Chem. Soc.* **2006**, *128*, 8350–8357.

- ⁴⁴ (a) Uddin, J.; Morales, C. M.; Maynard, J. H.; Landis, C. R. *Organometallics* **2006**, *25*, 5566–5581. (b) Stoutland, P. O.; Bergman, R. G.; Nolan, S. P.; Hoff, C. D. *Polyhedron* **1988**, *7*, 1429–1440.
- ⁴⁵ Shekhar, S.; Hartwig, J. F. *J. Am. Chem. Soc.* **2004**, *126*, 13016–13027.
- ⁴⁶ Pangborn, A. B.; Giardello, M. A.; Grubbs, R. H.; Rosen, R. K.; Timmers, F. J. *Organometallics* **1996**, *15*, 1518–1520.
- ⁴⁷ Danopoulos, A. A.; Tsoureas, N.; Wright, J. A.; Light, M. E. *Organometallics* **2004**, *23*, 166–168.
- ⁴⁸ Spee, M. P. R.; Boersma, J.; Meijer, M. D.; Slagt, M. Q.; van Koten, G.; Geus, J. W. *J. Org. Chem.* **2001**, *66*, 1647–1656.

CHAPTER 4

SYNTHESIS AND REACTIVITY OF AN ARYL-SUBSTITUTED BIS(PHENYLIMINO)PYRIDINE IRON DINITROGEN COMPOUND

4.1 Abstract

The dimeric pyridine di(imine) iron bis(dinitrogen) complex, $[(^{\text{Me}}\text{BPDI})\text{Fe}(\text{N}_2)]_2(\mu_2\text{-N}_2)$ ($^{\text{Me}}\text{BPDI} = 2,6\text{-}(2,6\text{-Me}_2\text{-C}_6\text{H}_3\text{N}=\text{CPh})_2\text{C}_5\text{H}_3\text{N}$), was prepared by reduction of the corresponding iron dichloride, $(^{\text{Me}}\text{BPDI})\text{FeCl}_2$ in THF using two equivalents of sodium and 5 mol % naphthalene. $[(^{\text{Me}}\text{BPDI})\text{Fe}(\text{N}_2)]_2(\mu_2\text{-N}_2)$ was characterized by a combination of infrared, NMR, and Mößbauer spectroscopies, as well as X-ray crystallography. *In situ* solution infrared and ^1H NMR spectroscopy demonstrated that the bis(dinitrogen) complex was present in solution in equilibrium with the THF adduct, $(^{\text{Me}}\text{BPDI})\text{Fe}(\text{THF})$. $[(^{\text{Me}}\text{BPDI})\text{Fe}(\text{N}_2)]_2(\mu_2\text{-N}_2)$, like the 2,6-diisopropyl aryl-substituted complex, $(^{\text{iPr}}\text{BPDI})\text{Fe}(\text{N}_2)_2$ ($^{\text{iPr}}\text{BPDI} = 2,6\text{-}(2,6\text{-}^{\text{iPr}}_2\text{-C}_6\text{H}_3\text{N}=\text{CPh})_2\text{C}_5\text{H}_3\text{N}$), underwent irreversible η^6 -arene formation. Both phenyl-substituted pyridine di(imine) iron bis(dinitrogen) complexes, $(^{\text{iPr}}\text{BPDI})\text{Fe}(\text{N}_2)_2$ and $[(^{\text{Me}}\text{BPDI})\text{Fe}(\text{N}_2)]_2(\mu_2\text{-N}_2)$ were assayed for the catalytic hydrogenation of ethyl 3,3-dimethylacrylate. $(^{\text{iPr}}\text{BPDI})\text{Fe}(\text{N}_2)_2$ showed no hydrogenation activity under 4 atm of H_2 at 23 °C after 24 hours, while the 2,6-dimethyl analogue, $[(^{\text{Me}}\text{BPDI})\text{Fe}(\text{N}_2)]_2(\mu_2\text{-N}_2)$, exhibited modest activity. Stoichiometric experiments suggested that low hydrogenation activities were due to the affinity of the iron center for coordination of the carbonyl oxygen.

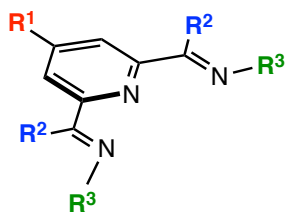
* Reproduced in part with permission from Russel, S. K.; Darmon, J. M.; Lobkovsky, E.; Chirik, P. J. *Inorg. Chem.* **2010**, *49*, 2782–2792. Copyright 2010 American Chemical Society.

4.2 Introduction

Ligand modularity has been an important concept in asymmetric homogenous catalysis.¹ The ability to generate a library of structurally related organic frameworks facilitates the search for appropriate “lock and key” interactions between substrate and catalyst that result in high levels of enantiomeric induction. The role of the ligand under these circumstances is to influence the reactivity and selectivity of the metal. However, a new trend in catalysis has emerged in which the ligand no longer plays a “spectator role,” but actively participates in the electronic structure and therefore the key bond-forming and -breaking events required for turnover.² This class of ligands is defined as “redox-active”.

First prepared in 1973,³ the pyridine di(imine) ligand architecture did not gain popularity until the independent reports of Brookhart⁴ and Gibson^{5,6} regarding the polymerization of ethylene by MAO-activated (MAO = methyl-aluminoxane) aryl-substituted pyridine di(imine) iron and cobalt dihalide complexes. One advantage of the pyridine di(imine) system was the relative ease with which ligand modifications were made, allowing for rapid synthesis of a catalyst library to probe substituent effects (**Figure 4.1**).⁷ Chiral variants have even been described,⁸ and are now being utilized to obtain high enantiomeric excesses for the hydrogenation of olefins.⁹ The pyridine di(imine) scaffold can also readily accept between one and three electrons,¹⁰ and is therefore classified as redox non-innocent.¹¹

In 2004, our laboratory published the synthesis of (*i*PrPDI)Fe(N₂)₂ (*i*PrPDI = 2,6-(2,6-*i*Pr₂-C₆H₃N=CCH₃)₂C₅H₃N) from the reduction of the corresponding iron dihalide, (*i*PrPDI)FeX₂ (X = Cl, Br) using excess sodium amalgam under an atmosphere of dinitrogen.¹² Since this initial report, (*i*PrPDI)Fe(N₂)₂ has demonstrated exceptional activity for the hydrogenation of olefins,¹³



Ease of Substitution:



Figure 4.1. Modularity of the pyridine di(imine) ligand architecture.

intra-,^{14,15} and intermolecular¹⁶ cyclization of unsaturates as well as the regioselective, anti-Markovnikov hydrosilylation of α -olefins with tertiary silanes.¹⁷ In some instances, the activity and selectivity of (*i*PrPDI)Fe(N₂)₂ has surpassed that of precious metal catalysts.¹⁷

Substitution of the backbone position, although more synthetically challenging, provided the second example of a pyridine di(imine) iron bis(dinitrogen) adduct, (*i*PrBPDI)Fe(N₂)₂ ((*i*PrBPDI = 2,6-(2,6-*i*Pr₂-C₆H₃N=CPh)₂C₅H₃N).¹⁸ This electron withdrawing analog of (*i*PrPDI)Fe(N₂)₂ exhibited higher activity for the catalytic hydrogenation of simple, unactivated olefins such as 1-hexene. Unfortunately, this complex also underwent irreversible η^6 -arene formation in solution, thereby reducing the overall hydrogenation activity for more hindered olefins.

Synthesis of these ligands has proven more challenging than the methyl-substituted analogs, as the condensation of anilines with dibenzoylpyridine typically requires harsher reaction conditions.⁷ Preparation of ^{Mes}BPDI, as reported by Esteruelas *et al.*, required activation of dibenzoylpyridine by complexation with anhydrous nickel dichloride prior to condensation of the aniline in acetic acid.¹⁹ Demetallation to give the free ligand was accomplished using aminopropyl silica gel in dichloromethane. This method was adapted by Archer *et al.* for the synthesis of (*i*PrBPDI)FeCl₂ in a one-pot procedure using dibenzoylpyridine, 2,6-

diisopropylaniline and iron dichloride.²⁰ Alternatively, ⁱPrBPDI can be prepared by an acid-catalyzed condensation using toluene and a Dean-stark trap.²¹

Attempts to prepare alkyl-substituted analogs (APDI; APDI = 2,6-(RN=CCH₃)₂C₅H₃N; R = Cy, ⁱPr, *cis*-myrtanyl), or aryl-substituted pyridine di(imine) derivatives in which the 2,6-substituents were smaller than ⁱPr groups (*i.e.* Et, Me, etc.), resulted in the formation of catalytically inactive bis(chelate) complexes (**Figure 4.2**).²² Spectroscopic and computational investigations established that these species were high-spin Fe^{II} (*S* = 2) complexes antiferromagnetically coupled to two pyridine di(imine) radical anions (*S* = 1/2). The differences in reduction behavior were attributed to the degree of steric protection about the iron-center. In 2010, our laboratory achieved reduction of the iron dihalide species to yield the corresponding iron dinitrogen compounds as dimeric species using an alternative reduction method. These complexes demonstrated increased activity for the hydrogenation of ethyl 3,3-dimethylacrylate.

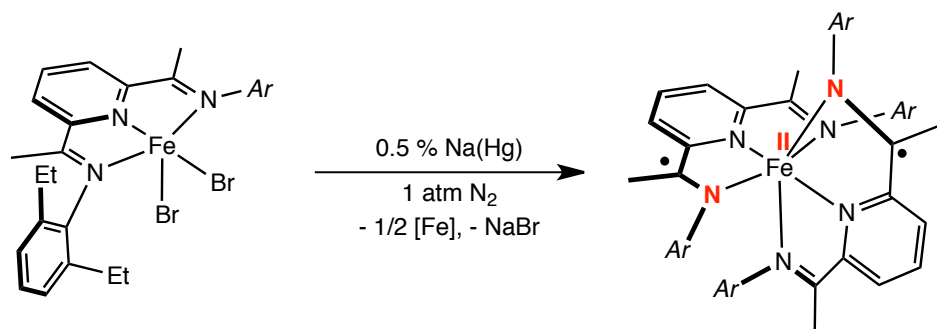


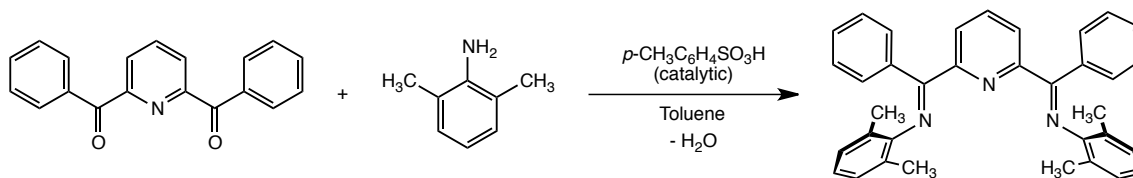
Figure 4.2. Sodium amalgam reduction of pyridine di(imine) iron dihalides with less steric protection.

Presented here is the reduction of (^{Me}BPDI)FeCl₂ using this methodology. The activity of the resulting dinitrogen compound, and that of 2,6-diisopropyl variant, (ⁱPrBPDI)Fe(N₂)₂, was evaluated for the hydrogenation of ethyl 3,3-dimethylacrylate, and exhibited diminished activities relative to (ⁱPrPDI)Fe(N₂)₂ due to a greater affinity for carbonyl coordination.

4.3 Characterization of the Reduction Products of $(^{\text{Me}}\text{BPDI})\text{FeCl}_2$

The high activity of $[(^{\text{Me}}\text{PDI})\text{Fe}(\text{N}_2)]_2(\mu_2\text{-N}_2)$ towards the hydrogenation of ethyl 3,3-dimethylacrylate, inspired investigation into the reduction chemistry of the $^{\text{Me}}\text{BPDI}$ iron dihalide analog. The early synthesis of $^{\text{Me}}\text{BPDI}$ ($^{\text{Me}}\text{BPDI} = 2,6\text{-}(2,6\text{-Me}_2\text{-C}_6\text{H}_3\text{N}=\text{CPh})_2\text{C}_5\text{H}_3\text{N}$) was accomplished by Schmidt *et al.*²³ from condensation of two equivalents of aniline with dibenzoyl pyridine. This reaction was carried out in refluxing toluene with catalytic *para*-toluenesulfonic acid. Our laboratory has exploited the method of Love *et al.*²⁴ for the preparation of sterically hindered imines. This procedure was applied to the synthesis of $^{\text{R}}\text{BPDI}$ (R = *i*Pr, Et, and Me) (**Figure 4.3**). Preparation of the corresponding iron dihalide was achieved by stirring a THF solution of ligand with one equivalent of FeCl_2 for 12 hours. Removal of solvent and trituration with pentane yielded $(^{\text{Me}}\text{BPDI})\text{FeCl}_2$ as a blue-green solid.

Schmidt's Method:



Currently Employed Method:

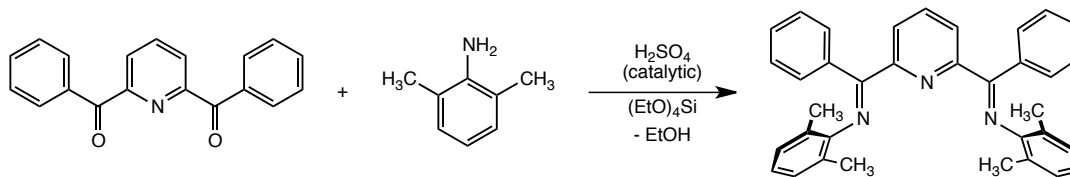


Figure 4.3. Synthetic methods for the preparation of $^{\text{Me}}\text{BPDI}$.

One concern regarding the reduction of the phenyl-substituted pyridine di(imine) iron dihalide complex was formation of η^6 -aryl and η^6 -phenyl complexes. Higher pressures of dinitrogen were required to suppress this pathway during the sodium amalgam reduction of the 2,6-diisopropyl aryl-substituted analog.¹⁸ This contrasts the behavior of $(^{\text{iPr}}\text{PDI})\text{FeCl}_2$, which was

ether, and a significant volume (approximately 75–100 mL) was required to extract $[(^{\text{Me}}\text{BPDI})\text{Fe}(\text{N}_2)]_2(\mu_2\text{-N}_2)$ from the residue. Reductions ran under these conditions—0.24 M [Fe] for approximately one hour—also prevented formation of significant amounts of η^6 -arene species.

Crystals of $[(^{\text{Me}}\text{BPDI})\text{Fe}(\text{N}_2)]_2(\mu_2\text{-N}_2)$ suitable for X-ray diffraction were grown from a concentrated diethyl ether solution at $-35\text{ }^\circ\text{C}$ (**Figure 4.5**). The asymmetric unit contains half of the dimer and the remainder of the molecule is related by a 2-fold axis that bisects the bridging dinitrogen unit. The molecular geometry is best described as idealized square pyramidal with the bridging dinitrogen occupying the apical position. This binding motif is well preceded for five-coordinate, pyridine di(imine) metal complexes with bridging dinitrogen moieties.²⁷ The metrical parameters of $[(^{\text{Me}}\text{BPDI})\text{Fe}(\text{N}_2)]_2(\mu_2\text{-N}_2)$ are presented in **Table 4.1**, and values for $(^{\text{iPr}}\text{BPDI})\text{Fe}(\text{N}_2)_2$ are included for comparison. No statistical deviations from the 2,6-diisopropyl aryl complex were observed. The $C_{\text{ipso}}\text{-}C_{\text{imine}}$ and $C_{\text{imine}}\text{-}N_{\text{imine}}$ bond lengths clearly signal reduction of the chelate, and are consistent with a BPDI^{2-} designation.²⁸

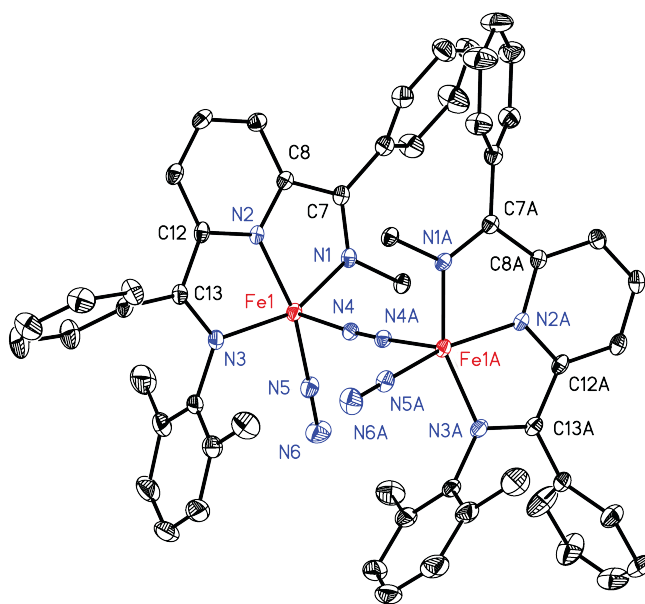


Figure 4.5. Solid state structure of $[(^{\text{Me}}\text{BPDI})\text{Fe}(\text{N}_2)]_2(\mu_2\text{-N}_2)$ at 30% probability ellipsoids. Hydrogen atoms and one aryl substituent from each ligand are omitted for clarity.

Table 4.1 Bond distances (Å) and angles (°) for $[(^{\text{Me}}\text{BPDI})\text{Fe}(\text{N}_2)]_2(\mu_2\text{-N}_2)$. The values for $(^{\text{iPr}}\text{BPDI})\text{Fe}(\text{N}_2)_2$ are included for comparison.

	$[(^{\text{Me}}\text{BPDI})\text{Fe}(\text{N}_2)]_2(\mu_2\text{-N}_2)$	$(^{\text{iPr}}\text{BPDI})\text{Fe}(\text{N}_2)_2^a$
Fe(1)-N(1)	1.9323(13)	1.927(4)
Fe(1)-N(2)	1.8388(13)	1.842(4)
Fe(1)-N(3)	1.9284(14)	1.935(5)
Fe(1)-N(4)	1.8803(13)	1.865(5)
Fe(1)-N(5)	1.8540(15)	1.841(5)
N(4)-N(4A)	1.123(3)	1.107(5)
N(5)-N(6)	1.102(2)	1.106(6)
N(1)-C(7)	1.340(2)	1.344(7)
N(3)-C(13)	1.341(2)	1.355(7)
C(7)-C(8)	1.437(2)	1.429(8)
C(12)-C(13)	1.419(3)	1.430(7)
Fe(1)-N(4)-N(4A)	174.95(12)	170.4(5)
Fe(1)-N(5)-N(6)	179.16(16)	178.5(5)
N(4)-Fe(1)-N(5)	93.84(6)	99.0(2)
N(1)-Fe(1)-N(5)	97.79(6)	96.6(2)
N(3)-Fe(1)-N(5)	95.79(6)	97.2(2)
N(1)-Fe(1)-N(2)	79.86(5)	79.3(2)
N(2)-Fe(1)-N(3)	80.09(6)	80.9(2)

^a Data taken from reference 18.

The benzene-*d*₆ ¹H NMR spectrum of the isolated material under an atmosphere of dinitrogen was broad and featureless at 23 °C. However, analysis by solid-state (KBr) infrared spectroscopy revealed two sharp and intense absorptions at 2104 and 2094 cm⁻¹, corresponding to the symmetric and asymmetric stretching frequencies of the terminal dinitrogen ligands. Attempts to obtain a solution infrared spectrum proved challenging, as dissolving the isolated material in toluene caused a significant decrease in intensity of these bands. This result denotes dinitrogen loss from the iron coordination sphere. The five-coordinate 2,6-diisopropyl aryl analog, $(^{\text{iPr}}\text{BPDI})\text{Fe}(\text{N}_2)_2$ is reported to lose an equivalent of dinitrogen in solution, existing in an equilibrium between $(^{\text{iPr}}\text{BPDI})\text{Fe}(\text{N}_2)_2$ and $(^{\text{iPr}}\text{BDPI})\text{Fe}(\text{N}_2)$.¹⁸ At 23 °C, however, the four-

coordinate species predominates. Evidence for dinitrogen exchange in the dimeric pyridine di(imine) iron dinitrogen complexes has been observed by ^{15}N NMR spectroscopy,²⁶ however, there is no evidence for a four-coordinate species in solution at 23 °C. Monitoring the intensity of the dinitrogen bands of $[(^{\text{Me}}\text{BPDI})\text{Fe}(\text{N}_2)]_2(\mu_2\text{-N}_2)$ at varying temperatures in toluene solution by *in situ* infrared spectroscopy revealed that loss of dinitrogen was the result of a chemical equilibrium. Lowering the temperature of the solution resulted in reconstitution of the intensity of the dinitrogen bands (**Figure 4.6**). Near -40 °C, the intensity plateaued, signaling that nearly all of the material was present in solution as $[(^{\text{Me}}\text{BPDI})\text{Fe}(\text{N}_2)]_2(\mu_2\text{-N}_2)$.

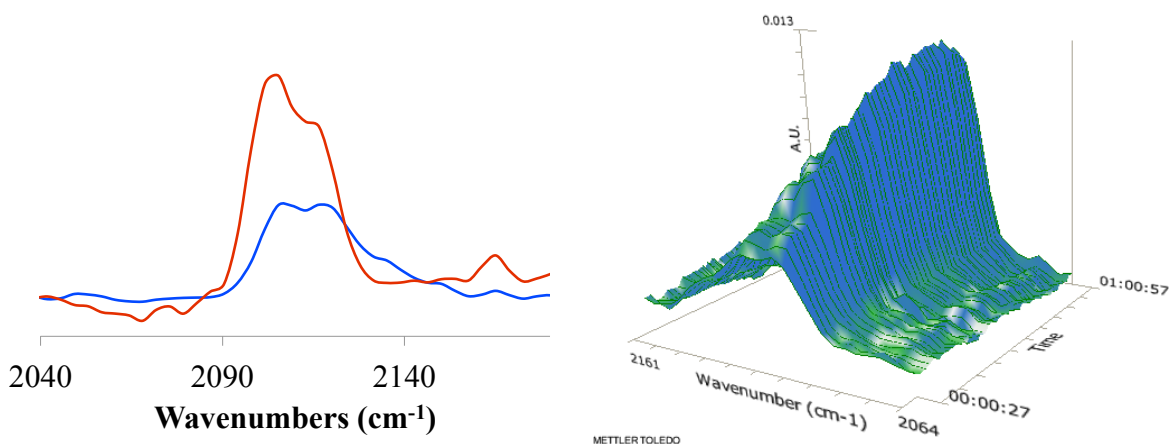


Figure 4.6. *In situ*, toluene solution infrared spectra of isolated $[(^{\text{Me}}\text{BPDI})\text{Fe}(\text{N}_2)]_2(\mu_2\text{-N}_2)$ at 22 °C (blue) and -35 °C (red). 3D Surface of the infrared spectra as the temperature was decreased from 22 °C to -40 °C (bottom).

In order to obtain some insight into the nature of the dominant species in solution at 23 °C, recrystallized samples of $[(^{\text{Me}}\text{BPDI})\text{Fe}(\text{N}_2)]_2(\mu_2\text{-N}_2)$ were analyzed by solid-state, zero-field ^{57}Fe Mößbauer spectroscopy (**Figure 4.7**). Consistent with the *in situ* infrared data, material crystallized at -35 °C was predominately $[(^{\text{Me}}\text{BPDI})\text{Fe}(\text{N}_2)]_2(\mu_2\text{-N}_2)$ (88%). A quadrupole doublet with an isomer shift of $0.37 \text{ mm}\cdot\text{s}^{-1}$ and a quadrupole splitting of $|0.34| \text{ mm}\cdot\text{s}^{-1}$ were observed

for $[(^{\text{Me}}\text{BPDI})\text{Fe}(\text{N}_2)]_2(\mu_2\text{-N}_2)$. These values are consistent with other monomeric and dimeric five-coordinate pyridine di(imine) iron bis(dinitrogen) complexes (**Table 4.2**). Therefore, a ground-structure similar to $(^{\text{iPr}}\text{PDI})\text{Fe}(\text{N}_2)_2$ is proposed: resonance structure between $[(^{\text{Me}}\text{BPDI}^0)\text{Fe}^0(\text{N}_2)]_2(\mu_2\text{-N}_2)$ and $[(^{\text{Me}}\text{BPDI}^{2-})\text{Fe}^{\text{II}}(\text{N}_2)]_2(\mu_2\text{-N}_2)$. A minor species, present in 12% in the solid state, exhibited an isomer shift of $0.35 \text{ mm}\cdot\text{s}^{-1}$ and a quadrupole splitting of $|2.17| \text{ mm}\cdot\text{s}^{-1}$. These parameters are consistent with those of other four-coordinate iron dinitrogen compounds.^{29,30} Further evidence, however, was needed to validate this claim. Typical batches of $[(^{\text{Me}}\text{BPDI})\text{Fe}(\text{N}_2)]_2(\mu_2\text{-N}_2)$ contained approximately 10–20% of this component.

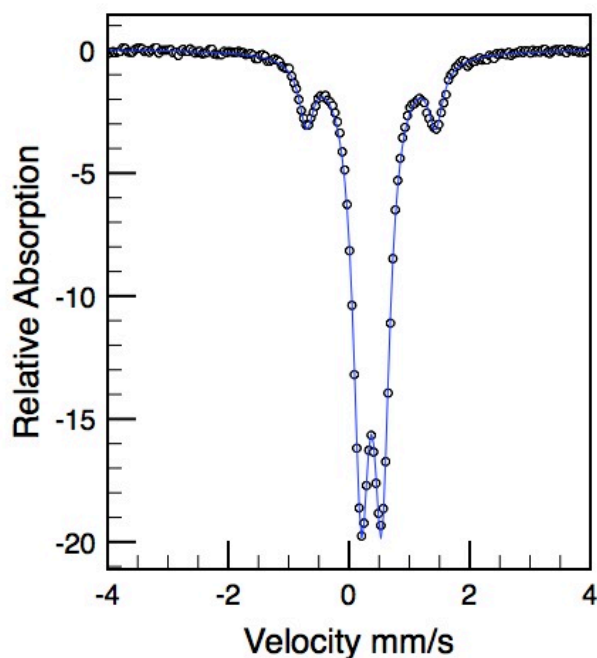


Figure 4.7. Zero-field ^{57}Fe Mößbauer spectrum of $[(^{\text{Me}}\text{BPDI})\text{Fe}(\text{N}_2)]_2(\mu_2\text{-N}_2)$ obtained at 80 K; $\delta = 0.37 \text{ mm}\cdot\text{s}^{-1}$, $|\Delta E_{\text{Q}}| = 0.34 \text{ mm}\cdot\text{s}^{-1}$.

Dissolving a sample of $[(^{\text{Me}}\text{BPDI})\text{Fe}(\text{N}_2)]_2(\mu_2\text{-N}_2)$ in toluene and stirring for thirty minutes prior to removal of solvent *in vacuo* yielded a material that was greater than 50% $[(^{\text{Me}}\text{BPDI})\text{Fe}(\text{N}_2)]_2(\mu_2\text{-N}_2)$ as judged by Mößbauer spectroscopy. This result suggested that the

Table 4.2. Zero-field ^{57}Fe Mößbauer parameters ($\text{mm}\cdot\text{s}^{-1}$) for representative four- and five-coordinate pyridine di(imine) iron dinitrogen complexes.

Complex	δ	$ \Delta E_Q $
$(i\text{PrPDI})\text{Fe}(\text{N}_2)_2^a$	0.39	0.53
$(i\text{PrPDI})\text{Fe}(\text{N}_2)^a$	0.38	1.72
$[(\text{MePDI})\text{Fe}(\text{N}_2)]_2(\mu_2\text{-N}_2)^a$	0.37	0.49
$(i\text{PrBPDI})\text{Fe}(\text{N}_2)_2$	0.43	0.41
$(i\text{PrBPDI})\text{Fe}(\text{N}_2)$	0.43	1.91
$[(\text{MeBPDI})\text{Fe}(\text{N}_2)]_2(\mu_2\text{-N}_2)$	0.37	0.34

^a Values are taken from reference 26.

dynamic behavior observed in solution was not due to an equilibrium between four- and five-coordinate iron dinitrogen compounds, as principally four-coordinate compounds was expected according to the *in situ* infrared spectroscopy data.

Alternatively, Archer *et al.* reported that $(i\text{PrBPDI})\text{Fe}(\text{N}_2)_2$ was susceptible to THF binding.¹⁸ Because synthesis of the dinitrogen complex utilized THF, this seemed a likely possibility. Analysis of the solid that resulted from stirring $[(\text{MeBPDI})\text{Fe}(\text{N}_2)]_2(\mu_2\text{-N}_2)$ in THF for 20 minutes by zero-field ^{57}Fe Mößbauer spectroscopy, revealed a mixture that contained 82% of the species that was identified from recrystallized $[(\text{MeBPDI})\text{Fe}(\text{N}_2)]_2(\mu_2\text{-N}_2)$ (**Figure 4.8**). This indicated that the solution equilibrium occurred between the iron bis(dinitrogen) complex, $[(\text{MeBPDI})\text{Fe}(\text{N}_2)]_2(\mu_2\text{-N}_2)$ and the THF adduct. The source of the THF was likely residual solvent from the synthesis of the complex. However, because the iron dinitrogen complex predominates at $-35\text{ }^\circ\text{C}$ (as established by *in situ* infrared spectroscopy), it is the major constituent of the recrystallized material. Attempts to prepare solely the THF adduct, $(\text{MeBPDI})\text{Fe}(\text{THF})$ from reduction of the iron dihalide under vacuum resulted in a mixture of

organometallic products (THF adduct and η^6 -arene species). Archer *et al.* has demonstrated that the half-life of $(i^{\text{Pr}}\text{BPDI})\text{Fe}(\text{N}_2)_2$ under vacuum was significantly shorter than under an atmosphere of dinitrogen (7.5 and 19 hours, respectively).¹⁸

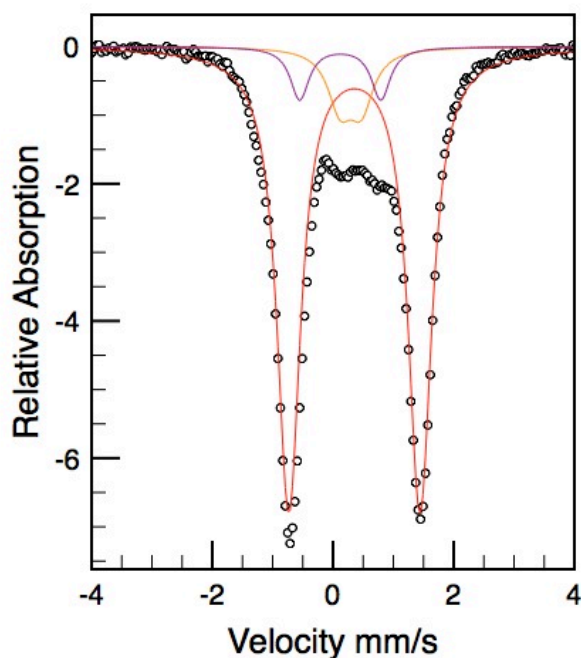


Figure 4.8. Zero-field ^{57}Fe Mössbauer spectrum of the isolated THF adduct (red) obtained at 80 K; $\delta = 0.35 \text{ mm}\cdot\text{s}^{-1}$, $|\Delta E_Q| = 2.17 \text{ mm}\cdot\text{s}^{-1}$.

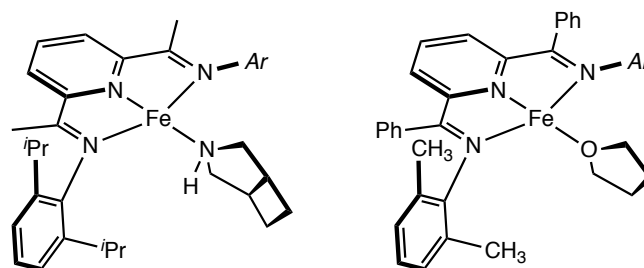
To determine the coordination number of the THF adduct, decomposition and computational experiments were performed. Decomposition of the adduct by addition of carbon monoxide suggested the presence of two equivalents of THF per metal center. However, because residual THF from the synthesis of the dinitrogen compound is known to persist, the results of the decomposition experiment are unreliable. The theoretical molecules, $(^{\text{Me}}\text{BDPI})\text{Fe}(\text{THF})_2$ and $(^{\text{Me}}\text{BPDI})\text{Fe}(\text{THF})$ were calculated using broken-symmetry (BS) DFT at the B3LYP level using models discussed in Section 1.5 for $(4\text{-R-}i^{\text{Pr}}\text{PDI})\text{Fe}(\text{DMAP})$. Initial geometries are provided in Appendix B. For $(^{\text{Me}}\text{BDPI})\text{Fe}(\text{THF})_2$, geometry optimization caused spontaneous ejection of the

apical THF molecule, resulting in an iron-oxygen distance of 4.22 Å in the converged solution. The iron-oxygen bond length in the input structure was 2.15 Å and was identical to the basal iron-oxygen distance. These results illustrate that $(^{\text{Me}}\text{BPDI})\text{Fe}(\text{THF})_2$ is computationally unstable.

The BS(2,2) calculation converged to a solution that is typical of pyridine di(imine) iron complexes with principally σ -donating ligands.^{13,29,30} The optimized geometry of $(^{\text{iPr}}\text{BPDI})\text{Fe}(\text{THF})$ is analogous to $(^{\text{iPr}}\text{PDI})\text{Fe}(\text{NHC}_6\text{H}_{10})$, which was previously obtained from the reaction of $(^{\text{iPr}}\text{PDI})\text{Fe}(\text{N}_2)$ with *N,N*-diallylamine.¹⁴ A comparison of the computed metrical parameters of $(^{\text{Me}}\text{BPDI})\text{Fe}(\text{THF})$ and the experimental values for $(^{\text{iPr}}\text{PDI})\text{Fe}(\text{NHC}_6\text{H}_{10})$ are reported in **Table 4.3**. A qualitative molecular orbital diagram is presented in **Figure 4.9**, and corresponds to an intermediate-spin, Fe^{II} ion ($S = 1$) antiferromagnetically coupled to a pyridine di(imine) triplet diradical dianion ($S = 1$).

Mössbauer parameters were computed in an attempt to validate the calculations. The isomer shift obtained from the BS(2,2) solution ($\delta^{\text{calc}} = 0.38 \text{ mm}\cdot\text{s}^{-1}$) was in excellent agreement with the experimentally observed value ($\delta^{\text{exp}} = 0.35 \text{ mm}\cdot\text{s}^{-1}$). Contrastingly, the quadrupole splitting parameter ($\Delta E_{\text{Q}}^{\text{calc}} = -1.08 \text{ mm}\cdot\text{s}^{-1}$) was not accurately reproduced ($|\Delta E_{\text{Q}}|^{\text{exp}} = |2.17| \text{ mm}\cdot\text{s}^{-1}$). This phenomenon is precedented,²⁹ and occurs because DFT cannot accurately calculate the electronic ground state of this class of molecules, which experience mixing from excited states by spin-orbit coupling. However, the experimental Mössbauer parameters for the isolated species are very similar to those of other four-coordinate pyridine di(imine) iron complexes bearing neutral ligands.²⁹ Therefore, this species will hereon be referred to as $(^{\text{Me}}\text{BPDI})\text{Fe}(\text{THF})$ (**Figure 4.10**).

Table 4.3. Comparison of experimental and computed bond lengths (Å) and angles (°) for (*i*PrPDI)Fe(NHC₆H₁₀) and (^{Me}BPDI)Fe(THF), respectively.



(*i*PrPDI)Fe(NHC₆H₁₀)

(^{Me}BPDI)Fe(THF)

	(<i>i</i> PrPDI)Fe(NHC ₆ H ₁₀) ^a	(^{Me} BPDI)Fe(THF) ^{calc}
Fe–N _{pyr}	1.819(3)	1.860
Fe–N _{imine}	1.910(3)	1.960
	1.921(4)	1.959
Fe–N/O	2.031	2.090
C _{imine} –N _{imine}	1.360(5)	1.370
	1.372(5)	1.370
C _{ipso} –C _{imine}	1.412(6)	1.436
	1.389(6)	1.437

^a Data from reference 14.

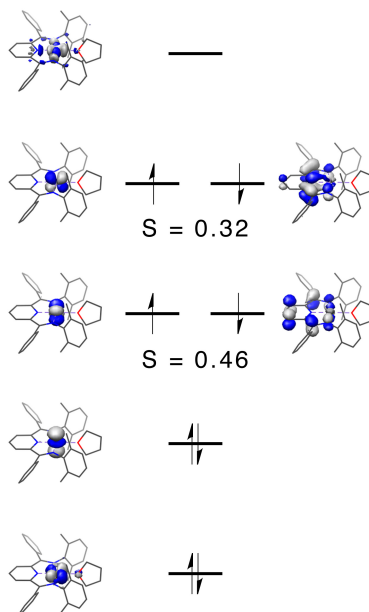


Figure 4.9. Qualitative molecular orbital diagram of (^{Me}BPDI)Fe(THF) obtained from a BS(2,2) calculation at the B3LYP level.

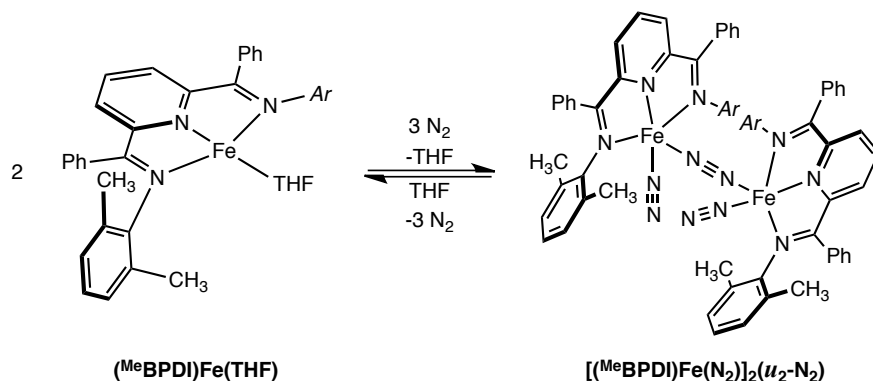


Figure 4.10. Solution equilibrium between $(^{\text{Me}}\text{BPDI})\text{Fe}(\text{THF})$ and $[(^{\text{Me}}\text{BPDI})\text{Fe}(\text{N}_2)]_2(\mu_2\text{-N}_2)$.

Efforts were made to observe $(^{\text{Me}}\text{BPDI})\text{Fe}(\text{THF})$ by ^1H NMR spectroscopy. Evacuating the head space of a J. Young tube containing a benzene- d_6 solution of $[(^{\text{Me}}\text{BPDI})\text{Fe}(\text{N}_2)]_2(\mu_2\text{-N}_2)$, and therefor shifting of the equilibrium towards the THF adduct, resulted in immediate appearance of broadened features. The number of resonances were consistent with molecular C_{2v} symmetry, and the range of chemical shift values was approximately 16 ppm. Notably, the *m*- and *p*-pyridine resonances were located at 15.30 and 7.44 ppm, respectively. These chemical shifts are indicative of temperature-independent paramagnetism.^{29,31} The broadness of the resonances was attributed to the dynamic between the dinitrogen and THF adducts. Addition of 1–2 drops of THF also resulted in the appearance of these features, further supporting that the resonances were due to the THF adduct. Under these conditions, the peak widths were much narrower resulting from a more dramatic shift in the equilibrium. The THF adduct, $(^{\text{Me}}\text{BPDI})\text{Fe}(\text{THF})$ was characterized by ^1H NMR in THF- d_8 to further support this assertion.

Consistent with the behavior of the 2,6-diisopropyl aryl analog, $[(^{\text{Me}}\text{BPDI})\text{Fe}(\text{N}_2)]_2(\mu_2\text{-N}_2)$ underwent ligand dissociation and formation of intramolecular η^6 -arene species in solution. Allowing a benzene- d_6 solution of $[(^{\text{Me}}\text{BPDI})\text{Fe}(\text{N}_2)]_2(\mu_2\text{-N}_2)$ to stand at 23 °C for 48 hours resulted in conversion to a 1.4:1 mixture of $(\kappa^2\text{-}^{\text{Me}}\text{BPDI})\text{Fe}(\eta^6\text{-phenyl})$ and $(\kappa^2\text{-}^{\text{Me}}\text{BPDI})\text{Fe}(\eta^6\text{-})$

aryl) (**Figure 4.11**). Each of the η^6 -arene complexes was diamagnetic—exhibiting sharp resonances with coupling—and was readily characterized by ^1H and ^{13}C NMR spectroscopy. The proton resonances for the hydrogens corresponding to the coordinated arene ring shift upfield, consistent with coordination to iron.¹⁸ As η^6 -formation is irreversible, the ratio of the two species is kinetically controlled and did not change as a function of time.

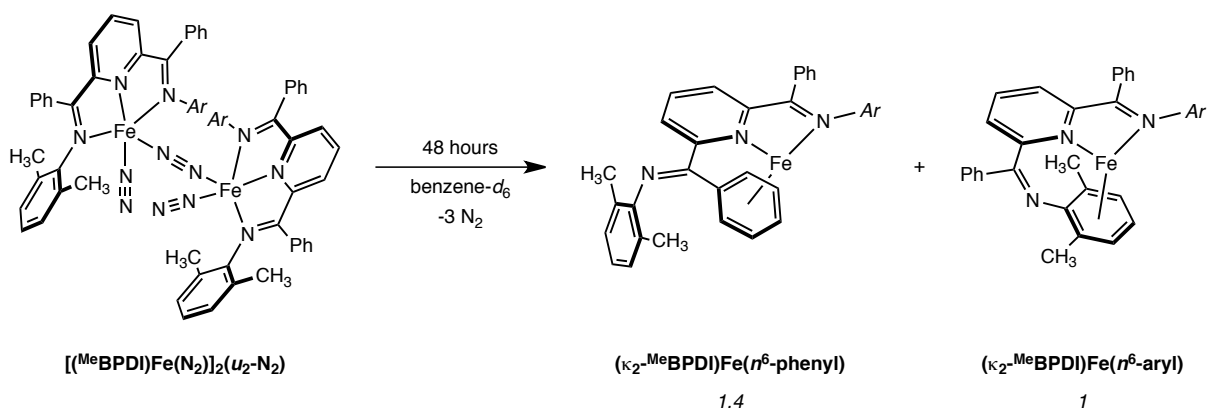
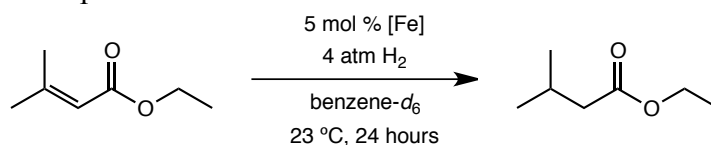


Figure 4.11. Formation of the η^6 -arene complexes, $(\kappa^2\text{-MeBPDI})\text{Fe}(\eta^6\text{-phenyl})$ and $(\kappa^2\text{-MeBPDI})\text{Fe}(\eta^6\text{-aryl})$.

4.4 Catalytic Olefin Hydrogenation Activity of $[(\text{MeBPDI})\text{Fe}(\text{N}_2)]_2(\mu_2\text{-N}_2)$

The phenyl-substituted pyridine di(imine) iron dinitrogen complexes, $(i\text{PrBPDI})\text{Fe}(\text{N}_2)_2$ and $[(\text{MeBPDI})\text{Fe}(\text{N}_2)]_2(\mu_2\text{-N}_2)$ were assayed for the catalytic hydrogenation of ethyl 3,3-dimethylacrylate. Typical reaction conditions employed a 0.92 M benzene- d_6 solution of the olefin, 5 mol % iron, and four atmospheres of dihydrogen at 23 °C. Conversion was assayed after 24 hours by ^1H NMR spectroscopy. The results of this study are presented in **Table 4.4**. $(i\text{PrBPDI})\text{Fe}(\text{N}_2)_2$ and $[(\text{MeBPDI})\text{Fe}(\text{N}_2)]_2(\mu_2\text{-N}_2)$ are included for comparison. Removal of steric bulk from the 2,6-disubstituted aryl group of complexes with methyl groups alpha to the imine results in a dramatic effect on the hydrogenation activity of this substrate.²⁶

Table 4.4. Catalytic hydrogenation of ethyl 3,3-dimethylacrylate using aryl substituted bis(imino)pyridine iron bis(dinitrogen) complexes. (*i*PrPDI)Fe(N₂)₂ and [(^{Me}PDI)Fe(N₂)₂]₂(μ₂-N₂) are included for comparison.²⁶



Precatalyst	Conversion
(<i>i</i> PrPDI)Fe(N ₂) ₂	50%
[(^{Me} PDI)Fe(N ₂) ₂] ₂ (μ ₂ -N ₂)	> 95% (1 hour)
(<i>i</i> PrBPDI)Fe(N ₂) ₂	0%
[(^{Me} BPDI)Fe(N ₂) ₂] ₂ (μ ₂ -N ₂)	21%

^a Conditions: 5.0 mol % [Fe], 0.92 M substrate in benzene-*d*₆ solution, 4 atm H₂, 23 °C. ^b Maximum 65% conversion due to catalyst deactivation. ^c 45% conversion after 72 hours.

The phenyl derivatives, in contrast, exhibited reduced turnover frequency and number with ethyl 3,3-dimethylacrylate. The 2,6-diisopropyl aryl variant, (*i*PrBPDI)Fe(N₂)₂ showed no turnover with ethyl 3,3-dimethylacrylate when stirred in the presence of 4 atm of dihydrogen for days at 23 °C. [(^{Me}BPDI)Fe(N₂)₂]₂(μ₂-N₂) achieved 21% conversion after 24 hours under standard conditions. Analysis by ¹H NMR spectroscopy of the reaction mixture following hydrogenation established formation of the unsaturated and saturated pyridine di(imine) iron ester adducts (*vide infra*) with little evidence for competitive η⁶-arene complex formation. A mixture of unidentified paramagnetic products was also observed, likely resulting from C–O bond cleavage.^{13,32} Allowing the hydrogenation to proceed for 72 hours resulted in 45% conversion, consistent with first order kinetics. The hydrogenation was also carried out in the presence of 2–5 equivalents (per iron) of THF with no significant deviation in activity. Because the THF adduct is favored in solution at 23 °C, there was little difference in using the THF adduct and the bis(dinitrogen) dimer, [(^{Me}BPDI)Fe(N₂)₂]₂(μ₂-N₂) as the precatalyst.

In order to understand the significant differences between the precatalysts screened with phenyl substituents and those with methyl substituents (BPDI vs. PDI), a series of NMR studies and stoichiometric experiments were undertaken. Analysis of the reaction mixture after attempted hydrogenation of ethyl 3,3-dimethylacrylate using (*i*PrBPDI)Fe(N₂)₂ demonstrated little deactivation by formation of η^6 -arene complexes. Instead, the diamagnetic ester complex, (*i*PrBPDI)Fe(OC(OEt)(CHC(CH₃)₂)) was observed. (*i*PrBPDI)Fe(OC(OEt)(CHC(CH₃)₂)) and (^{Me}BPDI)Fe(OC(OEt)(CHC(CH₃)₂)) were independently prepared as dark purple and black solids, respectively, by addition of 1 equivalent (per iron) of ethyl 3,3-dimethylacrylate to the corresponding iron dinitrogen compound (**Figure 4.12**). Monomeric dinitrogen complexes are depicted in **Figure 4.12** for simplicity. Both (*i*PrBPDI)Fe(OC(OEt)(CHC(CH₃)₂)) and (^{Me}BPDI)Fe(OC(OEt)(CHC(CH₃)₂)) exhibited ¹H NMR spectral features consistent with other pyridine di(imine) iron complexes with principally σ -donating ligands.^{13, 29,31}

The reaction of each complex, (^RBPDI)Fe(OC(OEt)(CHC(CH₃)₂)) (R = *i*Pr, Me), with hydrogen was explored (**Figure 4.13**). Exposure of (^{Me}BPDI)Fe(OC(OEt)(CHC(CH₃)₂)) to 4 atm of H₂ at 23 °C resulted in a color change from black to brown over 24 hours, signaling complete hydrogenation of the olefin and formation of the resulting ester adduct, (^{Me}BPDI)Fe(OC(OEt)(CH₂CH(CH₃)₂)). No evidence for the formation of paramagnetic products was observed under these conditions. Repeating this procedure with (*i*PrBPDI)Fe(OC(OEt)(CHC(CH₃)₂)) resulted in no change over the course of hours, indicating that this iron ester complex is not an initiator for hydrogenation.

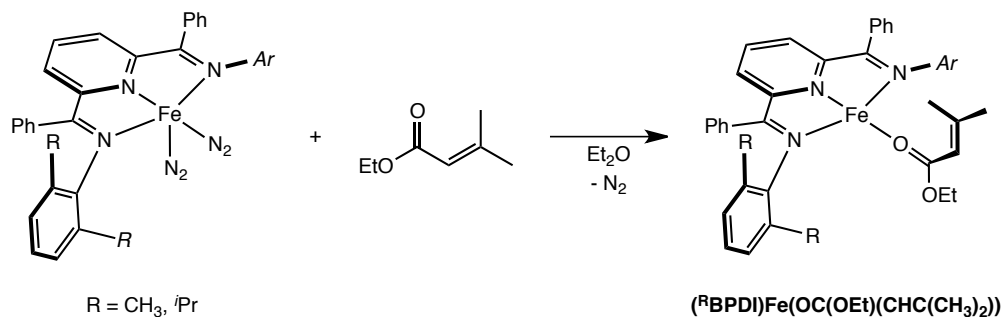


Figure 4.12. Synthesis of $(^{\text{R}}\text{BPDI})\text{Fe}(\text{OC}(\text{OEt})(\text{CHC}(\text{CH}_3)_2))$ ($\text{R} = \textit{i}\text{Pr}, \text{Me}$).

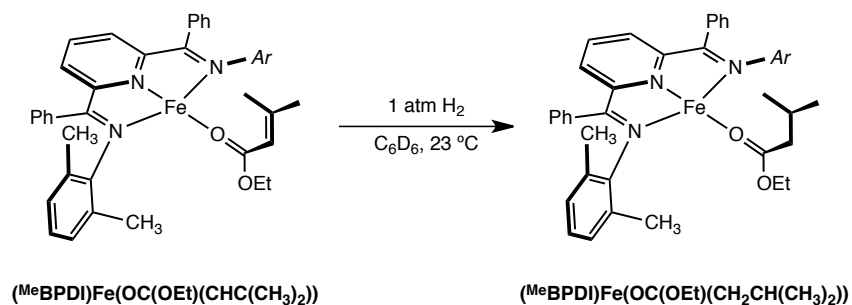
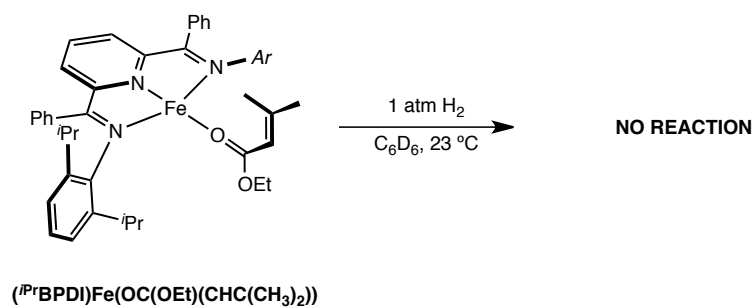


Figure 4.13. Addition of H_2 to $(^{\text{R}}\text{BPDI})\text{Fe}(\text{OC}(\text{OEt})(\text{CHC}(\text{CH}_3)_2))$ ($\text{R} = \textit{i}\text{Pr}, \text{Me}$).

The dramatic difference in hydrogenation activity between $(^{\textit{i}\text{Pr}}\text{PDI})\text{Fe}(\text{N}_2)_2$ and the phenyl-substituted derivatives, $(^{\textit{i}\text{Pr}}\text{BPDI})\text{Fe}(\text{N}_2)_2$ and $[(^{\text{Me}}\text{BPDI})\text{Fe}(\text{N}_2)]_2(\mu_2\text{-N}_2)$ are attributed to the affinity of the latter complexes to ligate the carbonyl moiety of the substrate. In the presence of stoichiometric ethyl 3,3-dimethylacrylate, $(^{\textit{i}\text{Pr}}\text{PDI})\text{Fe}(\text{N}_2)$ is in equilibrium with the ester adduct (see Section 1.6). This ultimately results due to the electron-rich or -poor nature of the iron-center as imparted by the pyridine di(imine) chelate. The sterically congested 2,6-

diisopropyl aryl variant, [(*i*PrBPDI)Fe] likely discourages coordination of the π -face of the olefin, and therefore favors coordination of the carbonyl oxygen. Removing some of this congestion, as is the case with [(^{Me}BPDI)Fe], allows for binding of the olefin over the carbonyl oxygen. However, hydrogenation of the olefin is sufficiently slow such that catalyst decomposition is competitive. This event may be overcome by increased hydrogen pressure.

4.5 Conclusions

In summary, the phenyl-substituted pyridine di(imine) iron bis(dinitrogen) dimer, [(^{Me}BPDI)Fe(N₂)]₂(μ_2 -N₂) was prepared from reduction of the corresponding iron dihalide, (^{Me}BPDI)FeCl₂ utilizing two equivalents of sodium and catalytic naphthalene. [(^{Me}BPDI)Fe(N₂)]₂(μ_2 -N₂) was characterized by X-ray diffraction, infrared, Mößbauer and NMR spectroscopies as a diamagnetic compound with a ground-state consistent with (*i*PrPDI)Fe(N₂)₂. *In situ* infrared, Mößbauer and ¹H NMR experiments established that [(^{Me}BPDI)Fe(N₂)]₂(μ_2 -N₂) was present in equilibrium with (^{Me}BPDI)Fe(THF) in solution. The source of THF was attributed to residual solvent from the synthesis of the complex. As with (*i*PrBPDI)Fe(N₂)₂, [(^{Me}BPDI)Fe(N₂)]₂(μ_2 -N₂) underwent irreversible η^6 -arene coordination in solution.

[(^{Me}BPDI)Fe(N₂)]₂(μ_2 -N₂) and the diisopropyl aryl variant, (*i*PrBPDI)Fe(N₂)₂ were assayed for the hydrogenation of ethyl 3,3-dimethylacrylate, and were found to be much less active than their methyl-substituted analogs, ((*i*PrPDI)Fe(N₂)₂ and [(^{Me}PDI)Fe(N₂)]₂(μ_2 -N₂)). Stoichiometric experiments revealed that the low activity of these catalysts was a result of the more electrophilic nature of the iron center engendered by the phenyl-substituted pyridine di(imine) chelate.

4.6 *Experimental*

All air- and moisture-sensitive manipulations were carried out using standard vacuum line, Schlenk, and cannula techniques or in an MBraun inert atmosphere dry box containing an atmosphere of purified nitrogen. Solvents for air- and moisture-sensitive manipulations were initially dried and deoxygenated using literature procedures.³³ Benzene-*d*₆ was purchased from Cambridge Isotope Laboratories, distilled from Na metal and dried over 4 Å molecular sieves. (MeBPDI)FeCl₂³⁴ and (*i*PrBPDI)Fe(N₂)₂¹⁸ were prepared according to literature procedures.

¹H NMR spectra were recorded on Varian Mercury 300, Inova 400, 500, and 600 spectrometers operating at 299.76, 399.78, 500.62, and 599.78 MHz, respectively. ¹³C NMR spectra were recorded on an Inova 500 spectrometer operating at 125.893 MHz. All ¹H and ¹³C NMR chemical shifts are reported relative to SiMe₄ using the ¹H (residual) and ¹³C chemical shifts of the solvent as a secondary standard. Infrared spectra were collected on a Thermo Nicolet spectrometer. Elemental analyses were performed at Robertson Microlit Laboratories, Inc., in Madison, NJ.

Single crystals suitable for X-ray diffraction were coated with polyisobutylene oil in a drybox, transferred to a nylon loop and then quickly transferred to the goniometer head of a Bruker X8 APEX2 diffractometer equipped with a molybdenum X-ray tube ($\lambda = 0.71073$ Å). Preliminary data revealed the crystal system. A hemisphere routine was used for data collection and determination of lattice constants. The space group was identified and the data were processed using the Bruker SAINT+ program and corrected for absorption using SADABS. The structures were solved using direct methods (SHELXS) completed by subsequent Fourier synthesis and refined by full-matrix least-squares procedures.

In situ solution infrared spectra were recorded with a Mettler Toledo ReactIR iC10 equipped with a DS Series 9.5mm x 1.5m AgX fiber conduit with a silicon probe tip on a 5 mM solution of the compound in toluene. The spectra were acquired at 30 second intervals with a resolution of eight cm^{-1} using a toluene background taken at 22 °C. The solution was cooled using an acetone/dry ice bath and the temperature was monitored using an external, low-temperature thermometer. Data was analyzed using the iC IR 4.0 software.

^{57}Fe Mößbauer spectra were recorded on a SEE Co. Mößbauer spectrometer (MS4) at 80 K in constant acceleration mode. $^{57}\text{Co/Rh}$ was used as the radiation source. WMOSS software was used for the quantitative evaluation of the spectral parameters (least squares fitting to Lorentzian peaks. The temperature of the samples was controlled by a Janis Research Co. CCS-850 He/N₂ cryostat within an accuracy of ± 1 K. Isomer shifts were determined relative to α -iron at 298 K.

All DFT calculations were performed with the *ORCA* program package.³⁵ The geometry optimizations of the complexes and single-point calculations on the optimized geometries were carried out at the B3LYP level³⁶ of DFT. This hybrid functional often gives better results for transition-metal compounds than pure gradient-corrected functionals, especially with regard to metal-ligand covalency.³⁷ The all-electron Gaussian basis sets were those developed by Ahlrichs' group.³⁸ Triple- ζ quality basis sets def2-TZVP with one set of polarization functions on the metals and on the atoms directly coordinated to the metal center were used. For the carbon and hydrogen atoms, slightly smaller polarized split-valence def2-SV(P) basis sets were used that were of double- ζ quality in the valence region and contained a polarizing set of d functions

on the non-hydrogen atoms. Auxiliary basis sets were chosen to match the orbital basis.³⁹ The RIJCOSX⁴⁰ approximation was used to accelerate the calculations.

Throughout this dissertation, computational results are described using the BS approach by Ginsberg⁴¹ and Noodleman et al.⁴² Because several BS solutions to the spin-unrestricted Kohn-Sham equations may be obtained, the general notation BS(*m,n*)⁴³ has been adopted, where *m* (*n*) denotes the number of spin-up (spin-down) electrons at the two interacting fragments. Canonical and corresponding⁴⁴ orbitals, as well as spin density plots, were generated with the program *Molekel*.⁴⁵

Nonrelativistic single-point calculations employed the CP(PPP) basis set for iron.⁴⁶ The Mößbauer isomer shifts were calculated from the computed electron densities at the iron centers as previously described.⁴⁷

Characterization of [(^{Me}BPDI)Fe(N₂)]₂(μ₂-N₂). A scintillation vial was charged with 0.750 g of (^{Me}BPDI)FeCl₂ (1.21 mmol), 0.058 g of sodium metal (2.5 mmol, 2.1 eq), and 0.008 g of naphthalene (0.06 mmol, 0.05 eq). To the vial was added 5 mL THF, and the resulting mixture was stirred for 1.5 hours. During this time, the solution turned from blue-green to brown. After reduction was complete (signaled by the formation of the brown solution), the THF was removed *in vacuo*. The dark residue was taken up in diethyl ether to yield a dark orange-brown mixture and was filtered through a plug of Celite. Removal of the solvent *in vacuo*, and recrystallization of the residue from ether at -35 °C afforded 0.321 g (45 %) of a brown solid identified as [(^{Me}BPDI)Fe(N₂)]₂(μ-N₂). Crystals suitable for X-ray diffraction were grown from a dilute diethyl ether solution. ¹H NMR (benzene-*d*₆, 20 °C): δ = 1.17 (bs, 12H, aryl CH₃), 6.57–7.48

(bm, 19H, *aryl*-, *phenyl*-, and *py*-H). ^{13}C $\{^1\text{H}\}$ NMR (benzene- d_6 , 20 °C): δ = 23.2 (b, CH_3), 108.2, 112.9, 124.9, 126.1, 128.6, 131.9, 134.1, 134.7, 136.7, 147.9 (b), 151.1 (b), 158.2 (b). IR (KBr): $\nu(\text{N}_2)$ = 2104, 2094 cm^{-1} . IR (toluene, 10 °C): $\nu(\text{N}_2)$ = 2120, 2109 cm^{-1} .

Allowing a benzene solution of $[(^{\text{Me}}\text{BPDI})\text{Fe}(\text{N}_2)]_2(\mu_2\text{-N}_2)$ to stand at 22 °C for 48 h furnished a 1.4:1 mixture of $[(\kappa^2\text{-}^{\text{Me}}\text{BPDI})\text{Fe}(\eta^6\text{-phenyl})]$ and $[(\kappa^2\text{-}^{\text{Me}}\text{BPDI})\text{Fe}(\eta^6\text{-aryl})]$, respectively.

Characterization of $(^{\text{Me}}\text{BPDI})\text{Fe}(\text{THF})$. A 100 mL round bottom flask was charged with 0.100 g of $[(^{\text{Me}}\text{BPDI})\text{Fe}(\text{N}_2)]_2(\mu_2\text{-N}_2)$ (0.090 mmol) and a needle valve attached. On a high vacuum line, the vessel was evacuated and 20 mL of THF was added by vacuum transfer. After stirring for 20 minutes, the solvent was removed *in vacuo* to afford 0.072 g (61%) of a dark solid identified as $(^{\text{Me}}\text{BPDI})\text{Fe}(\text{THF})$. ^1H NMR (benzene- d_6 , 20 °C): δ = 0.90 (11 Hz, 12H, CH_3), 1.45 (41 Hz, 8H, THF), 3.26 (24 Hz, 8H, THF), 6.77 (21 Hz, 4H, *m*-phenyl), 6.89 (19 Hz, 4H, *m*-aryl), 7.44 (19 Hz, 2H, *p*-Ar), 8.67 (26 Hz, 3H, *p*-pyr and *p*-aryl), 9.88 (18 Hz, 4H, *o*-phenyl), 15.30 (18 Hz, 2H, *m*-pyr). ^1H NMR (THF- d_8 , 20 °C): δ = 0.95 (41 Hz, 12H, CH_3), 6.78 (60 Hz, 4H, *m*-phenyl), 6.98 (62 Hz, 4H, *m*-aryl), 7.45 (23 Hz, 2H, *p*-aryl), 8.55 (21 Hz, 1H, *p*-pyr), 8.84 (49 Hz, 2H, *p*-phenyl), 9.71 (47 Hz, 4H, *o*-phenyl), 15.24 (48 Hz, 2H, *m*-pyr). ^{13}C $\{^1\text{H}\}$ NMR (THF- d_8 , 20 °C): δ = 22.7 (b, CH_3), 107.1, 111.8, 118.0 (b), 124.4 (b), 125.8 (b), 128.4 (b), 131.9 (b), 132.9 (b), 136.7.

Characterization of $[(\kappa^2\text{-}^{\text{Me}}\text{BPDI})\text{Fe}](\eta^6\text{-Phenyl})$. ^1H NMR (benzene- d_6 , 20 °C): δ = 2.25 (s, 6H, CH_3), 2.32 (s, 6H, CH_3), 3.69 (t, 6 Hz, 1H, *p*-Ph), 5.01 (dd, 2 Hz & 6 Hz, 2H, *m*-Ph), 5.59 (d,

4.1 Hz, 2H, *o*-Ph), 6.45 (dd, 8 Hz & 8 Hz, 1H, *p*-py), 6.83–7.02 (m, 11H, *m*- and *p*-aryl, and *o*-, *m*-, *p*-phenyl), 7.05 (d, 8 Hz, 1H, *m*-py), 7.60 (d, 8 Hz, 1H, *m*-py). ^{13}C $\{^1\text{H}\}$ NMR (benzene- d_6 , 20°C): δ = 18.9 (CH₃), 19.2 (CH₃), 19.5 (CH₃), 80.8 (*p*-Ph), 83.4 (*o*-Ph), 84.7 (*m*-Ph), 89.5 (quaternary-Ph), 108.9, 122.2, 123.2, 123.5, 124.0, 124.5, 126.1, 126.5, 129.3, 129.7, 130.8, 131.1, 134.1, 136.4, 143.5, 148.3, 149.4, 165.7, 168.5.

Characterization of $[(\kappa^2\text{-}^{\text{Me}}\text{BPDI})\text{Fe}](\eta^6\text{-Aryl})$. ^1H NMR (benzene- d_6 , 20 °C): δ = 2.12 (s, 6H, CH₃), 2.22 (s, 6H, CH₃), 4.09 (t, 6 Hz, 1H, *p*-Ar), 5.21 (d, 6 Hz, 2H, *m*-Ar), 6.43 (dd, 8 Hz & 8 Hz, 1H, *p*-pyr), 6.79–6.94 (m, 10H, *p*-py & phenyl), 7.28–7.34 (m, 2H, *p*-Ar & *p*-Ph), 7.41 (d, 8 Hz, 1H, *m*-pyr), 7.81 (d, 7 Hz, 2H, *m*-Ar). ^{13}C $\{^1\text{H}\}$ NMR (benzene- d_6 , 20°C): δ = 17.1 (CH₃), 17.3 (CH₃), 17.5 (CH₃), 19.2 (CH₃), 81.1, 86.3, 87.8, 108.2, 112.1, 124.9, 126.1, 127.0, 128.1, 129.0, 129.2, 129.3, 130.7, 131.9, 136.8, 162.6.

Characterization of $(^{\text{Me}}\text{BPDI})\text{Fe}(\text{OC}(\text{OEt})(\text{CHC}(\text{CH}_3)_2))$. A scintillation vial was charged with 0.10 g of $[(^{\text{Me}}\text{BPDI})\text{Fe}(\text{N}_2)]_2(\mu_2\text{-N}_2)$ (0.085 mmol) and 5 mL of diethyl ether. To this mixture was added 0.022 g of ethyl 3,3-dimethylacrylate (0.17 mmol, 2 eq), which elicited a color change from brown to black. After 0.5 hours, the solvent was removed *in vacuo*, and the crude solid was recrystallized from pentane to afford 0.088 g (77 %) of a black solid identified as $(^{\text{Me}}\text{BPDI})\text{Fe}(\text{OC}(\text{OEt})(\text{CHC}(\text{CH}_3)_2))$. ^1H NMR (benzene- d_6 , 20 °C): δ = 0.43 (s, 3H, olefin-CH₃), 0.73 (s, 1H, olefin-CH), 0.78 (t, 7 Hz, 3H, OCH₂CH₃), 1.10 (s, 3H, olefin-CH₃), 1.51 (s, 12H, aryl-CH₃), 3.31 (q, 7 Hz, 2H, OCH₂CH₃), 6.83 (d, 7 Hz, 4H, *m*-aryl), 6.94 (t, 8 Hz, 4H, *m*-phenyl), 7.27 (t, 7 Hz, 2H, *p*-aryl), 8.18 (t, 8 Hz, 1H, *p*-pyr), 8.20 (t, 8 Hz, 2H, *p*-phenyl), 9.43 (d,

7 Hz, 4H, *o*-phenyl), 11.75 (d, 8 Hz, 2H *m*-pyr). ^{13}C $\{^1\text{H}\}$ NMR (benzene- d_6 , 20 °C): δ = 21.3, 27.8, 32.3, 62.3, 76.5, 104.6, 108.1, 121.2, 122.8, 124.0, 126.7, 131.0, 131.9, 135.5, 140.3, 158.9, 167.3, 167.4, 169.5, 185.2.

Characterization of $(^{\text{Me}}\text{BPDI})\text{Fe}(\text{OC}(\text{OEt})(\text{CH}_2\text{CH}(\text{CH}_3)_2)$. A thick walled vessel was charged with a solution of 0.040 g (0.059 mmol) of $(^{\text{Me}}\text{BPDI})\text{Fe}(\text{ethyl 3,3-dimethylacrylate})$ in 5 mL of toluene. On the high-vacuum line, 4 atm of H_2 was added, and the resulting solution was allowed to stir for 24 hours eliciting a color change from black to brown. Removal of excess H_2 and solvent yielded 0.029 g (72 %) of a brown solid identified as $(^{\text{Me}}\text{BPDI})\text{Fe}(\text{OC}(\text{OEt})(\text{CH}_2\text{CH}(\text{CH}_3)_2)$. ^1H NMR (benzene- d_6 , 20 °C): δ = 0.05 (d, 7 Hz, 2H, CH_2), 0.24 (d, 6 Hz, 3H, $\text{CH}(\text{CH}_3)_2$), 0.86 (m, 1H, $\text{CH}(\text{CH}_3)_2$), 1.12 (t, 7 Hz, 3H, OCH_2CH_3), 1.50 (s, 12H, aryl- CH_3), 2.71 (q, 7 Hz, 2H, OCH_2CH_3), 6.84 (d, 7 Hz, 4H, *m*-aryl), 6.93 (t, 8 Hz, 4H, *m*-phenyl), 7.33 (t, 7 Hz, 2H, *p*-aryl), 8.15 (t, 8 Hz, 1H, *p*-pyr), 8.20 (t, 8 Hz, 2H, *p*-phenyl), 9.37 (d, 8 Hz, 4H, *o*-phenyl), 11.86 (d, 8 Hz, 2H, *m*-pyr). ^{13}C $\{^1\text{H}\}$ NMR (benzene- d_6 , 20 °C): δ = 21.4, 32.4, 40.9, 47.8, 55.5, 56.7, 104.3, 107.2, 120.9, 123.0, 126.7, 128.7, 131.0, 141.0, 159.5, 163.2, 167.5, 167.8, 186.3.

Characterization of $(^{\text{iPr}}\text{BPDI})\text{Fe}(\text{OC}(\text{OEt})(\text{CH}(\text{CH}_3)_2)$. A scintillation vial was charged with 0.060 g of $(^{\text{iPr}}\text{BPDI})\text{Fe}(\text{N}_2)_2$ (0.083 mmol) and approximately 5 mL of diethyl ether. To this mixture was added 0.013 g (0.10 mmol, 1.2 eq) of ethyl 3,3-dimethylacrylate resulting in a color change from brown to dark purple. After 0.5 hours, the solvent was removed *in vacuo*, and the remaining solid was recrystallized from pentane to afford 0.058 g (88 %) of a dark purple solid

identified as (*i*PrBPDI)Fe(OC(OEt)(CHC(CH₃)₂). ¹H-NMR (benzene-*d*₆, 20 °C): δ = -0.22 (d, 6 Hz, 12H, CH(CH₃)₂), 0.97 (t, 7 Hz, 3H, OCH₂CH₃), 1.01 (d, 7 Hz, 12H, CH(CH₃)₂), 1.12 (s, 3H, olefin-CH₃), 1.60 (s, 3H, olefin-CH₃), 2.07 (sep, 7 Hz, 4 H, CH(CH₃)₂), 3.34 (q, 7 Hz, 2H, OCH₂CH₃), 3.92 (s, 1H, olefin CH), 6.86 (t, 8 Hz, 4H, *m*-phenyl), 7.07 (d, 8 Hz, 4H, *m*-aryl), 7.48 (t, 8 Hz, 2H, *p*-aryl), 8.31 (t, 8 Hz, 1H, *p*-pyr), 8.47 (t, 8 Hz, 2H, *p*-phenyl), 9.53 (d, 8Hz, 4H, *o*-phenyl), 12.70 (d, 8 Hz, 2H, *m*-pyr). ¹³C {¹H} NMR (benzene-*d*₆, 20 °C): δ = 13.6, 23.3, 24.1, 30.1, 63.6, 104.6, 108.6, 116.5, 120.6, 121.1, 123.1, 123.9, 124.2, 124.4, 128.1, 129.0, 131.5, 136.6, 160.6, 167.8, 168.1, 188.0.

General Procedure for Catalytic Olefin Hydrogenation. In a typical experiment, a thick walled glass vessel was charged with a solution containing 0.016 mmol of the desired iron compound in 0.65 g (7.72 mmol) of benzene-*d*₆ and a magnetic stir bar. The vessel was placed in a liquid nitrogen cooled cold well for 20 minutes. Once the solution was frozen, 0.081 g (0.63 mmol) of ethyl 3,3-dimethylacrylate was layered on the reaction mixture. The vessel was taken out of the dry box and transferred to a high vacuum line while continuously submerged in liquid nitrogen. Following evacuation of the dinitrogen atmosphere, 1 atm of dihydrogen was admitted at 80 K. The solution was then thawed and stirred and ambient temperature. After the desired reaction time, the vessel was vented of dihydrogen and exposed to air. Decomposed iron compound was removed by filtration through Celite and the filtrate collected into an NMR tube. Conversions were determined by integrating the olefinic methyl resonances of the substrate against the isopropyl methyl groups of the product.

REFERENCES

- ¹ (a) Pfaltz, A.; Drury, W. J. *Proc. Natl. Acad. Sci. USA* **2004**, *101*, 5723–5726. (b) Hoveyda, A. H.; Hird, A. W.; Kacprzynski, M. A. *Chem. Comm.* **2004**, 1779–1785. (c) Martin, R.; Buchwald, S. L. *Acc. Chem. Res.* **2008**, *41*, 1461–1473.
- ² de Bruin, B. *Eur. J. Inorg. Chem.* **2012**, 340–342.
- ³ Alyea, E. C.; Merrell, P. H. *Inorg. Met.-Org. Chem.* **1974**, *4*, 535–544.
- ⁴ (a) Small, B. M.; Brookhart, M. *J. Am. Chem. Soc.* **1998**, *120*, 7143–7144. (b) Small, B. L.; Brookhart, M.; Bennett, A. M. A. *J. Am. Chem. Soc.* **1998**, *120*, 4049–4050.
- ⁵ Britovsek, G. J. P.; Gibson, V. C.; Kimberley, B. S.; Maddox, S. J.; Solan, G. A.; White, A. J. P.; Williams, D. J. *Chem. Commun.* **1998**, 849–850.
- ⁶ Britovsek, G. J. P.; Bruce, M.; Gibson, V. C.; Kimberley, B. S.; Maddox, P. J.; Mastroianni, S.; McTavish, S. J.; Redshaw, C.; Solan, G. A.; Strömberg, S.; White, A. J. P.; Williams, D. J. *J. Am. Chem. Soc.* **1999**, *121*, 8728–8740.
- ⁷ Gibson, V. C.; Redshaw, C.; Solan, G. A. *Chem. Rev.* **2007**, *107*, 1745–1776.
- ⁸ Bianchini, C.; Mantovani, G.; Meli, A.; Migliacci, F.; Zanobini, F.; Laschi, F.; Sommazzi, A. *Eur. J. Inorg. Chem.* **2003**, 1620–1631.
- ⁹ Monfette, S.; Turner, Z. R.; Semproni, S. P.; Chirik, P. J. *J. Am. Chem. Soc.* **2012**, *accepted for publication*.
- ¹⁰ (a) Knijnenburg, Q.; Gambarotta, S.; Budzelaar, P. H. M. *Dalton Trans.* **2006**, 5442–5448. (b) Gibson, V. C.; Redshaw, C.; Solan, G. A. *Chem. Rev.* **2007**, *107*, 1745–1776 and references therein.
- ¹¹ Chirik, P. J. *Inorg. Chem.* **2011**, *50*, 9737–9740.
- ¹² Bart, S. C.; Lobkovsky, E.; Chirik, P. J. *J. Am. Chem. Soc.* **2004**, *126*, 13794–13807.
- ¹³ Trovitch, R. J.; Lobkovsky, E.; Bill, E.; Chirik, P. J. *Organometallics* **2008**, *27*, 1470–1478.
- ¹⁴ Bouwkamp, M. W.; Bowman, A. C.; Lobkovsky, E.; Chirik, P. J. *J. Am. Chem. Soc.* **2006**, *128*, 13340–13341.
- ¹⁵ Sylvester, K. T.; Chirik, P. J. *J. Am. Chem. Soc.* **2009**, *131*, 8772–8774.
- ¹⁶ Russell, S. K.; Lobkovsky, E.; Chirik, P. J. *J. Am. Chem. Soc.* **2011**, *133*, 8858–8861.
- ¹⁷ Tondreau, A. M.; Atienza, C. C. H.; Weller, K. J.; Nye, S. A.; Lewis, K. M.; Delis, J. G. P.; Chirik, P. J. *Science* **2012**, *335*, 567–570.
- ¹⁸ Archer, A.; Bouwkamp, M.; Cortez, M.-P.; Lobkovsky, E.; Chirik, P. J. *Organometallics* **2006**, *25*, 4269–4278.

- ¹⁹ Esteruelas, M. A.; López, A. M.; Méndez, L.; Oliván, M.; Oñate, E. *Organometallics* **2003**, *22*, 395–406.
- ²⁰ Archer, A. M. Masters Thesis, Cornell University, Ithaca, NY, 2006.
- ²¹ Kleigrew, N.; Steffen, W.; Blömker, T.; Kehr, G.; Fröhlich, R.; Wibbeling, B.; Erker, G.; Wasilke, J.-C.; Wu, G.; Bazan, G. C. *J Am Chem Soc* **2005**, *127*, 13955–13968.
- ²² Wile, B. M.; Trovitch, R. J.; Bart, S. C.; Tondreau, A. M.; Lobkovsky, E.; Milsman, C.; Bill, E.; Wieghardt, K.; Chirik, P. J. *Inorg. Chem.* **2009**, *48*, 4190–4200.
- ²³ Schmidt, R.; Welch, M. B.; Palackal, S. J.; Alt, H. G. *J. Mol. Catal. A: Chem.* **2002**, *179*, 155–173.
- ²⁴ Love, B. E.; Ren, J. *J. Org. Chem.* **1993**, *58*, 5556–5557.
- ²⁵ Trovitch, R. J.; Lobkovsky, E.; Bouwkamp, M. W.; Chirik, P. J. *Organometallics* **2008**, *27*, 6264–6278.
- ²⁶ Russell, S. K.; Darmon, J. M.; Lobkovsky, E.; Chirik, P. J. *Inorg. Chem.* **2010**, *49*, 2782–2792.
- ²⁷ (a) Vidyaratne, I.; Scott, J.; Gambarotta, S.; Budzelaar, P. H. M. *Inorg Chem* **2007**, *46*, 7040–7049. (b) Vidyaratne, I.; Gambarotta, S.; Korobkov, I.; Budzelaar, P. H. M. *Inorg Chem* **2005**, *44*, 1187–1189. (c) Turner, Z. R.; Chirik, P. J. *Unpublished results*.
- ²⁸ Knijnenburg, Q.; Gambarotta, S.; Budzelaar, P. H. M. *Dalton Trans.* **2006**, 5442–5448.
- ²⁹ Bart, S. C.; Chłopek, K.; Bill, E.; Bouwkamp, M. W.; Lobkovsky, E.; Neese, F.; Wieghardt, K.; Chirik, P. J. *J. Am. Chem. Soc.* **2006**, *128*, 13901–13912.
- ³⁰ Stieber, S. C. E.; Milsman, C.; Hoyt, J. M.; Turner, Z. R.; Finkelstein, K. D.; Wieghardt, K.; DeBeer, S.; Chirik, P. J. *Inorg. Chem.* **2012**, *51*, 3770–3785.
- ³¹ Bart, S. C.; Lobkovsky, E.; Bill, E.; Wieghardt, K.; Chirik, P. J. *Inorg. Chem.* **2007**, *46*, 7055–7063.
- ³² Trovitch, R. J.; Lobkovsky, E.; Bouwkamp, M. W.; Chirik, P. J. *Organometallics* **2008**, *27*, 6264–6278.
- ³³ Pangborn, A. B.; Giardello, M. A.; Grubbs, R. H.; Rosen, R. K.; Timmers, F. J. *Organometallics* **1996**, *15*, 1518–1520.
- ³⁴ Schmidt, R.; Welch, M. B.; Palackal, S. J.; Alt, H. G. *J. Mol. Catal. A: Chem.* **2002**, *179*, 155–173.
- ³⁵ Neese, F. *ORCA: an ab initio, DFT and Semiempirical Electronic Structure Package*, version 2.8, revision 2287; Institut für Physikalische und Theoretische Chemie, Universität Bonn: Bonn, Germany, Nov 2010.

- ³⁶ (a) Becke, A. D. *J. Chem. Phys.* **1986**, *84*, 4524–4529. (b) Becke, A. D. *J. Chem. Phys.* **1993**, *98*, 5648–5652. (c) Lee, C. T.; Yang, W. T.; Parr, R. G. *Phys. Rev. B.* **1998**, *37*, 785–789.
- ³⁷ Neese, F.; Solomon, E. I. In *Magnetism: From Molecules to Materials*; Miller, J. S., Drillon, M., Eds.; Wiley: New York, 2002; Vol. 4, p 345.
- ³⁸ (a) Schäfer, A.; Horn, H.; Ahlrichs, R. *J. Chem. Phys.* **1992**, *97*, 2571–2577. (b) Schäfer, A.; Huber, C.; Ahlrichs, R. *J. Chem. Phys.* **1994**, *100*, 5829–5835. (c) Weigend, F.; Ahlrichs, R. *Phys. Chem. Chem. Phys.* **2005**, *7*, 3297–3305.
- ³⁹ (a) Eichkorn, K.; Weigend, F.; Treutler, O.; Ahlrichs, R. *Theor. Chem. Acc.* **1997**, *97*, 119–124. (b) Eichkorn, K.; Treutler, O.; Öhm, H.; Häser, M.; Ahlrichs, R. *Chem. Phys. Lett.* **1995**, *240*, 283–290. (c) Eichkorn, K.; Treutler, O.; Öhm, H.; Häser, M.; Ahlrichs, R. *Chem. Phys. Lett.* **1995**, *242*, 652–660.
- ⁴⁰ (a) Neese, F.; Wennmohs, F.; Hansen, A.; Becker, U. *Chem. Phys.* **2009**, *356*, 98–109. (b) Kossmann, S.; Neese, F. *Chem. Phys. Lett.* **2009**, *481*, 240–243. (c) Neese, F. *J. Comput. Chem.* **2003**, *24*, 1740–1747.
- ⁴¹ Ginsberg, A. P. *J. Am. Chem. Soc.* **1980**, *102*, 111–117.
- ⁴² Noodleman, L.; Peng, C. Y.; Case, D. A.; Mouesca, J. M. *Coord. Chem. Rev.* **1995**, *144*, 199–244.
- ⁴³ Kirchner, B.; Wennmohs, F.; Ye, S.; Neese, F. *Curr. Opin. Chem. Biol.* **2007**, *11*, 134–141.
- ⁴⁴ Neese, F. *J. Phys. Chem. Solids* **2004**, *65*, 781–785.
- ⁴⁵ *Molekel*, Advanced Interactive 3D-Graphics for Molecular Sciences, available under <http://www.cscs.ch/molkel/>.
- ⁴⁶ Neese, F. *Inorg. Chim. Acta.* **2002**, *337*, 181–192.
- ⁴⁷ (a) Sinnecker, S.; Slep, L. D.; Bill, E.; Neese, F. *Inorg. Chem.* **2005**, *44*, 2245–2254. (b) Römelt, M.; Ye, S.; Neese, F. *Inorg. Chem.* **2009**, *48*, 784–785.

CHAPTER 5

APPLICATION OF ENANTIOPURE BIS(OXAZOLINE) IRON DIALKYL COMPLEXES

TOWARDS CATALYTIC, ASYMMETRIC KETONE HYDROSILYLATION*

5.1 Abstract

A series of bis(oxazoline) iron dialkyl complexes, (*S,S*)-(RBox)Fe(R')₂ (R = *i*Pr, R' = CH₂Si(CH₃)₃, CH₂C(CH₃)₃; R = *t*Bu, R' = CH₂Si(CH₃)₃; R = Ph, R' = CH₂C(CH₃)₃) was prepared from alkylation of the corresponding iron dihalide, (*S,S*)-(RBox)FeCl₂ with the appropriate organolithium reagent. Each iron dialkyl was assayed for the catalytic hydrosilylation of various ketones using PhSiH₃ as the stoichiometric reductant for direct comparison with the tridentate pyridine bis(oxazoline) derivatives. While not as active, efficient turnover was observed at 23 °C using 1 mol % of the iron precatalyst. The nature of the chiral auxiliary and the alkyl substituent were demonstrated to have little influence as low enantiomeric excesses (< 35%) were observed. Activation of the precatalyst by treatment with a equivalent of B(C₆F₅)₃ *in situ*, allowed for an increase in asymmetric induction for the hindered acetophenone derivatives, 1-mesitylethanone, and α-tetralone to 93 and 54% e.e., respectively.

5.2 Introduction

The hydrogenation of ketones and aldehydes by transition metal-catalyzed H₂ addition, transfer hydrogenation, or hydrosilylation followed by hydrolysis are well established methods for the preparation of primary and secondary alcohols,¹ and have been applied to the synthesis of

* Reproduced in part with permission from Tondreau, A. M.; Darmon, J. M.; Wile, B. M.; Floyd, S. K.; Lobkovsky, E.; Chirik, P. J. *Organometallics* **2009**, 28, 3928–3940. Copyright 2009 American Chemical Society.

fine chemicals, perfumes, and important intermediates in pharmaceutical synthesis.² Traditionally, precious metal catalysts, specifically ruthenium and rhodium, have been favored for these transformations due to their exceptional activity, substrate scope, chemo- and enantioselectivity. Two well known classes are Noyori's *trans*-Ru(diphosphine)(diamine)Cl₂ compounds³ and Shvo-type cyclopentadienyl ruthenium hydride complexes.⁴

A movement is currently under way to replace the expensive and toxic precious metals with cheaper and more environmentally benign base-metal alternatives.⁵ Amongst these, iron has taken a prominent role.⁶ Our group has recently demonstrated that iron catalysis can confer significant advantages over platinum catalysts for the anti-Markovnikov hydrosilylation of alkenes.⁷ In the area of asymmetric ketone reduction, many groups have described alternative, well-defined iron catalysts.⁸ For example, Morris and co-workers^{9,10} have described a dicationic Fe^{II} system featuring a terdentate diiminophosphine ligand that exhibits exceptional turnover frequencies (53–4800 h⁻¹) for the asymmetric transfer hydrogenation of ketones with synthetically useful e.e.'s (14–99%) (**Figure 5.1**). To date, this system remains the only iron

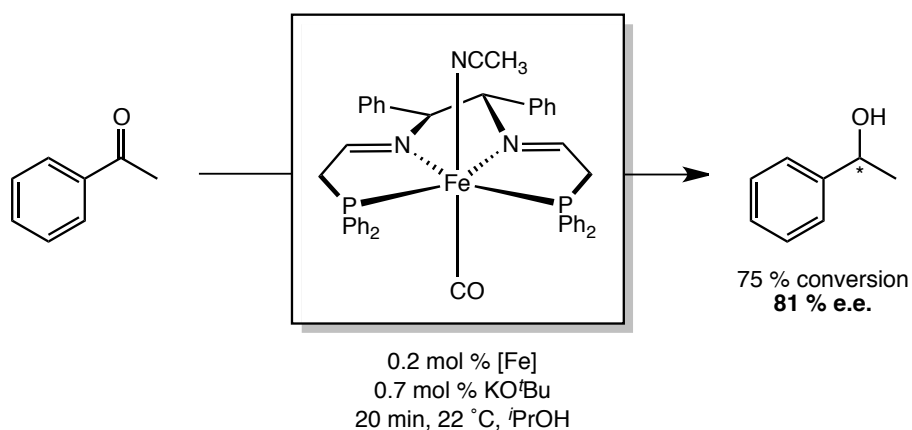


Figure 5.1. Morris' asymmetric transfer hydrogenation catalyst for the reduction of ketones.

catalyst to compete against platinum metal asymmetric transfer hydrogenation on the basis of activity and selectivity.

Our laboratory has used the method of Cámpora and co-workers¹¹ to prepare a family of alkyl- and aryl-substituted pyridine di(imine) iron dialkyl complexes that have demonstrated high activity for the hydrosilylation of aldehydes and ketones.¹² The silanes, PhSiH₃ and Ph₂SiH₂, were used as the stoichiometric reductants with low (0.1 mol %) catalyst loadings for the hydrosilylation of various acetophenone derivatives. Substituted enones were also tolerated. Tertiary silanes, while effective for the ill-defined Fe(OAc)₂ system,¹³ resulted in no turnover even upon heating to 65 °C with the pyridine di(imine) complexes.

The work of Tondreau *et al.*¹² inspired the synthesis of C₂ symmetric, *N,N*-bidentate bis(oxazoline) iron dialkyl complexes for assay in the catalytic, asymmetric hydrosilylation of ketones. Bis(oxazoline) ligands have been described as “privileged”^{14,15} due to their ability to engender high levels of enantiomeric induction for many different metal-catalyzed reactions.^{16,17} The capacity to readily prepare these ligands from their chiral precursors (amino alcohols) makes synthesis of a library of derivatives facile, which is advantageous as screening methods have dominated the search for effective chiral catalysts.^{15,18}

The first high-spin, tetrahedral bis(oxazoline) iron dialkyl complexes, (*S,S*)-(^{*t*}BuBox)Fe(R') (R' = CH₂Si(CH₃)₃, CH₂C₆H₅), were prepared by Bart *et al.*¹⁹ from the addition of an alkyl potassium or lithium reagent (*i.e.* KCH₂C₆H₅, LiCH₂Si(CH₃)₃) to the iron dichloride precursor. Described here is the synthesis and characterization of other members of the bis(oxazoline) iron dialkyl family and their application to the asymmetric hydrosilylation of ketones.

5.3 Synthesis and Characterization of Bis(oxazoline) Iron Dichloride and Iron Dialkyl Complexes

In order to probe the influence of the chiral auxiliary, the synthesis of two additional bis(oxazoline) ligands, (*S,S*)-^{*i*}PrBox and (*S,S*)-^{Ph}Box, and their iron dialkyl complexes were targeted. Following the procedure of Bart *et al.*¹⁹ the isopropyl and phenyl substituted bis(oxazoline) iron dichloride complexes, (*S,S*)-(^RBox)FeCl₂ (R = ^{*i*}Pr, Ph), were prepared as off-white solids in moderate yield (**Figure 6.2**). Each complex exhibited a magnetic moment of 4.7 μ_B as measured by a magnetic susceptibility balance, which is consistent with the high-spin, *d*⁶, *S* = 2 ground state description of the previously reported ^tBu substituted bis(oxazoline) iron dihalide.¹⁹ The complexes were also sufficiently soluble for analysis by ¹H NMR in benzene-*d*₆ solution at 22 °C. The spectrum of each complex exhibited paramagnetically shifted and broadened resonances consistent with molecular *C*₂ symmetry over a 40–75 ppm range.

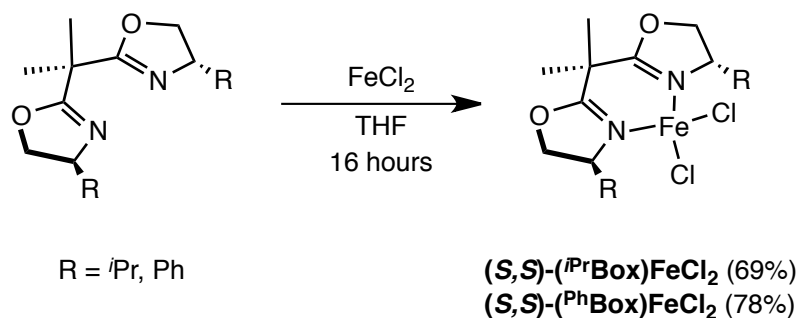


Figure 5.2. Synthesis of (*S,S*)-(^RBox)FeCl₂ (R = ^{*i*}Pr, Ph).

One advantage of the bis(oxazoline) ligand architecture is the ability to prepare ferrous dialkyl complexes with varying alkyl substituents. Many bi- and tridentate high-spin ferrous dichlorides have been reported to undergo reductive alkylation upon treatment with alkyl lithium reagents such as neopentyl lithium.^{19,20,21} Treatment with two equivalents of the corresponding

alkyl lithium reagents in diethyl ether furnished the dialkyl complexes, (S,S) - $(^R\text{Box})\text{Fe}(\text{R}')_2$ ($\text{R} = ^i\text{Pr}$, $\text{R}' = \text{CH}_2\text{Si}(\text{CH}_3)_3$, $\text{CH}_2\text{C}(\text{CH}_3)_3$; $\text{R} = \text{Ph}$, $\text{R}' = \text{CH}_2\text{C}(\text{CH}_3)_3$) as yellow solids in excellent yield (75–90% yield, **Figure 5.3**). Benzene- d_6 solution magnetic moments were measured for each complex and the observed values, between 4.8–4.8 μ_{B} , were consistent with the spin only value of four unpaired electrons. ^1H NMR spectra were collected for each complex in benzene- d_6 , and paramagnetically shifted and broadened resonances consistent with molecular C_2 symmetry were observed in a range of 70–80 ppm. This data was consistent with the experimentally measured quintet ground state.

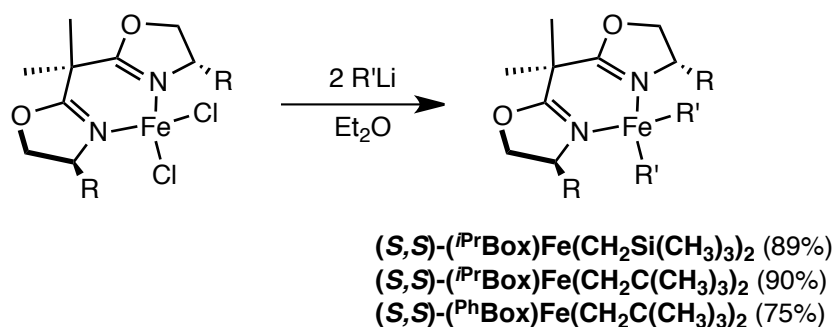


Figure 5.3. Synthesis of (S,S) - $(^R\text{Box})\text{Fe}(\text{R}')_2$ ($\text{R} = ^i\text{Pr}$, $\text{R}' = \text{CH}_2\text{Si}(\text{CH}_3)_3$, $\text{CH}_2\text{C}(\text{CH}_3)_3$; $\text{R} = \text{Ph}$, $\text{R}' = \text{CH}_2\text{C}(\text{CH}_3)_3$).

5.4 Catalytic, Asymmetric Hydrosilylation of Ketones

With this series of iron dialkyl complexes in hand, the catalytic, asymmetric hydrosilylation of ketones was explored. Initial screens demonstrated that the bis(oxazoline) iron dialkyl complexes were not as active as their pyridine bis(oxazoline) analogues, and required slightly higher catalyst loadings (1 mol % as compared to 0.3 mol %) in order to achieve similar turnover frequencies. Catalytic reactions (**Figure 6.4**) typically employed 0.40 M diethyl ether

solutions of the ketone substrate with 1 mol % of the iron dialkyl precatalyst. Two equivalents of PhSiH₃ (relative to substrate) were added with rapid stirring at 23 °C. The progress of each reaction was monitored by GC analysis of the silyl ether or the corresponding alcohol following basic hydrolysis, and enantioselectivities were determined from the resulting alcohols using chiral gas chromatography. The results of this study are presented in **Table 6.1**.

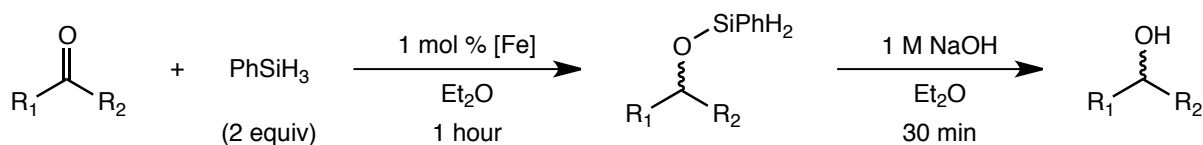
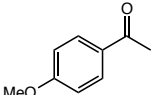
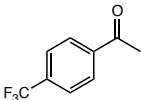
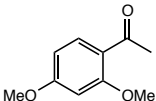
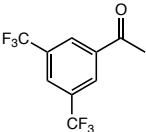
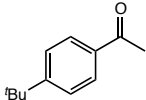
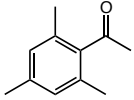
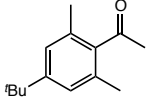
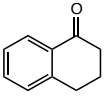
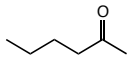


Figure 5.4. Conditions used for the catalytic, asymmetric hydrosilylation of ketones.

All of the bis(oxazoline) iron dialkyl complexes were very active for the hydrosilylation of several acetophenone derivatives. Introduction of electron donating, [OMe] and [^tBu] (entries 2 and 6), and electron withdrawing, [CF₃] (entry 3) groups into the *para*-position did not result in any significant difference in activity. Introduction of *ortho*- and *meta*-substituents (entries 4 and 5) also resulted in insignificant deviations from the activity observed with unsubstituted acetophenone. With few exceptions, all of the substrates were completely reduced in under an hour, corresponding to a turnover frequency of at least 330 h⁻¹. The two exceptions, 1-mesitylethanone and 1-(4-(*tert*-butyl)-2,6-dimethylphenyl)ethanone, entries 7 and 8, respectively, exhibited only modest conversion (< 20%) for each precatalyst screened, which is likely due to steric factors. For these two substrates, relatively minor differences were observed in conversion, suggesting that the chiral auxiliary has little to no effect on the efficiency of catalytic turnover. The only additional substrate examined, 2-hexenone (entry 10), also exhibited excellent conversion. Varying the iron alkyl substituents similarly had little to no effect on the

Table 5.1 Catalytic Ketone Hydrosilylation with (*S,S*)-(RBox)Fe(CH₂E(CH₃)₃)₂ Complexes.^a

Entry	Substrate	R = <i>i</i> Pr E = Si	R = <i>i</i> Pr E = C	R = <i>t</i> Bu E = Si	R = Ph E = C
1		99 (9)	99 (17)	99 (2)	99 (4)
2		99 (13)	97 (22)	99 (15)	97 (4)
3		99 (6)	89 (1)	98 (2)	94 (10)
4		99 (3)	98 (0)	99 (2)	96 (8)
5		99 (14)	99 (11)	99 (12)	99 (13)
6		98 (21)	98 (26)	99 (6)	94 (1)
7		11 (33)	1 (14)	18 (14)	3 (21)
8		14 (13)	1 (15)	1 (9)	3 (24)
9		95 (5)	96 (8)	86 (12)	96 (18)
10		98 (1)	97 (1)	97 (0)	97 (14)

^a Conversions are listed first in each column, followed by enantioselectivities below in parentheses. Conditions: 1 mol % [Fe], 1 equiv. of substrate, 2 equiv. of PhSiH₃, 1 hour, diethyl ether, 23 °C.

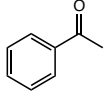
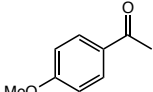
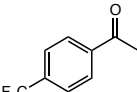
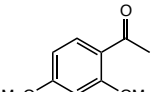
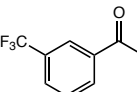
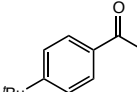
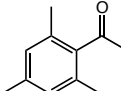
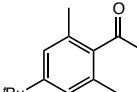
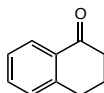
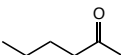
observed conversion.

Despite the observed activity of the bis(oxazoline) iron dialkyl complexes, modest to low enantiomeric excesses (< 35%) were observed regardless of the chiral auxiliary. Exceptions with specific substrate-catalyst combinations do exist; however, no systematic trends or variations in the data are apparent. Unfortunately, these data represent a synthetically ineffective strategy. Enantiomeric excesses observed when using the pyridine bis(oxazoline) analogues are typically higher (up to 50%); however, their synthetic utility is also questionable.²²

5.5 *In situ* Activation of Bis(oxazoline) Iron Dialkyl Complexes

Addition of the Lewis acidic, neutral borane, $B(C_6F_5)_3$, to metal dialkyl and alkyl species is a well-precedented strategy for promoting the activity of these complexes in catalytic processes.²³ Bart *et al.*¹⁹ has previously reported that addition of one equivalent of $B(C_6F_5)_3$ to (S,S) - $(tBuBox)Fe(CH_2Si(CH_3)_3)_2$ results in alkyl abstraction to yield the corresponding contact ion-pair, $[(S,S)$ - $(tBuBox)Fe(CH_2Si(CH_3)_3)_2][B(C_6F_5)_3(CH_2Si(CH_3)_3)]$ (**Figure 5.5**). In this study, one of the enantiopure bis(oxazoline) complexes, (S,S) - $(iPrBox)Fe(CH_2Si(CH_3)_3)_2$, was chosen as a representative example to screen the activity and enantioselectivity of the corresponding alkyl cation towards the asymmetric hydrogenation of ketones. For a typical experiment, 0.95 equivalents (*per equivalent iron*) of $B(C_6F_5)_3$ was added to the catalyst solution prior to addition of either ketone or silane in hopes of generating the contact ion-pair *in situ*. It was hoped that this would result in increased activity, amplify the chiral pocket, and result in an increase in enantiomeric excess. The results of this study are presented in **Table 5.2**.

Table 5.2. Catalytic Ketone Hydrosilylation with (S,S) - $(iPr)Box)Fe(CH_2Si(CH_3)_3)_2$ activated with $B(C_6F_5)_3$.^a

Entry	Substrate	(S,S) - $(iPr)Box)Fe(CH_2Si(CH_3)_3)_2$
1		99 (42)
2		99 (34)
3		98 (22)
4		97 (26)
5		99 (14)
6		98 (41)
7		16 (93)
8		1 (18)
9		99 (54)
10		99 (8)

^a Conversions are listed first in each column, followed by enantioselectivities below in parentheses. Conditions: 1 mol % [Fe], 1 mol % $B(C_6F_5)_3$, 1 equiv. of substrate, 2 equiv. of $PhSiH_3$, 1 hour, diethyl ether, 23 °C.

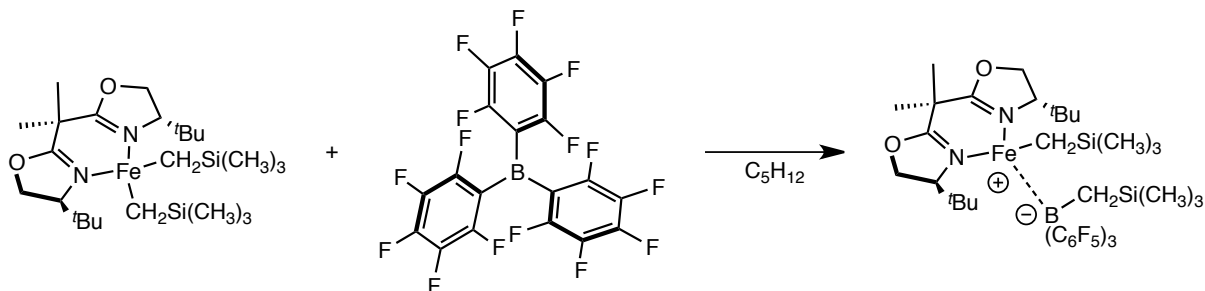


Figure 5.5. Alkyl abstraction of (S,S) - $(i\text{Bu})\text{Box}$ $\text{Fe}(\text{CH}_2\text{Si}(\text{CH}_3)_3)_2$ with $\text{B}(\text{C}_6\text{F}_5)_3$.

While *in situ* activation of the bis(oxazoline) iron dialkyl complex using $\text{B}(\text{C}_6\text{F}_5)_3$ typically resulted in higher levels of enantiomeric induction, significant differences in catalyst productivity were not observed. For example, unactivated and activated (S,S) - $(i\text{Pr})\text{Box}$ $\text{Fe}(\text{CH}_2\text{Si}(\text{CH}_3)_3)_2$ reduce both 1-mesitylethanone and 1-(4-(*tert*-butyl)-2,6-dimethylphenyl)ethanone (entries 7 and 8, respectively) to their corresponding alcohols in < 20% following work-up. Enantiomeric excesses, on the other hand, were equal to or profoundly better than those observed in the unactivated cases, and rivaled those observed for the analogous pyridine bis(oxazoline) iron dialkyl complex, (S,S) - $(i\text{Pr})\text{Pybox}$ $\text{Fe}(\text{CH}_2\text{Si}(\text{CH}_3)_3)_2$.²² For one ketone, 1-mesitylethanone (entry 7), the corresponding alcohol was obtained in 93% e.e. Attempts to increase the conversion with longer reaction times were unsuccessful, likely indicating a competitive catalyst deactivation pathway. Acetophenone and several other derivatives—*p-tert*-butylacetophenone and α -tetralone (entries 1, 6, and 9, respectively)—were obtained with moderate enantioselectivities of 42%, 41% and 54%, respectively.

5.6 Conclusions

Enantiopure bis(oxazoline) iron dialkyl complexes with various chiral auxiliaries and iron alkyl substituents have been prepared, characterized and screened as precatalysts for the

asymmetric hydrosilylation of ketones using PhSiH_3 as the stoichiometric reductant. The silyl ethers resulting from this process were then converted to the corresponding alcohols via a facile basic hydrolysis procedure. The bis(oxazoline) iron dialkyl complexes were not as active as their pyridine bis(oxazoline) iron dialkyl analogues; however, turnover frequencies corresponding to greater than 330 h^{-1} were observed for several substrates at $23 \text{ }^\circ\text{C}$ using 1 mol % of the iron complex. Low enantiomeric excesses were observed in all cases regardless of the chiral auxiliary and iron alkyl substituents used. Neutral borane, $\text{B}(\text{C}_6\text{F}_5)_3$ was added to activate a representative dialkyl complex *in situ* and generate the contact ion-pair, $[(S,S)\text{-}(i\text{PrBox})\text{Fe}(\text{CH}_2\text{Si}(\text{CH}_3)_3)_2][(\text{C}_6\text{F}_5)_3\text{B}(\text{CH}_2\text{Si}(\text{CH}_3)_3)]$, for screening as a precatalyst. Significantly higher levels of asymmetric induction were observed using this strategy, and in one case, 1-mesitylethanone, an enantiomeric excess of 93% was obtained.

5.7 *Experimental*

All air- and moisture-sensitive manipulations were carried out using standard vacuum line, Schlenk and cannula techniques or in an MBraun inert atmosphere dry box containing an atmosphere of purified nitrogen. Solvents for air- and moisture-sensitive manipulations were initially dried and deoxygenated using literature procedures.²⁴ Benzene- d_6 was purchased from Cambridge Isotope Laboratories and dried over 4 \AA molecular sieves. Bis(oxazoline) ligands,²⁵ $(S,S)\text{-}(t\text{BuBox})\text{FeCl}_2$, and $(S,S)\text{-}(t\text{BuBox})\text{Fe}(\text{CH}_2\text{SiMe}_3)_2$ were prepared according to literature procedures.²⁶ All aldehydes and ketones were purchased from commercial sources and were vacuum distilled from CaH_2 prior to use.

¹H NMR spectra were recorded on Varian Mercury 300, Inova 400 and 500 spectrometers operating at 299.76, 399.78 and 500.62 MHz, respectively. All ¹H NMR chemical shifts are reported relative to SiMe₄ using ¹H (residual) chemical shifts of the solvent as a secondary standard. ¹H NMR multiplicity and coupling constants are reported where applicable. Peak width at half height is given for paramagnetically broadened resonances, and all values were recorded at 21 °C unless otherwise noted. Solution magnetic moments were determined by Evans method²⁷ using a ferrocene standard and are the average value of at least three independent measurements. Magnetic susceptibility balance measurements were performed with a Johnson Matthey instrument that was calibrated with HgCo(SCN)₄. All solid state values were recorded at 21 °C unless otherwise noted. Elemental analyses were performed at Robertson Microlit Laboratories, Inc., in Madison, NJ.

Preparation of (S,S)-(iPrBox)FeCl₂. In a 100 mL round-bottom flask, a slurry of 0.227 g (1.79 mmol) FeCl₂ in 15 mL THF was prepared and a solution of 0.530 g (1.99 mmol) (S,S)-iPrBox in 30 mL of THF was added. After 16 h, the solvent was removed *in vacuo* to yield a white solid, which was triturated with pentane and collected by vacuum filtration to yield 0.484 g (69 %) of an off white solid. Analysis for C₁₅H₂₆Cl₂FeN₂O₂: Calcd C, 45.83; H, 6.67; N, 7.13. Found: C, 45.43; H, 6.42; N, 7.01. Magnetic susceptibility (magnetic susceptibility balance): μ_{eff} = 4.7 μ_B. ¹H NMR (benzene-*d*₆): δ = 14.22 (108.15 Hz, CMe₂), 5.06 (91.9 Hz, CH₂), 2.18 (77.0 Hz, CH₂), -13.27 (300.6 Hz, CHMe₂), -13.66 (67.1 Hz, CHMe₂), -21.7 (835.6 Hz, CH^{*i*}Pr), -46.1 (867.0 Hz, CHMe₂).

Preparation of (*S,S*)-(*i*PrBox)Fe(CH₂SiMe₃)₂. A slurry of 0.10 g (0.25 mmol) (*S,S*)-(*i*PrBox)FeCl₂ in approximately 5 mL diethyl ether and a solution of 0.048 g (0.51 mmol) LiCH₂SiMe₃ in 5 mL diethyl ether were independently prepared in separate 20 mL scintillation vials and chilled to -35 °C. The solution of alkyl lithium was then added dropwise to the cold slurry of iron dichloride and the reaction mixture became intense yellow. After stirring for 16 hours, the mixture was filtered through a pad of celite and the resulting solution concentrated *in vacuo* and yielded a yellow oil. The oil was triturated with pentane and 0.126 g (89 %) of an oily yellow solid was isolated. Recrystallization from pentane at -35 °C was used for additional purification. Analysis for C₂₃H₄₈FeN₂O₂Si₂: Calcd C, 55.62; H, 9.74; N, 5.64. Found: C, 55.34; H, 9.59; N, 5.82. Magnetic susceptibility (Evans, benzene-*d*₆): $\mu_{\text{eff}} = 4.8 \mu_{\text{B}}$. ¹H NMR (benzene-*d*₆): $\delta = 12.56$ (225 Hz, 18H, SiMe₃), 11.87 (200 Hz, 6H, CMe₂), -0.74 (396 Hz, 2H, CH₂), -1.10 (150 Hz, 2H, CH₂), -7.26 (279 Hz, 6H, CHMe₂), -13.88 (116 Hz, 6H, CHMe₂), -45.55 (1997 Hz, 2H, CH^{*i*}Pr), -50.00 (1639 Hz, 2H, CHMe₂).

Preparation of (*S,S*)-(*i*PrBox)Fe(CH₂CMe₃)₂. A procedure similar to that for (*S,S*)-(*i*PrBox)Fe(CH₂SiMe₃)₂ was used with 0.040 mg (0.51 mmol) of LiCH₂CMe₃ and 0.10 g (0.25 mmol) of (*S,S*)-(*i*PrBox)FeCl₂ and yielded 0.106 g (90 %) of a crystalline yellow solid. Analysis for C₂₅H₄₈FeN₂O₂: Calcd C, 64.64; H, 10.42; N, 6.03. Found: C, 64.42; H, 10.57; N, 6.27. Magnetic susceptibility (Evans, benzene-*d*₆): $\mu_{\text{eff}} = 4.8 \mu_{\text{B}}$. ¹H NMR (benzene-*d*₆): $\delta = 26.24$ (370 Hz, 18H, CMe₃), 12.02 (137 Hz, 6H, CMe₂), -0.06 (147 Hz, 2H, CH₂), 1.65 (101 Hz, 2H, CH₂), -8.10 (262 Hz, 6H, CHMe₂), -14.34 (119 Hz, 6H, CHMe₂), -50.10 (1009 Hz, 2H, CH^{*i*}Pr), -54.08 (1240 Hz, 2H, CHMe₂).

Preparation of (*S,S*)-(PhBox)FeCl₂. A procedure similar to that for (*S,S*)-(iPrBox)FeCl₂ was used with 0.176 g (1.39 mmol) FeCl₂ and 0.490 g (1.47 mmol) of (*S,S*)-PhBox and yielded 0.526 g (78%) of an off white solid. Analysis for C₂₁H₂₂Cl₂FeN₂O₂: Calcd C, 54.69; H, 4.81; N 6.07. Found: C, 54.35; H, 4.62; N, 5.90. Magnetic susceptibility (magnetic susceptibility balance): $\mu_{\text{eff}} = 4.7 \mu_{\text{B}}$. ¹H NMR (benzene-*d*₆): $\delta = 13.8$ (123.4 Hz, *CMe*₂), 6.3 (119.4 Hz, *p-aryl*), 0.2 (63.7 Hz, *m-aryl*), -13.3 (389.9 Hz, *o-aryl*), -16.8 (891.2 Hz, *CHPh*), methylene resonances not located.

Preparation of (*S,S*)-(PhBox)Fe(CH₂CMe₃)₂. A procedure similar to that for (*S,S*)-(iPrBox)Fe(CH₂SiMe₃)₂ was used with 0.034 g (0.44 mmol) of LiCH₂CMe₃ and 0.10 g (0.22 mmol) (*S,S*)-(PhBox)FeCl₂ and yielded 0.087 g (75 %) of a crystalline orange-yellow product. Purification was accomplished following recrystallization from pentane at -35 °C. Analysis for C₃₁H₄₄FeN₂O₂: Calcd C, 69.92; H, 8.33; N, 5.26. Found: C, 69.53; H, 8.18; N, 5.43. Magnetic susceptibility (Evans, benzene-*d*₆): $\mu_{\text{eff}} = 4.9 \mu_{\text{B}}$. ¹H NMR (benzene-*d*₆): $\delta = 48.64$ (342 Hz, 4H, *o/m-aryl*), 27.35 (346 Hz, 18H, *CMe*₃), 23.27 (155 Hz, 2H, *p-aryl*), 11.65 (133 Hz, 6H, *CMe*₂), -1.44 (104 Hz, 2H, *CH*₂), -3.70 (92 Hz, 2H, *CH*₂), -11.52 (299 Hz, 4H, *o/m-aryl*), -15.68 (165 Hz, 2H, *CHAr*).

General Procedure for Catalytic Hydrosilylation with Box Dialkyls. A scintillation vial was charged with 1 mL of a solution of 4×10^{-3} M catalyst precursor in the desired solvent, followed by the addition of 4×10^{-4} moles of the substrate. To the stirring solution was added 8×10^{-4} moles of PhSiH₃. The reaction was stirred for the allotted time, typically one hour, after which

time the vial was removed from the drybox and the reaction was quenched by the addition of moist diethyl ether. The reaction mixtures were stirred with an equal volume 1 M NaOH for approximately 30 minutes. The organic layer was separated the aqueous layer extracted twice with diethyl ether. The organic layers were combined and dried over MgSO₄. Conversions and enantiomeric excesses were determined by GC analysis.

Characterization of Hydrosilylation Products by Gas Chromatography. Gas chromatography for the diphenyl silyl ethers was performed on a Shimadzu GC-2010 gas chromatograph. GC analyses were performed using a Restek 15 m x 0.25 mm RTX-5 5% diphenyl-95% dimethyl polysiloxane column with a film thickness 0.25 μ m. The following temperature program was used: 30 °C, 3 min; 10 °C/min to 80 °C; and 15 °C/min to 245 °C, 5 min. The corresponding alcohols were analyzed on a Supelco 30 m x 0.25 mm BETA DEX 120 capillary column. Temperature programs for the various alcohols are as follows:

1-Phenylethanol. 60 °C; 5 °C/min to 100 °C; and 15 °C/min to 150 °C, 5 min. Enantiomer retention times: 13.8 min (R), 13.97 min

(1-(4-methoxyphenyl)ethanol. 80 °C; 5 °C/min to 140 °C, 5 min; and 15 °C/min to 170 °C, 10 min. Enantiomer retention times: 21.40 min, 21.59 min

(1-(4-(trifluoromethyl)phenyl)ethanol. 80 °C; 5 °C/min to 140 °C, 5 min; and 15 °C/min to 170 °C, 10 min. Enantiomer retention times: 14.54 min, 15.11 min.

(1-(2,4-dimethoxyphenyl)ethanol. 80 °C; 5 °C/min to 140 °C, 10 min; and 15 °C/min to 170 °C, 10 min. Enantiomer retention times: 33.18 min, 33.46 min.

(1-(3,5-bis(trifluoromethyl)phenyl)ethanol. 80 °C; 5 °C/min to 100 °C, 5 min; 5 °C/min to 100 °C, 5 min; and 15 °C/min to 170 °C, 8 min. Enantiomer retention times: 14.19 min, 14.88 min.

1-(4-*tert*-butylphenyl)ethanol. 80 °C; 5 °C/min to 140 °C, 5 min; and 15 °C/min to 170 °C, 10 min. Enantiomer retention times: 14.54 min, 15.11 min.

1-(2,4,6-trimethylphenyl)ethanol. 80 °C; 5 °C/min to 110 °C, 10 min; 5 °C/min to 140 °C, 30 min; 15 °C/min to 160 °C, 15 min. Enantiomer retention times: 41.95 min, 46.85 min.

1-(2,6-dimethyl-4-*tert*-butylphenyl)ethanol. 80 °C; 5 °C/min to 110 °C, 10 min; 5 °C/min to 140 °C, 30 min; 15 °C/min to 160 °C, 15 min. Enantiomer retention times: 63.11 min, 63.89 min.

1,2,3,4-tetrahydronaphthalen-1-ol. 80 °C, 10 min; 5 °C/min to 110 °C, 8 min; and 15 °C/min to 160 °C, 11 min. Enantiomer retention times: 28.29 min, 28.53 min.

2-Hexanol. 60 °C, 10 min; 2 °C/min to 70 °C, 5 min; and 15 °C/min to 160 °C, 5 min. Enantiomer retention times: 16.22 min, 16.53 min.

REFERENCES

- ¹ (a) Nishiyama, H. In *Transition Metals for Organic Synthesis*; Beller, M., Bolm, C., Ed.; Wiley-VCH: Weinheim, 2004. (b) Ohkuma, T.; Noyori, R. In *Comprehensive Asymmetric Catalysis*; Jacobsen, E. N., Pfaltz, A., Yamamoto, H. Eds.; Springer: Berlin, 1999.
- ² For recent reviews see: (a) Noyori, R. *Angew. Chem., Int. Ed.* **2002**, *41*, 2008–2022. (b) Muñiz, K. *Angew. Chem., Int. Ed.* **2005**, *44*, 6622–6627. (c) Samec, J. S. M.; Bäckvall, J.-E.; Andersson, P. G.; Brandt, P. *Chem. Soc. Rev.* **2006**, *35*, 237–248. (d) Ikariya, T.; Blacker, A. J. *Acc. Chem. Res.* **2007**, *40*, 1300–1308. (e) Blaser, H.-U.; Studer, M. *Acc. Chem. Res.* **2007**, *40*, 1348–1356. (f) Klingler, F. D. *Acc. Chem. Res.* **2007**, *40*, 1367–1376. (g) Morris, R. H. *Chem. Soc. Rev.* **2009**, *38*, 2282.
- ³ Sandoval, C. A.; Ohkuma, T.; Muñiz, K.; Noyori, R. *J. Am. Chem. Soc.* **2003**, *125*, 13490–13503.
- ⁴ (a) Shvo, Y.; Czarkie, D.; Rahamim, Y.; Chodosh, D. F. *J. Am. Chem. Soc.* **1986**, *108*, 7400–7402. (b) Casey, C. P.; Singer, S. W.; Powell, D. R.; Hayashi, R. K.; Kavana, M. *J. Am. Chem. Soc.* **2001**, *123*, 1090–1100. (c) Casey, C. P.; Johnson, J. B. *J. Am. Chem. Soc.* **2005**, *127*, 1883–1894. (d) Casey, C. P.; Beetner, S. E.; Johnson, J. B. *J. Am. Chem. Soc.* **2008**, *130*, 2285–2295. (e) Johnson, J. B.; Bäckvall, J.-E. *J. Org. Chem.* **2003**, *68*, 7681–7684. (f) Samec, J. S. M.; Éll, A. H.; Åberg, J. B.; Privalov, T.; Eriksson, L.; Bäckvall, J.-E. *J. Am. Chem. Soc.* **2006**, *128*, 14293–14305. (g) Privalov, T.; Samec, J. S. M.; Bäckvall, J.-E. *Organometallics* **2007**, *26*, 2840–2848.
- ⁵ Chirik, P. J.; Wieghardt, K. *Science* **2010**, *327*, 794–795.
- ⁶ For recent reviews on iron catalysis see: (a) Bolm, C.; Legros, J.; Paith, J. L.; Zani, L. *Chem. Rev.* **2004**, *104*, 6217–6254. (b) Correa, A.; Mancheño, O. G.; Bolm, C. *Chem. Soc. Rev.* **2008**, *37*, 1108–1117. (c) Sherry, B. D.; Fürstner, A.; *Acc. Chem. Res.* **2008**, *41*, 1500–1511. (d) Bauer, E. B. *Curr. Org. Chem.* **2008**, *12*, 1341–1369. (e) Gaillard, S.; Renaud, J. L. *ChemSusChem.* **2008**, *1*, 505–509. (f) Sarhan, A. A. O.; Bolm, C. *Chem. Soc. Rev.* **2009**, *38*, 2730–2744. (g) Czaplik, W. M.; Mayer, M.; Cvengros, J.; von Wangelin, J. *ChemSusChem.* **2009**, *2*, 396–417. (h) Liu, L. X. *Curr. Org. Chem.* **2010**, *14*, 1099–1126. (i) Nakazawa, H.; Itazaki, M. *Top. Organomet. Chem.* **2011**, *33*, 27–81. (j) Junge, K.; Schröder, K.; Beller, M. *Chem. Commun.* **2011**, *47*, 4849–4859. (k) Kandepi, V. V. K. M.; Cardoso, J. M. S.; Peris, E.; Royo, B. *Organometallics* **2010**, *29*, 2777–2782.
- ⁷ Tondreau, A. M.; Atienza, C. C. H.; Weller, K. J.; Nye, S. A.; Lewis, K. M.; Delis, J. G. P.; Chirik, P. J. *Science* **2012**, *335*, 567–570.

- ⁸ (a) Casey, C. P.; Guan, H. *J. Am. Chem. Soc.* **2007**, *129*, 5816–5817. (b) Casey, C. P.; Guan, H. *J. Am. Chem. Soc.* **2009**, *131*, 2499–2507. (c) Bullock, R. M.; *Angew. Chem., Int. Ed.* **2007**, *46*, 7360–7363. (d) Enthaler, S.; Erre, G.; Tse, M. K.; Junge, K.; Beller, M. *Tetrahedron Lett.* **2006**, *47*, 8095–8099. (e) Enthaler, S.; Hagemann, B.; Erre, G.; Junge, K.; Beller, M. *Chem. Asian J.* **2006**, *1*, 598–604. (f) Enthaler, S.; Spilker, B.; Erre, G.; Junge, K.; Tse, M. K.; Beller, M. *Tetrahedron* **2008**, *64*, 3867–3876. (g) Buchard, A.; Heuclin, H.; Auffrant, A.; Le Goff, X. F.; Le Floch, P. *Dalton Trans.* **2009**, 1659–1667.
- ⁹ Mikhailine, A.; Lough, A. J.; Morris, R. H. *J. Am. Chem. Soc.* **2009**, *131*, 1394–1395.
- ¹⁰ Mikhailine, A. A.; Morris, R. H. *Inorg. Chem.* **2010**, *49*, 11039–11044.
- ¹¹ Cámpora, J.; Naz, A. M.; Palma, P.; Álvarez, E.; Reyes, M. L. *Organometallics* **2005**, *24*, 4878–4881.
- ¹² Tondreau, A. M.; Lobkovsky, E.; Chirik, P. J. *Org. Lett.* **2008**, *10*, 2789–2792.
- ¹³ (a) Nishiyama, H.; Furuta, A. *Chem. Comm.* **2007**, 760–762. (b) Furuta, A.; Nishiyama, H. *Tet. Lett.* **2008**, *49*, 110–113. (c) Shaikh, N. S.; Junge, K.; Beller, M. *Org. Lett.* **2007**, *9*, 5429–5432. (d) Shaikh, N. S.; Enthaler, S.; Junge, K.; Beller, M. *Angew. Chem. Int. Ed.* **2008**, *47*, 2497–2501.
- ¹⁴ Yoon, T. P.; Jacobsen, E. N. *Science* **2003**, *299*, 1691–1693.
- ¹⁵ Pfaltz, A.; Drury, W. J. *Proc. Natl. Acad. Sci. USA* **2004**, *101*, 5723–5726.
- ¹⁶ Pfaltz, A. *Acc. Chem. Res.* **1993**, *26*, 339–345.
- ¹⁷ Ghosh, A.; Packiarajan, M.; Cappiello, J. *Tetrahedron: Asymmetry* **1998**, *9*, 1–45.
- ¹⁸ Hoveyda, A. H.; Hird, A. W.; Kacprzynski, M. A. *Chem. Comm.* **2004**, 1779–1785.
- ¹⁹ Bart, S. C.; Hawrelak, E.; Schmisser, A.; Lobkovsky, E. *Organometallics* **2004**, *23*, 237–246.
- ²⁰ Bouwkamp, M. W.; Bart, S. C.; Hawrelak, E. J.; Trovitch, R. J.; Lobkovsky, E.; Chirik, P. J. *Chem. Comm.* **2005**, 3406–3408.
- ²¹ Fernández, I.; Trovitch, R. J.; Lobkovsky, E.; Chirik, P. J. *Organometallics* **2008**, *27*, 109–118.
- ²² Tondreau, A. M.; Darmon, J. M.; Wile, B. M.; Floyd, S. K.; Lobkovsky, E.; Chirik, P. J. *Organometallics* **2009**, *28*, 3928–3940.
- ²³ Chen, E. Y. X.; Marks, T. J. *Chem. Rev.* **2000**, *100*, 1391–1434.
- ²⁴ Pangborn, A.B.; Giardello, M.A.; Grubbs, R.H.; Rosen, R.K.; Timmers, F.J. *Organometallics* **1996**, *15*, 1518–1520.
- ²⁵ Cornejo, A.; Fraile, J. M.; García, J. I.; Gil, M. J.; Martínez-Merino, V.; Mayoral, J. A.; Pires, E.; Villalba, I. *Synlett* **2005**, *15*, 2321–2324.

²⁶ Bart, S. C.; Hawrelak, E. J.; Schmisser, A. K.; Lobkovsky, E.; Chirik, P. J. *Organometallics* **2004**, *23*, 237–246.

²⁷ Sur, S. K. *J. Magn. Res.* **1989**, *82*, 169–173.

APPENDIX A
PRELIMINARY INVESTIGATIONS

A.1 Reduced *para*-Substituted Pyridine Di(imine) Cobalt Complexes

Pyridine di(imine) cobalt complexes have been the subject of many investigations over the course of the last two decades stemming from the independent reports of Brookhart¹ and Gibson^{2,3} describing the base metal catalyzed polymerization of ethylene upon activation with methylaluminoxane (MAO). Inspired by the preparation of *para*-substituted pyridine di(imine) ligands (**Chapter 1**), the electronic structure and reactivity of reduced pyridine di(imine) cobalt complexes featuring one of these chelates, 4-Me₂N-*i*PrPDI (4-Me₂N-*i*PrPDI = 2,6-(2,6-*i*Pr₂-C₆H₃N=CCH₃)₂-4-Me₂N-C₅H₂N) was explored. Complexation of 4-Me₂N-*i*PrPDI with cobalt dichloride was achieved by stirring the two compound in THF for 12–24 hours at 23 °C, and yielded (4-Me₂N-*i*PrPDI)CoCl₂ as a brown-yellow solid in excellent yields (99%, **Figure A.1.1**). The cobalt dihalide exhibited an $S = 3/2$ ground state, consistent with a high-spin d^7 configuration, and was characterized by ¹H NMR spectroscopy in chloroform-*d*₁ at 22 °C. The ¹H NMR spectrum exhibited 8 paramagnetically broadened resonances over a 250 ppm range.

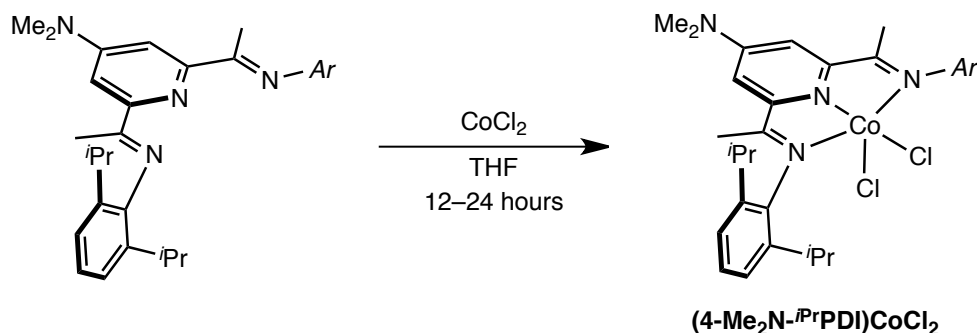


Figure A.1.1. Synthesis of (4-Me₂N-*i*PrPDI)CoCl₂.

Gal⁴ and Gibson⁵ have independently reported the synthesis of the diamagnetic pyridine

di(imine) cobalt alkyl complexes from the sequential treatment of the cobalt dihalide precursor with one equivalent of methyllithium followed by one equivalent of the appropriate alkyl lithium or magnesium reagent. Performing the same procedure with one equivalent of alkyl lithium reagent resulted in reduction of the cobalt dihalide to give the pyridine di(imine) cobalt monochloride, (^{Ar}PDI)CoCl.⁴ The ¹H NMR spectra of these complexes featured chemical shift values for the in-plane protons (*para*-pyridine and imine methyl) that significantly deviated from their diamagnetic reference values. This phenomenon was attributed to a thermal population of a triplet excited state, and was later verified in our laboratory by studying the spin-crossover behavior of *N*-alkyl substituted pyridine di(imine) cobalt halide complexes.^{6,7} Analysis of these complexes by ¹H NMR spectroscopy and density functional theory revealed that the formally low-spin Co(I) complexes were redox-active, and were actually low-spin Co(II) centers ($S = \frac{1}{2}$) antiferromagnetically coupled to a pyridine di(imine) radical anion, ^{Ar}PDI¹⁻ ($S = \frac{1}{2}$).⁶

The pyridine di(imine) cobalt monomethyl complex, (4-Me₂N-ⁱPrPDI)Co(CH₃) was prepared as a diamagnetic, blue-green solid in good yield (70%) from treatment of a thawing diethyl ether slurry of (4-Me₂N-ⁱPrPDI)CoCl₂ with two equivalents of methyllithium (**Figure A.1.2**). As expected, the benzene-*d*₆ ¹H NMR spectrum was consistent with solution C_{2v} molecular symmetry in solution, and exhibited signs of a thermally accessible triplet excited state. The imine methyl resonance was located upfield at -1.84 ppm, one of the most upfield shifted resonances observed for a pyridine di(imine) cobalt methyl complex, and is suggestive of a lower energy singlet-triplet gap.⁶ For comparison, the ¹H NMR chemical shifts of the in-plane protons of (4-Me₂N-ⁱPrPDI)Co(CH₃) and (ⁱPrPDI)Co(CH₃) are reported in **Table A.1.1**. These observations are consistent with the modest change in energy imparted by the *para*-substituent as

observed in the pyridine di(imine) iron complexes (**Chapter 1**) and predicted by DFT.⁸

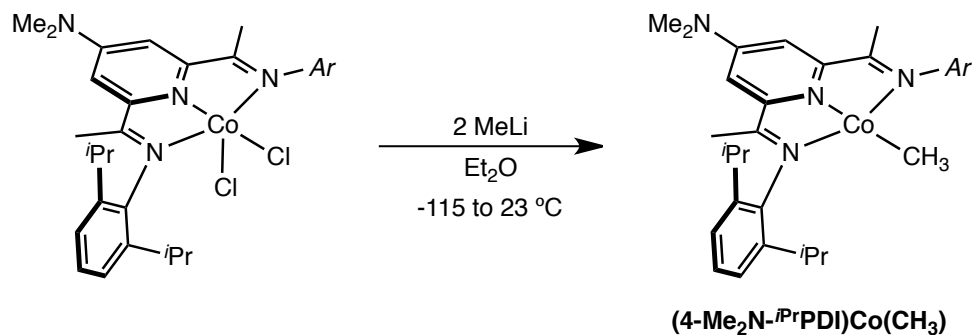


Figure A.1.2. Synthesis of (4-Me₂N-ⁱPrPDI)Co(CH₃).

Table A.1.1. ¹H NMR chemical shifts (ppm) of the in-plane pyridine di(imine) hydrogens of (4-R-ⁱPrPDI)Co(CH₃) collected in benzene-*d*₆ at 23 °C. Free ligand reference values are provided in parentheses.

Complex	<i>m</i> -pyr	imine CH ₃
(ⁱ PrPDI)Co(CH ₃) ^a	7.86 (8.51)	-1.15 (2.28)
(4-Me ₂ N- ⁱ PrPDI)Co(CH ₃)	8.15 (8.04)	-1.84 (2.4)

^a Data from reference 4.

Gibson^{9,10} and Gal¹¹ independently reported that addition of H₂ to a pyridine di(imine) cobalt alkyl, (ⁱPrPDI)Co(R) resulted in liberation of the corresponding alkane and formation of a new diamagnetic product assigned as the cobalt hydride, (ⁱPrPDI)Co(H). Gibson and co-workers were examining the role of the hydride in the context of β-hydrogen transfer as a model for chain transfer processes in polymerization and oligomerization catalysis,^{9,10} while Gal and co-workers were interested in using the pyridine di(imine) cobalt alkyl complexes as precatalysts for olefin hydrogenation.¹¹ The benzene-*d*₆ ¹H NMR spectrum of the putative hydride was similar to that of the alkyls; however, a hydride resonance was not observed. This is not unusual for cobalt hydrides,¹² and is most likely a result of fast relaxation on the NMR timescale (*I* = 7/2). The only other experimental evidence for a cobalt hydride was a band in the infrared spectrum at 2092 cm⁻¹,^{9,10} which was later assigned as an N₂ stretch in the neutral cobalt dinitrogen compound,

$(i\text{PrPDI})\text{Co}(\text{N}_2)$.¹³

The addition of 1 atmosphere of H_2 to a benzene- d_6 solution of $(4\text{-Me}_2\text{N-}i\text{PrPDI})\text{Co}(\text{CH}_3)$ (25 mM) was monitored by ^1H NMR spectroscopy. The gradual appearance of methane and a new diamagnetic, C_{2v} symmetric product assigned as $(4\text{-Me}_2\text{N-}i\text{PrPDI})\text{Co}(\text{H})$ was observed over the course of 1–2 hours (**Figure A.1.3**) at 23 °C. This contrasts the behavior of $(i\text{PrPDI})\text{Co}(\text{CH}_3)$, which rapidly extrudes methane with concomitant formation of the putative hydride. The benzene- d_6 ^1H NMR spectra of $(4\text{-Me}_2\text{N-}i\text{PrPDI})\text{Co}(\text{CH}_3)$ and $(4\text{-Me}_2\text{N-}i\text{PrPDI})\text{Co}(\text{H})$ are presented in **Figure A.1.4**. Consistent with previous observations,^{9–11} the imine methyl resonance shifts upfield to -2.43 ppm.

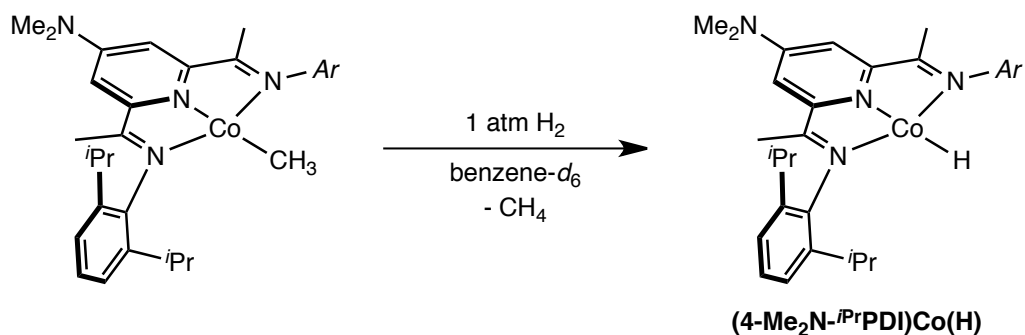


Figure A.1.3. In situ synthesis of $(4\text{-Me}_2\text{N-}i\text{PrPDI})\text{Co}(\text{H})$.

Rapid handling of a benzene- d_6 solution of $(4\text{-Me}_2\text{N-}i\text{PrPDI})\text{Co}(\text{H})$ under 1 atmosphere of N_2 allowed for observation of an absorption at 2125 cm^{-1} which is different from the neutral cobalt dinitrogen compound, $(4\text{-Me}_2\text{N-}i\text{PrPDI})\text{Co}(\text{N}_2)$ (vide infra), and has tentatively been assigned as the Co–H band. Attempts to prepare the cobalt deuteride were unsuccessful and the band at 2125 cm^{-1} remained. Two possibilities are consistent with these observations: the absorption may correspond to a cobalt dinitrogen complex, or rapid exchange with the isopropyl methyl groups results in formation of the cobalt hydride. Scrambling of the isotopic label into

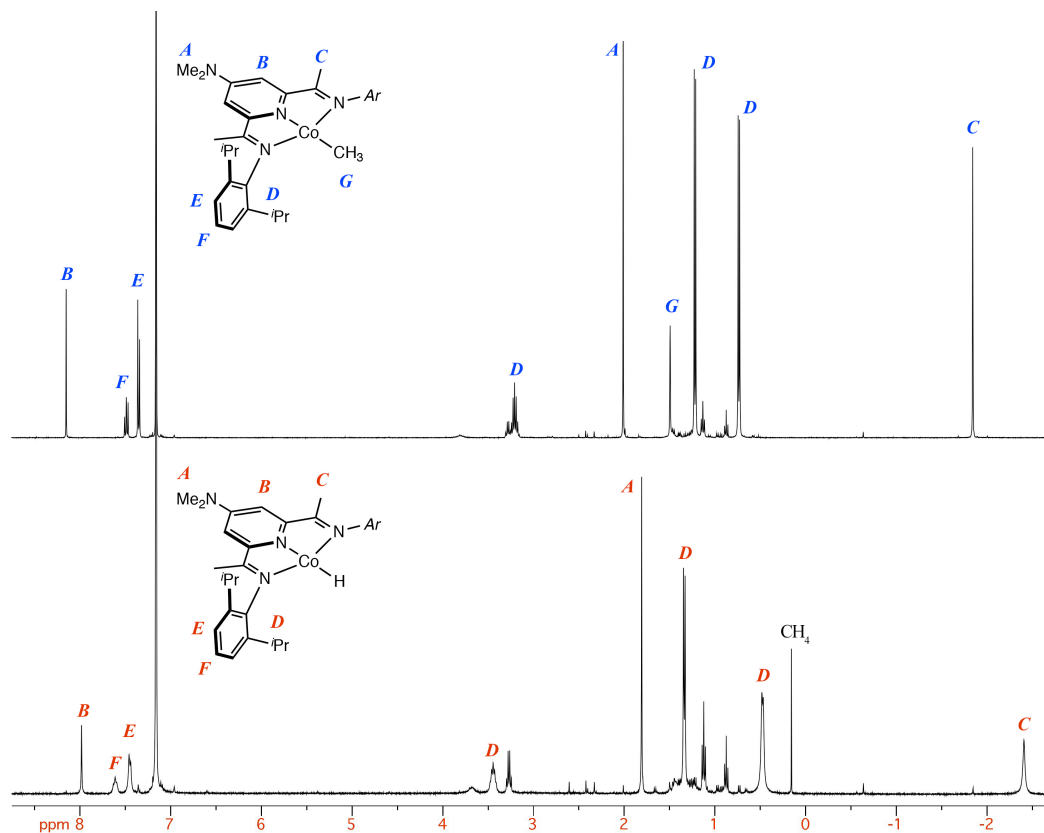


Figure A.1.4. Benzene- d_6 ^1H NMR spectra of $(4\text{-Me}_2\text{N-}i\text{PrPDI})\text{Co}(\text{CH}_3)$ (top) and $(4\text{-Me}_2\text{N-}i\text{PrPDI})\text{Co}(\text{H})$ (bottom) at 22 °C.

both isopropyl methyl groups was confirmed by ^2H NMR spectroscopy in benzene. C–H activation by pyridine di(imine) cobalt hydride complexes is well preceded, and several cyclometallated, C_1 symmetric pyridine di(imine) cobalt complexes have been prepared and crystallographically characterized upon upon addition of H_2 to the corresponding alkyl.¹⁴

Single crystals of $(4\text{-Me}_2\text{N-}i\text{PrPDI})\text{Co}(\text{H})$ suitable for X-ray diffraction (Mo $K\alpha$ radiation, $\lambda = 0.71073 \text{ \AA}$) precipitated from benzene- d_6 solution as clear, light green plates during the reaction of $(4\text{-Me}_2\text{N-}i\text{PrPDI})\text{Co}(\text{CH}_3)$ with H_2 . The asymmetric unit contained one half of the molecule. The hydride was located and refined isotropically with no distance or geometry constraints. A representation of the solid-state structure is presented in **Figure A.1.5**, and selected metrical parameters are reported in **Table A.1.2**. The geometry about cobalt is best described as

idealized square planar, with a cobalt–hydride bond length of 1.55 Å. The metrical parameters of the pyridine di(imine) chelate are consistent with a PDI¹⁻ designation, demonstrating that there is no significant difference between the electronic structure of the monoalkyls and the hydride.

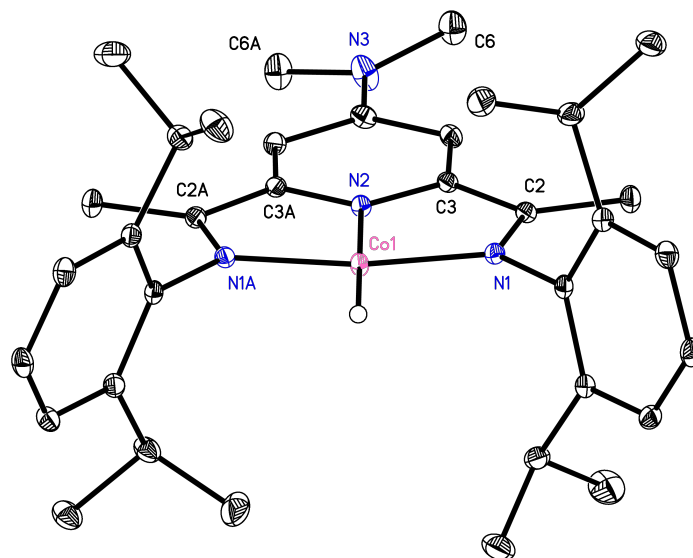


Figure A.1.5. Solid-state structure of (4-Me₂N-*i*PrPDI)Co(H) at 30% probability ellipsoids. Hydrogen atoms omitted for clarity.

Table A.1.2. Selected bond distances (Å) and angles (°) for (4-Me₂N-*i*PrPDI)Co(H).

Co(1)–N(1)	1.8820(12)	N(1)–C(2)	1.3335(18)
Co(1)–N(2)	1.8256(17)	C(2)–C(3)	1.4471(19)
Co(1)–H	1.55		
N(1)–Co(1)–N(2)	81.21 (4)		

Given the differences in the hydrogenation activity with 1,1-diphenylethylene for the pyridine di(imine) and pyridine di(carbene) iron dinitrogen complexes (**Chapter 1** and **Chapter 2**, respectively), the reactivity of (4-Me₂N-*i*PrPDI)Co(H) and 1,1-diphenylethylene was investigated. Addition of one equivalent of 1,1-diphenylethylene to a 25 mM solution of (4-Me₂N-*i*PrPDI)Co(H) under 1 atmosphere of dinitrogen did not result in immediate formation of

the primary or tertiary alkyl. Heating the solution to 65 °C for one week resulted in net hydrogenation of 1,1-diphenylethylene and smooth conversion to a C_s symmetric product identified as (4-Me₂N-^{*i*}PrPIEA)Co(N₂) (**Figure A.1.6**). This assignment was based upon the characteristic vinylic resonances in the ¹H NMR spectrum at 3.82 and 4.59 ppm. An intense N≡N band at 2127 cm⁻¹ was also observed by solution infrared spectroscopy in benzene-*d*₆.

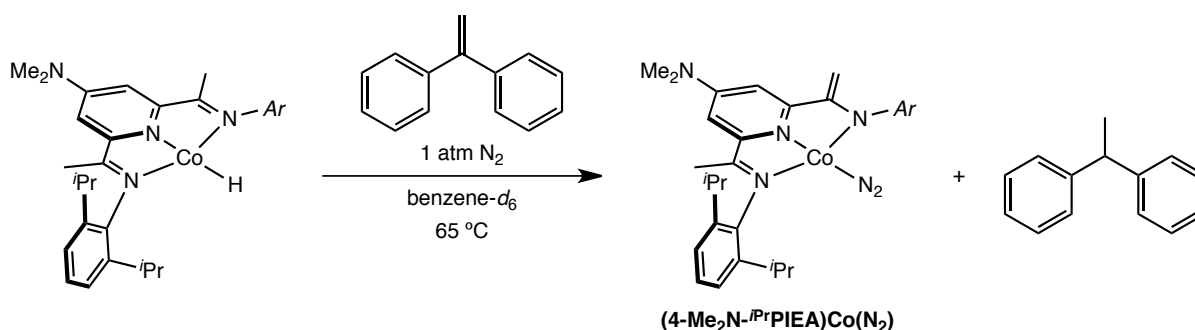


Figure A.1.6. Reactivity of (4-Me₂N-^{*i*}PrPDI)Co(H) with 1,1-diphenylethylene under 1 atmosphere of N₂.

Two mechanistic possibilities are proposed to account for this transformation (**Figure A.1.7**): (A) formation of an unstable tertiary alkyl followed by Co–C bond homolysis and H atom abstraction, or (B) H atom transfer to the olefin followed by H atom abstraction. These mechanisms are similar to those proposed by Arnold and coworkers where the isomerization of secondary and tertiary hydrotris(pyrazolyl)borate Co^{II} alkyls are believed to occur from a radical pathway.¹⁵

The neutral pyridine di(imine) cobalt dinitrogen complex, (4-Me₂N-^{*i*}PrPDI)Co(N₂) was also prepared. Stirring a toluene slurry of (4-Me₂N-^{*i*}PrPDI)CoCl₂ in the presence of 5 equivalents of 0.5% sodium amalgam for six hours followed by filtration and recrystallization from diethyl ether furnished a green solid identified as (4-Me₂N-^{*i*}PrPDI)Co(N₂) in good yield (74%, **Figure A.1.8**). (4-Me₂N-^{*i*}PrPDI)Co(N₂) is paramagnetic and a solution magnetic moment was measured

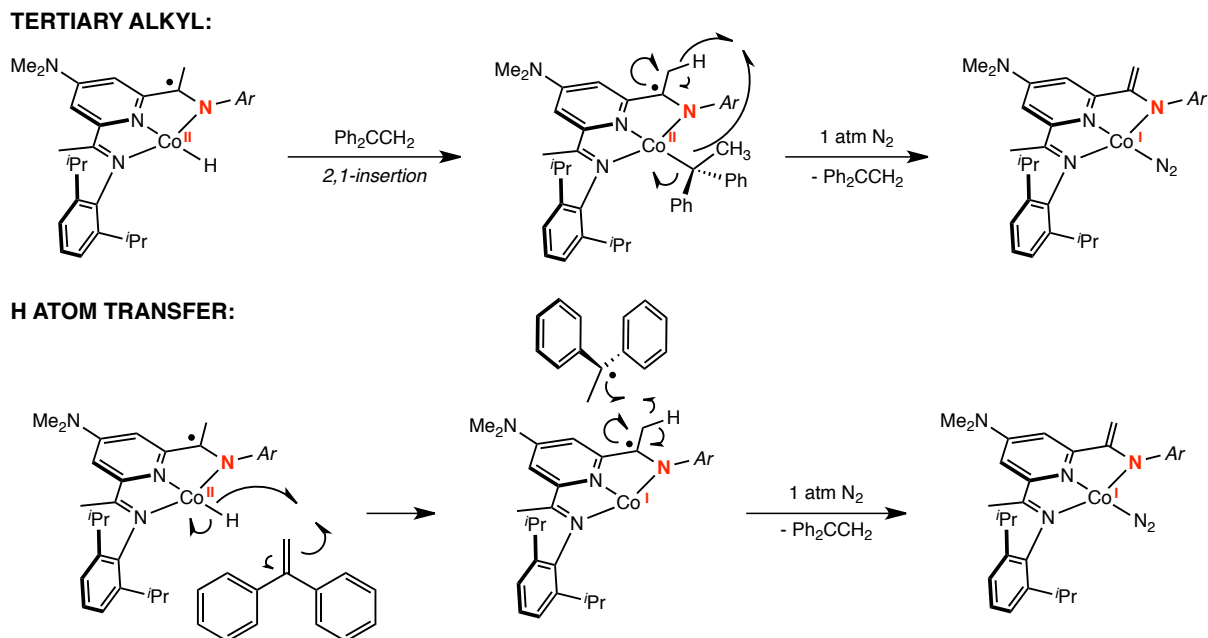


Figure A.1.7. Mechanisms accounting for the formation of (4-Me₂N-*i*PrPIEA)Co(N₂) from (4-Me₂N-*i*PrPDI)Co(H) and 1,1-diphenylethylene.

that is consistent with a doublet ground state ($\mu_{\text{eff}} = 1.3(2) \mu_{\text{B}}$) at 22 °C. The benzene-*d*₆ ¹H NMR spectrum at 22 °C exhibited 3 broad resonances, and was similar to the parent complex, (*i*PrPDI)Co(N₂).¹³ The presence of the dinitrogen ligand was confirmed by infrared spectroscopy. The toluene solution infrared spectrum exhibited an intense N≡N band at 2084 cm⁻¹. Consistent with previous findings (**Chapter 1**), the 4-Me₂N-*i*PrPDI chelate imparts a more electron-rich metal center by approximately 9 cm⁻¹ (**Table A.1.3**).

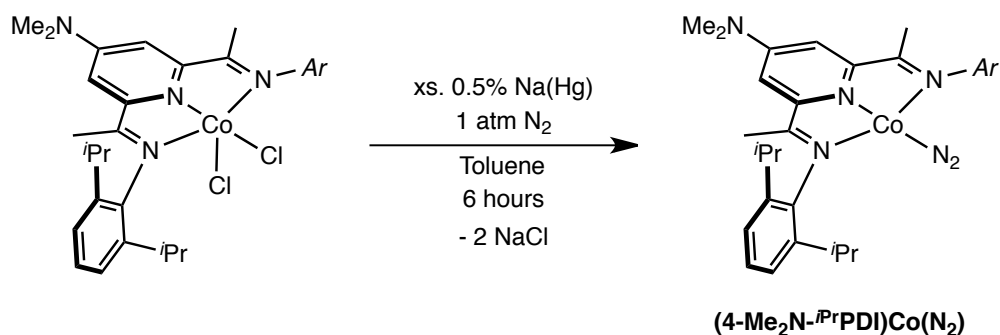


Figure A.1.8. Synthesis of (4-Me₂N-*i*PrPDI)Co(N₂).

Table A.1.3. Dinitrogen stretching frequencies of (4-R-*i*PrPDI)Co(N₂) measured by infrared spectroscopy in toluene.

Complex	$\nu(\text{N}\equiv\text{N})$ (cm ⁻¹)
(<i>i</i> PrBPDI)Co(N ₂) ^a	2111
(<i>i</i> PrPDI)Co(N ₂) ^a	2093
(4- <i>t</i> Bu- <i>i</i> PrPDI)Co(N ₂) ^b	2090
(4-Me ₂ N- <i>i</i> PrPDI)Co(N ₂)	2084

^a Data from reference 13.

^b Data from Bowman, A. C. Ph.D. Thesis, Cornell University, Ithaca, NY, 2010.

Single crystals of (4-Me₂N-*i*PrPDI)Co(N₂) suitable for X-ray diffraction (Mo K α radiation, $\lambda = 0.71073$ Å) were obtained from a concentrated diethyl ether solution at -35 °C as green plates. The asymmetric unit contained two molecules of (4-Me₂N-*i*PrPDI)Co(N₂) with statistically indistinguishable metrical parameters. A representation of the solid-state structure is presented in **Figure A.1.9**, and the metrical parameters of one of the molecules are reported in **Table A.1.4**. The metrical parameters of (*i*PrPDI)Co(N₂) are included for comparison. The geometry about the cobalt center is best described as idealized square planar. In most cases, the

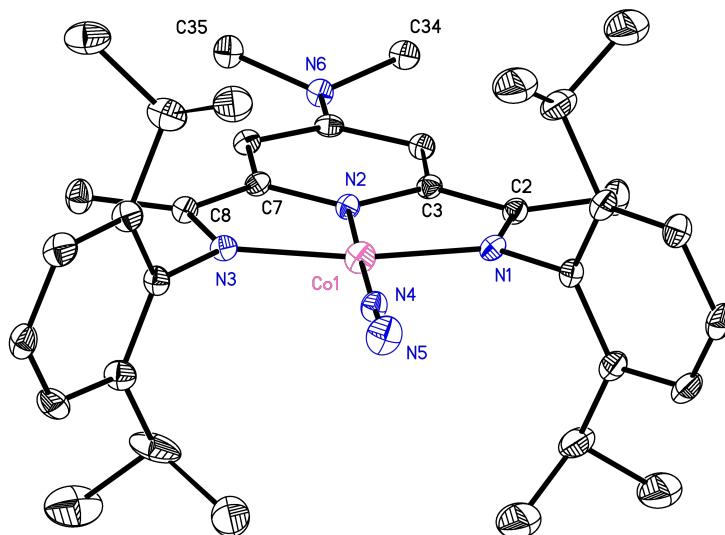


Figure A.1.9. Solid-state structure of (4-Me₂N-*i*PrPDI)Co(N₂) at 30% probability ellipsoids. Hydrogen atoms omitted for clarity.

Table A.1.4. Bond distances (Å) and angles (°) for (4-Me₂N-*i*PrPDI)Co(N₂) and (*i*PrPDI)Co(N₂).

	(4-Me ₂ N- <i>i</i> PrPDI)Co(N ₂)	(<i>i</i> PrPDI)Co(N ₂) ^a
Co(1)–N(1)	1.882(3)	1.8773(14)
Co(1)–N(2)	1.826(3)	1.8084(14)
Co(1)–N(3)	1.881(3)	1.8719(15)
Co(1)–N(4)	1.797(3)	1.7884(16)
N(1)–C(2)	1.348(5)	1.331(2)
N(3)–C(8)	1.350(5)	1.341(2)
C(2)–C(3)	1.442(5)	1.429(2)
C(7)–C(8)	1.442(5)	1.418(2)
N(4)–N(5)	1.108(5)	1.104(2)
N(1)–Co(1)–N(2)	81.33(13)	81.47(6)
N(2)–Co(1)–N(3)	81.65(13)	81.63(6)

^a Data from reference 13.

chelate distances are statistically indistinguishable from those of the parent complex, (*i*PrPDI)Co(N₂), and are consistent with a PDI¹⁻ description.

An X-band EPR spectrum of (4-Me₂N-*i*PrPDI)Co(N₂) recorded in fluid toluene solution was collected (**Figure A.1.10**), and was fit with similar parameters to the parent compound, (*i*PrPDI)Co(N₂).¹³ The spectrum is centered at an isotropic g_{iso} value of 1.992 and simulation gave an isotropic hyperfine coupling constant of $A_{\text{iso}} = 8.6 \times 10^{-4} \text{ cm}^{-1}$. These data conclusively show that the electronic structure of (4-Me₂N-*i*PrPDI)Co(N₂) does not significantly deviate from (*i*PrPDI)Co(N₂), and is consistent with our previous findings (**Chapter 1**).

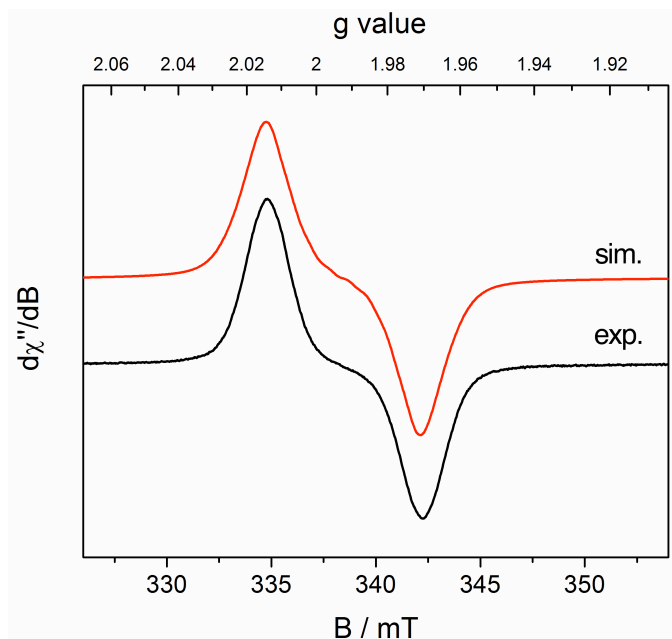


Figure A.1.10. Toluene solution EPR spectrum of (4-Me₂N-*i*PrPDI)Co(N₂) recorded at 23 °C (microwave frequency 9.44 GHz, power 1.00 mW, modulation frequency 1.0 mT).

Preparation of (4-Me₂N-*i*PrPDI)CoCl₂. A 100-mL round-bottom flask was charged with 0.18 g (1.3 mmol) of CoCl₂ and approximately 2 mL THF. A solution of 0.75 g (1.4 mmol) 4-Me₂N-*i*PrPDI in approximately 10 mL THF was then added to the slurry with rapid stirring, causing a rapid color change to brown-yellow. After 12 hours, 10 mL of pentane was added, causing the product to precipitate from solution. Filtration from THF/pentane and washing with diethyl ether yielded 0.90 g (99% yield) of analytically pure brown-yellow solid identified as (4-Me₂N-*i*PrPDI)CoCl₂. Solid state magnetic susceptibility (magnetic susceptibility balance, 295 K): $\mu_{\text{eff}} = 4.2(1) \mu_{\text{B}}$. ¹H NMR (chloroform-*d*₁, 22 °C): $\delta = -119.2$ (217 Hz, 4H, CH(CH₃)₂), -25.9 (29 Hz, 12H, CH(CH₃)₂), -22.6 (89 Hz, 12H, CH(CH₃)₂), -11.8 (26 Hz, 2H, *p*-aryl), -3.1 (54 Hz, 6H, C(N)CH₃), 2.9 (29 Hz, 4H, *m*-aryl), 35.8 (29 Hz, 6H, N(CH₃)₂), 125.6 (96 Hz, 2H, *m*-pyr).

Preparation of (4-Me₂N-ⁱPrPDI)Co(CH₃). A slurry of (4-Me₂N-ⁱPrPDI)CoCl₂ (0.30 g, 0.46 mmol) in approximately 5 mL diethyl ether was prepared and frozen in a liquid nitrogen cooled cold-well. A 1.6 M solution of methyllithium (0.92 mmol, 0.57 mL) in diethyl ether was diluted with approximately 10 mL diethyl ether, and frozen. Immediately upon thawing, the solution of methyllithium was added dropwise to the slurry of (4-Me₂N-ⁱPrPDI)CoCl₂ in a dropwise fashion causing a rapid color change to blue-green. The reaction mixture was stirred for 3 hours at 22 °C, filtered through Celite. Concentration of the resulting solution to approximately 5 mL and cooling to -35 °C afforded 0.19 g (70% yield) of a blue-green crystalline solid identified as (4-Me₂N-ⁱPrPDI)Co(CH₃). Analysis for C₃₆H₅₁N₄Co: Calc. C, 72.21; H, 8.59; N, 9.36. Found: C, 71.82; H, 8.27; N, 9.07. ¹H NMR (benzene-*d*₆, 22 °C): δ = -1.84 (s, 6H, CCH₃), 0.74 (d, 7 Hz, 12H, CH(CH₃)₂), 1.22 (d, 7 Hz, 12H, CH(CH₃)₂), 1.50 (s, 3H, CH₃), 2.01 (s, 6H, N(CH₃)₂), 3.21 (spt, 7 Hz, 4H, CH(CH₃)₂), 7.35 (d, 8Hz, 4H, *m*-aryl), 7.49 (t, 8 Hz, 2H, *p*-aryl), 8.15 (s, 2H, *m*-pyr). ¹³C {¹H} NMR (benzene-*d*₆, 22 °C): δ = 23.3 (CH(CH₃)₂), 24.1 (CH(CH₃)₂), 26.9 (CH₃), 28.4 (CH(CH₃)₂), 40.0 (N(CH₃)₂), 102.9 (*m*-pyr), 123.7 (*m*-aryl), 126.1 (*p*-aryl), 139.9 (aryl), 149.6 (*p*-pyr), 155.2 (aryl), 160.2 (C(N)CH₃), one resonance not located.

Characterization of (4-Me₂N-ⁱPrPDI)Co(H). In a typical experiment, a J. Young tube was charged with a solution of (4-Me₂N-ⁱPrPDI)Co(CH₃) (0.010 g, 17 μmol) in benzene-*d*₆ (0.650 g). On the high vacuum line, the headspace was evacuated and 1 atmosphere of H₂ was admitted. Upon thawing, the solution was shaken, but no significant color change was observed. After two hours of periodic shaking, complete conversion to (4-Me₂N-ⁱPrPDI)Co(H) had observed by ¹H NMR spectroscopy. ¹H NMR (benzene-*d*₆, 22 °C): δ = -2.43 (s, 6H, CCH₃), 0.45 (d, 7 Hz, 12H, CH(CH₃)₂), 1.33 (d, 7 Hz, 12H, CH(CH₃)₂), 1.80 (s, 6H, N(CH₃)₂), 3.43 (spt, 7 Hz, 4H,

$CH(CH_3)_2$, 7.42 (d, 8 Hz, 4H, *m-aryl*), 7.59 (t, 8 Hz, 2H, *p-aryl*), 7.98 (s, 2H, *m-pyr*). IR (benzene- d_6 , 23 °C): $\nu_{CoH} = 2125\text{ cm}^{-1}$.

Characterization of (4-Me₂N-*i*PrPIEA)Co(N₂). The cobalt hydride, (4-Me₂N-*i*PrPDI)Co(H) was prepared in the manner described above, and 1,1-diphenylethylene (3 μ L, 17 μ mol) was added by microsyringe under a dinitrogen atmosphere. The resulting solution was heated to 65 °C for one week, resulting in clean conversion to 1,1-diphenylethane and (*i*PrPIEA)Co(N₂). ¹H NMR (benzene- d_6 , 22 °C): $\delta = -0.63$ (s, 3H, CCH₃), 0.97 (d, 7 Hz, 6H, CH(CH₃)₂), 1.34 (d, 7 Hz, 6H, CH(CH₃)₂), 1.39 (d, 7 Hz, 6H, CH(CH₃)₂), 1.46 (d, 7 Hz, 6H, CH(CH₃)₂), 2.32 (s, 6H, N(CH₃)₂), 3.02 (spt, 7 Hz, 2H, CH(CH₃)₂), 3.54 (spt, 7 Hz, 2H, CH(CH₃)₂), 3.82 (s, 1H, CCH₂), 4.59 (s, 1H, CCH₂), 7.01–7.22 (m, 7H, *m-pyr*, *aryl*), 7.57 (d, 2 Hz, 1H, *m-pyr*). ¹³C {¹H} NMR (benzene- d_6 , 22 °C): $\delta = 19.9$ (CCH₃), 23.8 (CH(CH₃)₂), 24.0 (CH(CH₃)₂), 24.5 (CH(CH₃)₂), 25.6 (CH(CH₃)₂), 27.8 (CH(CH₃)₂), 27.9 (CH(CH₃)₂), 39.5 (N(CH₃)₂), 85.5 (CCH₂), 96.6 (*m-pyr*), 97.9 (*m-pyr*), 123.4 (*aryl*), 123.4 (*aryl*), 139.4 (*aryl*), 144.4 (*aryl*), 144.5 (CCH₃ or *pyr*), 147.7 (*aryl*), 153.8 (CCH₃ or *pyr*), 155.9 (*pyr*), 159.4 (CCH₂ or *pyr*), 162.8 (CCH₂ or *pyr*), three aryl resonances not located. IR (benzene- d_6 , 23 °C): $\nu_{NN} = 2127\text{ cm}^{-1}$.

Preparation of (4-Me₂N-*i*PrPDI)Co(N₂). A 250 mL round-bottom flask was charged with 15.8 g of mercury, approximately 100 mL of toluene and a magnetic stir bar. To the flask was added 0.079 g (3.4 mmol) of sodium in small pieces with vigorous stirring. The amalgam was stirred for 20 minutes, and the 0.45 g (0.69 mmol) of (4-Me₂N-*i*PrPDI)CoCl₂ was added to the flask. The reaction mixture was stirred for 6 hours, at which time the dark blue-green reaction mixture was

decanted away from the amalgam and filtered through Celite. The solvent was removed in vacuo and the resulting solid was recrystallized from diethyl ether at -35 °C to afford 0.313 g (74% yield) of a green crystalline solid identified as (4-Me₂N-*i*PrPDI)Co(N₂). Analysis for C₃₅H₄₈N₆Co: Calc. C, 68.72; H, 7.91; N, 13.74. Found: C, 68.49; H, 7.74; N, 13.44. Magnetic susceptibility (benzene-*d*₆, 295 K): $\mu_{\text{eff}} = 1.3(2) \mu_{\text{B}}$. ¹H NMR (benzene-*d*₆, 22 °C): $\delta = 3.46$ (270.9 Hz), 4.33 (638.5 Hz), 5.60 (133.3 Hz). IR (toluene, 23 °C): $\nu_{\text{NN}} = 2084 \text{ cm}^{-1}$.

A.2 Reduced Pyridine Di(carbene) Cobalt Complexes

Base metal pyridine di(carbene) complexes have not gained prominence as compared with pyridine di(imine) analogs due to their inactivity for ethylene polymerization when treated with MAO.¹⁶ Danopoulos and coworkers have prepared pyridine di(carbene) cobalt complexes in three different formal oxidation states – Co^I, Co^{II} and Co^{III} – including the formally Co^I monomethyl compound, (*i*PrCNC)Co(CH₃).¹⁷ Inspired by the similar electronic structures of (*i*PrPDI)Fe(N₂)₂ and (*i*PrCNC)Fe(N₂)₂ (**Chapter 1** and **2**, respectively), the chemistry of reduced pyridine di(carbene) cobalt complexes was further explored. Following the procedure of Danopoulos,¹⁷ (*i*PrCNC)Co(CH₃) was prepared by treating a chilled (-78 °C) toluene solution of the cobalt monobromide, (*i*PrCNC)CoBr with one equivalent of methyllithium (**Figure A.2.1**). Alternatively, (*i*PrCNC)Co(CH₃) was also prepared by treating a thawing diethyl ether slurry of (*i*PrCNC)CoBr₂ with two equivalents of methyllithium.

The benzene-*d*₆ ¹H NMR spectrum of (*i*PrCNC)Co(CH₃) is particularly noteworthy. Danopoulos and co-workers comment on the peculiar chemical shift of the *para*-pyridine proton at 10.65 ppm; however, no attempt to rationalize these observation were made.¹⁷ The similarities

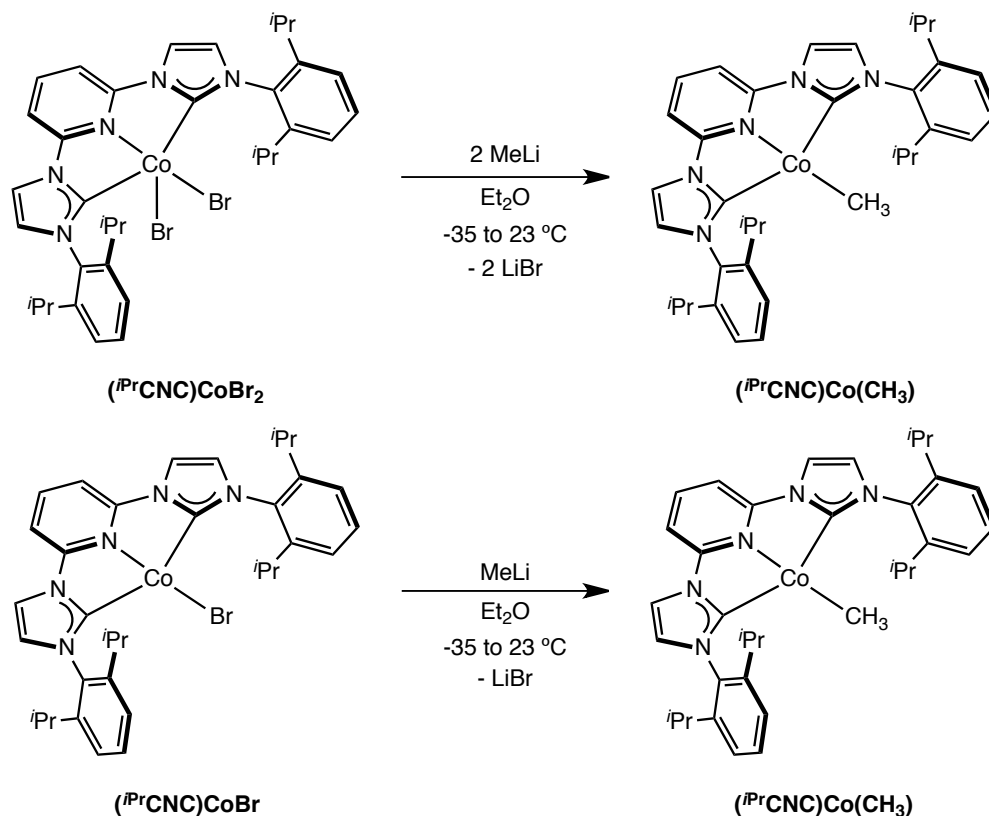


Figure A.2.1. Synthetic routes to $(iPrCNC)Co(CH_3)$.

between the benzene- d_6 1H NMR spectra of $(iPrPDI)Co(CH_3)$ and $(iPrCNC)Co(CH_3)$ (**Figure A.2.2**) indicate that the anomalous shifts are a result of thermal population of a nearby triplet excited state. Additionally, they suggest that $(iPrCNC)Co(CH_3)$ has a similar electronic structure and is a redox-active complex with a low-spin cobalt(II) center ($S = 1/2$) antiferromagnetically coupled to a pyridine di(carbene) radical ion ($S = 1/2$). Interestingly, this phenomenon was also observed for the pyridine bis(oxazoline) cobalt alkyl compound, $(iPrPybox)Co(CH_2Si(CH_3)_3)_2$;¹⁸ however, these results will not be discussed here.

The electronic structure of $(iPrCNC)Co(CH_3)$ was probed by density functional theory in an attempt to distinguish between the redox innocent ($((iPrCNC^0)Co^I(CH_3))$) and redox-active ($((iPrCNC^{1-})Co^{II}(CH_3))$) electronic structure descriptions. These two configurations correspond to a

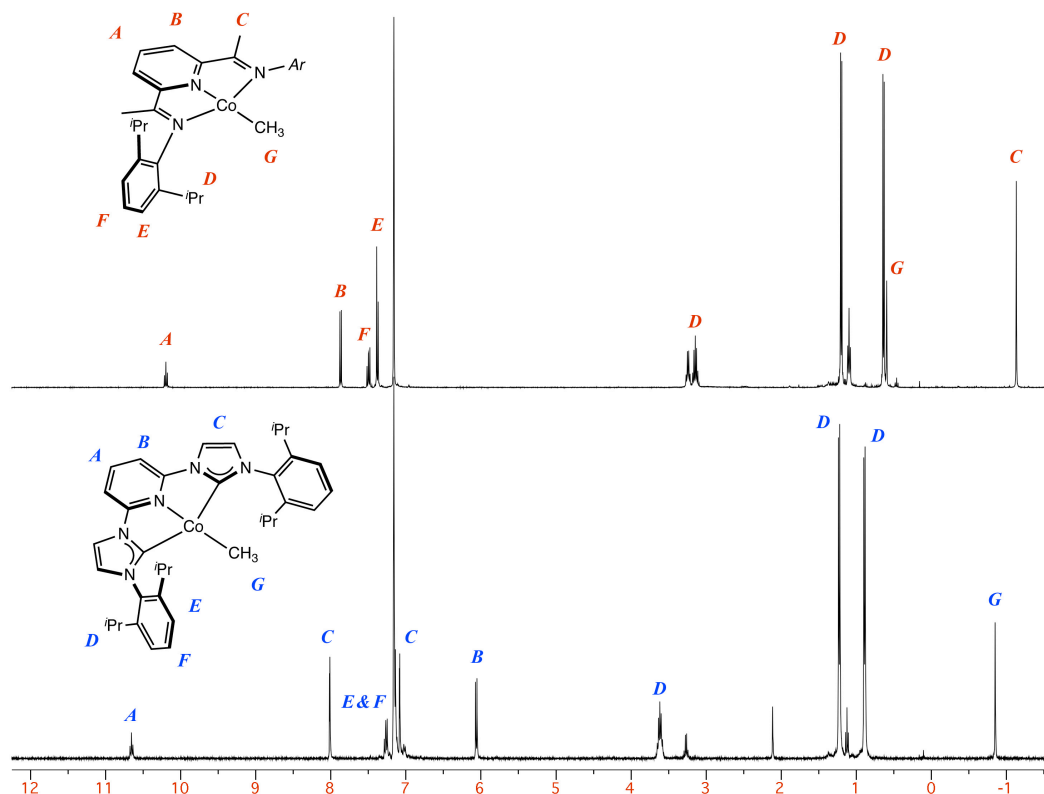


Figure A.2.2. Benzene- d_6 ^1H NMR spectra of $(i\text{PrPDI})\text{Co}(\text{CH}_3)$ (top) and $(i\text{PrCNC})\text{Co}(\text{CH}_3)$ (bottom) at 22 °C.

spin-restricted (RKS) and a BS(1,1) (broken-symmetry) singlet approach, respectively. Geometry optimization on each model was performed at the B3LYP level of DFT and resulted in the two solutions corresponding to the redox innocent and redox non-innocent descriptions. A comparison of the total energy indicated that the broken-symmetry solution was approximately 7 kcal/mol more stable than the spin-restricted solution. The geometric parameters of the RKS and BS(1,1) solutions are presented in **Table A.2.1**, and are in excellent agreement with the experimentally determined values.

Investigation of the frontier molecular orbital manifold of the BS(1,1) solution revealed three doubly filled metal d-orbitals and a d_{xz} SOMO, which is consistent with a low-spin, cobalt(II) description ($S = \frac{1}{2}$). A ligand b_2 SOMO ($S = \frac{1}{2}$) was found with opposite spin

Table A.2.1. Comparison of experimental and computational bond distances (Å) and angles (°) for (*i*PrCNC)Co(CH₃).

	Exp. ^a	RKS	BS(2,2)
Co–N _{pyr}	1.865(3)	1.887	1.902
Co–C _{carbene}	1.914(4)	1.930	1.955
	1.898(4)	1.934	1.954
Co–CH ₃	1.951(4)	1.975	1.986
N _{pyr} –C _{ipso}	1.358(5)	1.351	1.363
	1.357(5)	1.351	1.363
C _{ipso} –N _{carbene}	1.394(5)	1.393	1.397
	1.397(5)	1.394	1.398
N _{carbene} –C _{carbene}	1.399(5)	1.398	1.394
	1.400(5)	1.399	1.394
N–C _{carbene} –N	101.3(3)	101.99	102.48
	100.7(3)	102.09	102.55

^a Data from reference 17.

alignment, and antiferromagnetic coupling between the metal and ligand SOMOs accounts for the experimentally observed singlet ground state. These observations are reflected in the spin density plot obtained from Mulliken population analysis (**Figure A.2.3**). A triplet state was calculated at the B3LYP level of DFT from a simple spin-unrestricted approach that corresponds to a low-spin cobalt(II) center ($S = 1/2$) with a pyridine di(carbene) radical anion ($S = 1/2$) with parallel spin alignment. This solution was approximately 4.4 kcal/mol higher in energy than the broken-symmetry solution and is consistent with a thermally accessible triplet state as observed by ¹H NMR spectroscopy.⁶ On the basis of these results, the electronic structure of (*i*PrCNC)Co(CH₃) is best described as a low-spin cobalt(II) complex antiferromagnetically coupled to a pyridine di(carbene) radical anion (**Figure A.2.4**).

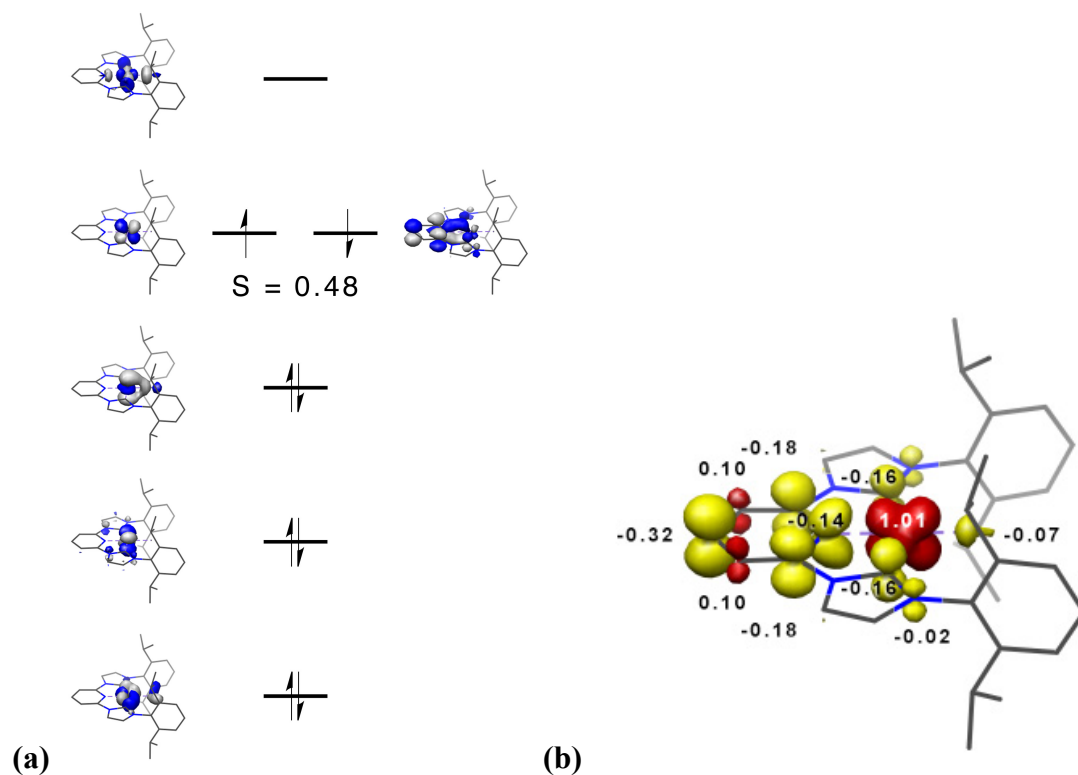


Figure A.2.3. (a) Qualitative MO diagram of $(iPrCNC)Co(CH_3)$ obtained from a BS(1,1) DFT calculation at the B3LYP level. (b) Spin density plot for $(iPrCNC)Co(CH_3)$ obtained from Mulliken population analysis.

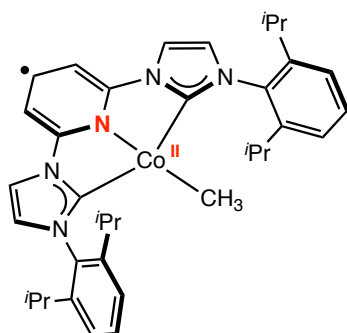


Figure A.2.4. Electronic structure of $(iPrCNC)Co(CH_3)$.

Similar to the reactivity observed with $(iPrPDI)Co(CH_3)$, monitoring the addition of 1 atmosphere of H_2 to a 25 mM benzene- d_6 solution of $(iPrCNC)Co(CH_3)$ by 1H NMR spectroscopy revealed the rapid release of methane and formation of a new diamagnetic, C_{2v} symmetric compound assigned as the cobalt hydride, $(iPrCNC)Co(H)$ (**Figure A.2.5**). No color change was

observed during the course of the reaction. The benzene- d_6 ^1H NMR spectrum of $(i^{\text{Pr}}\text{CNC})\text{Co}(\text{H})$ is similar to that of $(i^{\text{Pr}}\text{CNC})\text{Co}(\text{CH}_3)$ (**Figure A.2.6**). The resonance of the *para*-pyridine hydrogen was shifted downfield (11.3 ppm) relative to the chemical shift value in the cobalt methyl complex (10.65 ppm).¹⁷ The field strength of the non-chelating ligand was shown to inversely affect the singlet-triplet gap in the monoreduced pyridine di(imine) cobalt complexes,⁶ and our observations are consistent with these findings. The hydride resonance was not located, presumably due to fast relaxation.

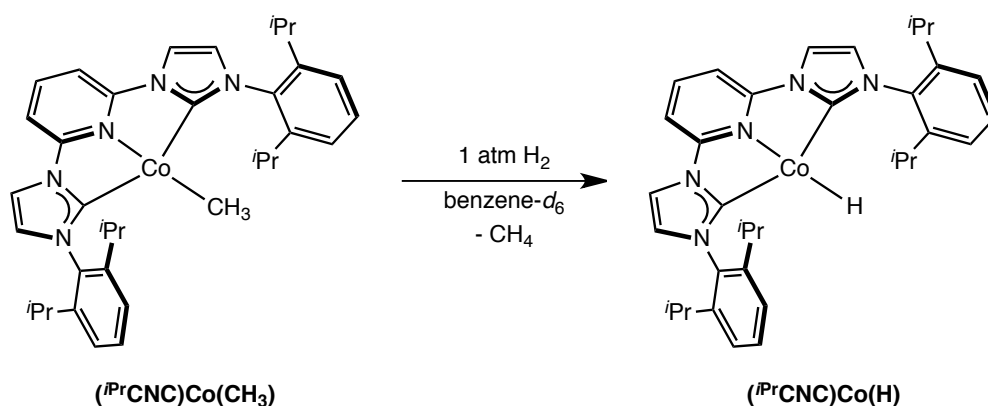


Figure A.2.5. In situ synthesis of $(i^{\text{Pr}}\text{CNC})\text{Co}(\text{H})$.

Addition of D_2 to a 25 mM benzene- d_6 solution of $(i^{\text{Pr}}\text{CNC})\text{Co}(\text{CH}_3)$ results in rapid and selective incorporation of deuterium into the *para*-pyridine, the downfield imidazolylidene and the upfield isopropyl methyl groups (**Figure A.2.7**). The rate of deuterium incorporation into the isopropyl methyl and imidazolylidene positions was significantly faster than the *para*-pyridine position, and complete isotopic labeling of these positions was observed at 6 hours with moderate shaking periodically in a J. Young tube.

Exposure of $(i^{\text{Pr}}\text{CNC})\text{Co}(\text{H})$ to 1 atmosphere of N_2 resulted in the disappearance of the peaks corresponding to the cobalt hydride as monitored by ^1H NMR spectroscopy in benzene- d_6 .

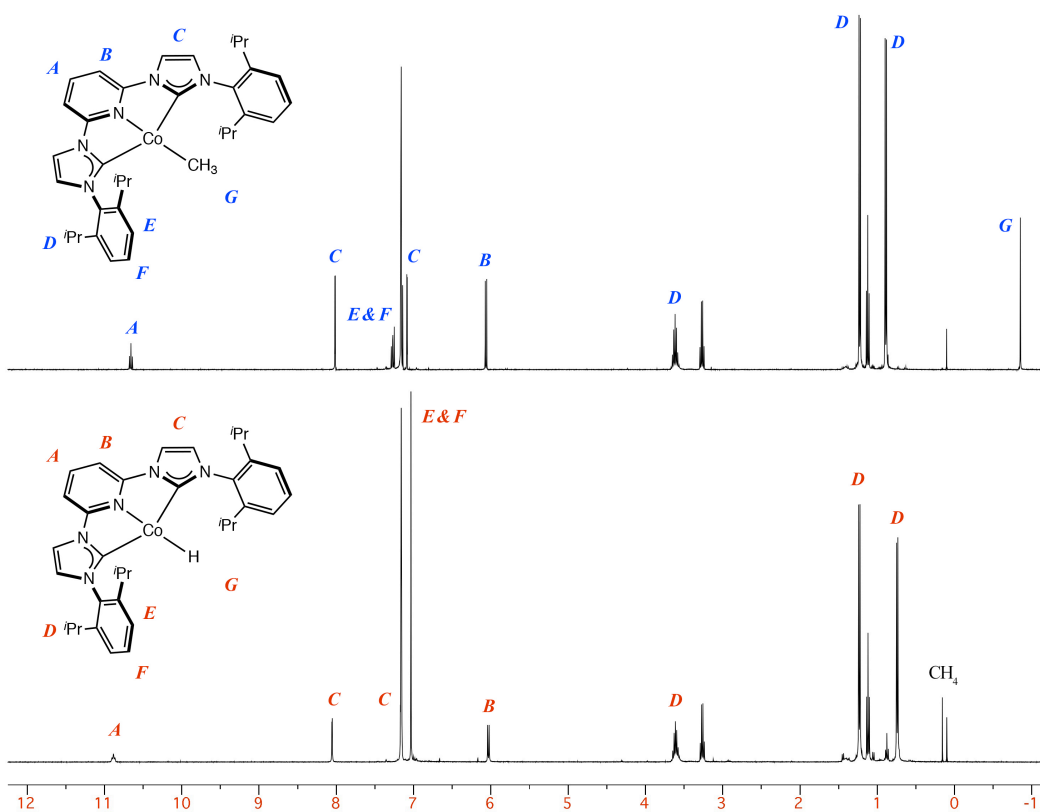


Figure A.2.6. Benzene-*d*₆ ¹H NMR spectra of (iPrCNC)Co(CH₃) (top) and (iPrCNC)Co(H) (bottom) at 22 °C.

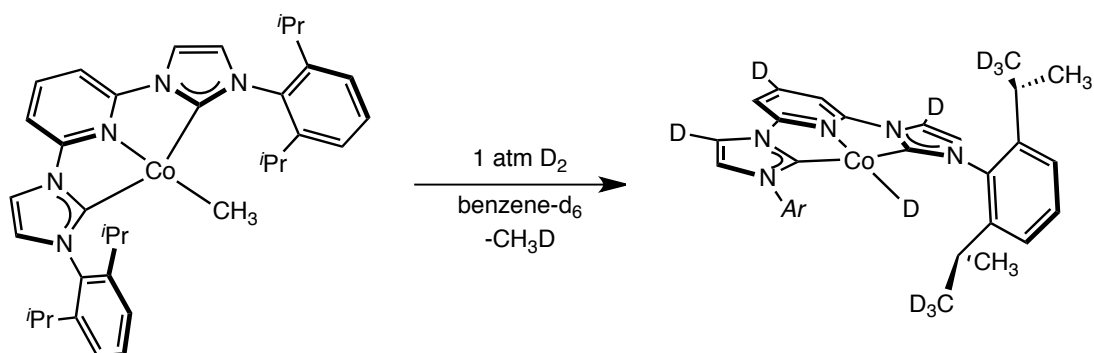


Figure A.2.7. Deuterium scrambling resulting from in situ synthesis of (iPrCNC)Co(D).

A gradual color change from brown-yellow to yellow-green to purple-black was observed over the course of hours. Analysis of the solution following these color changes by infrared spectroscopy revealed the appearance of two bands at 2079 and 2048 cm⁻¹ with medium and strong intensities, respectively, indicating the presence of dinitrogen ligands. Reduction of

$(i\text{PrCNC})\text{CoBr}_2$ with either five equivalents of 0.5% Na(Hg) or two equivalents of sodium in the presence of catalytic naphthalene in THF afforded similar color changes after 3–4 hours and 24 hours, respectively. Analysis of the resulting solutions by infrared spectroscopy revealed the presence of the same characteristic absorptions with dissimilar ratios. These data suggested a mixture of products; however, one of these bands is believed to correspond to the cobalt dinitrogen complex, $(i\text{PrCNC})\text{Co}(\text{N}_2)$ (**Figure A.2.7**). Further investigation is necessary to understand these observations.

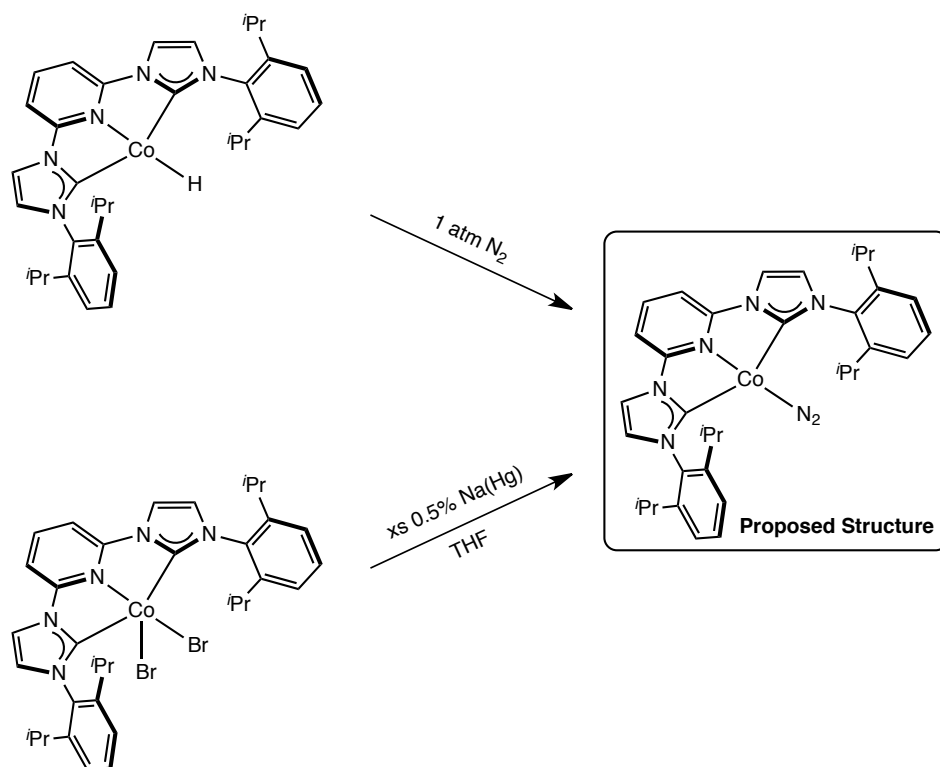


Figure A.2.8. Proposed product arising from the exposure of $(i\text{PrCNC})\text{Co}(\text{H})$ with 1 atm of N₂ or from reduction of $(i\text{PrCNC})\text{CoBr}_2$.

Because pyridine di(imine) cobalt alkyl complexes are known olefin hydrogenation precatalysts,^{11,14} and the pyridine di(carbene) iron bis(dinitrogen) compound is significantly more active than the pyridine di(imine) analog (**Chapter 2**), the activity of $(i\text{PrCNC})\text{Co}(\text{H})$ for the

hydrogenation of ethyl 3,3-dimethylacrylate was assayed. Standard conditions employed a 0.92 M solution of substrate in benzene- d_6 , 5 mol % ($i^{\text{Pr}}\text{CNC})\text{Co}(\text{CH}_3)$ and four atmospheres of dihydrogen. Under these conditions, >95% hydrogenation of ethyl 3,3-dimethylacrylate was observed in 1 hour as determined by ^1H NMR spectroscopy (**Figure A.2.9**). ($i^{\text{Pr}}\text{CNC})\text{Co}(\text{CH}_3)$ is therefore a more active precatalyst than many of the diaryl-substituted pyridine di(imine) iron dinitrogen and cobalt alkyl complexes. Further studies are necessary to determine how active ($i^{\text{Pr}}\text{CNC})\text{Co}(\text{CH}_3)$ is compared to the fastest pyridine di(imine) and pyridine di(carbene) base metal catalysts.

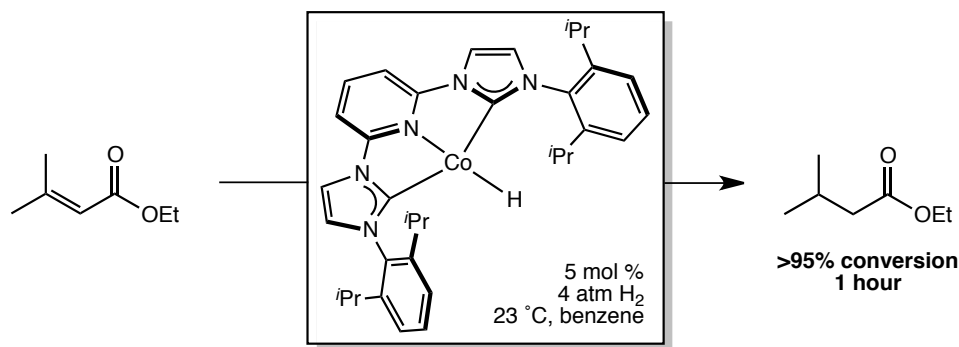


Figure A.2.9. Hydrogenation of ethyl 3,3-dimethylacrylate with 5 mol % ($i^{\text{Pr}}\text{CNC})\text{Co}(\text{CH}_3)$ and 4 atmospheres of H_2 .

The reaction of ($i^{\text{Pr}}\text{CNC})\text{Co}(\text{H})$ with 1,1-diphenylethylene was probed for comparison with the results obtained with (4-Me $_2$ N- $i^{\text{Pr}}\text{PDI})\text{Co}(\text{H})$. Addition of 1 equivalent of 1,1-diphenylethylene to a 25 mM benzene- d_6 solution of ($i^{\text{Pr}}\text{CNC})\text{Co}(\text{H})$ under one atmosphere of N_2 resulted in a rapid color change to deep blue. Smooth conversion of the cobalt hydride to a new, diamagnetic species identified as (4-C(Ph) $_2$ CH $_3$ -4-H- $i^{\text{Pr}}\text{CNC})\text{Co}(\text{N}_2)$ was observed by ^1H NMR spectroscopy (**Figure A.2.10**). (4-C(Ph) $_2$ CH $_3$ -4-H- $i^{\text{Pr}}\text{CNC})\text{Co}(\text{N}_2)$ is a redox innocent, low-spin, cobalt(I), d^8 complex. The presence of dinitrogen was confirmed by infrared spectroscopy. An intense $\text{N}\equiv\text{N}$ band was observed at 2050 cm^{-1} in benzene- d_6 solution. The benzene- d_6 ^1H NMR

spectrum of (4-C(Ph)₂CH₃-4-H-*i*PrCNC)Co(N₂) exhibits the number of resonances consistent for a C_s symmetric compound (**Figure A.2.11**). The allylic and vinylic (formerly the *para*- and *meta*-pyridine) resonances were located upfield at 4.90 and 4.33 ppm, respectively

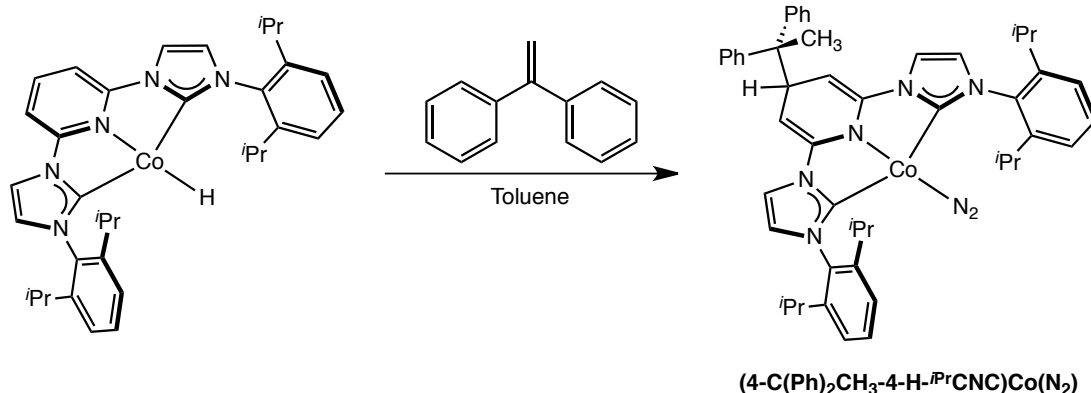


Figure A.2.10. Reactivity of (*i*PrCNC)Co(H) with 1,1-diphenylethylene under 1 atmosphere of N₂.

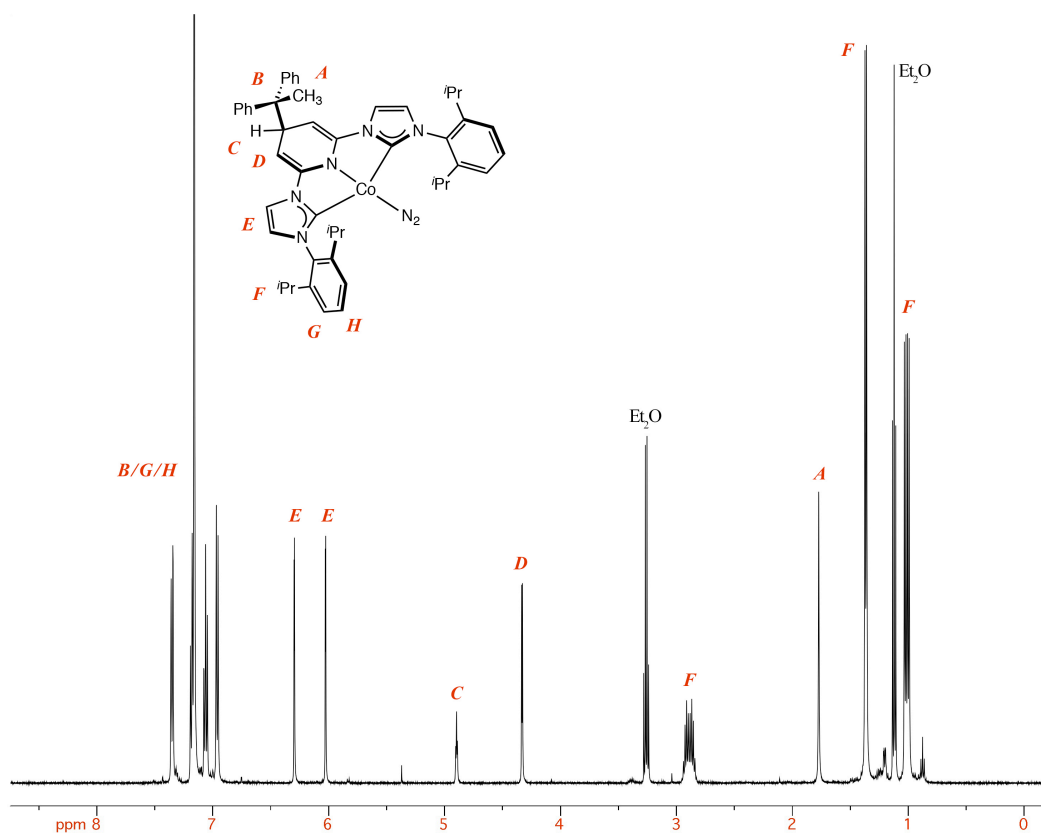


Figure A.2.11. Benzene-*d*₆ ¹H NMR spectra of (4-C(Ph)₂CH₃-4-H-*i*PrCNC)Co(N₂) at 22 °C.

Single crystals of (4-C(Ph)₂CH₃-4-H-*i*PrCNC)Co(N₂) suitable for X-ray diffraction (Cu K α radiation, $\lambda = 1.54178 \text{ \AA}$) were obtained from a concentrated diethyl ether solution at -35 °C as blue prisms. The asymmetric unit contained one molecule of (4-C(Ph)₂CH₃-4-H-*i*PrCNC)Co(N₂) and one molecule of diethyl ether. The geometry about the cobalt center is best described as square planar. A representation of the solid-state structure is presented in **Figure A.2.12** and the metrical parameters are reported in **Table A.2.2**. The values for (*i*PrCNC)Co(CH₃) are included for comparison. The cobalt–chelate distances are statistically indistinguishable from the those of the starting complex, (*i*PrCNC)Co(CH₃). The N(6)–N(7) distance of the dinitrogen ligand is 1.112(2) suggesting little perturbation by the cobalt center. The most significant changes occur in the chelate at the C_{ipso}–C_{meta} and C_{meta}–C_{para} bonds, and result from interruption of the π -system.

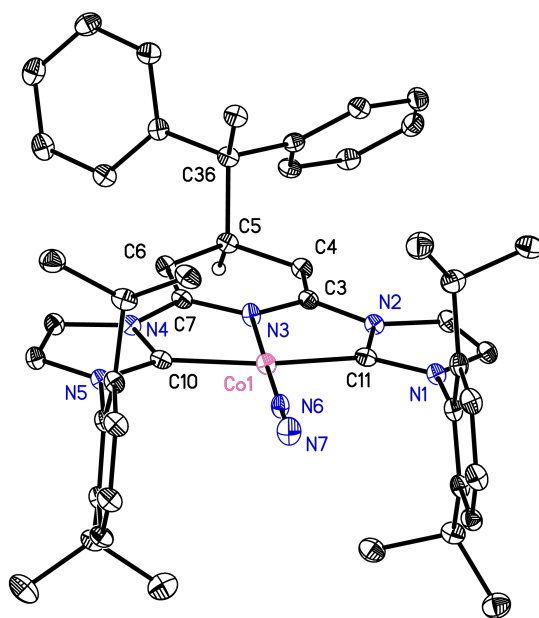


Figure A.2.12. Solid state structure of (4-C(Ph)₂CH₃-4-H-*i*PrCNC)Co(N₂) at 30% probability ellipsoids. Hydrogen atoms omitted for clarity.

Table A.2.2. Bond distances (Å) and angles (°) for (4-C(Ph)₂CH₃-4-H-ⁱPrCNC)Co(N₂).

	(4-C(Ph) ₂ CH ₃ -4-H- ⁱ PrCNC)Co(N ₂)	(ⁱ PrCNC)Co(CH ₃) ^a
Co(1)–N(3)	1.8553(16)	1.865(3)
Co(1)–C(10)	1.8980(19)	1.914(4)
Co(1)–C(11)	1.9015(19)	1.898(4)
Co(1)–N(6)	1.7500(17)	
C(3)–C(4)	1.333(3)	1.372(6)
C(6)–C(7)	1.335(3)	1.373(6)
C(4)–C(5)	1.513(3)	1.396(6)
C(5)–C(6)	1.526(2)	1.416(6)
N(1)–C(11)	1.357(3)	1.387(5)
C(11)–N(2)	1.381(2)	1.400(5)
N(4)–C(10)	1.377(2)	1.375(5)
C(10)–N(5)	1.366(2)	1.399(5)
N(6)–N(7)	1.112(2)	
N(1)–C(11)–N(2)	103.67(15)	101.3(3)
N(4)–C(10)–N(5)	103.28(16)	100.7(3)

^a Data from reference 17.

Two mechanisms similar to those proposed for the formation of (4-Me₂N-ⁱPrPIEA)Co(N₂) from the reaction of (4-Me₂N-ⁱPrPDI)Co(H) and 1,1-diphenylethylene under 1 atmosphere of dinitrogen account for the synthesis of (4-C(Ph)₂CH₃-4-H-ⁱPrCNC)Co(N₂) (**Figure A.2.13**). Formation of an unstable tertiary alkyl resulting in bond homolysis (**A**) or H atom transfer (**B**) both result in formation of the tertiary organic radical which undergoes C–C bond formation. The divergent outcome occurs due to the absence of a weak or acidic C–H bond in the pyridine di(carbene) chelate, which is present in the pyridine di(imine) ligand.

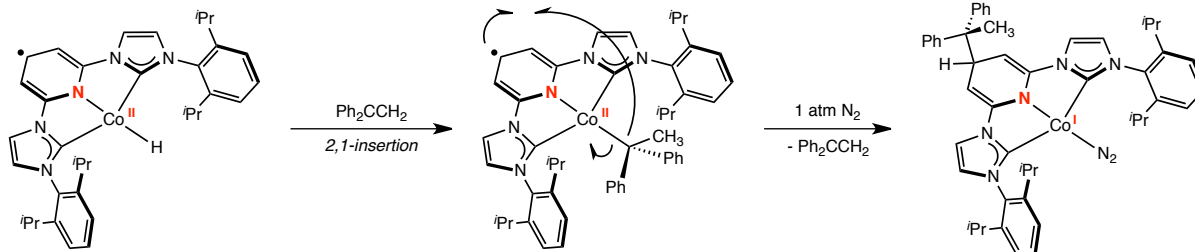
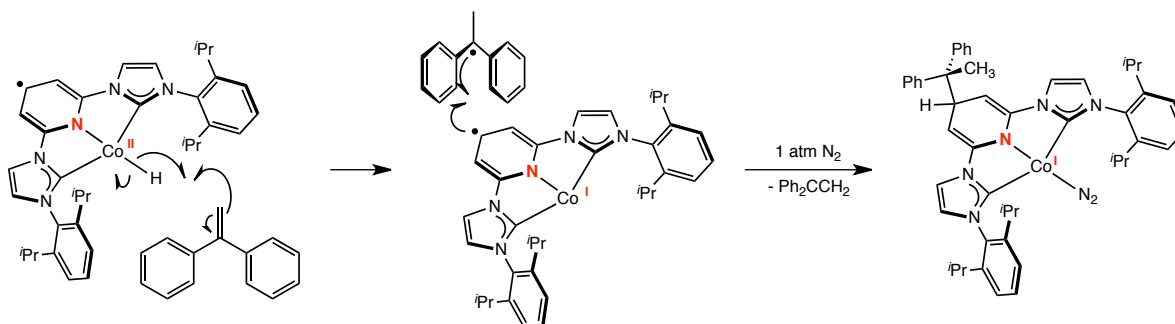
TERTIARY ALKYL:**H ATOM TRANSFER:**

Figure A.2.13. Mechanisms accounting for the formation of $(4-C(Ph)_2CH_3-4-H-iPrCNC)Co(N_2)$ from $(iPrCNC)Co(H)$ and 1,1-diphenylethylene.

In order to probe the viability of the proposed tertiary cobalt alkyls, the theoretical molecules, $(iPrCNC)Co(tBu)$ and $(iPrCNC)Co(C(Ph)_2CH_3)$ were geometry optimized at the B3LYP level of DFT using both broken-symmetry and spin-restricted singlet approaches. Representations of the geometry optimized structures are presented in **Figure A.2.14**. In both theoretical molecules, the steric crowding between the two aryl groups causes the alkyl group to lift out of the chelate plane. This occurs in both the broken-symmetry and restricted-spin solutions, and is more pronounced for $(iPrCNC)Co(C(Ph)_2CH_3)$. The $N_{pyr}-Co-C_{alkyl}$ angles are approximately 138° and 127° for $(iPrCNC)Co(tBu)$ and $(iPrCNC)Co(C(Ph)_2CH_3)$, respectively. Additionally, for $(iPrCNC)Co(C(Ph)_2CH_3)$, the aryl groups twist to a greater degree to avoid the steric interaction between the phenyl and isopropyl aryl groups. The lift of the alkyl fragment likely weakens the bond and makes it more susceptible to homolysis.

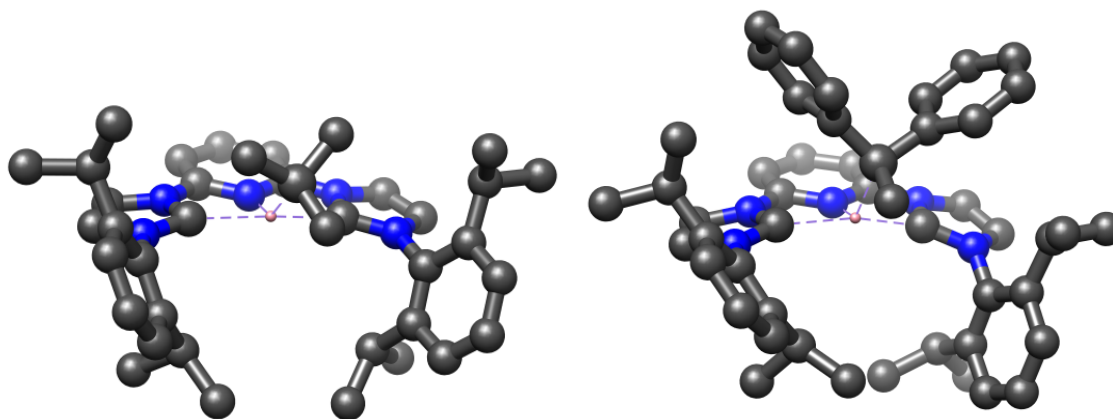


Figure A.2.14. Geometry optimization of the theoretical molecules, $(iPrCNC)Co(tBu)$ (left) and $(iPrCNC)Co(C(Ph)_2CH_3)$ (right), at the B3LYP level of DFT.

Characterization of $(iPrCNC)CoH$. In a typical experiment, a J. Young tube was charged with a solution of $(iPrCNC)Co(CH_3)$ (0.010 g, 17 μ mol) in benzene- d_6 (0.650 g). On the high vacuum line, the headspace was evacuated and 1 atmosphere of H_2 was admitted. Upon thawing, the solution was shaken, but no significant color change was observed. 1H NMR (benzene- d_6 , 22 $^\circ$ C): δ = 0.67 (d, 7 Hz, 12H, $CH(CH_3)_2$), 1.25 (d, 7 Hz, 12H, $CH(CH_3)_2$), 3.69 (spt, 7 Hz, 4H, $CH(CH_3)_2$), 5.93 (d, 7 Hz, 2H, *m-pyr*), 7.04 (s, 6H, *m-* and *p-aryl*), 7.24 (s, 2H, *imidazolylidene backbone*), 8.14 (s, 2H, *imidazolylidene backbone*), 11.32 (t, 7 Hz, 1H, *p-pyr*).

Preparation of $(4-C(Ph)_2CH_3-4-H-iPrCNC)Co(N_2)$. A thick-walled vessel was charged with a solution of $(iPrCNC)Co(CH_3)$ (0.10 g, 0.16 mmol) in approximately 10 mL of toluene. The vessel was cooled to -78 $^\circ$ C, and the headspace was evacuated and replaced with an atmosphere of H_2 . The reaction was warmed to room temperature and stirred for 15 minutes. The excess H_2 was removed at -78 $^\circ$ C and 0.030 g (0.17 mmol) of 1,1-diphenylethylene was added at 23 $^\circ$ C under an atmosphere of dinitrogen. A rapid color change to deep blue was observed, and the reaction was stirred for an additional 15 minutes. The solution was then filtered through Celite and

concentrated to dryness. The residue was redissolved in ether and stored at -35 °C to afford 0.082 g (62% yield) of blue solid identified as (4-C(Ph)₂CH₃-4-H-ⁱPrCNC)Co(N₂)₂. Analysis for C₄₉H₅₄N₇Co: Calc. C, 73.57; H, 6.80; N, 12.26. Found: C, 73.52; H, 6.66; N, 11.93. ¹H NMR (benzene-*d*₆, 22 °C): δ = 0.99 (d, 7 Hz, 6H, CH(CH₃)₂), 1.03 (d, 7 Hz, 6H, CH(CH₃)₂), 1.37 (d, 7 Hz, 12H, CH(CH₃)₂), 1.77 (s, 3H, Ph₂CCH₃), 2.87 (spt, 7 Hz, 2H, CH(CH₃)₂), 2.91 (spt, 7 Hz, 2H, CH(CH₃)₂), 4.33 (d, 4 Hz, 2H, 3-*pyr*), 4.90 (t, 4 Hz, 1H, 4-*pyr*), 6.03 (d, 2 Hz, 2H, *imidazolylidene backbone*), 6.30 (d, 2 Hz, 2H, *imidazolylidene backbone*), 6.96 (d, 7 Hz, 4H, *aryl* or *phenyl*), 7.06 (t, 7 Hz, 4H, *aryl* or *phenyl*), 7.18 (d, 7 Hz, 4H, *aryl* or *phenyl*), 7.35 (d, 7 Hz, 4H, *aryl* or *phenyl*). ¹³C {¹H} NMR (benzene-*d*₆, 22 °C): δ = 22.4 (Ph₂CCH₃), 23.9 (CH(CH₃)₂), 24.0 (CH(CH₃)₂), 24.4 (CH(CH₃)₂), 24.5 (CH(CH₃)₂), 28.5 (CH(CH₃)₂), 28.6 (CH(CH₃)₂), 45.2 (4-*pyr*), 53.1 (Ph₂CCH₃), 77.5 (3-*pyr*), 113.3 (*imidazolylidene backbone*), 123.0 (*imidazolylidene backbone*), 123.7 (*aryl*), 123.8 (*phenyl*), 125.6 (*aryl*), 128.3 (*phenyl*), 129.8 (*phenyl*), 136.0 (*aryl*), 145.9 (*aryl* or 2-*pyr*), 146.23 (*aryl* or 2-*pyr*), 146.25 (*aryl* or 2-*pyr*), 149.0 (*phenyl*), 194.1 (*carbene*), one resonance not located. IR (benzene-*d*₆, 23 °C): ν_{NN} = 2050 cm⁻¹.

A.3. Synthesis of a Reduced Pyridine Di(carbene) Manganese Dicarboxyl Complex

The pyridine di(carbene) manganese dibromide, (ⁱPrCNC)MnBr₂ (ⁱPrCNC = 2,6-((2,6-ⁱPr₂-C₆H₃)-imidazolin-2-ylidene)₂-C₅H₃N) was originally prepared by Danopoulos and coworkers from the complexation of manganese dibromide and ⁱPrCNC.¹⁹ Stirring a THF slurry of (ⁱPrCNC)MnBr₂ in the presence of excess 0.5% sodium amalgam under an atmosphere of CO for four hours followed by filtration and recrystallization of the product from diethyl ether at -35 °C

resulted in isolation of green solid identified as $(i\text{PrCNC})\text{Mn}(\text{CO})_2$ in 36% yield (**Figure A.3.1**). $(i\text{PrCNC})\text{Mn}(\text{CO})_2$ is a ^1H NMR silent compound, and a solution magnetic moment of $1.8(1) \mu_{\text{B}}$, was recorded in benzene- d_6 at 23°C , consistent with a doublet ground state. EPR spectroscopy is necessary to demonstrate if the unpaired spin is metal- or ligand-centered, and to elucidate the electronic structure of the compound. The infrared spectrum exhibited two bands at 1927 and 1894 cm^{-1} in benzene- d_6 solution. These bands are observed at 1926 and 1899 cm^{-1} in the solid state (KBr pellet). Interestingly, these values are less reduced than the neutral pyridine di(imine) manganese dicarbonyl, $(i\text{PrPDI})\text{Mn}(\text{CO})_2$ by approximately $30\text{--}60 \text{ cm}^{-1}$.²⁰

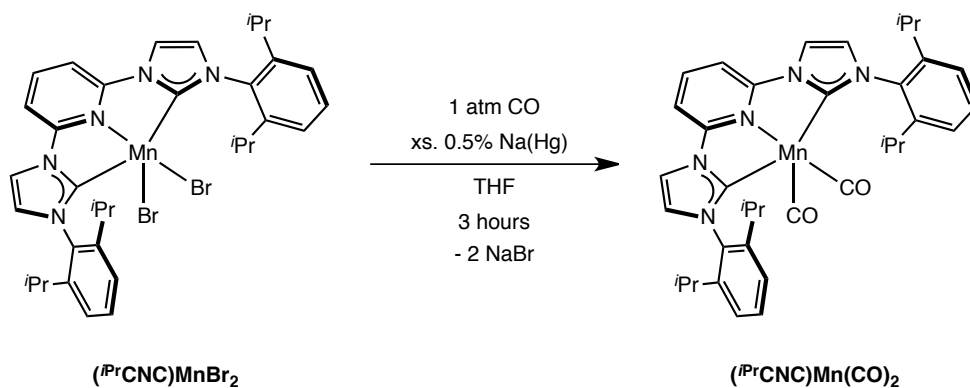


Figure A.3.1. Synthesis of $(i\text{PrCNC})\text{Mn}(\text{CO})_2$.

Single crystals of $(i\text{PrCNC})\text{Mn}(\text{CO})_2$ suitable for X-ray diffraction (Cu $K\alpha$ radiation, $\lambda = 1.54184 \text{ \AA}$) were grown from a toluene/diethyl ether solution as green diamonds. The asymmetric unit contained one molecule of $(i\text{PrCNC})\text{Mn}(\text{CO})_2$ and one molecule of toluene. A representation of the solid state structure is presented in **Figure A.3.2** and the metrical parameters are reported in **Table A.3.1**. The overall molecular geometry is best described as square pyramidal with carbonyl ligands in the apical and basal positions. The $\text{Mn}\text{--}\text{N}_{\text{pyr}}$ bond length of $1.976(4) \text{ \AA}$ and $\text{Mn}\text{--}\text{C}_{\text{carbene}}$ bond lengths of $1.987(5)$ and $1.973(5) \text{ \AA}$ are significantly shorter than the corresponding bonds in $(i\text{PrCNC})\text{MnBr}_2$, suggesting a low-spin configuration.

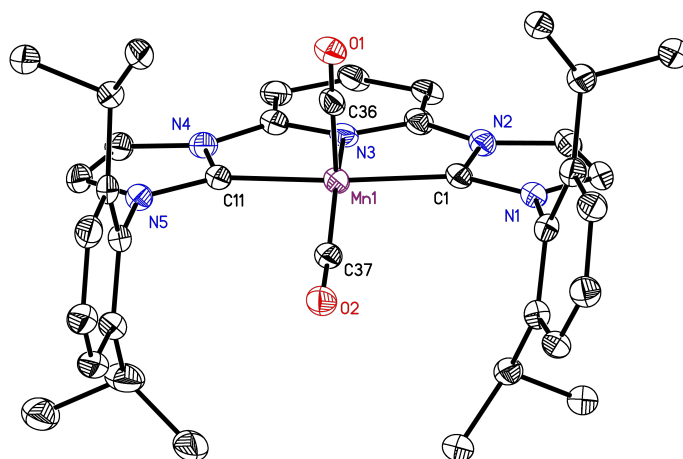


Figure A.3.2. Solid-state structure of (*i*PrCNC)Mn(CO)₂ at 30% probability ellipsoids. Hydrogen atoms omitted for clarity.

Table A.3.1. Bond distances (Å) and angles (°) for (*i*PrCNC)Mn(CO)₂.

Mn(1)–N(3)	1.976(4)	N(1)–C(1)	1.361(7)
Mn(1)–C(1)	1.987(5)	C(1)–N(2)	1.377(7)
Mn(1)–C(11)	1.973(5)	N(4)–C(11)	1.387(7)
Mn(1)–C(36)	1.764(6)	C(11)–N(5)	1.380(7)
Mn(1)–C(37)	1.808(6)		
C(36)–O(1)	1.171(7)	C(37)–O(2)	1.136(6)
N(1)–C(1)–N(2)	102.9(4)	N(4)–C(11)–N(5)	103.1(4)
N(3)–Mn(1)–C(36)	113.3(2)	N(3)–Mn(1)–C(37)	160.0(2)
C(36)–Mn(1)–C(37)	86.7(2)		

Preparation of (*i*PrCNC)Mn(CO)₂. A thick-walled vessel was charged with mercury (15.4 g) and approximately 5 mL of THF. Sodium (0.077 g, 3.3 mmol) was added in small pieces with rapid stirring. After 15 minutes, a slurry of (*i*PrCNC)MnBr₂ (0.50 g, 0.67 mmol) in approximately 20 mL of THF was added. The vessel was cooled to -78 °C, and the headspace was evacuated and replaced with an atmosphere of CO. The reaction mixture was warmed to 23 °C and rapidly

stirred for four hours. During this time, a rapid color change to brown-red and then a gradual change to brown-green was observed. The reaction mixture was then decanted away from the amalgam and concentrated to dryness *in vacuo*. The residue was extracted with diethyl ether and filtered through Celite. The resulting solution was concentrated and stored at -35 °C, which afforded 0.156 g (36% yield) of a green solid identified as (*i*PrCNC)Mn(CO)₂. Analysis for C₃₇H₄₁N₅O₂Mn: Calc. C, 69.15; H, 6.43; N, 10.90. Found: C, 69.04; H, 6.46; N, 10.66. Magnetic susceptibility (benzene-*d*₆, 295 K): $\mu_{\text{eff}} = 1.8(1) \mu_{\text{B}}$. IR (benzene-*d*₆, 23 °C): $\nu_{\text{CO}} = 1927, 1894 \text{ cm}^{-1}$. IR (KBr): $\nu_{\text{CO}} = 1926, 1899 \text{ cm}^{-1}$.

REFERENCES

- ¹ (a) Small, B. M.; Brookhart, M. *J. Am. Chem. Soc.* **1998**, *120*, 7143–7144. (b) Small, B. L.; Brookhart, M.; Bennett, A. M. A. *J. Am. Chem. Soc.* **1998**, *120*, 4049–4050.
- ² Britovsek, G. J. P.; Gibson, V. C.; Kimberley, B. S.; Maddox, S. J.; Solan, G. A.; White, A. J. P.; Williams, D. J. *Chem. Commun.* **1998**, 849–850.
- ³ Britovsek, G. J. P.; Bruce, M.; Gibson, V. C.; Kimberley, B. S.; Maddox, P. J.; Mastroianni, S.; McTavish, S. J.; Redshaw, C.; Solan, G. A.; Strömberg, S.; White, A. J. P.; Williams, D. J. *J. Am. Chem. Soc.* **1999**, *121*, 8728–8748.
- ⁴ Kooistra, T. M.; Knijnenburg, Q.; Smits, J. M. M.; Horton, A. D.; Budzelaar, P. H. M.; Gal, A. W. *Angew. Chem. Int. Ed.* **2001**, *40*, 4719–4722.
- ⁵ Gibson, V. C.; Humphries, M. J.; Tellmann, K. P.; Wass, D. F.; White, A. J. P.; Williams, D. J. *Chem. Comm.* **2001**, 2252–2253.
- ⁶ Knijnenburg, Q.; Hetterscheid, D.; Kooistra, T. M.; Budzelaar, P. H. M. *Eur. J. Inorg. Chem.* **2004**, 1204–1211.
- ⁷ Bowman, A. C.; Milsmann, C.; Bill, E.; Lobkovsky, E.; Weyhermüller, T.; Wieghardt, K.; Chirik, P. J. *Inorg. Chem.* **2010**, *49*, 6110–6123.
- ⁸ Zhu, D.; Budzelaar, P. H. A. *Organometallics* **2008**, *27*, 2699–2705.
- ⁹ Tellmann, K. P.; Humphries, M. J.; Rzepa, H. S.; Gibson, V. C. *Organometallics* **2004**, *23*, 5503–5513.
- ¹⁰ Humphries, M. J.; Tellmann, K. P.; Gibson, V. C.; White, A. J. P.; Williams, D. J. *Organometallics* **2005**, *24*, 2039–2050.
- ¹¹ Knijnenburg, Q.; Horton, A. D.; Heijden, H. V. D.; Kooistra, T. M.; Hetterscheid, D. G. H.; Smits, J. M. M.; Bruin, B. de; Budzelaar, P. H. M.; Gal, A. W. *J. Mol. Cat. A: Chem.* **2005**, *232*, 151–159.
- ¹² Ding, K.; Brennessel, W. W.; Holland, P. L. *J. Am. Chem. Soc.* **2009**, *131*, 10804–10805.
- ¹³ Bowman, A. C.; Milsmann, C.; Atienza, C. C. H.; Lobkovsky, E.; Wieghardt, K.; Chirik, P. J. *J. Am. Chem. Soc.* **2010**, *132*, 1676–1684.
- ¹⁴ Monfette, S.; Turner, Z. R.; Semproni, S. P.; Chirik, P. J. *J. Am. Chem. Soc.* **2012**, *134*, 4561–4564.
- ¹⁵ Kunishita, A.; Gianetti, T. L.; Arnold, J. *Organometallics* **2012**, *31*, 372–380.
- ¹⁶ McGuinness, D. S.; Gibson, V. C.; Steed, J. W. *Organometallics* **2004**, *23*, 6288–6292.

¹⁷ Danopoulos, A. A.; Wright, J. A.; Motherwell, W. B.; Ellwood, S. *Organometallics* **2004**, *23*, 4807–4810.

¹⁸ Monfette, S.; Chirik, P. J. *unpublished results*.

¹⁹ Pugh, D.; Wright, J. A.; Freeman, S.; Danopoulos, A. A. *Dalton Trans.* **2006**, 775–782.

²⁰ Russell, S. K.; Bowman, A. C.; Lobkovsky, E.; Wieghardt, K.; Chirik, P. J. *Eur. J. Inorg. Chem.* **2011**, *2012*, 535–545.

APPENDIX B

COMPUTATIONAL RESULTS

B.1. Computational Studies: Pyridine Di(carbene) Iron Complexes with Neutral Ligands

The electronic structure of $(i\text{PrCNC})\text{Fe}(\text{N}_2)_2$, as well as that of the free carbene, $i\text{PrCNC}$, has been the subject of several computational investigations.^{1,2,3} Danopoulos¹ and Zhang³ both describe the five-coordinate bis(dinitrogen) complex as a low-spin, Fe^0 compound with a neutral pyridine di(carbene) ligand, $(i\text{PrCNC}^0)\text{Fe}^0(\text{N}_2)_2$, and have presented computational evidence to support this assignment. One possibility that, to our knowledge, has not been addressed computationally is the potential of the pyridine di(carbene) ligand to be redox-active. Structural similarities between the pyridine di(carbene) and pyridine di(imine) frameworks prompted further investigation. However, despite the well-established ability of the pyridine di(imine) ligand to be redox-active,⁴ prior work by our laboratory regarding the five-coordinate pyridine di(imine) iron bis(dinitrogen) complex established a closed-shell singlet ground state with $(i\text{PrPDI}^0)\text{Fe}^0(\text{N}_2)_2$ and $(i\text{PrPDI}^{2-})\text{Fe}^{\text{II}}(\text{N}_2)_2$ resonance structures.⁵

Analogous to the computational treatment of $(i\text{PrPDI})\text{Fe}(\text{N}_2)_2$,⁵ broken-symmetry (BS) approaches for $(i\text{PrCNC})\text{Fe}(\text{N}_2)_2$ were investigated at the B3LYP level of DFT. Intermediate-spin Fe^{II} ($S = 1$) with a pyridine di(carbene) triplet dianion ($S = 1$) and low-spin Fe^{I} ($S = 1/2$) with a pyridine di(carbene) radical anion ($S = 1/2$) descriptions were probed corresponding to BS(2,2) and BS(1,1) models, respectively. In each case, antiferromagnetic coupling between the metal and ligand magnetic orbitals accounts for the experimentally observed singlet ground state. In order to compare these to a closed-shell description corresponding to $(i\text{PrCNC}^0)\text{Fe}^0(\text{N}_2)_2$, $(i\text{PrCNC}^{2-})\text{Fe}^{\text{II}}(\text{N}_2)_2$, or a hybrid structure of the two, the spin-restricted (RKS) model was

computed. Notably, in each of the closed-shell descriptions, the ligand and metal are in their singlet states ($S = 0$).

Geometry optimizations at the B3LYP level were performed for all three models, and produced two different solutions. The two broken-symmetry approaches converged to the same BS(1,1) solution, which was 2.2 kcal/mol lower in energy than the RKS solution. These results are similar to those of the five-coordinate pyridine di(imine) iron bis(dinitrogen) compound, (*i*PrPDI)Fe(N₂)₂, where the broken-symmetry solution was 2.4 kcal/mol lower in energy than the spin-restricted solution.⁵ The geometric parameters of both the RKS and the BS(1,1) solutions are in excellent agreement with the solid state structure (**Table B.1.1**). The largest deviation occurs in the iron–carbene bond distances for the BS(1,1) solution, and borders the generally

Table B.1.1. Comparison of experimental and computational bond distances (Å) and angles (°) for (*i*PrCNC)Fe(N₂)₂.

	Exp. ^a	RKS	BS(2,2)
Fe–N _{pyr}	1.890(2)	1.902	1.919
Fe–C _{carbene}	1.915(3)	1.956	1.976
	1.912(3)	1.957	1.976
Fe–N _{N₂,basal}	1.820(2)	1.837	1.842
Fe–N _{N₂,apical}	1.847(2)	1.827	1.881
N _{pyr} –C _{ipso}	1.367(3)	1.362	1.365
	1.364(3)	1.364	1.364
C _{ipso} –N _{carbene}	1.377(3)	1.384	1.390
	1.383(3)	1.384	1.390
N _{carbene} –C _{carbene}	1.402(3)	1.396	1.394
	1.394(3)	1.396	1.394
N≡N _{basal}	1.115(3)	1.110	1.111
N≡N _{apical}	1.113(3)	1.111	1.109
N–C _{carbene} –N	102.3(2)	102.58	102.63
	102.0(2)	102.54	102.62

^a Data from reference 1b.

accepted error range for DFT geometry optimizations.⁶ Neither solution is therefore excluded by energetic or structural arguments.

In an attempt to distinguish between the two models, ⁵⁷Fe Mößbauer parameters were computed for both solutions. This methodology, when compared to experimental data, has proven to be an excellent means of distinguishing between electronic structures.⁷ However, both parameters calculated for the spin-restricted ($\delta = 0.26 \text{ mm}\cdot\text{s}^{-1}$, $\Delta E_Q = +0.74 \text{ mm}\cdot\text{s}^{-1}$) and broken-symmetry ($\delta = 0.34 \text{ mm}\cdot\text{s}^{-1}$, $\Delta E_Q = +0.61 \text{ mm}\cdot\text{s}^{-1}$) solutions are in excellent agreement with the experimentally observed values ($\delta = 0.27 \text{ mm}\cdot\text{s}^{-1}$, $\Delta E_Q = |0.69| \text{ mm}\cdot\text{s}^{-1}$) and are indistinguishable from each other. This most likely results from the high overlap integral obtained between the two magnetic orbitals ($S = 0.75$, **Figure B.1.1**).

The HOMO obtained from the restricted calculation exhibits 43.7% Fe and 53.8% ligand and dinitrogen character. In agreement with the calculations of Zhu and Budzelaar,² the π -acceptor orbital is concentrated primarily on the pyridine ring and the carbene nitrogen atoms; however, significant electron density is also observed on the carbene carbons. These results are reflected in the spin density plot of (*i*PrCNC)Fe(N₂)₂ obtained from Mulliken population analysis of the BS(1,1) solution (**Figure B.1.1**). On the basis of these results, the electronic structure of (*i*PrCNC)Fe(N₂)₂ is best described as a closed-shell singlet with (*i*PrCNC⁰)Fe⁰(N₂)₂ and (*i*PrCNC²⁻)Fe^{II}(N₂)₂ resonance structures, and is similar to the five-coordinate pyridine di(imine) iron bis(dinitrogen) compound, (*i*PrPDI)Fe(N₂)₂ (**Figure B.1.2**).

Although there is no experimental evidence for the formation of a four-coordinate iron dinitrogen complex, computational investigations by Zhang have suggested that the theoretical molecule, (*i*PrCNC)Fe(N₂), would exist in a high-spin configuration.³ The low-spin singlet state

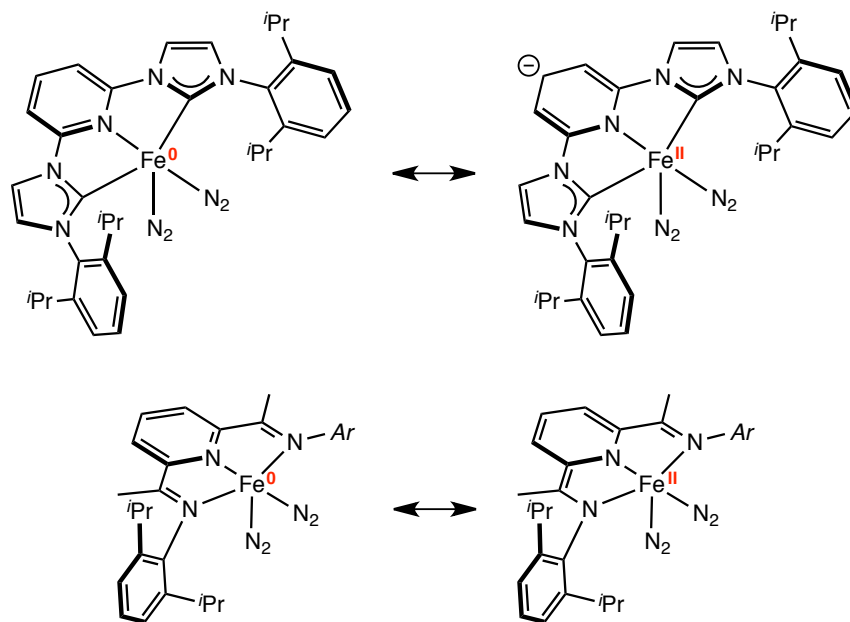


Figure B.1.2. Electronic structure of $(i\text{PrCNC})\text{Fe}(\text{N}_2)_2$ and $(i\text{PrPDI})\text{Fe}(\text{N}_2)_2$.

significantly lower in energy than the restricted singlet solution. For $(i\text{PrPDI})\text{Fe}(\text{N}_2)_2$, the broken-symmetry solution was found to be 17.1 kcal/mol lower in energy than the spin-restricted solution.⁵

To explore this possibility, both BS(2,2) and BS(1,1) approaches were investigated. The restricted singlet and unrestricted triplet models, previously examined by Zhang³, were recalculated for comparison. Consistent with the solutions obtained for the five-coordinate iron bis(dinitrogen) compound, the broken-symmetry models converged to the same BS(1,1) solution. A comparison of the total energies showed that this electronic configuration was 14.5 kcal/mol *more stable* than the restricted singlet solution, and 0.4 kcal/mol *more stable* than the unrestricted triplet ground state proposed by Zhang.

Geometry optimizations at the B3LYP level of DFT were performed on each model, and the results are reported in **Table B.1.2**. Differences between the metal-ligand and intraligand bond distances for both singlet solutions are similar to those observed for the five-coordinate

Table B.1.2. Comparison of computed bond distances (Å) and angles (°) for hypothetical (*i*PrCNC)Fe(N₂).

	<i>(i</i> PrCNC)Fe(N ₂) ₂ ^a	<i>(i</i> PrCNC)Fe(N ₂)		
		RKS	BS(2,2)	Triplet
Fe–N _{pyr}	1.890(2)	1.902	1.927	1.921
Fe–C _{carbene}	1.915(3)	1.942	1.971	1.968
	1.912(3)	1.942	1.971	1.968
Fe–N _{N₂,basal}	1.820(2)	1.794	1.804	1.803
Fe–N _{N₂,apical}	1.847(2)			
N _{pyr} –C _{ipso}	1.367(3)	1.358	1.366	1.366
	1.364(3)	1.358	1.366	1.366
C _{ipso} –N _{carbene}	1.377(3)	1.390	1.392	1.392
	1.383(3)	1.390	1.392	1.392
N _{carbene} –C _{carbene}	1.402(3)	1.398	1.398	1.398
	1.394(3)	1.398	1.399	1.398
N≡N _{basal}	1.115(3)	1.116	1.119	1.116
N–C _{carbene} –N	102.3(2)	102.08	102.45	102.40
	102.0(2)	102.08	102.46	102.40

^a Data from reference 1b.

complex, (*i*PrCNC)Fe(N₂)₂. One significant deviation was the position of the dinitrogen molecule relative to the idealized iron-chelate plane. For the restricted singlet calculation, the dinitrogen moiety lifts, resulting in a N_{pyr}–Fe–N_{N₂} angle of 163.6°, whereas for the BS(1,1) and unrestricted triplet calculations, the dinitrogen molecule lies in the plane of the chelate. This most likely occurs to maximize orbital overlap in the spin-restricted calculation, and is consistent with the observations of Budzelaar and coworkers for the pyridine di(imine) cobalt alkyl species.⁸

Qualitative molecular orbital diagrams for the RKS, BS(1,1) and unrestricted triplet solutions are presented in **Figure B.1.3**. The HOMO obtained from the restricted calculation exhibits 73.4% Fe character, and breaks symmetry to give two magnetic orbitals (metal d_{z²} and ligand b₂ π-orbital) with an overlap integral of 0.02 in the BS(1,1) solution. The electronic

structure description of the unrestricted triplet state as determined by frontier molecular orbital analysis is a low-spin Fe^{I} ($S = 1/2$) configuration with a pyridine di(carbene) radical anion ($S = 1/2$). The magnetic orbitals exhibit parallel spin-alignment, which accounts for the triplet ground state. This electronic structure configuration is similar to that of the unrestricted triplet state calculated for $(i^{\text{Pr}}\text{PDI})\text{Fe}(\text{N}_2)$.⁵ Importantly, the four-coordinate compound, $(i^{\text{Pr}}\text{CNC})\text{Fe}(\text{N}_2)$, has not been experimentally observed by infrared or Mößbauer spectroscopy. However, this species represents a possible 16 electron intermediate, and therefore the electronic structure is of interest.

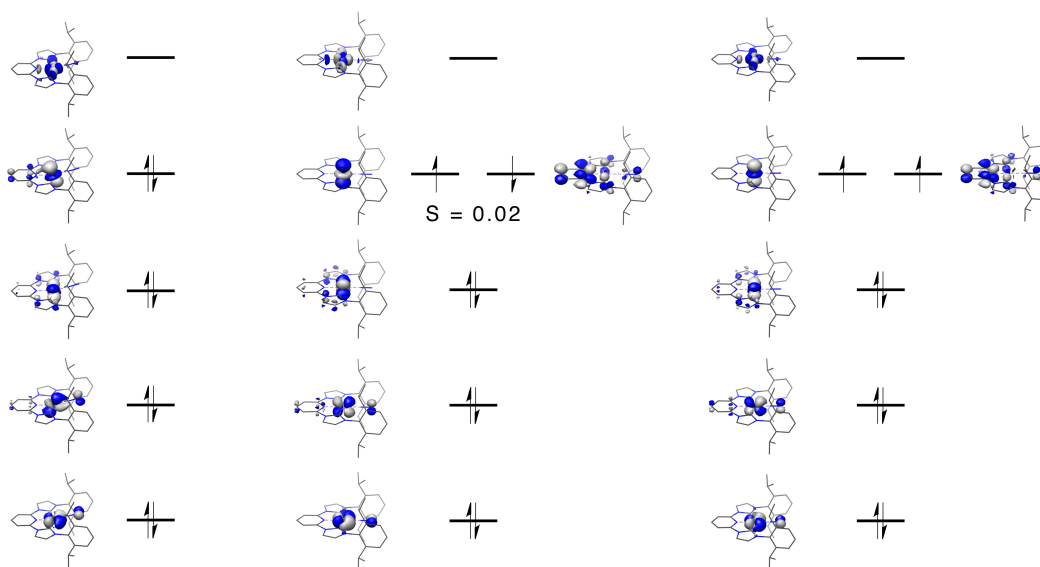


Figure B.1.3. Qualitative MO diagrams of hypothetical $(i^{\text{Pr}}\text{CNC})\text{Fe}(\text{N}_2)$ obtained from a RKS (left) and BS(2,2) (middle) singlet DFT calculation as well as an unrestricted triplet (right) DFT calculation at the B3LYP level.

For completion, the electronic structure of a pyridine di(carbene) iron complex bearing a principally σ -donating ligand, $(i^{\text{Pr}}\text{CNC})\text{Fe}(\text{DMAP})(\text{N}_2)$ was investigated. As stated in Section 2.1, the ^1H NMR spectrum of this complex does not exhibit features indicative of temperature independent paramagnetism, thereby differentiating it from the four-coordinate pyridine di(imine) iron compound, $(i^{\text{Pr}}\text{PDI})\text{Fe}(\text{DMAP})$.⁹ To investigate the electronic structure of this

complex, spin-restricted and BS(2,2) models were investigated. The above work demonstrated that BS(2,2) approaches would converge to a BS(1,1) solution, so the latter model was not explicitly calculated for $(i\text{PrCNC})\text{Fe}(\text{DMAP})(\text{N}_2)$. Additionally, RKS and BS(2,2) approaches for the theoretical four-coordinate complex, $(i\text{PrCNC})\text{Fe}(\text{DMAP})$ were investigated to determine the influence of the terminal dinitrogen molecule on the electronic structure.

Geometry optimizations at the B3LYP level of DFT were performed on all models and produced RKS and BS(1,1) solutions for the experimentally characterized five-coordinate iron DMAP compound, $(i\text{PrCNC})\text{Fe}(\text{DMAP})(\text{N}_2)$. The theoretical four-coordinate complex, $(i\text{PrCNC})\text{Fe}(\text{DMAP})$ converged to a BS(2,2) solution in which one of the overlap integrals was high ($S = 0.87$, *vide infra*), suggesting that a BS(1,1) description may be more accurate. Selected metrical parameters for all models are presented in **Table B.1.3**. For the five-coordinate complex, the broken-symmetry solution was 3 kcal/mol lower in energy than the spin-restricted solution, whereas for the theoretical four-coordinate complex, the broken-symmetry solution was 13 kcal/mol lower in energy than the corresponding spin-restricted model.

Similar to $(i\text{PrCNC})\text{Fe}(\text{N}_2)_2$, the HOMO obtained from the restricted calculation exhibits 37.7% Fe and 58.8% ligand, DMAP and dinitrogen character (**Figure B.1.4**). Analysis of the orbital manifolds for the BS(1,1) and BS(2,2) solution of the five- and hypothetical four-coordinate DMAP complexes, $(i\text{PrCNC})\text{Fe}(\text{DMAP})(\text{N}_2)$ and $(i\text{PrCNC})\text{Fe}(\text{DMAP})$, respectively, provided surprising insight. In the five-coordinate complex, coordination of dinitrogen provides a stabilizing interaction between the iron d_{xz} and dinitrogen π^* orbitals. As a result, the d_{z^2} orbital becomes the metal SOMO that interacts with the pyridine di(carbene) b_2 magnetic orbital. This electronic description, a low-spin Fe^{I} ($S = 1/2$) antiferromagnetically coupled to a pyridine

Table B.1.3. Comparison of selected computed bond distances (Å) and angles (°) for the (*i*PrCNC)Fe(DMAP)(N₂) and the theoretical (*i*PrCNC)Fe(DMAP) computed solutions.

	<i>(i</i> PrCNC)Fe(DMAP)(N ₂)			<i>(i</i> PrCNC)Fe(DMAP)	
	Exp.	RKS	BS(1,1)	RKS	BS(2,2)
Fe–N _{pyr}	1.8903(14)	1.897	1.926	1.860	1.909
Fe–C _{carbene}	1.9156(17)	1.960	1.976	1.954	1.967
	1.9179(17)	1.959	1.982	1.954	1.967
Fe–N _{N2}	1.7797(14)	1.806	1.801		
Fe–N _{DMAP}	2.0467(16)	2.043	2.209	2.003	2.007
N _{pyr} –C _{ipso}	1.369(2)	1.370	1.366	1.369	1.365
	1.369(2)	1.370	1.367	1.369	1.365
C _{ipso} –N _{carbene}	1.388(2)	1.383	1.390	1.384	1.381
	1.382(2)	1.383	1.390	1.384	1.381
N _{carbene} –C _{carbene}	1.406(2)	1.403	1.401	1.402	1.413
	1.405(2)	1.403	1.401	1.402	1.413
N≡N	1.1323(19)	1.117	1.119		
N–C _{carbene} –N	101.73(13)	102.00	102.11	101.26	101.25
	101.55(13)	101.95	102.04	101.26	101.25

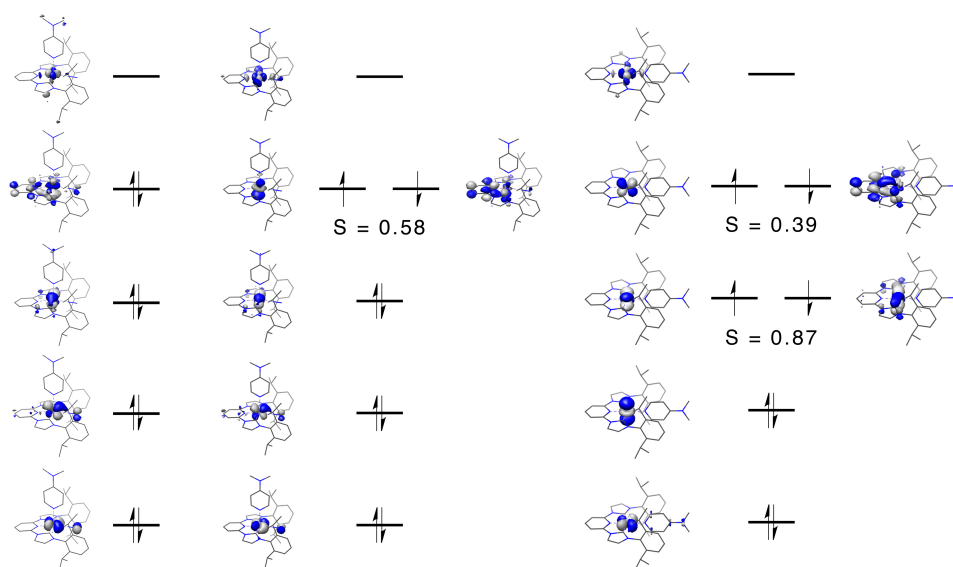


Figure B.1.4. Qualitative MO diagrams of (*i*PrCNC)Fe(DMAP)(N₂) obtained from a spin-restricted (left) and BS(2,2) (middle) DFT calculation and of hypothetical (*i*PrCNC)Fe(DMAP) (right) obtained from a BS(2,2) DFT calculation at the B3LYP level.

di(carbene) radical anion ($S = 1/2$), is similar to that computed for the five-coordinate nitrogen complex, $(i\text{PrCNC})\text{Fe}(\text{N}_2)_2$, using a broken-symmetry approach and is consistent with the Mößbauer and X-ray absorption data presented in Section 2.3. In the four-coordinate complex, assuming an idealized square planar geometry, absence of the stabilizing interaction provided by the dinitrogen ligand results in the d_{xz} becoming the magnetic orbital that antiferromagnetically couples to the pyridine di(carbene) b_2 SOMO.

The Mößbauer parameters calculated for $(i\text{PrCNC})\text{Fe}(\text{DMAP})(\text{N}_2)$ using the spin-restricted approach ($\delta = 0.28 \text{ mm}\cdot\text{s}^{-1}$, $\Delta E_Q = +0.73 \text{ mm}\cdot\text{s}^{-1}$) are in excellent agreement with the experimentally determined values ($\delta = 0.24 \text{ mm}\cdot\text{s}^{-1}$, $\Delta E_Q = |0.70| \text{ mm}\cdot\text{s}^{-1}$). In contrast, the values obtained using the broken-symmetry solution ($\delta = 0.36 \text{ mm}\cdot\text{s}^{-1}$, $\Delta E_Q = +0.50 \text{ mm}\cdot\text{s}^{-1}$) are much less accurate. In particular, the isomer shift is outside of the generally accepted range.⁷ In light of these results, the electronic structure of $(i\text{PrCNC})\text{Fe}(\text{DMAP})(\text{N}_2)$ is best described by a closed-shell singlet ground state with $(i\text{PrCNC}^0)\text{Fe}^0(\text{DMAP})(\text{N}_2)$ and $(i\text{PrCNC}^{2-})\text{Fe}^{\text{II}}(\text{DMAP})(\text{N}_2)$ resonance structures, and does not significantly differ from $(i\text{PrCNC})\text{Fe}(\text{N}_2)_2$.

In summary, the computational results for each of the experimentally characterized five-coordinate pyridine di(carbene) iron complexes support electronic structures best described by closed-shell singlet ground states with $(i\text{PrCNC}^0)\text{Fe}^0$ and $(i\text{PrCNC}^{2-})\text{Fe}^{\text{II}}$ resonance forms. To date, no evidence for a redox-active pyridine di(carbene) iron complex has been observed, although computations on hypothetical four-coordinate complexes suggest that the pyridine di(carbene) chelate may be able to support a ligand-centered radical.

B.2. Electronic Structure of Bis(oxazoline), Terpyridine, Bipyridine and Pyridine Di(carbene) Iron Dialkyl Complexes as Suggested by Density Functional Theory

The electronic structures of the pyridine di(imine) and pybox iron bis(neosilyl) complexes have been explored computationally.¹⁰ Each of these high-spin, $S = 2$ complexes break symmetry at the B3LYP level of density functional theory to give a broken-symmetry (BS) solution corresponding to a high-spin ferric ion antiferromagnetically coupled to a ligand-centered radical. The overlap values are relatively high and range from 0.73–0.76, indicating a high degree of covalency. Experimentally, these electronic structures are supported by the Mößbauer isomer shifts ($\delta = \sim 0.28 \text{ mm}\cdot\text{s}^{-1}$), which are inconsistent with the higher values ($\delta > 0.7 \text{ mm}\cdot\text{s}^{-1}$) exhibited by high-spin ferrous complexes.

The results obtained for the pyridine bis(oxazoline) iron dialkyl prompted computational investigation of the bis(oxazoline) iron dialkyl complexes. The solid state structure of the *tert*-butyl derivative, $(S,S)\text{-}(^t\text{BuBox})\text{Fe}(\text{CH}_2\text{Si}(\text{CH}_3)_3)_2$, prepared and crystallographically characterized by Bart *et al.*,¹¹ served as an initial geometry from which a BS(5,1) model was explored. Geometry optimization at the B3LYP level of DFT resulted in an unrestricted quintet solution corresponding to a high-spin, ferrous ion and a neutral bis(oxazoline). The experimental geometric parameters are acceptably reproduced by the computation (**Table B.2.1**). Therefore, the electronic structure is best described as $(S,S)\text{-}(^t\text{BuBox}^0)\text{Fe}^{\text{II}}(\text{CH}_2\text{Si}(\text{CH}_3)_3)_2$ with a high-spin ferrous ion ($S = 2$) and a neutral bis(oxazoline) ligand. A qualitative frontier molecular orbital diagram is presented in **Figure B.2.1**.

Terpyridine (terpy) and bipyridine (bipy),^{12,13} like the pyridine di(imine) ligands,^{4a} have demonstrated the ability to support ligand-centered radicals, and iron dialkyls of both have been

Table B.2.1. Experimental and computed bond distances (Å) for (*S,S*)-(*t*BuBox)Fe(CH₂Si(CH₃)₃)₂.

	Experimental	Unrestricted Quintet
Fe–N _{imine}	2.140(4)	2.214
	2.173(4)	2.256
Fe–C _{alkyl}	2.074(5)	2.098
	2.087(4)	2.114
C=N	1.271(6)	1.277
	1.263(6)	1.277
C–O	1.347(6)	1.347
	1.344(6)	1.345
N–C	1.503(6)	1.490
	1.497(6)	1.489

^a Data from reference 11.

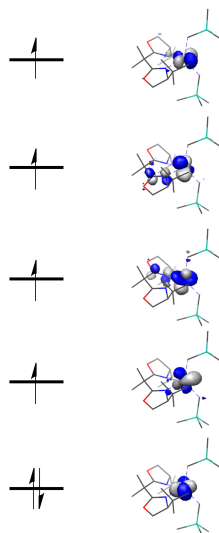


Figure B.2.1. Qualitative MO diagram for (*S,S*)-(*t*BuBox)Fe(CH₂Si(CH₃)₃)₂ obtained from a spin-unrestricted quintet DFT calculation at the B3LYP level.

reported (**Figure B.2.2**). The terpyridine iron bis(neosilyl) complex, prepared by Tondreau *et al.*¹⁰ from alkylation of the ferrous dihalide or by ligand substitution with (py)₂Fe(CH₂Si(CH₃)₂)₂, exhibits an *S* = 2 ground state. In contrast, the bis(bipyridine) iron diethyl complex,

$(\text{bipy})_2\text{Fe}(\text{Et})_2$ was prepared from alkylation of $(\text{bipy})_2\text{FeCl}_2$ and exhibits an $S = 0$ ground state.^{14,15}

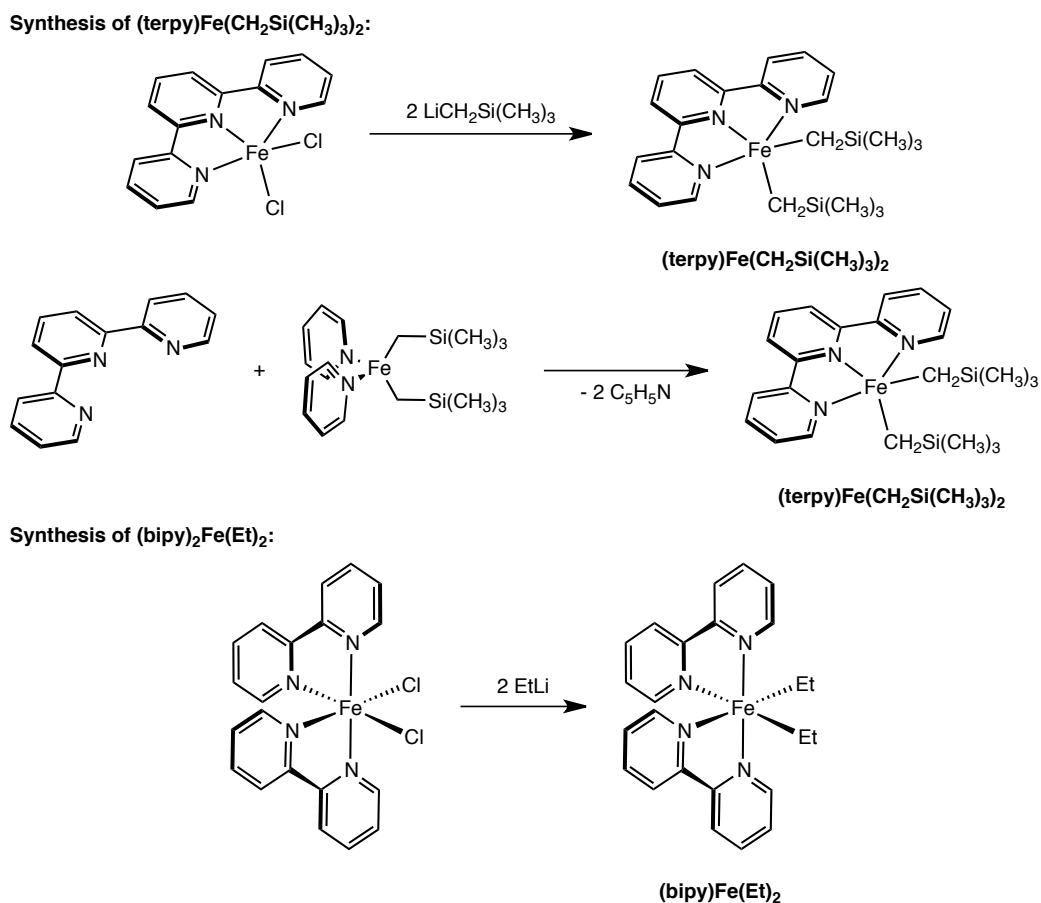


Figure B.2.2. Synthetic routes to $(\text{terpy})\text{Fe}(\text{CH}_2\text{Si}(\text{CH}_3)_3)_2$ and $(\text{bipy})_2\text{Fe}(\text{Et})_2$.

A spin-unrestricted quintet and a BS(5,1) model were explored at the B3LYP level of computation for $(\text{terpy})\text{Fe}(\text{CH}_2\text{Si}(\text{CH}_3)_3)_2$, and correspond to a redox innocent high-spin ferrous complex, and a redox-active high-spin ferric compound, respectively. Antiferromagnetic coupling accounts for the $S = 2$ ground state in the latter situation. Geometry optimization at the B3LYP level of DFT produced both solutions, where the redox-active form was 1.9 kcal/mol lower in energy. The geometric parameters of the optimized structures are reported in **Table B.2.2**. With few exceptions, the geometric parameters computed for the BS(5,1) solution were

more consistent with the experimentally determined bond distances and angles. However, neither solution can be excluded on the basis of structural or energetic arguments.

Table B.2.2. Experimental and computed bond distances (Å) for (terpy)Fe(CH₂Si(CH₃)₃)₂.

	Experimental	Unrestricted Quintet	BS(5,1)
Fe-N _{central}	2.014(2)	2.160	2.060
Fe-N	2.150(2)	2.241	2.206
	2.150(2)	2.241	2.206
Fe-C _{alkyl}	2.073(2)	2.087	2.103
	2.073(2)	2.087	2.104
N _{central} -C _{ipso}	1.375(2)	1.356	1.371
	1.375(2)	1.356	1.371
N-C _{ipso}	1.353(2)	1.351	1.358
	1.353(2)	1.351	1.358
C _{ipso} -C _{ipso}	1.457(2)	1.477	1.462
	1.457(2)	1.477	1.462

^a Data from reference 10.

Spin density plots for the spin-unrestricted quintet and BS(5,1) solutions obtained from Mulliken population analysis are presented in **Figure B.2.3**. For the unrestricted quintet solution, four unpaired electrons are delocalized over the metal and the terpyridine ligand, with a majority of the density (3.58) localized on the iron center. In contrast, the spin density plot for the broken-symmetry solution shows five unpaired electrons delocalized over the metal and alkyl ligands, suggesting significant covalency in the Fe-C_{alkyl} bonds. One unpaired electron of opposite spin is delocalized over the central pyridine ring. Closer analysis of the computed frontier molecular orbital scheme reveals significant commonalities between the electronic structure of the terpyridine iron dialkyl and that of the pyridine di(imine) and pybox iron dialkyl complexes, as is suggested experimentally by the similarity in Mößbauer parameters.¹⁰ Each example possesses

metal d_{xz} and ligand b_2 magnetic orbitals that exhibit a relatively high overlap integral of approximately 0.75.

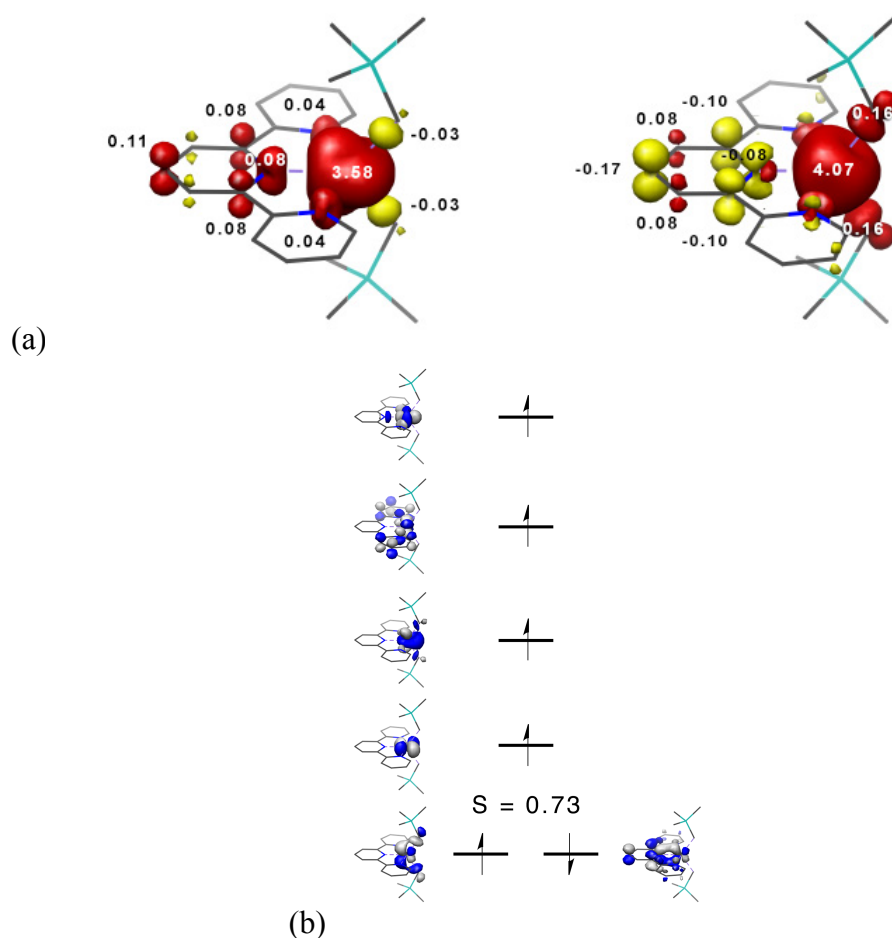


Figure B.2.3. (a) Spin density plots obtained from a Mulliken population analysis of the spin-unrestricted quintet (left) and BS(5,1) (right) solutions. (b) Qualitative MO diagram of (terpy)Fe(CH₂Si(CH₃)₃)₂ obtained from a BS(5,1) DFT calculation at the B3LYP level.

Mössbauer parameters were computed for the two electronic structure models predicted by DFT. Those values for the BS(5,1) model ($\delta = 0.22 \text{ mm}\cdot\text{s}^{-1}$, $\Delta E_Q = +2.62 \text{ mm}\cdot\text{s}^{-1}$) were more consistent with the with the experimentally determined values ($\delta = 0.29 \text{ mm}\cdot\text{s}^{-1}$, $\Delta E_Q = |2.37| \text{ mm}\cdot\text{s}^{-1}$). The values obtained from the spin-unrestricted quintet solution ($\delta = 0.45 \text{ mm}\cdot\text{s}^{-1}$, $\Delta E_Q = +2.92 \text{ mm}\cdot\text{s}^{-1}$) exhibited a significant deviation in the isomer shift and quadrupole splitting

parameters, suggesting that this state does not accurately describe the electronic structure of the compound. Therefore, the electronic structure is best described as (terpy¹⁻)Fe^{III}(CH₂Si(CH₃)₃)₂ with a high-spin ferric ion ($S = 3/2$) and a terpyridine radical anion.

In a seminal contribution from Kochi and coworkers, the effect of oxidation state on the reductive elimination of bis(bipyridine) iron diethyl complexes was investigated.¹⁵ The neutral complex, a formally low-spin iron(II) compound was crystallographically characterized. Closer analysis of the metrical parameters of the bipyridine ligands (see **Table B.2.3**) indicate intermediate values between the neutral (N–C_{ipso}: 1.346(2); C_{ipso}–C_{ipso}: 1.490(3)) and radical anion (N–C_{ipso}: 1.390(3); C_{ipso}–C_{ipso}: 1.431(3)) forms.¹³ Potential electronic structures accounting for a singlet ground state include low-spin iron(II) ($S = 0$), low-spin iron(III) ($S = 1/2$) with a bipyridine radical anion ($S = 1/2$), and intermediate-spin iron(IV) ($S = 1$) with two bipyridine radical anions ($S = 1$). In order to explore these possibilities, spin-restricted (RKS), BS(1,1) and BS(2,2) models were investigated.

Geometry optimization at the B3LYP level of DFT were performed for all models and produced two solutions. The two broken-symmetry approaches converged to the same BS(1,1) solution, which was 3.4 kcal/mol more stable than the spin-restricted solution. Both solutions acceptably reproduced the experimentally determined geometric parameters (**Table B.2.3**). Therefore, neither solution is favored on the basis of geometric or energetic arguments.

The Mulliken spin density plot of the broken-symmetry solution, presented in **Figure B.2.4**, shows one unpaired electron on the metal center and one unpaired electron of opposite spin delocalized over both bipyridine ligands. A closer inspection of the frontier molecular orbitals demonstrates that the iron is in a low-spin, ferric configuration with two doubly occupied d

orbitals and a singly occupied d orbital that is antiferromagnetically coupled to the ligand SOMO that contains equal contributions from both bipyridine ligands. This likely accounts for the intermediate ligand bond distances observed between bipy⁰ and bipy¹⁻.

Möbbauser parameters were computed in order to determine if experimental measurements would be able to distinguish between these two models. Although the computed isomer shifts were similar: 0.29 and 0.25 mm·s⁻¹ for the RKS and broken-symmetry solutions, respectively. The quadrupole splitting parameters – 1.329 mm·s⁻¹ and -1.281 mm·s⁻¹ for the RKS and broken-symmetry solutions, respectively – distinguish the two descriptions obtained by density functional theory. It is important to note that the calculations yielded an asymmetry parameter of the electric field gradient, η , of 0.05 and 0.68 for the spin-restricted and broken-symmetry solutions, respectively, which suggests that the sign of the quadrupole splitting is important.

The electronic structure of the pyridine di(carbene) iron dialkyl dinitrogen complexes was investigated by DFT in order to determine potential electronic differences as a function of alkyl group, and to further distinguish them from the high-spin, $S = 2$ tridentate iron dialkyls studied previously by our laboratory. Broken-symmetry DFT calculations at the B3LYP level were performed to better understand the electronic structure of (ⁱPrCNC)Fe(CH₃)₂(N₂), (ⁱPrCNC)Fe(4-CH₃-C₆H₄)(N₂) and (ⁱPrCNC)Fe(CH₂Si(CH₃)₃)₂(N₂). The X-ray diffraction data was utilized to provide an initial geometry from which geometry optimizations were performed in each case.

All complexes were calculated as spin-unrestricted singlets, in agreement with the experimentally established ground states. However, the calculations for each dialkyl converged to closed-shell solutions, demonstrating no BS character. The computed metrical parameters for

each complex are presented in **Table B.2.4** and are consistent with the experimentally determined values (see **Table 3.3** for comparison). The computed metal-ligand bond distances of (*i*PrCNC)Fe(CH₃)₂(N₂) are shorter than those of (*i*PrCNC)Fe(CH₂Si(CH₃)₃)₂(N₂), which is consistent with the experimentally observed increase in covalency as exhibited by the lower Mößbauer isomer shift.

Table B.2.4. Computed bond distances (Å) and angles (deg) for (*i*PrCNC)Fe(R)₂(N₂) (R = CH₃, 4-CH₃-C₆H₄, CH₂Si(CH₃)₃).

	CH ₃	4-CH ₃ -C ₆ H ₄	CH ₂ Si(CH ₃) ₃
Fe-N _{pyr}	1.908	1.913	1.909
Fe-C _{carbene}	1.947	1.986	1.976
	1.948	1.988	1.978
Fe-C _{alkyl}	2.128	2.106	2.169
	2.130	2.107	2.170
Fe-N _{N2}	1.824	1.833	1.844
N≡N	1.108	1.105	1.105
N _{pyr} -Fe-C _{alkyl}	88.52	89.18	95.61
	89.83	89.20	95.72
C _{alkyl} -Fe-N _{N2}	91.10	90.79	84.34
	90.55	90.84	84.33
N _{pyr} -Fe-C _{carbene}	80.34	80.34	80.04
	80.36	80.35	80.10

Qualitative molecular orbital diagrams for (*i*PrCNC)Fe(R)₂(N₂) (R = CH₃, CH₂Si(CH₃)₃) are presented in **Figure B.2.5**. Unpopulated orbitals were localized using the Pipek-Mezey method to provide a straightforward visual interpretation.¹⁶ From these studies, a closed-shell, low-spin, iron(II) description for each of the dialkyl dinitrogen complexes, (*i*PrCNC)Fe(R)₂(N₂) (R = CH₃, C₆H₄CH₃, CH₂Si(CH₃)₃), is supported with three doubly occupied metal orbitals corresponding to the t_{2g} set of an idealized octahedral ligand field. To further support the validity of the calculated electronic structure, ⁵⁷Fe Mößbauer parameters were computed (**Table B.2.5**).

The computed values are in excellent agreement with those measured experimentally, further validating the accuracy of the computational model.

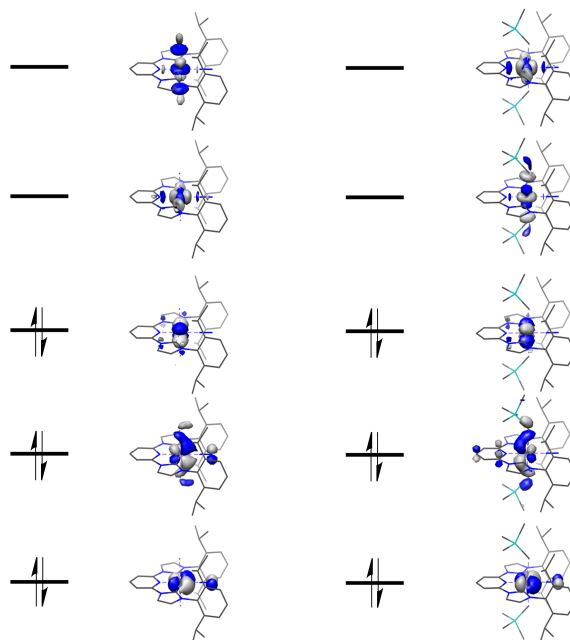


Figure B.2.5. Qualitative MO diagrams of $(i\text{PrCNC})\text{Fe}(\text{R})_2(\text{N}_2)$ ($\text{R} = \text{CH}_3, \text{CH}_2\text{Si}(\text{CH}_3)_3$) obtained from a spin-restricted singlet DFT calculation at the B3LYP level.

Table B.2.5. Experimental and computed Mößbauer parameters for $(i\text{PrCNC})\text{Fe}(\text{R})_2(\text{N}_2)$ ($\text{R} = \text{CH}_3, 4\text{-CH}_3\text{-C}_6\text{H}_4, \text{CH}_2\text{Si}(\text{CH}_3)_3$).

Complex	δ ($\text{mm}\cdot\text{s}^{-1}$)	ΔE_Q ($\text{mm}\cdot\text{s}^{-1}$)
$(i\text{PrCNC})\text{Fe}(\text{CH}_3)_2(\text{N}_2)$	0.06	1.61
<i>Computed</i>	0.05	1.67
$(i\text{PrCNC})\text{Fe}(4\text{-CH}_3\text{-C}_6\text{H}_4)_2(\text{N}_2)$	0.07	1.42
<i>Computed</i>	0.15	1.45
$(i\text{PrCNC})\text{Fe}(\text{CH}_2\text{Si}(\text{CH}_3)_2)_2(\text{N}_2)$	0.13	1.71
<i>Computed</i>	0.20	1.42

The electronic structure of several derivatives of the parent, pyridine di(carbene) iron dialkyl dinitrogen complexes, including the carbonyl adduct, $(i\text{PrCNC})\text{Fe}(\text{CH}_2\text{Si}(\text{CH}_3)_3)_2(\text{CO})$, the proposed 16 electron species, $(i\text{PrCNC})\text{Fe}(\text{CH}_3)_2$, and the disilyl complex,

(*i*PrCNC)Fe(SiH₂Mes)₂(N₂) were also investigated by DFT calculations at the B3LYP level. The initial geometry of the intermediate was generated by removing dinitrogen from the coordinates of the initial X-ray diffraction data for the iron dimethyl dinitrogen compound. All complexes were calculated as spin-unrestricted singlets using a BS(2,2) model, although the true ground state of the intermediate and the iron disilyl dinitrogen compound are not known. In all cases, the calculations converged to a closed-shell solution, indicating that low-spin, ferrous descriptions are computationally supported. The results for the iron bis(neosilyl) carbonyl and iron disilyl dinitrogen compound, including their qualitative molecular orbital diagrams and computed Mößbauer parameters can be found in Appendix B.3.

The computational results for the proposed intermediate exhibited several interesting features. A comparison of the selected metrical parameters of the parent pyridine di(carbene) iron dimethyl dinitrogen compound and the pyridine di(carbene) iron dimethyl intermediate is presented in **Table B.2.6**. The molecule adopts a pseudo-trigonal bipyrimidal geometry, as the *C_{alkyl}-Fe-C_{alkyl}* bond angle contracts by approximately 27°. The iron pyridine bond length decreases, as would be expected without the *trans*-influence of the dinitrogen ligand. Also, a significant iron methyl bond length increase of approximately 0.08 Å occurs, which indicates a weakening of the bond.

The lowest unoccupied molecular orbital with significant metal character (68.3%) is presented in **Figure B.2.6**. This metal LUMO indicates the electrophilicity of the iron center towards nucleophiles such as carbon monoxide, which has been experimentally verified. The full utility of these low-spin, ferrous dialkyls has yet to be extensively explored.

Table B.2.6. Computed bond distances (Å) and angles (°) for $(i^{\text{Pr}}\text{CNC})\text{Fe}(\text{CH}_3)_2(\text{N}_2)$ and $(i^{\text{Pr}}\text{CNC})\text{Fe}(\text{CH}_3)_2$.

	$(i^{\text{Pr}}\text{CNC})\text{Fe}(\text{CH}_3)_2(\text{N}_2)$	$(i^{\text{Pr}}\text{CNC})\text{Fe}(\text{CH}_3)_2$
Fe–N _{pyr}	1.908	1.837
Fe–C _{carbene}	1.947	1.950
	1.948	1.950
Fe–C _{alkyl}	2.128	2.049
	2.130	2.053
N _{pyr} –Fe–C _{alkyl}	88.52	105.41
	89.83	103.17
C _{alkyl} –Fe–C _{alkyl}	181.66	151.42
N _{pyr} –Fe–C _{carbene}	80.34	81.66
	80.36	81.66

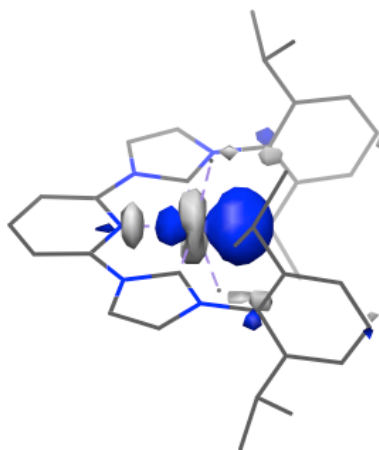


Figure B.2.6. Computed LUMO of the proposed intermediate, $(i^{\text{Pr}}\text{CNC})\text{Fe}(\text{CH}_3)_2$, involved in the reductive elimination of ethane obtained from a spin-restricted singlet DFT calculation at the B3LYP level.

B.3. Summary of Results for other Complexes

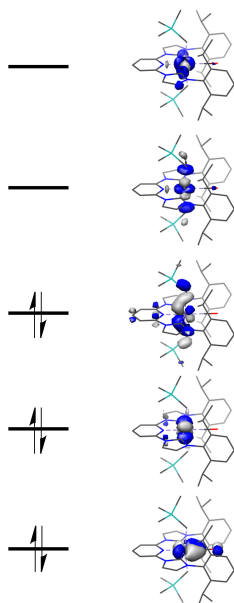


Figure B.3.1. Qualitative MO diagram for $(i\text{PrCNC})\text{Fe}(\text{CH}_2\text{Si}(\text{CH}_3)_3)_2(\text{CO})$ obtained from a restricted singlet DFT calculation at the B3LYP level.

Table B.3.1. Experimental and computed Mößbauer parameters for $(i\text{PrCNC})\text{Fe}(\text{R})_2(\text{CO})$ ($\text{R} = \text{CH}_2\text{Si}(\text{CH}_3)_3$).

Complex	δ ($\text{mm}\cdot\text{s}^{-1}$)	ΔE_Q ($\text{mm}\cdot\text{s}^{-1}$)
$(i\text{PrCNC})\text{Fe}(\text{CH}_2\text{Si}(\text{CH}_3)_2)_2(\text{CO})$	-0.03	0.65
<i>Computed</i>	0.05	0.50



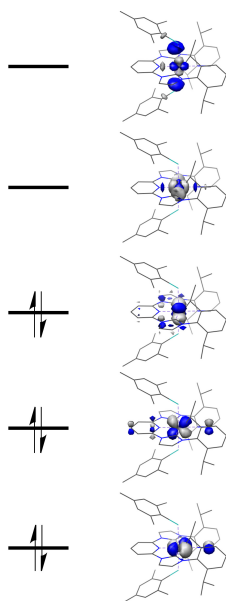


Figure B.3.2. Qualitative MO diagram for $(i\text{PrCNC})\text{Fe}(\text{SiH}_2\text{Mes})_2(\text{N}_2)$ obtained from a restricted singlet DFT calculation at the B3LYP level.

Table B.3.2. Computed Mößbauer parameters for $(i\text{PrCNC})\text{Fe}(\text{R})_2(\text{CO})$ ($\text{R} = \text{CH}_2\text{Si}(\text{CH}_3)_3$).

Complex	δ ($\text{mm}\cdot\text{s}^{-1}$)	ΔE_Q ($\text{mm}\cdot\text{s}^{-1}$)
$(i\text{PrCNC})\text{Fe}(\text{SiH}_2\text{Mes})_2(\text{CO})$?	?
<i>Computed</i>	<i>0.13</i>	<i>1.22</i>

B.4. Converged Geometries for Theoretical Molecules at the B3LYP Level of DFT

$(4\text{-CF}_3\text{-}i\text{PrPDI})\text{Fe}(\text{N}_2)$, BS(2,2)

Fe	-0.036865	-0.013110	-0.124459	C	1.576568	2.289421	-0.214785
N	0.281015	-1.940340	-0.053227	C	2.065500	3.708699	-0.262236
N	1.844163	-0.014670	-0.151124	C	-0.757367	-2.930876	0.002447
N	0.283554	1.916351	-0.185329	C	-1.235772	-3.373585	1.260584
N	-1.876505	-0.011189	-0.105388	C	-2.285815	-4.304128	1.282382
N	-2.986166	-0.009776	-0.100440	C	-2.852572	-4.786943	0.104272
C	6.094409	-0.042450	-0.258918	C	-2.375870	-4.334985	-1.125297
C	2.057871	-3.737637	0.006661	C	-1.331058	-3.402168	-1.204851
C	1.572717	-2.317870	-0.054751	C	-0.652469	-2.866850	2.579198
C	2.497122	-1.213674	-0.111883	C	-1.703186	-2.112275	3.415401
C	3.896263	-1.237305	-0.125302	C	-0.007497	-4.001249	3.397429
C	4.590953	-0.015888	-0.185865	C	-0.834503	-2.936006	-2.573026
C	3.899614	1.204183	-0.221379	C	-1.969404	-2.377994	-3.450639
C	2.498073	1.183156	-0.198959	C	-0.069336	-4.053305	-3.307547
				C	-0.752753	2.910342	-0.185782
				C	-1.268733	3.375937	1.049579

C	-2.309370	4.316553	1.023634
C	-2.836854	4.782028	-0.179759
C	-2.328817	4.302490	-1.385776
C	-1.287409	3.362620	-1.417676
C	-0.719583	2.893223	2.391683
C	0.064780	4.003681	3.115918
C	-1.820019	2.315857	3.299944
C	-0.765589	2.860937	-2.763693
C	-0.072963	3.981913	-3.561975
C	-1.873401	2.193056	-3.599549
H	2.634283	-3.921122	0.930684
H	2.732745	-3.961988	-0.837154
H	1.227609	-4.453086	-0.020492
H	4.438452	-2.182329	-0.083734
H	4.444225	2.146877	-0.260111
H	1.237434	4.426157	-0.225824
H	2.641634	3.899696	-1.184622
H	2.742170	3.922374	0.583068
H	-2.668283	-4.656777	2.243861
H	-3.670648	-5.511329	0.144353
H	-2.826587	-4.713126	-2.046215
H	0.143060	-2.147126	2.336196
H	-2.142984	-1.275142	2.850864
H	-1.248241	-1.702190	4.332112
H	-2.529167	-2.774000	3.723898
H	0.766754	-4.527835	2.817694
H	-0.753994	-4.749670	3.710340
H	0.463816	-3.602330	4.310697
H	-0.124472	-2.113027	-2.401241
H	-2.516700	-1.572932	-2.936097
H	-2.699957	-3.157276	-3.722356
H	-1.563711	-1.967855	-4.390227
H	0.774604	-4.429859	-2.708628
H	0.332990	-3.686412	-4.266115
H	-0.728092	-4.909900	-3.527151
H	-2.716419	4.690632	1.966511
H	-3.649496	5.513629	-0.177324
H	-2.751455	4.664564	-2.326522
H	-0.012015	2.076842	2.182939
H	0.885063	4.394723	2.493891
H	0.502113	3.624434	4.054133
H	-0.590047	4.852962	3.372500
H	-2.379964	1.514647	2.793143
H	-2.545412	3.086752	3.607292
H	-1.380494	1.895111	4.219436
H	-0.008086	2.090231	-2.557704
H	0.745984	4.441950	-2.987385
H	-0.782040	4.783178	-3.827860
H	0.350787	3.587744	-4.500283
H	-2.358647	1.374604	-3.045005
H	-1.456142	1.773480	-4.529831
H	-2.658486	2.911889	-3.885708
F	6.641454	1.158336	0.003571
F	6.528439	-0.413488	-1.481681
F	6.619055	-0.924397	0.615332

(4-CF₃-ⁱPrPDI)Fe(DMAP), BS(2,2)

Fe	-0.065629	0.006542	0.043974
C	2.074447	3.709351	0.401014
C	1.558108	2.308617	0.221672
C	2.458287	1.216397	0.084597
C	3.873858	1.243814	0.047139
C	4.561640	0.035116	-0.119881
C	3.877198	-1.182294	-0.236392
C	2.463429	-1.170705	-0.178355
C	1.570568	-2.275194	-0.239962
C	2.092421	-3.669382	-0.450827
F	6.624094	1.101756	0.371629
F	6.618426	-1.065340	0.295481
C	-0.759556	2.985720	0.208137
C	-1.042907	3.740473	-0.964154
C	-2.092668	4.672596	-0.926491
C	-2.845387	4.875602	0.228564
C	-2.549655	4.142661	1.378719
C	-1.515287	3.196246	1.395302
C	-0.241930	3.584902	-2.260467
C	-1.092254	3.042083	-3.424308
C	0.433936	4.906425	-2.676338
C	-1.176856	2.446589	2.683062
C	-2.402574	2.101036	3.542264
C	-0.139602	3.221327	3.519899
C	-0.726413	-2.984881	-0.034185
C	-1.566739	-3.233044	-1.154738
C	-2.574820	-4.201035	-1.041649
C	-2.763875	-4.918649	0.140192
C	-1.930195	-4.676618	1.230427
C	-0.902764	-3.721361	1.170632
C	-1.346486	-2.502291	-2.478374
C	-0.380704	-3.285552	-3.389803
C	-2.645948	-2.178417	-3.231873
C	-0.010673	-3.520471	2.399802
C	0.742145	-4.811136	2.777760
C	-0.789407	-2.993521	3.619876
C	-2.869062	0.707763	-0.740897
C	-4.254069	0.723961	-0.736221
C	-4.968256	-0.026304	0.232936
C	-4.168745	-0.766910	1.140834
C	-2.788326	-0.732157	1.035148
C	-7.014879	-0.826319	1.301501
C	-7.107013	0.745383	-0.663522
N	0.238442	1.966683	0.188433
N	1.802417	0.019327	-0.026839
N	0.252227	-1.949743	-0.109921
C	6.062964	0.040423	-0.239404
N	-2.116381	-0.007370	0.118751
N	-6.332094	-0.035529	0.288841
H	1.267911	4.422316	0.613111
H	2.609483	4.065772	-0.497623
H	2.798272	3.754420	1.233154
H	4.415166	2.183682	0.145598
H	4.421346	-2.118595	-0.351396
H	2.726773	-3.998945	0.391603
H	2.726199	-3.715767	-1.353451
H	1.282959	-4.401199	-0.566365
H	-2.322087	5.255216	-1.822932

H	-3.656591	5.609386	0.236363	C	-2.701489	-3.151935	-1.776300
H	-3.133902	4.316775	2.285007	C	-2.057615	-2.298130	-2.862694
H	0.554236	2.850499	-2.075710	C	-3.021622	-1.280513	-3.486916
H	-1.505340	2.046087	-3.203315	C	-1.429615	-3.201415	-3.942644
H	-0.478703	2.944037	-4.334933	C	-1.753117	-5.123702	1.444603
H	-1.935262	3.712075	-3.663471	C	-1.364170	-6.588513	1.156569
H	-0.309664	5.669493	-2.960122	C	-2.511920	-5.032437	2.776363
H	1.092645	4.747213	-3.546457	C	3.375939	-1.166041	0.859499
H	1.042800	5.326095	-1.862052	C	4.007774	0.058901	1.121501
H	-0.703589	1.498228	2.383318	C	3.301101	1.263510	0.986112
H	-2.859636	2.996649	3.995126	C	1.964979	1.190005	0.599839
H	-2.107345	1.440124	4.374241	C	-0.176736	1.867353	-0.157155
H	-3.178982	1.582944	2.958083	C	0.314959	4.053224	-0.652259
H	0.778986	3.415835	2.948343	C	1.395631	3.570107	0.003918
H	0.140736	2.651355	4.421732	C	-1.650272	3.076680	-1.786460
H	-0.544456	4.193781	3.846946	C	-1.276547	2.693329	-3.097345
H	-3.222536	-4.404732	-1.897411	C	-2.250564	2.769079	-4.103908
H	-3.555377	-5.670763	0.206877	C	-3.537430	3.225282	-3.829730
H	-2.077123	-5.246848	2.152004	C	-3.869684	3.633653	-2.539803
H	-0.856164	-1.546095	-2.236189	C	-2.937485	3.577109	-1.491206
H	0.587656	-3.461957	-2.899572	C	-3.303864	4.113954	-0.110580
H	-0.187650	-2.731111	-4.323519	C	-2.983647	5.619475	-0.003077
H	-0.803427	-4.267731	-3.660871	C	-4.772863	3.864851	0.265092
H	-3.135971	-3.084653	-3.625411	C	0.150955	2.294451	-3.474258
H	-2.430154	-1.532042	-4.098735	C	0.838406	3.435356	-4.252684
H	-3.369493	-1.652085	-2.589695	C	0.226578	0.975201	-4.259127
H	0.741383	-2.760646	2.145891	N	1.333637	0.011719	0.392255
H	0.049702	-5.597301	3.122487	N	1.215101	-2.212095	0.156885
H	1.455136	-4.618293	3.596645	N	-0.608427	-3.185874	-0.456247
H	1.305837	-5.218320	1.925842	N	1.102809	2.237949	0.284353
H	-1.261819	-2.019661	3.419305	N	-0.626502	3.023366	-0.761241
H	-0.110397	-2.855503	4.477101	H	0.259470	-5.104407	-0.985732
H	-1.582019	-3.693303	3.934290	H	2.605288	-3.854065	-0.205991
H	-2.326552	1.303092	-1.472402	H	-4.312418	-5.654437	0.760042
H	-4.763925	1.332627	-1.480919	H	-5.630720	-4.818963	-1.161263
H	-4.609514	-1.382037	1.923406	H	-4.604374	-3.263049	-2.787917
H	-2.181929	-1.319741	1.721112	H	-1.254091	-1.716397	-2.391127
H	-6.766466	-1.898929	1.217408	H	-3.829354	-1.760903	-4.064669
H	-8.099630	-0.718993	1.173948	H	-2.474713	-0.624497	-4.181284
H	-6.756822	-0.494781	2.322969	H	-3.478146	-0.640320	-2.716612
H	-6.864128	1.820681	-0.601991	H	-0.680779	-3.887403	-3.515028
H	-8.175807	0.626767	-0.444217	H	-0.924628	-2.593535	-4.712048
H	-6.933061	0.414174	-1.703016	H	-2.195708	-3.815111	-4.447868
F	6.465765	0.082558	-1.529115	H	-0.825117	-4.546962	1.569084

(*i*PrCNC)Fe(CH₂CH(Ph)₂)(H), RKS

Fe	-0.555666	-0.012491	0.128450
C	2.032184	-1.135965	0.493646
C	-0.153918	-1.964245	-0.007954
C	0.434719	-4.103171	-0.609494
C	1.580780	-3.498628	-0.220205
C	-1.982067	-3.599821	-0.644246
C	-2.535730	-4.523378	0.275803
C	-3.857505	-4.945812	0.063554
C	-4.600702	-4.481417	-1.017660
C	-4.022105	-3.599591	-1.928167

H	-2.260815	-7.223907	1.066958
H	-0.748803	-6.993966	1.977271
H	-0.791693	-6.695185	0.222405
H	-2.822861	-4.002960	2.992819
H	-1.869316	-5.372339	3.605116
H	-3.411511	-5.669499	2.782213
H	3.915765	-2.109594	0.945302
H	5.055908	0.075718	1.425735
H	3.784885	2.224705	1.162437
H	0.129857	5.037009	-1.070319
H	2.329926	4.045899	0.281901
H	-1.991856	2.473683	-5.123790
H	-4.283108	3.275906	-4.628122
H	-4.874676	4.011174	-2.345133

H	-2.680155	3.588091	0.626791	C	-1.510294	-5.847334	-1.478627
H	-1.921726	5.832175	-0.197699	C	-1.424459	-2.483687	3.222597
H	-3.215650	5.987850	1.009474	C	-0.889080	-3.641498	4.089095
H	-3.579931	6.203866	-0.724101	C	-2.155556	-1.463926	4.107128
H	-5.466154	4.449133	-0.361841	C	3.925940	-1.280118	0.404307
H	-4.949195	4.168005	1.307712	C	4.651508	-0.083500	0.318524
H	-5.039999	2.801352	0.169669	C	3.979179	1.138882	0.173113
H	0.718325	2.135968	-2.547866	C	2.589583	1.114645	0.103853
H	0.335090	3.625291	-5.215717	C	0.355250	1.900425	0.056351
H	1.888240	3.177835	-4.469247	C	0.760080	4.143536	0.310427
H	0.830949	4.378591	-3.683938	C	1.972828	3.556483	0.183745
H	-0.212112	0.152630	-3.677303	C	-1.544580	3.373086	0.770087
H	1.278536	0.721261	-4.469407	C	-2.610297	3.706781	-0.095435
H	-0.293999	1.035189	-5.228482	C	-3.870783	3.933559	0.478767
C	-1.960747	0.193282	1.965439	C	-4.063868	3.854416	1.856695
C	-2.510806	0.076444	0.554864	C	-2.988939	3.567034	2.694573
C	-2.425117	-0.840504	2.995977	C	-1.706989	3.330064	2.175954
C	-2.088357	1.557910	2.653468	C	-0.538987	3.117839	3.139139
C	-1.549805	-1.287186	3.999472	C	-0.170335	4.438290	3.844096
C	-3.771952	-1.229148	3.071743	C	-0.801832	2.002073	4.159100
C	-4.238108	-1.997388	4.143773	C	-2.399727	3.900118	-1.592719
C	-3.361826	-2.407916	5.153079	C	-2.020204	5.361859	-1.908354
C	-2.008998	-2.062492	5.067484	C	-3.607286	3.475804	-2.442267
C	-0.956583	2.247860	3.114703	C	-0.231756	-0.098174	-2.162659
C	-3.350281	2.104736	2.935697	C	-1.613741	-0.103725	-1.584456
C	-1.074919	3.450251	3.819911	N	1.879224	-0.038985	0.144166
C	-2.337570	3.982824	4.092615	N	1.625039	-2.250086	0.417581
C	-3.475112	3.298958	3.650078	N	-0.348851	-3.115900	0.579391
H	-0.766769	-0.075735	-1.350284	N	1.719707	2.195498	0.047434
H	-0.823010	0.027365	1.936724	N	-0.214911	3.141726	0.246343
H	-3.053219	0.957725	0.220368	C	0.177169	-1.326558	-2.956655
H	-3.103573	-0.822091	0.395156	C	0.149177	1.092599	-3.020211
H	-0.494527	-1.001078	3.954408	C	1.485839	-1.843782	-2.917737
H	-4.462866	-0.910158	2.288790	C	-0.704047	-1.897837	-3.895725
H	-5.294047	-2.279523	4.188503	C	1.492043	1.504280	-3.145083
H	-3.727122	-3.005911	5.992546	C	-0.790262	1.747736	-3.840664
H	-1.309029	-2.392719	5.840423	C	1.886978	-2.892417	-3.749010
H	0.035728	1.833000	2.925654	C	0.991332	-3.452752	-4.664860
H	-4.248029	1.583052	2.599462	C	-0.307559	-2.942205	-4.736419
H	-0.174655	3.967688	4.162740	C	-0.419015	2.780529	-4.708748
H	-2.436037	4.919351	4.647939	C	0.914216	3.188358	-4.793535
H	-4.470149	3.698052	3.867007	C	1.869163	2.534647	-4.007395

(ⁱPrCNC)Fe(C(Ph)₂CH₃)(H), RKS

Fe	0.034069	-0.020720	-0.099460
C	2.538377	-1.209868	0.317564
C	0.274550	-1.925102	0.271699
C	0.582128	-4.113613	0.884394
C	1.820205	-3.577109	0.782516
C	-1.764074	-3.327071	0.805768
C	-2.291694	-3.013254	2.082618
C	-3.651374	-3.271902	2.312871
C	-4.456945	-3.839326	1.328867
C	-3.910392	-4.169350	0.091929
C	-2.557176	-3.929381	-0.199412
C	-1.987715	-4.381199	-1.542455
C	-2.983202	-4.217691	-2.701871

C	-1.510294	-5.847334	-1.478627
C	-1.424459	-2.483687	3.222597
C	-0.889080	-3.641498	4.089095
C	-2.155556	-1.463926	4.107128
C	3.925940	-1.280118	0.404307
C	4.651508	-0.083500	0.318524
C	3.979179	1.138882	0.173113
C	2.589583	1.114645	0.103853
C	0.355250	1.900425	0.056351
C	0.760080	4.143536	0.310427
C	1.972828	3.556483	0.183745
C	-1.544580	3.373086	0.770087
C	-2.610297	3.706781	-0.095435
C	-3.870783	3.933559	0.478767
C	-4.063868	3.854416	1.856695
C	-2.988939	3.567034	2.694573
C	-1.706989	3.330064	2.175954
C	-0.538987	3.117839	3.139139
C	-0.170335	4.438290	3.844096
C	-0.801832	2.002073	4.159100
C	-2.399727	3.900118	-1.592719
C	-2.020204	5.361859	-1.908354
C	-3.607286	3.475804	-2.442267
C	-0.231756	-0.098174	-2.162659
C	-1.613741	-0.103725	-1.584456
N	1.879224	-0.038985	0.144166
N	1.625039	-2.250086	0.417581
N	-0.348851	-3.115900	0.579391
N	1.719707	2.195498	0.047434
N	-0.214911	3.141726	0.246343
C	0.177169	-1.326558	-2.956655
C	0.149177	1.092599	-3.020211
C	1.485839	-1.843782	-2.917737
C	-0.704047	-1.897837	-3.895725
C	1.492043	1.504280	-3.145083
C	-0.790262	1.747736	-3.840664
C	1.886978	-2.892417	-3.749010
C	0.991332	-3.452752	-4.664860
C	-0.307559	-2.942205	-4.736419
C	-0.419015	2.780529	-4.708748
C	0.914216	3.188358	-4.793535
C	1.869163	2.534647	-4.007395
H	0.271908	-5.116518	1.156388
H	2.799326	-4.013585	0.944151
H	-4.084867	-3.032123	3.284992
H	-5.513767	-4.034279	1.531089
H	-4.548652	-4.627683	-0.664930
H	-1.112212	-3.753047	-1.766700
H	-3.831048	-4.917130	-2.621106
H	-2.480121	-4.427752	-3.656394
H	-3.390937	-3.196450	-2.752876
H	-0.742512	-6.000593	-0.706214
H	-1.076135	-6.151722	-2.445003
H	-2.351342	-6.526074	-1.256425
H	-0.567381	-1.963249	2.774041
H	-1.717885	-4.190029	4.567980
H	-0.235400	-3.254636	4.889038
H	-0.304090	-4.363932	3.500748

H	-2.596638	-0.653917	3.508013
H	-1.451341	-1.012004	4.823257
H	-2.960065	-1.930284	4.698781
H	4.430703	-2.237180	0.539236
H	5.741553	-0.102114	0.378910
H	4.525458	2.081512	0.128311
H	0.494006	5.185423	0.454284
H	2.970836	3.980396	0.178512
H	-4.715807	4.185604	-0.164008
H	-5.056021	4.033884	2.279942
H	-3.146143	3.533900	3.775739
H	0.334374	2.800751	2.553727
H	0.067171	5.234148	3.120987
H	0.709592	4.297728	4.494344
H	-0.998881	4.800405	4.475455
H	-1.645803	2.236290	4.828963
H	0.087480	1.850934	4.793562
H	-1.017533	1.056109	3.645594
H	-1.547788	3.273797	-1.892543
H	-2.835230	6.052556	-1.632006
H	-1.819231	5.482596	-2.985621
H	-1.115774	5.677760	-1.366282
H	-3.932651	2.450100	-2.208114
H	-3.346137	3.515653	-3.511121
H	-4.472061	4.144639	-2.299485
H	-2.176213	-1.021355	-1.754202
H	-1.646706	-0.031353	-0.413035
H	2.208606	-1.407725	-2.229545
H	-1.718297	-1.502401	-3.989831
H	2.258932	0.998973	-2.557312
H	-1.835200	1.433109	-3.818673
H	2.911102	-3.271581	-3.683020
H	1.304766	-4.269700	-5.320809
H	-1.016055	-3.350596	-5.463578
H	-1.178617	3.259319	-5.334438
H	1.208473	3.995262	-5.470444
H	2.921245	2.829478	-4.067582
H	-0.623873	0.061003	1.295645
H	-2.232864	0.753245	-1.846634

(ⁱPrCNC)Fe(N₂), BS(1,1)

Fe	0.016433	0.020793	-0.516532
N	-1.758971	0.021577	-0.838117
N	-2.859996	0.022430	-1.036176
N	1.908271	0.020925	-0.150436
N	1.719136	2.263693	-0.185032
N	-0.194827	3.203146	-0.552449
N	1.715312	-2.221675	-0.165105
N	-0.199512	-3.160809	-0.528435
C	2.594053	1.194113	-0.014382
C	0.379871	1.956960	-0.446048
C	0.736952	4.218466	-0.366543
H	0.455437	5.265687	-0.414906
C	1.941595	3.633777	-0.134897
H	2.915379	4.069700	0.059755
C	-1.586626	3.453105	-0.815931

C	-2.470823	3.595041	0.275993
C	-3.813399	3.887139	-0.007654
H	-4.523595	4.006581	0.814536
C	-4.258165	4.028588	-1.321334
H	-5.308440	4.257951	-1.521411
C	-3.365967	3.877473	-2.381759
H	-3.727798	3.988264	-3.407062
C	-2.012773	3.585844	-2.155495
C	-1.056002	3.438236	-3.335866
H	-0.079705	3.127995	-2.937400
C	-0.849774	4.780508	-4.063039
H	-1.790415	5.149253	-4.505195
H	-0.115838	4.671383	-4.878843
H	-0.478039	5.558253	-3.376602
C	-1.510588	2.339021	-4.311052
H	-1.635270	1.375046	-3.793682
H	-0.764432	2.204085	-5.111304
H	-2.470948	2.588204	-4.792223
C	-2.009265	3.458162	1.724380
H	-0.956086	3.142985	1.710239
C	-2.074353	4.807596	2.464238
H	-1.473348	5.576608	1.952877
H	-1.690334	4.704278	3.492434
H	-3.108968	5.183301	2.531780
C	-2.791417	2.368918	2.479360
H	-3.859732	2.623802	2.579136
H	-2.386220	2.242047	3.496928
H	-2.723031	1.399392	1.962005
C	3.950530	1.241320	0.260024
H	4.468326	2.195677	0.366389
C	4.643299	0.021148	0.405151
H	5.711448	0.021340	0.628057
C	3.948285	-1.199208	0.271711
H	4.464242	-2.153423	0.387362
C	2.592032	-1.152083	-0.003459
C	0.376950	-1.914745	-0.430359
C	0.730212	-4.176181	-0.332959
H	0.446971	-5.223274	-0.374280
C	1.935414	-3.591623	-0.103845
H	2.908246	-4.027346	0.095834
C	-1.590941	-3.409512	-0.794607
C	-2.478388	-3.546119	0.295344
C	-3.821533	-3.833458	0.008761
H	-4.534350	-3.947976	0.829497
C	-4.263647	-3.975914	-1.305764
H	-5.314541	-4.200902	-1.508085
C	-3.367816	-3.831827	-2.364169
H	-3.727404	-3.944198	-3.390211
C	-2.013935	-3.545425	-2.134980
C	-1.053552	-3.406254	-3.313397
H	-0.072987	-3.113235	-2.912373
C	-1.490491	-2.294709	-4.282788
H	-2.456073	-2.524996	-4.762918
H	-0.743796	-2.168814	-5.083914
H	-1.597162	-1.331227	-3.760508
C	-0.866592	-4.747365	-4.047899
H	-1.810933	-5.097870	-4.496987
H	-0.511104	-5.535546	-3.364854

H	-0.127499	-4.645041	-4.859837
C	-2.021128	-3.405112	1.744784
H	-0.959511	-3.119758	1.733437
C	-2.777417	-2.284784	2.480000
H	-2.670815	-1.323330	1.954653
H	-2.381597	-2.160946	3.501571
H	-3.854295	-2.504374	2.566972
C	-2.127568	-4.742182	2.501894
H	-3.172636	-5.086712	2.572670
H	-1.742852	-4.636804	3.529602
H	-1.548586	-5.535332	2.002431

(ⁱPrCNC)Fe(DMAP)₂BS(2,2)

Fe	-0.318308	-0.000779	0.017534
N	-0.529252	3.219404	0.001092
N	1.408878	2.233985	0.002320
N	1.590944	-0.000284	0.013057
N	1.410170	-2.234650	0.025453
N	-0.527395	-3.221112	0.036569
N	-2.325668	-0.001329	0.023664
N	-6.547763	-0.002260	0.037949
C	0.027967	1.935187	0.007292
C	0.450446	4.207529	-0.006845
C	1.662016	3.598880	-0.006416
C	2.291005	1.171913	0.005701
C	3.680599	1.219502	0.002563
C	4.384710	0.000485	0.007161
C	3.681302	-1.218916	0.014896
C	2.291680	-1.172091	0.017727
C	0.029104	-1.936603	0.026655
C	1.664091	-3.599403	0.033967
C	0.452868	-4.208700	0.040668
C	-1.925374	3.550867	0.002668
C	-2.575469	3.772911	1.239637
C	-3.913602	4.194792	1.211238
C	-4.582081	4.389137	0.003179
C	-3.924802	4.159920	-1.205110
C	-2.586883	3.737738	-1.234081
C	-1.293383	4.980805	3.057832
C	-1.838077	3.622671	2.569674
C	-2.694149	2.973318	3.669401
C	-1.300611	4.892366	-3.083373
C	-1.860192	3.551397	-2.565414
C	-2.730886	2.891884	-3.647308
C	-1.923343	-3.553253	0.040167
C	-2.580180	-3.740556	1.279322
C	-3.918024	-4.163307	1.255212
C	-4.579694	-4.392518	0.049334
C	-3.915784	-4.197655	-1.161172
C	-2.577945	-3.775233	-1.194428
C	-2.716075	-2.895964	3.693507
C	-1.848685	-3.553857	2.607974
C	-1.285380	-4.894260	3.123324
C	-1.845459	-3.624536	-2.527102
C	-2.705704	-2.975244	-3.623597
C	-1.302088	-4.982430	-3.017422

C	-3.037903	-0.025208	-1.116640
C	-3.030131	0.022154	1.168800
C	-4.416351	0.022837	1.228246
C	-4.424464	-0.026488	-1.166706
C	-5.175894	-0.001971	0.033318
C	-7.269266	0.028702	1.297085
C	-7.277787	-0.033349	-1.216283
H	0.195875	5.262463	-0.012653
H	2.662598	4.016757	-0.011847
H	4.207991	2.174194	-0.003283
H	5.476866	0.000796	0.004716
H	4.209231	-2.173320	0.018584
H	2.664914	-4.016736	0.034992
H	0.198913	-5.263776	0.048441
H	-4.438713	4.383328	2.149983
H	-5.621879	4.727349	0.003150
H	-4.458862	4.321481	-2.143803
H	-0.734877	4.857753	4.000867
H	-2.116651	5.692052	3.239882
H	-0.612177	5.435961	2.323679
H	-0.976715	2.961504	2.390775
H	-2.071643	2.754367	4.552025
H	-3.145081	2.029966	3.329065
H	-3.509967	3.634244	4.008064
H	-0.749467	4.743206	-4.026949
H	-0.608993	5.352975	-2.362479
H	-2.115713	5.610471	-3.274810
H	-1.006397	2.882616	-2.378422
H	-2.115993	2.646406	-4.528312
H	-3.539092	3.557088	-3.995663
H	-3.192867	1.962081	-3.285343
H	-4.448566	-4.325171	2.195837
H	-5.619368	-4.731091	0.053219
H	-4.444305	-4.386252	-2.097994
H	-2.097970	-2.649673	4.572022
H	-3.521738	-3.562580	4.045066
H	-3.181123	-1.966878	3.333594
H	-0.996465	-2.883911	2.417938
H	-0.595667	-5.353587	2.399798
H	-2.098828	-5.613546	3.317297
H	-0.731101	-4.744790	4.065022
H	-0.983702	-2.963093	-2.351251
H	-2.086473	-2.755783	-4.508402
H	-3.155751	-2.032114	-3.281449
H	-3.522468	-3.636394	-3.959507
H	-0.746954	-4.858983	-3.962385
H	-2.125763	-5.693902	-3.196744
H	-0.618116	-5.437535	-2.285785
H	-2.452941	-0.044144	-2.038240
H	-2.438963	0.041225	2.086448
H	-4.892181	0.042582	2.207494
H	-4.906857	-0.046479	-2.142759
H	-8.348343	0.031058	1.097771
H	-7.031518	0.934278	1.884784
H	-7.042019	-0.853240	1.923898
H	-8.355485	-0.036314	-1.009657
H	-7.043549	-0.938689	-1.805733
H	-7.055238	0.848808	-1.844458

(ⁱPrCNC)Fe(CH₃)₂, RKS

Fe	0.429133	0.139779	-0.492778
C	0.328572	0.504420	-2.505850
C	-0.493424	-0.183825	1.307006
N	0.126710	3.265661	0.037123
N	2.036741	2.281776	0.235609
N	2.228107	0.074583	-0.131065
N	2.037163	-2.120508	-0.562338
N	0.130889	-2.973575	-1.105388
C	0.704260	2.024430	-0.085587
C	0.704882	-1.768087	-0.776074
C	-1.458121	4.570631	3.133984
C	-1.680134	3.260999	2.350262
C	-2.630067	2.327621	3.118673
C	2.907027	1.198760	0.215217
C	1.061038	4.233053	0.414461
C	2.906758	-1.099246	-0.201098
C	4.268250	1.194355	0.498457
C	-3.939124	4.251095	-0.574886
C	-3.001506	-3.370164	-3.096225
C	4.956121	-0.025089	0.420193
C	-1.691599	3.962579	-1.471171
C	-3.045268	4.288770	-1.643311
C	-0.258793	5.567445	-2.790593
C	-1.718041	-3.751555	1.036592
C	-2.161445	-3.549905	-0.410825
C	-1.654048	-3.118209	-2.795312
C	4.268407	-1.194487	0.065104
C	2.267096	-3.479130	-0.751071
C	1.068098	-4.010586	-1.092630
C	-3.496716	-3.790052	-0.770948
C	2.262848	3.619495	0.540650
C	-1.256776	-3.194046	-1.439196
C	-0.720480	4.102887	-2.641473
C	-3.492530	3.896412	0.696222
C	-2.150255	3.558842	0.927997
C	-1.266760	3.578978	-0.177131
C	-2.693524	-3.150036	2.060568
C	-0.215989	-4.168638	-4.585161
C	-0.661812	-2.848151	-3.924503
C	-3.916260	-3.696322	-2.096819
C	-1.291163	3.583080	-3.970940
C	-1.483599	-5.247668	1.327626
C	-1.199882	-1.872510	-4.982701
H	-1.075594	4.356107	4.145570
H	-2.401032	5.132563	3.241734
H	-0.733747	5.230165	2.631179
H	-0.711583	2.746399	2.279779
H	-2.187353	2.055290	4.090312
H	-2.813575	1.396354	2.563390
H	-3.601803	2.804090	3.329104
H	0.779874	5.270763	0.559972
H	4.782400	2.114820	0.777035
H	-4.989364	4.511459	-0.732994
H	-3.337410	-3.315506	-4.133511

H	6.024334	-0.065366	0.640446
H	-3.403663	4.585587	-2.630703
H	0.469396	5.660321	-3.613793
H	0.220188	5.943169	-1.873420
H	-1.111806	6.230031	-3.015147
H	-0.757955	-3.232768	1.164703
H	4.783151	-2.153746	0.000018
H	3.240392	-3.941408	-0.628884
H	0.791234	-5.032135	-1.331190
H	-4.219641	-4.061964	0.001041
H	3.235262	4.012205	0.816777
H	0.165598	3.494542	-2.412634
H	-4.199790	3.888119	1.528550
H	-2.263061	-3.216174	3.072971
H	-3.655148	-3.688457	2.083129
H	-2.892663	-2.089388	1.851416
H	0.229729	-4.861868	-3.854520
H	0.536751	-3.976829	-5.367920
H	-1.070430	-4.683398	-5.056068
H	0.227934	-2.381904	-3.480323
H	-4.961351	-3.888538	-2.354867
H	-0.504480	3.585103	-4.742363
H	-2.115334	4.213571	-4.345150
H	-1.659746	2.552169	-3.872928
H	-1.118750	-5.389016	2.358653
H	-0.739181	-5.687784	0.645587
H	-2.417432	-5.824784	1.219751
H	-0.401567	-1.614335	-5.696860
H	-1.554256	-0.936578	-4.526178
H	-2.028793	-2.309645	-5.563101
H	0.726872	-0.278263	-3.158795
H	0.753530	1.454790	-2.847137
H	-0.762631	0.553502	-2.677092
H	-1.562912	-0.123545	1.031637
H	-0.312563	0.565782	2.084689
H	-0.329695	-1.166766	1.761974

(ⁱPrCNC)Mn(CO)₃, unrestricted doublet

Mn	-0.053578	-0.046433	-0.018110
N	1.860028	-0.004760	0.257396
N	1.737571	-2.231076	0.186441
N	-0.234155	-3.094546	-0.079846
N	1.625859	2.213838	0.284364
N	-0.382815	2.990280	0.027317
O	0.002592	0.012001	-2.930295
O	-2.909753	-0.112648	-0.452750
C	2.608143	-1.164621	0.332260
C	0.410571	-1.879688	0.017463
C	0.680758	-4.138844	0.021887
H	0.359804	-5.172835	-0.037123
C	1.917714	-3.605521	0.189910
H	2.888877	-4.072009	0.309690
C	-1.650461	-3.336985	-0.236428
C	-2.183096	-3.438425	-1.541043
C	-3.545404	-3.747138	-1.663827
H	-3.989458	-3.828983	-2.657660
C	-4.342421	-3.954062	-0.540429

H	-5.402125	-4.194681	-0.660945
C	-3.790813	-3.859158	0.734936
H	-4.426530	-4.030268	1.606037
C	-2.434682	-3.552380	0.919916
C	-1.852163	-3.518410	2.331429
H	-0.896160	-2.976640	2.289501
C	-2.751150	-2.773563	3.332658
H	-3.019481	-1.771293	2.969931
H	-2.225622	-2.652024	4.292913
H	-3.682234	-3.326808	3.538627
C	-1.553110	-4.944601	2.838169
H	-2.478473	-5.540584	2.906118
H	-1.099194	-4.909313	3.842212
H	-0.858391	-5.481859	2.173896
C	-1.323553	-3.279952	-2.792876
H	-0.408641	-2.741353	-2.507670
C	-0.890723	-4.656531	-3.337741
H	-0.329523	-5.235450	-2.587238
H	-0.245253	-4.537321	-4.223672
H	-1.767915	-5.255554	-3.634849
C	-2.012009	-2.453049	-3.891984
H	-2.859672	-2.994631	-4.342697
H	-1.296366	-2.230987	-4.698668
H	-2.387523	-1.496001	-3.501628
C	3.970059	-1.177292	0.528838
H	4.505662	-2.126287	0.583848
C	4.652205	0.056448	0.662366
H	5.729127	0.080411	0.828651
C	3.907883	1.258886	0.587495
H	4.394700	2.230051	0.688969
C	2.548310	1.186562	0.387378
C	0.318998	1.805436	0.088102
C	0.478635	4.072856	0.180737
H	0.108211	5.091583	0.159345
C	1.738467	3.594112	0.342744
H	2.684286	4.102244	0.492330
C	-1.805086	3.169983	-0.156007
C	-2.308517	3.312890	-1.468723
C	-3.681491	3.558577	-1.613679
H	-4.103443	3.670680	-2.614093
C	-4.516757	3.665367	-0.504078
H	-5.584157	3.857923	-0.642501
C	-3.993783	3.531925	0.779897
H	-4.659711	3.624485	1.640401
C	-2.628667	3.284955	0.986934
C	-2.080868	3.206966	2.410283
H	-1.098031	2.716150	2.367449
C	-1.866908	4.617647	2.995849
H	-1.182094	5.219611	2.378729
H	-1.439585	4.553152	4.009982
H	-2.821949	5.164312	3.066186
C	-2.965305	2.366456	3.346785
H	-3.926998	2.862131	3.558391
H	-2.456621	2.216627	4.312065
H	-3.176604	1.374217	2.923143
C	-1.410202	3.265681	-2.702975
H	-0.476006	2.759477	-2.420763
C	-1.037176	4.689467	-3.164870

H	-1.937173	5.257918	-3.454039
H	-0.365955	4.649260	-4.038740
H	-0.524246	5.256098	-2.371853
C	-2.026753	2.464980	-3.862759
H	-2.355085	1.467932	-3.535275
H	-1.282216	2.329250	-4.662537
H	-2.893541	2.983794	-4.303657
C	0.023671	-0.009787	-1.768385
C	-1.749757	-0.085670	-0.275050
C	-0.502850	-0.087467	1.673807
O	-0.872548	-0.114511	2.775828

(iPrCNC)Co(CH₃), BS(1,1)

Co	0.030373	-0.006768	0.031094
C	0.370078	-1.930524	0.053755
C	0.729499	-4.190210	0.083006
H	0.439636	-5.235565	0.119673
C	1.954584	-3.609881	-0.001286
H	2.945526	-4.047712	-0.050783
C	0.362716	1.917677	-0.058289
C	0.712731	4.175723	-0.163831
H	0.419850	5.220530	-0.186426
C	1.939592	3.595944	-0.221480
H	2.928311	4.033776	-0.303738
C	2.626581	-1.176968	-0.102681
C	4.005706	-1.226595	-0.189360
H	4.535204	-2.180587	-0.195182
C	4.711085	-0.006079	-0.273291
H	5.799794	-0.005888	-0.346678
C	4.000043	1.214115	-0.266571
H	4.525053	2.168266	-0.333042
C	2.621287	1.163577	-0.176144
C	-2.234249	-3.571699	1.453432
C	-1.628589	-3.445478	0.184928
C	-2.342520	-3.634736	-1.018413
C	-3.704695	-3.954778	-0.920966
H	-4.287851	-4.102531	-1.833142
C	-4.327492	-4.087785	0.319206
H	-5.389490	-4.342002	0.372964
C	-3.597759	-3.898238	1.491808
H	-4.098041	-4.003781	2.457791
C	-3.605574	3.937533	1.297049
H	-4.102404	4.081402	2.259239
C	-4.337259	4.091188	0.120285
H	-5.396951	4.355849	0.168076
C	-3.719666	3.909218	-1.115990
H	-4.304689	4.031539	-2.031003
C	-2.360825	3.573008	-1.205386
C	-1.642424	3.428732	0.001483
C	-2.243715	3.603476	1.266867
C	-2.233037	-2.237685	-3.124432
H	-3.314124	-2.325136	-3.322853
H	-1.724318	-2.112564	-4.094656
H	-2.067773	-1.326885	-2.529961
C	-1.693663	-3.479391	-2.391159
H	-0.617140	-3.317275	-2.237577

C	-1.845278	-4.748681	-3.249500
H	-2.899757	-4.955697	-3.495605
H	-1.441771	-5.636794	-2.736957
H	-1.302808	-4.634301	-4.202020
C	-1.301333	-4.701796	3.519145
H	-2.278431	-5.111198	3.825295
H	-0.700951	-4.554208	4.432006
H	-0.797226	-5.464769	2.904346
C	-2.094968	-2.289811	3.642211
H	-2.193094	-1.339459	3.095974
H	-1.470276	-2.110198	4.532696
H	-3.096826	-2.583155	3.996353
C	-1.460611	-3.374097	2.754449
H	-0.452764	-3.021854	2.493426
C	-1.604952	4.734660	-3.325458
H	-2.600944	5.158415	-3.535980
H	-1.090277	4.599229	-4.290913
H	-1.040640	5.480709	-2.743346
C	-1.709555	3.393252	-2.575076
H	-0.686192	3.026097	-2.413132
C	-2.432096	2.334375	-3.426028
H	-2.479400	1.367849	-2.902010
H	-1.897501	2.179645	-4.377680
H	-3.462313	2.638243	-3.674525
C	-2.160657	2.585823	3.605051
H	-3.102417	3.031764	3.964665
H	-1.511895	2.440316	4.483973
H	-2.393857	1.595255	3.185905
C	-1.143802	4.867602	3.160004
H	-0.581429	5.493655	2.448849
H	-0.539574	4.773167	4.077544
H	-2.070405	5.406258	3.420750
C	-1.455860	3.478395	2.569247
H	-0.496334	2.996341	2.332555
C	-1.948881	0.024625	0.191458
H	-2.158318	0.359760	1.219952
H	-2.460078	-0.931714	0.053203
H	-2.423818	0.762224	-0.466695
N	-0.216188	-3.169011	0.114907
N	1.727109	-2.242698	-0.017796
N	1.927871	-0.006826	-0.094889
N	1.717560	2.229367	-0.154826
N	-0.228813	3.154980	-0.064895

(ⁱPrCNC)Co(C(Ph)₂CH₃), BS(1,1)

Co	-0.553127	-0.041299	0.096003
C	-0.227453	-1.944493	0.518514
C	0.235314	-4.049692	1.287436
C	1.411605	-3.537566	0.853996
C	-0.156614	1.888480	0.146976
C	0.335378	4.122768	0.182382
C	1.417054	3.503873	-0.349952
C	1.990078	-1.260228	-0.049288
C	3.315536	-1.375191	-0.434671
C	3.981712	-0.207625	-0.864128
C	3.298851	1.025425	-0.894354

C	1.978478	1.048543	-0.474577
C	-2.753846	-2.571289	2.433083
C	-2.137769	-3.344816	1.415548
C	-2.818048	-4.414697	0.781024
C	-4.141107	-4.674910	1.174774
C	-4.774488	-3.908052	2.146529
C	-4.083559	-2.867187	2.765131
C	-2.075830	3.484519	3.909307
C	-3.379258	3.882407	3.620894
C	-3.773088	4.064807	2.296668
C	-2.888976	3.831117	1.231033
C	-1.585433	3.386871	1.546232
C	-1.147311	3.240637	2.886040
C	-3.095131	-5.498708	-1.510085
C	-2.189431	-5.321085	-0.279292
C	-1.833751	-6.704602	0.304680
C	-1.124356	-2.158846	4.311352
C	-2.898029	-0.423586	3.824031
C	-1.993556	-1.504347	3.218945
C	-3.052076	5.604136	-0.558868
C	-3.317356	4.126633	-0.201276
C	-4.786317	3.771012	-0.481985
C	0.435065	1.640155	4.104918
C	0.957287	4.119504	3.971518
C	0.300467	2.918148	3.261942
C	-1.974479	-0.131776	-1.432538
N	-0.756832	-3.091824	1.070837
N	1.121680	-2.263763	0.386887
N	1.332582	-0.072771	-0.051141
N	1.124337	2.144716	-0.339924
N	-0.610758	3.145341	0.499338
C	-3.297817	-0.116276	-0.654253
C	-1.836252	1.045520	-2.400433
C	-1.853545	-1.366296	-2.340087
C	-2.986944	-1.897459	-2.990366
C	-0.609010	-1.919079	-2.702469
C	-2.933348	1.838179	-2.791149
C	-0.607698	1.323919	-3.042467
H	0.014071	-5.005267	1.746075
H	2.413810	-3.951917	0.861995
H	0.158151	5.173034	0.390441
H	2.355048	3.905097	-0.718581
H	3.824674	-2.340205	-0.423237
H	5.022980	-0.261706	-1.184635
H	3.797791	1.933971	-1.234834
H	-4.685302	-5.494015	0.700960
H	-5.807763	-4.124792	2.430187
H	-4.587293	-2.284575	3.536887
H	-1.766138	3.374769	4.951856
H	-4.087854	4.069303	4.432289
H	-4.788480	4.404513	2.084975
H	-4.002880	-6.077263	-1.272207
H	-2.556052	-6.046521	-2.299412
H	-3.398183	-4.529853	-1.926525
H	-1.262604	-4.846543	-0.631587
H	-2.744072	-7.239004	0.623622
H	-1.172196	-6.641430	1.182775
H	-1.329308	-7.325421	-0.454309

H	-1.753942	-2.680204	5.052032	H	-3.387272	-1.014370	-0.025320
H	-0.532387	-1.397745	4.846668	H	-4.209068	-0.083833	-1.285462
H	-0.421093	-2.894631	3.891897	H	2.022188	3.913706	4.168095
H	-3.562256	0.024656	3.069061	H	-3.977153	-1.499125	-2.762084
H	-2.285492	0.385632	4.246203	H	0.297917	-1.533790	-2.237415
H	-3.523388	-0.813799	4.644466	H	0.268868	0.724993	-2.792533
H	-1.314468	-0.993555	2.515696	H	-3.916890	1.650330	-2.360436
H	-3.646248	6.280370	0.078483	C	-2.882529	-2.900877	-3.959522
H	-3.321786	5.799866	-1.609575	C	-1.634793	-3.425957	-4.305070
H	-1.992000	5.871946	-0.434598	C	-0.496974	-2.928616	-3.662710
H	-2.695954	3.510344	-0.865693	C	-0.478394	2.336482	-3.991285
H	-5.018823	2.735397	-0.190938	C	-1.583168	3.120064	-4.352072
H	-4.996974	3.877430	-1.557521	C	-2.811583	2.857772	-3.745947
H	-5.485158	4.439205	0.048215	H	-3.787563	-3.270739	-4.450488
H	-0.102590	1.717744	5.063819	H	-1.549736	-4.208369	-5.064650
H	1.495257	1.446321	4.336226	H	0.491513	-3.323374	-3.916408
H	0.046412	0.767729	3.560179	H	0.494311	2.514700	-4.459760
H	0.894341	5.033411	3.359612	H	-1.485641	3.912770	-5.099274
H	0.476757	4.334738	4.940530	H	-3.695134	3.441202	-4.023157
H	0.866451	2.743267	2.338409				
H	-3.355095	0.760923	0.010631				

B.5. Experimental

All DFT calculations were performed with the *ORCA* program package.¹⁷ The geometry optimizations of the complexes and single-point calculations on the optimized geometries were carried out at the B3LYP level¹⁸ of DFT. This hybrid functional often gives better results for transition-metal compounds than pure gradient-corrected functionals, especially with regard to metal-ligand covalency.¹⁹ The all-electron Gaussian basis sets were those developed by Ahlrichs' group.²⁰ Triple- ζ quality basis sets def2-TZVP with one set of polarization functions on the metals and on the atoms directly coordinated to the metal center were used. For the carbon and hydrogen atoms, slightly smaller polarized split-valence def2-SV(P) basis sets were used that were of double- ζ quality in the valence region and contained a polarizing set of d functions on the non-hydrogen atoms. Auxiliary basis sets were chosen to match the orbital basis.²¹ The RIJCOSX²² approximation was used to accelerate the calculations.

Throughout this dissertation, computational results are described using the BS approach by Ginsberg²³ and Noodleman et al.²⁴ Because several BS solutions to the spin-unrestricted Kohn-Sham equations may be obtained, the general notation BS(m,n)²⁵ has been adopted, where m (n) denotes the number of spin-up (spin-down) electrons at the two interacting fragments. Canonical and corresponding²⁶ orbitals, as well as spin density plots, were generated with the program *Molekel*.²⁷

Nonrelativistic single-point calculations employed the CP(PPP) basis set for iron.²⁸ The Mößbauer isomer shifts were calculated from the computed electron densities at the iron centers as previously described.²⁹

REFERENCES

- ¹ (a) Danopoulos, A. A.; Pugh, D.; Smith, H.; Saßmannshausen, J. *Chem. Eur. J.* **2009**, *15*, 5491–5502. (b) Danopoulos, A. A.; Wright, J. A.; Motherwell, W. B. *Chem. Commun.* **2005**, 784–786.
- ² Zhu, D.; Budzelaar, P. H. A. *Organometallics* **2008**, *27*, 2699–2705.
- ³ Zhang, X. *International Journal of Quantum Chemistry* **2010**, *110*, 1880–1889.
- ⁴ (a) Knijnenburg, Q.; Gambarotta, S.; Budzelaar, P. H. M. *Dalton Trans.* **2006**, 5442–5448. (b) Gibson, V. C.; Redshaw, C.; Solan, G. A. *Chem. Rev.* **2007**, *107*, 1745–1776. and references therein.
- ⁵ Stieber, S. C. E.; Milsmann, C.; Hoyt, J. M.; Turner, Z. R.; Finkelstein, K. D.; Wieghardt, K.; DeBeer, S.; Chirik, P. J. *Inorg. Chem.* **2012**, *51*, 3770–3785.
- ⁶ Neese, F. *J. Biol. Inorg. Chem.* **2006**, *11*, 702–711.
- ⁷ Römelt, M.; Ye, S.; Neese, F. *Inorg Chem* **2009**, *48*, 784–785.
- ⁸ Knijnenburg, Q.; Hetterscheid, D.; Kooistra, T. M.; Budzelaar, P. H. M. *Eur. J. Inorg. Chem.* **2004**, *2004*, 1204–1211.
- ⁹ Bart, S. C.; Chłopek, K.; Bill, E.; Bouwkamp, M. W.; Lobkovsky, E.; Neese, F.; Wieghardt, K.; Chirik, P. J. *J. Am. Chem. Soc.* **2006**, *128*, 13901–13912.
- ¹⁰ Tondreau, A. M. Ph.D. Thesis, Cornell University, Ithaca, NY, 2011.
- ¹¹ Bart, S. C.; Hawrelak, E.; Schmisser, A.; Lobkovsky, E. *Organometallics* **2004**, *23*, 237–246.
- ¹² Jones, G. D.; Martin, J. L.; McFarland, C.; Allen, O. R.; Hall, R. E.; Haley, A. D.; Brandon, R. J.; Kanovalova, T.; Desrochers, P. J.; Pulay, P.; Vicic, D. A., *J. Am. Chem. Soc.*, **2006**, *128*, 13175–13183.
- ¹³ Scarborough, C. C.; Sproules, S.; Weyhermüller, T.; DeBeer, S.; Wieghardt, K. *Inorg Chem* **2011**, *50*, 12446–12462.
- ¹⁴ Yamamoto, A.; Morifuji, K.; Ikeda, S. *J. Am. Chem. Soc.* **1965**, *87*, 4652–4653.
- ¹⁵ Lau, W.; Huffman, J.; Kochi, J. K. *Organometallics* **1982**, *1*, 155–169.
- ¹⁶ Pipek, J.; Mezey, P. G. *J. Chem. Phys.* **1989**, *90*, 4916–4926.
- ¹⁷ Neese, F. *ORCA: an ab initio, DFT and Semiempirical Electronic Structure Package*, version 2.8, revision 2287; Institut für Physikalische und Theoretische Chemie, Universität Bonn: Bonn, Germany, Nov 2010.
- ¹⁸ (a) Becke, A. D. *J. Chem. Phys.* **1986**, *84*, 4524–4529. (b) Becke, A. D. *J. Chem. Phys.* **1993**, *98*, 5648–5652. (c) Lee, C. T.; Yang, W. T.; Parr, R. G. *Phys. Rev. B.* **1998**, *37*, 785–789.

- ¹⁹ Neese, F.; Solomon, E. I. In *Magnetism: From Molecules to Materials*; Miller, J. S., Drillon, M., Eds.; Wiley: New York, 2002; Vol. 4, p 345.
- ²⁰ (a) Schäfer, A.; Horn, H.; Ahlrichs, R. *J. Chem. Phys.* **1992**, *97*, 2571–2577. (b) Schäfer, A.; Huber, C.; Ahlrichs, R. *J. Chem. Phys.* **1994**, *100*, 5829–5835. (c) Weigend, F.; Ahlrichs, R. *Phys. Chem. Chem. Phys.* **2005**, *7*, 3297–3305.
- ²¹ (a) Eichkorn, K.; Weigend, F.; Treutler, O.; Ahlrichs, R. *Theor. Chem. Acc.* **1997**, *97*, 119–124. (b) Eichkorn, K.; Treutler, O.; Öhm, H.; Häser, M.; Ahlrichs, R. *Chem. Phys. Lett.* **1995**, *240*, 283–290. (c) Eichkorn, K.; Treutler, O.; Öhm, H.; Häser, M.; Ahlrichs, R. *Chem. Phys. Lett.* **1995**, *242*, 652–660.
- ²² (a) Neese, F.; Wennmohs, F.; Hansen, A.; Becker, U. *Chem. Phys.* **2009**, *356*, 98–109. (b) Kossmann, S.; Neese, F. *Chem. Phys. Lett.* **2009**, *481*, 240–243. (c) Neese, F. *J. Comput. Chem.* **2003**, *24*, 1740–1747.
- ²³ Ginsberg, A. P. *J. Am. Chem. Soc.* **1980**, *102*, 111–117.
- ²⁴ Noodleman, L.; Peng, C. Y.; Case, D. A.; Mouesca, J. M. *Coord. Chem. Rev.* **1995**, *144*, 199–244.
- ²⁵ Kirchner, B.; Wennmohs, F.; Ye, S.; Neese, F. *Curr. Opin. Chem. Biol.* **2007**, *11*, 134–141.
- ²⁶ Neese, F. *J. Phys. Chem. Solids* **2004**, *65*, 781–785.
- ²⁷ *Molekel*, Advanced Interactive 3D-Graphics for Molecular Sciences, available under <http://www.cscs.ch/molkel/>.
- ²⁸ Neese, F. *Inorg. Chim. Acta.* **2002**, *337*, 181–192.
- ²⁹ (a) Sinnecker, S.; Slep, L. D.; Bill, E.; Neese, F. *Inorg. Chem.* **2005**, *44*, 2245–2254. (b) Römelt, M.; Ye, S.; Neese, F. *Inorg. Chem.* **2009**, *48*, 784–785.

APPENDIX C
CRYSTAL STRUCTURE DATA

Table C.1. Compilation of X-ray data for compounds discussed in this manuscript.

Compound	X-Ray ID	Location
[2,6-pyr-(CH ₂ NDipp)(CH ₂ N(H)Dipp)] ₂ Fe	jmd1	Appendix A
[(^{Me} BPDI)Fe(N ₂)] ₂ (μ ² -N ₂)	jmd3	<i>Inorg. Chem.</i> 2010 , <i>49</i> , 2782.
(4-Me ₂ N- ^{iPr} PDI)Fe(N ₂) ₂	jmd5	<i>Organometallics</i> 2012 , <i>31</i> , 2275.
(^{iPr} CNC)Fe(CH ₃) ₂ (N ₂)·2LiBr(Et ₂ O) ₂	jmd9	<i>Not Publishable</i>
(^{iPr} CNC)Fe(CH ₂ Si(CH ₃) ₃) ₂ (N ₂)	jmd11	<i>Not Publishable</i>
(4-Me ₂ N- ^{iPr} PDI)Co(H)	jmd12	Appendix A
(4-CF ₃ - ^{iPr} PDI)Fe(Cl) ₂	jmd14	<i>Organometallics</i> 2012 , <i>31</i> , 2275.
(^{iPr} CNC)Fe(η ² ,η ² -(CH ₂ CHCH ₂) ₂ N ^t Bu)	jmd16	Appendix A
(4-Me ₂ N- ^{iPr} PDI)Fe(DMAP)	jmd17	Appendix A
(4-Me ₂ N- ^{iPr} PDI)Fe(CO) ₂	jmd18	<i>Organometallics</i> 2012 , <i>31</i> , 2275.
(^{iPr} CNC)Fe(N ₂)(DMAP)	jmd20	Appendix A
(4- ^t Bu- ^{iPr} PDI)Fe(N ₂) ₂	jmd23	<i>Organometallics</i> 2012 , <i>31</i> , 2275.
(4-Me ₂ N- ^{Me} PDI)Co(CH ₃)	jmd24	Appendix A
(4-Me ₂ N- ^{iPr} PDI)Fe(Cl) ₂	jmd25	<i>Organometallics</i> 2012 , <i>31</i> , 2275.
(^{iPr} CNC)Fe(CH ₂ Si(CH ₃) ₃) ₂ (N ₂)	jmd27	Appendix A
(^{iPr} CNC)Fe(CH ₂ Si(CH ₃) ₃) ₂ (CO)	jmd28	Appendix A
(^{iPr} CNC)Fe(C ₆ H ₄ CH ₃) ₂ (N ₂)·2LiBr(Et ₂ O) ₂	jmd29	Appendix A
(^{Me} PDI)Fe(2,2'-biphenyl)	jmd31	<i>Organometallics</i> 2012 , <i>31</i> , 2275.
(^{iPr} CNC)Mn(CO) ₂	jmd32	Appendix A
(4-Me ₂ N- ^{iPr} PDI)Co(N ₂)	jmd33	Appendix A
(4-C(Ph) ₂ CH ₃ -4-H- ^{iPr} CNC)Co(N ₂)	jmd34	Appendix A

Structure: [2,6-pyr-(CH₂NDipp)(CH₂N(H)Dipp)]₂Fe

ID: jmd1

Crystallographer: Emil Lobkovsky

Table C.2. Crystal data and structure refinement for jmd1.

Identification code	jmd1	
Empirical formula	C ₆₆ H ₉₄ Fe N ₆ O	
Formula weight	1043.32	
Temperature	173(2) K	
Wavelength	0.71073 Å	
Crystal system	Triclinic	
Space group	P-1	
Unit cell dimensions	a = 15.5963(7) Å	α = 117.193(2)°.
	b = 15.8667(7) Å	β = 91.551(2)°.
	c = 16.1131(7) Å	γ = 116.179(2)°.
Volume	3049.4(2) Å ³	
Z	2	
Density (calculated)	1.136 Mg/m ³	
Absorption coefficient	0.292 mm ⁻¹	
F(000)	1132	
Crystal size	0.40 x 0.35 x 0.25 mm ³	
Theta range for data collection	1.52 to 28.28°.	
Index ranges	-20 ≤ h ≤ 15, -21 ≤ k ≤ 21, -21 ≤ l ≤ 21	
Reflections collected	65497	
Independent reflections	14902 [R(int) = 0.0521]	
Completeness to theta = 28.28°	98.4 %	
Absorption correction	Semi-empirical from equivalents	
Max. and min. transmission	0.9305 and 0.8920	
Refinement method	Full-matrix least-squares on F ²	
Data / restraints / parameters	14902 / 3 / 849	
Goodness-of-fit on F ²	1.007	
Final R indices [I > 2σ(I)]	R1 = 0.0492, wR2 = 0.1158	
R indices (all data)	R1 = 0.0701, wR2 = 0.1270	
Largest diff. peak and hole	0.623 and -0.535 e.Å ⁻³	

Table C.3. Atomic coordinates ($\times 10^4$) and equivalent isotropic displacement parameters ($\text{\AA}^2 \times 10^3$) for jmd1. $U(\text{eq})$ is defined as one third of the trace of the orthogonalized U^{ij} tensor.

	x	y	z	$U(\text{eq})$
Fe(1)	7239(1)	8354(1)	2379(1)	18(1)
N(1)	7996(1)	5465(1)	701(1)	32(1)
N(2)	6550(1)	6824(1)	998(1)	20(1)
N(3)	6177(1)	8465(1)	1890(1)	21(1)
N(4)	8490(1)	9099(1)	-69(1)	25(1)
N(5)	8714(1)	9122(1)	2221(1)	20(1)
N(6)	8001(1)	8862(1)	3634(1)	26(1)
C(1)	7537(1)	6085(1)	1255(1)	28(1)
C(2)	6792(1)	6028(1)	593(1)	23(1)
C(3)	6372(1)	5205(1)	-377(1)	31(1)
C(4)	5697(1)	5190(1)	-959(1)	35(1)
C(5)	5442(1)	5985(1)	-553(1)	31(1)
C(6)	5869(1)	6787(1)	433(1)	22(1)
C(7)	5582(1)	7648(1)	902(1)	24(1)
C(8)	8581(1)	5281(1)	1215(1)	34(1)
C(9)	8085(1)	4482(1)	1453(2)	46(1)
C(10)	8650(2)	4304(2)	1961(2)	63(1)
C(11)	9666(2)	4859(2)	2189(2)	63(1)
C(12)	10147(1)	5577(1)	1879(2)	50(1)
C(13)	9621(1)	5808(1)	1391(1)	37(1)
C(14)	6951(1)	3722(1)	1079(2)	54(1)
C(15)	6678(1)	2583(2)	258(2)	55(1)
C(16)	6493(2)	3658(2)	1883(2)	74(1)
C(17)	10144(1)	6562(1)	1009(1)	40(1)
C(18)	11197(1)	6790(2)	983(2)	56(1)
C(19)	10175(1)	7656(1)	1572(2)	48(1)
C(20)	5809(1)	9175(1)	2404(1)	22(1)
C(21)	6195(1)	10196(1)	2470(1)	27(1)
C(22)	5843(1)	10895(1)	2998(1)	33(1)
C(23)	5124(1)	10600(1)	3445(1)	36(1)
C(24)	4738(1)	9595(1)	3372(1)	34(1)

C(25)	5064(1)	8871(1)	2856(1)	27(1)
C(26)	7011(1)	10558(1)	2012(1)	34(1)
C(27)	6923(2)	11210(2)	1600(2)	65(1)
C(28)	8038(1)	11210(2)	2730(2)	56(1)
C(29)	4625(1)	7790(1)	2820(1)	32(1)
C(30)	3497(1)	7095(1)	2370(1)	42(1)
C(31)	4889(1)	7977(1)	3829(1)	45(1)
C(32)	8180(1)	8703(1)	593(1)	22(1)
C(33)	9006(1)	9296(1)	1502(1)	20(1)
C(34)	9987(1)	9957(1)	1600(1)	26(1)
C(35)	10703(1)	10450(1)	2454(1)	31(1)
C(36)	10417(1)	10249(1)	3172(1)	31(1)
C(37)	9413(1)	9584(1)	3036(1)	24(1)
C(38)	9066(1)	9359(1)	3810(1)	32(1)
C(39)	7891(1)	8334(1)	-1061(1)	25(1)
C(40)	8068(1)	7482(1)	-1629(1)	32(1)
C(41)	7485(2)	6730(1)	-2588(1)	45(1)
C(42)	6759(2)	6827(2)	-2977(1)	50(1)
C(43)	6611(1)	7685(1)	-2419(1)	41(1)
C(44)	7167(1)	8458(1)	-1449(1)	29(1)
C(45)	8891(1)	7378(1)	-1239(1)	40(1)
C(46)	8491(2)	6282(2)	-1298(2)	63(1)
C(47)	9698(1)	7532(1)	-1757(2)	51(1)
C(48)	7028(1)	9429(1)	-842(1)	34(1)
C(49)	7833(1)	10467(1)	-791(1)	38(1)
C(50)	6009(1)	9241(2)	-1194(2)	60(1)
C(51)	7709(1)	9014(1)	4495(1)	23(1)
C(52)	7811(1)	10028(1)	5181(1)	27(1)
C(53)	7525(1)	10151(1)	6023(1)	33(1)
C(54)	7132(1)	9295(1)	6186(1)	35(1)
C(55)	7020(1)	8305(1)	5514(1)	34(1)
C(56)	7302(1)	8141(1)	4664(1)	30(1)
C(57)	8194(1)	10985(1)	5020(1)	37(1)
C(58)	7455(1)	11373(1)	5061(1)	48(1)
C(59)	9207(2)	11961(2)	5739(2)	68(1)
C(60)	7258(3)	7045(3)	3956(3)	41(1)

C(61)	7663(4)	6661(4)	4459(4)	71(2)
C(62)	6211(3)	6285(3)	3327(3)	58(2)
C(60')	7084(4)	7014(4)	3920(4)	41(1)
C(61')	7866(4)	6811(4)	4218(6)	103(3)
C(62')	6048(3)	6038(3)	3718(4)	60(2)
O(1S)	2436(2)	5326(2)	5003(2)	147(1)
C(1S)	655(3)	4195(3)	4680(4)	169(2)
C(2S)	1489(3)	5131(3)	4647(4)	145(2)
C(3S)	3284(2)	6167(2)	4941(2)	86(1)
C(4S)	4228(2)	6381(2)	5448(3)	107(1)

Structure: (4-Me₂N-*i*PrPDI)CoH

ID: jmd12

Crystallographer: Scott Semproni

Table C.4. Crystal data

C ₃₅ H ₄₉ CoN ₄	$F(000) = 1256$
$M_r = 584.71$	$D_x = 1.196 \text{ Mg m}^{-3}$
Monoclinic, $C2/c$	Mo $K\alpha$ radiation, $\lambda = 0.71073 \text{ \AA}$
$a = 13.800 (3) \text{ \AA}$	Cell parameters from 9994 reflections
$b = 11.062 (2) \text{ \AA}$	$\theta = 2.4\text{--}27.5^\circ$
$c = 21.302 (4) \text{ \AA}$	$\mu = 0.56 \text{ mm}^{-1}$
$\beta = 93.177 (2)^\circ$	$T = 100 \text{ K}$
$V = 3246.9 (11) \text{ \AA}^3$	Plate, clear light green
$Z = 4$	$0.23 \times 0.14 \times 0.08 \text{ mm}$

Table C.5. Data collection

Bruker APEX II CCD diffractometer	3365 reflections with $I > 2\sigma(I)$
Radiation source: fine-focus tube	$R_{\text{int}} = 0.022$
Triumph curved-crystal	$\theta_{\text{max}} = 27.5^\circ$, $\theta_{\text{min}} = 1.9^\circ$
Absorption correction: multi-scan SADABS V2008/1 (Bruker AXS)	$h = -17 \rightarrow 17$
$T_{\text{min}} = 0.683$, $T_{\text{max}} = 0.746$	$k = -14 \rightarrow 14$
17966 measured reflections	$l = -27 \rightarrow 27$
3683 independent reflections	

Table C.6. Refinement

Refinement on F^2	Primary atom site location: structure-invariant direct methods
Least-squares matrix: full	Secondary atom site location: difference Fourier map
$R[F^2 > 2\sigma(F^2)] = 0.032$	Hydrogen site location: inferred from neighbouring sites
$wR(F^2) = 0.080$	H atoms treated by a mixture of independent and constrained refinement
$S = 1.06$	$w = 1/[\sigma^2(F_o^2) + (0.0366P)^2 + 4.1167P]$ where $P = (F_o^2 + 2F_c^2)/3$
3683 reflections	$(\Delta/\sigma)_{\text{max}} < 0.001$
191 parameters	$\Delta)_{\text{max}} = 0.37 \text{ e \AA}^{-3}$
0 restraints	$\Delta)_{\text{min}} = -0.34 \text{ e \AA}^{-3}$

Special details

Geometry. All s.u.'s (except the s.u. in the dihedral angle between two l.s. planes) are estimated using the full covariance matrix. The cell s.u.'s are taken into account individually in

the estimation of s.u.'s in distances, angles and torsion angles; correlations between s.u.'s in cell parameters are only used when they are defined by crystal symmetry. An approximate (isotropic) treatment of cell s.u.'s is used for estimating s.u.'s involving l.s. planes.

Refinement. Refinement of F^2 against ALL reflections. The weighted R-factor wR and goodness of fit S are based on F^2 , conventional R-factors R are based on F , with F set to zero for negative F^2 . The threshold expression of $F^2 > 2\sigma(F^2)$ is used only for calculating R-factors(gt) etc. and is not relevant to the choice of reflections for refinement. R-factors based on F^2 are statistically about twice as large as those based on F , and R-factors based on ALL data will be even larger.

Table C.7. Fractional atomic coordinates and isotropic or equivalent isotropic displacement parameters (\AA^2)

	x	y	z	$U_{\text{iso}}^*/U_{\text{eq}}$
C1	0.03145 (11)	0.60495 (14)	0.07826 (7)	0.0203 (3)
H1A	0.0542	0.5381	0.0544	0.030*
H1B	0.0773	0.6701	0.0774	0.030*
H1C	-0.0302	0.6315	0.0602	0.030*
C2	0.02061 (10)	0.56629 (13)	0.14471 (6)	0.0154 (3)
C3	0.01190 (10)	0.65202 (13)	0.19540 (6)	0.0148 (3)
C4	0.01380 (10)	0.77758 (13)	0.19413 (7)	0.0171 (3)
H4	0.0241	0.8181	0.1568	0.020*
C5	0.0000	0.84350 (18)	0.2500	0.0190 (4)
C6	0.03369 (14)	1.03297 (15)	0.19681 (8)	0.0293 (4)
H6A	0.0968	1.0041	0.1873	0.044*
H6B	0.0373	1.1176	0.2067	0.044*
H6C	-0.0107	1.0208	0.1611	0.044*
C7	0.02531 (10)	0.35519 (12)	0.11929 (6)	0.0153 (3)
C8	0.11829 (10)	0.31855 (13)	0.10321 (7)	0.0176 (3)
C9	0.12448 (11)	0.22165 (14)	0.06155 (7)	0.0211 (3)
H9	0.1851	0.1956	0.0502	0.025*
C10	0.04185 (12)	0.16356 (13)	0.03688 (7)	0.0215 (3)
H10	0.0473	0.1003	0.0085	0.026*
C11	-0.04870 (11)	0.19974 (13)	0.05449 (7)	0.0204 (3)
H11	-0.1037	0.1597	0.0381	0.025*
C12	-0.05897 (10)	0.29532 (13)	0.09640 (6)	0.0166 (3)
C13	-0.15831 (11)	0.33207 (14)	0.11769 (7)	0.0217 (3)
H13	-0.1478	0.3825	0.1553	0.026*
C14	-0.21823 (13)	0.22277 (17)	0.13603 (9)	0.0341 (4)
H14A	-0.2328	0.1736	0.0996	0.051*
H14B	-0.2776	0.2499	0.1528	0.051*
H14C	-0.1820	0.1762	0.1672	0.051*
C15	-0.21333 (13)	0.40868 (19)	0.06751 (10)	0.0386 (4)
H15A	-0.1758	0.4792	0.0587	0.058*
H15B	-0.2747	0.4329	0.0826	0.058*

H15C	-0.2239	0.3620	0.0298	0.058*
C16	0.20895 (11)	0.37713 (16)	0.13365 (7)	0.0241 (3)
H16	0.1919	0.4600	0.1450	0.029*
C17	0.29298 (12)	0.38433 (16)	0.09021 (8)	0.0282 (4)
H17A	0.3152	0.3042	0.0813	0.042*
H17B	0.3451	0.4300	0.1103	0.042*
H17C	0.2715	0.4234	0.0517	0.042*
C18	0.23922 (13)	0.3106 (2)	0.19447 (9)	0.0437 (5)
H18A	0.1859	0.3093	0.2215	0.066*
H18B	0.2934	0.3514	0.2153	0.066*
H18C	0.2575	0.2292	0.1848	0.066*
Co1	0.0000	0.42607 (2)	0.2500	0.01422 (8)
N1	0.01661 (8)	0.45176 (10)	0.16392 (5)	0.0146 (2)
N2	0.0000	0.59111 (15)	0.2500	0.0146 (3)
N3	0.0000	0.96750 (17)	0.2500	0.0288 (4)
H1	0.0000	0.286 (2)	0.2500	0.022 (6)*

Structure: (*i*PrCNC)Fe(η^2, η^2 -(CH₂CHCH₂)₂N^{*t*}Bu)

ID: jmd16

Crystallographer: Zoë Turner

Table C.8. Crystal data

C ₄₅ H ₆₀ FeN ₆	$F(000) = 796$
$M_r = 740.84$	$D_x = 1.253 \text{ Mg m}^{-3}$
Monoclinic, $P2_1$	Mo $K\alpha$ radiation, $\lambda = 0.71073 \text{ \AA}$
$a = 10.1532 (10) \text{ \AA}$	Cell parameters from 9990 reflections
$b = 14.2472 (14) \text{ \AA}$	$\theta = 2.5\text{--}27.4^\circ$
$c = 13.6316 (14) \text{ \AA}$	$\mu = 0.42 \text{ mm}^{-1}$
$\beta = 95.492 (1)^\circ$	$T = 100 \text{ K}$
$V = 1962.8 (3) \text{ \AA}^3$	Shard, brown
$Z = 2$	$0.17 \times 0.13 \times 0.05 \text{ mm}$

Table C.9. Data collection

Bruker APEX-II CCD diffractometer	8668 independent reflections
Radiation source: fine-focus sealed tube	7679 reflections with $I > 2\sigma(I)$
graphite	$R_{\text{int}} = 0.027$
PHI AND OMEGA SCANS scans	$\theta_{\text{max}} = 27.5^\circ$, $\theta_{\text{min}} = 2.0^\circ$
Absorption correction: multi-scan <i>SADABS</i>	$h = -13 \rightarrow 13$
$T_{\text{min}} = 0.931$, $T_{\text{max}} = 0.979$	$k = -18 \rightarrow 17$
22273 measured reflections	$l = -17 \rightarrow 17$

Table C.10. Refinement

Refinement on F^2	Secondary atom site location: difference Fourier map
Least-squares matrix: full	Hydrogen site location: inferred from neighbouring sites
$R[F^2 > 2\sigma(F^2)] = 0.035$	Riding
$wR(F^2) = 0.081$	$w = 1/[\sigma^2(F_o^2) + (0.0429P)^2]$ where $P = (F_o^2 + 2F_c^2)/3$
$S = 1.02$	$(\Delta/\sigma)_{\text{max}} = 0.001$
8668 reflections	$\Delta_{\text{max}} = 0.35 \text{ e \AA}^{-3}$

559 parameters	$\Delta\rho_{\min} = -0.18 \text{ e } \text{\AA}^{-3}$
37 restraints	Absolute structure: Flack H D (1983), Acta Cryst. A39, 876-881
Primary atom site location: structure-invariant direct methods	Flack parameter: 0.004 (10)

Special details

Experimental. Collected, solved and refined by Dr. Zoe R. Turner

PLAT230_ALERT_2_B Hirshfeld Test Diff for C42 –C44A .. 8.00 su PLAT230_ALERT_2_B Hirshfeld Test Diff for C42 –C43A .. 11.25 su PLAT230_ALERT_2_B Hirshfeld Test Diff for C42 –C45 .. 12.50 su PLAT230_ALERT_2_C Hirshfeld Test Diff for C42 –C44 .. 7.00 su

The tert butyl group of C42 is disordered and has been modeled as best as possible as a two component disorder. The above alerts are a result of this disorder.

PLAT411_ALERT_2_C Short Inter H··H Contact H2 .. H41B .. 2.10 Ang. This is a result of crystal packing.

Geometry. All s.u.'s (except the s.u. in the dihedral angle between two l.s. planes) are estimated using the full covariance matrix. The cell s.u.'s are taken into account individually in the estimation of s.u.'s in distances, angles and torsion angles; correlations between s.u.'s in cell parameters are only used when they are defined by crystal symmetry. An approximate (isotropic) treatment of cell s.u.'s is used for estimating s.u.'s involving l.s. planes.

Refinement. Refinement of F^2 against ALL reflections. The weighted R-factor wR and goodness of fit S are based on F^2 , conventional R-factors R are based on F , with F set to zero for negative F^2 . The threshold expression of $F^2 > 2\sigma(F^2)$ is used only for calculating R-factors(gt) etc. and is not relevant to the choice of reflections for refinement. R-factors based on F^2 are statistically about twice as large as those based on F , and R-factors based on ALL data will be even larger.

Table C.11. Fractional atomic coordinates and isotropic or equivalent isotropic displacement parameters (\AA^2)

	<i>x</i>	<i>y</i>	<i>z</i>	<i>U</i> _{iso} */ <i>U</i> _{eq}	Occ. (<1)
C1	0.6690 (2)	1.03048 (14)	0.05946 (14)	0.0243 (4)	
C2	0.5502 (2)	1.14424 (16)	-0.03188 (16)	0.0319 (5)	
C3	0.6227 (2)	1.10205 (16)	-0.09398 (16)	0.0327 (5)	
C4	0.7798 (2)	0.96677 (14)	-0.07164 (15)	0.0279 (5)	
C5	0.8132 (2)	0.95327 (16)	-0.16715 (15)	0.0363 (6)	
H5	0.7766	0.9917	-0.2198	0.044*	
C6	0.9015 (2)	0.88203 (18)	-0.18319 (16)	0.0401 (6)	
H6	0.9261	0.8711	-0.2477	0.048*	
C7	0.9544 (2)	0.82655 (16)	-0.10521 (16)	0.0348 (5)	
H7	1.0152	0.7776	-0.1150	0.042*	
C8	0.9150 (2)	0.84533 (15)	-0.01328 (15)	0.0284 (4)	
C9	1.0413 (2)	0.72310 (15)	0.08747 (18)	0.0335 (5)	
C10	1.0483 (2)	0.70386 (16)	0.18378 (18)	0.0351 (5)	
C11	0.9049 (2)	0.83003 (16)	0.15992 (16)	0.0275 (5)	
C12	0.4958 (2)	1.12895 (15)	0.13913 (15)	0.0262 (4)	
C13	0.5367 (2)	1.20429 (14)	0.20104 (15)	0.0304 (5)	
C14	0.4543 (2)	1.22977 (16)	0.27286 (17)	0.0386 (5)	
H14	0.4801	1.2795	0.3170	0.046*	
C15	0.3361 (2)	1.18411 (18)	0.28107 (18)	0.0417 (6)	
H15	0.2827	1.2015	0.3317	0.050*	
C16	0.2949 (2)	1.11324 (17)	0.21607 (17)	0.0378 (5)	
H16	0.2122	1.0834	0.2214	0.045*	
C17	0.3729 (2)	1.08491 (15)	0.14290 (15)	0.0300 (5)	
C18	0.6569 (2)	1.26255 (15)	0.18519 (16)	0.0361 (5)	
H18	0.7142	1.2254	0.1437	0.043*	
C19	0.6121 (3)	1.35190 (19)	0.1280 (2)	0.0578 (8)	
H19A	0.5574	1.3346	0.0676	0.087*	
H19B	0.6900	1.3867	0.1109	0.087*	
H19C	0.5605	1.3913	0.1691	0.087*	
C20	0.7398 (3)	1.28960 (18)	0.28054 (18)	0.0445 (6)	
H20A	0.6887	1.3320	0.3190	0.067*	

H20B	0.8208	1.3212	0.2647	0.067*	
H20C	0.7630	1.2329	0.3191	0.067*	
C21	0.3186 (2)	1.01500 (16)	0.06566 (16)	0.0327 (5)	
H21	0.3927	0.9954	0.0268	0.039*	
C22	0.2133 (2)	1.06278 (19)	-0.00464 (18)	0.0424 (6)	
H22A	0.1413	1.0850	0.0324	0.064*	
H22B	0.1783	1.0178	-0.0550	0.064*	
H22C	0.2527	1.1162	-0.0365	0.064*	
C23	0.2619 (2)	0.9273 (2)	0.10916 (17)	0.0427 (6)	
H23A	0.3281	0.8997	0.1578	0.064*	
H23B	0.2384	0.8817	0.0565	0.064*	
H23C	0.1828	0.9438	0.1412	0.064*	
C24	0.9580 (2)	0.75959 (14)	0.33317 (15)	0.0279 (4)	
C25	1.0517 (2)	0.80738 (15)	0.39707 (16)	0.0311 (5)	
C26	1.0472 (2)	0.79249 (18)	0.49744 (17)	0.0417 (6)	
H26	1.1083	0.8246	0.5428	0.050*	
C27	0.9570 (3)	0.7328 (2)	0.53282 (18)	0.0477 (7)	
H27	0.9557	0.7247	0.6019	0.057*	
C28	0.8685 (2)	0.68465 (18)	0.46876 (18)	0.0404 (6)	
H28	0.8072	0.6429	0.4941	0.049*	
C29	0.8676 (2)	0.69635 (15)	0.36717 (16)	0.0310 (5)	
C30	1.1590 (2)	0.86705 (17)	0.35892 (18)	0.0380 (5)	
H30	1.1288	0.8856	0.2897	0.046*	
C31	1.2861 (2)	0.8095 (2)	0.3567 (2)	0.0511 (7)	
H31A	1.3215	0.7944	0.4243	0.077*	
H31B	1.3516	0.8460	0.3246	0.077*	
H31C	1.2665	0.7512	0.3199	0.077*	
C32	1.1868 (3)	0.95683 (17)	0.4187 (2)	0.0494 (7)	
H32A	1.1036	0.9904	0.4244	0.074*	
H32B	1.2471	0.9970	0.3855	0.074*	
H32C	1.2275	0.9407	0.4847	0.074*	
C33	0.7769 (2)	0.63706 (17)	0.29762 (17)	0.0407 (6)	

H33	0.7729	0.6668	0.2309	0.049*	
C34	0.8368 (3)	0.53893 (18)	0.2894 (2)	0.0567 (8)	
H34A	0.9246	0.5443	0.2656	0.085*	
H34B	0.7793	0.5010	0.2431	0.085*	
H34C	0.8449	0.5088	0.3544	0.085*	
C35	0.6366 (3)	0.6315 (2)	0.3268 (2)	0.0571 (8)	
H35A	0.6365	0.5978	0.3894	0.086*	
H35B	0.5807	0.5981	0.2756	0.086*	
H35C	0.6020	0.6951	0.3341	0.086*	
C36	0.9131 (2)	1.03893 (16)	0.18584 (17)	0.0294 (5)	
H36A	1.0066	1.0271	0.1748	0.035*	
H36B	0.8854	1.1047	0.1724	0.035*	
C37	0.8718 (5)	1.0004 (3)	0.2650 (3)	0.0248 (10)	0.479 (4)
H37	0.9403	0.9590	0.3004	0.030*	0.479 (4)
C38	0.7885 (6)	1.0482 (4)	0.3332 (4)	0.0267 (12)	0.479 (4)
H38A	0.7300	1.0936	0.2952	0.032*	0.479 (4)
H38B	0.8466	1.0842	0.3821	0.032*	0.479 (4)
C39	0.6144 (5)	0.9387 (5)	0.3205 (4)	0.0279 (11)	0.479 (4)
H39A	0.5599	0.9874	0.2841	0.033*	0.479 (4)
H39B	0.5545	0.8993	0.3563	0.033*	0.479 (4)
C40	0.6777 (5)	0.8779 (4)	0.2470 (3)	0.0262 (10)	0.479 (4)
H40	0.7294	0.8254	0.2808	0.031*	0.479 (4)
C37A	0.8056 (5)	1.0384 (3)	0.2489 (3)	0.0221 (9)	0.521 (4)
H37A	0.7452	1.0934	0.2362	0.027*	0.521 (4)
C38A	0.8187 (5)	1.0099 (4)	0.3554 (4)	0.0249 (10)	0.521 (4)
H38C	0.8837	0.9581	0.3648	0.030*	0.521 (4)
H38D	0.8538	1.0637	0.3958	0.030*	0.521 (4)
C39A	0.6474 (5)	0.8983 (4)	0.3348 (3)	0.0241 (10)	0.521 (4)
H39C	0.5648	0.8798	0.3629	0.029*	0.521 (4)
H39D	0.7107	0.8455	0.3451	0.029*	0.521 (4)
C40A	0.6176 (5)	0.9151 (3)	0.2257 (3)	0.0221 (10)	0.521 (4)
H40A	0.5454	0.9623	0.2113	0.027*	0.521 (4)
C41	0.6179 (2)	0.84963 (15)	0.15382 (15)	0.0287 (5)	
H41A	0.5291	0.8757	0.1334	0.034*	
H41B	0.6273	0.7826	0.1365	0.034*	

C42	0.6800 (3)	0.9985 (2)	0.49024 (18)	0.0528 (8)	
N1	0.57615 (17)	1.10277 (12)	0.06120 (12)	0.0253 (4)	
N2	0.69318 (17)	1.03263 (12)	-0.04037 (12)	0.0268 (4)	
N3	0.82866 (17)	0.91392 (11)	0.00625 (12)	0.0266 (4)	
N4	0.95585 (17)	0.79855 (12)	0.07358 (12)	0.0287 (4)	
N5	0.96748 (17)	0.76690 (12)	0.22801 (12)	0.0284 (4)	
N6	0.7037 (2)	0.98193 (13)	0.38775 (13)	0.0353 (5)	
Fe1	0.77835 (3)	0.93592 (2)	0.135037 (18)	0.02491 (8)	
C43	0.5415 (6)	0.9571 (6)	0.5152 (4)	0.057 (2)	0.521 (4)
H43A	0.5280	0.9716	0.5838	0.086*	0.521 (4)
H43B	0.5410	0.8889	0.5058	0.086*	0.521 (4)
H43C	0.4703	0.9854	0.4713	0.086*	0.521 (4)
C44	0.7051 (6)	1.0843 (4)	0.5342 (4)	0.0471 (15)	0.479 (4)
H44A	0.6569	1.1332	0.4951	0.071*	0.479 (4)
H44B	0.8002	1.0974	0.5381	0.071*	0.479 (4)
H44C	0.6762	1.0834	0.6008	0.071*	0.479 (4)
C45	0.7759 (6)	0.9168 (4)	0.5498 (3)	0.0540 (19)	0.479 (4)
H45A	0.8682	0.9269	0.5369	0.081*	0.479 (4)
H45B	0.7473	0.8543	0.5264	0.081*	0.479 (4)
H45C	0.7683	0.9215	0.6207	0.081*	0.479 (4)
C43A	0.6094 (7)	0.9306 (5)	0.5362 (4)	0.0467 (16)	0.479 (4)
H43D	0.6562	0.8704	0.5355	0.070*	0.479 (4)
H43E	0.5211	0.9240	0.5010	0.070*	0.479 (4)
H43F	0.6012	0.9493	0.6045	0.070*	0.479 (4)
C44A	0.5858 (5)	1.0961 (4)	0.4753 (4)	0.0503 (14)	0.521 (4)
H44D	0.5637	1.1183	0.5397	0.075*	0.521 (4)
H44E	0.5043	1.0815	0.4337	0.075*	0.521 (4)
H44F	0.6349	1.1451	0.4438	0.075*	0.521 (4)
C45A	0.8017 (6)	1.0383 (4)	0.5519 (3)	0.0494 (15)	0.521 (4)
H45D	0.8361	1.0922	0.5176	0.074*	0.521 (4)
H45E	0.8702	0.9898	0.5612	0.074*	0.521 (4)
H45F	0.7766	1.0585	0.6163	0.074*	0.521 (4)
H2	0.486 (3)	1.189 (2)	-0.044 (2)	0.059*	
H3	0.638 (3)	1.114 (2)	-0.164 (2)	0.059*	
H9	1.083 (3)	0.698 (2)	0.035 (2)	0.059*	
H10	1.095 (3)	0.659 (2)	0.220 (2)	0.059*	

Structure: (4-Me₂N-ⁱPrPDI)Fe(DMAP)

ID: jmd17

Crystallographer: Scott Semproni

Table C.12. Crystal data

C ₄₂ H ₅₈ FeN ₆	Z = 2
M _r = 702.79	F(000) = 756
Triclinic, P $\bar{1}$	D _x = 1.235 Mg m ⁻³
a = 8.4601 (2) Å	Cu Kα radiation, λ = 1.54178 Å
b = 11.8033 (2) Å	Cell parameters from 8962 reflections
c = 20.4841 (4) Å	θ = 4.4–65.2°
α = 90.921 (2)°	μ = 3.48 mm ⁻¹
β = 101.881 (1)°	T = 100 K
γ = 108.531 (1)°	Plate, clear dark red-purple
V = 1890.54 (7) Å ³	0.09 × 0.07 × 0.06 mm

Table C.13. Data collection

Bruker APEX II CCD diffractometer	5160 reflections with I > 2σ(I)
Radiation source: fine-focus sealed tube	R _{int} = 0.050
none	θ _{max} = 65.9°, θ _{min} = 2.2°
Absorption correction: multi-scan S _{AD} ABS V2008/1 (Bruker AXS)	h = -9→9
T _{min} = 0.615, T _{max} = 0.753	k = -13→13
21363 measured reflections	l = -23→22
6161 independent reflections	

Table C.14. Refinement

Refinement on F ²	Primary atom site location: structure-invariant direct methods
Least-squares matrix: full	Secondary atom site location: difference Fourier map
R[F ² > 2σ(F ²)] = 0.041	Hydrogen site location: inferred from neighbouring sites
wR(F ²) = 0.103	H-atom parameters constrained
S = 1.04	w = 1/[σ ² (F _o ²) + (0.0535P) ² + 0.4914P] where P = (F _o ² + 2F _c ²)/3
6161 reflections	(Δ/σ) _{max} < 0.001
456 parameters	Δ _{max} = 0.36 e Å ⁻³
0 restraints	Δ _{min} = -0.33 e Å ⁻³

Special details

Experimental. Collected, solved and refined by Scott P. Semproni PLAT029_ALERT_3_A
_diffm_measured_fraction_theta_full Low 0.94 PLAT022_ALERT_3_C Ratio Unique / Expected
Reflections (too) Low .. 0.94 Author response: This was a very small and weakly diffracting crystal. Not

all reflections could be collected during the experiment.

Geometry. All s.u.'s (except the s.u. in the dihedral angle between two l.s. planes) are estimated using the full covariance matrix. The cell s.u.'s are taken into account individually in the estimation of s.u.'s in distances, angles and torsion angles; correlations between s.u.'s in cell parameters are only used when they are defined by crystal symmetry. An approximate (isotropic) treatment of cell s.u.'s is used for estimating s.u.'s involving l.s. planes.

Refinement. Refinement of F^2 against ALL reflections. The weighted R-factor wR and goodness of fit S are based on F^2 , conventional R-factors R are based on F, with F set to zero for negative F^2 . The threshold expression of $F^2 > 2\sigma(F^2)$ is used only for calculating R-factors(gt) etc. and is not relevant to the choice of reflections for refinement. R-factors based on F^2 are statistically about twice as large as those based on F, and R- factors based on ALL data will be even larger.

Table C.15. Fractional atomic coordinates and isotropic or equivalent isotropic displacement parameters (\AA^2)

	x	y	z	$U_{\text{iso}}^*/U_{\text{eq}}$
C1	0.7708 (3)	0.5333 (2)	0.79281 (13)	0.0324 (6)
H1A	0.6776	0.5481	0.7608	0.049*
H1B	0.8800	0.5754	0.7812	0.049*
H1C	0.7727	0.5628	0.8381	0.049*
C2	0.7435 (3)	0.4017 (2)	0.79042 (12)	0.0232 (5)
C3	0.8386 (3)	0.3539 (2)	0.84096 (11)	0.0221 (5)
C4	0.9786 (3)	0.4154 (2)	0.89262 (12)	0.0258 (5)
H4	1.0230	0.5005	0.8960	0.031*
C5	1.0535 (3)	0.3514 (2)	0.93944 (12)	0.0257 (5)
C6	0.9838 (3)	0.2251 (2)	0.93329 (11)	0.0230 (5)
H6	1.0319	0.1798	0.9645	0.028*
C7	0.8431 (3)	0.1668 (2)	0.88094 (11)	0.0203 (5)
C8	0.7523 (3)	0.0426 (2)	0.86667 (11)	0.0206 (5)
C9	0.7942 (3)	-0.0510 (2)	0.90836 (12)	0.0254 (5)
H9A	0.7302	-0.0643	0.9439	0.038*
H9B	0.9170	-0.0242	0.9284	0.038*
H9C	0.7628	-0.1261	0.8801	0.038*
C10	1.2713 (3)	0.5395 (2)	0.99185 (13)	0.0313 (6)
H10A	1.3060	0.5589	0.9495	0.047*
H10B	1.3721	0.5668	1.0290	0.047*
H10C	1.1897	0.5798	0.9979	0.047*
C11	1.2758 (3)	0.3441 (2)	1.03457 (13)	0.0331 (6)
H11A	1.1951	0.2931	1.0587	0.050*
H11B	1.3730	0.3996	1.0668	0.050*
H11C	1.3168	0.2938	1.0082	0.050*
C12	0.5053 (3)	0.35713 (19)	0.69702 (11)	0.0208 (5)
C13	0.5592 (3)	0.41003 (19)	0.64082 (11)	0.0230 (5)
C14	0.4486 (3)	0.4561 (2)	0.59741 (12)	0.0254 (5)
H14	0.4841	0.4941	0.5599	0.031*
C15	0.2891 (3)	0.4475 (2)	0.60778 (12)	0.0255 (5)
H15	0.2174	0.4814	0.5784	0.031*

C16	0.2344 (3)	0.3890 (2)	0.66145 (11)	0.0235 (5)
H16	0.1231	0.3807	0.6676	0.028*
C17	0.3395 (3)	0.3423 (2)	0.70629 (11)	0.0219 (5)
C18	0.7326 (3)	0.4217 (2)	0.62587 (13)	0.0314 (6)
H18	0.7920	0.3809	0.6602	0.038*
C19	0.7139 (4)	0.3607 (2)	0.55619 (14)	0.0398 (7)
H19A	0.6388	0.2773	0.5527	0.060*
H19B	0.8266	0.3626	0.5502	0.060*
H19C	0.6645	0.4036	0.5215	0.060*
C20	0.8460 (3)	0.5518 (3)	0.62902 (16)	0.0458 (7)
H20A	0.7925	0.5926	0.5942	0.069*
H20B	0.9580	0.5545	0.6217	0.069*
H20C	0.8604	0.5920	0.6731	0.069*
C21	0.2809 (3)	0.2808 (2)	0.76589 (11)	0.0264 (5)
H21	0.3356	0.2172	0.7745	0.032*
C22	0.0885 (3)	0.2180 (3)	0.75300 (13)	0.0360 (6)
H22A	0.0301	0.2780	0.7483	0.054*
H22B	0.0609	0.1711	0.7906	0.054*
H22C	0.0506	0.1644	0.7117	0.054*
C23	0.3442 (3)	0.3672 (3)	0.82954 (12)	0.0372 (6)
H23A	0.4691	0.4020	0.8387	0.056*
H23B	0.3104	0.3233	0.8674	0.056*
H23C	0.2937	0.4314	0.8233	0.056*
C24	0.5068 (3)	-0.10393 (19)	0.79767 (11)	0.0210 (5)
C25	0.5107 (3)	-0.1754 (2)	0.74272 (11)	0.0232 (5)
C26	0.3931 (3)	-0.2909 (2)	0.72848 (13)	0.0290 (5)
H26	0.3961	-0.3407	0.6922	0.035*
C27	0.2722 (3)	-0.3345 (2)	0.76611 (13)	0.0315 (6)
H27	0.1923	-0.4133	0.7554	0.038*
C28	0.2681 (3)	-0.2633 (2)	0.81925 (12)	0.0293 (6)
H28	0.1842	-0.2939	0.8448	0.035*
C29	0.3840 (3)	-0.1472 (2)	0.83663 (11)	0.0225 (5)
C30	0.6426 (3)	-0.1280 (2)	0.70067 (12)	0.0265 (5)
H30	0.6582	-0.0409	0.6972	0.032*
C31	0.8161 (3)	-0.1370 (2)	0.73482 (14)	0.0356 (6)
H31A	0.8544	-0.0930	0.7793	0.053*
H31B	0.8996	-0.1025	0.7077	0.053*
H31C	0.8056	-0.2215	0.7394	0.053*
C32	0.5852 (3)	-0.1886 (2)	0.62934 (13)	0.0365 (6)
H32A	0.5784	-0.2730	0.6306	0.055*
H32B	0.6680	-0.1480	0.6030	0.055*
H32C	0.4726	-0.1838	0.6087	0.055*
C33	0.3724 (3)	-0.0706 (2)	0.89439 (12)	0.0261 (5)
H33	0.4870	-0.0077	0.9100	0.031*
C34	0.3320 (4)	-0.1416 (2)	0.95410 (13)	0.0411 (7)
H34A	0.2155	-0.1990	0.9418	0.062*
H34B	0.3411	-0.0864	0.9920	0.062*
H34C	0.4133	-0.1851	0.9668	0.062*
C35	0.2438 (4)	-0.0065 (3)	0.87170 (14)	0.0449 (7)
H35A	0.2776	0.0442	0.8362	0.067*
H35B	0.2403	0.0435	0.9097	0.067*
H35C	0.1303	-0.0658	0.8546	0.067*
C36	0.4517 (3)	0.0974 (2)	0.62475 (12)	0.0262 (5)
H36	0.5529	0.1620	0.6244	0.031*
C37	0.3521 (3)	0.0405 (2)	0.56414 (12)	0.0286 (5)

H37	0.3860	0.0653	0.5238	0.034*
C38	0.1996 (3)	-0.0547 (2)	0.56193 (12)	0.0268 (5)
C39	0.1614 (3)	-0.0845 (2)	0.62439 (12)	0.0265 (5)
H39	0.0600	-0.1477	0.6264	0.032*
C40	0.2697 (3)	-0.0229 (2)	0.68248 (12)	0.0253 (5)
H40	0.2395	-0.0459	0.7237	0.030*
C41	-0.0656 (3)	-0.2066 (3)	0.50356 (14)	0.0407 (7)
H41A	-0.0431	-0.2797	0.5182	0.061*
H41B	-0.1384	-0.2233	0.4583	0.061*
H41C	-0.1237	-0.1796	0.5343	0.061*
C42	0.1394 (4)	-0.0907 (2)	0.43945 (12)	0.0386 (6)
H42A	0.1070	-0.0223	0.4224	0.058*
H42B	0.0789	-0.1617	0.4076	0.058*
H42C	0.2630	-0.0724	0.4450	0.058*
N1	0.6169 (2)	0.31577 (16)	0.74623 (9)	0.0212 (4)
N2	0.7734 (2)	0.23098 (16)	0.83529 (9)	0.0203 (4)
N3	0.6204 (2)	0.01773 (16)	0.81139 (9)	0.0194 (4)
N4	1.1917 (3)	0.41107 (18)	0.99064 (11)	0.0362 (5)
N5	0.4162 (2)	0.06835 (16)	0.68492 (9)	0.0220 (4)
N6	0.0940 (3)	-0.11401 (19)	0.50335 (10)	0.0346 (5)
Fe1	0.59320 (4)	0.15276 (3)	0.765864 (17)	0.01965 (11)

Structure: (*i*PrCNC)Fe(N₂)(DMAP)

ID: jmd20

Crystallographer: Scott Semproni

Table C.16. Crystal data

C ₄₆ H ₆₁ FeN ₉ O	$F(000) = 1736$
$M_r = 811.89$	$D_x = 1.246 \text{ Mg m}^{-3}$
Monoclinic, $P2_1/n$	Cu $K\alpha$ radiation, $\lambda = 1.54187 \text{ \AA}$
$a = 11.098 (5) \text{ \AA}$	Cell parameters from 9948 reflections
$b = 23.513 (5) \text{ \AA}$	$\theta = 4.6\text{--}65.6^\circ$
$c = 16.613 (5) \text{ \AA}$	$\mu = 3.15 \text{ mm}^{-1}$
$\beta = 92.883 (5)^\circ$	$T = 100 \text{ K}$
$V = 4330 (3) \text{ \AA}^3$	Cube, black
$Z = 4$	$0.08 \times 0.07 \times 0.06 \text{ mm}$

Table C.17. Data collection

Bruker APEX-II CCD diffractometer	7424 independent reflections
Radiation source: sealed tube graphite	6845 reflections with $I > 2\sigma(I)$
ϕ and ω scans	$R_{\text{int}} = 0.033$
Absorption correction: multi-scan <i>SADABS</i> V2008/1 (Bruker AXS)	$\theta_{\text{max}} = 66.3^\circ$, $\theta_{\text{min}} = 3.3^\circ$
$T_{\text{min}} = 0.690$, $T_{\text{max}} = 0.753$	$h = -13 \rightarrow 12$
45763 measured reflections	$k = -27 \rightarrow 27$
	$l = -18 \rightarrow 19$

Table C.18. Refinement

Refinement on F^2	Primary atom site location: structure-invariant direct methods
Least-squares matrix: full	Secondary atom site location: difference Fourier map
$R[F^2 > 2\sigma(F^2)] = 0.031$	Hydrogen site location: inferred from neighbouring sites
$wR(F^2) = 0.086$	H-atom parameters constrained
$S = 1.02$	$w = 1/[\sigma^2(F_o^2) + (0.0491P)^2 + 1.7647P]$ where $P = (F_o^2 + 2F_c^2)/3$
7424 reflections	$(\Delta/\sigma)_{\text{max}} = 0.001$
526 parameters	$\Delta)_{\text{max}} = 0.29 \text{ e \AA}^{-3}$
0 restraints	$\Delta)_{\text{min}} = -0.28 \text{ e \AA}^{-3}$

Special details

Geometry. All s.u.'s (except the s.u. in the dihedral angle between two l.s. planes) are estimated using the full covariance matrix. The cell s.u.'s are taken into account individually in the estimation of

s.u.'s in distances, angles and torsion angles; correlations between s.u.'s in cell parameters are only used when they are defined by crystal symmetry. An approximate (isotropic) treatment of cell s.u.'s is used for estimating s.u.'s involving l.s. planes.

Refinement. Refinement of F^2 against ALL reflections. The weighted R-factor wR and goodness of fit S are based on F^2 , conventional R-factors R are based on F , with F set to zero for negative F^2 . The threshold expression of $F^2 > 2\sigma(F^2)$ is used only for calculating R-factors(gt) etc. and is not relevant to the choice of reflections for refinement. R-factors based on F^2 are statistically about twice as large as those based on F , and R-factors based on ALL data will be even larger.

Table C.19. Fractional atomic coordinates and isotropic or equivalent isotropic displacement parameters (\AA^2)

	<i>x</i>	<i>y</i>	<i>z</i>	$U_{\text{iso}}^*/U_{\text{eq}}$
C1	0.20320 (15)	0.04598 (7)	0.26809 (10)	0.0256 (4)
H1	0.2126	0.0106	0.2953	0.031*
C1S	0.5188 (2)	0.08183 (10)	0.15311 (15)	0.0517 (6)
H1S1	0.4849	0.0638	0.1038	0.078*
H1S2	0.4743	0.1169	0.1634	0.078*
H1S3	0.5121	0.0557	0.1986	0.078*
C2	0.22185 (15)	0.05541 (7)	0.19013 (10)	0.0270 (4)
H2	0.2463	0.0283	0.1518	0.032*
C2S	0.6487 (2)	0.09570 (9)	0.14313 (14)	0.0474 (5)
H2S1	0.6554	0.1238	0.0992	0.057*
H2S2	0.6839	0.1128	0.1935	0.057*
C3	0.21083 (14)	0.14663 (7)	0.10946 (9)	0.0225 (3)
C3S	0.8396 (2)	0.05631 (11)	0.12118 (13)	0.0513 (6)
H3S1	0.8746	0.0654	0.1757	0.062*
H3S2	0.8533	0.0891	0.0855	0.062*
C4	0.24301 (15)	0.13077 (8)	0.03347 (10)	0.0283 (4)
H4	0.2571	0.0920	0.0208	0.034*
C4S	0.8987 (2)	0.00452 (13)	0.08941 (19)	0.0687 (7)
H4S1	0.8859	-0.0276	0.1255	0.103*
H4S2	0.9854	0.0114	0.0863	0.103*
H4S3	0.8635	-0.0043	0.0356	0.103*
C5	0.25424 (15)	0.17347 (8)	-0.02422 (10)	0.0305 (4)
H5	0.2757	0.1638	-0.0771	0.037*
C6	0.23408 (15)	0.23009 (8)	-0.00451 (10)	0.0260 (4)
H6	0.2414	0.2594	-0.0433	0.031*
C7	0.20319 (13)	0.24248 (7)	0.07298 (9)	0.0218 (3)
C8	0.19375 (14)	0.34981 (7)	0.07610 (10)	0.0249 (4)
H8	0.2091	0.3598	0.0222	0.030*
C9	0.17416 (15)	0.38539 (7)	0.13675 (10)	0.0246 (4)
H9	0.1727	0.4257	0.1335	0.030*
C10	0.16299 (13)	0.29533 (7)	0.18989 (9)	0.0192 (3)
C11	0.16609 (13)	0.14108 (7)	0.24690 (9)	0.0191 (3)
C12	0.14560 (14)	0.10441 (6)	0.38641 (9)	0.0199 (3)
C13	0.24194 (15)	0.11971 (7)	0.43953 (10)	0.0234 (3)
C14	0.21832 (15)	0.12773 (7)	0.52032 (10)	0.0260 (4)

H14	0.2821	0.1383	0.5576	0.031*
C15	0.10310 (16)	0.12044 (8)	0.54685 (10)	0.0282 (4)
H15	0.0883	0.1262	0.6021	0.034*
C16	0.00917 (15)	0.10485 (8)	0.49332 (10)	0.0269 (4)
H16	-0.0694	0.0999	0.5124	0.032*
C17	0.02805 (14)	0.09637 (7)	0.41205 (10)	0.0216 (3)
C18	0.36960 (15)	0.12575 (8)	0.41175 (11)	0.0319 (4)
H18	0.3656	0.1264	0.3515	0.038*
C19	0.44549 (18)	0.07407 (9)	0.43960 (16)	0.0507 (6)
H19A	0.4557	0.0741	0.4985	0.076*
H19B	0.5248	0.0760	0.4163	0.076*
H19C	0.4044	0.0391	0.4217	0.076*
C20	0.43049 (16)	0.18040 (8)	0.44176 (13)	0.0372 (4)
H20A	0.3811	0.2131	0.4244	0.056*
H20B	0.5103	0.1835	0.4195	0.056*
H20C	0.4392	0.1797	0.5007	0.056*
C21	-0.07311 (15)	0.07716 (7)	0.35327 (10)	0.0256 (4)
H21	-0.0594	0.0949	0.2998	0.031*
C22	-0.07106 (17)	0.01253 (8)	0.34262 (13)	0.0392 (5)
H22A	0.0074	0.0009	0.3235	0.059*
H22B	-0.1351	0.0012	0.3031	0.059*
H22C	-0.0841	-0.0059	0.3944	0.059*
C23	-0.19851 (15)	0.09480 (8)	0.37804 (11)	0.0284 (4)
H23A	-0.2193	0.0733	0.4259	0.043*
H23B	-0.2579	0.0869	0.3338	0.043*
H23C	-0.1987	0.1356	0.3903	0.043*
C24	0.13136 (14)	0.37907 (7)	0.28160 (9)	0.0205 (3)
C25	0.22341 (15)	0.38116 (7)	0.34299 (10)	0.0230 (3)
C26	0.19747 (16)	0.40948 (7)	0.41362 (10)	0.0281 (4)
H26	0.2575	0.4116	0.4564	0.034*
C27	0.08592 (17)	0.43462 (8)	0.42299 (11)	0.0313 (4)
H27	0.0709	0.4542	0.4715	0.038*
C28	-0.00334 (16)	0.43133 (7)	0.36216 (10)	0.0284 (4)
H28	-0.0797	0.4483	0.3694	0.034*
C29	0.01743 (15)	0.40330 (7)	0.29018 (10)	0.0226 (3)
C30	0.34574 (15)	0.35379 (7)	0.33251 (10)	0.0255 (4)
H30	0.3311	0.3159	0.3065	0.031*
C31	0.41702 (16)	0.34352 (8)	0.41242 (11)	0.0324 (4)
H31A	0.4402	0.3801	0.4368	0.049*
H31B	0.4897	0.3214	0.4026	0.049*
H31C	0.3668	0.3225	0.4491	0.049*
C32	0.42227 (17)	0.38904 (9)	0.27614 (12)	0.0367 (4)
H32A	0.3803	0.3918	0.2229	0.055*
H32B	0.5006	0.3705	0.2709	0.055*
H32C	0.4346	0.4273	0.2986	0.055*
C33	-0.08146 (15)	0.40121 (7)	0.22326 (10)	0.0244 (4)
H33	-0.0558	0.3741	0.1810	0.029*
C34	-0.20111 (16)	0.38024 (8)	0.25423 (11)	0.0300 (4)
H34A	-0.1896	0.3426	0.2787	0.045*
H34B	-0.2614	0.3778	0.2092	0.045*
H34C	-0.2290	0.4069	0.2946	0.045*
C35	-0.09899 (17)	0.45982 (8)	0.18432 (12)	0.0346 (4)
H35A	-0.1268	0.4868	0.2244	0.052*
H35B	-0.1592	0.4572	0.1393	0.052*
H35C	-0.0222	0.4730	0.1644	0.052*

C36	-0.09581 (14)	0.22947 (7)	0.14038 (10)	0.0223 (3)
H36	-0.0437	0.2304	0.0968	0.027*
C37	-0.21743 (15)	0.23432 (7)	0.12239 (10)	0.0241 (3)
H37	-0.2467	0.2387	0.0680	0.029*
C38	-0.29898 (14)	0.23282 (7)	0.18502 (10)	0.0238 (4)
C39	-0.24571 (15)	0.22645 (7)	0.26293 (10)	0.0238 (4)
H39	-0.2953	0.2248	0.3079	0.029*
C40	-0.12245 (14)	0.22256 (7)	0.27483 (10)	0.0220 (3)
H40	-0.0903	0.2190	0.3287	0.026*
C41	-0.47757 (17)	0.23808 (9)	0.09066 (12)	0.0383 (5)
H41A	-0.4282	0.2607	0.0554	0.057*
H41B	-0.5579	0.2552	0.0925	0.057*
H41C	-0.4850	0.1992	0.0697	0.057*
C42	-0.49918 (16)	0.22985 (10)	0.23846 (12)	0.0386 (5)
H42A	-0.4861	0.1922	0.2627	0.058*
H42B	-0.5836	0.2334	0.2188	0.058*
H42C	-0.4807	0.2593	0.2790	0.058*
N1	0.16766 (11)	0.09704 (6)	0.30248 (8)	0.0200 (3)
N2	0.19829 (12)	0.11271 (6)	0.17667 (8)	0.0218 (3)
N3	0.19073 (11)	0.20187 (6)	0.13106 (8)	0.0194 (3)
N4	0.18710 (11)	0.29517 (6)	0.10768 (8)	0.0206 (3)
N5	0.15626 (11)	0.35316 (6)	0.20561 (8)	0.0203 (3)
N6	0.14409 (11)	0.24034 (6)	0.33803 (8)	0.0194 (3)
N7	0.14601 (13)	0.25287 (6)	0.40389 (8)	0.0265 (3)
N8	-0.04452 (11)	0.22347 (5)	0.21565 (8)	0.0191 (3)
N9	-0.42067 (13)	0.23677 (7)	0.17143 (9)	0.0322 (3)
Fe1	0.13913 (2)	0.221220 (10)	0.234263 (14)	0.01591 (8)
O1S	0.71374 (13)	0.04575 (6)	0.12467 (9)	0.0458 (4)

Structure: (4-Me₂N-MePDI)Co(CH₃)

ID: jmd24

Crystallographer: Zoë Turner

Table C.20. Crystal data

C ₂₈ H ₃₅ CoN ₄	$F(000) = 2064$
$M_r = 486.53$	$D_x = 1.258 \text{ Mg m}^{-3}$
Orthorhombic, <i>Pbca</i>	Cu $K\alpha$ radiation, $\lambda = 1.54178 \text{ \AA}$
Hall symbol: -P 2ac 2ab	Cell parameters from 7693 reflections
$a = 15.0075 (3) \text{ \AA}$	$\theta = 3.9\text{--}65.2^\circ$
$b = 15.0761 (4) \text{ \AA}$	$\mu = 5.39 \text{ mm}^{-1}$
$c = 22.7027 (5) \text{ \AA}$	$T = 100 \text{ K}$
$V = 5136.6 (2) \text{ \AA}^3$	Block, blue
$Z = 8$	$0.20 \times 0.06 \times 0.04 \text{ mm}$

Table C.21. Data collection

Bruker APEX-II CCD diffractometer	4376 independent reflections
Radiation source: fine-focus sealed tube	3943 reflections with $I > 2\sigma(I)$
graphite	$R_{\text{int}} = 0.046$
Detector resolution: 0 pixels mm ⁻¹	$\theta_{\text{max}} = 66.1^\circ$, $\theta_{\text{min}} = 3.9^\circ$
phi and ω scans	$h = -16 \rightarrow 17$
Absorption correction: multi-scan <i>SADABS</i>	$k = -16 \rightarrow 14$
$T_{\text{min}} = 0.412$, $T_{\text{max}} = 0.813$	$l = -26 \rightarrow 26$
51236 measured reflections	

Table C.22. Refinement

Refinement on F^2	Primary atom site location: structure-invariant direct methods
Least-squares matrix: full	Secondary atom site location: difference Fourier map
$R[F^2 > 2\sigma(F^2)] = 0.031$	Hydrogen site location: inferred from neighbouring sites
$wR(F^2) = 0.080$	H-atom parameters constrained
$S = 1.05$	$w = 1/[\sigma^2(F_o^2) + (0.0381P)^2 + 3.1199P]$ where $P = (F_o^2 + 2F_c^2)/3$
4376 reflections	$(\Delta/\sigma)_{\text{max}} < 0.001$
305 parameters	$\Delta\rho_{\text{max}} = 0.28 \text{ e \AA}^{-3}$

0 restraints	$\Delta_{\min} = -0.31 \text{ e } \text{\AA}^{-3}$
--------------	--

Special details

Geometry. All s.u.'s (except the s.u. in the dihedral angle between two l.s. planes) are estimated using the full covariance matrix. The cell s.u.'s are taken into account individually in the estimation of s.u.'s in distances, angles and torsion angles; correlations between s.u.'s in cell parameters are only used when they are defined by crystal symmetry. An approximate (isotropic) treatment of cell s.u.'s is used for estimating s.u.'s involving l.s. planes.

Refinement. Refinement of F^2 against ALL reflections. The weighted R-factor wR and goodness of fit S are based on F^2 , conventional R-factors R are based on F , with F set to zero for negative F^2 . The threshold expression of $F^2 > 2\sigma(F^2)$ is used only for calculating R-factors(gt) etc. and is not relevant to the choice of reflections for refinement. R-factors based on F^2 are statistically about twice as large as those based on F , and R-factors based on ALL data will be even larger.

Table C.23. Fractional atomic coordinates and isotropic or equivalent isotropic displacement parameters (\AA^2)

	<i>x</i>	<i>y</i>	<i>z</i>	<i>U</i> _{iso} */ <i>U</i> _{eq}	Occ. (<1)
C1	0.42002 (13)	0.21756 (13)	0.25926 (9)	0.0301 (4)	
H1A	0.3940	0.2644	0.2838	0.045*	0.50
H1B	0.4773	0.2378	0.2434	0.045*	0.50
H1C	0.4293	0.1642	0.2832	0.045*	0.50
H1D	0.4730	0.1799	0.2565	0.045*	0.50
H1E	0.3898	0.2065	0.2968	0.045*	0.50
H1F	0.4378	0.2800	0.2571	0.045*	0.50
C2	0.35831 (11)	0.19674 (12)	0.20968 (8)	0.0213 (4)	
C3	0.37840 (11)	0.13008 (12)	0.16598 (8)	0.0204 (4)	
C4	0.45109 (11)	0.07378 (12)	0.16207 (8)	0.0222 (4)	
H4	0.4963	0.0755	0.1913	0.027*	
C5	0.45766 (11)	0.01386 (12)	0.11447 (8)	0.0224 (4)	
C6	0.38757 (11)	0.01196 (12)	0.07298 (8)	0.0220 (4)	
H6	0.3888	-0.0293	0.0413	0.026*	
C7	0.31682 (11)	0.07071 (12)	0.07869 (8)	0.0203 (4)	
C8	0.24040 (11)	0.08420 (12)	0.04093 (8)	0.0214 (4)	
C9	0.22737 (12)	0.03552 (13)	-0.01563 (8)	0.0274 (4)	

H9A	0.1717	0.0550	-0.0341	0.041*	0.50
H9B	0.2244	-0.0283	-0.0078	0.041*	0.50
H9C	0.2774	0.0479	-0.0421	0.041*	0.50
H9D	0.2773	-0.0053	-0.0219	0.041*	0.50
H9E	0.2246	0.0781	-0.0482	0.041*	0.50
H9F	0.1716	0.0018	-0.0139	0.041*	0.50
C10	0.25218 (12)	0.30870 (12)	0.23762 (8)	0.0210 (4)	
C11	0.20086 (12)	0.28887 (13)	0.28737 (8)	0.0242 (4)	
C12	0.16432 (12)	0.35901 (14)	0.31936 (8)	0.0290 (4)	
H12	0.1298	0.3469	0.3535	0.035*	
C13	0.17767 (13)	0.44584 (14)	0.30198 (9)	0.0313 (5)	
H13	0.1518	0.4929	0.3239	0.038*	
C14	0.22883 (12)	0.46429 (13)	0.25262 (9)	0.0285 (4)	
H14	0.2378	0.5242	0.2411	0.034*	
C15	0.26714 (12)	0.39637 (13)	0.21981 (8)	0.0240 (4)	
C16	0.18282 (14)	0.19407 (13)	0.30373 (9)	0.0318 (5)	
H16A	0.1382	0.1920	0.3352	0.048*	
H16B	0.2381	0.1662	0.3174	0.048*	
H16C	0.1604	0.1620	0.2692	0.048*	
C17	0.32093 (13)	0.41634 (14)	0.16553 (9)	0.0319 (4)	
H17A	0.3814	0.3930	0.1704	0.048*	
H17B	0.3236	0.4807	0.1596	0.048*	
H17C	0.2928	0.3884	0.1313	0.048*	
C18	0.10870 (12)	0.17032 (12)	0.02590 (8)	0.0213 (4)	
C19	0.02590 (12)	0.13066 (12)	0.03630 (8)	0.0246 (4)	
C20	-0.04678 (12)	0.15962 (13)	0.00317 (9)	0.0297 (4)	
H20	-0.1036	0.1338	0.0098	0.036*	
C21	-0.03785 (13)	0.22517 (13)	-0.03906 (8)	0.0295 (4)	
H21	-0.0879	0.2434	-0.0616	0.035*	
C22	0.04459 (13)	0.26403 (13)	-0.04824 (8)	0.0274 (4)	
H22	0.0505	0.3095	-0.0769	0.033*	
C23	0.11902 (12)	0.23744 (12)	-0.01607 (8)	0.0235 (4)	
C24	0.01571 (13)	0.05982 (14)	0.08265 (9)	0.0330 (5)	

H24A	0.0484	0.0066	0.0705	0.050*	
H24B	-0.0475	0.0453	0.0874	0.050*	
H24C	0.0396	0.0815	0.1202	0.050*	
C25	0.20800 (13)	0.28137 (14)	-0.02468 (9)	0.0321 (5)	
H25A	0.2303	0.3028	0.0133	0.048*	
H25B	0.2015	0.3315	-0.0518	0.048*	
H25C	0.2502	0.2385	-0.0412	0.048*	
C26	0.59122 (13)	-0.05115 (14)	0.15777 (10)	0.0351 (5)	
H26A	0.6196	0.0055	0.1675	0.053*	
H26B	0.6371	-0.0948	0.1477	0.053*	
H26C	0.5570	-0.0723	0.1918	0.053*	
C27	0.53584 (12)	-0.10419 (13)	0.06087 (9)	0.0288 (4)	
H27A	0.4893	-0.1489	0.0669	0.043*	
H27B	0.5944	-0.1331	0.0610	0.043*	
H27C	0.5265	-0.0745	0.0230	0.043*	
C28	0.10636 (12)	0.26699 (13)	0.14967 (8)	0.0267 (4)	
H28A	0.0558	0.2378	0.1304	0.040*	
H28B	0.1125	0.3275	0.1345	0.040*	
H28C	0.0961	0.2690	0.1923	0.040*	
N1	0.28108 (9)	0.23795 (10)	0.19997 (6)	0.0198 (3)	
N2	0.31296 (9)	0.12878 (10)	0.12454 (6)	0.0199 (3)	
N3	0.18407 (9)	0.14537 (10)	0.06147 (6)	0.0211 (3)	
N4	0.53204 (10)	-0.03918 (11)	0.10802 (7)	0.0288 (4)	
Co1	0.215031 (17)	0.200660 (19)	0.133486 (12)	0.01874 (10)	

Structure: (*i*PrCNC)Fe(CH₂Si(CH₃)₃)₂(N₂)

ID: jmd27

Crystallographer: Zoë Turner

Table C.24. Crystal data

C ₄₃ H ₆₃ FeN ₇ Si ₂	$F(000) = 5088$
$M_r = 790.03$	$D_x = 1.122 \text{ Mg m}^{-3}$
Monoclinic, $P2_1/c$	Cu $K\alpha$ radiation, $\lambda = 1.54178 \text{ \AA}$
Hall symbol: $-P 2_1/c$	Cell parameters from 9858 reflections
$a = 16.4987 (2) \text{ \AA}$	$\theta = 2.7\text{--}64.9^\circ$
$b = 32.6224 (5) \text{ \AA}$	$\mu = 3.34 \text{ mm}^{-1}$
$c = 26.0839 (4) \text{ \AA}$	$T = 100 \text{ K}$
$\beta = 91.121 (1)^\circ$	Needle, purple
$V = 14036.4 (3) \text{ \AA}^3$	$0.21 \times 0.05 \times 0.02 \text{ mm}$
$Z = 12$	

Table C.25. Data collection

Bruker APEX-II CCD diffractometer	24062 independent reflections
Radiation source: fine-focus sealed tube	15353 reflections with $I > 2\sigma(I)$
graphite	$R_{\text{int}} = 0.089$
phi and ω scans	$\theta_{\text{max}} = 66.2^\circ$, $\theta_{\text{min}} = 2.2^\circ$
Absorption correction: multi-scan <i>SADABS</i>	$h = -19 \rightarrow 18$
$T_{\text{min}} = 0.541$, $T_{\text{max}} = 0.936$	$k = -33 \rightarrow 38$
105771 measured reflections	$l = -30 \rightarrow 29$

Table C.26. Refinement

Refinement on F^2	Primary atom site location: structure-invariant direct methods
Least-squares matrix: full	Secondary atom site location: difference Fourier map
$R[F^2 > 2\sigma(F^2)] = 0.056$	Hydrogen site location: inferred from neighbouring sites
$wR(F^2) = 0.181$	H-atom parameters constrained
$S = 0.73$	$w = 1/[\sigma^2(F_o^2) + (0.1502P)^2 + 8.9379P]$ where $P = (F_o^2 + 2F_c^2)/3$
24062 reflections	$(\Delta/\sigma)_{\text{max}} = 0.001$
1474 parameters	$\Delta)_{\text{max}} = 0.43 \text{ e \AA}^{-3}$
0 restraints	$\Delta)_{\text{min}} = -0.30 \text{ e \AA}^{-3}$

Special details

Experimental. Collected, solved and refined by Dr. Zoe R. Turner

Geometry. All s.u.'s (except the s.u. in the dihedral angle between two l.s. planes) are estimated

using the full covariance matrix. The cell s.u.'s are taken into account individually in the estimation of s.u.'s in distances, angles and torsion angles; correlations between s.u.'s in cell parameters are only used when they are defined by crystal symmetry. An approximate (isotropic) treatment of cell s.u.'s is used for estimating s.u.'s involving l.s. planes.

Refinement. Refinement of F^2 against ALL reflections. The weighted R-factor wR and goodness of fit S are based on F^2 , conventional R-factors R are based on F, with F set to zero for negative F^2 . The threshold expression of $F^2 > 2\sigma(F^2)$ is used only for calculating R-factors(gt) etc. and is not relevant to the choice of reflections for refinement. R-factors based on F^2 are statistically about twice as large as those based on F, and R-factors based on ALL data will be even larger.

Table C.27. Fractional atomic coordinates and isotropic or equivalent isotropic displacement parameters (\AA^2)

	x	y	z	$U_{\text{iso}}^*/U_{\text{eq}}$
C1	0.1335 (3)	0.44734 (14)	0.02918 (15)	0.0450 (10)
H1	0.1101	0.4660	0.0052	0.054*
C2	0.1325 (2)	0.40652 (14)	0.02546 (15)	0.0413 (10)
H2	0.1083	0.3906	-0.0013	0.050*
C3	0.1918 (2)	0.35246 (13)	0.08416 (14)	0.0350 (9)
C4	0.1718 (2)	0.31613 (13)	0.05959 (15)	0.0394 (10)
H4	0.1421	0.3161	0.0280	0.047*
C5	0.1963 (2)	0.27982 (13)	0.08250 (16)	0.0408 (10)
H5	0.1845	0.2544	0.0661	0.049*
C6	0.2381 (2)	0.28021 (12)	0.12945 (15)	0.0367 (9)
H6	0.2547	0.2554	0.1457	0.044*
C7	0.2547 (2)	0.31763 (12)	0.15135 (14)	0.0329 (9)
C8	0.3216 (2)	0.29838 (12)	0.23490 (14)	0.0358 (9)
H8	0.3191	0.2693	0.2340	0.043*
C9	0.3537 (3)	0.32175 (12)	0.27220 (15)	0.0378 (9)
H9	0.3780	0.3121	0.3032	0.045*
C10	0.3050 (2)	0.36637 (11)	0.21097 (14)	0.0311 (8)
C11	0.2013 (2)	0.42352 (12)	0.10059 (14)	0.0345 (9)
C12	0.1844 (3)	0.49912 (13)	0.09274 (17)	0.0444 (10)
C13	0.2511 (3)	0.52198 (15)	0.07701 (19)	0.0551 (12)
C14	0.2614 (4)	0.56116 (17)	0.0989 (2)	0.0725 (17)
H14	0.3063	0.5776	0.0895	0.087*
C15	0.2072 (4)	0.57579 (18)	0.1337 (2)	0.0768 (17)
H15	0.2164	0.6018	0.1492	0.092*
C16	0.1399 (3)	0.55352 (15)	0.1465 (2)	0.0621 (13)
H16	0.1024	0.5647	0.1699	0.075*
C17	0.1258 (3)	0.51492 (13)	0.12588 (16)	0.0474 (11)
C18	0.3056 (3)	0.50637 (18)	0.0346 (2)	0.0707 (16)
H18	0.3019	0.4758	0.0339	0.085*
C19	0.2739 (4)	0.52280 (18)	-0.0175 (2)	0.0761 (16)
H19A	0.2183	0.5132	-0.0237	0.114*
H19B	0.3087	0.5128	-0.0449	0.114*
H19C	0.2746	0.5528	-0.0171	0.114*
C20	0.3945 (3)	0.5182 (2)	0.0418 (3)	0.115 (3)
H20A	0.4006	0.5478	0.0370	0.172*

H20B	0.4270	0.5037	0.0164	0.172*
H20C	0.4132	0.5106	0.0764	0.172*
C21	0.0477 (3)	0.49182 (15)	0.13512 (17)	0.0517 (11)
H21	0.0596	0.4618	0.1326	0.062*
C22	-0.0163 (3)	0.50255 (17)	0.09304 (19)	0.0648 (14)
H22A	-0.0297	0.5318	0.0950	0.097*
H22B	-0.0654	0.4862	0.0982	0.097*
H22C	0.0056	0.4964	0.0592	0.097*
C23	0.0115 (3)	0.49987 (17)	0.18754 (18)	0.0631 (14)
H23A	0.0522	0.4941	0.2144	0.095*
H23B	-0.0356	0.4820	0.1922	0.095*
H23C	-0.0054	0.5286	0.1897	0.095*
C24	0.3809 (2)	0.39531 (12)	0.28808 (14)	0.0344 (9)
C25	0.4622 (3)	0.40537 (13)	0.27974 (15)	0.0401 (10)
C26	0.4972 (3)	0.43524 (14)	0.31141 (17)	0.0521 (12)
H26	0.5518	0.4433	0.3065	0.063*
C27	0.4524 (3)	0.45342 (13)	0.35043 (16)	0.0514 (12)
H27	0.4768	0.4738	0.3716	0.062*
C28	0.3745 (3)	0.44212 (13)	0.35823 (16)	0.0465 (11)
H28	0.3453	0.4548	0.3849	0.056*
C29	0.3362 (3)	0.41227 (12)	0.32786 (14)	0.0380 (9)
C30	0.5120 (3)	0.38324 (14)	0.24000 (16)	0.0467 (11)
H30	0.4737	0.3725	0.2130	0.056*
C31	0.5566 (3)	0.34634 (16)	0.26396 (18)	0.0588 (13)
H31A	0.5953	0.3560	0.2902	0.088*
H31B	0.5857	0.3316	0.2373	0.088*
H31C	0.5172	0.3279	0.2797	0.088*
C32	0.5733 (3)	0.41085 (18)	0.21372 (19)	0.0659 (15)
H32A	0.5456	0.4351	0.1999	0.099*
H32B	0.5985	0.3958	0.1857	0.099*
H32C	0.6152	0.4194	0.2387	0.099*
C33	0.3735 (2)	0.41707 (12)	0.12982 (16)	0.0384 (9)
H33A	0.3684	0.4444	0.1136	0.046*
H33B	0.4112	0.4205	0.1595	0.046*
C34	0.2525 (3)	0.39742 (14)	0.34161 (16)	0.0449 (10)
H34	0.2324	0.3796	0.3128	0.054*
C35	0.4572 (3)	0.33417 (15)	0.1098 (2)	0.0697 (16)
H35A	0.4960	0.3379	0.1383	0.105*
H35B	0.4824	0.3180	0.0827	0.105*
H35C	0.4091	0.3198	0.1220	0.105*
C36	0.2564 (3)	0.37101 (17)	0.38974 (19)	0.0637 (14)
H36A	0.2953	0.3487	0.3850	0.096*
H36B	0.2027	0.3595	0.3961	0.096*
H36C	0.2738	0.3878	0.4191	0.096*
C37	0.1916 (3)	0.43204 (17)	0.3476 (2)	0.0662 (15)
H37A	0.2074	0.4489	0.3773	0.099*
H37B	0.1376	0.4205	0.3530	0.099*
H37C	0.1907	0.4490	0.3166	0.099*
C38	0.3667 (4)	0.3775 (3)	0.0244 (2)	0.110 (3)
H38A	0.3365	0.3517	0.0265	0.165*
H38B	0.4029	0.3765	-0.0049	0.165*
H38C	0.3285	0.4003	0.0199	0.165*
C39	0.5239 (3)	0.41030 (16)	0.0635 (2)	0.0638 (14)
H39A	0.5114	0.4368	0.0476	0.096*
H39B	0.5512	0.3927	0.0388	0.096*

H39C	0.5594	0.4145	0.0936	0.096*
C40	0.1498 (2)	0.40719 (14)	0.20530 (15)	0.0418 (10)
H40A	0.1687	0.4068	0.2416	0.050*
H40B	0.1279	0.4350	0.1991	0.050*
C41	0.0875 (3)	0.31953 (17)	0.2217 (2)	0.0741 (16)
H41A	0.1125	0.3055	0.1928	0.111*
H41B	0.0382	0.3049	0.2313	0.111*
H41C	0.1256	0.3200	0.2510	0.111*
C42	0.0054 (3)	0.37098 (18)	0.13951 (19)	0.0628 (14)
H42A	-0.0092	0.3988	0.1287	0.094*
H42B	-0.0439	0.3545	0.1429	0.094*
H42C	0.0402	0.3585	0.1138	0.094*
C43	-0.0153 (3)	0.39054 (19)	0.2511 (2)	0.0727 (16)
H43A	0.0082	0.3881	0.2858	0.109*
H43B	-0.0640	0.3734	0.2482	0.109*
H43C	-0.0298	0.4192	0.2444	0.109*
N1	0.17471 (19)	0.45783 (10)	0.07434 (12)	0.0383 (8)
N2	0.17389 (19)	0.39207 (10)	0.06842 (11)	0.0347 (7)
N3	0.23316 (18)	0.35403 (9)	0.12939 (11)	0.0308 (7)
N4	0.29298 (19)	0.32535 (9)	0.19808 (11)	0.0325 (7)
N5	0.34522 (19)	0.36298 (9)	0.25765 (11)	0.0315 (7)
N6	0.2781 (2)	0.45248 (11)	0.19477 (13)	0.0398 (8)
N7	0.2901 (2)	0.48186 (12)	0.21560 (15)	0.0507 (9)
Si1	0.42695 (7)	0.38508 (4)	0.08384 (4)	0.0430 (3)
Si2	0.06110 (7)	0.37307 (4)	0.20280 (4)	0.0459 (3)
Fe1	0.25775 (4)	0.404116 (18)	0.16147 (2)	0.03141 (15)
C1A	-0.0067 (2)	0.58689 (12)	0.38938 (14)	0.0337 (9)
H1A	-0.0345	0.5812	0.3580	0.040*
C2A	-0.0202 (2)	0.56893 (12)	0.43450 (15)	0.0364 (9)
H2A	-0.0587	0.5481	0.4413	0.044*
C3A	0.0467 (2)	0.58016 (12)	0.52156 (14)	0.0342 (9)
C4A	0.0072 (2)	0.55283 (13)	0.55259 (16)	0.0408 (10)
H4A	-0.0353	0.5359	0.5396	0.049*
C5A	0.0321 (3)	0.55117 (14)	0.60377 (16)	0.0447 (11)
H5A	0.0076	0.5320	0.6261	0.054*
C6A	0.0926 (2)	0.57728 (13)	0.62277 (15)	0.0422 (10)
H6A	0.1099	0.5763	0.6577	0.051*
C7A	0.1265 (2)	0.60472 (13)	0.58882 (14)	0.0350 (9)
C8A	0.2197 (3)	0.64760 (15)	0.64537 (15)	0.0458 (11)
H8A	0.2113	0.6365	0.6785	0.055*
C9A	0.2671 (3)	0.67879 (16)	0.63359 (16)	0.0509 (12)
H9A	0.2993	0.6942	0.6572	0.061*
C10A	0.2097 (2)	0.65754 (12)	0.55819 (14)	0.0318 (8)
C11A	0.0825 (2)	0.61656 (11)	0.44684 (13)	0.0293 (8)
C12A	0.0924 (2)	0.63698 (12)	0.35454 (13)	0.0326 (9)
C13A	0.1501 (2)	0.61613 (13)	0.32598 (14)	0.0350 (9)
C14A	0.1844 (2)	0.63759 (15)	0.28536 (15)	0.0461 (11)
H14A	0.2240	0.6244	0.2651	0.055*
C15A	0.1625 (3)	0.67693 (15)	0.27410 (16)	0.0498 (11)
H15A	0.1877	0.6909	0.2467	0.060*
C16A	0.1037 (3)	0.69679 (14)	0.30226 (16)	0.0453 (10)
H16A	0.0882	0.7240	0.2935	0.054*
C17A	0.0672 (2)	0.67712 (13)	0.34314 (15)	0.0383 (9)
C18A	0.1717 (2)	0.57182 (13)	0.33563 (15)	0.0396 (10)
H18A	0.1566	0.5650	0.3716	0.048*

C19A	0.1231 (3)	0.54386 (14)	0.29941 (17)	0.0516 (11)
H19D	0.0650	0.5481	0.3046	0.077*
H19E	0.1370	0.5152	0.3066	0.077*
H19F	0.1361	0.5504	0.2638	0.077*
C20A	0.2629 (2)	0.56305 (15)	0.33010 (16)	0.0490 (11)
H20D	0.2777	0.5660	0.2941	0.074*
H20E	0.2747	0.5350	0.3416	0.074*
H20F	0.2943	0.5825	0.3511	0.074*
C21A	0.0001 (3)	0.69808 (13)	0.37253 (15)	0.0402 (10)
H21A	-0.0024	0.6847	0.4069	0.048*
C22A	-0.0824 (3)	0.69141 (16)	0.34553 (18)	0.0548 (12)
H22D	-0.0814	0.7034	0.3111	0.082*
H22E	-0.1249	0.7046	0.3653	0.082*
H22F	-0.0935	0.6620	0.3429	0.082*
C23A	0.0166 (3)	0.74377 (13)	0.38154 (17)	0.0524 (12)
H23D	0.0708	0.7472	0.3971	0.079*
H23E	-0.0240	0.7549	0.4046	0.079*
H23F	0.0138	0.7584	0.3487	0.079*
C24A	0.3095 (3)	0.71536 (13)	0.55516 (15)	0.0432 (10)
C25A	0.3866 (3)	0.70426 (13)	0.53777 (14)	0.0392 (9)
C26A	0.2534 (2)	0.60525 (12)	0.47053 (14)	0.0313 (8)
H26A	0.2462	0.6022	0.4330	0.038*
H26B	0.3031	0.6219	0.4759	0.038*
C27A	0.4327 (3)	0.73413 (14)	0.51443 (16)	0.0513 (11)
H27A	0.4845	0.7271	0.5018	0.062*
C28A	0.4050 (4)	0.77382 (15)	0.50906 (18)	0.0590 (13)
H28A	0.4374	0.7937	0.4925	0.071*
C29A	0.3309 (4)	0.78462 (15)	0.5275 (2)	0.0629 (14)
H29A	0.3130	0.8122	0.5240	0.075*
C30A	0.2812 (3)	0.75626 (15)	0.55137 (18)	0.0548 (12)
C31A	0.4206 (3)	0.66126 (13)	0.54669 (15)	0.0399 (10)
H31D	0.3741	0.6423	0.5526	0.048*
C32A	0.4757 (3)	0.66105 (15)	0.59514 (18)	0.0584 (13)
H32D	0.5240	0.6777	0.5891	0.088*
H32E	0.4921	0.6329	0.6031	0.088*
H32F	0.4460	0.6724	0.6240	0.088*
C33A	0.4684 (3)	0.64494 (15)	0.50171 (17)	0.0506 (11)
H33C	0.4362	0.6481	0.4700	0.076*
H33D	0.4807	0.6159	0.5073	0.076*
H33E	0.5191	0.6604	0.4989	0.076*
C34A	0.1997 (3)	0.76968 (17)	0.5729 (2)	0.0677 (15)
H34A	0.1673	0.7444	0.5797	0.081*
C35A	0.2118 (4)	0.7924 (2)	0.6240 (3)	0.111 (3)
H35D	0.2357	0.7737	0.6496	0.167*
H35E	0.1593	0.8022	0.6360	0.167*
H35F	0.2481	0.8158	0.6192	0.167*
C36A	0.1508 (4)	0.79644 (18)	0.5353 (3)	0.105 (3)
H36D	0.1754	0.8237	0.5336	0.157*
H36E	0.0949	0.7989	0.5470	0.157*
H36F	0.1508	0.7838	0.5012	0.157*
C37A	0.3047 (3)	0.55252 (14)	0.56518 (15)	0.0459 (10)
H37D	0.3419	0.5751	0.5734	0.069*
H37E	0.3308	0.5264	0.5738	0.069*
H37F	0.2552	0.5555	0.5850	0.069*
C38A	0.1952 (2)	0.51489 (13)	0.48201 (18)	0.0460 (10)

H38D	0.1491	0.5208	0.5039	0.069*
H38E	0.2156	0.4873	0.4894	0.069*
H38F	0.1778	0.5166	0.4459	0.069*
C39A	0.3712 (2)	0.53293 (12)	0.46232 (15)	0.0398 (9)
H39D	0.3620	0.5330	0.4251	0.060*
H39E	0.3818	0.5048	0.4739	0.060*
H39F	0.4181	0.5502	0.4710	0.060*
C40A	0.0730 (2)	0.69160 (12)	0.50753 (14)	0.0324 (8)
H40C	0.1057	0.7129	0.5254	0.039*
H40D	0.0605	0.7028	0.4730	0.039*
C41A	-0.0622 (3)	0.74655 (15)	0.54271 (18)	0.0572 (13)
H41D	-0.0297	0.7620	0.5679	0.086*
H41E	-0.1192	0.7468	0.5527	0.086*
H41F	-0.0573	0.7592	0.5088	0.086*
C42A	-0.0205 (3)	0.67287 (15)	0.60803 (16)	0.0493 (11)
H42D	-0.0162	0.6429	0.6083	0.074*
H42E	-0.0699	0.6812	0.6254	0.074*
H42F	0.0268	0.6847	0.6259	0.074*
C43A	-0.1041 (3)	0.66116 (19)	0.50511 (19)	0.0661 (15)
H43D	-0.1039	0.6683	0.4686	0.099*
H43E	-0.1573	0.6673	0.5192	0.099*
H43F	-0.0926	0.6318	0.5092	0.099*
N1A	0.05542 (17)	0.61552 (9)	0.39657 (11)	0.0295 (7)
N2A	0.03344 (17)	0.58688 (9)	0.46937 (11)	0.0306 (7)
N3A	0.10576 (17)	0.60572 (9)	0.53885 (11)	0.0289 (7)
N4A	0.18429 (19)	0.63421 (10)	0.59932 (11)	0.0351 (7)
N5A	0.2621 (2)	0.68526 (10)	0.58092 (12)	0.0377 (8)
N6A	0.20129 (18)	0.68079 (10)	0.45211 (12)	0.0335 (7)
N7A	0.2280 (2)	0.70461 (11)	0.42693 (14)	0.0438 (8)
Si1A	0.27838 (6)	0.55356 (3)	0.49501 (4)	0.0332 (2)
Si2A	-0.02441 (7)	0.69165 (4)	0.54024 (4)	0.0399 (3)
Fe1A	0.15556 (3)	0.642955 (18)	0.49451 (2)	0.02825 (14)
C29B	0.5467 (2)	0.68644 (12)	0.36968 (13)	0.0326 (9)
C17B	0.7570 (2)	0.71165 (12)	0.14054 (14)	0.0357 (9)
C33B	0.4725 (2)	0.69590 (13)	0.33600 (15)	0.0394 (9)
H33F	0.4708	0.6755	0.3074	0.047*
C24B	0.5816 (2)	0.64733 (12)	0.37090 (13)	0.0318 (8)
C30B	0.6780 (2)	0.59327 (12)	0.40854 (15)	0.0371 (9)
H30B	0.6625	0.5785	0.3762	0.045*
C13B	0.8694 (3)	0.67037 (13)	0.17584 (14)	0.0397 (10)
C25B	0.6462 (2)	0.63712 (12)	0.40443 (14)	0.0318 (8)
C11B	0.6931 (2)	0.61830 (12)	0.16961 (14)	0.0330 (8)
C12B	0.7929 (2)	0.67380 (12)	0.15278 (13)	0.0348 (9)
C27B	0.6445 (2)	0.70705 (13)	0.43465 (15)	0.0393 (9)
H27B	0.6663	0.7278	0.4564	0.047*
C10B	0.5731 (2)	0.60530 (11)	0.29089 (14)	0.0306 (8)
C35B	0.4759 (3)	0.73880 (13)	0.31210 (17)	0.0493 (11)
H35G	0.4712	0.7595	0.3391	0.074*
H35H	0.4311	0.7420	0.2872	0.074*
H35I	0.5276	0.7423	0.2947	0.074*
C3B	0.6056 (3)	0.56200 (13)	0.15803 (15)	0.0446 (10)
C9B	0.4857 (2)	0.58978 (12)	0.35520 (16)	0.0382 (9)
H9B	0.4595	0.5913	0.3873	0.046*
C28B	0.5802 (3)	0.71588 (12)	0.40192 (15)	0.0405 (10)
H28B	0.5583	0.7428	0.4015	0.049*

C8B	0.4695 (2)	0.56261 (12)	0.31814 (15)	0.0368 (9)
H8B	0.4303	0.5413	0.3184	0.044*
C32B	0.7697 (2)	0.59103 (14)	0.41527 (16)	0.0447 (10)
H32G	0.7954	0.6066	0.3878	0.067*
H32H	0.7872	0.5623	0.4137	0.067*
H32I	0.7857	0.6027	0.4486	0.067*
C21B	0.6807 (2)	0.71415 (14)	0.10730 (15)	0.0410 (10)
H21B	0.6495	0.6882	0.1118	0.049*
C18B	0.9131 (3)	0.62980 (15)	0.17908 (15)	0.0470 (11)
H18B	0.8720	0.6074	0.1762	0.056*
C34B	0.3947 (3)	0.69091 (15)	0.36666 (17)	0.0491 (11)
H34B	0.3911	0.6627	0.3794	0.074*
H34C	0.3476	0.6968	0.3444	0.074*
H34D	0.3957	0.7100	0.3957	0.074*
C40B	0.5634 (2)	0.66653 (12)	0.21097 (14)	0.0355 (9)
H40E	0.5503	0.6819	0.2425	0.043*
H40F	0.5971	0.6852	0.1905	0.043*
C31B	0.6376 (3)	0.57163 (14)	0.45308 (18)	0.0490 (11)
H31E	0.6517	0.5857	0.4852	0.074*
H31F	0.6564	0.5432	0.4549	0.074*
H31G	0.5786	0.5721	0.4478	0.074*
C1B	0.7557 (3)	0.61646 (14)	0.09273 (16)	0.0573 (13)
H1B	0.7909	0.6239	0.0659	0.069*
C6B	0.4871 (3)	0.52173 (14)	0.21075 (18)	0.0548 (12)
H6B	0.4461	0.5084	0.2296	0.066*
C14B	0.9079 (3)	0.70613 (14)	0.19088 (15)	0.0451 (10)
H14B	0.9596	0.7048	0.2074	0.054*
C16B	0.7975 (3)	0.74666 (13)	0.15636 (15)	0.0424 (10)
H16B	0.7745	0.7728	0.1496	0.051*
C20B	0.9622 (3)	0.62358 (15)	0.22849 (17)	0.0512 (11)
H20G	1.0067	0.6434	0.2301	0.077*
H20H	0.9843	0.5957	0.2293	0.077*
H20I	0.9271	0.6276	0.2579	0.077*
C4B	0.5660 (3)	0.52948 (15)	0.13455 (18)	0.0636 (14)
H4B	0.5794	0.5212	0.1008	0.076*
C36B	0.7449 (2)	0.58662 (12)	0.26702 (14)	0.0341 (9)
H36G	0.7934	0.6000	0.2527	0.041*
H36H	0.7460	0.5930	0.3041	0.041*
C37B	0.8638 (3)	0.51938 (13)	0.29677 (16)	0.0457 (10)
H37G	0.9071	0.5360	0.2821	0.069*
H37H	0.8764	0.4902	0.2924	0.069*
H37I	0.8595	0.5256	0.3334	0.069*
C22B	0.7047 (3)	0.71720 (18)	0.05072 (17)	0.0631 (14)
H22G	0.7358	0.7424	0.0455	0.095*
H22H	0.6556	0.7177	0.0289	0.095*
H22I	0.7378	0.6934	0.0417	0.095*
C5B	0.5062 (3)	0.50928 (16)	0.16151 (18)	0.0656 (15)
H5B	0.4782	0.4868	0.1462	0.079*
C43B	0.4226 (3)	0.71594 (15)	0.16669 (18)	0.0550 (12)
H43G	0.3908	0.7230	0.1968	0.082*
H43H	0.3875	0.7166	0.1359	0.082*
H43I	0.4666	0.7358	0.1630	0.082*
C15B	0.8719 (3)	0.74372 (14)	0.18214 (16)	0.0491 (11)
H15B	0.8984	0.7679	0.1939	0.059*
C7B	0.5305 (2)	0.55461 (13)	0.23126 (15)	0.0405 (10)

C23B	0.6255 (3)	0.74981 (14)	0.12014 (18)	0.0524 (12)
H23G	0.6127	0.7489	0.1567	0.079*
H23H	0.5753	0.7478	0.0996	0.079*
H23I	0.6529	0.7757	0.1124	0.079*
C41B	0.4779 (3)	0.64060 (16)	0.10901 (17)	0.0589 (13)
H41G	0.5173	0.6568	0.0900	0.088*
H41H	0.4253	0.6413	0.0908	0.088*
H41I	0.4967	0.6122	0.1118	0.088*
C38B	0.7752 (3)	0.51128 (15)	0.19542 (17)	0.0587 (13)
H38G	0.7214	0.5091	0.1790	0.088*
H38H	0.8007	0.4842	0.1966	0.088*
H38I	0.8089	0.5301	0.1757	0.088*
C39B	0.6852 (3)	0.50054 (14)	0.29540 (19)	0.0541 (12)
H39G	0.6763	0.5116	0.3297	0.081*
H39H	0.7033	0.4720	0.2982	0.081*
H39I	0.6345	0.5017	0.2753	0.081*
C2B	0.7043 (3)	0.58498 (15)	0.09209 (17)	0.0600 (14)
H2B	0.6961	0.5657	0.0652	0.072*
C19B	0.9693 (4)	0.6273 (2)	0.13201 (19)	0.0791 (18)
H19G	0.9369	0.6309	0.1004	0.119*
H19H	0.9959	0.6004	0.1314	0.119*
H19I	1.0105	0.6489	0.1345	0.119*
C42B	0.3877 (3)	0.63211 (17)	0.20840 (19)	0.0633 (14)
H42G	0.4013	0.6029	0.2064	0.095*
H42H	0.3348	0.6369	0.1918	0.095*
H42I	0.3857	0.6405	0.2444	0.095*
C26B	0.6772 (2)	0.66806 (13)	0.43581 (15)	0.0384 (9)
H26C	0.7216	0.6623	0.4584	0.046*
N6B	0.69633 (19)	0.66310 (10)	0.26553 (11)	0.0316 (7)
N4B	0.52243 (18)	0.57225 (10)	0.27916 (11)	0.0341 (7)
N5B	0.54768 (17)	0.61564 (9)	0.33882 (11)	0.0300 (7)
N1B	0.7491 (2)	0.63654 (10)	0.13934 (11)	0.0384 (8)
N2B	0.6656 (2)	0.58612 (10)	0.13852 (11)	0.0405 (8)
N7B	0.7266 (2)	0.69030 (10)	0.28351 (12)	0.0361 (7)
N3B	0.5886 (2)	0.57485 (10)	0.20575 (12)	0.0373 (8)
Si2B	0.46679 (7)	0.66280 (4)	0.17501 (4)	0.0434 (3)
Si1B	0.76454 (7)	0.53156 (3)	0.26290 (4)	0.0381 (3)
Fe1B	0.64374 (3)	0.619697 (18)	0.23582 (2)	0.02960 (15)

Structure: (*i*PrCNC)Fe(CH₂Si(CH₃)₃)₂(CO)

ID: jmd28

Crystallographer: Zoë Turner

Table C.28. Crystal data

2(C ₄₄ H ₆₃ FeN ₅ OSi ₂)-C ₅ H ₁₂	$F(000) = 3560$
$M_r = 1652.19$	$D_x = 1.148 \text{ Mg m}^{-3}$
Orthorhombic, $P2_12_12_1$	Cu $K\alpha$ radiation, $\lambda = 1.54178 \text{ \AA}$
Hall symbol: P 2ac 2ab	Cell parameters from 9908 reflections
$a = 17.2582 (2) \text{ \AA}$	$\theta = 5.6\text{--}65.6^\circ$
$b = 18.5402 (2) \text{ \AA}$	$\mu = 3.29 \text{ mm}^{-1}$
$c = 29.8709 (3) \text{ \AA}$	$T = 100 \text{ K}$
$V = 9557.81 (18) \text{ \AA}^3$	Plate, purple
$Z = 4$	$0.09 \times 0.04 \times 0.04 \text{ mm}$

Table C.29. Data collection

Bruker APEX-II CCD diffractometer	16355 independent reflections
Radiation source: fine-focus sealed tube	13615 reflections with $I > 2\sigma(I)$
graphite	$R_{\text{int}} = 0.070$
phi and ω scans	$\theta_{\text{max}} = 66.2^\circ$, $\theta_{\text{min}} = 5.4^\circ$
Absorption correction: multi-scan <i>SADABS</i> 2008/2	$h = -19 \rightarrow 20$
$T_{\text{min}} = 0.756$, $T_{\text{max}} = 0.880$	$k = -21 \rightarrow 21$
78910 measured reflections	$l = -28 \rightarrow 35$

Table C.30. Refinement

Refinement on F^2	Secondary atom site location: difference Fourier map
Least-squares matrix: full	Hydrogen site location: inferred from neighbouring sites
$R[F^2 > 2\sigma(F^2)] = 0.039$	H-atom parameters constrained
$wR(F^2) = 0.083$	$w = 1/[\sigma^2(F_o^2) + (0.P)^2]$ where $P = (F_o^2 + 2F_c^2)/3$
$S = 0.95$	$(\Delta/\sigma)_{\text{max}} = 0.001$
16355 reflections	$\Delta_{\text{max}} = 0.36 \text{ e \AA}^{-3}$
1018 parameters	$\Delta_{\text{min}} = -0.31 \text{ e \AA}^{-3}$
0 restraints	Absolute structure: Flack H D (1983), Acta Cryst. A39, 876-881
Primary atom site location: structure-invariant direct methods	Flack parameter: $-0.010 (2)$

Special details

Experimental. Collected, solved and refined by Dr. Zoe R. Turner

Geometry. All s.u.'s (except the s.u. in the dihedral angle between two l.s. planes) are estimated using the full covariance matrix. The cell s.u.'s are taken into account individually in the estimation of

s.u.'s in distances, angles and torsion angles; correlations between s.u.'s in cell parameters are only used when they are defined by crystal symmetry. An approximate (isotropic) treatment of cell s.u.'s is used for estimating s.u.'s involving l.s. planes.

Refinement. Refinement of F^2 against ALL reflections. The weighted R-factor wR and goodness of fit S are based on F^2 , conventional R-factors R are based on F , with F set to zero for negative F^2 . The threshold expression of $F^2 > 2\sigma(F^2)$ is used only for calculating R-factors(gt) etc. and is not relevant to the choice of reflections for refinement. R-factors based on F^2 are statistically about twice as large as those based on F , and R-factors based on ALL data will be even larger.

Table C.31. Fractional atomic coordinates and isotropic or equivalent isotropic displacement parameters (\AA^2)

	<i>x</i>	<i>y</i>	<i>z</i>	$U_{\text{iso}}^*/U_{\text{eq}}$
C2S	0.1323 (5)	0.4975 (3)	0.5863 (2)	0.110 (2)
H2S1	0.1775	0.5033	0.5662	0.132*
H2S2	0.1344	0.5367	0.6087	0.132*
C5S	0.2192 (4)	0.3366 (4)	0.6506 (3)	0.135 (3)
H5S1	0.1780	0.3295	0.6728	0.202*
H5S2	0.2697	0.3310	0.6652	0.202*
H5S3	0.2139	0.3007	0.6267	0.202*
C3S	0.1393 (4)	0.4269 (4)	0.6099 (2)	0.120 (2)
H3S1	0.0989	0.4243	0.6334	0.145*
H3S2	0.1292	0.3876	0.5883	0.145*
C1S	0.0575 (4)	0.5063 (4)	0.5583 (2)	0.122 (2)
H1S1	0.0426	0.4595	0.5457	0.183*
H1S2	0.0668	0.5406	0.5340	0.183*
H1S3	0.0158	0.5243	0.5775	0.183*
C4S	0.2126 (4)	0.4152 (5)	0.6300 (2)	0.126 (3)
H4S1	0.2208	0.4513	0.6539	0.152*
H4S2	0.2537	0.4218	0.6072	0.152*
C1	0.95736 (17)	0.31009 (15)	0.31567 (8)	0.0281 (6)
H1	0.9375	0.3463	0.2963	0.034*
C2	0.91881 (17)	0.27916 (16)	0.34927 (8)	0.0285 (6)
H2	0.8671	0.2887	0.3585	0.034*
C3	0.96193 (16)	0.18246 (15)	0.40378 (7)	0.0245 (6)
C4	0.89759 (17)	0.17244 (16)	0.43102 (8)	0.0300 (6)
H4	0.8513	0.1993	0.4267	0.036*
C5	0.90399 (17)	0.12114 (17)	0.46501 (8)	0.0320 (7)
H5	0.8609	0.1123	0.4840	0.038*
C6	0.97217 (17)	0.08286 (16)	0.47150 (8)	0.0296 (7)
H6	0.9769	0.0484	0.4949	0.035*
C7	1.03310 (16)	0.09690 (15)	0.44246 (8)	0.0250 (6)
C8	1.13957 (17)	0.01437 (16)	0.47009 (8)	0.0308 (7)
H8	1.1168	-0.0077	0.4956	0.037*
C9	1.21065 (18)	0.00248 (17)	0.45331 (8)	0.0323 (7)
H9	1.2481	-0.0299	0.4652	0.039*
C10	1.15630 (16)	0.08677 (15)	0.40767 (7)	0.0235 (6)
C11	1.04211 (16)	0.23047 (15)	0.34654 (8)	0.0234 (6)
C12	1.08458 (16)	0.29982 (15)	0.27786 (8)	0.0239 (6)

C13	1.06850 (17)	0.27246 (15)	0.23485 (8)	0.0262 (6)
C14	1.11225 (19)	0.30031 (16)	0.19952 (8)	0.0329 (7)
H14	1.1024	0.2839	0.1699	0.040*
C15	1.16929 (19)	0.35100 (17)	0.20644 (9)	0.0359 (7)
H15	1.1976	0.3697	0.1817	0.043*
C16	1.18544 (18)	0.37478 (17)	0.24931 (9)	0.0332 (7)
H16	1.2259	0.4088	0.2538	0.040*
C17	1.14355 (17)	0.34984 (15)	0.28585 (8)	0.0261 (6)
C18	1.00668 (18)	0.21681 (16)	0.22554 (8)	0.0311 (7)
H18	0.9910	0.1953	0.2549	0.037*
C19	0.9347 (2)	0.25035 (19)	0.20447 (10)	0.0455 (8)
H19A	0.9147	0.2884	0.2241	0.068*
H19B	0.8949	0.2132	0.2005	0.068*
H19C	0.9481	0.2710	0.1753	0.068*
C20	1.0374 (2)	0.15525 (18)	0.19575 (9)	0.0431 (8)
H20A	1.0474	0.1737	0.1656	0.065*
H20B	0.9988	0.1166	0.1943	0.065*
H20C	1.0856	0.1363	0.2085	0.065*
C21	1.16126 (17)	0.37907 (16)	0.33240 (9)	0.0298 (6)
H21	1.1351	0.3471	0.3547	0.036*
C22	1.1284 (2)	0.45461 (17)	0.33778 (9)	0.0378 (7)
H22A	1.1561	0.4879	0.3179	0.057*
H22B	1.1346	0.4703	0.3689	0.057*
H22C	1.0732	0.4544	0.3300	0.057*
C23	1.24837 (18)	0.37713 (18)	0.34185 (10)	0.0362 (7)
H23A	1.2689	0.3295	0.3341	0.054*
H23B	1.2575	0.3866	0.3737	0.054*
H23C	1.2744	0.4140	0.3238	0.054*
C24	1.28732 (17)	0.03913 (17)	0.38647 (8)	0.0300 (7)
C25	1.29038 (17)	-0.02018 (16)	0.35761 (8)	0.0293 (7)
C26	1.35730 (18)	-0.02836 (19)	0.33134 (9)	0.0380 (7)
H26	1.3617	-0.0688	0.3120	0.046*
C27	1.4159 (2)	0.02049 (19)	0.33312 (10)	0.0438 (8)
H27	1.4607	0.0137	0.3151	0.053*
C28	1.41119 (18)	0.08006 (19)	0.36097 (10)	0.0404 (8)
H28	1.4522	0.1142	0.3613	0.048*
C29	1.34697 (18)	0.09065 (17)	0.38865 (9)	0.0359 (7)
C30	1.22553 (18)	-0.07455 (17)	0.35394 (9)	0.0338 (7)
H30	1.1782	-0.0527	0.3677	0.041*
C31	1.2066 (2)	-0.09227 (18)	0.30520 (10)	0.0412 (8)
H31A	1.1994	-0.0474	0.2884	0.062*
H31B	1.1590	-0.1209	0.3039	0.062*
H31C	1.2494	-0.1198	0.2921	0.062*
C32	1.2435 (2)	-0.14417 (18)	0.37921 (10)	0.0426 (8)
H32A	1.2910	-0.1657	0.3672	0.064*
H32B	1.2004	-0.1781	0.3756	0.064*
H32C	1.2507	-0.1334	0.4111	0.064*
C33	1.3438 (2)	0.15397 (18)	0.42003 (11)	0.0429 (8)
H33	1.2880	0.1677	0.4233	0.051*
C34	1.3731 (3)	0.1325 (2)	0.46665 (11)	0.0658 (12)
H34A	1.3433	0.0911	0.4776	0.099*
H34B	1.3666	0.1732	0.4873	0.099*
H34C	1.4280	0.1195	0.4649	0.099*
C35	1.3865 (2)	0.2202 (2)	0.40394 (12)	0.0552 (9)
H35A	1.4422	0.2102	0.4031	0.083*

H35B	1.3764	0.2604	0.4244	0.083*
H35C	1.3685	0.2329	0.3738	0.083*
C36	1.09208 (17)	0.09042 (15)	0.31720 (8)	0.0265 (6)
H36A	1.0920	0.1199	0.2896	0.032*
H36B	1.1378	0.0584	0.3152	0.032*
C37	0.9979 (2)	-0.03401 (18)	0.36107 (8)	0.0388 (8)
H37A	1.0484	-0.0564	0.3667	0.058*
H37B	0.9600	-0.0714	0.3535	0.058*
H37C	0.9808	-0.0083	0.3880	0.058*
C38	0.9105 (2)	0.07884 (19)	0.30997 (11)	0.0436 (8)
H38A	0.8994	0.1024	0.3386	0.065*
H38B	0.8696	0.0438	0.3033	0.065*
H38C	0.9125	0.1152	0.2862	0.065*
C39	1.01406 (19)	-0.02615 (17)	0.26150 (9)	0.0366 (7)
H39A	1.0134	0.0050	0.2350	0.055*
H39B	0.9701	-0.0596	0.2603	0.055*
H39C	1.0626	-0.0536	0.2622	0.055*
C40	1.15806 (18)	0.23863 (16)	0.42003 (8)	0.0299 (7)
H40A	1.1918	0.2091	0.4396	0.036*
H40B	1.1936	0.2703	0.4030	0.036*
C41	1.0322 (2)	0.36285 (18)	0.43612 (10)	0.0441 (8)
H41A	1.0511	0.3847	0.4083	0.066*
H41B	1.0212	0.4008	0.4580	0.066*
H41C	0.9847	0.3356	0.4300	0.066*
C42	1.0604 (2)	0.2514 (2)	0.50684 (9)	0.0418 (8)
H42A	1.0100	0.2328	0.4972	0.063*
H42B	1.0530	0.2847	0.5320	0.063*
H42C	1.0935	0.2112	0.5163	0.063*
C43	1.1862 (2)	0.3596 (2)	0.48376 (11)	0.0552 (10)
H43A	1.2242	0.3293	0.4993	0.083*
H43B	1.1631	0.3936	0.5050	0.083*
H43C	1.2120	0.3864	0.4597	0.083*
C44	1.19546 (17)	0.18226 (15)	0.33819 (7)	0.0250 (4)
N1	1.03160 (13)	0.28055 (12)	0.31357 (6)	0.0219 (5)
N2	0.97044 (13)	0.22988 (12)	0.36804 (7)	0.0246 (5)
N3	1.02734 (13)	0.14436 (12)	0.40876 (6)	0.0229 (5)
N4	1.10613 (13)	0.06606 (12)	0.44205 (6)	0.0242 (5)
N5	1.22021 (13)	0.04596 (13)	0.41533 (6)	0.0253 (5)
O1	1.24881 (12)	0.19294 (11)	0.31552 (6)	0.0332 (3)
Si1	1.00645 (5)	0.03116 (4)	0.31351 (2)	0.02842 (18)
Si2	1.10774 (5)	0.30064 (5)	0.45910 (2)	0.03196 (19)
Fe1	1.11525 (2)	0.16344 (2)	0.370933 (11)	0.02102 (10)
C1A	0.73177 (18)	0.52658 (17)	0.29523 (8)	0.0329 (7)
H1A	0.7661	0.4908	0.2841	0.039*
C2A	0.72140 (18)	0.59143 (16)	0.27786 (8)	0.0305 (7)
H2A	0.7466	0.6112	0.2524	0.037*
C3A	0.63651 (16)	0.69451 (15)	0.30384 (7)	0.0227 (6)
C4A	0.65532 (17)	0.74953 (16)	0.27463 (8)	0.0286 (6)
H4A	0.6922	0.7427	0.2514	0.034*
C5A	0.61817 (18)	0.81548 (16)	0.28059 (8)	0.0301 (6)
H5A	0.6301	0.8547	0.2613	0.036*
C6A	0.56374 (17)	0.82461 (15)	0.31450 (8)	0.0275 (6)
H6A	0.5375	0.8692	0.3185	0.033*
C7A	0.54941 (16)	0.76639 (15)	0.34204 (8)	0.0233 (6)
C8A	0.45318 (16)	0.81497 (15)	0.39769 (8)	0.0263 (6)

H8A	0.4471	0.8635	0.3880	0.032*
C9A	0.41890 (16)	0.78310 (15)	0.43273 (8)	0.0256 (6)
H9A	0.3833	0.8052	0.4528	0.031*
C10A	0.49473 (16)	0.69644 (15)	0.40058 (8)	0.0231 (6)
C11A	0.64064 (16)	0.58041 (15)	0.33941 (7)	0.0235 (6)
C12A	0.69118 (18)	0.45835 (15)	0.36284 (8)	0.0290 (7)
C13A	0.63415 (19)	0.40400 (16)	0.36207 (9)	0.0335 (7)
C14A	0.6456 (2)	0.34485 (18)	0.39051 (10)	0.0432 (8)
H14A	0.6080	0.3074	0.3912	0.052*
C15A	0.7103 (2)	0.33996 (19)	0.41751 (10)	0.0442 (8)
H15A	0.7171	0.2991	0.4363	0.053*
C16A	0.7646 (2)	0.39354 (18)	0.41735 (10)	0.0395 (8)
H16A	0.8084	0.3896	0.4364	0.047*
C17A	0.75717 (18)	0.45391 (16)	0.38993 (8)	0.0304 (7)
C18A	0.5662 (2)	0.40706 (18)	0.33025 (11)	0.0472 (8)
H18A	0.5526	0.4590	0.3259	0.057*
C19A	0.5902 (3)	0.3769 (3)	0.28466 (11)	0.0877 (17)
H19D	0.6033	0.3257	0.2877	0.132*
H19E	0.6354	0.4034	0.2736	0.132*
H19F	0.5472	0.3822	0.2635	0.132*
C20A	0.4945 (2)	0.3691 (2)	0.34678 (12)	0.0569 (10)
H20D	0.4510	0.3800	0.3268	0.085*
H20E	0.4823	0.3856	0.3771	0.085*
H20F	0.5036	0.3169	0.3471	0.085*
C21A	0.81917 (18)	0.51136 (16)	0.39022 (9)	0.0337 (7)
H21A	0.7977	0.5552	0.3752	0.040*
C22A	0.8907 (2)	0.48731 (18)	0.36413 (10)	0.0442 (8)
H22D	0.9297	0.5257	0.3648	0.066*
H22E	0.8761	0.4771	0.3330	0.066*
H22F	0.9121	0.4436	0.3778	0.066*
C23A	0.8431 (2)	0.53253 (19)	0.43808 (10)	0.0423 (8)
H23D	0.8696	0.4918	0.4524	0.063*
H23E	0.7968	0.5451	0.4554	0.063*
H23F	0.8781	0.5741	0.4369	0.063*
C24A	0.41906 (16)	0.66381 (15)	0.47007 (7)	0.0236 (6)
C25A	0.35960 (16)	0.61517 (16)	0.46164 (8)	0.0269 (6)
C26A	0.33190 (18)	0.57396 (17)	0.49735 (9)	0.0326 (7)
H26A	0.2922	0.5394	0.4923	0.039*
C27A	0.36194 (18)	0.58294 (17)	0.54028 (9)	0.0344 (7)
H27A	0.3419	0.5553	0.5644	0.041*
C28A	0.42002 (17)	0.63122 (17)	0.54770 (8)	0.0305 (7)
H28A	0.4398	0.6367	0.5772	0.037*
C29A	0.45136 (16)	0.67294 (15)	0.51318 (8)	0.0244 (6)
C30A	0.32243 (18)	0.60812 (17)	0.41587 (9)	0.0338 (7)
H30A	0.3593	0.6285	0.3934	0.041*
C31A	0.24812 (19)	0.6529 (2)	0.41406 (10)	0.0435 (8)
H31D	0.2253	0.6494	0.3841	0.065*
H31E	0.2602	0.7035	0.4207	0.065*
H31F	0.2112	0.6346	0.4363	0.065*
C32A	0.3067 (2)	0.52992 (18)	0.40304 (10)	0.0445 (8)
H32D	0.3540	0.5014	0.4072	0.067*
H32E	0.2907	0.5276	0.3716	0.067*
H32F	0.2654	0.5105	0.4220	0.067*
C33A	0.51463 (17)	0.72695 (16)	0.52342 (8)	0.0290 (6)
H33A	0.5396	0.7404	0.4944	0.035*

C34A	0.4824 (2)	0.79651 (18)	0.54449 (10)	0.0424 (8)
H34D	0.4436	0.8177	0.5245	0.064*
H34E	0.5248	0.8310	0.5490	0.064*
H34F	0.4585	0.7852	0.5734	0.064*
C35A	0.57740 (18)	0.69579 (18)	0.55347 (8)	0.0369 (7)
H35D	0.5559	0.6866	0.5833	0.055*
H35E	0.6203	0.7302	0.5559	0.055*
H35F	0.5965	0.6505	0.5406	0.055*
C36A	0.47556 (18)	0.58516 (17)	0.32835 (9)	0.0326 (7)
H36C	0.5030	0.5474	0.3111	0.039*
H36D	0.4368	0.5593	0.3468	0.039*
C37A	0.4775 (2)	0.6685 (2)	0.23807 (9)	0.0468 (9)
H37D	0.5013	0.7145	0.2465	0.070*
H37E	0.4445	0.6755	0.2117	0.070*
H37F	0.5182	0.6333	0.2310	0.070*
C38A	0.3465 (3)	0.5663 (2)	0.26181 (12)	0.0672 (12)
H38D	0.3752	0.5275	0.2470	0.101*
H38E	0.3128	0.5904	0.2400	0.101*
H38F	0.3148	0.5460	0.2860	0.101*
C39A	0.3574 (2)	0.7126 (2)	0.30569 (10)	0.0504 (9)
H39D	0.3266	0.6981	0.3317	0.076*
H39E	0.3227	0.7283	0.2816	0.076*
H39F	0.3918	0.7525	0.3140	0.076*
C40A	0.64042 (16)	0.63920 (15)	0.42952 (8)	0.0265 (6)
H40C	0.6096	0.6397	0.4575	0.032*
H40D	0.6733	0.5955	0.4308	0.032*
C41A	0.76526 (18)	0.71052 (18)	0.48570 (8)	0.0347 (7)
H41D	0.7304	0.7113	0.5116	0.052*
H41E	0.8011	0.7514	0.4874	0.052*
H41F	0.7948	0.6654	0.4857	0.052*
C42A	0.77893 (18)	0.72161 (19)	0.38610 (8)	0.0377 (7)
H42D	0.8063	0.6754	0.3839	0.057*
H42E	0.8163	0.7602	0.3923	0.057*
H42F	0.7522	0.7316	0.3578	0.057*
C43A	0.6589 (2)	0.80755 (17)	0.43425 (10)	0.0396 (7)
H43D	0.6412	0.8206	0.4041	0.059*
H43E	0.6961	0.8436	0.4449	0.059*
H43F	0.6144	0.8059	0.4546	0.059*
C44A	0.53341 (17)	0.55079 (15)	0.40918 (8)	0.0250 (4)
N1A	0.68377 (14)	0.51937 (12)	0.33289 (6)	0.0264 (5)
N2A	0.66571 (13)	0.62479 (12)	0.30478 (6)	0.0248 (5)
N3A	0.58569 (13)	0.70260 (12)	0.33749 (6)	0.0229 (5)
N4A	0.49936 (13)	0.76233 (11)	0.37852 (6)	0.0223 (5)
N5A	0.44451 (13)	0.71164 (12)	0.43473 (6)	0.0224 (5)
O1A	0.51692 (12)	0.50264 (11)	0.43205 (6)	0.0332 (3)
Si2A	0.41707 (5)	0.63392 (5)	0.28593 (2)	0.0357 (2)
Si03	0.70643 (5)	0.71710 (4)	0.43250 (2)	0.02747 (17)
Fe1A	0.56026 (2)	0.62295 (2)	0.375913 (11)	0.02215 (10)

Structure: (*i*PrCNC)Fe(4-CH₃-C₆H₄)₂(N₂)·2LiBr(Et₂O)₂

ID: jmd29

Crystallographer: Zoë Turner

Table C.32. Crystal data

2(C ₄₉ H ₅₅ FeN ₇)·C ₁₆ H ₄₀ Br ₂ Li ₂ O ₄ ·C ₄ H ₁₀ O	$F(000) = 2268$
$M_r = 2140.00$	$D_x = 1.215 \text{ Mg m}^{-3}$
Monoclinic, $P2_1/c$	Mo $K\alpha$ radiation, $\lambda = 0.71073 \text{ \AA}$
Hall symbol: -P 2ybc	Cell parameters from 9948 reflections
$a = 17.668 (5) \text{ \AA}$	$\theta = 3.4\text{--}65.4^\circ$
$b = 18.251 (5) \text{ \AA}$	$\mu = 0.99 \text{ mm}^{-1}$
$c = 24.071 (5) \text{ \AA}$	$T = 100 \text{ K}$
$\beta = 131.088 (13)^\circ$	Block, purple
$V = 5850 (3) \text{ \AA}^3$	$0.12 \times 0.07 \times 0.06 \text{ mm}$
$Z = 2$	

Table C.33. Data collection

Bruker APEX-II CCD diffractometer	9907 independent reflections
Radiation source: fine-focus sealed tube	7772 reflections with $I > 2\sigma(I)$
graphite	$R_{\text{int}} = 0.072$
phi and ω scans	$\theta_{\text{max}} = 24.9^\circ$, $\theta_{\text{min}} = 1.5^\circ$
Absorption correction: multi-scan <i>SADABS</i> 2008/2	$h = -20 \rightarrow 20$
$T_{\text{min}} = 0.891$, $T_{\text{max}} = 0.943$	$k = -21 \rightarrow 21$
61467 measured reflections	$l = -28 \rightarrow 25$

Table C.34. Refinement

Refinement on F^2	Primary atom site location: structure-invariant direct methods
Least-squares matrix: full	Secondary atom site location: difference Fourier map
$R[F^2 > 2\sigma(F^2)] = 0.072$	Hydrogen site location: inferred from neighbouring sites
$wR(F^2) = 0.200$	H-atom parameters constrained
$S = 1.02$	$w = 1/[\sigma^2(F_o^2) + (0.1008P)^2 + 18.6987P]$ where $P = (F_o^2 + 2F_c^2)/3$
9907 reflections	$(\Delta/\sigma)_{\text{max}} = 0.001$
655 parameters	$\Delta)_{\text{max}} = 4.69 \text{ e \AA}^{-3}$
0 restraints	$\Delta)_{\text{min}} = -0.56 \text{ e \AA}^{-3}$

Special details

Experimental. Collected, integrated, solved and refined by Dr. Zoe R. Turner

Geometry. All s.u.'s (except the s.u. in the dihedral angle between two l.s. planes) are estimated using the full covariance matrix. The cell s.u.'s are taken into account individually in the estimation of s.u.'s in distances, angles and torsion angles; correlations between s.u.'s in cell parameters are only used

when they are defined by crystal symmetry. An approximate (isotropic) treatment of cell s.u.'s is used for estimating s.u.'s involving l.s. planes.

Refinement. Refinement of F^2 against ALL reflections. The weighted R-factor wR and goodness of fit S are based on F^2 , conventional R-factors R are based on F , with F set to zero for negative F^2 . The threshold expression of $F^2 > 2\sigma(F^2)$ is used only for calculating R-factors(gt) etc. and is not relevant to the choice of reflections for refinement. R-factors based on F^2 are statistically about twice as large as those based on F , and R- factors based on ALL data will be even larger.

Table C.35. Fractional atomic coordinates and isotropic or equivalent isotropic displacement parameters (\AA^2)

	x	y	z	$U_{\text{iso}}^*/U_{\text{eq}}$	Occ. (<1)
O3S	0.0000	0.5000	0.5000	0.163 (6)	
C10S	0.0727 (13)	0.6042 (12)	0.4850 (9)	0.207 (10)	
H10A	0.0717	0.6570	0.4918	0.310*	0.50
H10B	0.0419	0.5945	0.4339	0.310*	0.50
H10C	0.1422	0.5867	0.5184	0.310*	0.50
H10D	0.0989	0.5685	0.4709	0.310*	0.50
H10E	0.1287	0.6310	0.5289	0.310*	0.50
H10F	0.0283	0.6388	0.4444	0.310*	0.50
C9S	0.0183 (18)	0.5675 (12)	0.5004 (14)	0.105 (10)	0.49 (3)
H9S1	0.0496	0.5843	0.5506	0.126*	0.49 (3)
H9S2	-0.0489	0.5907	0.4671	0.126*	0.49 (3)
C9T	0.0707 (14)	0.5418 (13)	0.4988 (12)	0.097 (8)	0.51 (3)
H9T1	0.1368	0.5343	0.5486	0.116*	0.51 (3)
H9T2	0.0734	0.5135	0.4651	0.116*	0.51 (3)
C1	0.5478 (4)	0.3263 (3)	0.9308 (3)	0.0332 (10)	
H1	0.5716	0.3175	0.9056	0.040*	
C2	0.4906 (4)	0.3823 (3)	0.9190 (3)	0.0328 (10)	
H2	0.4665	0.4212	0.8848	0.039*	
C3	0.4143 (3)	0.4124 (3)	0.9756 (2)	0.0292 (10)	
C4	0.3580 (4)	0.4746 (3)	0.9374 (3)	0.0325 (10)	
H4	0.3579	0.4966	0.9016	0.039*	
C5	0.3021 (4)	0.5035 (3)	0.9537 (3)	0.0345 (10)	
H5	0.2622	0.5459	0.9281	0.041*	
C6	0.3029 (4)	0.4718 (3)	1.0068 (3)	0.0333 (10)	
H6	0.2653	0.4917	1.0186	0.040*	
C7	0.3613 (3)	0.4098 (3)	1.0412 (2)	0.0284 (10)	
C8	0.3372 (3)	0.3800 (3)	1.1313 (2)	0.0319 (10)	
H8	0.2923	0.4175	1.1213	0.038*	
C9	0.3767 (4)	0.3274 (3)	1.1813 (3)	0.0351 (11)	
H9	0.3655	0.3206	1.2146	0.042*	
C10	0.4393 (3)	0.3091 (3)	1.1240 (2)	0.0296 (10)	
C11	0.5191 (3)	0.3095 (2)	1.0098 (2)	0.0289 (10)	
C12	0.6238 (4)	0.2152 (2)	1.0101 (2)	0.0291 (10)	
C13	0.7293 (4)	0.2189 (3)	1.0574 (3)	0.0356 (11)	
C14	0.7815 (4)	0.1533 (3)	1.0762 (3)	0.0479 (13)	
H14	0.8527	0.1540	1.1081	0.057*	
C15	0.7314 (4)	0.0874 (3)	1.0490 (4)	0.0518 (14)	
H15	0.7684	0.0432	1.0636	0.062*	

C16	0.6286 (4)	0.0851 (3)	1.0012 (3)	0.0431 (12)	
H16	0.5954	0.0392	0.9817	0.052*	
C17	0.5715 (4)	0.1485 (3)	0.9805 (3)	0.0338 (10)	
C18	0.7864 (4)	0.2902 (3)	1.0835 (3)	0.0425 (12)	
H18	0.7438	0.3286	1.0811	0.051*	
C19	0.8070 (5)	0.3147 (4)	1.0335 (4)	0.0552 (15)	
H19A	0.8480	0.2776	1.0345	0.083*	
H19B	0.8429	0.3615	1.0512	0.083*	
H19C	0.7432	0.3205	0.9829	0.083*	
C20	0.8864 (4)	0.2869 (4)	1.1628 (3)	0.0545 (15)	
H20A	0.8750	0.2691	1.1952	0.082*	
H20B	0.9162	0.3360	1.1786	0.082*	
H20C	0.9321	0.2535	1.1654	0.082*	
C21	0.4582 (4)	0.1461 (3)	0.9259 (3)	0.0359 (11)	
H21	0.4336	0.1871	0.9379	0.043*	
C22	0.4170 (4)	0.1582 (3)	0.8474 (3)	0.0474 (13)	
H22A	0.4415	0.2051	0.8448	0.071*	
H22B	0.3434	0.1588	0.8131	0.071*	
H22C	0.4397	0.1184	0.8340	0.071*	
C23	0.4166 (4)	0.0746 (3)	0.9295 (3)	0.0458 (13)	
H23A	0.4312	0.0343	0.9109	0.069*	
H23B	0.3438	0.0790	0.8992	0.069*	
H23C	0.4481	0.0647	0.9807	0.069*	
C24	0.4902 (4)	0.2190 (3)	1.2232 (2)	0.0322 (10)	
C25	0.5944 (4)	0.2228 (3)	1.2820 (3)	0.0347 (11)	
C26	0.6416 (4)	0.1596 (3)	1.3236 (3)	0.0395 (12)	
H26	0.7124	0.1597	1.3627	0.047*	
C27	0.5889 (4)	0.0976 (3)	1.3097 (3)	0.0448 (13)	
H27	0.6236	0.0550	1.3386	0.054*	
C28	0.4861 (4)	0.0956 (3)	1.2544 (3)	0.0450 (13)	
H28	0.4505	0.0523	1.2467	0.054*	
C29	0.4336 (4)	0.1566 (3)	1.2094 (3)	0.0400 (12)	
C30	0.6511 (4)	0.2927 (3)	1.3010 (3)	0.0404 (12)	
H30	0.6201	0.3187	1.2538	0.049*	
C31	0.6408 (5)	0.3426 (4)	1.3466 (4)	0.0560 (15)	
H31A	0.5695	0.3491	1.3210	0.084*	
H31B	0.6711	0.3903	1.3530	0.084*	
H31C	0.6751	0.3203	1.3949	0.084*	
C32	0.7631 (4)	0.2808 (4)	1.3415 (3)	0.0541 (15)	
H32A	0.7967	0.2587	1.3898	0.081*	
H32B	0.7945	0.3280	1.3481	0.081*	
H32C	0.7692	0.2481	1.3123	0.081*	
C33	0.3201 (4)	0.1534 (3)	1.1504 (3)	0.0494 (14)	
H33	0.2979	0.1913	1.1122	0.059*	
C34	0.2717 (5)	0.1711 (4)	1.1835 (4)	0.0604 (17)	
H34A	0.2958	0.1363	1.2231	0.091*	
H34B	0.1985	0.1673	1.1450	0.091*	
H34C	0.2899	0.2210	1.2034	0.091*	
C35	0.2827 (5)	0.0786 (4)	1.1124 (3)	0.0589 (16)	
H35A	0.3213	0.0634	1.0983	0.088*	
H35B	0.2114	0.0821	1.0682	0.088*	
H35C	0.2914	0.0425	1.1463	0.088*	
C36	0.6211 (4)	0.3643 (3)	1.1556 (3)	0.0412 (12)*	
C37	0.7104 (4)	0.3433 (3)	1.1802 (3)	0.0425 (12)	
H37	0.7177	0.2982	1.1645	0.051*	

C38	0.7933 (4)	0.3883 (3)	1.2295 (3)	0.0509 (14)	
H38	0.8573	0.3740	1.2468	0.061*	
C39	0.7835 (4)	0.4541 (3)	1.2539 (3)	0.0472 (14)	
C40	0.6873 (4)	0.4715 (3)	1.2261 (3)	0.0405 (12)	
H40	0.6758	0.5152	1.2410	0.049*	
C41	0.6088 (4)	0.4244 (3)	1.1766 (3)	0.0379 (11)*	
H41	0.5433	0.4371	1.1573	0.045*	
C42	0.8707 (5)	0.5044 (4)	1.3056 (4)	0.070 (2)	
H42A	0.8461	0.5544	1.2995	0.104*	
H42B	0.9152	0.5033	1.2946	0.104*	
H42C	0.9079	0.4883	1.3565	0.104*	
C43	0.3654 (4)	0.2335 (3)	0.9987 (3)	0.0331 (10)*	
C44	0.2910 (4)	0.2548 (3)	0.9259 (3)	0.0402 (12)	
H44	0.2984	0.3005	0.9111	0.048*	
C45	0.2063 (4)	0.2132 (3)	0.8734 (3)	0.0429 (12)	
H45	0.1590	0.2302	0.8240	0.052*	
C46	0.1903 (4)	0.1473 (3)	0.8926 (3)	0.0438 (12)	
C47	0.2620 (4)	0.1255 (3)	0.9653 (3)	0.0461 (13)	
H47	0.2531	0.0806	0.9804	0.055*	
C48	0.3465 (4)	0.1676 (3)	1.0167 (3)	0.0395 (11)	
H48	0.3935	0.1508	1.0662	0.047*	
C49	0.0998 (4)	0.0999 (4)	0.8369 (3)	0.0590 (16)	
H49A	0.1183	0.0481	0.8497	0.088*	
H49B	0.0766	0.1090	0.7877	0.088*	
H49C	0.0459	0.1116	0.8371	0.088*	
Fe1	0.49255 (5)	0.29499 (4)	1.07560 (4)	0.0338 (2)	
N1	0.5670 (3)	0.2823 (2)	0.9868 (2)	0.0277 (8)	
N2	0.4731 (3)	0.3722 (2)	0.9672 (2)	0.0277 (8)	
N3	0.4158 (3)	0.3806 (2)	1.02635 (19)	0.0274 (8)	
N4	0.3753 (3)	0.3690 (2)	1.0964 (2)	0.0283 (8)	
N5	0.4378 (3)	0.2832 (2)	1.1769 (2)	0.0299 (8)	
N6	0.5667 (3)	0.2125 (2)	1.1221 (2)	0.0326 (9)	
N7	0.6123 (3)	0.1627 (3)	1.1504 (2)	0.0435 (10)	
C1S	0.9118 (5)	0.6647 (4)	0.8936 (4)	0.0625 (17)	
H1S1	0.9445	0.6171	0.9043	0.094*	
H1S2	0.9219	0.6946	0.8650	0.094*	
H1S3	0.8398	0.6575	0.8650	0.094*	
C2S	0.9561 (9)	0.7024 (5)	0.9633 (4)	0.120 (4)	
H2S1	1.0286	0.7105	0.9916	0.144*	
H2S2	0.9238	0.7509	0.9523	0.144*	
C3S	0.9002 (5)	0.6987 (4)	1.0325 (6)	0.096 (3)	
H3S1	0.8759	0.6628	1.0486	0.115*	
H3S2	0.8420	0.7279	0.9916	0.115*	
C4S	0.9756 (7)	0.7479 (5)	1.0950 (6)	0.112 (4)	
H4S1	1.0382	0.7209	1.1312	0.167*	
H4S2	0.9498	0.7656	1.1183	0.167*	
H4S3	0.9883	0.7897	1.0766	0.167*	
C5S	1.2192 (6)	0.5108 (5)	1.2380 (4)	0.086 (3)	
H5S1	1.2086	0.4829	1.2672	0.129*	
H5S2	1.2893	0.5270	1.2699	0.129*	
H5S3	1.2041	0.4796	1.1987	0.129*	
C6S	1.1515 (5)	0.5761 (4)	1.2049 (3)	0.0642 (18)	
H6S1	1.1550	0.6007	1.2433	0.077*	
H6S2	1.1757	0.6113	1.1882	0.077*	
C7S	0.9940 (6)	0.5204 (5)	1.1609 (4)	0.077 (2)	

H7S1	1.0338	0.4777	1.1927	0.092*	
H7S2	0.9299	0.5017	1.1147	0.092*	
C8S	0.9723 (8)	0.5674 (7)	1.1985 (6)	0.120 (4)	
H8S1	1.0355	0.5835	1.2459	0.181*	
H8S2	0.9329	0.5399	1.2068	0.181*	
H8S3	0.9340	0.6104	1.1678	0.181*	
O1S	0.9433 (4)	0.6606 (2)	1.0071 (2)	0.0790 (16)	
O2S	1.0486 (3)	0.5578 (2)	1.1436 (2)	0.0549 (10)	
Br1	1.13343 (4)	0.53177 (3)	1.04106 (3)	0.04056 (17)	
Li1	0.9981 (7)	0.5623 (5)	1.0437 (5)	0.046 (2)	

Structure: (*i*PrCNC)Mn(CO)₂

ID: jmd32

Crystallographer: Scott Semproni

Table C.36. Crystal data

C ₄₄ H ₄₉ MnN ₅ O ₂	$F(000) = 1556$
$M_r = 734.82$	$D_x = 1.271 \text{ Mg m}^{-3}$
Monoclinic, $P2_1/c$	Cu $K\alpha$ radiation, $\lambda = 1.54184 \text{ \AA}$
$a = 16.467 (5) \text{ \AA}$	Cell parameters from 2268 reflections
$b = 13.832 (5) \text{ \AA}$	$\theta = 2.8\text{--}64.7^\circ$
$c = 17.668 (5) \text{ \AA}$	$\mu = 3.13 \text{ mm}^{-1}$
$\beta = 107.448 (5)^\circ$	$T = 100 \text{ K}$
$V = 3839 (2) \text{ \AA}^3$	Diamond, green
$Z = 4$	$0.06 \times 0.05 \times 0.02 \text{ mm}$

Table C.37. Data collection

Bruker APEX II CCD diffractometer	6464 independent reflections
Radiation source: fine-focus sealed tube	3883 reflections with $I > 2\sigma(I)$
graphite	$R_{\text{int}} = 0.118$
phi and ω scans	$\theta_{\text{max}} = 66.2^\circ$, $\theta_{\text{min}} = 2.8^\circ$
Absorption correction: multi-scan <i>SADABS</i> V2008/1 (Bruker AXS)	$h = -19 \rightarrow 15$
$T_{\text{min}} = 0.492$, $T_{\text{max}} = 0.753$	$k = -15 \rightarrow 15$
15987 measured reflections	$l = -20 \rightarrow 17$

Table C.38. Refinement

Refinement on F^2	Primary atom site location: structure-invariant direct methods
Least-squares matrix: full	Secondary atom site location: difference Fourier map
$R[F^2 > 2\sigma(F^2)] = 0.075$	Hydrogen site location: inferred from neighbouring sites
$wR(F^2) = 0.209$	H-atom parameters constrained
$S = 0.99$	$w = 1/[\sigma^2(F_o^2) + (0.1021P)^2]$ where $P = (F_o^2 + 2F_c^2)/3$
6464 reflections	$(\Delta/\sigma)_{\text{max}} < 0.001$
478 parameters	$\Delta)_{\text{max}} = 0.80 \text{ e \AA}^{-3}$
0 restraints	$\Delta)_{\text{min}} = -0.62 \text{ e \AA}^{-3}$

Special details

Experimental. Collected, solved and refined by Scott P. Semproni

Geometry. All s.u.'s (except the s.u. in the dihedral angle between two l.s. planes) are estimated using the full covariance matrix. The cell s.u.'s are taken into account individually in the estimation of s.u.'s in distances, angles and torsion angles; correlations between s.u.'s in cell parameters are only used

when they are defined by crystal symmetry. An approximate (isotropic) treatment of cell s.u.'s is used for estimating s.u.'s involving l.s. planes.

Refinement. Refinement of F^2 against ALL reflections. The weighted R-factor wR and goodness of fit S are based on F^2 , conventional R-factors R are based on F, with F set to zero for negative F^2 . The threshold expression of $F^2 > 2\sigma(F^2)$ is used only for calculating R-factors(gt) etc. and is not relevant to the choice of reflections for refinement. R-factors based on F^2 are statistically about twice as large as those based on F, and R- factors based on ALL data will be even larger.

Table C.39. Fractional atomic coordinates and isotropic or equivalent isotropic displacement parameters (\AA^2)

	x	y	z	$U_{\text{iso}}^*/U_{\text{eq}}$
C1	0.3317 (3)	0.3655 (4)	0.0216 (3)	0.0353 (11)
C1S	0.0664 (5)	0.5902 (6)	0.3453 (4)	0.070 (2)
H1S1	0.1166	0.5981	0.3918	0.106*
H1S2	0.0148	0.5923	0.3620	0.106*
H1S3	0.0648	0.6426	0.3075	0.106*
C2	0.2867 (3)	0.2521 (4)	-0.0753 (3)	0.0365 (11)
H2	0.2499	0.2100	-0.1126	0.044*
C2S	0.0713 (4)	0.4945 (5)	0.3064 (3)	0.0517 (15)
C3	0.3712 (3)	0.2624 (4)	-0.0619 (3)	0.0372 (11)
H3	0.4055	0.2292	-0.0882	0.045*
C3S	0.1131 (4)	0.4838 (5)	0.2492 (4)	0.0522 (15)
H3S	0.1377	0.5385	0.2321	0.063*
C4	0.4776 (3)	0.3733 (4)	0.0299 (3)	0.0360 (12)
C4S	0.1188 (4)	0.3937 (5)	0.2172 (4)	0.0509 (15)
H4S	0.1483	0.3866	0.1788	0.061*
C5	0.5512 (3)	0.3541 (4)	0.0115 (3)	0.0384 (12)
H5	0.5530	0.3050	-0.0255	0.046*
C5S	0.0816 (4)	0.3132 (5)	0.2410 (4)	0.0561 (16)
H5S	0.0849	0.2515	0.2185	0.067*
C6	0.6245 (3)	0.4095 (4)	0.0493 (3)	0.0397 (12)
H6	0.6764	0.3987	0.0375	0.048*
C6S	0.0400 (4)	0.3237 (5)	0.2974 (4)	0.0572 (17)
H6S	0.0160	0.2686	0.3147	0.069*
C7	0.6194 (3)	0.4800 (4)	0.1041 (3)	0.0391 (12)
H7	0.6676	0.5180	0.1306	0.047*
C7S	0.0329 (4)	0.4136 (5)	0.3295 (3)	0.0559 (16)
H7S	0.0021	0.4205	0.3669	0.067*
C8	0.5428 (3)	0.4931 (4)	0.1188 (3)	0.0363 (12)
C9	0.5723 (4)	0.6355 (4)	0.2144 (3)	0.0401 (12)
H9	0.6308	0.6481	0.2218	0.048*
C10	0.5210 (3)	0.6843 (4)	0.2462 (3)	0.0391 (12)
H10	0.5367	0.7384	0.2807	0.047*
C11	0.4400 (3)	0.5654 (3)	0.1700 (3)	0.0317 (11)
C12	0.1776 (3)	0.3190 (4)	-0.0202 (3)	0.0348 (11)

C13	0.1496 (3)	0.2439 (4)	0.0189 (3)	0.0359 (11)
C14	0.0639 (4)	0.2451 (4)	0.0154 (3)	0.0413 (12)
H14	0.0425	0.1952	0.0411	0.050*
C15	0.0095 (3)	0.3169 (4)	-0.0242 (3)	0.0408 (12)
H15	-0.0490	0.3148	-0.0271	0.049*
C16	0.0398 (4)	0.3917 (4)	-0.0598 (3)	0.0388 (12)
H16	0.0023	0.4422	-0.0849	0.047*
C17	0.1243 (3)	0.3947 (4)	-0.0597 (3)	0.0365 (12)
C18	0.2083 (4)	0.1638 (4)	0.0620 (3)	0.0420 (13)
H18	0.2679	0.1836	0.0661	0.050*
C19	0.2041 (4)	0.1464 (4)	0.1454 (3)	0.0442 (13)
H19A	0.1463	0.1264	0.1432	0.066*
H19B	0.2187	0.2060	0.1763	0.066*
H19C	0.2445	0.0953	0.1705	0.066*
C20	0.1900 (4)	0.0693 (4)	0.0147 (3)	0.0511 (14)
H20A	0.2311	0.0199	0.0418	0.077*
H20B	0.1948	0.0801	-0.0386	0.077*
H20C	0.1322	0.0473	0.0106	0.077*
C21	0.1584 (3)	0.4734 (4)	-0.1004 (3)	0.0377 (12)
H21	0.2199	0.4820	-0.0704	0.045*
C22	0.1148 (4)	0.5717 (4)	-0.1014 (3)	0.0433 (13)
H22A	0.0553	0.5674	-0.1344	0.065*
H22B	0.1443	0.6209	-0.1232	0.065*
H22C	0.1169	0.5896	-0.0472	0.065*
C23	0.1535 (4)	0.4437 (4)	-0.1851 (3)	0.0445 (13)
H23A	0.1875	0.3852	-0.1836	0.067*
H23B	0.1758	0.4960	-0.2106	0.067*
H23C	0.0941	0.4309	-0.2154	0.067*
C24	0.3666 (3)	0.6800 (4)	0.2372 (3)	0.0365 (12)
C25	0.3221 (4)	0.7560 (4)	0.1909 (3)	0.0444 (13)
C26	0.2516 (4)	0.7925 (4)	0.2092 (3)	0.0513 (15)
H26	0.2207	0.8449	0.1791	0.062*
C27	0.2258 (4)	0.7544 (4)	0.2697 (3)	0.0494 (14)
H27	0.1765	0.7792	0.2803	0.059*
C28	0.2718 (4)	0.6794 (4)	0.3158 (3)	0.0441 (13)
H28	0.2539	0.6544	0.3583	0.053*
C29	0.3432 (3)	0.6403 (4)	0.3006 (3)	0.0364 (12)
C30	0.3493 (5)	0.7989 (5)	0.1233 (4)	0.0573 (17)
H30	0.3957	0.7570	0.1157	0.069*
C31	0.3868 (5)	0.9010 (5)	0.1449 (4)	0.0611 (17)
H31A	0.3427	0.9442	0.1524	0.092*
H31B	0.4072	0.9257	0.1019	0.092*
H31C	0.4343	0.8980	0.1940	0.092*
C32	0.2768 (5)	0.7982 (5)	0.0457 (3)	0.066 (2)
H32A	0.2536	0.7326	0.0351	0.099*
H32B	0.2984	0.8189	0.0022	0.099*
H32C	0.2319	0.8425	0.0498	0.099*
C33	0.3961 (4)	0.5624 (4)	0.3524 (3)	0.0400 (12)
H33	0.4218	0.5225	0.3183	0.048*

C34	0.4696 (4)	0.6077 (4)	0.4183 (3)	0.0472 (14)
H34A	0.5019	0.6516	0.3946	0.071*
H34B	0.5072	0.5564	0.4474	0.071*
H34C	0.4464	0.6438	0.4549	0.071*
C35	0.3443 (4)	0.4948 (4)	0.3883 (3)	0.0464 (14)
H35A	0.3172	0.5322	0.4212	0.070*
H35B	0.3820	0.4461	0.4211	0.070*
H35C	0.3004	0.4627	0.3457	0.070*
C36	0.3486 (3)	0.3960 (4)	0.1830 (3)	0.0405 (13)
C37	0.2622 (4)	0.5216 (4)	0.0983 (3)	0.0375 (12)
N1	0.2638 (3)	0.3147 (3)	-0.0240 (2)	0.0340 (9)
N2	0.3982 (3)	0.3306 (3)	-0.0026 (2)	0.0347 (10)
N3	0.4728 (3)	0.4403 (3)	0.0838 (2)	0.0337 (9)
N4	0.5238 (3)	0.5630 (3)	0.1687 (2)	0.0357 (10)
N5	0.4395 (3)	0.6419 (3)	0.2199 (2)	0.0355 (10)
O1	0.3371 (3)	0.3487 (3)	0.2338 (2)	0.0433 (9)
O2	0.1990 (2)	0.5557 (3)	0.0968 (2)	0.0428 (9)
Mn1	0.36377 (5)	0.46655 (6)	0.10522 (5)	0.0329 (2)

Structure: (4-Me₂N-ⁱPrPDI)Co(N₂)

ID: jmd33

Crystallographer: Zoë Turner

Table C.40. Crystal data

C ₃₅ H ₄₈ CoN ₆	Z = 4
$M_r = 611.72$	$F(000) = 1308$
Triclinic, $P\bar{1}$	$D_x = 1.213 \text{ Mg m}^{-3}$
Hall symbol: -P 1	Mo $K\alpha$ radiation, $\lambda = 0.71073 \text{ \AA}$
$a = 8.6211 (2) \text{ \AA}$	Cell parameters from 9759 reflections
$b = 12.3344 (3) \text{ \AA}$	$\theta = 3.9\text{--}65.6^\circ$
$c = 32.3803 (8) \text{ \AA}$	$\mu = 0.54 \text{ mm}^{-1}$
$\alpha = 91.511 (2)^\circ$	$T = 100 \text{ K}$
$\beta = 95.534 (2)^\circ$	Plate, green
$\gamma = 101.867 (2)^\circ$	$0.17 \times 0.08 \times 0.05 \text{ mm}$
$V = 3350.13 (14) \text{ \AA}^3$	

Table C.41. Data collection

Bruker APEX-II CCD diffractometer	11159 independent reflections
Radiation source: fine-focus sealed tube	9419 reflections with $I > 2\sigma(I)$
graphite	$R_{\text{int}} = 0.044$
phi and ω scans	$\theta_{\text{max}} = 24.9^\circ$, $\theta_{\text{min}} = 1.8^\circ$
Absorption correction: multi-scan SADABS 2008/2	$h = -10 \rightarrow 9$
$T_{\text{min}} = 0.913$, $T_{\text{max}} = 0.973$	$k = -14 \rightarrow 14$
47964 measured reflections	$l = -33 \rightarrow 36$

Table C.42. Refinement

Refinement on F^2	Primary atom site location: structure-invariant direct methods
Least-squares matrix: full	Secondary atom site location: difference Fourier map
$R[F^2 > 2\sigma(F^2)] = 0.065$	Hydrogen site location: inferred from neighbouring sites
$wR(F^2) = 0.175$	H-atom parameters constrained
$S = 1.24$	$w = 1/[\sigma^2(F_o^2) + (0.0623P)^2 + 6.567P]$ where $P = (F_o^2 + 2F_c^2)/3$
11159 reflections	$(\Delta/\sigma)_{\text{max}} = 0.047$
757 parameters	$\Delta)_{\text{max}} = 1.32 \text{ e \AA}^{-3}$
28 restraints	$\Delta)_{\text{min}} = -1.02 \text{ e \AA}^{-3}$

Special details

Experimental. Collected, solved and refined by Dr. Zoe R. Turner

Geometry. All s.u.'s (except the s.u. in the dihedral angle between two l.s. planes) are estimated using the full covariance matrix. The cell s.u.'s are taken into account individually in the estimation of

s.u.'s in distances, angles and torsion angles; correlations between s.u.'s in cell parameters are only used when they are defined by crystal symmetry. An approximate (isotropic) treatment of cell s.u.'s is used for estimating s.u.'s involving l.s. planes.

Refinement. Refinement of F^2 against ALL reflections. The weighted R-factor wR and goodness of fit S are based on F^2 , conventional R-factors R are based on F , with F set to zero for negative F^2 . The threshold expression of $F^2 > 2\sigma(F^2)$ is used only for calculating R-factors(gt) etc. and is not relevant to the choice of reflections for refinement. R-factors based on F^2 are statistically about twice as large as those based on F , and R- factors based on ALL data will be even larger.

Fractional atomic coordinates and isotropic or equivalent isotropic displacement parameters (\AA^2)

	x	y	z	$U_{\text{iso}}^*/U_{\text{eq}}$
C1	0.2329 (5)	0.6494 (3)	0.15037 (14)	0.0350 (10)
H1A	0.1269	0.6019	0.1508	0.052*
H1B	0.3018	0.6374	0.1750	0.052*
H1C	0.2791	0.6310	0.1253	0.052*
C2	0.2192 (4)	0.7673 (3)	0.15051 (11)	0.0219 (8)
C3	0.3038 (4)	0.8504 (3)	0.18143 (11)	0.0202 (7)
C4	0.4075 (4)	0.8395 (3)	0.21579 (11)	0.0206 (8)
H4	0.4339	0.7697	0.2210	0.025*
C5	0.4740 (4)	0.9323 (3)	0.24298 (11)	0.0202 (7)
C6	0.4259 (4)	1.0328 (3)	0.23526 (11)	0.0209 (8)
H6	0.4636	1.0953	0.2540	0.025*
C7	0.3230 (4)	1.0405 (3)	0.20011 (11)	0.0200 (7)
C8	0.2615 (4)	1.1343 (3)	0.18535 (11)	0.0211 (8)
C9	0.3050 (5)	1.2457 (3)	0.20689 (13)	0.0308 (9)
H9A	0.3767	1.2960	0.1908	0.046*
H9B	0.3586	1.2401	0.2346	0.046*
H9C	0.2083	1.2745	0.2095	0.046*
C10	0.0327 (4)	0.7359 (3)	0.08988 (11)	0.0208 (8)
C11	0.0972 (5)	0.7153 (3)	0.05295 (12)	0.0281 (9)
C12	0.0004 (5)	0.6458 (4)	0.02240 (13)	0.0341 (10)
H12	0.0423	0.6313	-0.0028	0.041*
C13	-0.1555 (5)	0.5969 (3)	0.02739 (13)	0.0333 (10)
H13	-0.2192	0.5487	0.0061	0.040*
C14	-0.2179 (5)	0.6189 (3)	0.06374 (13)	0.0299 (9)
H14	-0.3255	0.5864	0.0671	0.036*
C15	-0.1255 (5)	0.6878 (3)	0.09539 (12)	0.0280 (9)
C16	0.2670 (5)	0.7706 (4)	0.04555 (15)	0.0432 (8)
H16	0.3234	0.8065	0.0724	0.052*
C17	0.3608 (7)	0.6877 (5)	0.0302 (2)	0.0660 (8)
H17A	0.3544	0.6262	0.0489	0.099*
H17B	0.4726	0.7248	0.0296	0.099*
H17C	0.3156	0.6590	0.0021	0.099*
C18	0.2632 (8)	0.8613 (5)	0.0140 (2)	0.0660 (8)
H18A	0.2111	0.8273	-0.0129	0.099*

H18B	0.3724	0.8997	0.0107	0.099*
H18C	0.2037	0.9146	0.0239	0.099*
C19	-0.1969 (5)	0.7097 (4)	0.13506 (14)	0.0432 (8)
H19	-0.1144	0.7653	0.1526	0.052*
C20	-0.2348 (8)	0.6107 (5)	0.1594 (2)	0.0660 (8)
H20A	-0.3093	0.5519	0.1425	0.099*
H20B	-0.2835	0.6290	0.1841	0.099*
H20C	-0.1367	0.5851	0.1680	0.099*
C21	-0.3403 (7)	0.7609 (5)	0.1266 (2)	0.0660 (8)
H21A	-0.4253	0.7081	0.1100	0.099*
H21B	-0.3112	0.8284	0.1113	0.099*
H21C	-0.3778	0.7796	0.1530	0.099*
C22	0.0993 (4)	1.1988 (3)	0.13132 (11)	0.0229 (8)
C23	0.1869 (5)	1.2652 (3)	0.10359 (12)	0.0295 (9)
C24	0.1264 (5)	1.3528 (3)	0.08729 (13)	0.0337 (10)
H24	0.1839	1.3984	0.0683	0.040*
C25	-0.0149 (5)	1.3750 (3)	0.09797 (13)	0.0329 (10)
H25	-0.0531	1.4362	0.0868	0.040*
C26	-0.0999 (5)	1.3091 (4)	0.12465 (14)	0.0350 (10)
H26	-0.1984	1.3242	0.1314	0.042*
C27	-0.0456 (5)	1.2196 (3)	0.14229 (12)	0.0284 (9)
C28	0.3399 (6)	1.2400 (5)	0.08970 (17)	0.0529 (13)
H28	0.3794	1.1894	0.1099	0.063*
C29	0.4704 (6)	1.3426 (6)	0.0886 (2)	0.0726 (18)
H29A	0.4380	1.3908	0.0673	0.109*
H29B	0.5687	1.3208	0.0820	0.109*
H29C	0.4892	1.3826	0.1158	0.109*
C30	0.3080 (8)	1.1800 (5)	0.0468 (2)	0.078 (2)
H30A	0.2268	1.1118	0.0476	0.118*
H30B	0.4067	1.1614	0.0389	0.118*
H30C	0.2700	1.2283	0.0264	0.118*
C31	-0.1444 (5)	1.1483 (4)	0.17145 (15)	0.0391 (11)
H31	-0.0809	1.0946	0.1829	0.047*
C32	-0.1820 (6)	1.2147 (5)	0.20798 (15)	0.0476 (12)
H32A	-0.0826	1.2571	0.2228	0.071*
H32B	-0.2391	1.1641	0.2269	0.071*
H32C	-0.2487	1.2659	0.1978	0.071*
C33	-0.2993 (6)	1.0807 (4)	0.14804 (18)	0.0536 (14)
H33A	-0.3668	1.1311	0.1377	0.080*
H33B	-0.3561	1.0297	0.1669	0.080*
H33C	-0.2736	1.0382	0.1246	0.080*
C34	0.6086 (4)	0.8168 (3)	0.28889 (12)	0.0261 (8)
H34A	0.5124	0.7791	0.3006	0.039*
H34B	0.7003	0.8259	0.3100	0.039*
H34C	0.6269	0.7725	0.2650	0.039*
C35	0.6277 (5)	1.0119 (3)	0.30818 (12)	0.0277 (9)
H35A	0.6556	1.0840	0.2958	0.042*
H35B	0.7184	1.0000	0.3269	0.042*
H35C	0.5357	1.0104	0.3239	0.042*

N1	0.1270 (3)	0.8100 (3)	0.12198 (9)	0.0218 (7)
N2	0.2659 (3)	0.9506 (2)	0.17356 (9)	0.0189 (6)
N3	0.1627 (3)	1.1093 (3)	0.14991 (9)	0.0205 (6)
N4	-0.0135 (4)	0.9706 (3)	0.08450 (10)	0.0257 (7)
N5	-0.1011 (5)	0.9740 (3)	0.05746 (12)	0.0406 (9)
N6	0.5883 (3)	0.9251 (3)	0.27567 (9)	0.0217 (7)
Co1	0.12597 (6)	0.96183 (5)	0.128619 (17)	0.03041 (17)
C1A	0.1180 (5)	0.5017 (3)	0.26662 (13)	0.0299 (9)
H1A1	0.1983	0.4703	0.2537	0.045*
H1A2	0.0666	0.5442	0.2463	0.045*
H1A3	0.0377	0.4416	0.2759	0.045*
C2A	0.1961 (4)	0.5761 (3)	0.30288 (11)	0.0213 (8)
C3A	0.1788 (4)	0.6887 (3)	0.30848 (11)	0.0183 (7)
C4A	0.0949 (4)	0.7504 (3)	0.28320 (11)	0.0203 (7)
H4A	0.0368	0.7181	0.2579	0.024*
C5A	0.0961 (4)	0.8612 (3)	0.29515 (11)	0.0194 (7)
C6A	0.1897 (4)	0.9080 (3)	0.33198 (11)	0.0186 (7)
H6A	0.1968	0.9837	0.3399	0.022*
C7A	0.2718 (4)	0.8430 (3)	0.35674 (11)	0.0185 (7)
C8A	0.3721 (4)	0.8714 (3)	0.39529 (11)	0.0211 (8)
C9A	0.4042 (5)	0.9829 (3)	0.41685 (12)	0.0271 (8)
H9A1	0.4002	0.9746	0.4468	0.041*
H9A2	0.3235	1.0236	0.4063	0.041*
H9A3	0.5101	1.0239	0.4117	0.041*
C10A	0.3192 (4)	0.4360 (3)	0.33464 (11)	0.0214 (8)
C11A	0.2131 (4)	0.3508 (3)	0.35191 (12)	0.0231 (8)
C12A	0.2549 (5)	0.2481 (3)	0.35544 (12)	0.0272 (8)
H12A	0.1866	0.1901	0.3677	0.033*
C13A	0.3944 (5)	0.2286 (3)	0.34136 (13)	0.0296 (9)
H13A	0.4202	0.1576	0.3437	0.036*
C14A	0.4951 (5)	0.3125 (3)	0.32402 (13)	0.0295 (9)
H14A	0.5895	0.2983	0.3141	0.035*
C15A	0.4614 (4)	0.4179 (3)	0.32075 (12)	0.0255 (8)
C16A	0.0600 (5)	0.3719 (3)	0.36730 (13)	0.0283 (9)
H16A	0.0286	0.4330	0.3509	0.034*
C17A	-0.0776 (5)	0.2717 (4)	0.35993 (18)	0.0463 (12)
H17D	-0.0933	0.2481	0.3304	0.069*
H17E	-0.1751	0.2916	0.3681	0.069*
H17F	-0.0530	0.2109	0.3765	0.069*
C18A	0.0863 (6)	0.4121 (4)	0.41281 (15)	0.0478 (12)
H18D	0.1168	0.3539	0.4299	0.072*
H18E	-0.0124	0.4292	0.4213	0.072*
H18F	0.1713	0.4789	0.4165	0.072*
C19A	0.5795 (5)	0.5116 (3)	0.30400 (14)	0.0337 (10)
H19A	0.5499	0.5827	0.3123	0.040*
C20A	0.5693 (7)	0.5052 (5)	0.25772 (18)	0.0655 (17)
H20D	0.5995	0.4370	0.2484	0.098*
H20E	0.6419	0.5695	0.2482	0.098*
H20F	0.4599	0.5051	0.2462	0.098*

C21A	0.7493 (5)	0.5170 (4)	0.32297 (18)	0.0514 (13)
H21D	0.7875	0.4530	0.3125	0.077*
H21E	0.7519	0.5159	0.3533	0.077*
H21F	0.8181	0.5855	0.3153	0.077*
C22A	0.5332 (4)	0.8002 (3)	0.44824 (11)	0.0216 (8)
C23A	0.4653 (4)	0.7700 (3)	0.48488 (12)	0.0242 (8)
C24A	0.5655 (5)	0.7775 (3)	0.52175 (12)	0.0275 (9)
H24A	0.5216	0.7551	0.5467	0.033*
C25A	0.7286 (5)	0.8172 (3)	0.52246 (12)	0.0296 (9)
H25A	0.7954	0.8235	0.5479	0.036*
C26A	0.7930 (5)	0.8475 (3)	0.48612 (13)	0.0293 (9)
H26A	0.9045	0.8754	0.4869	0.035*
C27A	0.6990 (4)	0.8384 (3)	0.44822 (12)	0.0244 (8)
C28A	0.2868 (5)	0.7296 (4)	0.48566 (13)	0.0311 (9)
H28A	0.2350	0.7284	0.4566	0.037*
C29A	0.2189 (5)	0.8090 (4)	0.51251 (17)	0.0475 (12)
H29D	0.2715	0.8142	0.5409	0.071*
H29E	0.1041	0.7811	0.5129	0.071*
H29F	0.2376	0.8827	0.5009	0.071*
C30A	0.2459 (5)	0.6128 (4)	0.50112 (15)	0.0402 (11)
H30D	0.2976	0.5638	0.4854	0.060*
H30E	0.1302	0.5855	0.4972	0.060*
H30F	0.2837	0.6138	0.5307	0.060*
C31A	0.7771 (5)	0.8638 (4)	0.40843 (13)	0.0302 (9)
H31A	0.6907	0.8642	0.3855	0.036*
C32A	0.8898 (6)	0.9762 (4)	0.41098 (15)	0.0412 (11)
H32D	0.8330	1.0336	0.4186	0.062*
H32E	0.9299	0.9912	0.3839	0.062*
H32F	0.9795	0.9764	0.4320	0.062*
C33A	0.8646 (6)	0.7728 (4)	0.39738 (17)	0.0484 (13)
H33D	0.9519	0.7720	0.4190	0.073*
H33E	0.9078	0.7873	0.3707	0.073*
H33F	0.7901	0.7007	0.3953	0.073*
C34A	-0.0721 (4)	0.8815 (3)	0.23108 (11)	0.0244 (8)
H34D	0.0086	0.8822	0.2117	0.037*
H34E	-0.1449	0.9289	0.2212	0.037*
H34F	-0.1323	0.8055	0.2328	0.037*
C35A	0.0332 (5)	1.0414 (3)	0.28032 (12)	0.0271 (8)
H35D	0.0116	1.0564	0.3088	0.041*
H35E	-0.0376	1.0732	0.2609	0.041*
H35F	0.1443	1.0749	0.2770	0.041*
N1A	0.2884 (3)	0.5456 (2)	0.33463 (9)	0.0200 (6)
N2A	0.2634 (3)	0.7351 (2)	0.34500 (9)	0.0193 (6)
N3A	0.4331 (3)	0.7859 (2)	0.40950 (9)	0.0197 (6)
N4A	0.4859 (4)	0.5715 (3)	0.40844 (10)	0.0276 (7)
N5A	0.5539 (5)	0.5204 (3)	0.42732 (13)	0.0460 (10)
N6A	0.0056 (4)	0.9230 (3)	0.27186 (9)	0.0227 (7)
Co1A	0.37577 (6)	0.65296 (4)	0.377085 (17)	0.02820 (16)

Structure: (4-C(Ph)₂CH₃-C^{4-H}NC)Co(N₂)

ID: jmd34

Crystallographer: Scott Semproni

Table C.43. Crystal data

C ₅₃ H ₆₄ CoN ₇ O	Z = 2
M _r = 874.04	F(000) = 932
Triclinic, P $\bar{1}$	D _x = 1.233 Mg m ⁻³
a = 12.0909 (3) Å	Cu Kα radiation, λ = 1.54178 Å
b = 12.8468 (3) Å	Cell parameters from 9908 reflections
c = 16.0768 (4) Å	θ = 2.9–65.7°
α = 93.285 (2)°	μ = 3.21 mm ⁻¹
β = 108.604 (2)°	T = 100 K
γ = 93.618 (2)°	Prism, blue
V = 2354.06 (10) Å ³	0.12 × 0.06 × 0.06 mm

Table C.44. Data collection

Bruker APEX II CCD diffractometer	7638 independent reflections
Radiation source: fine-focus sealed tube graphite	6709 reflections with I > 2σ(I)
phi and ω scans	R _{int} = 0.037
Absorption correction: multi-scan SADABS V2008/1 (Bruker AXS)	θ _{max} = 66.1°, θ _{min} = 2.9°
T _{min} = 0.586, T _{max} = 0.753	h = -14→13
20551 measured reflections	k = -14→14
	l = -18→18

Table C.45. Refinement

Refinement on F ²	Primary atom site location: structure-invariant direct methods
Least-squares matrix: full	Secondary atom site location: difference Fourier map
R[F ² > 2σ(F ²)] = 0.038	Hydrogen site location: inferred from neighbouring sites
wR(F ²) = 0.096	H-atom parameters constrained
S = 1.03	w = 1/[σ ² (F _o ²) + (0.0507P) ² + 0.6501P] where P = (F _o ² + 2F _c ²)/3
7638 reflections	(Δ/σ) _{max} < 0.001
570 parameters	Δ _{max} = 0.31 e Å ⁻³
0 restraints	Δ _{min} = -0.28 e Å ⁻³

Special details

Experimental. Collected, solved and refined by Scott P. Semproni

Geometry. All s.u.'s (except the s.u. in the dihedral angle between two l.s. planes) are estimated using the full covariance matrix. The cell s.u.'s are taken into account individually in the estimation of

s.u.'s in distances, angles and torsion angles; correlations between s.u.'s in cell parameters are only used when they are defined by crystal symmetry. An approximate (isotropic) treatment of cell s.u.'s is used for estimating s.u.'s involving l.s. planes.

Refinement. Refinement of F^2 against ALL reflections. The weighted R-factor wR and goodness of fit S are based on F^2 , conventional R-factors R are based on F , with F set to zero for negative F^2 . The threshold expression of $F^2 > 2\sigma(F^2)$ is used only for calculating R-factors(gt) etc. and is not relevant to the choice of reflections for refinement. R-factors based on F^2 are statistically about twice as large as those based on F , and R-factors based on ALL data will be even larger.

Table C.46. Fractional atomic coordinates and isotropic or equivalent isotropic displacement parameters (\AA^2)

	x	y	z	$U_{\text{iso}}^*/U_{\text{eq}}$
C1	0.09716 (17)	0.14490 (15)	0.07130 (12)	0.0238 (4)
H1	0.0197	0.1592	0.0390	0.029*
C1S	0.1158 (2)	0.8499 (2)	0.16850 (17)	0.0472 (6)
H1S1	0.0397	0.8709	0.1329	0.071*
H1S2	0.1575	0.8232	0.1296	0.071*
H1S3	0.1622	0.9105	0.2061	0.071*
C2	0.16271 (17)	0.07717 (16)	0.04543 (12)	0.0234 (4)
H2	0.1404	0.0344	-0.0084	0.028*
C2S	0.0975 (2)	0.7657 (2)	0.22505 (18)	0.0500 (7)
H2S1	0.0546	0.7027	0.1875	0.060*
H2S2	0.1741	0.7462	0.2632	0.060*
C3	0.37107 (16)	0.02855 (15)	0.12356 (11)	0.0199 (4)
C3S	0.0048 (3)	0.7275 (2)	0.32972 (18)	0.0643 (9)
H3S1	0.0771	0.7108	0.3752	0.077*
H3S2	-0.0318	0.6625	0.2923	0.077*
C4	0.39126 (17)	-0.04011 (15)	0.06583 (12)	0.0220 (4)
H4	0.3338	-0.0559	0.0095	0.026*
C4S	-0.0786 (3)	0.7706 (3)	0.3727 (2)	0.0776 (10)
H4S1	-0.0433	0.8368	0.4070	0.116*
H4S2	-0.0949	0.7203	0.4118	0.116*
H4S3	-0.1519	0.7827	0.3272	0.116*
C5	0.50397 (16)	-0.09340 (15)	0.08831 (12)	0.0207 (4)
H5	0.5412	-0.0781	0.0425	0.025*
C6	0.58877 (17)	-0.04716 (15)	0.17699 (12)	0.0219 (4)
H6	0.6659	-0.0689	0.1974	0.026*
C7	0.55509 (16)	0.02360 (15)	0.22595 (11)	0.0201 (4)
C8	0.73885 (17)	0.06722 (16)	0.36072 (12)	0.0227 (4)
H8	0.7924	0.0223	0.3488	0.027*
C9	0.75902 (17)	0.13631 (16)	0.43163 (12)	0.0238 (4)
H9	0.8301	0.1491	0.4795	0.029*
C10	0.57125 (16)	0.14843 (15)	0.34546 (11)	0.0195 (4)
C11	0.27137 (16)	0.15236 (15)	0.18171 (11)	0.0201 (4)
C12	0.12896 (16)	0.26705 (16)	0.20762 (12)	0.0219 (4)

C13	0.08517 (17)	0.23125 (16)	0.27334 (12)	0.0243 (4)
C14	0.05833 (18)	0.30797 (17)	0.32715 (13)	0.0290 (5)
H14	0.0280	0.2874	0.3720	0.035*
C15	0.07479 (18)	0.41274 (17)	0.31681 (13)	0.0298 (5)
H15	0.0572	0.4633	0.3552	0.036*
C16	0.11681 (17)	0.44520 (16)	0.25103 (13)	0.0269 (4)
H16	0.1267	0.5178	0.2442	0.032*
C17	0.14486 (17)	0.37255 (16)	0.19457 (12)	0.0241 (4)
C18	0.06689 (19)	0.11557 (17)	0.28339 (13)	0.0301 (5)
H18	0.1265	0.0795	0.2640	0.036*
C19	0.0833 (2)	0.0907 (2)	0.37869 (15)	0.0419 (6)
H19A	0.1590	0.1235	0.4174	0.063*
H19B	0.0812	0.0147	0.3822	0.063*
H19C	0.0202	0.1180	0.3972	0.063*
C20	-0.0547 (2)	0.07007 (18)	0.22336 (14)	0.0353 (5)
H20A	-0.1151	0.1046	0.2404	0.053*
H20B	-0.0638	-0.0052	0.2293	0.053*
H20C	-0.0629	0.0818	0.1621	0.053*
C21	0.19305 (18)	0.40793 (16)	0.12330 (13)	0.0272 (5)
H21	0.1642	0.3539	0.0722	0.033*
C22	0.32746 (19)	0.41588 (18)	0.15412 (14)	0.0338 (5)
H22A	0.3583	0.4730	0.2006	0.051*
H22B	0.3548	0.4299	0.1043	0.051*
H22C	0.3551	0.3499	0.1771	0.051*
C23	0.1508 (2)	0.51262 (18)	0.09044 (15)	0.0387 (5)
H23A	0.0653	0.5096	0.0744	0.058*
H23B	0.1740	0.5266	0.0388	0.058*
H23C	0.1861	0.5687	0.1372	0.058*
C24	0.64437 (16)	0.26858 (15)	0.48196 (11)	0.0210 (4)
C25	0.59471 (17)	0.24265 (16)	0.54679 (12)	0.0232 (4)
C26	0.58612 (18)	0.32514 (17)	0.60456 (12)	0.0272 (5)
H26	0.5548	0.3106	0.6502	0.033*
C27	0.62190 (18)	0.42648 (16)	0.59678 (12)	0.0272 (5)
H27	0.6152	0.4810	0.6370	0.033*
C28	0.66769 (17)	0.44982 (16)	0.53070 (12)	0.0257 (4)
H28	0.6911	0.5205	0.5254	0.031*
C29	0.67994 (16)	0.37102 (15)	0.47181 (11)	0.0218 (4)
C30	0.55037 (18)	0.13213 (16)	0.55391 (12)	0.0276 (5)
H30	0.5411	0.0910	0.4970	0.033*
C31	0.6393 (2)	0.08128 (18)	0.62690 (14)	0.0356 (5)
H31A	0.7146	0.0836	0.6159	0.053*
H31B	0.6111	0.0083	0.6278	0.053*
H31C	0.6493	0.1193	0.6838	0.053*
C32	0.43036 (19)	0.12745 (18)	0.56719 (14)	0.0342 (5)
H32A	0.4388	0.1582	0.6263	0.051*
H32B	0.3982	0.0544	0.5606	0.051*
H32C	0.3773	0.1668	0.5231	0.051*
C33	0.72573 (17)	0.40003 (16)	0.39752 (12)	0.0248 (4)
H33	0.7316	0.3338	0.3640	0.030*

C34	0.8475 (2)	0.4582 (2)	0.43278 (15)	0.0391 (6)
H34A	0.8441	0.5235	0.4662	0.059*
H34B	0.8750	0.4742	0.3834	0.059*
H34C	0.9017	0.4142	0.4714	0.059*
C35	0.6400 (2)	0.46463 (19)	0.33430 (14)	0.0382 (5)
H35A	0.5630	0.4251	0.3113	0.057*
H35B	0.6686	0.4798	0.2853	0.057*
H35C	0.6333	0.5304	0.3656	0.057*
C36	0.47853 (17)	-0.21641 (15)	0.08359 (11)	0.0210 (4)
C37	0.42994 (18)	-0.24218 (16)	0.15823 (12)	0.0256 (4)
H37A	0.4008	-0.3162	0.1504	0.038*
H37B	0.3658	-0.1987	0.1568	0.038*
H37C	0.4924	-0.2281	0.2150	0.038*
C38	0.39072 (17)	-0.24976 (14)	-0.00858 (12)	0.0211 (4)
C39	0.42878 (18)	-0.24377 (15)	-0.08168 (12)	0.0238 (4)
H39	0.5085	-0.2220	-0.0731	0.029*
C40	0.35263 (18)	-0.26888 (16)	-0.16647 (12)	0.0267 (4)
H40	0.3804	-0.2643	-0.2153	0.032*
C41	0.23627 (19)	-0.30055 (16)	-0.18022 (13)	0.0298 (5)
H41	0.1839	-0.3179	-0.2382	0.036*
C42	0.19686 (19)	-0.30673 (16)	-0.10839 (14)	0.0306 (5)
H42	0.1170	-0.3283	-0.1173	0.037*
C43	0.27342 (17)	-0.28164 (15)	-0.02350 (13)	0.0249 (4)
H43	0.2453	-0.2863	0.0251	0.030*
C44	0.58703 (17)	-0.27610 (15)	0.09269 (11)	0.0213 (4)
C45	0.57886 (19)	-0.38406 (16)	0.09898 (13)	0.0283 (5)
H45	0.5064	-0.4179	0.0985	0.034*
C46	0.6721 (2)	-0.44351 (17)	0.10595 (13)	0.0322 (5)
H46	0.6635	-0.5168	0.1102	0.039*
C47	0.7790 (2)	-0.39535 (18)	0.10669 (13)	0.0323 (5)
H47	0.8445	-0.4350	0.1131	0.039*
C48	0.78839 (19)	-0.28960 (18)	0.09796 (13)	0.0311 (5)
H48	0.8605	-0.2566	0.0971	0.037*
C49	0.69386 (17)	-0.23029 (16)	0.09040 (12)	0.0251 (4)
H49	0.7020	-0.1575	0.0836	0.030*
N1	0.16445 (13)	0.19019 (12)	0.15457 (10)	0.0211 (4)
N2	0.26896 (13)	0.08212 (12)	0.11272 (9)	0.0198 (3)
N3	0.44786 (14)	0.06205 (13)	0.20550 (10)	0.0219 (4)
N4	0.62452 (13)	0.07511 (12)	0.30910 (9)	0.0199 (3)
N5	0.65691 (13)	0.18533 (12)	0.42186 (9)	0.0206 (3)
N6	0.38025 (14)	0.25660 (13)	0.34840 (10)	0.0240 (4)
N7	0.35808 (16)	0.31307 (15)	0.39445 (11)	0.0341 (4)
Co1	0.41394 (3)	0.16454 (2)	0.277604 (18)	0.01955 (10)
O1S	0.03203 (16)	0.80415 (13)	0.27760 (11)	0.0470 (4)



RightsLink®

[Home](#)[Create Account](#)[Help](#)

ACS Publications
High quality. High impact.

Title: Electronic Effects in 4-Substituted Bis(imino)pyridines and the Corresponding Reduced Iron Compounds

Author: Jonathan M. Darmon et al.

Publication: Organometallics

Publisher: American Chemical Society

Date: Mar 1, 2012

Copyright © 2012, American Chemical Society

User ID
<input type="text"/>
Password
<input type="text"/>
<input type="checkbox"/> Enable Auto Login
<input type="button" value="LOGIN"/>
Forgot Password/User ID?
If you're a copyright.com user , you can login to RightsLink using your copyright.com credentials. Already a RightsLink user or want to learn more?

PERMISSION/LICENSE IS GRANTED FOR YOUR ORDER AT NO CHARGE

This type of permission/license, instead of the standard Terms & Conditions, is sent to you because no fee is being charged for your order. Please note the following:

- Permission is granted for your request in both print and electronic formats.
- If figures and/or tables were requested, they may be adapted or used in part.
- Please print this page for your records and send a copy of it to your publisher/graduate school.
- Appropriate credit for the requested material should be given as follows: "Reprinted (adapted) with permission from (COMPLETE REFERENCE CITATION). Copyright (YEAR) American Chemical Society." Insert appropriate information in place of the capitalized words.
- One-time permission is granted only for the use specified in your request. No additional uses are granted (such as derivative works or other editions). For any other uses, please submit a new request.

[BACK](#)[CLOSE WINDOW](#)

Copyright © 2012 [Copyright Clearance Center, Inc.](#) All Rights Reserved. [Privacy statement.](#) Comments? We would like to hear from you. E-mail us at customercare@copyright.com



RightsLink[®]

[Home](#)[Create Account](#)[Help](#)

ACS Publications
High quality. High impact.

Title: Synthesis of Aryl-Substituted Bis(imino)pyridine Iron Dinitrogen Complexes
Author: Sarah K. Russell et al.
Publication: Inorganic Chemistry
Publisher: American Chemical Society
Date: Mar 1, 2010
Copyright © 2010, American Chemical Society

User ID
<input type="text"/>
Password
<input type="text"/>
<input type="checkbox"/> Enable Auto Login
<input type="button" value="LOGIN"/>
Forgot Password/User ID?
If you're a copyright.com user , you can login to Rightslink using your copyright.com credentials. Already a Rightslink user or want to learn more?

PERMISSION/LICENSE IS GRANTED FOR YOUR ORDER AT NO CHARGE

This type of permission/license, instead of the standard Terms & Conditions, is sent to you because no fee is being charged for your order. Please note the following:

- Permission is granted for your request in both print and electronic formats.
- If figures and/or tables were requested, they may be adapted or used in part.
- Please print this page for your records and send a copy of it to your publisher/graduate school.
- Appropriate credit for the requested material should be given as follows: "Reprinted (adapted) with permission from (COMPLETE REFERENCE CITATION). Copyright (YEAR) American Chemical Society." Insert appropriate information in place of the capitalized words.
- One-time permission is granted only for the use specified in your request. No additional uses are granted (such as derivative works or other editions). For any other uses, please submit a new request.

[BACK](#)[CLOSE WINDOW](#)

Copyright © 2012 [Copyright Clearance Center, Inc.](#) All Rights Reserved. [Privacy statement.](#) Comments? We would like to hear from you. E-mail us at customer care@copyright.com



RightsLink®

Home

Create Account

Help



ACS Publications
High quality. High impact.

Title: Enantiopure Pyridine Bis(oxazoline) "Pybox" and Bis(oxazoline) "Box" Iron Dialkyl Complexes: Comparison to Bis(imino)pyridine Compounds and Application to Catalytic Hydrosilylation of Ketones

Author: Aaron M. Tondreau et al.

Publication: Organometallics

Publisher: American Chemical Society

Date: Jul 1, 2009

Copyright © 2009, American Chemical Society

User ID
<input type="text"/>
Password
<input type="text"/>
<input type="checkbox"/> Enable Auto Login
<input type="button" value="LOGIN"/>
Forgot Password/User ID?
If you're a copyright.com user, you can login to Rightslink using your copyright.com credentials. Already a Rightslink user or want to learn more?

PERMISSION/LICENSE IS GRANTED FOR YOUR ORDER AT NO CHARGE

This type of permission/license, instead of the standard Terms & Conditions, is sent to you because no fee is being charged for your order. Please note the following:

- Permission is granted for your request in both print and electronic formats.
- If figures and/or tables were requested, they may be adapted or used in part.
- Please print this page for your records and send a copy of it to your publisher/graduate school.
- Appropriate credit for the requested material should be given as follows: "Reprinted (adapted) with permission from (COMPLETE REFERENCE CITATION). Copyright (YEAR) American Chemical Society." Insert appropriate information in place of the capitalized words.
- One-time permission is granted only for the use specified in your request. No additional uses are granted (such as derivative works or other editions). For any other uses, please submit a new request.

BACK

CLOSE WINDOW

Copyright © 2012 [Copyright Clearance Center, Inc.](#) All Rights Reserved. [Privacy statement.](#)
Comments? We would like to hear from you. E-mail us at customercare@copyright.com